

Developing Nuclear Magnetic Resonance Spectroscopy and Mass Spectrometry Methods to Identify Biomarkers and Mechanisms in Neurological Disease

Tereza Kacerova

Somerville College, University of Oxford

Trinity Term 2025

A thesis submitted to the Board of the Faculty of Mathematical, Physical & Life Sciences in partial fulfilment of the requirements for the degree of Doctor of Philosophy at the University of Oxford

Abstract

Neurological diseases represent a growing global health burden, yet early diagnosis and effective management remain limited by overlapping clinical features, incomplete understanding of pathophysiology, and a lack of scalable, minimally invasive biomarkers. While magnetic resonance imaging (MRI), positron emission tomography (PET), and cerebrospinal fluid (CSF) analysis are standard clinical tools, they are costly, invasive, and often insufficiently sensitive to detect early molecular changes or subtle disease progression. Their limited repeatability also constrains use in routine longitudinal monitoring. In contrast, metabolomics offers a non-invasive, high-throughput approach to profile routinely sampled biofluids such as blood or urine. Reflecting interactions between genetic, environmental, and disease-related factors, the metabolome provides a near-instantaneous snapshot of physiological and pathological states, supporting early diagnosis, patient stratification, and therapeutic decision-making.

This thesis addresses key limitations in current neurological diagnostics by developing and applying integrated metabolomics and multi-omics workflows aimed at biomarker discovery, disease classification, and treatment monitoring. The approach combines nuclear magnetic resonance (NMR) spectroscopy with mass spectrometry coupled to diverse liquid chromatography (multi-LC-MS) systems to enable high-resolution metabolic profiling of peripheral blood samples. The metabolomics foundation is further strengthened through the integration of additional omics layers, including targeted proteomics, glycomics, and neuroimaging data. Multivariate statistical modelling and machine learning (ML) were applied to refine classification accuracy, identify predictive biomarker signatures, and improve biological interpretability. The workflow was implemented across three exemplar conditions - multiple sclerosis, neuromyelitis optica spectrum disorders (NMOSDs), and mild cognitive impairment (MCI) - to establish a translational framework for precision medicine in neurology.

Initially, the project focused on developing a robust sample preparation protocol enabling sequential NMR and multi-LC-MS profiling from a single clinical serum aliquot. By facilitating complementary metabolite coverage while preserving sample integrity, the workflow provides an efficient solution for volume-constrained studies. Analytical reproducibility was further enhanced by optimising serum protein depletion strategies, particularly through formic acid pre-treatment, which improved metabolite detection and classification accuracy in LC-MS datasets. These technical advancements were then applied across a series of clinical studies. In multiple sclerosis, NMR-based metabolomics combined with serum glial fibrillary acidic protein (sGFAP) and neurofilament light chain (sNfL) enabled accurate prediction of disease progression, with performance validated in two independent cohorts. In parallel, targeted LC-MS glycomics demonstrated that plasma *N*-glycan signatures can distinguish multiple sclerosis from other NMOSDs and differentiate between disease-specific phenotypes. Finally, untargeted multi-omics profiling was applied to the VITACOG trial, a randomised controlled study investigating B vitamin supplementation as a treatment strategy for MCI. This study assessed the potential of the developed metabolomics workflow to monitor therapeutic response and revealed supplementation-associated metabolic shifts that may contribute to the observed neuroprotective effects.

These studies demonstrate that integrated, multiplatform workflows can address major challenges in biofluid-based biomarker discovery, offering a reproducible and scalable strategy for capturing disease-associated metabolic changes. The validated multi-omics pipeline is applicable across diverse neurological conditions, as demonstrated in three representative case studies. Crucially, the synergy between platforms revealed molecular features inaccessible to individual methods, enabling early disease detection, progression prediction, and treatment monitoring. By bridging methodological development with translational application, this thesis offers a practical framework for integrating multi-omics biomarkers into neurology and advancing personalised healthcare.

Declaration

I, Tereza Kacerova, declare that the thesis I am submitting is entirely my own work, except where otherwise indicated in the text, captions, footnotes, or bibliography. This thesis has not been submitted, in whole or in part, for any other academic degree or professional qualification.

01/07/2025



Signature

Date

Acknowledgments

First of all, I would like to thank Dr Fay Probert for giving me the chance to join her group, for supporting me through funding, and especially for letting me work on such a wide range of exciting and diverse projects. I really appreciated your input on data analysis which encouraged me to view data from new and creative perspectives. I'm really sorry that you weren't able to see me submit this thesis, but I truly hope you're off to great new things. I'll always be proud to say I was your first primary DPhil student. You taught me so much, and your approach really helped me grow into an independent scientist.

I would also like to thank Professor James McCullagh. When I first arrived in Oxford, I didn't expect to find myself moving from NMR back to mass spec - but looking back, I'm so glad I did. Thank you for welcoming me into your group and for letting me analyse an insane number of samples across so many platforms! The formic acid project, with all its troubleshooting, is something I'll never forget - it taught me patience and gave me a deep appreciation for the complexity, rigour, and creativity that underpins good analytical chemistry. It's been an incredible learning experience, and I really hope that wherever my future career takes me, I'll always stay connected to both NMR and mass spec.

Many thanks to Professor Daniel Anthony - despite me "being a chemist", you never gave up on me and were always encouraging throughout my DPhil journey. I'll never forget the day I came to your office with the draft of the Extreme Phenotypes manuscript, feeling rather down about my DPhil - your guidance and perspective were genuinely game-changing. The wine and cheese evenings in Pharmacology were also a much-needed break from the long days (and nights) in the basement. I'm really grateful that you introduced me to so many fantastic collaborations around the world and gave me the trust to work independently on several projects. Although it hasn't been that long, it certainly feels like a journey - and I'm so glad it's not over yet. I'm genuinely excited about the projects ahead of us... let's see what happens with multinuclear NMR!

Speaking of collaborations, I'd like to thank Professor Jens Kuhle and Professor David Leppert in Basel for introducing me to the world of GFAP and NfL; Professor Tianrong Yeo in Singapore for all his clinical insights into multiple sclerosis; and Professor David Smith for allowing me to work on the OPTIMA and VITACOG studies, and for always showing such genuine enthusiasm for our results - I really admire your dedication. I'm also very grateful to Professor Helga Refsum and Dr Thomas Olsen in Oslo for arranging the proteomics studies in VITACOG; to Professor Fredrik Jernerén in Uppsala for introducing me to tau proteins; and to Professor Alex Dickens in Turku for letting us perform LC-MS experiments in his lab - while some may complain about the cold, I had a great time in Finland! Many thanks to everyone at Ludger Ltd for their advice on glycans. I'm also grateful to the whole team at Numares - it was always a pleasure to visit Regensburg for NMR experiments. Thank you to Numares and EPSRC for funding my DPhil. And going even further back, a sincere thanks to the Bakala Foundation for supporting my undergraduate studies - your support helped shape the path that led me here.

A huge thank you to Elisabete Pires - you are truly the Queen of Mass Spec! I can't put into words how grateful I am that you took on a first-year DPhil student and, even on weekends, patiently taught me all the LC-MS and SFC-MS tricks. I've learnt so much from you - especially through all those attempts to calibrate the various Xevos (each with their own issues!). I'll also never forget our lunch breaks, your constant support, and your incredible friendship. You've been such an important part of this journey.

Many thanks to Dr Coral Mycroft - always helpful with NMR, no matter the day or hour, and always up for a chat about NMR, PhDs, and life in general.

Huge thanks as well to Victor, Izzy, Ross, and Dan - you were always so supportive and willing to help. Victor and Dan were my go-to coding experts, Ross was always calm and reassuring, and Izzy was always up for a run - any time of day!

Thanks to everyone in my office - especially Rachel and John - for always being up for a chat about IC problems. I've learnt so much from you both! Also, big thanks to the rest of the mass spec crew, especially Victor and Luciana, for all your help and good company.

I'm also very grateful to the Part II students I had the privilege to supervise in Fay's group - Charlotte, Marisa, Katie, and Jiayi. Each of you was so talented, curious, and enthusiastic, and I genuinely learnt a lot from working with you. Thank you for being such brilliant students!

Many thanks to the CRL management team - Billy, Allan, and Domingo - for fixing whatever needed fixing in the lab and always greeting us with a smile in the corridor. These little things really can brighten a day in the basement. Thanks also to Debbie, our CRL safety officer - I might not have always worn a lab coat when sprinting between the mass spec room and the wet lab, but you were always firm yet compassionate, and I really appreciated that!

A big thank you to my friends Sam and Carolina! Sam - our 11pm chats by the 600 MHz about absolutely everything will always stay with me. And Carolina - you're simply an amazing person, always encouraging and full of positivity. I can't wait to see you back in Oxford (or else I'll just have to come on another holiday to Portugal!).

Listi and Shoba - we met on our very first day as Oxford DPhils, and this friendship has lasted through these long and often difficult three years. Love you both, and I know we'll stay in touch.

And finally, many thanks to Ali, Charlie, and everyone in the Catalyst Running Club. Ali's Saturday runs were *supposed* to be 16 km, but somehow always turned into 28 km thanks to "poor GPS signal" - no complaints from me! I think those runs helped me realise that research really is a lot like a marathon.

I'd also like to thank my undergraduate friends George and Joseph - the London trio may have taken different PhD paths, but we've stayed in touch and encouraged each other just like before. You're both brilliant chemists, and I'm proud to call you my friends.

Samanta - even though you went back to Prague for your PhD, nothing has really changed. It's been great having someone I could message anytime, no matter what was going on.

And thank you to my high school teacher, Klára, for always keeping me supplied with book recommendations (I promise I'll catch up eventually!) and for listening to all my DPhil stories over the years.

I can't put into words how thankful I am to my family - and I'm sorry if I haven't called or visited as much as I should have over the past three years. Special thanks to my grandparents in Pilsen, grandma Hana and grandpa Milan, for always supporting me and believing in me.

I would like to dedicate this thesis to my grandma Věra, a loving grandmother, and to my grandpa Petr, an exceptional surgeon and a true inspiration in his dedication to work. You both passed away last year - but I know you know that I finished writing.

Finally, huge thanks to my parents. Dad - we may argue about science now and then, but you've always been the model of what a Professor should be. Thank you for teaching me that if you cheat at work, you're only cheating yourself. And Mum - thank you for all your love and constant support. You're the best mum and the best friend. Love you both!

List of Publications

This integrated thesis is based on the following five manuscripts, with my contributions detailed in the Statement of Authorship at the beginning of each chapter.

Kacerova, T., Pires, E., Walsby-Tickle, J., Probert, F. & McCullagh, J.: **Integrating NMR and multi-LC-MS-based untargeted metabolomics for comprehensive analysis of blood serum samples.** *Anal Chim Acta* **1356**, 343979 (2025)

Kacerova, T., Pires, E., Dixon, A., Williams, R., Legge, I., Hippisley, M., Yates, A. G., Smith, A. D., Anthony, D. C., Probert, F. & McCullagh, J.: **Refining Precision: Formic Acid Treatment Enhances Reproducibility in Untargeted Serum and Plasma Metabolomics**. Manuscript submitted (20/06/2025) to: *Analytical Chemistry*.

Kacerova, T., Willemse, E., Oechtering, J., Radford-Smith, D.E., Xiong, W., Maleska Maceski, A., Yeo, T., De Luca, G., Palace, J., Leppert, D., Kuhle, J., Anthony, D. C., Probert. F.: **Serum GFAP and NfL Augment a Metabolomics-Driven Strategy for Long-Term Prediction of Multiple Sclerosis Progression**. Manuscript submitted (06/03/2025) to: *Communications Medicine* – under review.

Kacerova, T., Sealey, M., Saldana, L., Xiong, W., Woodhall, M., Waters, P., Sénard, T., Cheeseman, J., Urbanowicz, P., Elgood Hunt, G., Spencer, D.I.R., McCullagh, J.S.O., Leite, M.I., DeLuca, G., Palace, J., Anthony, D.C., Yeo, T., Probert, F.: **Plasma N-Glycan Profiling Enhances Diagnostic Precision in Multiple Sclerosis, AQP4-Ab NMOSD, and MOGAD.** Manuscript submitted (17/03/2025) to: *Neurology: Neuroimmunology and Neuroinflammation*) – revised manuscript submitted.

Kacerova, T., Yates, A.G., Dai, J., Shepherd, D., Pires, E., de Jel, S., Gong, Q., Schiffer, E., Jernerén, F., Olsen, T., De Jager Loots, C.A., Refsum, H., Smith, A.D., McCullagh, J.S.O., Anthony, D.C., Probert, F.: **Role of B vitamins in modulating homocysteine and metabolic pathways linked to brain atrophy: metabolomics insights from the VITACOG trial**. Manuscript accepted (26/06/2025) by: *Alzheimer's & Dementia*).

Two additional co-authored publications are indirectly related to the research presented in this thesis:

Radford-Smith, D., Yates, A., **Kacerova, T.**, Nylund, M., Sucksdorff, M., Matilainen, M., Willimse, E., Oechtering, J., Maleska Maceski, A., Leppert, D., Kuhle, J., Probert, F., Anthony, D.C., Airas, L.: **Integrated Serum Metabolomics and TSPO-PET Imaging for Predicting Disease Progression in Multiple Sclerosis**. *BMJ Neurology Open* **7**, e001026 (2025).

Williams, R., Walsby-Tickle, J., Hvinden, I., Legge, I., **Kacerova, T.,** Lee, K., Misheva, M., Haughton, D., Ngere, J., Sidda, J., Pires, E., Cadoux-Hudson, T., McCullagh, J.S.O.: **Metabolomics Using Anion-Exchange Chromatography Mass Spectrometry for the Analysis of Cells, Tissues and Biofluids**. Manuscript submitted to: *Nature Protocols* – accepted (29/05/2025).

List of Abbreviations

- **4,4-DSS** – 4,4-dimethyl-4-silapentane-1-sulfonic acid
- **A** – Antenna (branching pattern in glycan structures)
- **AD** – Alzheimer's disease
- **AEC** – Anion-exchange chromatography
- **AI** – Artificial intelligence
- **ANCOVA** – Analysis of covariance
- **ANOVA** – Analysis of variance
- **APCI** – Atmospheric pressure chemical ionisation
- **AQP4-Ab** – Aquaporin-4 antibody
- **AUC** – Area under the curve
- **ApoE** – Apolipoprotein E
- **$A\beta_{42}/A\beta_{40}$** – Amyloid-beta 42/40 ratio
- **B** – Bisecting N-acetylglucosamine
- **B cell** – B lymphocyte
- **BEH** – Bridged ethylene hybrid
- ***B_0*** – Main external magnetic field (in NMR)
- ***B_1*** – Oscillating magnetic field from radiofrequency pulse
- **C18** – Octadecylsilane
- **CE** – Capillary electrophoresis
- **CHI3L1** – Chitinase-3-like protein 1
- **CID** – Collision-induced dissociation
- **CIS** – Clinically isolated syndrome
- **CNS** – Central nervous system
- **CPMG** – Carr–Purcell–Meiboom–Gill (pulse sequence)
- **CRM** – Charge residue model
- **CSF** – Cerebrospinal fluid
- **CV** – Coefficient of variation
- **CXCL13** – Chemokine ligand 13
- **DANTE** – Delays Alternating with Nutations for Tailored Excitation
- **DART** – Direct analysis in real time
- **DC** – Direct current
- **DESI** – Desorption electrospray ionisation
- **DI-MS** – Direct infusion mass spectrometry
- **DSS** – 4,4-dimethyl-4-silapentane-1-sulfonic acid
- **EDSS** – Expanded Disability Status Scale
- **eGFR** – estimated glomerular filtration rate
- **EI** – Electron ionisation
- **ESI** – Electrospray ionisation
- ***E_k*** – Kinetic energy
- **F** – Fucose
- **FDR** – False discovery rate
- **FID** – Free induction decay
- **FLAIR** – Fluid-attenuated inversion recovery
- **FTD** – Frontotemporal dementia
- **G** – Galactose
- **GC-MS** – Gas chromatography–mass spectrometry

- **GFAP** – Glial fibrillary acidic protein
- **GlcNAc** – N-acetylglucosamine
- **HDL** – High-density lipoprotein
- **HILIC** – Hydrophilic interaction liquid chromatography
- **HRMS** – High-resolution mass spectrometry
- **Hcy** – Homocysteine
- **IC** – Ion chromatography
- **IEM** – Ion evaporation model
- **IQR** – Interquartile range
- **IR** – Infrared (spectroscopy)
- **JRES -** J-resolved spectroscopy
- **KNN** – k-nearest neighbours (imputation)
- **LASSO** – Least absolute shrinkage and selection operator
- **LBD** – Lewy body dementia
- **LC** – Liquid chromatography
- **LC-MS** – Liquid chromatography–mass spectrometry
- **LDL** – Low-density lipoprotein
- **LOESS** – Locally Estimated Scatterplot Smoothing
- **LRMS** – Low-resolution mass spectrometry
- **M** – Core mannose
- **MALDI** – Matrix-assisted laser desorption/ionisation
- **MALDI-MSI** – Matrix-assisted laser desorption/ionisation mass spectrometry imaging
- **MCI** – Mild cognitive impairment
- **MFA** – Metabolic flux analysis
- **ML** – Machine learning
- **MMSE** – Mini-Mental State Examination
- **MOG** – Myelin oligodendrocyte glycoprotein
- **MOGAD** – Myelin oligodendrocyte glycoprotein antibody-associated disease
- **MRI** – Magnetic resonance imaging
- **MRM** – Multiple reaction monitoring
- **MS** – Mass spectrometry
- **MS/MS** – Tandem mass spectrometry
- **MSI** – Mass spectrometry imaging / Metabolomics Standards Initiative
- **MoCA** – Montreal Cognitive Assessment
- ***m/z*** – Mass-to-charge ratio
- **NMOSD** – Neuromyelitis optica spectrum disorder
- **NMR** – Nuclear magnetic resonance
- **NOE** – Nuclear Overhauser Effect
- **NOESY** – Nuclear Overhauser Effect Spectroscopy
- **NSE** – Neuron-specific enolase
- **NfL** – Neurofilament light chain
- **OCB** – Oligoclonal band
- **OPLS-DA** – Orthogonal partial least squares discriminant analysis
- **OR** – Odds ratio
- **PCA** – Principal component analysis
- **PET** – Positron emission tomography
- **PLS-DA** – Partial least squares discriminant analysis
- **PROJECT** – Periodic Refocusing of J Evolution by Coherence Transfer
- **PUFA** – Polyunsaturated fatty acid

- **p-tau** – Phosphorylated tau
- **Q-Orbitrap** – Quadrupole-Orbitrap hybrid mass spectrometer
- **Q-TOF** – Quadrupole time-of-flight mass spectrometer
- Q^2 – Cross-validated explained variance (predictive ability)
- **QC** – Quality control
- **QqQ** – Triple quadrupole mass spectrometer
- R^2 – Explained variance (goodness of fit)
- **RF** – Radiofrequency
- **ROC** – Receiver operating characteristic
- **RPLC** – Reversed-phase liquid chromatography
- **RRMS** – Relapsing–remitting multiple sclerosis
- **S** – Sialic acid
- **SCFA** – Short-chain fatty acid
- **SFC** – Supercritical fluid chromatography
- **SPMS** – Secondary progressive multiple sclerosis
- **SRM** – Selected reaction monitoring
- **T25FW** – Timed 25-Foot Walk
- **tHcy** – Total homocysteine
- **TICS** – Telephone Interview for Cognitive Status
- **TMS** – Tetramethylsilane
- **TOF** – Time-of-flight
- **TSPO** – 18 kDa Translocator protein
- **t-tau** – Total tau
- **UHPLC** – Ultra-high-performance liquid chromatography
- **UPC²** – Ultra-performance convergence chromatography
- **UV** – Ultraviolet (spectroscopy)
- **VIP** – Variable importance in projection
- **VLDL** – Very-low-density lipoprotein
- **VaD** – Vascular dementia
- **WATERGATE** – Water suppression by Gradient Tailored Excitation

Table of Contents

Abstract 2

Declaration 3

Acknowledgments 4

List of Publications 6

List of Abbreviations 7

Chapter 1 Introduction 13

1. 1 Context and rationale 13

1. 2 Neurological disorders 13

1. 2. 1 Demyelinating diseases of the central nervous system 14

1. 2. 2 Neurodegenerative diseases 15

1. 3 Diagnosis and monitoring of neurological disorders 16

1. 3. 1 Functional scoring 16

1. 3. 2 Imaging approaches 16

1. 3. 3 Biofluid-based approaches 17

1. 3. 4 'Omics' sciences for disease diagnosis and monitoring 18

1. 4 Metabolomics in biomedical research 19

1. 4.1 From Hippocrates to high-throughput: the evolution of metabolomics 21

1. 4. 2 Metabolomics strategies: targeted, untargeted, and hybrid approaches 21

1. 5 Metabolomics platforms and analytical workflows 22

1. 5. 1 Mass spectrometry and NMR-based methods 23

1. 5. 2 Nuclear magnetic resonance-based metabolomics 25

1. 5. 2. 1 Fundamental principles of NMR signal generation 25

1. 5. 2. 1. 1 Larmor precession, resonance, and energy transitions in NMR 26

1. 5. 2. 1. 2 Radiofrequency excitation and magnetisation dynamics in NMR 27

1. 5. 2. 2 Pulse sequences for NMR-based metabolomics of biofluids 28

1. 5. 2. 2. 1 Presaturated 1D Nuclear Overhauser Effect Spectroscopy in biofluid metabolomics 29

1. 5. 2. 2. 2 The Carr-Purcell-Meiboom-Gill sequence 29

1. 5. 2. 2. 3 Water suppression in biofluid NMR metabolomics 30

1. 5. 2. 3 NMR lipoprotein profiling 31

1. 5. 2. 4 Clinical relevance of NMR metabolomics and application in this thesis 32

1. 5. 3 Mass spectrometry-based metabolomics 32

1. 5. 3. 1 Ionisation techniques in mass spectrometry 34

1. 5. 3. 2 Mass analysers for untargeted metabolomics 35

1. 5. 3. 2. 1 Quadrupole mass analyser 35

1. 5. 3. 2. 2 Time of flight mass analyser 37

1. 5. 3. 2. 3 Ion trap mass analyser 38
1. 5. 3. 2. 4 Orbitrap mass analyser 38
1. 5. 4 Chromatographic strategies for enhancing MS-based metabolomics 39
1. 5. 4. 1 Reversed-phase liquid chromatography 40
1. 5. 4. 2 Hydrophilic interaction liquid chromatography 41
1. 5. 4. 3 Ion chromatography 42
1. 5. 4. 4 Supercritical fluid chromatography 43
1. 5. 5 Multi-LC-MS analysis expands metabolome coverage 44
1. 6 Metabolomics data processing and metabolite identification 44
1. 6. 1 Pre-processing and quality control in NMR and MS metabolomics 44
1. 6. 2 Integration and pre-processing strategies in ^{1}H NMR data analysis 45
1. 6. 3 Alignment, feature annotation, and drift correction in LC-MS 46
1. 6. 4 Data transformation, normalisation, and scaling for omics analysis 48
1. 7 Statistical analysis of omics datasets 50
1. 7. 1 Multivariate analysis and machine learning for metabolomics 50
1. 7. 1. 1 OPLS-DA: model construction, validation, and interpretation 51
1. 7. 1. 2 Random Forest: a non-parametric approach to metabolomics classification 53
1. 7. 1. 3 Comparative evaluation of OPLS-DA and random forest in metabolomics 54
1. 7. 2 ROC analysis for assessing predictive model accuracy 56
1. 8 Thesis scope: analytical framework and clinical context 58
1. 8. 1 Aims and objectives 58
1. 9 References 61
Chapter 2 Developing an Integrated NMR and LC-MS Workflow for Serum Metabolomics 71
2. 1 Project context and chapter overview 73
2. 3 Manuscript information 73
2. 4 Authorship declaration 74
2. 5 Manuscript 75
2. 6 Supplementary information 91
Chapter 3 Optimisation of Protein Removal Strategies for LC-MS-Based Metabolomics 128
3.1 Project context and chapter overview 128
3. 2 References 132
3. 3 Manuscript information 132
3. 4 Authorship declaration 133
3. 5 Manuscript 134
3. 6 Supplementary information 144
Chapter 4 Combining Serum NMR Metabolomics and Protein Biomarkers to Predict Disease Progression in Multiple Sclerosis 169
4. 1 Project context and chapter overview 169

4. 2 References 171
4. 3 Manuscript information 171
4. 4 Authorship declaration 172
4. 5 Manuscript 173
4. 6 Supplementary information 188
Chapter 5 Plasma *N*-Glycomics as a Diagnostic Tool in Demyelinating Neuroinflammatory Disorders 202
5. 1 Project context and chapter overview 202
5. 2 References 204
5. 3 Manuscript information 204
5. 4 Authorship declaration 205
5. 5 Manuscript 206
5. 6 Supplementary information 221
Chapter 6 Multi-Platform Serum Metabolomics Reveals B Vitamin-Induced Metabolic Reprogramming in Mild Cognitive Impairment 239
6.1 Project context and chapter overview 239
6. 2 References 241
6. 3 Manuscript information 241
6. 4 Authorship declaration 242
6. 5 Manuscript 243
6. 6 Supplementary information 262
Chapter 7 Summary, Discussion, and Conclusions 284
7. 1 Integrated multi-omics strategies for blood-based biomarkers in neurological diseases 284
7. 2 Sample preparation and platform compatibility optimisation 285
7. 3 Development and validation of a reproducible multi-omics data analysis pipeline 287
7. 4 Multi-omics biomarkers of disability progression in multiple sclerosis 288
7. 5 *N*-Glycomics discriminates between MS and Ab-defined demyelinating disorders 290
7.6 Monitoring treatment response in MCI using a multi-omics approach 291
7. 7 Future directions 293
7. 7. 1 Scaling multi-omics for early diagnosis and progression modelling 293
7. 7. 2 Future research will integrate metabolomics and proteomics for early stratification and progression modelling in AD 294
7.7.3 Expanding platform coverage: lipidomics and proteomics integration 294
7. 8 Concluding remarks 296
7. 9 References 297

Chapter 1 Introduction

1. 1 Context and rationale

This thesis focuses on developing and applying metabolomics and integrated multi-omics approaches to advance early disease detection, mechanistic understanding, and patient stratification in neurological disorders. It establishes a blood-based multi-platform approach for diagnosis that combines nuclear magnetic resonance (NMR) spectroscopy, liquid chromatography-mass spectrometry (LC-MS), and multivariate modelling focussed on metabolic alterations. This analytical strategy overcomes the limitations of individual techniques, enabling a more comprehensive view of disease-associated perturbations. Extending beyond metabolomics, the integration of additional omics layers reveals that converging molecular signals across biological systems provides deeper mechanistic insight and increases the reliability of candidate biomarkers.[1] Together, these strategies address the growing clinical need for scalable tools to enhance prediction of neurological disease, monitor progression, and support therapeutic response, thereby advancing the translation of omics science into personalised healthcare.

1. 2 Neurological disorders

Nowhere is the need for accessible, molecularly informed diagnostics more pressing than in neurological disease, where both the inaccessibility of brain tissue and the complexity of surrogate matrices constrain effective monitoring. Within the calvarium, the central nervous system (CNS) is protected by anatomical and immunological barriers that preserve homeostasis but render tissue sampling unfeasible outside of invasive procedures such as biopsy. As a result, clinical assessments rely heavily on indirect measures such as neuroimaging, cerebrospinal fluid (CSF), or blood analyses.[2] Yet each of these has limitations: CSF collection is invasive and not routinely performed, while neuroimaging is expensive and typically infrequent - for instance, many UK patients with multiple sclerosis receive only minimal magnetic resonance imaging (MRI) scans throughout their disease course.[3] Moreover, the molecular heterogeneity of CSF and blood, combined with the subtlety of early pathological changes, poses challenges for sensitive and specific detection.[4, 5]

Omics-based platforms offer a promising route to non-invasive molecular diagnostics, with growing evidence that neurological disorders induce characteristic alterations in peripheral biofluids. A recent study by Oka *et al.* demonstrated that integrated plasma metabolomic, lipidomic, and genomic profiling improves prediction of Alzheimer's disease (AD) progression.[6] However, clinical translation remains limited due to challenges in analytical reproducibility, standardisation, and regulatory implementation.[7] To address these barriers and explore the translational potential of multi-omics, this thesis develops a multiplatform strategy that integrates NMR and LC-MS metabolomics with complementary omics and analytical techniques. This thesis focuses on three exemplar disorders - multiple sclerosis, neuromyelitis optica spectrum disorders (NMOSDs), and mild cognitive impairment (MCI), a prodromal stage of AD - which collectively encompass both inflammatory and neurodegenerative mechanisms. Together, these conditions provide a representative framework for evaluating the diagnostic and prognostic potential of omics-based approaches in neurology.

1. 2. 1 Demyelinating diseases of the central nervous system

Demyelinating diseases of the CNS are characterised by immune-mediated destruction of the myelin sheath, resulting in impaired neuronal conduction and progressive neurological dysfunction.[8] The most prevalent of these is multiple sclerosis, which affects approximately 2.8 million people worldwide.[9] Multiple sclerosis typically manifests in young adults between the ages of 20 and 30, with a notable female predominance (~75%).[9, 10] As the leading cause of non-traumatic neurological disability in young adults, multiple sclerosis exhibits a broad clinical spectrum encompassing visual, motor, sensory, and coordination impairments.[10] While advances in imaging and immunological assays have improved early multiple sclerosis diagnosis and differentiation from related demyelinating conditions,[11] they offer limited utility in predicting or monitoring disease progression.[12, 13] The clinical course is highly variable, ranging from relapsing–remitting (RRMS) episodes to a steady, irreversible decline in progressive forms such as secondary progressive multiple sclerosis (SPMS).[13] This pronounced variability reflects underlying pathology, initially marked by focal inflammatory demyelination, which evolves into chronic axonal loss, cortical atrophy, and compartmentalised inflammation behind an intact blood–brain barrier in SPMS.[14]

Importantly, the delineation of antibody (Ab)-associated neurological syndromes has led to the recognition of NMOSDs as distinct from multiple sclerosis. NMOSDs now encompass aquaporin-4 Ab-positive (AQP4-Ab NMOSD) disease, myelin oligodendrocyte glycoprotein Ab-associated disease (MOGAD), and double-

seronegative NMOSD, where patients meet clinical and radiological criteria but lack detectable AQP4 or MOG Ab levels.[15] These subtypes are immunopathologically distinct and differ in their treatment response and prognosis. For instance, AQP4-Ab-positive NMOSD typically responds well to B cell-targeted therapies, whereas MOGAD often requires alternative immunosuppressive strategies tailored to its specific pathophysiology.[16] Importantly, multiple sclerosis-specific treatments can trigger relapses in Ab-positive NMOSD, making accurate early diagnosis essential for guiding appropriate therapy.[17-19] Despite advances in classification, early-stage differentiation remains challenging, particularly in seronegative individuals with overlapping clinical symptoms.[11, 20] This diagnostic uncertainty underscores the need for improved molecular stratification, not only to refine differential diagnosis (explored in **Chapter 5**), but also to enable more precise monitoring of disease activity and progression (addressed in **Chapter 4**).

1. 2. 2 Neurodegenerative diseases

Neurodegenerative diseases, similar to demyelinating disorders, represent a clinically and biologically heterogeneous group of conditions marked by insidious onset and overlapping features. Enhanced molecular characterisation is thus essential to facilitate earlier diagnosis, improve prognostic accuracy, and inform the development of targeted therapeutic strategies.

MCI is a clinically diverse syndrome marked by measurable cognitive decline, most commonly affecting memory, that does not yet significantly interfere with daily activities.[21] Increasing recognition of its role as a prodromal stage has linked MCI to several neurodegenerative disorders, most notably AD, but also vascular dementia (VaD), frontotemporal dementia (FTD), and Lewy body dementia (LBD).[21-23] Notably, individuals with amnestic MCI are at particularly high risk of progressing to AD.[23, 24] However, the clinical course of MCI is highly variable due to underlying biological heterogeneity and overlapping pathophysiological mechanisms.[21] Despite its prognostic importance, the accurate diagnosis and longitudinal monitoring of MCI remain challenging. Current diagnostic tools, such as CSF biomarkers and advanced neuroimaging, are invasive, costly, and often unavailable outside specialised centres.[25] At the same time, existing pharmacological interventions for AD offer limited benefit when initiated at advanced disease stages, underscoring the need for early intervention. The growing global burden of cognitive impairment, exacerbated by ageing populations, highlights the urgency of developing scalable, minimally invasive tools for early detection, longitudinal monitoring, and improved stratification. Such approaches are essential not

only for timely diagnosis and care planning but also for the successful development and implementation of disease-modifying therapies - and potentially adjunct therapies, as examined in **Chapter 6**.[26]

1. 3 Diagnosis and monitoring of neurological disorders

In current clinical practice, both diagnosis and disease monitoring still rely heavily on functional scoring systems, which offer limited biological insight.

1. 3. 1 Functional scoring

In multiple sclerosis, the Expanded Disability Status Scale (EDSS) is the most common clinical metric, assessing disability primarily through ambulatory function.[10] Similarly, the Timed 25-Foot Walk (T25FW) test provides a quantitative measure of gait speed.[27] However, both tests are limited by their focus on mobility and may not capture the full extent of disease progression, particularly in non-motor domains. Moreover, their predictive value for future clinical outcomes is minimal and they often show limited correlation with imaging or molecular biomarkers.[10, 28] In AD and other dementias, cognitive impairment is typically assessed using tools such as the Mini-Mental State Examination (MMSE), the Telephone Interview for Cognitive Status (TICS),[29] or the Montreal Cognitive Assessment (MoCA).[30] While these tests offer a general indication of cognitive decline, their sensitivity is limited and the performance can also be affected by non-pathological day-to-day variability and patient-related factors such as education or mood.[30] Although clinical tests offer insights into disease severity and progression, their interpretation is strengthened when combined with imaging and biofluid biomarkers, which provide more objective and sensitive measures, particularly at prodromal or preclinical stages.[24]

1. 3. 2 Imaging approaches

Alongside clinical scoring systems, conventional MRI continues to play an important role in the structural assessment of both multiple sclerosis and neurodegenerative diseases. In multiple sclerosis, MRI is routinely used to detect new or active lesions and monitor lesion load, which correlates with relapse activity.[11] However, longitudinal studies have shown that radiological measures often fail to predict long-term progression, particularly in progressive subtypes.[31, 32] In neurological disorders, MRI can reveal characteristic changes including cortical and hippocampal atrophy, ventricular enlargement, and white

matter abnormalities, particularly visible on T2-weighted or FLAIR sequences.[33] These structural changes can identify early disease processes and assist in differentiating AD from other dementias, such as FTD, which often presents with frontal lobe atrophy, or LBD, which affects the medial temporal and occipital lobes.[33, 34] Nevertheless, MRI lacks the molecular specificity required for early or definitive diagnosis.[31, 32]

While MRI provides essential structural information, positron emission tomography (PET) offers a complementary imaging modality capable of detecting molecular pathology *in vivo*. In AD, PET is primarily used for visualising amyloid-β plaques and tau neurofibrillary tangles.[35] Tracers such as ^{18}F-florbetapir and ^{11}C-PiB enable early amyloid detection, often years before cognitive symptoms manifest, while tau-specific tracers such as ^{18}F-flortaucipir are more closely associated with symptom severity and neurodegenerative progression.[35] Beyond amyloid and tau, inflammation-targeted PET tracers such as translocator protein (TSPO) ligands have shown utility in both neurodegeneration and demyelination. In multiple sclerosis, Sucksdorff *et al.* demonstrated that increased TSPO binding, reflecting microglial and astrocytic activation, is observed in progressive disease stages and is associated with clinical deterioration.[36, 37] TSPO PET imaging therefore provides insight into non-lesional neuroinflammation, which may underlie neurodegenerative processes in both multiple sclerosis and AD.[37, 38] Additionally, metabolic PET imaging using ^{18}F-fluorodeoxyglucose (FDG-PET) enables assessment of neuronal glucose metabolism, offering a functional readout of synaptic activity. Jones *et al.* recently demonstrated that FDG-PET could effectively map functional patterns of neurodegeneration in AD, linking glucose hypometabolism to symptom domains and large-scale brain networks.[39] However, the widespread application of PET imaging is limited by high costs and the need for specialised infrastructure. In contrast, scalable biofluid-based biomarkers with clinical relevance offer a more accessible and adaptable strategy for advancing personalised medicine.

1. 3. 3 Biofluid-based approaches

Among biofluid-based approaches to biomarker discovery, CSF provides a direct window into CNS pathology and has yielded clinically validated biomarkers. In demyelinating disorders, the detection of CSF-specific oligoclonal bands (OCBs) is a well-established diagnostic marker and shows prognostic value, particularly in identifying individuals with clinically isolated syndrome (CIS) who are at risk of developing multiple sclerosis. Additionally, the quantification of protein biomarkers such as neurofilament light chain (NfL),[40, 41] chitinase-3-like protein 1 (CHI3L1),[40] and more recently glial fibrillary acidic protein (GFAP),[42]

has demonstrated utility in both diagnosis and longitudinal monitoring of disease progression, as evidenced by work from the Kuhle group and others.[43] In neurodegenerative diseases, especially AD, CSF biomarkers offer high diagnostic specificity. Measurement of amyloid-β peptides, total tau (t-tau), and phosphorylated tau (p-tau) constitutes the core diagnostic framework, reflecting hallmark AD pathologies.[44, 45] In addition, NfL and GFAP have emerged as valuable indicators of neuroaxonal injury and glial activation, respectively, and were suggested to correlate with AD severity.[42] Although CSF-based diagnostics offer high specificity, their invasive nature restricts their suitability for routine monitoring and application in large-scale screenings, highlighting the growing need for blood-based biomarkers.

Notably, several CSF biomarkers have now been successfully translated into blood-based assays, offering more accessible tools for monitoring neurological diseases. NfL and GFAP,[42, 46] both studied extensively in multiple sclerosis and AD, can now be reliably quantified in plasma.[47] In AD, blood-based $A\beta_{42}/A\beta_{40}$ ratios[48] and p-tau[49-52] also show promising diagnostic utility. Additionally, genotyping for apolipoprotein E (ApoE), particularly the ε4 allele, is widely recognised as a major genetic risk factor for late-onset AD.[53] Despite recent advances, blood-based biomarkers for demyelinating and neurodegenerative diseases remain insufficiently accurate for early detection, prognosis, and treatment monitoring. Ongoing challenges, including limited sensitivity, poor disease specificity, and inter-individual variability, have driven interest in more comprehensive molecular approaches. Among these, omics-based analyses are gaining traction for their ability to capture the complex molecular networks underlying disease progression**.** In multiple sclerosis, a recent proteomic study by Chitnis *et al.* identified a 20-protein serum panel that outperformed individual biomarkers in reflecting both clinical and radiographic disease activity.[54] Similarly, several independent metabolomics studies have reported significant differences between the serum metabolome of individuals with RRMS and SPMS, highlighting its potential for disease stratification.[55-57] In cognitive decline, Grande *et al.* demonstrated that multi-marker model combining serum p-tau, NfL, and GFAP significantly improved prediction of long-term dementia risk.[58] In parallel, Vignoli *et al.* showed that a serum metabolomics model integrating lipoproteins and small metabolites could stratify AD progression with high accuracy.[59]

1. 3. 4 'Omics' sciences for disease diagnosis and monitoring

To overcome the limitations of traditional approaches to biomarker discovery and disease monitoring, research efforts are increasingly focused on the application of omics-based technologies. These platforms

enable high-throughput molecular profiling across genomic, transcriptomic, proteomic, and metabolomic layers. By quantifying molecular alterations across diverse pathways and regulatory levels, often from a single blood, urine, or saliva sample, omics approaches provide a comprehensive view of disease biology. Such samples act as molecular fingerprints, capturing the biochemical state of an individual together with disease-associated perturbations.[60] Notably, omics platforms generate high-dimensional datasets that require advanced statistical and computational methods, such as multivariate analysis and machine learning (ML), to identify disease-specific patterns relevant to diagnosis, risk stratification, progression, and therapeutic response (Fig. 1.1).[61, 62] For example, a recent *Nature Medicine* study based on UK Biobank data demonstrated that NMR-derived metabolomic profiles could predict the onset of multiple common diseases, including diabetes, heart failure, and neurological conditions, outperforming conventional clinical predictors in several cases and highlighting the potential of metabolomics for population-wide risk stratification.[63]

In summary, effective clinical management of demyelinating and neurodegenerative disorders is hindered by substantial clinical and pathological heterogeneity.[13, 24] Biofluid-based omics approaches offer valuable tools for disease diagnosis and monitoring. Metabolomics, in particular, enables sensitive detection of biochemical alterations and can provide deeper insights when integrated with other omics layers. Although still an emerging approach in neurology, this thesis investigates the clinical utility of omics for tracking disease progression, improving diagnostic accuracy, and assessing treatment response. For example, **Chapter 4** investigates markers of progression in demyelinating disease, **Chapter 5** focuses on differential diagnosis, and **Chapter 6** explores the use of metabolomics for assessing treatment response in MCI.

1. 4 Metabolomics in biomedical research

The human metabolome comprises all low-molecular-weight molecules present in cells, tissues, or biofluids at a given time point. These molecules, spanning amino acids, lipids, nucleotides, carbohydrates, and organic acids, reflect the endpoint of cellular function and provide a direct readout of physiological state. Positioned downstream of the genome, transcriptome, and proteome, metabolomics captures the cumulative outcome of genetic, transcriptional, post-translational, and environmental effects.[64, 65] In contrast to other omics that capture upstream regulatory layers, such as inherited variation in genomics, gene expression in transcriptomics, or protein abundance and modification in proteomics, metabolomics provides a dynamic and integrative measure of biochemical activity.

Given the ability of the metabolome to reflect the biochemical status of an individual with high sensitivity, metabolomics offers a powerful approach for detecting molecular alterations associated with disease. By enabling the simultaneous quantification of thousands of small molecules in a single assay, it provides detailed insight into disrupted metabolic pathways and biochemical networks.[62] This capacity to capture subtle, system-wide alterations underpins the increasing use of metabolomics in biomarker discovery, disease stratification, and longitudinal monitoring - often revealing molecular changes prior to the onset of clinical symptoms. In particular, blood-based metabolomic profiling is minimally invasive, compatible with routine clinical workflows, and scalable for large-cohort studies, making it a valuable tool in translational research and precision medicine (Fig. 1.1).[61, 62]

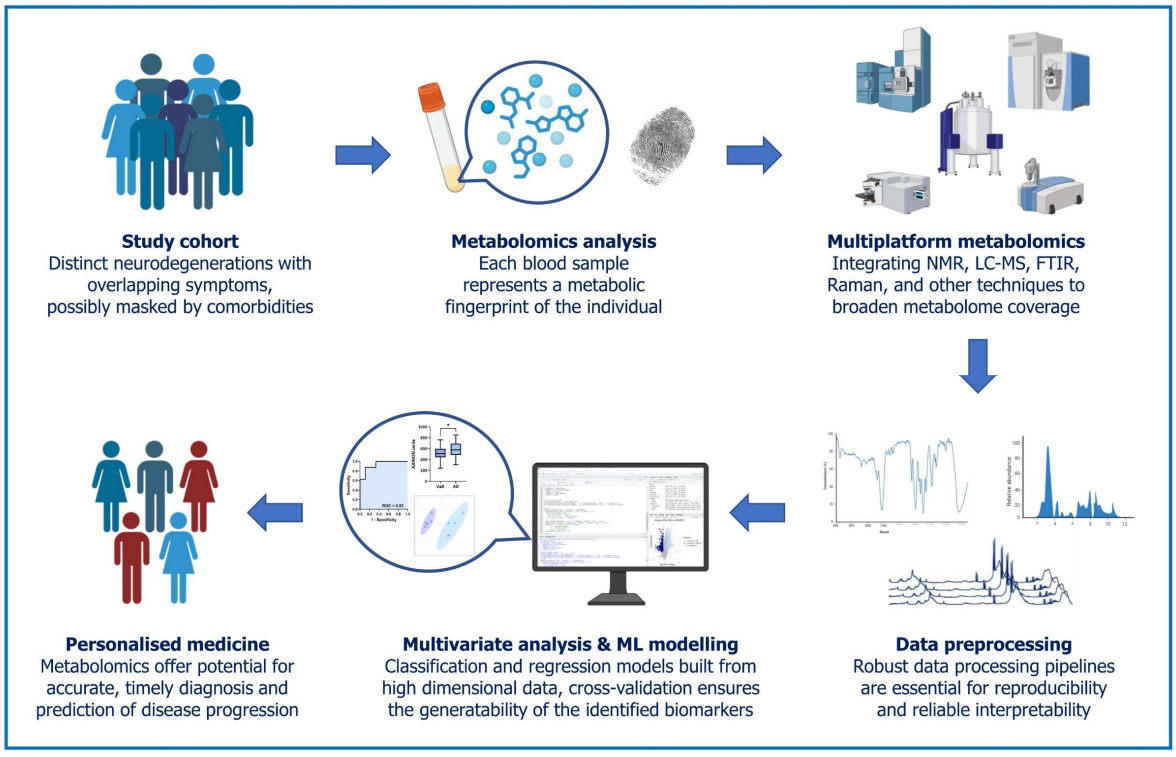

Figure 1.1. Overview of a multi-step metabolomics pipeline for stratifying neurodegenerative diseases, as applied in this thesis. The workflow begins with the selection of a clinically diverse study cohort, often characterised by overlapping symptoms and comorbidities. Metabolomics analysis is then performed on biofluid samples, such as blood or urine, each representing a metabolic fingerprint of the individual. Multiplatform analytical techniques (e.g., NMR, various LC-MS systems, FTIR, and Raman spectroscopy) are integrated to maximise metabolome coverage. Following spectral acquisition, robust data pre-processing and curation are applied to ensure reproducibility and interpretability, while minimising the risk of model overfitting due to non-specific noise. Multivariate statistical and machine learning (ML) models are subsequently constructed to identify discriminatory patterns and develop predictive classifiers. A critical component of this process is rigorous cross-validation to assess model stability. The resulting insights support the development of personalised diagnostic and prognostic tools, advancing precision medicine in neurodegeneration.

1. 4.1 From Hippocrates to high-throughput: the evolution of metabolomics

The notion that physiological changes are reflected in bodily fluids has been recognised since ancient times. Hippocrates examined urine for changes in colour and odour, using sensory cues to infer disease. Though rudimentary, this practice reflects a foundational idea in personalised diagnostics: that internal biochemical changes can precede - and sometimes even predict - clinical symptoms. Centuries later, the principle remains, but the scale and precision have transformed. In 1959, physicist Richard Feynman delivered his iconic lecture *"There's Plenty of Room at the Bottom"*, urging scientists to explore the molecular frontier.[66] That vision now finds concrete realisation in metabolomics - the comprehensive analysis of small-molecule metabolites that capture the dynamic biochemical state of cells, tissues, and organisms. Emerging in the 1990s alongside genomics, metabolomics addressed a critical gap by providing insight into real-time physiological states and treatment responses - factors that the genome alone could not fully capture.[67]

The launch of the Human Metabolome Project in 2004 catalysed the field, providing reference databases and enabling high-throughput profiling by NMR and MS.[68] Since then, metabolomics has evolved into a powerful tool for biomedical research, with growing relevance to personalised medicine through its ability to reveal real-time molecular signatures of disease onset, progression, and therapeutic response. Today, the field is entering a new era driven by artificial intelligence (AI). ML methods are essential for interpreting complex, high-dimensional data and uncovering predictive patterns beyond human recognition. By integrating metabolomics with AI, we move closer to scalable, non-invasive approaches for disease diagnosis, enabling detection of biochemical changes that reflect not just genetic risk, but the real-time phenotype shaped by both genetic and environmental factors (Fig. 1.1).

1. 4. 2 Metabolomics strategies: targeted, untargeted, and hybrid approaches

The application of metabolomics in translational research depends on established analytical strategies, which are typically classified as targeted, untargeted, or hybrid approaches. The primary approach adopted in this thesis is untargeted metabolomics, which aims to detect as many metabolites as possible within a given biological sample without prior knowledge of their identity. This comprehensive profiling typically yields thousands of features, often corresponding to distinct chemical entities or adducts, which are subsequently analysed using multivariate statistical techniques and ML models to identify those most strongly associated

with the biological condition of interest.[60, 69] For instance, Hajjar *et al.* applied untargeted metabolomics to CSF in MCI individuals, uncovering disruptions in sugar, methionine, and tyrosine pathways that correlated with AD phenotypes and highlighted potential therapeutic targets, illustrating the strength of untargeted analysis in generating novel biological hypotheses without initial assumptions.[70] Following feature detection and assignment, the discriminatory metabolites are examined in the context of metabolic pathways and biochemical networks, supporting hypothesis generation and the identification of putative biomarkers or perturbed pathways. Consequently, untargeted metabolomics is inherently exploratory and particularly well suited to discovery-driven research.[62, 69]

In contrast, targeted metabolomics focuses on the quantitative analysis of a predefined panel of metabolites, selected based on prior biological knowledge or specific hypotheses. Targeted workflows rely on validated reference standards, enabling accurate quantification of metabolite concentrations.[71] This approach is commonly applied in clinical validation studies, nutritional research, and mechanistic investigations where specific metabolic pathways are of interest.[69] For instance, Meng *et al.* applied targeted metabolomics to evaluate a predefined panel of plasma metabolites, identifying uric acid, pyruvic acid, and isolithocholic acid as a biomarker set that effectively distinguished individuals with MCI from healthy controls, underscoring the utility of targeted platforms for early-stage disease screening and quantitative biomarker development.[72]

A more recent advancement in the field is the development of semi-targeted, or pseudo-targeted, metabolomics - which integrates elements of both targeted and untargeted strategies.[73] In this hybrid framework, a predefined set of known metabolites is identified and quantified using reference standards, while additional unknown or partially annotated features are retained to support broader pattern recognition.[74] This approach balances analytical rigour with exploratory scope, offering a more comprehensive view of the metabolic landscape.[73] In this thesis, semi-targeted metabolomics was applied in selected LC-MS experiments (**Chapter 6**) to maximise both quantification accuracy and discovery potential.

1. 5 Metabolomics platforms and analytical workflows

Given the broad range of physicochemical properties represented by different metabolites - from volatile compounds to highly polar or lipophilic molecules - selecting an appropriate analytical platform is a critical aspect of any metabolomics experiment. Traditionally, NMR and MS have been the most established

technologies in the field and remain the most widely used, owing to their high reproducibility, quantitative precision, and broad metabolite coverage.[60] Among MS-based approaches, gas chromatography-MS (GC-MS) and LC-MS are the most commonly employed, offering complementary coverage of volatile and non-volatile metabolites, respectively (Fig. 1.2). However, as metabolomics continues to evolve, a number of complementary and emerging platforms are increasingly being integrated into workflows to capture specific classes of metabolite or to provide additional spatial, temporal, or functional insights. These include infrared (IR) and Raman spectroscopy for rapid, non-destructive fingerprinting;[75] capillary electrophoresis (CE) for high-resolution separation of charged or polar compounds;[76] and imaging mass spectrometry for spatial metabolite mapping in tissues.[77] Additionally, metabolic flux analysis (MFA) using stable isotope tracers is being employed to elucidate pathway dynamics,[42] while breathomics[78] and optical metabolic imaging[79] are gaining traction in clinical and *in vivo* applications.

1. 5. 1 Mass spectrometry and NMR-based methods

The expanding range of analytical platforms highlights the need to tailor experimental design to the specific biological question and the physicochemical properties of the target metabolite classes. This thesis primarily combines multi-LC-MS and NMR approaches to maximise metabolite coverage and ensure analytical robustness across both targeted and untargeted applications. Among the platforms used in this thesis, NMR spectroscopy offers a robust, non-destructive, and inherently quantitative approach for metabolic profiling. It enables the precise identification and absolute quantification of a defined subset of predominantly high-abundance metabolites in biological fluids.[60, 80] These include not only hydrophilic compounds such as amino acids, organic acids, and monosaccharides, but also amphipathic and hydrophobic species, notably lipoprotein subclasses, polyunsaturated fatty acids (PUFAs), and glycoprotein acetylation signals.[60, 81] Given its minimal sample preparation requirements and exceptional reproducibility across large cohorts, NMR is particularly well-suited to longitudinal studies and clinical applications, where analytical consistency, throughput, and quantitative stability are essential.[81, 82]

In contrast, LC-MS offers superior sensitivity and a much broader dynamic range, enabling the detection and semi-quantitative analysis of low-abundance metabolites and hydrophobic species that are typically undetectable by NMR (Fig. 1.2).[83, 84] The metabolite coverage of LC-MS is significantly enhanced by the variety of chromatographic separation techniques that can be hyphenated to MS, including reversed-phase

(RPLC), hydrophilic interaction liquid chromatography (HILIC), and ion-pairing LC, among others.[82] These allow for the targeted or untargeted profiling of chemically diverse metabolite classes, encompassing not only lipids, acylcarnitines, bile acids, and micronutrients, but also organic acids, phosphates, sugars, and other polar or charged small molecules. However, a substantial proportion of detected features in untargeted LC-MS datasets remain unidentified, contributing to what is often referred to as the *dark matter* of metabolomics or the *dark metabolome*.[85] LC-MS is also inherently more susceptible to analytical variability, arising from factors such as matrix effects, ion suppression, and batch-to-batch variation.[86]

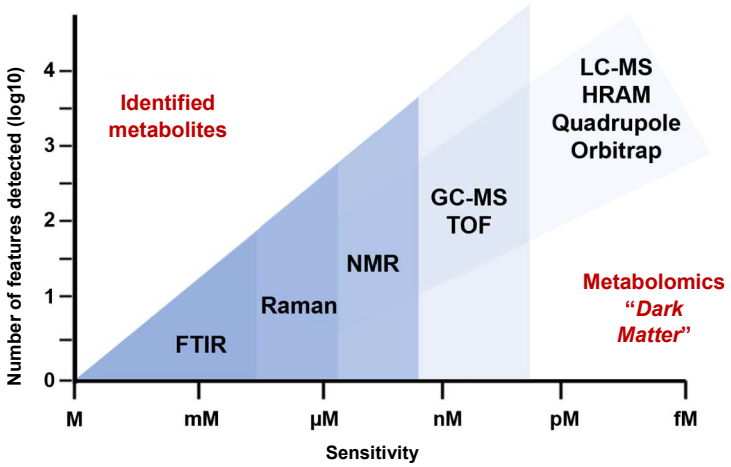

Figure 1.2. Sensitivity and feature detection across major metabolomics platforms. Comparison of common analytical techniques in metabolomics based on sensitivity (*x*-axis) and number of features detected (*y*-axis). Techniques such as FTIR and Raman spectroscopy offer rapid, low-resolution fingerprinting, while NMR provides quantitative and reproducible profiling of high-abundance metabolites. Mass spectrometry-based approaches (e.g., GC-MS, LC-MS) enable higher sensitivity and broader metabolite coverage, particularly with high-resolution instruments (e.g. high resolution accurate mass (HRAM), Orbitrap, time-of-flight (TOF), and quadrupole systems). Despite advances in analytical technologies, only a subset of detected features, particularly in LC-MS experiments, can be reliably annotated; the remainder, often referred to as *metabolomics dark matter*, continues to represent a significant challenge for data interpretation and downstream application. Modified from:[87]

Nevertheless, these two platforms offer complementary analytical capabilities: NMR provides high reproducibility, robust structural elucidation, and precise quantification, while LC-MS delivers enhanced sensitivity and broader chemical coverage.[60, 82] The integration of both techniques enables more comprehensive metabolome profiling and increases confidence in metabolite identification, quantification, and biomarker discovery.[82, 88, 89] This integrative rationale forms the basis of the multi-platform metabolomics approach adopted in this thesis, which combines NMR and LC-MS technologies, including distinct chromatographic modalities, to comprehensively profile a broad spectrum of metabolites across varied chemical classes.[90, 91] In view of the experimental work being centred on NMR and LC-MS, these two analytical platforms will be discussed in greater detail in the subsequent sections.

1. 5. 2 Nuclear magnetic resonance-based metabolomics

NMR spectroscopy remains one of the most widely used techniques in metabolomics, particularly in clinical and population-based studies, due to its high reproducibility, quantitative reliability, and minimal sample preparation requirements. Globally, NMR is most commonly employed for structural elucidation, where fine spectral resolution and peak assignment are critical. In contrast, metabolomics applications typically prioritise reliable identification and relative quantification of key metabolites over full spectral interpretation, even in the presence of overlapping signals.[92] Solution-state ^{1}H NMR is particularly well suited to this task, offering a non-destructive, high-throughput approach for profiling a broad range of metabolites. NMR techniques can be broadly categorised into solid-state and solution-state methods, each offering distinct advantages depending on the sample matrix and molecular environment. While solid-state NMR is valuable for studying insoluble or crystalline materials such as membranes, tissues, or macromolecular complexes, solution-state NMR is the preferred method in metabolomics.[60, 92] Several NMR-active nuclei are relevant in this context, including ^{1}H, ^{13}C, and ^{15}N, each offering complementary insights into metabolic pathways. However, this thesis primarily focuses on ^{1}H NMR experiments owing to the high natural abundance and favourable sensitivity of the proton nucleus, as well as its broad applicability in profiling clinical samples. The following section outlines key NMR principles and introduces the pulse sequences used in the metabolomics analyses described in **Chapters 4 and 6.** Two methodological challenges, water suppression and lipoprotein profiling, are also discussed, given their importance in acquiring high-quality ^{1}H NMR data.

1. 5. 2. 1 Fundamental principles of NMR signal generation

In NMR spectroscopy, the resonance frequencies of atomic nuclei are measured in the presence of a strong and uniform external magnetic field. Each nucleus is characterised by a nuclear spin quantum number (I), which can take values that are integer or half-integer multiples of ½ and must be greater than or equal to zero. Nuclei with $I = 0$, such as ^{12}C, have no net spin and are therefore NMR-inactive (or NMR silent).[93] In contrast, many elements have at least one naturally occurring NMR-active isotope with a non-zero spin quantum number, making them NMR-detectable.

Spinning nuclei possess angular momentum (P) and, due to their charge and motion, generate an associated magnetic moment (μ). The magnetic properties of each nuclide are further defined by its gyromagnetic ratio (γ) - a nucleus-specific constant that relates its magnetic moment to its angular momentum (Equation 1.1).[93]

$$\mu = \gamma P \tag{1.1}$$

As shown in Equation 1.1, both magnetic moment and angular momentum are vector quantities. In the presence of an external magnetic field (B_0), the magnetic moment adopts one of a limited number of quantised orientations, corresponding to discrete energy states. For a nucleus with a spin quantum number l, there are $2l + 1$ possible spin states in the magnetic field.[93, 94] For instance, the most widely studied nucleus in metabolomics, ^{1}H (proton), possesses $l = ½$, resulting in two allowed spin states. These are conventionally described as parallel (α) and anti-parallel (β) relative to the external magnetic field, with the β state representing the higher energy configuration.[93, 94]

1. 5. 2. 1. 1 Larmor precession, resonance, and energy transitions in NMR

While often described as adopting discrete parallel or anti-parallel orientations in a static magnetic field (B_0), nuclear spin populations are subject to thermal fluctuations that slightly perturb this alignment.[93] Nonetheless, the lower-energy parallel state remains marginally favoured, generating a net magnetisation along the z-axis, known as the bulk magnetisation vector. In the absence of external perturbation, no net transverse (xy-plane) magnetisation is present, as such states are energetically disfavoured. However, upon application of a radiofrequency (RF) pulse, the magnetisation vector is tipped away from the z-axis and undergoes precession around B_0 due to the resulting torque.[93] This precessional motion, termed Larmor precession, occurs at an angular frequency proportional to γ and B_0, as described in Equation 1.2.[93] The direction of precession depends on the sign of γ and is constant for each nucleus. The corresponding Larmor frequency (ν) defines the specific resonance condition for each nuclide. NMR signals are generated when nuclei absorb RF energy matching this frequency, enabling transitions between spin states. Resonance occurs when the applied RF field precisely matches the Larmor frequency of the studied nucleus.[93, 94]

$$\nu = \frac{|\gamma| B_0}{2\pi} \text{ (Hz)} \tag{1.2}$$

The energy difference (ΔE) between the two spin states in a magnetic field is relatively small (Equation 1.3),[93] and is directly proportional to γ and B_0 .

$$\Delta E = h\nu = \frac{h\gamma B_0}{2\pi} \text{ (J)} \tag{1.3}$$

Consequently, the population imbalance between spin states - dictated by the Boltzmann distribution (Equation 1.4) - is relatively small, with only a slight excess of nuclei in the α state. This subtle population difference underlies the net magnetisation and ultimately gives rise to the detectable NMR signal.[93]

$$\frac{N_\alpha}{N_\beta} = e^{\Delta E/k_B T} \tag{1.4}$$

This limited population difference is a key reason why NMR is inherently less sensitive than other spectroscopic techniques, such as IR or ultraviolet (UV) spectroscopy, where the energy transitions involve much larger gaps between ground and excited states.[93] To compensate for this low sensitivity and to achieve high-resolution detection, NMR experiments require the use of high-field superconducting magnets, typically operating at frequencies in the range of several hundred megahertz (e.g., 400-1200 MHz for ^{1}H). Higher magnetic fields not only improve sensitivity but also enhance spectral dispersion, facilitating more accurate identification and quantification of metabolites.[93, 94]

1. 5. 2. 1. 2 Radiofrequency excitation and magnetisation dynamics in NMR

As described above, generation of an NMR signal requires the application of electromagnetic radiation at the Larmor frequency of the target nuclei. This is achieved by applying oscillating RF pulses to the sample, delivered at a defined amplitude and duration (t_p). Upon termination of the RF pulse, the RF field is switched off, and signal acquisition begins during the relaxation period. During RF irradiation, the oscillating magnetic field component (B_1), oriented perpendicular to B_0, applies a torque to the bulk magnetisation vector, tipping it away from the z-axis.[93, 94] According to classical electromagnetic theory, this torque causes the magnetisation vector to rotate away from its equilibrium position along the z-axis and toward the xy-plane. The rate of rotation, or nutation frequency, is proportional to the product γB_1 and the angle through

which the magnetisation vector is rotated (known as the nutation angle (θ), pulse flip angle, or tip angle) is determined by both the strength and duration of the RF pulse, as described in Equation 1.5.[93]

$$\theta = \frac{360\gamma B_1 t_p}{2\pi} \tag{1.5}$$

The bulk magnetisation vector represents the sum of individual magnetic moments of all NMR-active nuclei in the sample. The most commonly applied excitation pulse is the 90° RF pulse, which rotates the magnetisation from its equilibrium position along the *z*-axis into the *xy*-plane. This equalises the populations of the α and β spin states, effectively eliminating net longitudinal magnetisation and generating transverse magnetisation.[93] During excitation, the spins become phase-coherent, with their magnetic moments precessing in a synchronised manner - a state induced by the RF pulse. In contrast, a 180° pulse inverts the spin state populations, reorienting the net magnetisation along the negative *z*-axis. Although a 180° pulse does not directly generate a detectable signal - since only transverse magnetisation induces current in the receiver coil - it plays a crucial role in pulse sequence design. In spin-echo sequences, it refocuses dephasing spins and compensates for magnetic field inhomogeneities, thereby enhancing signal recovery.[93] Maximum signal intensity is achieved when the magnetisation lies entirely in the *xy*-plane, as with 90° or 270° pulses. In contrast, 180° or 360° pulses produce no net transverse magnetisation immediately after excitation and thus do not generate a detectable signal on their own.

The following sections will primarily discuss the pulse sequences applied throughout the experimental work, with particular emphasis on water suppression strategies and the optimisation of spectral resolution for diagnostically relevant signals, such as lipoprotein subclasses.

1. 5. 2. 2 Pulse sequences for NMR-based metabolomics of biofluids

In NMR-based metabolomics, the choice of pulse sequence is guided by the sample matrix and specific analytical objectives. For human biofluids such as plasma and serum, critical requirements include efficient suppression of the water signal and broad macromolecular resonances, alongside high spectral reproducibility across large sample cohorts.[60, 92]

Commonly used sequences in this context include 1D projection of the J-resolved spectroscopy (JRES) experiment,[95] which aids in resolving overlapping multiplets, and Periodic Refocusing of J Evolution by Coherence Transfer (PROJECT), an alternative to spin-echo-based filtering for macromolecular signal suppression.[96] However, the most widely applied sequences in untargeted metabolomics remain 1D NOESY (Nuclear Overhauser Effect Spectroscopy) and CPMG (Carr-Purcell-Meiboom-Gill).[97] The NOESY-presaturation sequence enables effective water suppression while preserving small-molecule signals, making it suitable for detecting low-abundance metabolites in biofluids. Conversely, the CPMG sequence employs a train of refocusing pulses to attenuate broad signals from slowly tumbling macromolecules, thereby enhancing the relative visibility of small metabolites.[57, 97] Together, these complementary sequences underpin the acquisition protocols used throughout this thesis, particularly in **Chapters 2, 4, and 6**.

1. 5. 2. 2. 1 Presaturated 1D Nuclear Overhauser Effect Spectroscopy in biofluid metabolomics

The 1D NOESY-presaturation sequence is widely used in biofluid metabolomics and represents a simplified adaptation of the conventional 2D NOESY experiment.[97-99] It employs a short mixing time to achieve efficient water suppression while preserving signals from low-molecular-weight metabolites. The pulse train consists of two calibrated 90° pulses (p1) followed by a variable read pulse (p0), with presaturation applied during the relaxation delay and mixing time. The very short mixing period does not generate significant Nuclear Overhauser Effects (NOE); instead, it mainly serves to suppress water and broad macromolecular resonances. In the commonly used noesypr1d sequence, a minimum of eight scans is required to enable phase cycling and suppress artefacts. The final p0 pulse then initiates acquisition of the free induction decay (FID).[93, 98] In untargeted metabolomics, 1D NOESY-presaturation is especially effective for detecting low-abundance metabolites in biofluids such as plasma or urine, where small-molecule signals are often obscured by water and macromolecular resonances.[57, 99] Presaturation selectively attenuates the water peak, reducing spectral distortion and improving quantification. Although based on the NOESY block structure, the sequence does not rely on NOE transfer; its robustness comes from efficient solvent and background suppression, providing reproducible performance across a wide range of biological samples.[60, 73]

1. 5. 2. 2. 2 The Carr-Purcell-Meiboom-Gill sequence

The CPMG pulse sequence is widely used in NMR-based metabolomics to enhance the detection of low-molecular-weight metabolites in complex biological matrices such as plasma, serum, and urine.[57, 60, 92, 99] It

exploits the spin-echo principle to attenuate signals from macromolecules, which exhibit short transverse relaxation times (T_2). Following a 90° RF pulse, a series of 180° refocusing pulses are applied at regular intervals to generate spin echoes and correct for magnetic field inhomogeneities.[93] Accurate calibration of the 180° pulse is essential to ensure efficient refocusing and reliable quantification. As the echo train evolves, signals from macromolecules decay rapidly due to their short T_2 values, whereas signals from small metabolites, with longer T_2 times, are preserved. The CPMG sequence thus acts as a T_2 filter, suppressing broad background signals and improving the spectral resolution and quantification of small molecules.[93] While highly effective for enhancing small-molecule detection, CPMG has limitations.[99] Metabolites with intrinsically short T_2 values may also be suppressed, potentially biasing quantification. Moreover, overlapping signals with similar T_2 relaxation times can complicate spectral deconvolution.[93, 97]

As described above, both NOESY and CPMG sequences typically incorporate water suppression, most commonly via presaturation, to improve spectral quality in complex biofluids.[81] In the case of CPMG, combining T_2 filtering with water suppression attenuates both macromolecular and solvent signals, enhancing the visibility of low-concentration metabolites, which is particularly effective for plasma and serum samples.[81, 97] Although signal loss may occur for metabolites near the water resonance or those with short T_2 values, CPMG remains one of the most widely used sequences in NMR metabolomics.

1. 5. 2. 2. 3 Water suppression in biofluid NMR metabolomics

As highlighted in the context of CPMG acquisition, water suppression is critical for improving spectral quality in NMR metabolomics. In biofluids such as plasma, serum, or urine, the dominant water signal can obscure low-abundance metabolites, compromising both identification and quantification.[96] Effective suppression of this signal is therefore essential, and a range of techniques has been developed, each with specific advantages and limitations depending on the sample matrix and analytical goal.[100]

A widely employed solvent suppression method is presaturation, where a continuous low-power RF pulse is applied at the water resonance during the relaxation delay preceding acquisition. This selectively saturates water protons, attenuating their signal and improving the observation of adjacent metabolite resonances. After a 1–3 second delay, a 90° RF pulse is applied to excite the remaining protons for signal acquisition.[93] While presaturation is simple and commonly used approach, it can partially or fully suppress signals from

exchangeable protons, particularly those involved in hydrogen bonding or undergoing rapid exchange with water.[96, 100] Nevertheless, several metabolomics pulse sequences, such as 1D NOESY and CPMG, incorporate presaturation modules to enhance spectral quality by simultaneously suppressing solvent and, in the case of CPMG, broad macromolecular signals.[81, 97] These integrated approaches provide robust solutions for improving the resolution and quantification of low-concentration metabolites in complex biofluids.

Another widely used solvent suppression technique is WATERGATE, which achieves effective water signal attenuation while preserving overall spectral resolution.[96, 100] This method employs selective excitation of the water resonance followed by a series of gradient and RF pulses that refocus and dephase water magnetisation, removing its contribution from the detected signal.[96] However, it may still result in sensitivity loss for metabolites resonating near the water peak. Additional methods, such as Delays Alternating with Nutations for Tailored Excitation (DANTE), offer greater flexibility by using tailored pulse trains to selectively suppress the water signal.[101] These approaches are particularly effective for precise separation of solvent and metabolite resonances, as the adaptability of the pulse sequence allows for optimisation based on sample-specific parameters such as water content and spectral complexity.

1. 5. 2. 3 NMR lipoprotein profiling

While proton NMR spectroscopy is widely used for the analysis of small molecules, it also enables the characterisation of larger molecular assemblies, such as lipoproteins. Although primarily studied in cardiometabolic contexts, lipoprotein alterations have been linked to neuroinflammation, blood–brain barrier dysfunction, and cognitive decline, highlighting their relevance in neurodegenerative disease.[81, 102]

Lipoproteins are spherical particles comprising a hydrophobic core of cholesterol esters and triglycerides, encased by a monolayer of phospholipids, unesterified cholesterol, and apolipoproteins,[103] which stabilise the structure and regulate interactions with enzymes and receptors. Based on density, size, and composition, lipoproteins are classified into chylomicrons, very-low-density lipoproteins (VLDL), low-density lipoproteins (LDL), and high-density lipoproteins (HDL).[103] Traditional diagnostic lipid panels measure total cholesterol concentrations but do not account for particle size, number, or composition - parameters increasingly recognised as more predictive of disease risk. [57, 81, 102, 104] Compared to these standard cholesterol assays, NMR offers a robust platform for the detailed characterisation of lipoprotein subclasses,

including quantification of particle size, particle number, and subclass distribution.[102] These parameters are derived from the aliphatic region of the ^{1}H NMR spectrum, which contains prominent methyl (-CH_3) and methylene (-CH_2-) signals originating from lipoprotein components.[57] The relaxation properties of these resonances reflect differences in molecular environment and mobility: core lipids show longer T_2 relaxation times and sharper signals, while surface lipids - being more restricted - yield shorter T_2 times and broader peaks.[93]

A key advantage of NMR-based profiling is its ability to resolve overlapping spectral features by exploiting subtle differences in chemical shift, line width, and signal intensity, allowing discrimination of lipoprotein subclasses.[104] For example, smaller, denser LDL particles produce broader signals that are slightly shifted to higher ppm values due to the more deshielded environments created by tighter lipid packing.[105] In addition to subclass differentiation, quantitative information on particle concentration can be obtained by integrating deconvolved signal areas, providing total particle counts per subclass.[102, 104] These measurements capture lipoprotein heterogeneity in structure and function, offering added value beyond conventional lipid panels.

1. 5. 2. 4 Clinical relevance of NMR metabolomics and application in this thesis

Given its precision, reproducibility, and suitability for high-throughput profiling, NMR spectroscopy plays a central role in the metabolomics analyses conducted in this thesis. Its ability to quantify both small-molecule metabolites and lipoprotein subfractions from a single serum sample is particularly relevant to the clinical studies in **Chapters 4 and 6**, where the focus is on disease stratification and biomarker discovery. However, given the low abundance of many metabolites in biological systems, including biofluids, NMR lacks the sensitivity required for comprehensive metabolome coverage. Consequently, MS-based metabolomics is often employed to extend coverage and access a broader range of metabolite classes.

1. 5. 3 Mass spectrometry-based metabolomics

MS complements NMR as a core analytical platform, offering distinct advantages in sensitivity, dynamic range, and molecular coverage. Widely adopted in both targeted and untargeted metabolomics workflows, MS can be coupled with diverse separation techniques to enhance metabolome coverage and quantitative results. This chapter provides a brief overview of the fundamental principles of MS, including the most commonly used ionisation techniques and mass analysers in metabolomics, with particular emphasis on

those employed in the research presented in this thesis. While several configurations exist, this thesis primarily employed electrospray ionisation (ESI) in combination with quadrupole-time-of-flight (Q-TOF) and quadrupole-Orbitrap (Q-Orbitrap) analysers. In addition, common chromatographic separation strategies are reviewed, with a focus on LC-MS workflows used in this study. The primary techniques discussed include RPLC, IC, HILIC, and supercritical fluid chromatography (SFC). Of these, RPLC and IC were used in **Chapter 6** to comprehensively screen treatment-induced alterations in the metabolome, while HILIC was used in **Chapter 5** for glycomics analysis in disease diagnosis.

A key step in MS analysis is the conversion of analytes into gas-phase ions, as compounds are detected and separated based on their mass-to-charge ratio (*m/z*). The core components of a mass spectrometer include the sample inlet, where the sample enters the system; the ion source, where ionisation of analytes occurs; the mass analyser, separating ions based on their *m/z*; and the detector, recording the ion signal.[106] Importantly, MS accommodates samples in solid, liquid, or gaseous form, depending on the ionisation technique used.

For solid samples, desorption-based ionisation is commonly employed, with matrix-assisted laser desorption/ionisation (MALDI) being among the most established techniques.[107] In MALDI, the sample is co-crystallised with a matrix on a metal target; a laser pulse excites the matrix, promoting gentle desorption and ionisation of analytes with minimal fragmentation.[108] Despite being widely used for the analysis of large biomolecules, particularly peptides and intact proteins, recent advances in matrix-assisted laser desorption/ionisation mass spectrometry imaging (MALDI-MSI) have extended its application to metabolomics, enabling the spatially resolved detection of small molecules directly from tissue sections.[109] This technique offers simultaneous chemical and anatomical information without the need for labelling or extensive sample preparation, making it particularly valuable for studying tissue-specific metabolic alterations, mapping metabolic pathways, and identifying disease-associated biomarkers.[109-111] MALDI-MSI has shown utility in diverse fields including oncology, neurodegeneration, and metabolic disease research. Moreover, its adaptation to minimally invasive sampling formats, such as dried blood spots, highlights its emerging role in point-of-care diagnostics and personalised medicine.[112, 113] Complementary ambient ionisation techniques - such as desorption electrospray ionisation (DESI)[111, 114] and direct analysis in real time (DART)[115] - further enhance the scope of spatial metabolomics by enabling rapid, *in situ* profiling of metabolites with minimal sample processing.

While spatially resolved techniques like MALDI-MSI offer valuable insights into metabolite localisation, GC-MS and LC-MS remain the primary approach for high-throughput metabolomics. Their scalability, reproducibility, and broad metabolite coverage have established LC-MS as a reliable platform for both discovery-driven studies and clinically oriented biomarker research.[60, 116]

1. 5. 3. 1 Ionisation techniques in mass spectrometry

A critical step in all MS-based workflows is ionisation, which enables the generation of charged species suitable for mass analysis. MS relies on the ionisation of analyte molecules to generate charged species that can be separated based on their *m/z* ratios. Ionisation techniques are broadly classified as hard or soft, depending on the degree of fragmentation induced during the ionisation process.[106] Hard ionisation methods, such as electron ionisation (EI), subject analytes to high-energy collisions, resulting in excessive fragmentation.[106, 117] While this can facilitate structural elucidation, it may also limit the detection of intact molecular ions. In contrast, soft ionisation techniques - such as electrospray ionisation (ESI), atmospheric pressure chemical ionisation (APCI), and MALDI - induce minimal fragmentation, allowing intact molecular species to be preserved and detected.[106, 117]

Among these, ESI is the most widely used ionisation method in metabolomics due to its compatibility with LC and its ability to ionise a wide range of polar and thermally labile metabolites.[60, 82] In ESI, analytes in solution are introduced into a high-voltage capillary, where an electric field induces the formation of charged microdroplets. A coaxial flow of inert gas, typically nitrogen, promotes solvent evaporation during droplet desolvation. As the solvent evaporates, charge density on the droplet surface increases (Fig. 1.3). When electrostatic repulsion exceeds the cohesive force of surface tension - a condition defined as the Rayleigh limit - the droplet becomes unstable and undergoes Coulombic fission, producing smaller progeny droplets with increased charge density. This process continues until desolvation is complete and gas-phase ions are formed.[106, 117] Final ion formation is described by two complementary models: the charge residue model (CRM), in which droplets shrink to a single ion, and the ion evaporation model (IEM), where ions are ejected from the droplet surface. Both likely operate in parallel, depending on analyte and solvent properties.[106, 117]

Depending on the ionisation mode, ESI can generate cations or anions, making it suitable for a wide variety of analytes. Ion formation is often enhanced by LC mobile phase additives that promote either protonation or deprotonation.[118, 119] For example, a small amount (~0.1%) of formic acid is commonly used to enhance

protonation in positive ion mode, while ammonium hydroxide or other basic modifiers can facilitate deprotonation in negative ion mode. In addition to the formation of protonated ($[M+H]^+$) or deprotonated ($[M-H]^-$) species during ESI, other adduct ions, such as sodium ($[M+Na]^+$) or potassium ($[M+K]^+$), may also form as a result of trace salt contamination in the mobile phase or sample matrix.[120] The presence of such adducts must be carefully considered during spectral interpretation, as they can affect relative abundance measurements, interfere with automated peak-picking algorithms, and complicate accurate metabolite identification.

1. 5. 3. 2 Mass analysers for untargeted metabolomics

Following ionisation, gas-phase ions are transferred into the mass analyser for separation based on their *m/z* ratios. A wide array of mass analysers has been developed, each offering distinct advantages in terms of resolving power, mass accuracy, scan speed, and dynamic range. These include low-resolution (LRMS) and high-resolution (HRMS) instruments, as well as hybrid configurations that combine complementary analyser types to enhance performance. In untargeted metabolomics, HRMS platforms are particularly valued for their ability to provide accurate mass measurements, enabling the resolution of molecular species with very similar masses. These attributes are also leveraged in proteomics, where the complexity of peptide mixtures necessitates high mass accuracy and resolution.[106, 117] For the purposes of this thesis, the following sections will predominantly focus on three representative mass analysers commonly employed in metabolomics workflows: the quadrupole, time-of-flight (TOF), and Q-Orbitrap analysers.

1. 5. 3. 2. 1 Quadrupole mass analyser

The quadrupole mass analyser is one of the most widely used LRMS instruments in metabolomics, either as a standalone device or, more commonly, in the triple-quadrupole (QqQ) configuration, particularly well-suited for targeted analyses that demand high sensitivity and reproducibility. Acting as a mass filter, the quadrupole selectively transmits ions based on their *m*/*z* ratios. The main components include four parallel cylindrical rods arranged in a square configuration, with opposing pairs connected to a direct current (DC) voltage and an oscillating RF voltage. As ions enter the quadrupole (Fig. 1.3 - quadrupole 1), they are subjected to an oscillating electric field that affects their trajectories. Only ions with specific *m*/*z* values exhibit stable oscillations and reach the detector, while others are destabilised and filtered out. By systematically adjusting the RF and DC potentials, the quadrupole can scan across a defined *m*/*z* range,

enabling rapid, sequential ion selection for mass analysis.[117] Notably, quadrupoles are frequently employed in tandem MS (MS/MS) set-ups, particularly in QqQ configurations. In this arrangement, the first quadrupole (Q1) isolates precursor ions, the second (q2) acts as a collision cell, typically filled with an inert gas such as argon, for fragmentation via collision-induced dissociation (CID), and the third (Q3) analyses the resulting product ions (Fig. 1.3).[121] This configuration enables targeted quantification and structural elucidation of analytes with high sensitivity and specificity, particularly in selected reaction monitoring (SRM) and multiple reaction monitoring (MRM) modes.[117, 121]

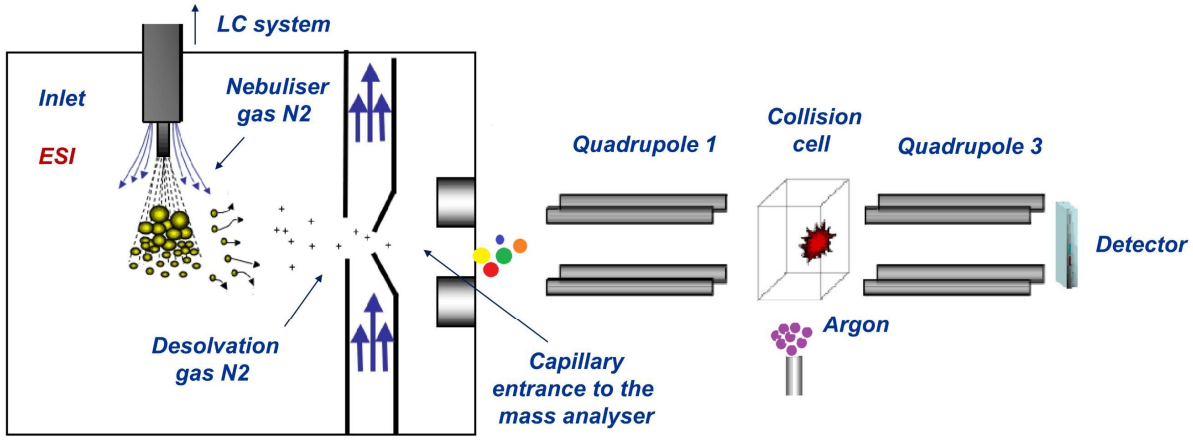

Figure 1.3. Schematic representation of electrospray ionisation (ESI) coupled with a triple quadrupole (QqQ) mass spectrometer. In ESI, a high voltage is applied to a liquid sample emerging from the LC system, producing a fine aerosol of charged droplets, which are desolvated by a stream of nitrogen gas to release ions. The triple quadrupole mass spectrometer consists of three main parts: Quadrupole 1 (Q1) selects precursor ions based on their mass-to-charge ratio (*m/z*); the collision cell induces fragmentation of selected ions via collision-induced dissociation with an inert gas (argon); and Quadrupole 3 (Q3) analyses the resulting fragment ions, which are then detected for quantification. Figure created by the author based on references [117, 121].

In metabolomics, QqQ systems are primarily utilised for targeted analyses, offering precise quantification of predefined metabolites in complex biological matrices.[122, 123] Their robustness, rapid duty cycle, and high sensitivity make them particularly suitable for validation studies, clinical assays, and biomarker quantification. Although limited in resolution compared to high-resolution platforms, quadrupole-based systems remain indispensable for routine and large-scale quantitative metabolomics applications.

1. 5. 3. 2. 2 Time of flight mass analyser

In contrast to quadrupole analysers, TOF analysers offer HRMS analysis by separating ions based on their velocities after acceleration in a uniform electric field. Since all ions receive the same kinetic energy, their velocities become inversely proportional to the square root of their *m/z* (equations 1.6 and 1.7). As a result,

lighter ions travel faster and reach the detector before heavier ones. By measuring the time taken for each ion to traverse the flight tube ("the flight time") the corresponding *m/z* is determined with high accuracy.[106]

$$E_k = \frac{1}{2}mv^2 = zeV \tag{1.6}$$

Where m = ion mass (kg), v = ion velocity (m/s), z = charge state, e = elementary charge (1.602×10^{-19} C), and V = accelerating voltage (V). Expressing v from this equation then clearly shows the inversely proportional relationship between v and square root of the corresponding *m/z*.[117]

$$v = \sqrt{\frac{2zeV}{m}} \tag{1.7}$$

To improve mass resolution, TOF systems often utilise extended flight paths or incorporate a reflectron – an electrostatic ion mirror that reverses the trajectory of ions. Reflectrons compensate for slight variations in kinetic energy among ions of the same *m/z,* thereby improving mass accuracy and peak sharpness without increasing instrument size.[117] TOF-based platforms are particularly well-suited for metabolomics due to their short acquisition time, broad mass detection range, and capacity for accurate mass measurement across complex mixtures. These capabilities enable comprehensive untargeted profiling, allowing for the simultaneous detection of thousands of metabolite features with high fidelity.

A common hybrid configuration is the Q-TOF mass spectrometer, which integrates the ion filtering and precursor selection capabilities of a quadrupole with the high-resolution detection of a TOF analyser.[117] Q-TOF systems are widely used in metabolomics for both untargeted screening and structural elucidation, enabling MS/MS analysis with high sensitivity and mass accuracy for both precursor and fragment ion.[82] In this thesis, Q-TOF instruments are used primarily for untargeted profiling of medium-polar compounds and lipids, typically coupled with RPLC or SFC. Although these pairings are common, Q-TOF platforms remain highly versatile and compatible with various ionisation techniques and chromatographic modes, depending on analytical objectives.

1. 5. 3. 2. 3 Ion trap mass analyser

While Q-TOF systems excel in high-resolution MS/MS analysis, ion traps offer a complementary advantage through their capacity for detailed, multi-stage fragmentation (MS^n), making them especially valuable for structural elucidation. The ion trap is a mass analyser that stores ions using oscillating electric fields,

allowing controlled isolation, fragmentation, and detection. In the common quadrupole ion trap (QIT), ions are confined in a three-dimensional potential well and sequentially ejected by varying the RF voltage.[106] This enables robust MS^n, making ion traps particularly useful for structural elucidation and targeted metabolite analysis. Although ion traps offer lower resolution and mass accuracy than TOF or Orbitrap systems, they provide high sensitivity and are often integrated into hybrid instruments.[117] Their capacity for in-depth fragmentation makes them valuable for targeted metabolomics and drug metabolism studies.

1. 5. 3. 2. 4 Orbitrap mass analyser

Despite being the most recent mass analyser technology, the Orbitrap has become one of the most widely used HRMS platforms in untargeted metabolomics, valued for its exceptional mass accuracy, resolving power, and dynamic range. Unlike TOF or ion trap systems, which rely on flight time or sequential ion ejection, the Orbitrap separates ions based on their oscillation frequencies within an electrostatic field. It consists of a central spindle-shaped electrode surrounded by a coaxial barrel-like electrode, with a strong electrostatic potential generated between them. Ions are initially accumulated in a curved linear trap (C-trap) and then injected as a coherent ion packet into the Orbitrap.[124] Upon injection, ions orbit the central electrode while simultaneously oscillating along the axial (z) axis. The frequency of this axial motion is inversely proportional to the square root of the ion m/z and is largely independent of initial ion energy or spatial dispersion. The resulting image current induced by the axial oscillation is measured over time and converted to a mass spectrum via Fourier transformation, yielding exceptionally high mass resolution and accuracy.[106, 117, 124] Orbitrap platforms are particularly well suited to untargeted metabolomics and lipidomics, where the ability to distinguish isobaric species and detect low-abundance compounds is critical. The high mass accuracy and resolving power also support proteomic applications, including both data-dependent and data-independent acquisition strategies for reliable peptide identification and quantification. To expand analytical flexibility, Orbitrap analysers are often coupled with quadrupole mass filters in Q-Orbitrap hybrid configurations, which combine precursor ion selection with high-resolution mass detection, supporting both targeted and discovery-driven analyses across diverse sample types.[74, 117, 125] In this thesis, a Q-Orbitrap platform is used for glycomics analysis (**Chapter 5**), providing high-resolution characterisation of *N*-glycan structures. In parallel, a Q-Orbitrap mass spectrometer is employed for untargeted metabolomics, primarily in combination with IC to enhance coverage of polar and charged metabolites (**Chapters 2, 3, and 6**). While

IC is the main separation technique used throughout this work, both Orbitrap and Q-Orbitrap platforms are fully compatible with a range of chromatographic methods, which can be selected based on the physicochemical properties of the analytes of interest.

1. 5. 4 Chromatographic strategies for enhancing MS-based metabolomics

Since mass spectrometers operate on gas-phase ions and biological samples typically contain thousands of co-eluting species, chromatographic separation is essential to reduce complexity, improve quantification, and maximise metabolome coverage. While direct infusion MS (DI-MS) offers rapid analysis, it often suffers from ion suppression and limited resolution in complex matrices. To overcome these limitations, MS is often coupled with LC, GC, or SFC.[90, 126, 127] Each technique offers unique advantages based on analyte properties, but none provides complete metabolome coverage. A multiplatform approach using orthogonal chromatographic systems is therefore considered the gold standard in untargeted metabolomics (Fig. 1.4)[89] By broadening metabolite class coverage and improving sensitivity to low-abundance compounds, integrated workflows enhance both reproducibility and the robustness of systems-level metabolic profiling.[82, 90]

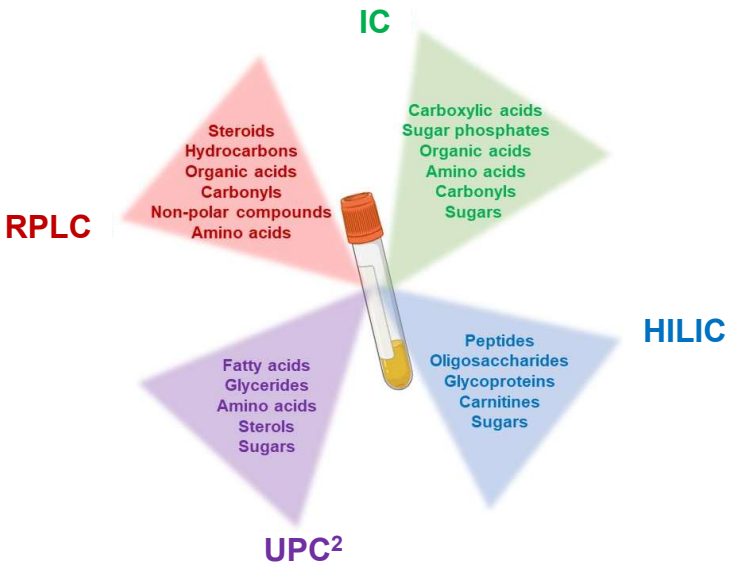

Figure 1.4. Expanded metabolome coverage achieved through the integration of multiple chromatographic platforms. Metabolite classes detectable by reversed-phase liquid chromatography (RPLC), ion chromatography (IC), hydrophilic interaction liquid chromatography (HILIC), and supercritical fluid chromatography (UPC^2/SFC) are shown. Combining complementary separation techniques substantially enhances the breadth of detectable metabolites across chemical classes.

Among the available chromatographic techniques, GC-MS and RPLC-MS remain the most widely adopted in metabolomics. GC-MS is particularly suited for volatile and thermally stable compounds, such as short-chain fatty acids (SCFAs), certain PUFAs, and ketone bodies.[128] However, it often requires chemical derivatisation to enhance compound volatility and thermal stability.[129] This additional processing step can

introduce variability, complicate quantification, and reduce throughput, particularly when reactions are incomplete.[129] Given that many of these metabolites are also accessible by LC-MS, particularly when combined with ESI, LC-MS is generally preferred for its broader applicability and reduced sample preparation demands.[130, 131] RPLC-MS, although effective for moderately polar and lipophilic metabolites, provides limited retention of highly polar compounds, analytes that are abundant in biofluids and central to many metabolic pathways.[132] To address this gap, alternative separation methods have been introduced, including mixed-mode chromatography,[133] HILIC,[134] and IC.[74] In addition, SFC–MS has emerged as a promising platform, particularly for untargeted lipidomics, offering high throughput and improved resolution for non-polar and amphiphilic species (Fig. 1.4).[126]

1. 5. 4. 1 Reversed-phase liquid chromatography

RPLC-MS is among the most established analytical platforms, both globally and within metabolomics, offering broad coverage for medium to non-polar compound.[135, 136] The system uses a non-polar stationary phase, most commonly octadecylsilane (C18), to facilitate hydrophobic interactions with analytes. Although both isocratic and gradient elution can be applied, gradient elution is generally preferred in untargeted metabolomics to separate a wider range of metabolites. This approach typically uses a polar weak solvent (e.g., water) and a strong organic solvent (e.g., methanol or acetonitrile); by gradually increasing the proportion of the organic phase, analyte retention is reduced and elution is facilitated (Fig. 1.5).[82, 135, 136]

Despite its versatility, RPLC is generally unsuitable for highly polar or ionic metabolites, which exhibit poor retention and often elute close to the column void volume. In some instances, chemical derivatisation may be used to modify the physicochemical properties of polar compounds to improve retention;[137] however, derivatisation introduces additional complexity, potential artefacts, and may reduce analytical throughput. Although specialised RP columns have been developed to enhance the retention of polar compounds, achieving sufficient separation, particularly retention beyond the void volume, remains challenging. Consequently, alternative chromatographic methods, such as HILIC or IC, are often preferred for the analysis of polar and ionic metabolites.[74, 132, 134, 138] Given these limitations, RPLC was employed throughout this thesis (**Chapters 2, 3, and 6**) for the untargeted analysis of medium to less polar compounds, but consistently integrated with orthogonal analytical platforms to ensure broader overall metabolome coverage.

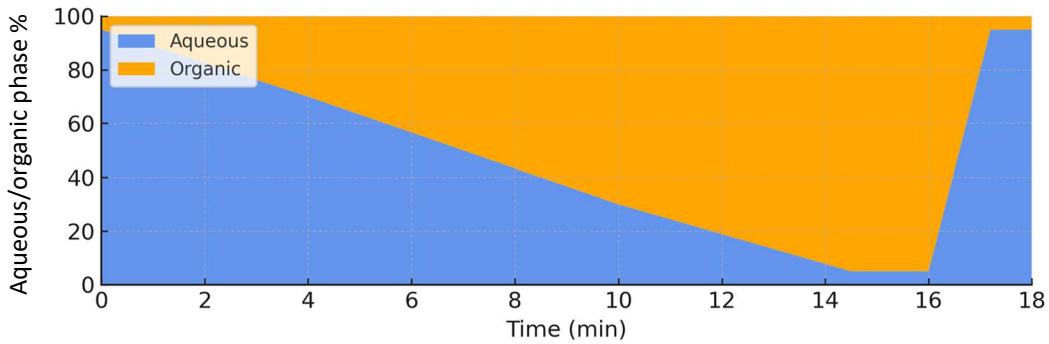

Figure 1.5. Example of a reverse-phase liquid chromatography (RPLC) gradient method for metabolomics (18 min total run time). The gradient starts with high aqueous content (95%) and transitions to high organic (typically MeOH or MeCN) content, allowing for the elution of a broad range of compounds with diverse polarities. This method supports comprehensive metabolite coverage across both polar and non-polar analytes.

1. 5. 4. 2 Hydrophilic interaction liquid chromatography

HILIC-MS has emerged as a key platform in untargeted metabolomics for profiling polar metabolites.[138] HILIC employs a polar stationary phase, such as amide, zwitterionic, or bare silica, combined with a predominantly organic mobile phase, usually 60-70% acetonitrile.[134, 139] This configuration promotes the formation of a water-enriched layer on the surface of the stationary phase, providing a medium into which polar metabolites partition. Retention is governed by a combination of hydrophilic partitioning, hydrogen bonding, electrostatic interactions, and dipole–dipole forces. As the aqueous content of the mobile phase increases, these interactions are progressively disrupted, leading to analyte elution.[134, 138] However, this intricate interplay of retention mechanisms often necessitates careful method development and rigorous column equilibration to ensure reproducible performance. Variability in retention time and peak area, along with difficulties in predicting elution order, can compromise reproducibility, which is an important consideration in large-scale untargeted metabolomics.[134] Furthermore, sample preparation must be adapted to the high organic content of the mobile phase required for HILIC, which may reduce the solubility and ionisation efficiency of certain highly polar analytes, particularly at higher concentration. Nonetheless, when optimally configured, HILIC provides superior resolution for specific polar metabolite classes. In this thesis, it was employed in **Chapter 5** for plasma *N*-glycan profiling, facilitating detailed structural characterisation relevant to disease stratification.

1. 5. 4. 3 Ion chromatography

Historically, IC was used primarily for the detection of inorganic compounds. However, recent advances, particularly the development of electrolytic ion suppressors, have enabled IC-MS coupling and expanded its

application to metabolomics, where it is now valued for analysing highly polar and ionic metabolites, especially in cases where other methods are inadequate.[132] In IC, separation is based on electrostatic interactions between charged analytes and stationary phase materials functionalised with oppositely charged groups.[132, 140] Depending on the nature of the target compounds, IC can operate in either cation- or anion-exchange mode. In metabolomics, anion-exchange chromatography (AEC) is more commonly applied due to its suitability for separating negatively charged metabolites such as organic acids, sugar phosphates, and nucleotides.[74, 125, 132]

In AEC, separation is achieved via reversible electrostatic interactions between anionic metabolites and a positively charged resin-based stationary phase. Analytes are eluted by increasing the ionic strength of the mobile phase, typically using a hydroxide ion gradient (e.g., KOH), displacing analytes according to their binding affinity.[74, 132] To render the mobile phase MS-compatible, an ion suppressor is employed downstream of the analytical column. Protons generated electrolytically from water combine with hydroxide ions to form neutral water, while residual cations (e.g., K^+ from KOH eluents) are removed via a semi-permeable membrane (Fig. 1.6).[141] This results in a low-conductivity aqueous eluent containing only the resolved analyte ions, which are readily introduced into the electrospray ion source for MS analysis.[132]

This setup allows for highly selective and reproducible detection of ionic metabolites without the need for derivatisation or organic modifiers, supporting robust metabolomic profiling of biofluids, tissues, and cellular extracts with minimal sample preparation.[132]

Throughout this thesis, IC-MS, specifically AEC-MS, was employed alongside RPLC-MS to provide complementary metabolome coverage across various untargeted analyses (**Chapters 2, 3, and 6**). Given the relative novelty of IC in metabolomics and the predominance of prior applications within *in vitro* systems, this work represents one of the first comprehensive uses of IC-MS for profiling human biofluids.

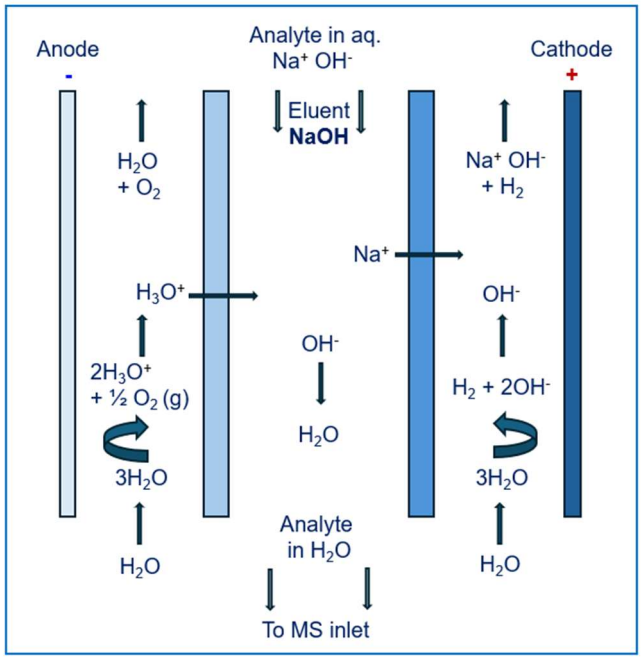

Figure 1.6. Schematic representation of an ion suppressor mechanism for the chemical neutralisation of hydroxide-based eluents following anion-exchange chromatography, enabling conversion of the analyte matrix to pure water prior to mass spectrometry detection. Figure adapted from: [141]

1. 5. 4. 4 Supercritical fluid chromatography

SFC remains a relatively underutilised yet increasingly valuable platform in omics research. With broad applicability to non-polar and moderately polar compounds, its modern implementation, ultra-performance convergence chromatography (UPC^2-MS), has re-emerged as a powerful tool in both metabolomics and lipidomics.[126, 142] SFC employs supercritical CO_2 as the major component of the mobile phase, often modified with polar organic solvents, enabling separations akin to normal-phase chromatography while offering operational simplicity comparable to RPLC.[143, 144] The low viscosity and high diffusivity of supercritical CO_2 enable faster mass transfer, leading to shorter analytical run times, lower solvent usage, and improved throughput. Earlier limitations in robustness and quantitative reproducibility constrained the use of SFC in bioanalysis; however, recent advances in instrumentation and stationary phase materials have significantly enhanced method stability, sensitivity, and peak resolution.[143, 144] In particular, novel stationary phases, such as ethylene-bridged hybrid (BEH) materials and modified silica particles, have expanded SFC applicability to a wider range of analytes, including polar and chiral compounds.[145]

While SFC has been well established in targeted analyses, including enantiomeric separations in clinical pharmacokinetics and anti-doping studies,[146, 147] its application to untargeted metabolomics remains relatively limited. Nonetheless, recent work by Wolrab *et al.* has demonstrated that SFC-MS/MS can extend

beyond traditional lipid profiling to capture polar metabolites, such as serotonin and melatonin from the tryptophan pathway, when coupled with appropriate extraction strategies.[148] Moreover, Yamada *et al.* showed that coupling SFC with Orbitrap-MS enables rapid, comprehensive lipid profiling by capturing both fatty acid composition and headgroup polarity, highlighting its potential for biomarker discovery and disease stratification in lipid-related disorders, and complementing NMR-based approaches.[149]

1. 5. 5 Multi-LC-MS analysis expands metabolome coverage

Compared to NMR, LC-MS, particularly when coupled with HRMS, offers markedly higher sensitivity and broader metabolite coverage. A key strength of LC-MS lies in its adaptability to orthogonal chromatographic approaches, as demonstrated in **Chapters 2 and 3**, where method optimisation and multiplatform workflows enabled more comprehensive metabolic profiling and internal cross-validations. This versatility extends to clinically-relevant applications, with **Chapter 5** showcasing its role in glycomics and **Chapter 6** illustrating its capacity to support large-scale metabolomics studies.

1. 6 Metabolomics data processing and metabolite identification

Given that one of the overarching aims of this thesis is to integrate multi-platform datasets generated by both LC-MS and NMR, robust and harmonised data analysis is essential for reliable interpretation. A critical first step is the careful processing of raw data, as the complexity and variability of metabolomics datasets requires appropriate pre-processing to ensure statistical and biological efficiency and validity.[150, 151] Following raw metabolomics data acquisition, spectral alignment and peak integration are essential for cross-sample comparability and must precede any form of metabolite quantification. Once a feature matrix is obtained, additional pre-processing, such as handling missing values, filtering low-quality features, correcting batch effects, and applying appropriate transformation, normalisation, and scaling, is required to minimise technical variability and ensure robust, interpretable statistical and ML analyses.[150]

1. 6. 1 Pre-processing and quality control in NMR and MS metabolomics

Metabolomics data processing begins with raw spectral handling using vendor-specific software aligned with the instrumentation. In NMR-based workflows, raw FIDs are typically processed using TopSpin (Bruker) or historically VNMRJ (Varian), which enables Fourier transformation, phasing, baseline correction, and spectral alignment. For LC-MS data, processing is inherently instrument-dependent. In this

thesis, data were acquired using Waters and Thermo Fisher platforms, with MassLynx and Xcalibur software used, respectively, for initial data inspection and export.

To ensure analytical robustness, quality control (QC) samples - typically pooled aliquots representative of the study cohort - are injected at regular intervals throughout the LC-MS acquisition to monitor system stability, sensitivity, and reproducibility.[152, 153] In NMR spectroscopy, pooled serum or plasma samples are similarly used as QC references across the analytical run.[152, 154] Additionally, given the inherent susceptibility of LC-MS systems to both retention time drift and fluctuations in ion intensity, the inclusion of analytical standards is a critical component of robust metabolomics workflows.[154] Standards may consist of compound mixtures prepared in solvent, which are used for retention time alignment and compound identification in targeted or semi-targeted analyses. Alternatively, internal standards can be spiked into either QC samples or directly into biological samples to correct for matrix effects, such as ion suppression or enhancement.[153, 154] In targeted workflows, the use of isotope-labelled standards (e.g., deuterium-labelled analogues) is common, allowing for compensation of compound degradation and providing improved accuracy in quantification.[155] Collectively, these strategies ensure data quality, support analytical reproducibility, and facilitate the detection and correction of technical variability prior to statistical analysis.

1. 6. 2 Integration and pre-processing strategies in ^{1}H NMR data analysis

Following spectral acquisition and alignment, the subsequent step in ^{1}H NMR data processing involves extracting integral values from the spectra. Several software platforms - both commercial and open-source - are commonly employed for this purpose, including ACD/Labs, NMRProcFlow,[156] and MestReNova. While differing in interface and usability, these tools generally employ comparable algorithms for spectral pre-processing and integration. A critical pre-processing step involves the removal of spectral regions that are biologically uninformative or prone to introducing artefacts in downstream analyses. These typically include the spectral region below ~0.5 ppm and above ~10 ppm, both of which are often dominated by noise; the water resonance (~4.7 ppm in D_2O), which can obscure neighbouring signals; and peaks arising from internal reference standards (e.g., maleic acid, 4,4-dimethyl-4-silapentane-1-sulfonic acid (DSS), or tetramethylsilane (TMS)),[157] which are excluded to prevent distortion of spectral normalisation.

Spectral integration may then proceed via two main approaches. Manual integration involves assigning and quantifying individual peaks, allowing precise metabolite-specific annotation but requiring considerable time and operator expertise. Alternatively, the spectrum can be divided into uniform segments, commonly 0.1–0.2 ppm wide, in a process known as "*bucketing*" or "*binning*".[156] While this method may split individual peaks across multiple bins, it offers a consistent and reproducible strategy that minimises variability introduced by subjective interpretation. Recently, advanced algorithms, including AI-based tools, automate peak detection and integration, combining manual accuracy with scalable automation.

1. 6. 3 Alignment, feature annotation, and drift correction in LC-MS

Similar to NMR workflows, several software platforms are available for LC-MS data processing, ranging from open-source to commercial solutions. Common open-source tools include MZmine,[158] which supports feature detection, alignment, and deconvolution in untargeted workflows, and Skyline,[159] widely used for targeted quantitative analysis. LaCyTools is specialised for high-throughput quality control and quantification of targeted and semi-targeted datasets.[160] Among commercial options, Progenesis QI offers an integrated environment for feature extraction, alignment, normalisation, and database-driven annotation. Other frequently used platforms include XCMS[161] and MS-DIAL,[162] which are particularly common in untargeted metabolomics and lipidomics for peak picking and spectral deconvolution.

LC-MS data analysis involves several key steps, beginning with spectral alignment, usually referenced to a pooled QC sample, to correct for retention time shifts across the run. This is followed by peak detection (or "*peak picking*"), which requires careful parameter optimisation to accurately identify chromatographic features corresponding to individual compounds.[150, 154] Subsequent deconvolution enables the resolution of co-eluting species and the identification of related ion forms, such as adducts, isotopologues, and in-source fragments. Feature annotation and compound identification are then performed through database matching, spectral libraries, or analytical standards, followed by manual or semi-automated review.[163] QC samples and internal standards are employed throughout the run to monitor system performance and assess feature stability.[163, 164] Metrics such as the coefficient of variation (CV) are used to evaluate reproducibility, with typical thresholds of 30% for untargeted and 15% for targeted metabolomics.[164]

Since metabolite annotation serves as the critical bridge between analytical data and biological interpretation, it is essential to report the confidence of each identification transparently. The Metabolomics Standards Initiative (MSI) provides a widely adopted tiered framework for classifying levels of metabolite identification confidence (Table 1.1).[165, 166] Throughout this thesis, all reported metabolites comply with MSI Level 1 identification, confirmed by comparison with authentic reference standards, unless stated otherwise.

Another critical aspect of LC-MS data pre-processing, particularly in large-scale studies, is the correction of signal intensity drift. This phenomenon typically arises from progressive alterations in instrument sensitivity, accumulation of endogenous matrix components, such as proteins and lipids, in the ionisation source (particularly during analysis of blood and tissue), and environmental variability, including fluctuations in temperature and humidity.[154, 167, 168] Uncorrected drift can significantly impair inter-sample comparability, attenuate biological signals, and introduce systematic error into downstream statistical modelling.

Table 1.1. Levels of metabolite identification confidence as defined by the Metabolomics Standards Initiative.[166]

Identification level	Description	Minimum analytical data requirement
Level 0	Identified (3D structure)	Comprehensive three-dimensional structural elucidation from isolated pure compounds.
Level 1	Identified (2D structure)	Two independent and orthogonal properties - such as retention time and mass spectrum, accurate mass and isotope pattern, or $^{1}H/^{13}C$ and 2D NMR spectra - are compared to those of an authentic standard measured under identical conditions.
Level 2	Annotated compounds	Matching experimental measurements to literature values reported for authentic compounds by other laboratories or listed in public databases, without requiring direct analysis of an authentic standard.
Level 3	Characterised compounds	A reproducible spectral signal is observed, and the associated physicochemical properties are consistent with those expected for the specific compound class.
Level 4	Unknown compounds	A reproducible spectral signal is identified and quantifiable using NMR, MS, or another technique.

To correct for signal drift, computational algorithms use QC sample intensities to model temporal trends and adjust feature values in biological samples accordingly. One widely adopted approach is Locally Estimated Scatterplot Smoothing (LOESS) regression, a non-parametric technique that fits a locally weighted curve to the QC data for each feature, enabling the correction of intra-batch variation with minimal assumptions about the underlying trend (Fig. 1.7).[82, 154, 164, 168] A number of computational tools have been developed to facilitate QC-based drift correction. Open-source packages in Python and R, such as *statTarget*,[169] *batchCorr*,[167] and *normalyzerDE*,[170] include functionality for QC-based drift correction. In addition, platforms such as *MetaboDrift* offer dedicated workflows for visualising and correcting drift using robust curve-fitting algorithms.[168] In this thesis, *MetaboDrift* was employed as the primary approach for drift correction due to its flexibility, ease of implementation, and visual diagnostic outputs that support quality control throughout the pre-processing pipeline (Fig. 1.7, 1.8).

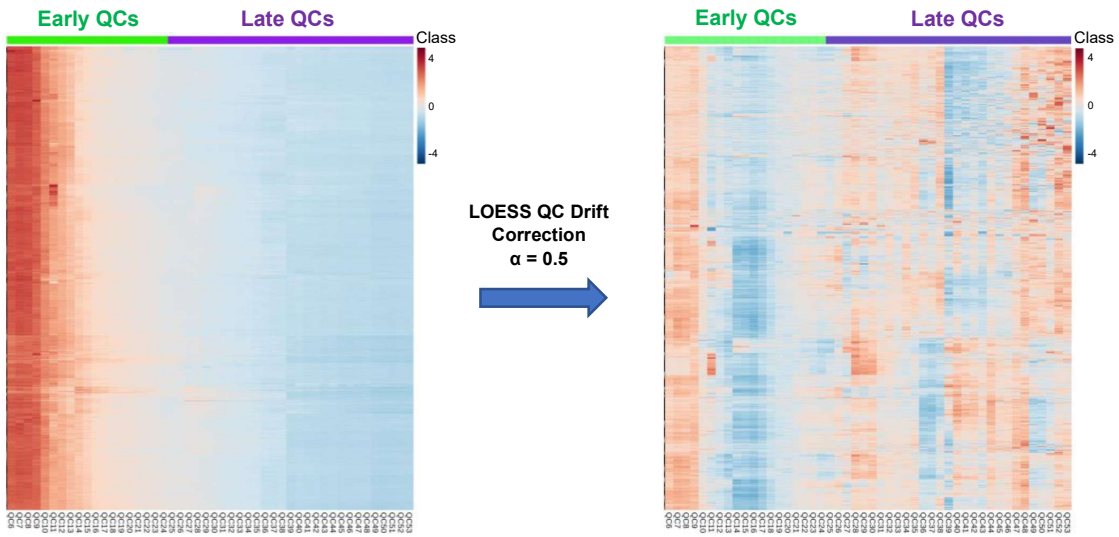

Figure 1.7. Effect of LOESS-based drift correction on RPLC-MS signal intensities in positive ion mode. Heatmaps of scaled feature intensities from early (green, injection 5–20) and late (purple, injection 21-50) QC samples in a large-scale serum metabolomics dataset (n = 400), acquired using reversed-phase LC-MS in positive ion mode. **Left:** Raw data show a pronounced intensity gradient due to signal drift over time, with early QCs exhibiting systematically higher responses. **Right:** After LOESS correction (α = 0.5) applied using *MetaboDrift*,[168] the drift is effectively minimised, yielding more consistent feature intensities across the run. This correction enhances data quality and comparability, supporting robust downstream statistical analyses.

1. 6. 4 Data transformation, normalisation, and scaling for omics analysis

Following initial pre-processing and feature extraction, metabolomics data undergo further refinement to ensure suitability for multivariate statistical modelling and ML workflows. This includes systematic

handling of missing values, appropriate normalisation, data transformation, and scaling, each essential for mitigating technical artefacts and improving the interpretability of underlying biological variation.

Missing values are common in untargeted metabolomics due to intermittent detection near the limit of quantification or inconsistencies in peak alignment. Appropriate imputation strategies, such as *k*-nearest neighbours (KNN), probabilistic principal component analysis (PCA), or replacement with a small constant (e.g., half-minimum), are required to avoid bias and preserve statistical power.[171, 172] The optimal method depends on the extent and structure of missingness, as improper imputation can distort downstream analyses.

Following imputation, additional post-processing steps are required to correct for sample-to-sample variability, heteroscedasticity, and differences in measurement scale.[173] Normalisation mitigates technical variation arising from differences in sample preparation, injection volume, or total ion count. Common approaches include median, sum, or quantile normalisation to align intensity distributions across samples. Transformation is applied to stabilise variance and reduce skewness in feature distributions, with log transformation being frequently used to approximate normality and diminish the influence of extreme values. Scaling adjusts for disparities in units or dynamic range, ensuring that all variables contribute comparably to multivariate models. Auto-scaling (mean-centred and scaled by the standard deviation (SD)) and Pareto-scaling (scaled by the square root of the SD) are widely used in metabolomics workflows.[173, 174]

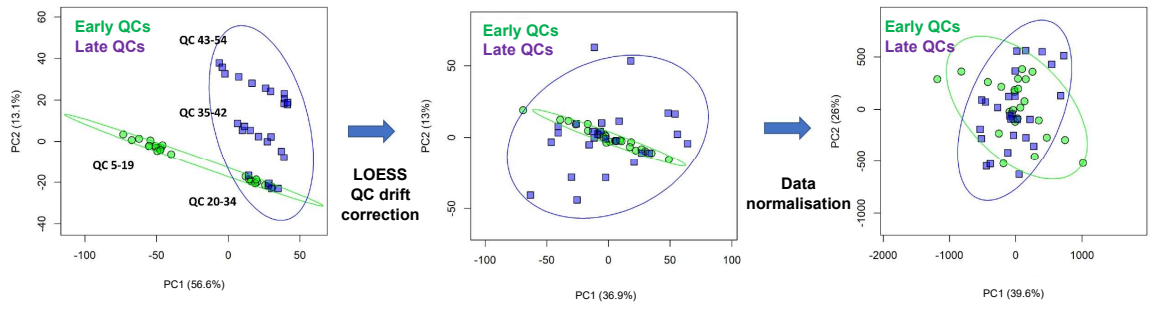

Figure 1.8. Correction of signal drift and data normalisation in untargeted LC-MS serum metabolomics. Principal component analysis (PCA) of QC samples (green = early QCs (injection 5–20), blue = late QCs (injection 21–50)) from a 400-sample serum metabolomics run (reversed-phase liquid chromatography mass spectrometry; positive ion mode). **Left:** PCA of raw data reveals systematic drift along PC1, reflecting temporal signal instability across the run. **Middle:** LOESS-based drift correction (α = 0.5), applied via *MetaboDrift*,[168] reduces the separation between early and late QCs by accounting for time-dependent intensity variation. **Right:** Further processing with sum normalisation, log transformation, and *z*-score scaling harmonises feature distributions across samples. This sequential correction and normalisation strategy enables convergence of QC samples over time, minimising platform-derived technical variation.

Collectively, these data processing steps provide a robust foundation for downstream statistical modelling, pattern recognition, and predictive analysis. In studies involving the integration of multiple analytical methods, an additional challenge arises from the heterogeneous nature of the data generated across platforms. When integrating datasets such as NMR, LC-MS, targeted protein assays, or clinical measures, raw intensity scales often differ substantially. In such cases, standardisation using *z*-scores (mean = 0, SD = 1) is essential to harmonise variable magnitudes while preserving each variable's relative structure within its respective platform.[175] This approach facilitates integrated multivariate analysis and clustering across heterogeneous datasets. In this thesis, different data processing strategies were applied depending on the analytical platform and study design; however, *z*-score standardisation was generally employed for multi-platform integration to ensure comparability and maintain biological interpretability in downstream analysis (Fig. 1.8).

1. 7 Statistical analysis of omics datasets

Once datasets have been processed and a data table produced, statistical analysis becomes the next critical step in identifying biologically meaningful differences between groups or predicting clinical outcomes. Univariate methods - such as t-tests, analysis of variance (ANOVA), and linear regression - are commonly used to evaluate individual variables, typically corrected for multiple testing using false discovery rate (FDR) procedures. While informative, univariate approaches do not account for interdependencies among variables and may overlook multivariate patterns. In contrast, multivariate statistical and ML methods analyse multiple features simultaneously, allowing for dimensionality reduction, classification, and discovery of complex biological signatures. The following sections describe the application of multivariate supervised approaches, orthogonal partial least squares discriminant analysis (OPLS-DA) and random forest, chosen for their complementary strengths and suitability for high-dimensional omics data.

1. 7. 1 Multivariate analysis and machine learning for metabolomics

Given the substantially higher number of variables relative to the number of samples, dimensionality reduction through multivariate analysis is essential to mitigate overfitting and enhance model interpretability. These methods can be broadly categorised as either supervised or unsupervised, depending on whether sample class information is incorporated during model construction.[176, 177] The most widely used unsupervised approach is PCA, which is particularly effective in scenarios involving pronounced metabolic

shifts, such as drug-induced reprogramming within *in vitro* systems. In contrast, clinical studies aimed at detecting subtle metabolic differences, typically require more advanced supervised ML methods to achieve sufficient sensitivity and specificity.[176, 177] While a variety of ML algorithms can be applied to high-dimensional omics data, this thesis primarily focuses on two supervised methods: OPLS-DA and random forest. These approaches were selected based on their widespread use in metabolomics, suitability for handling multicollinearity, and complementary strengths in classification and feature selection. Due to the supervised nature of both methods, rigorous validation is essential to mitigate overfitting and ensure robust, generalisable results. The implementation and evaluation of OPLS-DA and random forest models are described in more detail in the following sections.

1. 7. 1. 1 OPLS-DA: model construction, validation, and interpretation

OPLS-DA is a supervised multivariate modelling technique widely used in metabolomics for dimensionality reduction and class discrimination. Its primary objective is to maximise separation between predefined groups, such as patients and healthy controls, or treated versus untreated individuals, while simultaneously identifying the features most responsible for this distinction. OPLS-DA builds upon the basic framework of partial least squares (PLS) by introducing an orthogonal signal correction, which removes variation in the predictor matrix (X) that is unrelated to the response variable (Y). In standard PLS, the method identifies linear combinations of predictors that maximise the covariance between X and Y, thereby modelling their relationship while simultaneously reducing dimensionality.[178] However, traditional PLS does not explicitly partition variance into predictive and non-predictive components, which may result in models being influenced by systematic variation unrelated to the dependent variable. OPLS-DA addresses this limitation by partitioning the variance in X into predictive components (associated with group differences) and orthogonal components (unrelated to group separation). As a result, the first component in OPLS-DA captures the variation directly linked to class discrimination, while the orthogonal components account for non-predictive variation, such as biological or technical noise. This separation yields a more interpretable model, in which the components reflect the true underlying structure relevant to the biological question rather than confounding factors.[178] By projecting the data into a lower-dimensional space optimised for class separation, OPLS-DA enhances both the clarity and robustness of the resulting model.

The performance of the OPLS-DA model is typically assessed through cross-validation, often employing a 10-fold approach in combination with permutation testing to ensure model robustness and to mitigate the risk of overfitting (Fig. 1.9). In 10-fold cross-validation (applied in this thesis), the dataset is split into ten subsets; the model is iteratively trained on nine subsets and validated on the remaining one, with this process repeated across all subsets. To further enhance model robustness and interpretability, a feature selection step, such as least absolute shrinkage and selection operator (LASSO) regression or other regularisation techniques, can be implemented to prioritise the most informative variables and reduce dimensionality (Fig. 1.9).[81] Model performance is then quantified using metrics such as R^2 and Q^2. R^2 represents the proportion of variance in the data explained by the model (goodness of fit), while Q^2 reflects the model predictive ability, indicating how accurately it generalises to independent, unseen data.[179] Ideally, both R^2 and Q^2 values should exhibit high magnitudes, demonstrating both a strong fit and reliable predictive performance. Discrepancies between these metrics, such as a high R^2 coupled with a low Q^2, may suggest overfitting, whereas simultaneously low values indicate poor model performance.[178, 179]

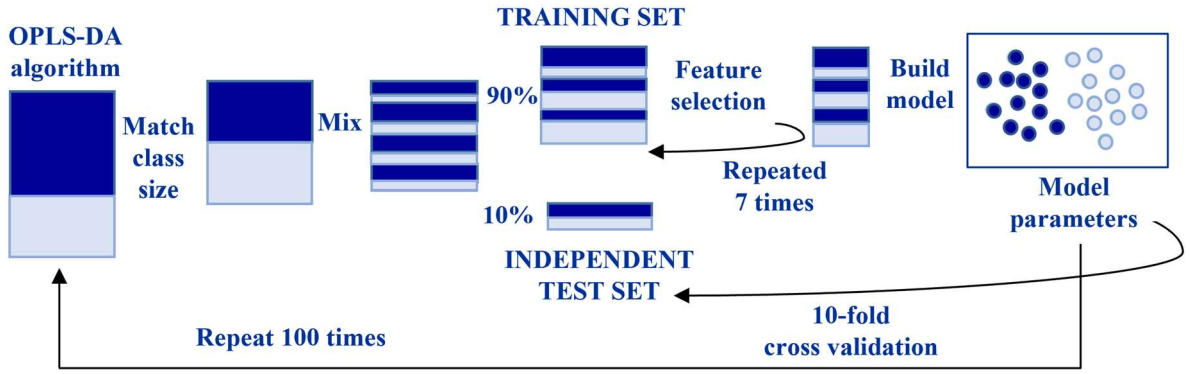

Figure 1.9. Workflow of OPLS-DA model evaluation using repeated training/test splitting and 10-fold cross-validation. The dataset is first balanced by matching class sizes, followed by random mixing and repeated partitioning into 90% training and 10% independent test sets. Within the training set, feature selection and model construction are iteratively performed. The final model is validated using 10-fold cross-validation, where the training data is divided into 10 subsets; the model is trained on nine subsets and tested on the remaining one, rotating through all subsets. This entire process is repeated 100 times to ensure robustness. Model performance is evaluated using R^2 (explained variance) and Q^2 (predictive ability) metrics. A high R^2 and Q^2 indicate good model fit and generalisability, respectively, while discrepancies between these values can signal overfitting or poor predictive performance. The original R script for cross-validated OPLS-DA was developed by Dr Fay Probert.[81]

In OPLS-DA, variable importance in projection (VIP) scores are computed from the predictive components of the underlying PLS model to quantify each variable contribution to class separation. Variables with VIP scores exceeding 1 are generally considered to exert a significant influence on the model and are therefore prioritised as putative biomarkers. To enhance the specificity of feature selection, the VIP distribution is

examined for an inflection point, delineating the threshold beyond which additional variables contribute minimally to model discrimination.[57, 81] Focusing on variables preceding this point improves interpretability, reduces the dimensionality of the dataset, and mitigates the risk of overfitting.

In addition to internal validation metrics such as R^2 and Q^2, model classification performance is further assessed using external metrics calculated on unseen data from an independent test set (Fig. 1.9). These include accuracy, sensitivity, and specificity. Accuracy is defined as the proportion of correct classifications, encompassing both true positives (TPs) and true negatives (TNs), relative to the total number of predictions. Sensitivity quantifies the proportion of true positives correctly identified, whereas specificity measures the proportion of true negatives correctly classified. In this context, TPs refer to instances where the model correctly predicts the positive class, while false positives (FPs) correspond to incorrect positive predictions. Conversely, true negatives TNs denote correctly identified negative instances, and false negatives (FNs) represent instances where the positive class is incorrectly classified as negative.[178, 180] Together with the confusion matrix, these metrics offer a comprehensive assessment of the model ability to distinguish between groups when applied to previously unseen data, reflecting its generalisability and overall performance.

1. 7. 1. 2 Random Forest: a non-parametric approach to metabolomics classification

An alternative to OPLS-DA in metabolomics is random forest, a versatile and robust ML algorithm capable of effectively handling complex, high-dimensional data with minimal pre-processing.

In random forest, a collection of decision trees is constructed to classify data or perform regression, making it particularly well-suited for complex, non-linear relationships.[181] The algorithm introduces randomness in two ways: by drawing bootstrap samples (with replacement) from the original dataset to train each tree, and by randomly selecting a subset of features at each node to determine the optimal split (Fig. 1.10). This randomness helps reduce overfitting and allows the model to capture intricate, non-linear interactions between variables, which are often present in metabolomics datasets.[182, 183] Predictions are made by aggregating the outputs (e.g., majority voting for classification) across all trees, enhancing the model accuracy and robustness.

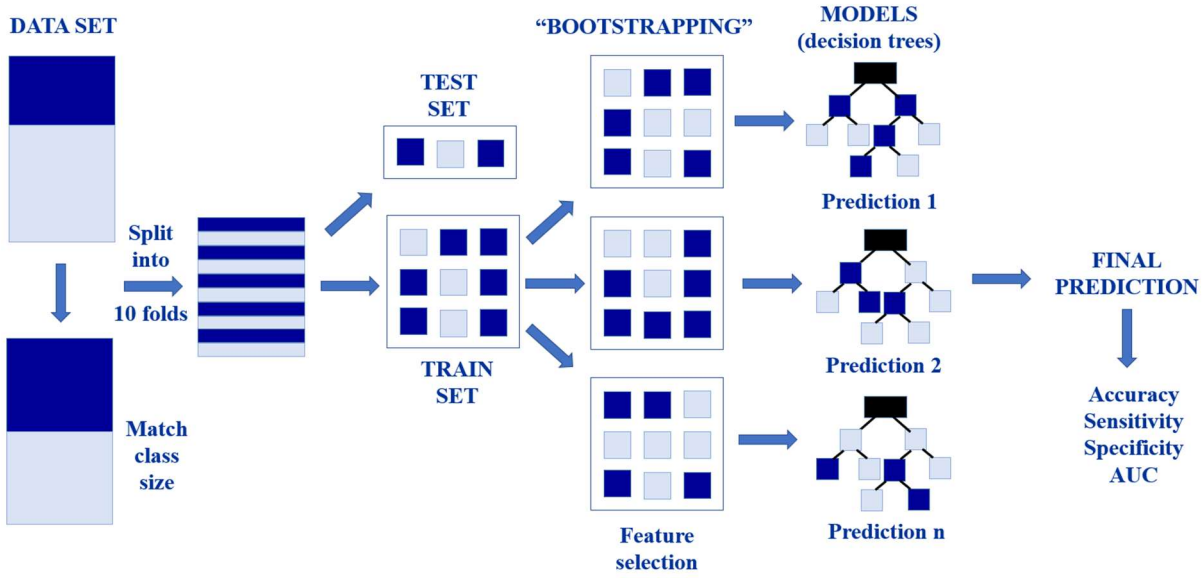

Figure 1.10. Schematic overview of random forest model construction and evaluation using 10-fold cross validation and bootstrapping. The dataset is class-balanced and partitioned into 10 folds for cross-validation. In each iteration, 9 folds are used for training and 1 for testing. Within the training set, bootstrapping is applied to generate multiple resampled subsets, each used to construct an individual decision tree. At each split within the tree, a random subset of features is selected, introducing stochasticity that reduces overfitting and enhances model generalisability. The ensemble of decision trees generates predictions, which are aggregated (e.g., by majority vote) to yield a final classification. Model performance is assessed using metrics such as accuracy, sensitivity, specificity, and area under the receiver operating characteristic curve (AUC). Variable importance is derived from measures such as the mean decrease in Gini index, facilitating interpretation and biomarker selection in metabolomics studies. The original R script for random forest was developed by Dr Daniel Radford-Smith.[183]

1. 7. 1. 3 Comparative evaluation of OPLS-DA and random forest in metabolomics

OPLS-DA and random forest are widely used supervised methods in metabolomics, valued for handling high-dimensional, complex datasets. Their complementary strengths make them well suited to address challenges posed by correlated variables and limited sample sizes.

Random forest offers flexibility in modelling complex data structures without requiring assumptions about variable distributions or linearity.[181, 184, 185] Its capacity to model non-linear relationships is particularly advantageous when analysing metabolite networks, where interactions are often intricate and not adequately captured by linear methods (Table 1.2). The ensemble architecture, based on aggregating predictions from multiple decision trees trained on bootstrapped subsets, enhances both model stability and generalisability, while reducing the risk of overfitting to noise or specific sample characteristics.[182, 184] These properties make random forest effective in high-dimensional settings with multicollinearity and limited sample sizes.

In contrast, OPLS-DA is often preferred for its interpretability and structured approach to dimensionality reduction. By explicitly separating variation that is orthogonal to the response variable, the method facilitates

clearer identification of metabolic changes directly associated with the biological condition or phenotype of interest.[178] This method is particularly effective in datasets dominated by linear trends, where minimising noise is critical to uncover meaningful patterns. However, the inherently linear nature of OPLS-DA limits its capacity to capture non-linear relationships or higher-order interactions, potentially reducing its performance in more complex datasets.[179, 185] Furthermore, OPLS-DA requires careful data pre-processing, including appropriate normalisation and scaling, and is prone to overfitting if not rigorously validated using techniques such as cross-validation and permutation testing (Table 1.2).

Table 1.2. Comparison of key characteristics of random forest and OPLS-DA for omics data analysis. In broad terms, random forest is suited to complex, non-linear datasets, whereas OPLS-DA provides an interpretable framework for analysing predominantly linear relationships.

Aspect	Random Forest	OPLS-DA
Type of Method	Non-linear, ensemble-based ML	Linear, statistical modelling and chemometrics
Data Requirements	Minimal pre-processing, handles non-linearities	Requires careful pre-processing, assumes linearity
Output	Predictions, feature importance, decision trees	Discriminant components, score/loading plots
Feature Interactions	Captures complex interactions implicitly	Models linear combinations of features
Robustness	Resistant to overfitting with proper tuning	Sensitive to noise-driven overfitting
Interpretability	Less interpretable due to black-box nature	Highly interpretable with clear visual outputs
Use Case	Large, complex datasets, non-linear relationships	Metabolomics, omics data with interpretability needs

Nevertheless, these two methods are often regarded as complementary: random forest can be employed to explore complex relationships and rank features based on their importance, whereas OPLS-DA offers a refined and interpretable framework for investigating the most relevant metabolites. The selection between these approaches should be informed by the specific characteristics of the dataset and the primary objectives of the study. In many cases, applying both algorithms in parallel can offer an additional layer of indirect validation, enabling cross-comparison of results and strengthening confidence in the robustness of observed patterns (as demonstrated in **Chapter 4**).[185]

Notably, while internal pseudo cross-validation provides a robust assessment of model stability in both random forest and OPLS-DA, external validation using an independent cohort remains the most reliable test

of generalisability. The availability of such datasets allows for critical confirmation that the identified patterns are not specific to the original sample, thereby reinforcing both the reproducibility and translational relevance of the findings.

1. 7. 2 ROC analysis for assessing predictive model accuracy

In addition to cross-validation and external validation on independent cohorts, rigorous performance evaluation is necessary to quantify the discriminatory power of models such as OPLS-DA and random forest. Receiver operating characteristic (ROC) curve analysis provides a well-established framework for this purpose, allowing systematic assessment of classification performance across varying decision thresholds. This approach is particularly relevant for evaluating models designed to predict disease progression and distinguish clinically meaningful phenotypes, which are key objectives of this thesis. By evaluating sensitivity and specificity across the full range of thresholds, ROC analysis yields a comprehensive measure of discriminative capacity.[186]

Thresholds play a critical role in ROC analysis, as they define the cut-off values used to convert continuous predicted probabilities into binary outcomes. For each threshold, observations with predicted probabilities above the threshold are classified as positive, and those below as negative. By varying the threshold, different combinations of TPs, FPs, TNs, and FNs are generated, producing the ROC curve. The area under the ROC curve (AUC) provides a single quantitative measure of discriminative performance, where an AUC of 0.5 indicates random classification and an AUC of 1.0 indicates perfect discrimination.[186, 187] ROC analysis therefore enables both visual and quantitative comparison of classification models based on their ability to separate classes across the full range of possible thresholds.

In the evaluation of a single metabolite, the threshold corresponds to a specific concentration level used to classify samples as positive or negative. Adjusting this threshold generates different rates of TPs and FPs, allowing the ROC curve to capture the sensitivity-specificity trade-off.[187] In contrast, multivariate models integrate information from multiple metabolites to generate a combined prediction score, which can then be evaluated using ROC analysis. Techniques such as OPLS-DA, which separates predictive from orthogonal variation, and random forest, which aggregates predictions from multiple decision trees, are commonly applied for multivariate classification. Both approaches output continuous prediction scores that can be

thresholded to generate ROC curves.[177, 181, 186] The AUC provides a quantitative measure of overall discriminative performance, facilitating comparison between different models. These multivariate models allow for a more comprehensive assessment of the collective discriminative power of multiple metabolites and often achieve superior classification performance compared to single-metabolite analyses.[187, 188]

Occasionally, discrepancies arise between multivariate model accuracy and AUC values, reflecting the fact that these metrics capture different aspects of classification performance. Accuracy measures the proportion of correct classifications at a specific decision threshold, providing a straightforward assessment of predictive success. However, accuracy alone may not fully represent discriminative ability, particularly in the presence of class imbalance or when the chosen threshold is suboptimal.[188] In contrast, AUC evaluates the capacity to correctly rank observations across all possible thresholds, offering a threshold-independent measure of overall discrimination. As a result, a classification model may achieve only moderate accuracy at a given threshold while still exhibiting a high AUC, indicating strong overall class separation.[188] Together, accuracy and AUC provide a comprehensive evaluation of classification performance, with each offering distinct and complementary insights into predictive success and discriminative ability.

In summary, multivariate and ML methods play a key role in this thesis, enabling disease classification, biomarker discovery, and progression modelling in high-dimensional omics datasets. Techniques such as OPLS-DA, random forest, and ROC analysis are applied across **Chapters 3–6**, with cross-validation used to ensure model robustness and biological relevance.

1. 8 Thesis scope: analytical framework and clinical context

This chapter established the clinical rationale and methodological framework for the thesis, outlining key limitations in the sensitivity and specificity of current diagnostic and prognostic tools for demyelinating and neurodegenerative disorders. These limitations underscore the need for novel, biologically grounded approaches capable of capturing disease-relevant molecular alterations. In response, a rationale for a blood-based multiplatform metabolomics approach was presented, along with critical considerations for data integration. This thesis further highlights the importance of rigorous data processing and multivariate statistical modelling as essential components for drawing robust and reliable conclusions. These concepts underpin the analytical pipeline developed in this thesis, with the following chapters detailing the design of multi-platform strategies for biomarker discovery (**Chapters 2 and 3**) and their application to diagnostic and prognostic modelling across clinical cohorts (**Chapters 4–6**).

1. 8. 1 Aims and objectives

The aim of this thesis was to develop and apply robust, multi-platform metabolomics workflows - centred on the combined use of NMR spectroscopy and LC-MS - to advance biomarker discovery, improve disease classification, and support treatment monitoring, focusing on neurological disorders. The project was structured around four key objectives:

1. To develop and optimise sample preparation methods for reproducible, high-quality analysis across NMR and LC-MS platforms using human plasma and serum samples.
2. To integrate NMR and LC-MS profiling for biomarker discovery in MS, Ab-mediated demyelinating syndromes, and MCI.
3. To apply ML and multivariate modelling techniques to enhance the diagnostic and prognostic power of multi-omics datasets.
4. To investigate how therapeutic interventions shape metabolism at the systemic level, using untargeted, comprehensive multi-omics profiling.

This integrated thesis comprises five experimental chapters, each based on published or submitted manuscripts for which I was the primary and lead author. Together, they reflect a progression from

methodological development to clinical application, demonstrating how optimised multi-platform and multi-omics workflows enhance biomarker discovery in diverse neurological disease contexts.

The experimental work begins in **Chapter 2** (Kacerova, T., Pires, E., Walsby-Tickle, J., Probert, F. & McCullagh, J.: Integrating NMR and multi-LC-MS-based untargeted metabolomics for comprehensive analysis of blood serum samples. *Anal Chim Acta* 1356, 343979 (2025)), where an integrated NMR and LC-MS workflow for serum metabolomics is designed. To address the practical limitations of volume-constrained clinical samples, a protocol was developed to enable sequential NMR and multi-LC-MS analysis from a single aliquot. This workflow underpins the thesis, providing a reproducible foundation for multi-platform analysis without compromising sample integrity.

Building on this foundation, **Chapter 3** (Kacerova, T., Pires, E., Dixon, A., Williams, R., Legge, I., Hippisley, M., Yates, A. G., Smith, A. D., Anthony, D. C., Probert, F. & McCullagh, J.: Refining Precision: Formic Acid Treatment Enhances Reproducibility in Untargeted Serum and Plasma Metabolomics. *Analytical Chemistry*) addresses a key technical challenge in LC-MS metabolomics improving the removal of abundant proteins from blood samples. Multiple protein depletion strategies were systematically evaluated to identify the optimal balance between extraction efficiency, analytical reproducibility, and cross-platform compatibility. This work refined the workflow introduced in Chapter 2, making it more suitable for larger-scale studies by enhancing analytical robustness.

With the technical foundations established, **Chapter 4** (Kacerova, T., Willemse, E., Oechtering, J., Radford-Smith, D.E., Xiong, W., Maleska Maceski, A., Yeo, T., De Luca, G., Palace, J., Leppert, D., Kuhle, J., Anthony, D. C., Probert. F.: Serum GFAP and NfL Augment a Metabolomics-Driven Strategy for Long-Term Prediction of Multiple Sclerosis Progression. *Communications Medicine*) presents the first major clinical application of the workflow. In this study, the optimised multi-omics strategy is applied to a well-characterised MS cohort, combining serum metabolomics with protein biomarkers to identify predictors of disease progression. Notably, the results were externally validated in an independent cohort, reinforcing their clinical relevance and demonstrating the translational potential of this approach.

Chapter 5 (Kacerova, T., Sealey, M., Saldana, L., Xiong, W., Woodhall, M., Waters, P., Sénard, T., Cheeseman, J., Urbanowicz, P., Elgood Hunt, G., Spencer, D.I.R., McCullagh, J.S.O., Leite, M.I., DeLuca,

G., Palace, J., Anthony, D.C., Yeo, T., Probert, F.: Plasma N-Glycan Profiling Enhances Diagnostic Precision in Multiple Sclerosis, AQP4-Ab NMOSD and MOGAD. *Neurology: Neuroimmunology and Neuroinflammation*) shifts the focus toward differential diagnosis. Building on insights from earlier NMR-based studies, this chapter introduces a targeted LC-MS glycomics approach to distinguish MS from Ab-mediated conditions, specifically AQP4-Ab NMOSD and MOGAD. The findings highlight the utility of glycan profiling as a complementary tool to improve diagnostic precision in demyelinating diseases.

Finally, **Chapter 6** (Kacerova, T., Yates, A.G., Dai, J., Shepherd, D., Pires, E., de Jel, S., Gong, Q., Schiffer, E., Jernerén, F., Olsen, T., De Jager Loots, C.A., Refsum, H., Smith, A.D., McCullagh, J.S.O., Anthony, D.C., Probert, F. Role of B vitamins in modulating homocysteine and metabolic pathways linked to brain atrophy: metabolomics insights from the VITACOG trial. *Alzheimer's & Dementia*) applies multiplatform metabolomics to monitor treatment effects in individuals with MCI using samples from the VITACOG trial. Untargeted metabolomics is used to investigate the effects of B vitamin supplementation on metabolic pathways, with the aim of identifying candidate biomarkers predictive of therapeutic response. This chapter extends the thesis into a therapeutic context, linking biomarker discovery with potential clinical utility in early neurodegenerative disease.

In summary, the first part of this thesis focuses on the development and optimisation of sample preparation protocols, employing multi-platform and multi-omics strategies to enhance metabolite coverage and minimise technical variability. These methodologies are subsequently applied across a range of neurological conditions, establishing a translational framework for integrated, biomarker-driven approaches in neurology. Taken together, the studies reported in this thesis contribute to a growing body of research addressing key analytical and clinical challenges in biomarker discovery for neurological diseases.

1. 9 References

(1) Hasin, Y.; Seldin, M.; Lusis, A. Multi-omics approaches to disease. *Genome Biol* **2017**, *18* (1), 83. DOI: 10.1186/s13059-017-1215-1 From NLM Medline.
(2) Feigin, V. L.; Vos, T.; Nichols, E.; Owolabi, M. O.; Carroll, W. M.; Dichgans, M.; Deuschl, G.; Parmar, P.; Brainin, M.; Murray, C. The global burden of neurological disorders: translating evidence into policy. *Lancet Neurol* **2020**, *19* (3), 255–265. DOI: 10.1016/S1474-4422(19)30411-9 From NLM Medline.
(3) Fernandes, L.; Allen, C. M.; Williams, T.; Tallantyre, E.; Evangelou, N.; Chataway, J.; Ford, H. L.; Trials, U. M.; Registries Consortium, i. The contemporary role of MRI in the monitoring and management of people with multiple sclerosis in the UK. *Mult Scler Relat Disord* **2021**, *55*, 103190. DOI: 10.1016/j.msard.2021.103190 From NLM Medline.
(4) Zhang, J.; Zhang, Y.; Wang, J.; Xia, Y.; Zhang, J.; Chen, L. Recent advances in Alzheimer's disease: Mechanisms, clinical trials and new drug development strategies. *Signal Transduct Target Ther* **2024**, *9* (1), 211. DOI: 10.1038/s41392-024-01911-3 From NLM Medline.
(5) Gadhave, D. G.; Sugandhi, V. V.; Jha, S. K.; Nangare, S. N.; Gupta, G.; Singh, S. K.; Dua, K.; Cho, H.; Hansbro, P. M.; Paudel, K. R. Neurodegenerative disorders: Mechanisms of degeneration and therapeutic approaches with their clinical relevance. *Ageing Res Rev* **2024**, *99*, 102357. DOI: 10.1016/j.arr.2024.102357 From NLM Medline.
(6) Oka, T.; Matsuzawa, Y.; Tsuneyoshi, M.; Nakamura, Y.; Aoshima, K.; Tsugawa, H.; Alzheimer's Disease Metabolomics, C. Multiomics analysis to explore blood metabolite biomarkers in an Alzheimer's Disease Neuroimaging Initiative cohort. *Sci Rep* **2024**, *14* (1), 6797. DOI: 10.1038/s41598-024-56837-1 From NLM Medline.
(7) Gowda, G. A. N.; Zhang, S. C.; Gu, H. W.; Asiago, V.; Shanaiah, N.; Raftery, D. Metabolomics-based methods for early disease diagnostics. *Expert Rev Mol Diagn* **2008**, *8* (5), 617–633. DOI: 10.1586/14737159.8.5.617.
(8) Coutinho Costa, V. G.; Araujo, S. E.; Alves-Leon, S. V.; Gomes, F. C. A. Central nervous system demyelinating diseases: glial cells at the hub of pathology. *Front Immunol* **2023**, *14*, 1135540. DOI: 10.3389/fimmu.2023.1135540 From NLM Medline.
(9) Walton, C.; King, R.; Rechtman, L.; Kaye, W.; Leray, E.; Marrie, R. A.; Robertson, N.; La Rocca, N.; Uitdehaag, B.; van der Mei, I.; et al. Rising prevalence of multiple sclerosis worldwide: Insights from the Atlas of MS, third edition. *Mult Scler* **2020**, *26* (14), 1816–1821. DOI: 10.1177/1352458520970841 From NLM Medline.
(10) Jakimovski, D.; Bittner, S.; Zivadinov, R.; Morrow, S. A.; Benedict, R. H.; Zipp, F.; Weinstock-Guttman, B. Multiple sclerosis. *Lancet* **2024**, *403* (10422), 183–202. DOI: 10.1016/S0140-6736(23)01473-3 From NLM Medline.
(11) Matthews, L.; Marasco, R.; Jenkinson, M.; Küker, W.; Luppe, S.; Leite, M. I.; Giorgio, A.; De Stefano, N.; Robertson, N.; Johansen-Berg, H.; et al. Distinction of seropositive NMO spectrum disorder and MS brain lesion distribution. *Neurology* **2013**, *80* (14), 1330–1337. DOI: 10.1212/WNL.0b013e3182887957.
(12) McGinley, M. P.; Goldschmidt, C. H.; Rae-Grant, A. D. Diagnosis and Treatment of Multiple Sclerosis: A Review. *JAMA* **2021**, *325* (8), 765–779. DOI: 10.1001/jama.2020.26858 From NLM Medline.
(13) Dobson, R.; Giovannoni, G. Multiple sclerosis - a review. *Eur J Neurol* **2019**, *26* (1), 27–40. DOI: 10.1111/ene.13819 From NLM Medline.
(14) Bruck, W. The pathology of multiple sclerosis is the result of focal inflammatory demyelination with axonal damage. *J Neurol* **2005**, *252 Suppl 5*, v3–9. DOI: 10.1007/s00415-005-5002-7 From NLM Medline.
(15) Wingerchuk, D. M.; Banwell, B.; Bennett, J. L.; Cabre, P.; Carroll, W.; Chitnis, T.; de Seze, J.; Fujihara, K.; Greenberg, B.; Jacob, A.; et al. International consensus diagnostic criteria for neuromyelitis optica spectrum disorders. *Neurology* **2015**, *85* (2), 177–189. DOI: 10.1212/WNL.0000000000001729 From NLM Medline.
(16) Cacciaguerra, L.; Flanagan, E. P. Updates in NMOSD and MOGAD Diagnosis and Treatment: A Tale of Two Central Nervous System Autoimmune Inflammatory Disorders. *Neurol Clin* **2024**, *42* (1), 77–114. DOI: 10.1016/j.ncl.2023.06.009 From NLM Medline.
(17) Yamamura, T.; Kleiter, I.; Fujihara, K.; Palace, J.; Greenberg, B.; Zakrzewska-Pniewska, B.; Patti, F.; Tsai, C. P.; Saiz, A.; Yamazaki, H.; et al. Trial of Satralizumab in Neuromyelitis Optica Spectrum Disorder. *New Engl J Med* **2019**, *381* (22), 2114–2124. DOI: 10.1056/NEJMoa1901747.
(18) Selmaj, K.; Cree, B. A. C.; Barnett, M.; Thompson, A.; Hartung, H. P. Multiple sclerosis: time for early treatment with high-efficacy drugs. *J Neurol* **2024**, *271* (1), 105–115. DOI: 10.1007/s00415-023-11969-8 From NLM Medline.
(19) Cree, B. A. C.; Bennett, J. L.; Kim, H. J.; Weinshenker, B. G.; Pittock, S. J.; Wingerchuk, D. M.; Fujihara, K.; Paul, F.; Cutter, G. R.; Marignier, R.; et al. Inebilizumab for the treatment of neuromyelitis optica spectrum disorder (N-MOmentum): a double-blind, randomised placebo-controlled phase 2/3 trial. *Lancet* **2019**, *394* (10206), 1352–1363. DOI: 10.1016/S0140-6736(19)31817-3.

(20) Jurynczyk, M.; Probert, F.; Yeo, T.; Tackley, G.; Claridge, T. D. W.; Cavey, A.; Woodhall, M. R.; Arora, S.; Winkler, T.; Schiffer, E.; et al. Metabolomics reveals distinct, antibody-independent, molecular signatures of MS, AQP4-antibody and MOG-antibody disease. *Acta Neuropathol Com* **2017**, *5*. DOI: ARTN 9510.1186/s40478-017-0495-8.
(21) Knopman, D. S.; Petersen, R. C. Mild cognitive impairment and mild dementia: a clinical perspective. *Mayo Clin Proc* **2014**, *89* (10), 1452–1459. DOI: 10.1016/j.mayocp.2014.06.019 From NLM Medline.
(22) Salemme, S.; Lombardo, F. L.; Lacorte, E.; Sciancalepore, F.; Remoli, G.; Bacigalupo, I.; Piscopo, P.; Zamboni, G.; Rossini, P. M.; Cappa, S. F.; et al. The prognosis of mild cognitive impairment: A systematic review and meta-analysis. *Alzheimers Dement (Amst)* **2025**, *17* (1), e70074. DOI: 10.1002/dad2.70074 From NLM PubMed-not-MEDLINE.
(23) Smith, A. D.; Smith, S. M.; de Jager, C. A.; Whitbread, P.; Johnston, C.; Agacinski, G.; Oulhaj, A.; Bradley, K. M.; Jacoby, R.; Refsum, H. Homocysteine-lowering by B vitamins slows the rate of accelerated brain atrophy in mild cognitive impairment: a randomized controlled trial. *Plos One* **2010**, *5* (9), e12244. DOI: 10.1371/journal.pone.0012244 From NLM Medline.
(24) Scheltens, P.; De Strooper, B.; Kivipelto, M.; Holstege, H.; Chetelat, G.; Teunissen, C. E.; Cummings, J.; van der Flier, W. M. Alzheimer's disease. *Lancet* **2021**, *397* (10284), 1577–1590. DOI: 10.1016/S0140-6736(20)32205-4 From NLM Medline.
(25) Simonsen, A. H.; Herukka, S. K.; Andreasen, N.; Baldeiras, I.; Bjerke, M.; Blennow, K.; Engelborghs, S.; Frisoni, G. B.; Gabryelewicz, T.; Galluzzi, S.; et al. Recommendations for CSF AD biomarkers in the diagnostic evaluation of dementia. *Alzheimers Dement* **2017**, *13* (3), 274–284. DOI: 10.1016/j.jalz.2016.09.008 From NLM Medline.
(26) Yiannopoulou, K. G.; Anastasiou, A. I.; Zachariou, V.; Pelidou, S. H. Reasons for Failed Trials of Disease-Modifying Treatments for Alzheimer Disease and Their Contribution in Recent Research. *Biomedicines* **2019**, *7* (4). DOI: 10.3390/biomedicines7040097 From NLM PubMed-not-MEDLINE.
(27) Kalinowski, A.; Cutter, G.; Bozinov, N.; Hinman, J. A.; Hittle, M.; Motl, R.; Odden, M.; Nelson, L. M. The timed 25-foot walk in a large cohort of multiple sclerosis patients. *Mult Scler* **2022**, *28* (2), 289–299. DOI: 10.1177/13524585211017013 From NLM Medline.
(28) Cohen, M.; Bresch, S.; Thommel Rocchi, O.; Morain, E.; Benoit, J.; Levraut, M.; Fakir, S.; Landes, C.; Lebrun-Frenay, C. Should we still only rely on EDSS to evaluate disability in multiple sclerosis patients? A study of inter and intra rater reliability. *Mult Scler Relat Disord* **2021**, *54*, 103144. DOI: 10.1016/j.msard.2021.103144 From NLM Medline.
(29) de Jager, C. A.; Oulhaj, A.; Jacoby, R.; Refsum, H.; Smith, A. D. Cognitive and clinical outcomes of homocysteine-lowering B-vitamin treatment in mild cognitive impairment: a randomized controlled trial. *Int J Geriatr Psychiatry* **2012**, *27* (6), 592–600. DOI: 10.1002/gps.2758 From NLM Medline.
(30) Jia, X.; Wang, Z.; Huang, F.; Su, C.; Du, W.; Jiang, H.; Wang, H.; Wang, J.; Wang, F.; Su, W.; et al. A comparison of the Mini-Mental State Examination (MMSE) with the Montreal Cognitive Assessment (MoCA) for mild cognitive impairment screening in Chinese middle-aged and older population: a cross-sectional study. *BMC Psychiatry* **2021**, *21* (1), 485. DOI: 10.1186/s12888-021-03495-6 From NLM Medline.
(31) Chard, D.; Trip, S. A. Resolving the clinico-radiological paradox in multiple sclerosis. *F1000Res* **2017**, *6*, 1828. DOI: 10.12688/f1000research.11932.1 From NLM PubMed-not-MEDLINE.
(32) Kearney, H.; Miller, D. H.; Ciccarelli, O. Spinal cord MRI in multiple sclerosis--diagnostic, prognostic and clinical value. *Nat Rev Neurol* **2015**, *11* (6), 327–338. DOI: 10.1038/nrneurol.2015.80 From NLM Medline.
(33) Brickman, A. M.; Honig, L. S.; Scarmeas, N.; Tatarina, O.; Sanders, L.; Albert, M. S.; Brandt, J.; Blacker, D.; Stern, Y. Measuring cerebral atrophy and white matter hyperintensity burden to predict the rate of cognitive decline in Alzheimer disease. *Arch Neurol* **2008**, *65* (9), 1202–1208. DOI: 10.1001/archneur.65.9.1202 From NLM Medline.
(34) Barber, R.; Ballard, C.; McKeith, I. G.; Gholkar, A.; O'Brien, J. T. MRI volumetric study of dementia with Lewy bodies: a comparison with AD and vascular dementia. *Neurology* **2000**, *54* (6), 1304–1309. DOI: 10.1212/wnl.54.6.1304 From NLM Medline.
(35) Chapleau, M.; Iaccarino, L.; Soleimani-Meigooni, D.; Rabinovici, G. D. The Role of Amyloid PET in Imaging Neurodegenerative Disorders: A Review. *J Nucl Med* **2022**, *63* (Suppl 1), 13S–19S. DOI: 10.2967/jnumed.121.263195 From NLM Medline.
(36) Radford-Smith, D. E.; Yates, A. G.; Kacerova, T.; Nylund, M.; Sucksdorff, M.; Matilainen, M.; Willemse, E.; Oechtering, J.; Maleska Maceski, A.; Leppert, D.; et al. Integrating TSPO-PET imaging with metabolomics for enhanced prognostic accuracy in multiple sclerosis. *BMJ Neurol Open* **2025**, *7* (1), e001026. DOI: 10.1136/bmjno-2025-001026 From NLM PubMed-not-MEDLINE.
(37) Sucksdorff, M.; Matilainen, M.; Tuisku, J.; Polvinen, E.; Vuorimaa, A.; Rokka, J.; Nylund, M.; Rissanen, E.; Airas, L. Brain TSPO-PET predicts later disease progression independent of relapses in multiple sclerosis. *Brain* **2020**, *143* (11), 3318–3330. DOI: 10.1093/brain/awaa275 From NLM Medline.

(38) Garland, E. F.; Dennett, O.; Lau, L. C.; Chatelet, D. S.; Bottlaender, M.; Nicoll, J. A. R.; Boche, D. The mitochondrial protein TSPO in Alzheimer's disease: relation to the severity of AD pathology and the neuroinflammatory environment. *J Neuroinflammation* **2023**, *20* (1), 186. DOI: 10.1186/s12974-023-02869-9 From NLM Medline.
(39) Jones, D.; Lowe, V.; Graff-Radford, J.; Botha, H.; Barnard, L.; Wiepert, D.; Murphy, M. C.; Murray, M.; Senjem, M.; Gunter, J.; et al. A computational model of neurodegeneration in Alzheimer's disease. *Nat Commun* **2022**, *13* (1), 1643. DOI: 10.1038/s41467-022-29047-4 From NLM Medline.
(40) Cubas-Nunez, L.; Gil-Perotin, S.; Castillo-Villalba, J.; Lopez, V.; Solis Tarazona, L.; Gasque-Rubio, R.; Carratala-Bosca, S.; Alcala-Vicente, C.; Perez-Miralles, F.; Lassmann, H.; et al. Potential Role of CHI3L1+ Astrocytes in Progression in MS. *Neurol Neuroimmunol Neuroinflamm* **2021**, *8* (3). DOI: 10.1212/NXI.0000000000000972 From NLM Medline.
(41) Kuhle, J.; Barro, C.; Disanto, G.; Mathias, A.; Soneson, C.; Bonnier, G.; Yaldizli, O.; Regeniter, A.; Derfuss, T.; Canales, M.; et al. Serum neurofilament light chain in early relapsing remitting MS is increased and correlates with CSF levels and with MRI measures of disease severity. *Mult Scler* **2016**, *22* (12), 1550–1559. DOI: 10.1177/1352458515623365 From NLM Medline.
(42) Abdelhak, A.; Foschi, M.; Abu-Rumeileh, S.; Yue, J. K.; D'Anna, L.; Huss, A.; Oeckl, P.; Ludolph, A. C.; Kuhle, J.; Petzold, A.; et al. Blood GFAP as an emerging biomarker in brain and spinal cord disorders. *Nat Rev Neurol* **2022**, *18* (3), 158–172. DOI: 10.1038/s41582-021-00616-3 From NLM Medline.
(43) Cross, A. H.; Gelfand, J. M.; Thebault, S.; Bennett, J. L.; von Budingen, H. C.; Cameron, B.; Carruthers, R.; Edwards, K.; Fallis, R.; Gerstein, R.; et al. Emerging Cerebrospinal Fluid Biomarkers of Disease Activity and Progression in Multiple Sclerosis. *JAMA Neurol* **2024**, *81* (4), 373–383. DOI: 10.1001/jamaneurol.2024.0017 From NLM Publisher.
(44) Sauvee, M.; DidierLaurent, G.; Latarche, C.; Escanye, M. C.; Olivier, J. L.; Malaplate-Armand, C. Additional use of Abeta(4)(2)/Abeta(4)(0) ratio with cerebrospinal fluid biomarkers P-tau and Abeta(4)(2) increases the level of evidence of Alzheimer's disease pathophysiological process in routine practice. *J Alzheimers Dis* **2014**, *41* (2), 377–386. DOI: 10.3233/JAD-131838 From NLM Medline.
(45) Visser, P. J.; Reus, L. M.; Gobom, J.; Jansen, I.; Dicks, E.; van der Lee, S. J.; Tsolaki, M.; Verhey, F. R. J.; Popp, J.; Martinez-Lage, P.; et al. Cerebrospinal fluid tau levels are associated with abnormal neuronal plasticity markers in Alzheimer's disease. *Mol Neurodegener* **2022**, *17* (1), 27. DOI: 10.1186/s13024-022-00521-3 From NLM Medline.
(46) Meier, S.; Willemse, E. A. J.; Schaedelin, S.; Oechtering, J.; Lorscheider, J.; Melie-Garcia, L.; Cagol, A.; Barakovic, M.; Galbusera, R.; Subramaniam, S.; et al. Serum Glial Fibrillary Acidic Protein Compared With Neurofilament Light Chain as a Biomarker for Disease Progression in Multiple Sclerosis. *JAMA Neurol* **2023**, *80* (3), 287–297. DOI: 10.1001/jamaneurol.2022.5250 From NLM Publisher.
(47) Meier, S.; Willemse, E. A. J.; Schaedelin, S.; Oechtering, J.; Lorscheider, J.; Melie-Garcia, L.; Cagol, A.; Barakovic, M.; Galbusera, R.; Subramaniam, S.; et al. Serum Glial Fibrillary Acidic Protein Compared With Neurofilament Light Chain as a Biomarker for Disease Progression in Multiple Sclerosis. *Jama Neurology* **2023**, *80* (3), 287–297. DOI: 10.1001/jamaneurol.2022.5250.
(48) Doecke, J. D.; Perez-Grijalba, V.; Fandos, N.; Fowler, C.; Villemagne, V. L.; Masters, C. L.; Pesini, P.; Sarasa, M.; Group, A. R. Total Abeta(42)/Abeta(40) ratio in plasma predicts amyloid-PET status, independent of clinical AD diagnosis. *Neurology* **2020**, *94* (15), e1580–e1591. DOI: 10.1212/WNL.0000000000009240 From NLM Medline.
(49) Feizpour, A.; Doecke, J. D.; Dore, V.; Krishnadas, N.; Huang, K.; Bourgeat, P.; Laws, S. M.; Fowler, C.; Robertson, J.; Mackintosh, L.; et al. Detection and staging of Alzheimer's disease by plasma pTau217 on a high throughput immunoassay platform. *Ebiomedicine* **2024**, *109*, 105405. DOI: 10.1016/j.ebiom.2024.105405 From NLM Medline.
(50) Palmqvist, S.; Warmenhoven, N.; Anastasi, F.; Pilotto, A.; Janelidze, S.; Tideman, P.; Stomrud, E.; Mattsson-Carlgren, N.; Smith, R.; Ossenkoppele, R.; et al. Plasma phospho-tau217 for Alzheimer's disease diagnosis in primary and secondary care using a fully automated platform. *Nat Med* **2025**. DOI: 10.1038/s41591-025-03622-w From NLM Publisher.
(51) Cano, A.; Capdevila, M.; Puerta, R.; Arranz, J.; Montrreal, L.; de Rojas, I.; Garcia-Gonzalez, P.; Olive, C.; Garcia-Gutierrez, F.; Sotolongo-Grau, O.; et al. Clinical value of plasma pTau181 to predict Alzheimer's disease pathology in a large real-world cohort of a memory clinic. *Ebiomedicine* **2024**, *108*, 105345. DOI: 10.1016/j.ebiom.2024.105345 From NLM Medline.
(52) Horie, K.; Salvado, G.; Koppisetti, R. K.; Janelidze, S.; Barthelemy, N. R.; He, Y.; Sato, C.; Gordon, B. A.; Jiang, H.; Benzinger, T. L. S.; et al. Plasma MTBR-tau243 biomarker identifies tau tangle pathology in Alzheimer's disease. *Nat Med* **2025**. DOI: 10.1038/s41591-025-03617-7 From NLM Publisher.
(53) Genin, E.; Hannequin, D.; Wallon, D.; Sleegers, K.; Hiltunen, M.; Combarros, O.; Bullido, M. J.; Engelborghs, S.; De Deyn, P.; Berr, C.; et al. APOE and Alzheimer disease: a major gene with semi-dominant inheritance. *Mol Psychiatry* **2011**, *16* (9), 903–907. DOI: 10.1038/mp.2011.52 From NLM Medline.

(54) Chitnis, T.; Qureshi, F.; Gehman, V. M.; Becich, M.; Bove, R.; Cree, B. A. C.; Gomez, R.; Hauser, S. L.; Henry, R. G.; Katrib, A.; et al. Inflammatory and neurodegenerative serum protein biomarkers increase sensitivity to detect clinical and radiographic disease activity in multiple sclerosis. *Nat Commun* **2024**, *15* (1), 4297. DOI: 10.1038/s41467-024-48602-9 From NLM Medline.
(55) Oppong, A. E.; Coelewij, L.; Robertson, G.; Martin-Gutierrez, L.; Waddington, K. E.; Donnes, P.; Nytrova, P.; Farrell, R.; Pineda-Torra, I.; Jury, E. C. Blood metabolomic and transcriptomic signatures stratify patient subgroups in multiple sclerosis according to disease severity. *iScience* **2024**, *27* (3), 109225. DOI: 10.1016/j.isci.2024.109225 From NLM PubMed-not-MEDLINE.
(56) Dickens, A. M.; Larkin, J. R.; Griffin, J. L.; Cavey, A.; Matthews, L.; Turner, M. R.; Wilcock, G. K.; Davis, B. G.; Claridge, T. D.; Palace, J.; et al. A type 2 biomarker separates relapsing-remitting from secondary progressive multiple sclerosis. *Neurology* **2014**, *83* (17), 1492–1499. DOI: 10.1212/WNL.0000000000000905 From NLM Medline.
(57) Yeo, T.; Sealey, M.; Zhou, Y.; Saldana, L.; Loveless, S.; Claridge, T. D. W.; Robertson, N.; DeLuca, G.; Palace, J.; Anthony, D. C.; et al. A blood-based metabolomics test to distinguish relapsing-remitting and secondary progressive multiple sclerosis: addressing practical considerations for clinical application. *Sci Rep* **2020**, *10* (1), 12381. DOI: 10.1038/s41598-020-69119-3 From NLM Medline.
(58) Grande, G.; Valletta, M.; Rizzuto, D.; Xia, X.; Qiu, C.; Orsini, N.; Dale, M.; Andersson, S.; Fredolini, C.; Winblad, B.; et al. Blood-based biomarkers of Alzheimer's disease and incident dementia in the community. *Nat Med* **2025**. DOI: 10.1038/s41591-025-03605-x From NLM Publisher.
(59) Vignoli, A.; Bellomo, G.; Paoletti, F. P.; Luchinat, C.; Tenori, L.; Parnetti, L. Studying Alzheimer's disease through an integrative serum metabolomic and lipoproteomic approach. *J Transl Med* **2025**, *23* (1), 119. DOI: 10.1186/s12967-025-06148-4 From NLM Medline.
(60) Wishart, D. S.; Cheng, L. L.; Copie, V.; Edison, A. S.; Eghbalnia, H. R.; Hoch, J. C.; Gouveia, G. J.; Pathmasiri, W.; Powers, R.; Schock, T. B.; et al. NMR and Metabolomics-A Roadmap for the Future. *Metabolites* **2022**, *12* (8). DOI: ARTN 67810.3390/metabo12080678.
(61) Castelli, F. A.; Rosati, G.; Moguet, C.; Fuentes, C.; Marrugo-Ramirez, J.; Lefebvre, T.; Volland, H.; Merkoci, A.; Simon, S.; Fenaille, F.; et al. Metabolomics for personalized medicine: the input of analytical chemistry from biomarker discovery to point-of-care tests. *Anal Bioanal Chem* **2022**, *414* (2), 759–789. DOI: 10.1007/s00216-021-03586-z From NLM Medline.
(62) Wishart, D. S. Emerging applications of metabolomics in drug discovery and precision medicine. *Nat Rev Drug Discov* **2016**, *15* (7), 473–484. DOI: 10.1038/nrd.2016.32 From NLM Medline.
(63) Buergel, T.; Steinfeldt, J.; Ruyoga, G.; Pietzner, M.; Bizzarri, D.; Vojinovic, D.; Upmeier Zu Belzen, J.; Loock, L.; Kittner, P.; Christmann, L.; et al. Metabolomic profiles predict individual multidisease outcomes. *Nat Med* **2022**, *28* (11), 2309–2320. DOI: 10.1038/s41591-022-01980-3 From NLM Medline.
(64) Clish, C. B. Metabolomics: an emerging but powerful tool for precision medicine. *Csh Mol Case Stud* **2015**, *1* (1). DOI: ARTN a00058810.1101/mcs.a000588.
(65) Kaspy, M. S.; Semnani-Azad, Z.; Malik, V. S.; Jenkins, D. J. A.; Hanley, A. J. Metabolomic profile of combined healthy lifestyle behaviours in humans: A systematic review. *Proteomics* **2022**, *22* (18), e2100388. DOI: 10.1002/pmic.202100388 From NLM Medline.
(66) P., F. R. There's plenty of room at the bottom. In Annual Meeting of the American Physical Society, California Institute of Technology, Pasadena, California, USA; 1959.
(67) Aharoni, A.; Goodacre, R.; Fernie, A. R. Plant and microbial sciences as key drivers in the development of metabolomics research. *Proc Natl Acad Sci U S A* **2023**, *120* (12), e2217383120. DOI: 10.1073/pnas.2217383120 From NLM Medline.
(68) Wishart, D. S.; Tzur, D.; Knox, C.; Eisner, R.; Guo, A. C.; Young, N.; Cheng, D.; Jewell, K.; Arndt, D.; Sawhney, S.; et al. HMDB: the Human Metabolome Database. *Nucleic Acids Res* **2007**, *35* (Database issue), D521–526. DOI: 10.1093/nar/gkl923 From NLM Medline.
(69) Almontashiri, N. A. M.; Zha, L.; Young, K.; Law, T.; Kellogg, M. D.; Bodamer, O. A.; Peake, R. W. A. Clinical Validation of Targeted and Untargeted Metabolomics Testing for Genetic Disorders: A 3 Year Comparative Study. *Sci Rep* **2020**, *10* (1), 9382. DOI: 10.1038/s41598-020-66401-2 From NLM Medline.
(70) Hajjar, I.; Liu, C.; Jones, D. P.; Uppal, K. Untargeted metabolomics reveal dysregulations in sugar, methionine, and tyrosine pathways in the prodromal state of AD. *Alzheimers Dement (Amst)* **2020**, *12* (1), e12064. DOI: 10.1002/dad2.12064 From NLM PubMed-not-MEDLINE.
(71) McMillen, T. S.; Leslie, A.; Chisholm, K.; Penny, S.; Gallant, J.; Cohen, A.; Drucker, A.; Fawcett, J. P.; Pinto, D. M. A large-scale, targeted metabolomics method for the analysis and quantification of metabolites in human plasma via liquid chromatography-mass spectrometry. *Anal Chim Acta* **2023**, *1279*, 341791. DOI: 10.1016/j.aca.2023.341791 From NLM Medline.
(72) Meng, Y.; Cheng, M.; Qu, H.; Song, Z.; Zhang, L.; Zeng, Y.; Zhang, D.; Li, S. Targeted plasma metabolomics reveals potential biomarkers of the elderly with mild cognitive impairment in Qingdao rural area. *Front Aging Neurosci* **2024**, *16*, 1511437. DOI: 10.3389/fnagi.2024.1511437 From NLM PubMed-not-MEDLINE.

(73) Baiges-Gaya, G.; Iftimie, S.; Castane, H.; Rodriguez-Tomas, E.; Jimenez-Franco, A.; Lopez-Azcona, A. F.; Castro, A.; Camps, J.; Joven, J. Combining Semi-Targeted Metabolomics and Machine Learning to Identify Metabolic Alterations in the Serum and Urine of Hospitalized Patients with COVID-19. *Biomolecules* **2023**, *13* (1). DOI: 10.3390/biom13010163 From NLM Medline.
(74) Walsby-Tickle, J.; Gannon, J.; Hvinden, I.; Bardella, C.; Abboud, M. I.; Nazeer, A.; Hauton, D.; Pires, E.; Cadoux-Hudson, T.; Schofield, C. J.; et al. Anion-exchange chromatography mass spectrometry provides extensive coverage of primary metabolic pathways revealing altered metabolism in IDH1 mutant cells. *Commun Biol* **2020**, *3* (1), 247. DOI: 10.1038/s42003-020-0957-6 From NLM Medline.
(75) Lopes, J.; Correia, M.; Martins, I.; Henriques, A. G.; Delgadillo, I.; da Cruz, E. S. O.; Nunes, A. FTIR and Raman Spectroscopy Applied to Dementia Diagnosis Through Analysis of Biological Fluids. *J Alzheimers Dis* **2016**, *52* (3), 801–812. DOI: 10.3233/JAD-151163 From NLM Medline.
(76) Sasaki, K.; Sagawa, H.; Suzuki, M.; Yamamoto, H.; Tomita, M.; Soga, T.; Ohashi, Y. Metabolomics Platform with Capillary Electrophoresis Coupled with High-Resolution Mass Spectrometry for Plasma Analysis. *Anal Chem* **2019**, *91* (2), 1295–1301. DOI: 10.1021/acs.analchem.8b02994 From NLM Medline.
(77) Abu Sammour, D.; Cairns, J. L.; Boskamp, T.; Marsching, C.; Kessler, T.; Ramallo Guevara, C.; Panitz, V.; Sadik, A.; Cordes, J.; Schmidt, S.; et al. Spatial probabilistic mapping of metabolite ensembles in mass spectrometry imaging. *Nat Commun* **2023**, *14* (1), 1823. DOI: 10.1038/s41467-023-37394-z From NLM Medline.
(78) Malik, M.; Demetrowitsch, T.; Schwarz, K.; Kunze, T. New perspectives on 'Breathomics': metabolomic profiling of non-volatile organic compounds in exhaled breath using DI-FT-ICR-MS. *Commun Biol* **2024**, *7* (1), 258. DOI: 10.1038/s42003-024-05943-x From NLM Medline.
(79) Pouli, D.; Thieu, H. T.; Genega, E. M.; Baecher-Lind, L.; House, M.; Bond, B.; Roncari, D. M.; Evans, M. L.; Rius-Diaz, F.; Munger, K.; et al. Label-free, High-Resolution Optical Metabolic Imaging of Human Cervical Precancers Reveals Potential for Intraepithelial Neoplasia Diagnosis. *Cell Rep Med* **2020**, *1* (2). DOI: 10.1016/j.xcrm.2020.100017 From NLM Medline.
(80) Smolinska, A.; Blanchet, L.; Buydens, L. M. C.; Wijmenga, S. S. NMR and pattern recognition methods in metabolomics: From data acquisition to biomarker discovery: A review. *Anal Chim Acta* **2012**, *750*, 82–97. DOI: 10.1016/j.aca.2012.05.049.
(81) Yeo, T.; Probert, F.; Sealey, M.; Saldana, L.; Geraldes, R.; Hoeckner, S.; Schiffer, E.; Claridge, T. D. W.; Leppert, D.; DeLuca, G.; et al. Objective biomarkers for clinical relapse in multiple sclerosis: a metabolomics approach. *Brain Commun* **2021**, *3* (4), fcab240. DOI: 10.1093/braincomms/fcab240 From NLM PubMed-not-MEDLINE.
(82) Kacerova, T.; Pires, E.; Walsby-Tickle, J.; Probert, F.; McCullagh, J. S. O. Integrating NMR and Multi-LC-MS-Based Untargeted Metabolomics for Comprehensive Analysis of Blood Serum Samples. *Anal Chim Acta* **2025**, *1356*. DOI: 10.1016/j.aca.2025.343979.
(83) Alseekh, S.; Aharoni, A.; Brotman, Y.; Contrepois, K.; D'Auria, J.; Ewald, J.; Ewald, J. C.; Fraser, P. D.; Giavalisco, P.; Hall, R. D.; et al. Mass spectrometry-based metabolomics: a guide for annotation, quantification and best reporting practices. *Nat Methods* **2021**, *18* (7), 747–756. DOI: 10.1038/s41592-021-01197-1.
(84) Barrett, D. Advances in Metabolic Profiling. *Bioanalysis* **2012**, *4* (6), 643–644. DOI: 10.4155/Bio.12.23.
(85) MohammadiPeyhani, H.; Hafner, J.; Sveshnikova, A.; Viterbo, V.; Hatzimanikatis, V. Expanding biochemical knowledge and illuminating metabolic dark matter with ATLASx. *Nat Commun* **2022**, *13* (1), 1560. DOI: 10.1038/s41467-022-29238-z From NLM Medline.
(86) Beltran, A.; Suarez, M.; Rodriguez, M. A.; Vinaixa, M.; Samino, S.; Arola, L.; Correig, X.; Yanes, O. Assessment of Compatibility between Extraction Methods for NMR- and LC/MS-Based Metabolomics. *Anal Chem* **2012**, *84* (14), 5838–5844. DOI: 10.1021/ac3005567.
(87) Stringer, K. A.; McKay, R. T.; Karnovsky, A.; Quemerais, B.; Lacy, P. Metabolomics and Its Application to Acute Lung Diseases. *Front Immunol* **2016**, *7*, 44. DOI: 10.3389/fimmu.2016.00044 From NLM PubMed-not-MEDLINE.
(88) Marshall, D. D.; Powers, R. Beyond the paradigm: Combining mass spectrometry and nuclear magnetic resonance for metabolomics. *Prog Nucl Mag Res Sp* **2017**, *100*, 1–16. DOI: 10.1016/j.pnmrs.2017.01.001.
(89) Psychogios, N.; Hau, D. D.; Peng, J.; Guo, A. C.; Mandal, R.; Bouatra, S.; Sinelnikov, I.; Krishnamurthy, R.; Eisner, R.; Gautam, B.; et al. The human serum metabolome. *Plos One* **2011**, *6* (2), e16957. DOI: 10.1371/journal.pone.0016957 From NLM Medline.
(90) Bieber, S.; Greco, G.; Grosse, S.; Letzel, T. RPLC-HILIC and SFC with Mass Spectrometry: Polarity-Extended Organic Molecule Screening in Environmental (Water) Samples. *Anal Chem* **2017**, *89* (15), 7907–7914. DOI: 10.1021/acs.analchem.7b00859 From NLM PubMed-not-MEDLINE.
(91) Lange, M.; Fedorova, M. Evaluation of lipid quantification accuracy using HILIC and RPLC MS on the example of NIST(R) SRM(R) 1950 metabolites in human plasma. *Anal Bioanal Chem* **2020**, *412* (15), 3573–3584. DOI: 10.1007/s00216-020-02576-x From NLM Medline.
(92) Gowda, G. A. N.; Raftery, D. Quantitating Metabolites in Protein Precipitated Serum Using NMR Spectroscopy. *Anal Chem* **2014**, *86* (11), 5433–5440. DOI: 10.1021/ac5005103.

(93) Claridge, T. *High-Resolution NMR Techniques in Organic Chemistry*; Elsevier, 2009.
(94) Keeler, J. Understanding NMR spectroscopy. 2nd ed.; John Wiley and Sons: Chichester, 2010.
(95) Rodriguez-Martinez, A.; Posma, J. M.; Ayala, R.; Harvey, N.; Jimenez, B.; Neves, A. L.; Lindon, J. C.; Sonomura, K.; Sato, T. A.; Matsuda, F.; et al. J-Resolved (1)H NMR 1D-Projections for Large-Scale Metabolic Phenotyping Studies: Application to Blood Plasma Analysis. *Anal Chem* **2017**, *89* (21), 11405–11412. DOI: 10.1021/acs.analchem.7b02374 From NLM Medline.
(96) Aguilar, J. A.; Cassani, J.; Probert, F.; Palace, J.; Claridge, T. D. W.; Botana, A.; Kenwright, A. M. Reliable, high-quality suppression of NMR signals arising from water and macromolecules: application to bio-fluid analysis. *Analyst* **2019**, *144* (24), 7270–7277. DOI: 10.1039/c9an01005j.
(97) Verhoeven, A.; Slagboom, E.; Wuhrer, M.; Giera, M.; Mayboroda, O. A. Automated quantification of metabolites in blood-derived samples by NMR. *Anal Chim Acta* **2017**, *976*, 52–62. DOI: 10.1016/j.aca.2017.04.013 From NLM Medline.
(98) Bouatra, S.; Aziat, F.; Mandal, R.; Guo, A. C.; Wilson, M. R.; Knox, C.; Bjorndahl, T. C.; Krishnamurthy, R.; Saleem, F.; Liu, P.; et al. The human urine metabolome. *Plos One* **2013**, *8* (9), e73076. DOI: 10.1371/journal.pone.0073076 From NLM Medline.
(99) Mulder, F. A. A.; Tenori, L.; Licari, C.; Luchinat, C. Practical considerations for rapid and quantitative NMR-based metabolomics. *J Magn Reson* **2023**, *352*, 107462. DOI: 10.1016/j.jmr.2023.107462 From NLM Medline.
(100) Giraudeau, P.; Silvestre, V.; Akoka, S. Optimizing water suppression for quantitative NMR-based metabolomics: a tutorial review. *Metabolomics* **2015**, *11*, 1041–1055.
(101) Freeman, R.; Morris, G. A. The 'DANTE' experiment. *J Magn Reson* **2011**, *213* (2), 244–246. DOI: 10.1016/j.jmr.2011.08.020 From NLM Medline.
(102) Baumstark, D.; Kremer, W.; Boettcher, A.; Schreier, C.; Sander, P.; Schmitz, G.; Kirchhoefer, R.; Huber, F.; Kalbitzer, H. R. H NMR spectroscopy quantifies visibility of lipoproteins, subclasses, and lipids at varied temperatures and pressures[S]. *J Lipid Res* **2019**, *60* (9), 1516–1534. DOI: 10.1194/jlr.M092643.
(103) Cox, R. A.; García-Palmieri, M. R. Cholesterol, Triglycerides, and Associated Lipoproteins. In *Clinical Methods: The History, Physical, and Laboratory Examinations*, 3rd ed.; Walker, H. K., Hall, W. D., Hurst, J. W. Eds.; Butterworths, 1990.
(104) Hajjar, G.; Merchak, N.; Daniel, C.; Rizk, T.; Akoka, S.; Bejjani, J. Improved lipid mixtures profiling by (1)H NMR using reference lineshape adjustment and deconvolution techniques. *Talanta* **2020**, *208*, 120475. DOI: 10.1016/j.talanta.2019.120475 From NLM PubMed-not-MEDLINE.
(105) Kanonidou, C. Small dense low-density lipoprotein: Analytical review. *Clin Chim Acta* **2021**, *520*, 172–178. DOI: 10.1016/j.cca.2021.06.012 From NLM Medline.
(106) McCullagh, J.; Oldham, N. *Mass spectrometry*; Oxford University Press, 2023.
(107) Clark, A. E.; Kaleta, E. J.; Arora, A.; Wolk, D. M. Matrix-assisted laser desorption ionization-time of flight mass spectrometry: a fundamental shift in the routine practice of clinical microbiology. *Clin Microbiol Rev* **2013**, *26* (3), 547–603. DOI: 10.1128/CMR.00072-12 From NLM Medline.
(108) Beaufour, M.; Ginguene, D.; Le Meur, R.; Castaing, B.; Cadene, M. Liquid Native MALDI Mass Spectrometry for the Detection of Protein-Protein Complexes. *J Am Soc Mass Spectrom* **2018**, *29* (10), 1981–1994. DOI: 10.1007/s13361-018-2015-x From NLM Medline.
(109) Schwaiger-Haber, M.; Stancliffe, E.; Anbukumar, D. S.; Sells, B.; Yi, J.; Cho, K.; Adkins-Travis, K.; Chheda, M. G.; Shriver, L. P.; Patti, G. J. Using mass spectrometry imaging to map fluxes quantitatively in the tumor ecosystem. *Nat Commun* **2023**, *14* (1), 2876. DOI: 10.1038/s41467-023-38403-x From NLM Medline.
(110) Levasseur, M.; Nicol, E.; Elie, N.; Houel, E.; Eparvier, V.; Touboul, D. Spatialized Metabolomic Annotation Combining MALDI Imaging and Molecular Networks. *Anal Chem* **2024**, *96* (1), 18–22. DOI: 10.1021/acs.analchem.3c03482 From NLM Medline.
(111) He, M. J.; Pu, W.; Wang, X.; Zhang, W.; Tang, D.; Dai, Y. Comparing DESI-MSI and MALDI-MSI Mediated Spatial Metabolomics and Their Applications in Cancer Studies. *Front Oncol* **2022**, *12*, 891018. DOI: 10.3389/fonc.2022.891018 From NLM PubMed-not-MEDLINE.
(112) Martin, N. J.; Bunch, J.; Cooper, H. J. Dried blood spot proteomics: surface extraction of endogenous proteins coupled with automated sample preparation and mass spectrometry analysis. *J Am Soc Mass Spectrom* **2013**, *24* (8), 1242–1249. DOI: 10.1007/s13361-013-0658-1 From NLM Medline.
(113) Vreeker, G. C. M.; Bladergroen, M. R.; Nicolardi, S.; Mesker, W. E.; Tollenaar, R.; van der Burgt, Y. E. M.; Wuhrer, M. Dried blood spot N-glycome analysis by MALDI mass spectrometry. *Talanta* **2019**, *205*, 120104. DOI: 10.1016/j.talanta.2019.06.104 From NLM Medline.
(114) Hale, O. J.; Cooper, H. J. Native Mass Spectrometry Imaging of Proteins and Protein Complexes by Nano-DESI. *Anal Chem* **2021**, *93* (10), 4619–4627. DOI: 10.1021/acs.analchem.0c05277 From NLM Medline.
(115) Choucair, I.; Shang, E.; Tran, M. N.; Cassella-McLane, G.; El-Khoury, J. M. Direct analysis in real time mass spectrometry (DART-MS/MS) for rapid urine opioid detection in a clinical setting. *Clin Chim Acta* **2025**, *564*, 119939. DOI: 10.1016/j.cca.2024.119939 From NLM Medline.

(116) Vuckovic, D. Current trends and challenges in sample preparation for global metabolomics using liquid chromatography-mass spectrometry. *Anal Bioanal Chem* **2012**, *403* (6), 1523–1548. DOI: 10.1007/s00216-012-6039-y.
(117) de Hoffmann, E.; Stroobant, V. *Mass Spectrometry: Principles and Applications*; Wiley, 2012.
(118) Birdsall, R. E.; Kellett, J.; Yu, Y. Q.; Chen, W. Application of mobile phase additives to reduce metal-ion mediated adsorption of non-phosphorylated peptides in RPLC/MS-based assays. *J Chromatogr B Analyt Technol Biomed Life Sci* **2019**, *1126-1127*, 121773. DOI: 10.1016/j.jchromb.2019.121773 From NLM Medline.
(119) Cajka, T.; Hricko, J.; Kulhava, L. R.; Paucova, M.; Novakova, M.; Kuda, O. Optimization of Mobile Phase Modifiers for Fast LC-MS-Based Untargeted Metabolomics and Lipidomics. *Int J Mol Sci* **2023**, *24* (3). DOI: ARTN 198710.3390/ijms24031987.
(120) Janda, M.; Seah, B. K. B.; Jakob, D.; Beckmann, J.; Geier, B.; Liebeke, M. Determination of Abundant Metabolite Matrix Adducts Illuminates the Dark Metabolome of MALDI-Mass Spectrometry Imaging Datasets. *Anal Chem* **2021**, *93* (24), 8399–8407. DOI: 10.1021/acs.analchem.0c04720 From NLM Medline.
(121) Schwaiger-Haber, M.; Stancliffe, E.; Arends, V.; Thyagarajan, B.; Sindelar, M.; Patti, G. J. A Workflow to Perform Targeted Metabolomics at the Untargeted Scale on a Triple Quadrupole Mass Spectrometer. *ACS Meas Sci Au* **2021**, *1* (1), 35–45. DOI: 10.1021/acsmeasuresciau.1c00007 From NLM PubMed-not-MEDLINE.
(122) Zhou, J.; Yin, Y. Strategies for large-scale targeted metabolomics quantification by liquid chromatography-mass spectrometry. *Analyst* **2016**, *141* (23), 6362–6373. DOI: 10.1039/c6an01753c From NLM Medline.
(123) Syslova, K.; Bohmova, A.; Mikoska, M.; Kuzma, M.; Pelclova, D.; Kacer, P. Multimarker screening of oxidative stress in aging. *Oxid Med Cell Longev* **2014**, *2014*, 562860. DOI: 10.1155/2014/562860 From NLM Medline.
(124) Zubarev, R. A.; Makarov, A. Orbitrap mass spectrometry. *Anal Chem* **2013**, *85* (11), 5288–5296. DOI: 10.1021/ac4001223 From NLM Medline.
(125) Reinbold, R.; Hvinden, I. C.; Rabe, P.; Herold, R. A.; Finch, A.; Wood, J.; Morgan, M.; Staudt, M.; Clifton, I. J.; Armstrong, F. A.; et al. Resistance to the isocitrate dehydrogenase 1 mutant inhibitor ivosidenib can be overcome by alternative dimer-interface binding inhibitors. *Nat Commun* **2022**, *13* (1). DOI: ARTN 478510.1038/s41467-022-32436-4.
(126) Shulaev, V.; Isaac, G. Supercritical fluid chromatography coupled to mass spectrometry - A metabolomics perspective. *J Chromatogr B* **2018**, *1092*, 499–505. DOI: 10.1016/j.jchromb.2018.06.021.
(127) Dunn, W. B.; Bailey, N. J.; Johnson, H. E. Measuring the metabolome: current analytical technologies. *Analyst* **2005**, *130* (5), 606–625. DOI: 10.1039/b418288j From NLM Medline.
(128) Schott, H. F.; Konings, M.; Schrauwen-Hinderling, V. B.; Mensink, R. P.; Plat, J. A Validated Method for Quantification of Fatty Acids Incorporated in Human Plasma Phospholipids by Gas Chromatography-Triple Quadrupole Mass Spectrometry. *ACS Omega* **2021**, *6* (2), 1129–1137. DOI: 10.1021/acsomega.0c03874 From NLM PubMed-not-MEDLINE.
(129) Antolin, E. M.; Delange, D. M.; Canavaciolo, V. G. Evaluation of five methods for derivatization and GC determination of a mixture of very long chain fatty acids (C24:0-C36:0). *J Pharm Biomed Anal* **2008**, *46* (1), 194–199. DOI: 10.1016/j.jpba.2007.09.015 From NLM Medline.
(130) Zeki, O. C.; Eylem, C. C.; Recber, T.; Kir, S.; Nemutlu, E. Integration of GC-MS and LC-MS for untargeted metabolomics profiling. *J Pharm Biomed Anal* **2020**, *190*, 113509. DOI: 10.1016/j.jpba.2020.113509 From NLM Medline.
(131) Doerfler, H.; Lyon, D.; Nagele, T.; Sun, X.; Fragner, L.; Hadacek, F.; Egelhofer, V.; Weckwerth, W. Granger causality in integrated GC-MS and LC-MS metabolomics data reveals the interface of primary and secondary metabolism. *Metabolomics* **2013**, *9* (3), 564–574. DOI: 10.1007/s11306-012-0470-0 From NLM PubMed-not-MEDLINE.
(132) Ngere, J. B.; Ebrahimi, K. H.; Williams, R.; Pires, E.; Walsby-Tickle, J.; McCullagh, J. S. O. Ion-Exchange Chromatography Coupled to Mass Spectrometry in Life Science, Environmental, and Medical Research. *Anal Chem* **2023**, *95* (1), 152–166. DOI: 10.1021/acs.analchem.2c04298.
(133) Zhang, K.; Liu, X. Mixed-mode chromatography in pharmaceutical and biopharmaceutical applications. *J Pharm Biomed Anal* **2016**, *128*, 73–88. DOI: 10.1016/j.jpba.2016.05.007 From NLM Medline.
(134) Tang, D. Q.; Zou, L.; Yin, X. X.; Ong, C. N. HILIC-MS for metabolomics: An attractive and complementary approach to RPLC-MS. *Mass Spectrom Rev* **2016**, *35* (5), 574–600. DOI: 10.1002/mas.21445 From NLM Medline.
(135) Zhang, G. F.; Li, Q. L.; Li, L.; Kasumov, T. Metabolomics Research with Tandem Mass Spectrometry. *Tandem Mass Spectroscopy - Applications and Principles* **2012**, 309–330. DOI: Book_Doi 10.5772/1327.
(136) Zhang, A. H.; Sun, H.; Wang, P.; Han, Y.; Wang, X. J. Modern analytical techniques in metabolomics analysis. *Analyst* **2012**, *137* (2), 293–300. DOI: 10.1039/c1an15605e.
(137) Bian, X.; Li, N.; Tan, B.; Sun, B.; Guo, M. Q.; Huang, G.; Fu, L.; Hsiao, W. L. W.; Liu, L.; Wu, J. L. Polarity-Tuning Derivatization-LC-MS Approach for Probing Global Carboxyl-Containing Metabolites in

Colorectal Cancer. *Anal Chem* **2018**, *90* (19), 11210–11215. DOI: 10.1021/acs.analchem.8b01873 From NLM Medline.
(138) Cai, X.; Zou, L.; Dong, J.; Zhao, L.; Wang, Y.; Xu, Q.; Xue, X.; Zhang, X.; Liang, X. Analysis of highly polar metabolites in human plasma by ultra-performance hydrophilic interaction liquid chromatography coupled with quadrupole-time of flight mass spectrometry. *Anal Chim Acta* **2009**, *650* (1), 10–15. DOI: 10.1016/j.aca.2009.01.054 From NLM Medline.
(139) Bosman, P.; Pichon, V.; Acevedo, A. C.; Chardin, H.; Combes, A. Development of analytical methods to study the salivary metabolome: impact of the sampling. *Anal Bioanal Chem* **2022**, *414* (23), 6899–6909. DOI: 10.1007/s00216-022-04255-5 From NLM Medline.
(140) Cummins, P. M.; Rochfort, K. D.; O'Connor, B. F. Ion-Exchange Chromatography: Basic Principles and Application. *Methods Mol Biol* **2017**, *1485*, 209–223. DOI: 10.1007/978-1-4939-6412-3_11 From NLM Medline.
(141) Inc., T. F. S. Product Manual for the DRS 600 Suppressor. Inc, T. F. S., Ed.; Waltham, MA, USA, 2021.
(142) Kozlov, O.; Hancova, E.; Cifkova, E.; Lisa, M. Comprehensive Single-Platform Lipidomic/Metabolomic Analysis Using Supercritical Fluid Chromatography-Mass Spectrometry. *Anal Chem* **2024**, *96* (3), 1320–1327. DOI: 10.1021/acs.analchem.3c04771 From NLM Medline.
(143) Folprechtova, D.; Schmid, M. G.; Armstrong, D. W.; Kalikova, K. The Enantioselective Potential of NicoShell and TeicoShell Columns for Basic Pharmaceuticals and Forensic Drugs in Sub/Supercritical Fluid Chromatography. *Molecules* **2023**, *28* (3). DOI: 10.3390/molecules28031202 From NLM Medline.
(144) Kalikova, K.; Martinkova, M.; Schmid, M. G.; Tesarova, E. Cellulose tris-(3,5-dimethylphenylcarbamate)-based chiral stationary phase for the enantioseparation of drugs in supercritical fluid chromatography: comparison with HPLC. *J Sep Sci* **2018**, *41* (6), 1471–1478. DOI: 10.1002/jssc.201701341 From NLM Medline.
(145) Storbeck, K. H.; Gilligan, L.; Jenkinson, C.; Baranowski, E. S.; Quanson, J. L.; Arlt, W.; Taylor, A. E. The utility of ultra-high performance supercritical fluid chromatography-tandem mass spectrometry (UHPSFC-MS/MS) for clinically relevant steroid analysis. *J Chromatogr B Analyt Technol Biomed Life Sci* **2018**, *1085*, 36–41. DOI: 10.1016/j.jchromb.2018.03.033 From NLM Medline.
(146) Fassauer, G. M.; Hofstetter, R.; Hasan, M.; Oswald, S.; Modess, C.; Siegmund, W.; Link, A. Ketamine metabolites with antidepressant effects: Fast, economical, and eco-friendly enantioselective separation based on supercritical-fluid chromatography (SFC) and single quadrupole MS detection. *J Pharm Biomed Anal* **2017**, *146*, 410–419. DOI: 10.1016/j.jpba.2017.09.007 From NLM Medline.
(147) Segawa, H.; Iwata, Y. T.; Okada, Y.; Yamamuro, T.; Kuwayama, K.; Tsujikawa, K.; Kanamori, T. Rapid enantiomeric analysis of zopiclone in serum by supercritical fluid chromatography-tandem mass spectrometry. *J Forensic Sci* **2023**, *68* (4), 1352–1358. DOI: 10.1111/1556-4029.15279 From NLM Medline.
(148) Wolrab, D.; Fruhauf, P.; Gerner, C. Quantification of the neurotransmitters melatonin and N-acetyl-serotonin in human serum by supercritical fluid chromatography coupled with tandem mass spectrometry. *Anal Chim Acta* **2016**, *937*, 168–174. DOI: 10.1016/j.aca.2016.08.012 From NLM Medline.
(149) Yamada, T.; Uchikata, T.; Sakamoto, S.; Yokoi, Y.; Nishiumi, S.; Yoshida, M.; Fukusaki, E.; Bamba, T. Supercritical fluid chromatography/Orbitrap mass spectrometry based lipidomics platform coupled with automated lipid identification software for accurate lipid profiling. *J Chromatogr A* **2013**, *1301*, 237–242. DOI: 10.1016/j.chroma.2013.05.057 From NLM Medline.
(150) Karaman, I. Preprocessing and Pretreatment of Metabolomics Data for Statistical Analysis. *Adv Exp Med Biol* **2017**, *965*, 145–161. DOI: 10.1007/978-3-319-47656-8_6 From NLM Medline.
(151) Ebbels, T. M.; Lindon, J. C.; Coen, M. Processing and modeling of nuclear magnetic resonance (NMR) metabolic profiles. *Methods Mol Biol* **2011**, *708*, 365–388. DOI: 10.1007/978-1-61737-985-7_21 From NLM Medline.
(152) Gonzalez-Dominguez, A.; Estanyol-Torres, N.; Brunius, C.; Landberg, R.; Gonzalez-Dominguez, R. QComics: Recommendations and Guidelines for Robust, Easily Implementable and Reportable Quality Control of Metabolomics Data. *Anal Chem* **2024**, *96* (3), 1064–1072. DOI: 10.1021/acs.analchem.3c03660 From NLM Medline.
(153) Broeckling, C. D.; Beger, R. D.; Cheng, L. L.; Cumeras, R.; Cuthbertson, D. J.; Dasari, S.; Davis, W. C.; Dunn, W. B.; Evans, A. M.; Fernandez-Ochoa, A.; et al. Current Practices in LC-MS Untargeted Metabolomics: A Scoping Review on the Use of Pooled Quality Control Samples. *Anal Chem* **2023**, *95* (51), 18645–18654. DOI: 10.1021/acs.analchem.3c02924 From NLM Medline.
(154) Dunn, W. B.; Broadhurst, D.; Begley, P.; Zelena, E.; Francis-McIntyre, S.; Anderson, N.; Brown, M.; Knowles, J. D.; Halsall, A.; Haselden, J. N.; et al. Procedures for large-scale metabolic profiling of serum and plasma using gas chromatography and liquid chromatography coupled to mass spectrometry. *Nat Protoc* **2011**, *6* (7), 1060–1083. DOI: 10.1038/nprot.2011.335 From NLM Medline.
(155) Tokuoka, S. M.; Yasumoto, A.; Kita, Y.; Shimizu, T.; Yatomi, Y.; Oda, Y. Limitations of deuterium-labeled internal standards for quantitative electrospray ionization mass spectrometry analysis of fatty acid metabolites. *Rapid Commun Mass Spectrom* **2020**, *34* (13), e8814. DOI: 10.1002/rcm.8814 From NLM Medline.

(156) Jacob, D.; Deborde, C.; Lefebvre, M.; Maucourt, M.; Moing, A. NMRProcFlow: a graphical and interactive tool dedicated to 1D spectra processing for NMR-based metabolomics. *Metabolomics* **2017**, *13* (4), 36. DOI: 10.1007/s11306-017-1178-y From NLM PubMed-not-MEDLINE.
(157) Rundlof, T.; Mathiasson, M.; Bekiroglu, S.; Hakkarainen, B.; Bowden, T.; Arvidsson, T. Survey and qualification of internal standards for quantification by 1H NMR spectroscopy. *J Pharm Biomed Anal* **2010**, *52* (5), 645–651. DOI: 10.1016/j.jpba.2010.02.007 From NLM Medline.
(158) Schmid, R.; Heuckeroth, S.; Korf, A.; Smirnov, A.; Myers, O.; Dyrlund, T. S.; Bushuiev, R.; Murray, K. J.; Hoffmann, N.; Lu, M.; et al. Integrative analysis of multimodal mass spectrometry data in MZmine 3. *Nat Biotechnol* **2023**, *41* (4), 447–449. DOI: 10.1038/s41587-023-01690-2 From NLM Medline.
(159) MacLean, B.; Tomazela, D. M.; Shulman, N.; Chambers, M.; Finney, G. L.; Frewen, B.; Kern, R.; Tabb, D. L.; Liebler, D. C.; MacCoss, M. J. Skyline: an open source document editor for creating and analyzing targeted proteomics experiments. *Bioinformatics* **2010**, *26* (7), 966–968. DOI: 10.1093/bioinformatics/btq054 From NLM Medline.
(160) Jansen, B. C.; Falck, D.; de Haan, N.; Hipgrave Ederveen, A. L.; Razdorov, G.; Lauc, G.; Wuhrer, M. LaCyTools: A Targeted Liquid Chromatography-Mass Spectrometry Data Processing Package for Relative Quantitation of Glycopeptides. *J Proteome Res* **2016**, *15* (7), 2198–2210. DOI: 10.1021/acs.jproteome.6b00171 From NLM Medline.
(161) Tautenhahn, R.; Patti, G. J.; Rinehart, D.; Siuzdak, G. XCMS Online: a web-based platform to process untargeted metabolomic data. *Anal Chem* **2012**, *84* (11), 5035–5039. DOI: 10.1021/ac300698c From NLM Medline.
(162) Takeda, H.; Matsuzawa, Y.; Takeuchi, M.; Takahashi, M.; Nishida, K.; Harayama, T.; Todoroki, Y.; Shimizu, K.; Sakamoto, N.; Oka, T.; et al. MS-DIAL 5 multimodal mass spectrometry data mining unveils lipidome complexities. *Nat Commun* **2024**, *15* (1), 9903. DOI: 10.1038/s41467-024-54137-w From NLM Medline.
(163) Hoffmann, M. A.; Nothias, L. F.; Ludwig, M.; Fleischauer, M.; Gentry, E. C.; Witting, M.; Dorrestein, P. C.; Duhrkop, K.; Bocker, S. High-confidence structural annotation of metabolites absent from spectral libraries. *Nat Biotechnol* **2022**, *40* (3), 411–421. DOI: 10.1038/s41587-021-01045-9 From NLM Medline.
(164) Liu, Q.; Walker, D.; Uppal, K.; Liu, Z.; Ma, C.; Tran, V.; Li, S.; Jones, D. P.; Yu, T. Addressing the batch effect issue for LC/MS metabolomics data in data preprocessing. *Sci Rep* **2020**, *10* (1), 13856. DOI: 10.1038/s41598-020-70850-0 From NLM Medline.
(165) Sumner, L. W.; Amberg, A.; Barrett, D.; Beale, M. H.; Beger, R.; Daykin, C. A.; Fan, T. W.; Fiehn, O.; Goodacre, R.; Griffin, J. L.; et al. Proposed minimum reporting standards for chemical analysis Chemical Analysis Working Group (CAWG) Metabolomics Standards Initiative (MSI). *Metabolomics* **2007**, *3* (3), 211–221. DOI: 10.1007/s11306-007-0082-2 From NLM PubMed-not-MEDLINE.
(166) Fiehn, O.; Robertson, D.; Griffin, J. L.; van der Werf, M. J.; Nikolau, B.; Morrison, N.; Sumner, L. W.; Goodacre, R.; Taylor, C. A.; Fostel, J.; et al. The metabolomics standards initiative (MSI). *Metabolomics* **2007**, *3*, 175–178. DOI: https://doi.org/10.1007/s11306-007-0070-6.
(167) Brunius, C.; Shi, L.; Landberg, R. Large-scale untargeted LC-MS metabolomics data correction using between-batch feature alignment and cluster-based within-batch signal intensity drift correction. *Metabolomics* **2016**, *12* (11), 173. DOI: 10.1007/s11306-016-1124-4 From NLM PubMed-not-MEDLINE.
(168) Thonusin, C.; IglayReger, H. B.; Soni, T.; Rothberg, A. E.; Burant, C. F.; Evans, C. R. Evaluation of intensity drift correction strategies using MetaboDrift, a normalization tool for multi-batch metabolomics data. *J Chromatogr A* **2017**, *1523*, 265–274. DOI: 10.1016/j.chroma.2017.09.023 From NLM Medline.
(169) Luan, H.; Ji, F.; Chen, Y.; Cai, Z. statTarget: A streamlined tool for signal drift correction and interpretations of quantitative mass spectrometry-based omics data. *Anal Chim Acta* **2018**, *1036*, 66–72. DOI: 10.1016/j.aca.2018.08.002 From NLM Medline.
(170) Willforss, J.; Chawade, A.; Levander, F. NormalyzerDE: Online Tool for Improved Normalization of Omics Expression Data and High-Sensitivity Differential Expression Analysis. *J Proteome Res* **2019**, *18* (2), 732–740. DOI: 10.1021/acs.jproteome.8b00523 From NLM Medline.
(171) Chilimoniuk, J.; Grzesiak, K.; Kala, J.; Nowakowski, D.; Kretowski, A.; Kolenda, R.; Ciborowski, M.; Burdukiewicz, M. imputomics: web server and R package for missing values imputation in metabolomics data. *Bioinformatics* **2024**, *40* (3). DOI: 10.1093/bioinformatics/btae098 From NLM Medline.
(172) Wei, R.; Wang, J.; Su, M.; Jia, E.; Chen, S.; Chen, T.; Ni, Y. Missing Value Imputation Approach for Mass Spectrometry-based Metabolomics Data. *Sci Rep* **2018**, *8* (1), 663. DOI: 10.1038/s41598-017-19120-0 From NLM Medline.
(173) van den Berg, R. A.; Hoefsloot, H. C.; Westerhuis, J. A.; Smilde, A. K.; van der Werf, M. J. Centering, scaling, and transformations: improving the biological information content of metabolomics data. *BMC Genomics* **2006**, *7*, 142. DOI: 10.1186/1471-2164-7-142 From NLM Medline.

(174) Xia, J.; Psychogios, N.; Young, N.; Wishart, D. S. MetaboAnalyst: a web server for metabolomic data analysis and interpretation. *Nucleic Acids Res* **2009**, *37* (Web Server issue), W652–660. DOI: 10.1093/nar/gkp356 From NLM Medline.
(175) Miller, M. J.; Kennedy, A. D.; Eckhart, A. D.; Burrage, L. C.; Wulff, J. E.; Miller, L. A.; Milburn, M. V.; Ryals, J. A.; Beaudet, A. L.; Sun, Q.; et al. Untargeted metabolomic analysis for the clinical screening of inborn errors of metabolism. *J Inherit Metab Dis* **2015**, *38* (6), 1029–1039. DOI: 10.1007/s10545-015-9843-7 From NLM Medline.
(176) Bartel, J.; Krumsiek, J.; Theis, F. J. Statistical methods for the analysis of high-throughput metabolomics data. *Comput Struct Biotechnol J* **2013**, *4*, e201301009. DOI: 10.5936/csbj.201301009 From NLM PubMed-not-MEDLINE.
(177) Fonville, J. M.; Richards, S. E.; Barton, R. H.; Boulange, C. L.; Ebbels, T. M.; Nicholson, K. N.; Holmes, E.; Dumas, M. E. The evolution of partial least squares models and related chemometric approaches in metabonomics and metabolic phenotyping. *Journal of Chemometrics* **2010**, *24*, 636–649. DOI: https://doi.org/10.1002/cem.1359.
(178) Worley, B.; Powers, R. PCA as a practical indicator of OPLS-DA model reliability. *Curr Metabolomics* **2016**, *4* (2), 97–103. DOI: 10.2174/2213235X04666160613122429 From NLM PubMed-not-MEDLINE.
(179) Golbraikh, A.; Tropsha, A. Beware of q2! *J Mol Graph Model* **2002**, *20* (4), 269–276. DOI: 10.1016/s1093-3263(01)00123-1 From NLM Medline.
(180) Thevenot, E. A.; Roux, A.; Xu, Y.; Ezan, E.; Junot, C. Analysis of the Human Adult Urinary Metabolome Variations with Age, Body Mass Index, and Gender by Implementing a Comprehensive Workflow for Univariate and OPLS Statistical Analyses. *J Proteome Res* **2015**, *14* (8), 3322–3335. DOI: 10.1021/acs.jproteome.5b00354 From NLM Medline.
(181) Breiman, L. Random forests. *Mach Learn* **2001**, *45* (1), 5–32. DOI: Doi 10.1023/A:1010933404324.
(182) Jin, Y.; Lan, A.; Dai, Y.; Jiang, L.; Liu, S. Development and testing of a random forest-based machine learning model for predicting events among breast cancer patients with a poor response to neoadjuvant chemotherapy. *Eur J Med Res* **2023**, *28* (1), 394. DOI: 10.1186/s40001-023-01361-7 From NLM Medline.
(183) Radford-Smith, D. E.; Anthony, D. C.; Benz, F.; Grist, J. T.; Lyman, M.; Miller, J. J.; Probert, F. A multivariate blood metabolite algorithm stably predicts risk and resilience to major depressive disorder in the general population. *Ebiomedicine* **2023**, *93*, 104643. DOI: 10.1016/j.ebiom.2023.104643 From NLM Medline.
(184) Nguyen, J. M.; Jezequel, P.; Gillois, P.; Silva, L.; Ben Azzouz, F.; Lambert-Lacroix, S.; Juin, P.; Campone, M.; Gaultier, A.; Moreau-Gaudry, A.; et al. Random forest of perfect trees: concept, performance, applications and perspectives. *Bioinformatics* **2021**, *37* (15), 2165–2174. DOI: 10.1093/bioinformatics/btab074 From NLM PubMed-not-MEDLINE.
(185) Smith, P. F.; Zheng, Y. Applications of Multivariate Statistical and Data Mining Analyses to the Search for Biomarkers of Sensorineural Hearing Loss, Tinnitus, and Vestibular Dysfunction. *Front Neurol* **2021**, *12*, 627294. DOI: 10.3389/fneur.2021.627294 From NLM PubMed-not-MEDLINE.
(186) Bradley, A. P. The use of the area under the ROC curve in the evaluation of machine learning algorithms. *Pattern Recognition* **1997**, *30* (7). DOI: 1145-1159https://doi.org/10.1016/S0031-3203(96)00142-2.
(187) Robin, X.; Turck, N.; Hainard, A.; Tiberti, N.; Lisacek, F.; Sanchez, J. C.; Muller, M. pROC: an open-source package for R and S+ to analyze and compare ROC curves. *Bmc Bioinformatics* **2011**, *12*, 77. DOI: 10.1186/1471-2105-12-77 From NLM Medline.
(188) Probert, F.; Yeo, T. R.; Zhou, Y. F.; Sealey, M.; Arora, S.; Palace, J.; Claridge, T. D. W.; Hillenbrand, R.; Oechtering, J.; Kuhle, J.; et al. Determination of CSF GFAP, CCN5, and vWF Levels Enhances the Diagnostic Accuracy of Clinically Defined MS From Non-MS Patients With CSF Oligoclonal Bands. *Front Immunol* **2022**, *12*. DOI: ARTN 81135110.3389/fimmu.2021.811351.

2. 4 Statement of Authorship

Title of paper	Integrating NMR and multi-LC-MS-based untargeted metabolomics for comprehensive analysis of blood serum samples
Publication status	Published
Publication details	Kacerova, T., Pires, E., Walsby-Tickle, J., Probert, F. & McCullagh, J.: **Integrating NMR and multi-LC-MS-based untargeted metabolomics for comprehensive analysis of blood serum samples.** *Anal Chim Acta* **1356**, 343979 (2025)

Student confirmation

Student name	Tereza Kacerova
Contribution to the paper	T.K. Conceptualisation of the study, Sample preparation, NMR, and LC-MS analysis, Data analysis and interpretation, Manuscript writing; E.P. and J. W. T. provided initial LC-MS training and assistance; F. P. and J. S. O. M. are the principal investigators/supervisors of the research described in the manuscript, contributed extensively to project/data conceptualisation and visualisation, and manuscript reviewing/editing.
Date	30/06/2025
Signature	

Supervisor confirmation

By signing the Statement of Authorship, you are certifying that the candidate made a substantial contribution to the publication, and that the description described above is accurate.

Supervisor name	Prof James S. O. McCullagh
Contribution to the paper	I am happy to state that the candidate made a major and substantial contribution this publication, and that the description above is accurate.
Date	29th June 2025
Signature	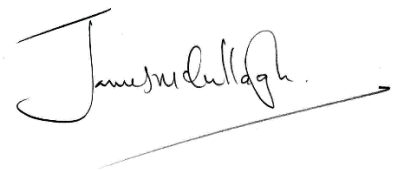

Chapter 2 Developing an Integrated NMR and LC-MS Workflow for Serum-Based Metabolomics

2. 1 Project context and chapter overview

Robust analytical foundations are essential for any metabolomics study, particularly when integrating data across multiple platforms and bridging exploratory research with clinical application. NMR and LC-MS constitute analytically complementary platforms in metabolomics, each defined by distinct physicochemical principles, performance characteristics, and methodological considerations. Integrating these can expand metabolome coverage by capturing a wider spectrum of diverse compound classes and provide cross-platform validation for common metabolites. However, despite their complementarity, the routine integration of NMR and LC-MS remains limited - primarily due to challenges in standardising sample preparation across platforms, especially when working with limited sample volumes. This constraint is common in comprehensive studies involving multiple analytical modalities or when only a single aliquot of biological sample is available. Common approaches to multiplatform metabolomics include parallel processing of separate aliquots using platform-specific protocols, computational alignment of independently acquired datasets, and sample-splitting strategies with tailored extraction procedures for each technique.[1-3] While these methods enable dual-platform analysis, they often require larger sample volumes, increase the risk of analyte loss, and add complexity to data analysis and integration. Given the limited serum volumes available in the clinical studies presented in this thesis, such strategies were not feasible.

This chapter reports the development of a method that enables sequential NMR and multi-platform LC-MS analyses to be performed on a single serum aliquot, without compromising analytical quality or metabolite coverage. The primary aim was to establish a workflow compatible with low-volume, biobanked clinical cohorts such as VITACOG (**Chapter 6**), where maximising analytical output from limited sample input is essential for untargeted, discovery-driven metabolomics. The protocol was designed to support direct, sequential application of NMR and LC-MS, including both RPLC-MS and IC-MS, without the need for solvent exchange or extensive sample reprocessing. This approach preserves sample integrity, minimises sample consumption, and facilitates broad, physicochemically diverse metabolite coverage across complementary analytical platforms.

Although this protocol was developed within the context of neurodegenerative disease research, its primary aim is to support biomarker discovery in research settings, particularly in retrospective clinical cohorts where sample volumes are limited and pre-analytical variability cannot be controlled. Designed as a flexible and efficient workflow, the approach enables sequential NMR and multi-platform LC-MS analyses from a single serum aliquot, maximising metabolite coverage while minimising sample consumption.

To establish a robust, cross-platform analytical pipeline, key methodological variables were systematically evaluated, including deuterated solvent use, phosphate buffering, protein removal strategies, and dilution parameters. These optimisation steps were essential to ensure compatibility between NMR and LC-MS platforms without the need for solvent exchange or sample reprocessing.

The resulting protocol offers a streamlined approach for high-throughput, untargeted metabolomics and establishes the analytical foundation for the biomarker discovery studies described in the subsequent chapters, which collectively focus on early disease detection, mechanistic insight, and patient stratification in volume-constrained clinical cohorts.

2. 2 References

(1) Bird, S. S.; Sheldon, D. P.; Gathungu, R. M.; Vouros, P.; Kautz, R.; Matson, W. R.; Kristal, B. S. Structural Characterization of Plasma Metabolites Detected via LC-Electrochemical Coulometric Array Using LC-UV Fractionation, MS, and NMR. *Anal Chem* **2012**, *84* (22), 9889-9898. DOI: 10.1021/ac302278u.
(2) Psychogios, N.; Hau, D. D.; Peng, J.; Guo, A. C.; Mandal, R.; Bouatra, S.; Sinelnikov, I.; Krishnamurthy, R.; Eisner, R.; Gautam, B.; et al. The Human Serum Metabolome. *Plos One* **2011**, *6* (2). DOI: ARTN e1695710.1371/journal.pone.0016957.
(3) Marshall, D. D.; Lei, S. L.; Worley, B.; Huang, Y. T.; Garcia-Garcia, A.; Franco, R.; Dodds, E. D.; Powers, R. Combining DI-ESI-MS and NMR datasets for metabolic profiling. *Metabolomics* **2015**, *11* (2), 391-402. DOI: 10.1007/s11306-014-0704-4.

2. 3 Manuscript information

This chapter consists of the following published article:

Kacerova, T., Pires, E., Walsby-Tickle, J., Probert, F. & McCullagh, J.: **Integrating NMR and multi-LC-MS-based untargeted metabolomics for comprehensive analysis of blood serum samples**. *Anal Chim Acta* **1356**, 343979 (2025).

It is reproduced with publisher permission here in its original published form.

Analytica Chimica Acta 1356 (2025) 343979

Contents lists available at ScienceDirect

Analytica Chimica Acta

journal homepage: www.elsevier.com/locate/aca

Integrating NMR and multi-LC-MS-based untargeted metabolomics for comprehensive analysis of blood serum samples

Tereza Kacerova, Elisabete Pires, John Walsby-Tickle, Fay Probert **, James S.O. McCullagh *

Chemistry Research Laboratory, Department of Chemistry, University of Oxford, Oxford, OX1 3TA, UK

HIGHLIGHTS

- A serum preparation protocol for untargeted metabolomics using sequential NMR and multi-platform LC-MS analysis.
- No metabolite deuteration was observed when analysing samples in deuterated buffer using multiple LC-MS methods.
- LC-MS compound-feature abundances are minimally affected by NMR buffers and protein removal.
- A single serum sample preparation process for sequential NMR and multiple LC-MS platform analysis.

GRAPHICAL ABSTRACT

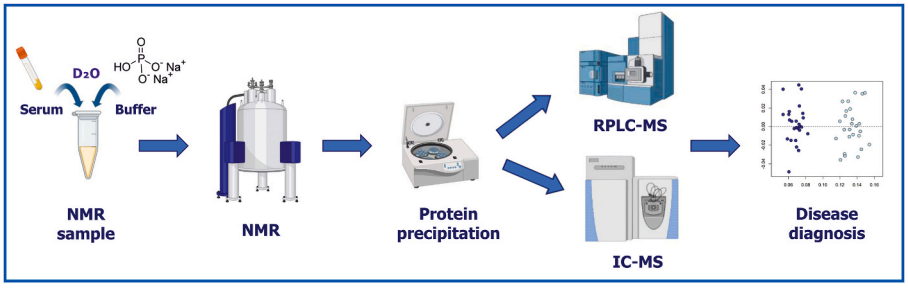

ARTICLE INFO

Handling Editor: Xiu-Ping Yan

Keywords:
Sample preparation
Nuclear magnetic resonance
Mass spectrometry
Multi-platform metabolomics
Untargeted metabolomics

ABSTRACT

Background: Mass spectrometry (MS) and nuclear magnetic resonance (NMR) have emerged as pivotal tools in biofluid metabolomics, facilitating investigation of disease mechanisms and biomarker discovery. Despite complementary capabilities, these techniques are rarely combined, although their integration is often beneficial. Typically, different sample preparation approaches are used, and compatibility challenges potentially arise due to the requirement for deuterated buffered solvents in NMR but not MS techniques. Additionally, MS-based approaches necessitate protein removal from samples whilst in NMR proteins can be potentially useful biomarkers. In this study, we developed a blood serum preparation protocol enabling sequential NMR and multi-LC-MS untargeted metabolomics analysis using a single serum aliquot in a research discovery setting.

Results: We analysed human serum samples using various untargeted NMR and multi-LC-MS platforms to assess the impact of deuterated solvents and buffers on detected compound-features. Employing multiple LC-MS profiling approaches, we observed no evidence of deuterium incorporation into metabolites following sample preparation with deuterated solvents. Furthermore, we demonstrated that buffers used in NMR were well tolerated by LC-MS. Protein removal, involving both solvent precipitation and molecular weight cut-off (MWCO) filtration, was identified as a primary factor influencing metabolite abundance. Our findings led to the development and validation of a serum sample preparation protocol enabling a combined NMR and multi-LC-MS analysis.

Significance: Using a single clinical serum aliquot for simultaneous untargeted profiling via NMR and multi-LC-MS represents a highly efficient alternative to current methods. This approach reduces sample volume

* Corresponding author.
** Corresponding author
E-mail address: james.mccullagh@chem.ox.ac.uk (J.S.O. McCullagh).

https://doi.org/10.1016/j.aca.2025.343979
Received 2 August 2024; Received in revised form 17 March 2025; Accepted 27 March 2025
Available online 4 April 2025
0003-2670/© 2025 The Authors. Published by Elsevier B.V. This is an open access article under the CC BY license (http://creativecommons.org/licenses/by/4.0/).

requirements and substantially expands the potential for broader metabolome coverage. Our study offers comprehensive insights into the impact of sample preparation on complex metabolic biofluid profiles, highlighting the compatibility and complementarity of LC-MS and NMR in metabolomics research.

1. Introduction

Metabolomics focuses on detecting, identifying and quantifying small molecules in biological samples [1–3]. The field has rapidly developed with applications found in multiple research areas, including medicine, the pharmaceutical industry, agriculture, and environmental science [3–6]. Notably, metabolomics offers insights into the biochemical state of an organism, providing information on metabolic changes occurring as a response to intrinsic and extrinsic factors, including pathological processes, lifestyle and environmental exposures [7–9]. The profiling of biofluids holds significant promise for personalised medicine, encompassing biomarker identification and diagnostic and prognostic assessments at an individual level [10–12]. Blood and urine are of particular interest as systemic biofluids, reflecting the overall state of the entire organism rather than focusing on a specific organ or tissue type. In contrast, other matrices, such as cerebrospinal fluid, breast milk, exhaled breath condensate, and faecal samples, can be more invasive to collect or represent more specific physiological processes [13]. Furthermore, the routine collection of blood and urine for clinical testing purposes enhances sample accessibility [10,11]. Serum, derived from spontaneously coagulated blood and devoid of additives, is considered the gold standard for disease diagnosis [10], closely mirroring the endogenous blood metabolome composition.

Liquid chromatography coupled to mass spectrometry (LC-MS) has emerged as the predominant analytical technique used in metabolomics [1–3,11–13], with reversed-phase LC-MS (RPLC-MS) [14,15] being the most widely applied approach, albeit with limitations for the analysis of highly polar metabolites, which are often the most abundant in cells and biofluids [16,17]. Alternative LC-MS retention mechanisms are often used to characterise these metabolites, including mixed-mode chromatography-MS [18], hydrophilic interaction chromatography-MS (HILIC-MS) [19,20], ion-exchange chromatography-MS (IC-MS) [16,17,21,22], and combinations of these methods to obtain broader metabolome coverage. While LC-MS-based metabolomics offers high compound coverage with low sample volume requirements, challenges such as susceptibility to batch effects, low compound-feature number to metabolite identification ratio, and selective quantification capabilities persist [1,23]. On the other hand, despite its lower sensitivity, nuclear magnetic resonance (NMR) provides highly reproducible and quantitative analysis, is non-destructive and can measure peptides, lipoproteins, glycoproteins and other small proteins, in addition to low molecular weight metabolites [24–29]. Combining NMR and LC-MS approaches, therefore, has the potential to significantly enrich metabolite coverage [30–35]. The Venn diagram in Fig. 1 represents indicative coverage of different compound classes reported using the complementary analytical platforms: NMR, RPLC-MS, and IC-MS [16,27,29,30,36–40].

The complementarity between NMR and MS, and the enhancement of quantitative analyte coverage, were underscored by Psychogios et al., who characterised the human serum metabolome by combining a cross-section of targeted and untargeted methods [30], which showcased the benefits of integrating these platforms. This combined approach compensated for limited sensitivity and separation capacity while

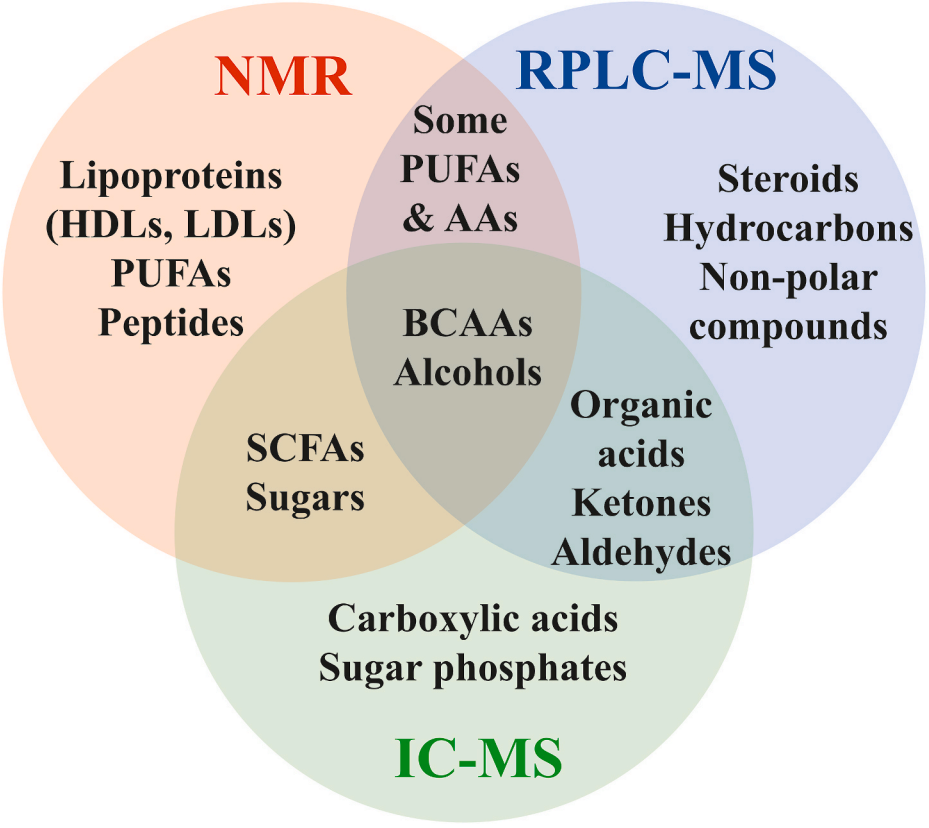

Fig. 1. The scope and overlap of the individual analytical platforms addressed in this study. (HDLs – high-density lipoproteins; LDLs – low-density lipoproteins; PUFAs – polyunsaturated fatty acids; BCAAs – branched-chain amino acids; SCFAs – short-chain fatty acids; AAs – amino acids).

significantly increasing uniquely detected compounds [30]. Nevertheless, despite the apparent benefits of integrating NMR and LC-MS for metabolomics applications, surprisingly few studies utilise this combinatorial approach. This paucity is reflected in the results of a PubMed search using keywords "MS metabolomics", "NMR metabolomics", and "MS NMR metabolomics", which illustrated that MS-based metabolomics is still the most prevalent approach (Fig. 2), while fewer than 10 % of publications mentioned both techniques. Additionally, the vast majority of these 10 % applied the techniques independently (i.e. using different sample aliquots and preparation approaches for analysis on each platform) [41,42]. Only a small number of combinatorial studies have conducted NMR and MS metabolomics analyses using the same sample aliquot [31,32,41,43,44]. Currently, the standard sample preparation workflow for parallel NMR and MS analysis involves dividing the sample and following a separate sample preparation procedure for each technique [34,45–47]. Nevertheless, this approach can introduce sample preparation biases and artifacts independently. Additionally, processing each sample twice significantly increases preparation time, resources required, and, in particular, the amount of sample needed, which is often limited in patient-derived studies. Therefore, preparing a single sample suitable for both platforms has significant advantages, not only for the 10 % of studies utilising both approaches, but particularly for clinical and large cohort studies where limited sample volumes often determine which analytical studies can be performed [16,17].

The principal obstacles impeding the use of a unified sample preparation approach for NMR and LC-MS metabolomics include the necessity for deuterated solvents and buffered sample pH for NMR analysis, along with the removal of macromolecules, such as proteins, for LC-MS. Regarding deuterated solvents, the main concern arises from the possible exchange of acidic hydrogens for deuterium in metabolite molecules. This exchange can alter the metabolite mass, which may lead to the failure of automated data processing software, potentially affecting data accuracy and metabolite identification. A previously published study by Beltran et al. examined liver extracts using both NMR and MS untargeted metabolomics while performing metabolite extraction in deuterated water and comparing it to Milli-Q water as the metabolite extraction solvent. The study found no evidence that metabolites extracted in deuterated water were themselves deuterated [43]. Similar results were observed for cell extracts prepared in deuterated water and Milli-Q water [31,32,43,44]. However, to our knowledge, no studies have been conducted on more complex biofluid samples, such as blood samples. As larger cohort metabolomics studies, which frequently involve biofluid analysis, become more prevalent, streamlined approaches to facilitate the combination of NMR and MS analyses would be advantageous.

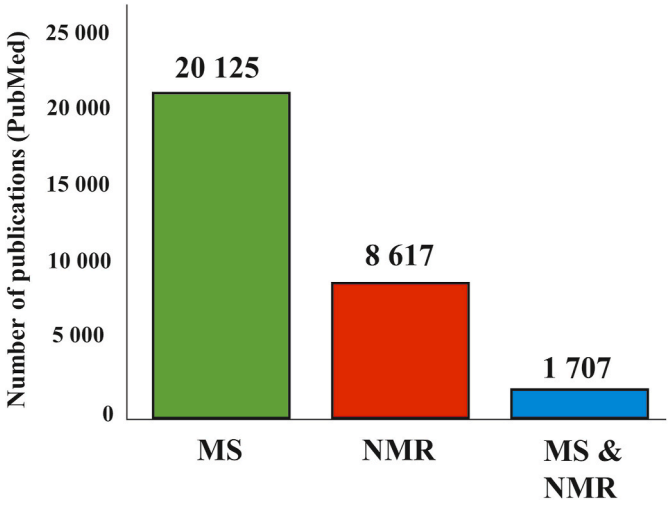

Fig. 2. Results of PubMed search for "MS metabolomics" (MS, green) vs "NMR metabolomics" (NMR, red) vs "MS NMR metabolomics" (MS & NMR, blue) (Date of the search: July 30, 2024). (For interpretation of the references to colour in this figure legend, the reader is referred to the Web version of this article.)

Whilst protein precipitation or membrane-based molecular weight cut-off (MWCO) filtration are used in LC-MS sample preparation [48], the broad baseline macromolecular signals in NMR spectra [40,49] are routinely suppressed "*on-instrument*" [49], negating the need for physical removal. Methods such as spin-echo experiments (e.g. Carr-Purcell-Meiboom-Gill (CPMG) pulse sequence) use transverse relaxation times (T_2) to generate a one-dimensional hydrogen spectrum depicting the slowly relaxing signals that correspond to small molecules [50–54]. Furthermore, current CPMG filters can allow the differentiation of macromolecular structures with specific T_2 properties, such as the lipoprotein signals that can be maintained in the filtered spectra and used as a metabolomic parameter (e.g. for disease diagnosis) [38,39,50,51,55].

A separate challenge is the need for buffered NMR samples. This is due to the pH-dependent nature of NMR spectral chemical shift values, necessitating samples to be buffered to maintain a constant sample pH. However, the increased sample salt concentrations resulting from the use of such buffers could theoretically pose a challenge for MS-based analytical methods, as certain salts (e.g. phosphates) can affect ionisation efficiency and sensitivity [56]. To our knowledge, all studies focusing on the combination of NMR and MS [31,32,43,44] have to date been performed using pure deuterated water without buffering salts or other additives, meaning that the potential changes in the metabolome occurring either as a result of altered pH or metabolite interactions with buffer ions have not been investigated in detail.

Given the potential benefits of combining NMR with comprehensive multi-LC-MS analysis for enhanced metabolome coverage and biomarker discovery in a research context, we explored ways to prepare serum samples that would allow for sequential NMR and MS analysis. Our primary aim was to develop a sample preparation method for untargeted metabolomics using a single sample aliquot suitable for analysis on both NMR and multiple LC-MS platforms. To do so, we explored sample preparation using deuterated solvents and sought evidence of whether this led to deuteration across the serum metabolome. Furthermore, we investigated changes in the LC-MS metabolome in response to the addition of NMR buffer to serum samples. Finally, we compared different approaches for protein removal (precipitation in organic solvent and MWCO filtration) and their impact on serum metabolome coverage. This led to an optimised blood serum sample preparation workflow for untargeted metabolomics suitable for a research context, prioritising broad metabolite coverage and use of minimal sample volumes. This approach facilitates metabolite discovery and highlights key considerations for implementing a multiplatform strategy.

2. Materials and methods

All experiments used commercially available, sterile AB-type human serum (Merck H3667, Merck, UK). The serum aliquots were stored at −80 °C until the day of analysis. All samples analysed (both NMR and MS) were prepared in triplicate. Detailed workflows depicting the individual sample preparation can be found in the supplementary information (SI Methods 1-3).

2.1. Sample preparation for NMR analysis

The serum aliquots were thawed at 4 °C and the samples were visually checked for any protein precipitation. A volume of 150 μL of the sample was then diluted with 400 μL of 75 mM sodium phosphate buffer prepared in D_2O (pH 7.4). The mixture was transferred to a 5-mm NMR tube.

To investigate the effect of standard MS sample preparation on the

NMR analysis, serum samples were prepared in MeCN (1 : 2.33 (v/v)) according to an established protocol [57]. The solvent was subsequently removed via lyophilisation using a FreeZone® Benchtop Freeze Dryer (Labconco, USA) (safe temperature −25 °C; collector temperature −40 °C; vacuum pressure 0.22 mbar; 16h) and resuspended in the NMR phosphate buffer.

2.2. NMR spectroscopy analysis and spectra processing

The ^{1}H NMR experiments comparing serum extracted in aqueous phosphate buffer with and without MWCO filtration were performed using a 700-MHz Bruker AVIII spectrometer operating at 16.4 T equipped with a ^{1}H (^{13}C/^{15}N) TCI cryoprobe. The ^{1}H NMR experiments comparing serum extracted in MeCN with and without MWCO filtration were performed using a 600-MHz Bruker AVIII spectrometer operating at 14.0 T equipped with a dedicated 5 mm ^{1}H(^{13}C/^{15}N) inverse TCI cryoprobe. The sample temperature was stable at 298 K. ^{1}H NMR spectra were acquired using a 1D NOESY pre-saturation scheme and a spin-echo Carr-Purcell-Meiboom-Gill (CPMG) sequence. The technical details of NMR sample preparation and NMR acquisition parameters have been previously published [38,39,55]. The spectra were processed in Topspin 4.1.4 (Bruker, Germany) and ACD/Labs Spectrus Processor Academic Edition 12.01 (Advanced Chemistry Development, Inc.), as previously described [38,39,55]. The regions of the spectra between 0.50–4.20 ppm and 5.20–8.50 ppm were divided into 0.02 ppm width "buckets" that were used for statistical analysis.

2.3. Sample preparation for LC-MS analysis

Metabolites were extracted in MeCN (1:2.33 (v/v)) and vortexed for 1 min, following a well-established extraction method [57] commonly used in untargeted MS metabolomics studies of serum samples. The same v/v ratio was used for all extraction solvents investigated: Milli-Q water, deuterated water, and NMR buffer (75 mM sodium phosphate in D_2O; pH adjusted to 7.4). All extractions were performed at room temperature. The specific solvent (1:2.33 (v/v)) was added to each serum aliquot, and the sample was vortexed for 1 min [57]. The samples were centrifuged (16 000×*g*; 15 min, 4 °C) and filtered with MWCO filters (Amicon® Ultra-10 Centrifugal Unit; 30 min; 16 000×*g*). The filtrate was transferred into the total-recovery MS vials.

2.4. Sample preparation for LC-MS analysis using precipitation in acetonitrile for protein removal

Two different sets of "artificial NMR" samples were prepared: i) high buffer concentration samples (serum: NMR buffer 0.43 : 1.00 (v/v)); ii) low buffer concentration samples (serum: NMR buffer 4.00 : 1.00 (v/v)). For the high buffer concentration samples, 167 μL of the "NMR serum" sample was mixed with 85 μL MeCN. For the low buffer concentration samples, 62.5 μL of the "NMR serum" sample was mixed with 105 μL MeCN. A control serum sample without any buffer additives was prepared by mixing 50 μL serum with 117 μL MeCN. The samples were centrifuged (16 000×*g*; 15 min, 4 °C), and the supernatant was transferred into total-recovery MS vials.

2.5. Sample protein concentration measurement

The total protein concentration for each extraction method was determined using Pierce™ Rapid Gold BCA Protein Assay Kit-1 (Thermo Fisher Scientific, UK). The protein concentration was measured in the derivatised supernatant/filtrate (μg μL^{-1}) blanked with a working reagent (1:10) using ClarioStar Plus (BMG LABTECH, Germany) with an LVis plate (480 nm).

2.6. Anion-exchange chromatography-MS analysis

Anion-exchange chromatography-MS analysis was carried out using a Dionex ICS-5000+ high-pressure ion chromatography system equipped with a continuously regenerated trap column, Dionex ERS 500e suppressor and AS11-HC (2 × 250 mm, 4 μm) column, from Dionex (Sunnyvale, CA, USA), coupled to a Q-Exactive hybrid quadrupole-Orbitrap MS via a HESI II probe (Thermo Fisher, San Jose, CA, USA). The technical parameters for the untargeted metabolomics method have been previously published in Ref. [17].

2.7. Reversed-phase ultra-performance liquid chromatography-MS analysis

C18 reversed-phase analysis was performed using an Acquity UPLC liquid chromatograph (Waters, UK) system with a gradient elution program coupled directly to a high-resolution tandem mass spectrometer, Xevo G2-XS QTOF (Waters, UK). A 5 μL partial loop injection was used for all analyses with pre- and post-injection wash programs. A Waters CORTECS UPLC T3 column (2.1 × 100 mm, 1.6 μm; Waters PLC, Milford, MA, USA) was used with a flow rate of 0.3 mL/min. The total run time was 18 min. Mobile phase A comprised Milli-Q water with 0.1 % formic acid, and mobile phase B was 100 % methanol with 0.1 % formic acid. The gradient elution program was as follows: 0 min, 5 % B; 4 min, 50 % B; 12 min, 99 % B; 15 min, 99 % B; 15.1 min, 5 % B; 18 min, 5 % B. The column temperature was kept at 40 °C throughout the experiment. Mass spectrometry analysis was performed separately in positive and negative ion modes using a scan range from *m/z* 50–900. The centroid data were collected in MS^{E} mode, and the time was set to 0.2 s. All the parent ions were fragmented with an energy ramp of 20–40 eV, and the fragment information was collected. Tune file source parameters were set as follows: source temperature 140 °C; cone gas flow 50 L/h; desolvation gas flow 800 L/h; cone voltage and capillary voltage were set to 40.0 V and 2.5 kV in positive (pos.) ionisation mode and 40.0 V and 2.0 kV in negative (neg.) ionisation mode, respectively. Full scan data were acquired in continuum mode.

2.8. LC-MS data pre-processing and analysis

Unprocessed chromatographic and MS data were examined using vendor-specific LC-MS software - MassLynx 4.2 (Waters, Elstree, UK) for RPLC-MS and FreeStyle 1.8 (Thermo Fisher Scientific, Waltham, MA, USA) for IC-MS. The untargeted metabolomics data were then processed in Progenesis QI (Nonlinear Dynamics, Waters, Elstree, UK), and the detected compound-features were compared between the different extraction methods. A % coefficient of variation (CV) cut-off of 30 % was used for routine filtering of the untargeted metabolomics data and for evaluating the efficacy of sample preparation efficiency across independent datasets.

To compare the abundance and variability of metabolites, compound-features were matched by both retention time and *m/z* across the different sample preparation methods. Metabolite identification was based on matching multiple experimental data to metabolite databases. In-house libraries of over 450 (IC-MS) and 150 (RPLC-MS) authentic metabolite standards with matching of multiple independent measurements under the same experimental conditions to provide Level 1 identifications (e.g. retention time (R_t error <2 min; accurate-mass <5 ppm (IC-MS) and 20 ppm (RPLC-MS)); isotope and fragmentation patterns >90 %).

2.9. Statistical analysis

The data were imported into R software 4.2.1 (R Foundation for Statistical Computing, Vienna, Austria) and analysed with in-house R scripts while using the *corrr*, *ggplot2*, *ggpubr*, and *dplyr* packages. The data in section 3.4 were analysed in MetaboAnalyst 5.0 [58]. The

features were filtered based on the interquartile range (IQR) values. All datasets, including more than 1000 features, were reduced by 40 % based on the IQR value. Each dataset was Pareto scaled (if not stated otherwise). Univariate statistical analysis included determining fold-change (FC) and *t*-test p-values between different extraction methods for compound-features and combined in volcano plots. The FC threshold was set to 2 and the p-value cut-off was set to 0.05 to determine significance. To control the false discovery rate (FDR), FDR-corrected p-values were calculated using the Benjamini-Hochberg method [59,60]. For multiple groups comparisons, One-Way ANOVA with Tukey's and Dunnett's *post hoc* tests was employed as appropriate (p-value cut-off was set to 0.05). The data were projected using an unsupervised principal component analysis (PCA), which allowed the similarities within the individual datasets to be shown. The rest of the data analysis was performed using GraphPad Prism 9 software. The significance cut-off was set at $p < 0.05$ for all data sets.

3. Results and discussion

3.1. No detectable hydrogen exchange was observed in the untargeted mass spectra of metabolites from serum samples prepared using deuterated solvents

To investigate the potential deuteration of serum metabolites in NMR samples prepared with deuterated solvents, we analysed and compared human serum (Merck, UK) that had been prepared with (i) Milli-Q water and (ii) deuterated water. Both sample extracts (each condition in triplicate) were analysed using two different untargeted LC-MS methods (IC-MS and RPLC-MS (+ve/-ve ion mode)) to provide a broad metabolome coverage. Mass spectral peak-picking and chromatographic peak alignment were conducted using Progenesis QI (Nonlinear Dynamics, Waters, Elstree, UK).

To assess the potential for compound-feature deuteration, we compared the *m/z* (nominal mass obtained by rounding the measured *m/z* values to the nearest integer) of all compound-features measured in the Milli-Q water extracts with those detected in the deuterated water extracts, using each analytical method (Table 1). It was hypothesised that the presence of deuteration would manifest as a shift of at least one *m/z* unit in samples where a deuteron had replaced a hydrogen atom in the deuterated water sample compared to the corresponding analyte in the Milli-Q water sample, for retention time-matched compound-features. To illustrate the relationship between *m/z* values in the two datasets we performed a correlation plot using *m/z* values from deuterated and Milli-Q water extracts. For each compound-feature, we expected to see a 1:1 correlation between the deuterated and non-deuterated samples in the absence of deuteration. Our results revealed that over 98.5 % of compound-features showed a direct 1:1 correlation, suggesting that very few, if any, deuterated compounds were present (the sum of all compound-features from all analytical platforms was 11 073 (1378 features for IC-MS (neg. ionisation); 3246 features for RPLC-MS (neg. ionisation); 6449 features for RPLC-MS (pos. ionisation))). The results are illustrated in Fig. 3. Approximately 1.5 % of the compound-features were detected exclusively in only one of the solvent extracts (Fig. 3; SI Fig. 1). These could have been potential candidates for deuteration but further investigation found no evidence of *m/z* values that corresponded to a deuteration profile. Specifically, none of the 68 compound-features (0.6 %) uniquely detected in the deuterated water samples showed evidence of deuteration when their *m/z* values and isotope abundances were compared to the corresponding non-deuterated *m/z* values (*M*) at the same retention time. We used a combination of automated and manual methods to examine the data. Progenesis QI (Nonlinear Dynamics, Waters, Elstree, UK) was used to automatically identify unique compound-features in either the deuterated or non-deuterated groups. Manual inspection of extracted ion chromatograms (EICs) in MassLynx 4.2 (for RPLC-MS) and FreeStyle 1.8 (for IC-MS) was performed to assess whether any compound-features corresponded to *m/z* shifts consistent with deuteration. Deuterated compounds would be expected to show an *m/z* value of $M + Dn$ in the deuterated samples specifically (where $D = 1.0063$ Da, representing the mass difference for deuteration, and *n* is a chemically feasible number of hydrogen atom substitutions). No such patterns were observed in the data. Similarly, the small number of remaining unique compound-features detected in the Milli-Q water extracts (90; 0.8 % of all detected features) were not deuteration-related and could be formed due to small differences in metabolite extraction reproducibility. A significant proportion of the unique features in both solvent extracts were either present in the void volume or were characterised by relatively high nominal mass values, corresponding to high molecular weight adducts, dimers and trimers likely formed during ionisation (SI Tables 1 and 2). In summary, we found no evidence of deuterated metabolites after examining over 11 000 LC-MS compound-features, from the analysis of samples prepared using deuterated water.

To evaluate the efficiency and reproducibility of the two extraction methods, correlation plots of the decimal logarithm values of peak areas (raw abundance) for all compound-feature measurements were also created for both Milli-Q and deuterated water samples (all compound-features with a %CV < 30 were included). Despite the indirect nature of peak area as an indicator of metabolite deuteration (it is noteworthy that peak area may be affected by several secondary factors, such as solvent effects or injection reproducibility), a strong correlation was observed between deuterated and non-deuterated extracts ($R^2 = 0.9933$, $R^2 = 0.9956$ for IC-MS and RPLC-MS, respectively). Generally, greater variation was observed at lower abundances, as expected. To account for method preparation variability, an interval was determined by comparing the peak intensities of two technical replicates extracted in Milli-Q water, representing the inherent technical variability of the method. This interval is depicted as red dashed lines in Figs. 4 and 5, illustrating the expected variation between technical replicates. Fig. 4A and B illustrate these plots for each LC-MS method comparison (Bland-Altman and linear correlation plots for all tested methods, including IC-MS in neg. ionisation mode, RPLC-MS in both neg. and pos. ionisation modes, can be found in SI Fig. 2). We found no systematic changes in *m/z* or compound-feature abundance correlated with the use of deuterated solvents for sample preparation. We speculate that while reversible deuteration is likely to occur for acidic hydrogen atoms in metabolite structures, any exchanged deuterium atoms would have reverted to hydrogen by the time the metabolites were analysed by MS (having been

Table 1
The number of compound-features detected by different LC-MS systems for the individual extractions (all extractions were repeated in sample triplicate).

Extraction	Instrument	Total features	%CV < 30	Median CV (%)
Milli-Q water	IC-MS neg.	1785	1366	14.61
Deuterated water	IC-MS neg.	1832	1252	15.06
Phosphate D_2O buffer	IC-MS neg.	1702	1357	14.41
MeCN	IC-MS neg.	2257	1534	17.73
Milli-Q water	RPLC-MS neg.	3581	3257	6.19
Deuterated water	RPLC-MS neg.	3387	3027	4.89
Phosphate D_2O buffer	RPLC-MS neg.	4021	3499	6.45
MeCN	RPLC-MS neg.	2422	2359	4.22
Milli-Q water	RPLC-MS pos.	6875	6298	5.45
Deuterated water	RPLC-MS pos.	7150	6288	8.29
Phosphate D_2O buffer	RPLC-MS pos.	8753	7162	10.37
MeCN	RPLC-MS pos.	6918	6295	6.69

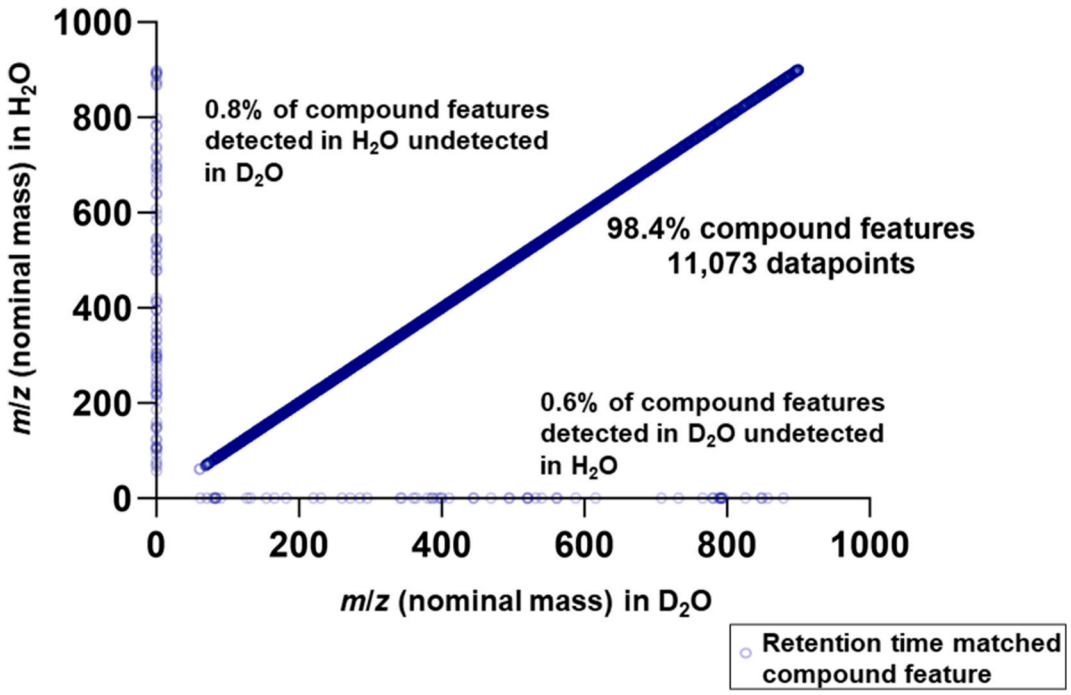

Fig. 3. Correlation plot using compound-feature *m/z* values generated from Milli-Q water (H_2O) and deuterated water (D_2O) metabolite extractions from the same blood serum samples (nominal mass values were used for compound-features matched by retention time). The plot includes datapoints for all three LC-MS methods (e.g. data generated via IC-MS (neg. ionisation mode), RPLC-MS (neg. ionisation mode) and RPLC-MS (pos. ionisation mode)). The unpaired datapoints on the x and y axes represent compound-features that were not associated with any "deuterated counterparts" (i.e., compound-features characterised by identical retention times and a mass difference corresponding to deuteration). All extractions were repeated in sample triplicate.

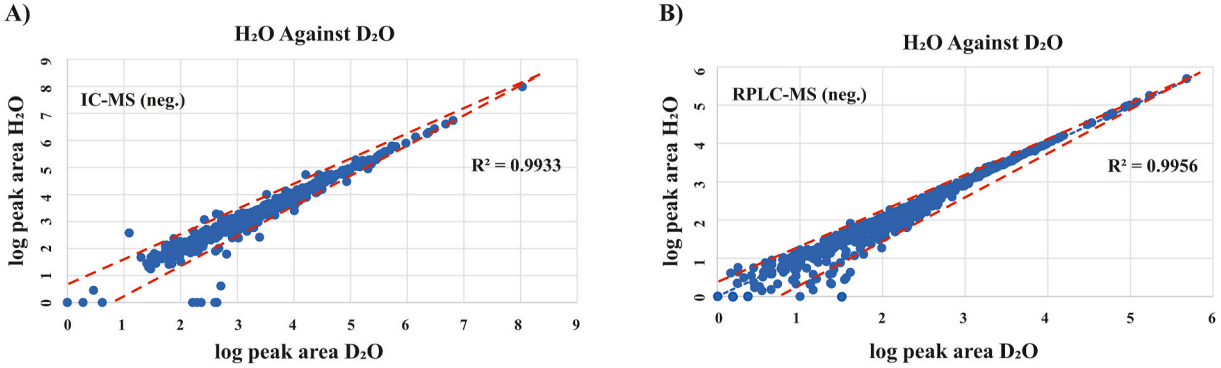

Fig. 4. Plots showing the correlation between serum metabolites extracted in Milli-Q water and deuterated water. The graphs depict the chromatographic peak areas (log values), normalising the data by compressing the wide range of raw values, thereby emphasising the key trends. The method accuracy interval, determined by comparing the peak areas of two technical replicates extracted in Milli-Q water, is represented by the red dashed lines. **(A)** IC-MS (neg. ionisation mode) data; **(B)** RPLC-MS (neg. ionisation mode) data. All extractions were repeated in sample triplicate. (For interpretation of the references to colour in this figure legend, the reader is referred to the Web version of this article.)

chromatographically resolved). This is presumably due to the large excess of exchangeable protons present in the mobile phase solutions used for each of the LC-MS platforms.

3.2. NMR phosphate buffer induces some changes in compound-feature abundances by LC-MS

In NMR metabolomics studies, deuterated aqueous buffers, such as phosphate buffer, are commonly used to ensure high chemical shift reproducibility between samples, mitigating the influence of even slight variations in pH (*note:* the buffer pH is usually kept at serum levels of around pH 7.4). Conversely, MS sample preparation, typically avoids the addition of buffers due to their potential to induce chemical artifacts and/or ion suppression, thereby affecting sensitivity and peak area reproducibility. It is worth noting that there is an exception with anion-exchange chromatography-MS, where hydroxide ions are employed for gradient elution and subsequently removed through electrochemical suppression prior to MS analysis [16]. Very few studies have investigated the impact of NMR buffers on compound-feature profiles using untargeted LC-MS methods. Our objective was, therefore, to assess the effect of phosphate buffer in samples on analyte chromatographic peak area reproducibility across the metabolome using both IC-MS and RPLC-MS platforms.

We directly compared the compound-feature abundance profile from the analysis of serum samples extracted in deuterated phosphate buffer (75 mM) with serum samples extracted using an equivalent volume of Milli-Q water. We constructed correlation plots which represented compound-feature abundance with and without the presence of

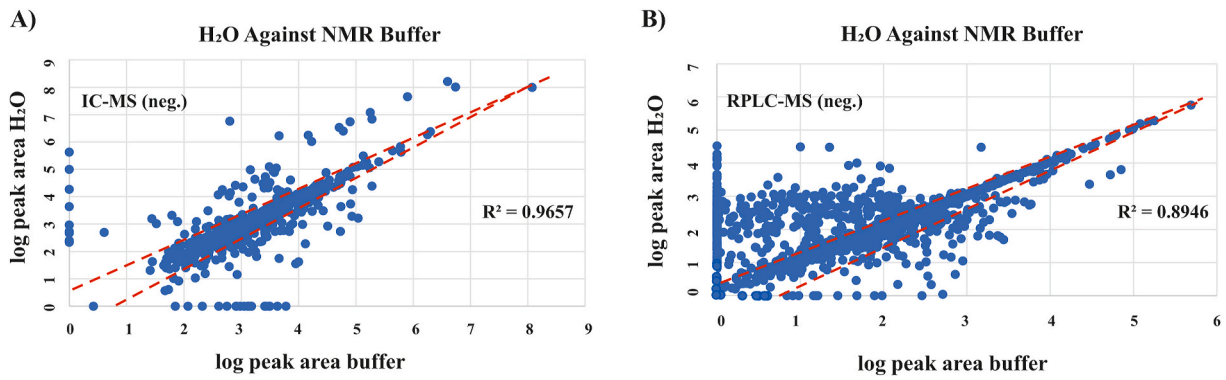

Fig. 5. Plots showing the correlation between serum metabolites extracted in Milli-Q water and deuterated phosphate buffer. The graphs depict the chromatographic peak areas (log values), normalising the data by compressing the wide range of raw values, thereby emphasising the key trends. The method accuracy interval, determined by comparing the peak areas of two technical replicates extracted in Milli-Q water, is represented by the red dashed lines. **(A)** IC-MS (neg. ionisation mode) data; **(B)** RPLC-MS (neg. ionisation mode) data. All extractions were repeated in sample triplicate. (For interpretation of the references to colour in this figure legend, the reader is referred to the Web version of this article.)

phosphate buffer using both LC-MS platforms. Fig. 5A and B illustrate the results demonstrating that while the majority of compound-features remained directly correlated on the 1:1 line, the linearity for IC-MS data reduced from 0.99 to 0.96, and for RPLC analysis, from 0.99 to 0.89 in the presence of phosphate buffer. Therefore, in response to the addition of phosphate buffer, 3 % of the IC-MS and 18 % of the RPLC-MS detected features were significantly altered in abundance (FDR (Benjamini-Hochberg) corrected p-values <0.05) (note: the linear correlation plots, Bland-Altman plots and hierarchical clustering heatmaps for all tested methods, including IC-MS in neg. ionisation mode, RPLC-MS in both neg. and pos. ionisation modes, can be found in the SI Figs. 3–8). Despite the relatively high number of significantly altered features, only 1.7 % (21) and 2.5 % (186) of compound-features were detected exclusively in the phosphate buffer extracts on the IC-MS and RPLC-MS (both pos./neg. ionisation modes) systems, respectively (Fig. 6). Furthermore, our findings indicated that, within the scope of metabolites covered by our in-house database of authentic standards (primarily targeting the polar metabolome that ionises in neg. ionisation mode using IC-MS), the majority of these metabolites were not significantly altered in abundance (7 out of the 74 identified metabolites were associated with an ANOVA p-value < 0.05; refer to SI Tables 4 and 5). To visualise the most significant changes in more detail, hierarchical clustering was performed, comparing the 50 compound-features with the lowest p-values from ANOVA for serum samples extracted in deuterated phosphate buffer with those extracted in deuterated water and Milli-Q water. A heatmap of the results highlighted that the addition of buffer (and not deuteration) had the greatest impact on feature abundance (SI Figs. 6–8). Taken together these results indicate that adding 75 mM of phosphate has a small but appreciable impact, creating some artifacts and altering some compound-feature abundances across the whole extracted metabolome profile. Interestingly, RPLC-MS analysis was affected to a greater extent than IC-MS analysis, presumably because IC-MS uniquely incorporates an anion removal step via electrochemical suppression prior to ESI-MS analysis [16]. While we have not observed any adverse effects on the performance of the mass spectrometers over two years of routine use with 75 mM phosphate, this is in the context of

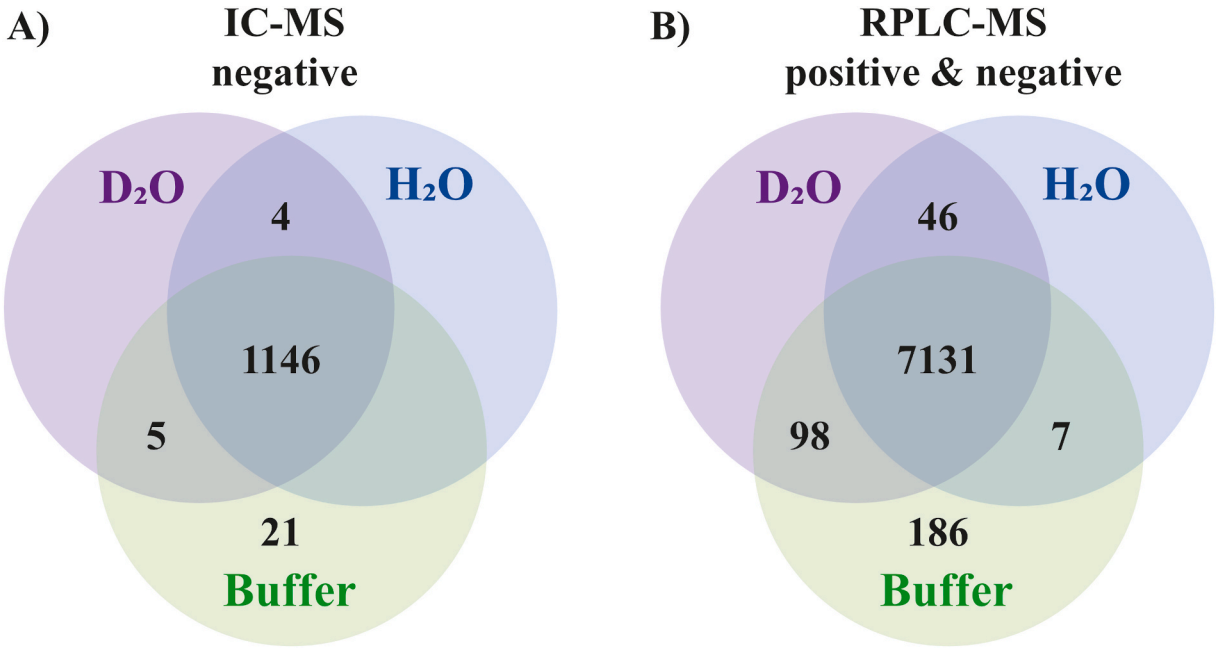

Fig. 6. Venn diagrams for the individual analytical techniques **(A)** IC-MS (neg. ionisation mode); **(B)** RPLC-MS (neg. and pos. ionisation mode); show the overlap of compound-features for the various tested extractions (Milli-Q water, deuterated water, aqueous deuterated phosphate buffer). *Note:* As each method targets different physiochemical properties of the metabolome, the total number of detected compound-features varies considerably between the methods.

regular source cleaning between projects and it should be recognised that phosphate-containing buffers may pose the risk of salt build-up in the ion-source. Therefore, we recommend regular cleaning and monitoring to ensure consistent instrument performance.

3.3. The effect of serum deproteination on NMR and LC-MS serum metabolite profiles

The removal of protein from serum samples is essential for all metabolomics applications using LC-MS approaches, as even small amounts of protein can induce ion suppression and lead to protein precipitation during the chromatographic process [48,61,62]. This is particularly important for IC-MS, where proteins can also be deposited in the electrochemical suppressor, reducing its effectiveness and useable lifetime [16]. Conversely, protein removal is not mandatory for NMR-based metabolomics, as protein signals can be selectively suppressed during data acquisition to enhance the signals of low molecular weight metabolites. Omitting the protein removal step in NMR analysis allows for the detection of biologically relevant macromolecular signals, such as lipoproteins and *N*-acetyl glycoproteins, which are known markers of inflammation. However, it is noteworthy that several studies have also demonstrated improved quantitation of some low molecular weight metabolites by NMR when protein removal is carried out during sample preparation [63,64].

Various standard approaches are used to remove protein from biological extracts, with denaturation and precipitation using organic solvents being the most commonly employed in metabolomics [62,65–67]. MWCO filtration is also utilised [17,48,68,69]. However, several studies report that irrespective of the method, the process of removing protein can alter the metabolite profile [48,63]. For example, MWCO filtration of serum samples has been shown to favour hydrophilic metabolite recovery, while potentially leading to a decrease or loss of hydrophobic compounds [48]. In contrast, precipitation in organic solvents is generally reported to be less effective for protein removal [48,70]. Nevertheless, the absence of additional mechanical sample processing should lead to extracts that more accurately reflect the intact serum composition [48,70]. Considering the potential for perturbation of the serum metabolite profile and the distinct requirements of LC-MS and NMR-based sample preparation for metabolomics, we assessed the effect of protein removal methods on the metabolome profile, with the aim to ascertain an optimal sample preparation workflow suitable for integrating untargeted NMR and LC-MS analyses. Two strategies were considered: (i) Implementing a common protein removal step, resulting in a deproteinated extract that was identical for both NMR and LC-MS analyses. (ii) Employing a sequential approach wherein NMR data acquisition was performed prior to protein removal (using an on-instrument protein signal suppression technique), followed by the removal of protein from the sample prior to LC-MS analysis. Although the latter approach allows NMR to capture additional macromolecular signals, it results in NMR analysis of samples that have been processed differently compared to the corresponding LC-MS samples.

3.3.1. Protein removal improves the detection of selected signals but also the loss of several serum metabolites

To evaluate the two strategies (i and ii), we assessed the impact of protein removal methods on the NMR spectral profile. Initially, we compared metabolite extraction from serum in NMR phosphate buffer with and without 10 kDa MWCO filtration. Total protein content (assessed by UV/vis spectrometry) showed a reduction from 1750 ± 80 μg/mL to 130 ± 10 μg/mL after filtration. Subsequent NMR analysis revealed a significantly improved spectral baseline by eliminating the residual signals arising from albumin, glycoproteins, and lipoproteins, particularly in the 0.8–2.0 ppm region (Fig. 7A). The removal of undesired signals, including the propylene glycol contaminant originating from blood collection tubes, was also achieved. Importantly, 10 kDa MWCO filtration facilitated the detection of specific metabolites, including branched-chain amino acids (BCAAs) and lactate, previously obscured by broad lipoprotein signals in unfiltered samples (Fig. 7B). Additionally, signals such as 2-hydroxybutyrate (0.90 ppm) and lysine (1.38 ppm, 1.73 ppm) were revealed only after the filtration step. However, MWCO filtration also led to a reduction in additional NMR spectral features, including lipoproteins, *N*-acetyl glycoproteins and medium-chain fatty acids (2.02 ppm). Furthermore, in filtered samples, the spectral region from 3.0 to 4.0 ppm showed chemical shifts associated with glycerol (3.54–3.58, 3.64–3.67, 3.76–3.80 ppm), released from the MWCO filter coating during filtration (Fig. 7C–SI Figs. 9–14). The glycerol multiplets interfered with carbohydrate signals and entirely overlapped with the glycine signal (3.56 ppm). Attempts to mitigate this interference through pre-washing MWCO filters using Milli-Q water and various organic solvents showed partial reduction but did not entirely eliminate the glycerol signal from the resulting spectra (SI Table 3; SI Figs. 9–12). Thus, while filtration effectively removes significant overlap in the NMR spectrum, enabling the measurement of additional low molecular weight compounds, it also results in the loss or obscuring of several biologically meaningful metabolites.

As an alternative method for the removal of protein from serum samples, the addition of acetonitrile to precipitate protein (serum: acetonitrile ratio of 1 : 2.33 (v/v)) was also tested (Fig. 7D). Although less efficient in total protein removal (levels of 210 ± 20 μg/mL were measured after precipitation compared to 130 ± 10 μg/mL for MWCO), the NMR spectra closely resembled those of MWCO-filtered samples (SI Fig. 13B vs 14B). Both protein removal methods effectively eliminated macromolecular signals, including lipoproteins, *N*-acetyl glycoproteins and medium-chain fatty acids. The implementation of MWCO filters further resulted in a decreased relative abundance of lysine (1.40 ppm; $p = 0.008$), acetate (1.92 ppm; $p = 0.003$), glutamine (2.35 ppm, $p = 0.02$), and citrate (2.52–2.56; 2.64–2.68 ppm, $p = 0.01$ (note that the citrate signal was enhanced by the presence of sodium citrate-based anticoagulant)).

In conclusion, our findings related to protein removal indicate that MWCO filtration and protein precipitation using acetonitrile reduce the protein content in serum samples by approximately 95 % and 90 %, respectively. In both scenarios, there was a complete elimination of signals corresponding to lipoproteins, *N*-acetyl glycoproteins, and medium-chain fatty acids observed in the NMR spectra (Fig. 7A). Furthermore, the analysis of CPMG spectra for individual extractions revealed a reduction in the relative abundance of certain metabolites associated with MWCO filtration of serum samples. Conversely, protein removal enabled the detection of certain compounds that were obscured in unfiltered samples. Our observations thus highlight both advantages and disadvantages associated with protein removal prior to NMR analysis. The incorporation of the protein removal step may prove beneficial for studies exclusively focusing on low-molecular-weight metabolites, as it enhances compound detection by eliminating broad overlapping signals. Conversely, for clinical studies, quantifying macromolecular signals, such as lipoproteins, *N*-acetyl glycoproteins, and medium-chain fatty acids, may be desirable, given that they could serve as useful diagnostic biomarkers. Indeed, this has been demonstrated in various studies of conditions, including cancer, autoimmune disorders, and cardiovascular and neurological diseases [38,55,71–73].

3.3.2. Combining protein precipitation by acetonitrile and MWCO filtration shows a minimal effect on the polar metabolome but reduces hydrophobic compounds extraction reproducibility

To assess the influence of protein removal on the metabolome in more detail, we compared acetonitrile-based precipitation with a combination of acetonitrile precipitation and MWCO filtration using multi-platform LC-MS analysis.

A comparative analysis between MWCO-filtered and unfiltered samples, both extracted in acetonitrile, demonstrated that the combined approach involving acetonitrile extraction with MWCO filtration was significantly more efficient than either method alone. The protein

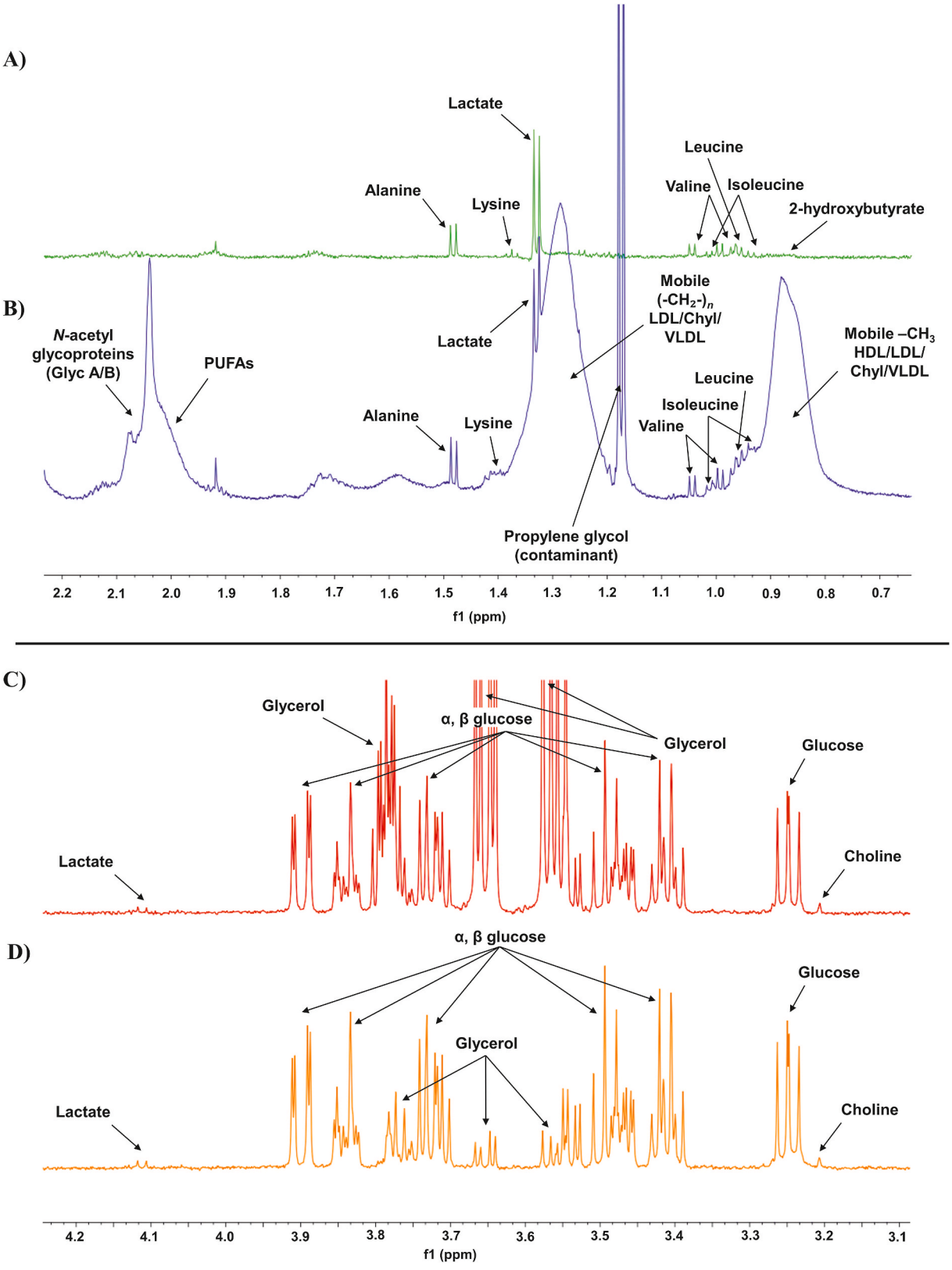

Fig. 7. ^{1}H CPMG NMR spectra of serum samples illustrating the effect of MWCO filtration. **(A, B)** The 0.7–2.2 ppm spectral region of **(A)** a 10 kDa MWCO-filtered sample and **(B)** an unfiltered serum sample in aqueous phosphate buffer. Panel A, compared to panel B, highlights the absence of lipoprotein, PUFA (δ 0.86, 1.28, and 1.99 ppm), *N*-acetyl glycoprotein (GlycA/B, δ 2.00–2.10 ppm), and propylene glycol contaminant (released from blood collection tubes, δ 1.17 ppm) signals following filtration. **(C, D)** The 3.1–4.2 ppm spectral region of **(C)** a 10 kDa MWCO-filtered sample in acetonitrile (distorted by glycerol contamination peaks at δ 3.56 (m), 3.65 (m), and 3.78 (m)); and **(D)** an acetonitrile-precipitated sample, which contains only physiological glycerol signals. Similar to MWCO-filtered samples in aqueous phosphate buffer, the acetonitrile-precipitated samples also lack signals corresponding to lipoproteins, PUFAs, and *N*-acetyl glycoproteins. For complete NMR spectra of all extraction methods, refer to SI Figs. 13 and 14.

content of serum samples using the combined approach decreased to 20 ± 10 μg/mL (compared to 210 ± 20 and 130 ± 10 μg/mL for acetonitrile and MWCO, respectively, when applied separately). Analysis of both sets of samples by IC-MS revealed very few significant differences in metabolite abundance between the two approaches. Specifically, only 5 compound-features (0.3 % of the total number of compound-features) exhibited a significant decrease in abundance during the IC-MS analysis. Conversely, 12 compound-features (0.8 % of the total compound-features number) showed an increase in abundance due to MWCO filtration (Fig. 8A). Notably, one of the most significantly altered signals was glycerol (5-fold change, $p = 0.0004$), which increased in the filtered samples (in alignment with NMR results presented in section 3.3.1). The presence of glycerol in the MWCO-filtered samples was not surprising, as it is used to coat MWCO filters during manufacture to provide a filter-protecting layer.

The impact of MWCO filtration on RPLC-MS results was particularly pronounced in pos. ionisation mode. In the combined acetonitrile and filtered samples, 12 % of compound-features (603) showed a significant reduction upon filtration, while 11 % (539) displayed a significant increase (Fig. 8B). In contrast, for RPLC-MS in neg. ionisation mode, 3 % (64) of compound-features exhibited a decrease, and 4 % (90) demonstrated an increase when filtered (SI Fig. 15). Additionally, particularly for RPLC-MS, the implementation of MWCO filtration led to a decrease in extraction reproducibility (data not shown). The exact factors driving this difference in relative abundance are unclear but may be related to interactions between more hydrophobic metabolites and the MWCO filter membrane.

3.4. *Effects of sample dilution on serum metabolite profiles analysed by LC-MS*

Our experiments revealed that the addition of phosphate buffer during sample preparation induced alterations in a specific subset of compound-feature abundances, resulting in the generation of artifacts within LC-MS profiles (as discussed in section 3.2). To investigate whether these changes were primarily due to the presence of phosphate ions in the sample or the dilution effect of adding the buffer solution, we extracted metabolites from serum using two different buffer concentrations: a “low” buffer concentration (serum: buffer ratio of 4 : 1 (v/v)) and a “high” buffer concentration (serum: buffer ratio of 0.43 : 1.00 (v/v)), while controlling for volume (and hence the organic/aqueous solvent ratio) and buffer concentration separately. The two concentrations emulated typical sample preparation approaches. For example, the designation “high” buffer concentration, indicated by a serum: buffer ratio of 0.43 : 1.00 (v/v), aligns with NMR studies typically encountering limitations due to restricted biological sample volumes, primarily employed for research purposes. Conversely, the "low" buffer concentration, characterised by a serum to buffer ratio of 4.00 : 1.00 (v/v), was more relevant to experiments focused on maintaining sample integrity, typically employed in industrial or clinical NMR measurements. To precisely evaluate buffer and dilution effects, control extractions were conducted using Milli-Q water, deuterated water, and undiluted serum (no aqueous solvent was added). Protein removal, essential for LC-MS analysis, was achieved through protein precipitation in acetonitrile, with an additional aliquot of each sample subjected to MWCO filtration. Subsequently, the samples were analysed using IC-MS and RPLC-MS platforms.

We then assessed the impact of various sample preparation variables on the total number of detected compound-features and the reproducibility of extractions, quantified by the number of compound-features exhibiting a %CV < 30. The results are illustrated in a bar chart (Fig. 9A, B) and a PCA plot (Fig. 9C and D). Detailed information about the experimental groups is summarised in Table 2 and SI Methods 3. The bar charts in Fig. 9A, B illustrate the influence of serum dilution and variation in phosphate buffer ion concentration independently for both RPLC-MS (pos. ionisation mode; Fig. 9A) and IC-MS (neg. ionisation mode; Fig. 9B) analyses. Results from both platforms are primarily affected by serum sample dilutions, evidenced by the significant difference ($p < 0.0001$) in the number of well-characterised features (%CV < 30) between control samples (**a** in Fig. 9A, B) and those with higher dilution using pure Milli-Q water (**d** in Fig. 9A, B), corresponding to a percentage change of the well-characterised features (%CV < 30) of 39 ± 5 % and 25 ± 4 % for RPLC-MS and IC-MS, respectively. Moreover, the phosphate buffer ion concentration had a significant impact predominantly on the IC-MS profiles ($p = 0.0001$), where the number of well-characterised features (%CV < 30) changed by 15 ± 5 % for the comparison of samples with a low (**b** in Fig. 9B) and high (**c** in Fig. 9B) proportions of the phosphate buffer additive. In contrast, phosphate ion concentration had no significant effect on the RPLC-MS analysis ($p = 0.44$), as there were no significant changes in the total number of well-characterised features (%CV < 30; change of 8 ± 9 %). Although the factors driving the observed differences between platforms remain unclear, the results summarised in Fig. 9A, B indicate that the dilution effect (rather than the addition of phosphate ions) has the greatest impact on altering the proportion of both the total number of compound-features and those characterised by a %CV < 30. Notably, on both platforms, the number of features with a %CV < 30 decreased more rapidly than the total number of compound-features measured.

The PCA plots (Fig. 9C and D) offer visual insights into the impact of the various assessed parameters. For RPLC-MS analysis (Fig. 9C) the

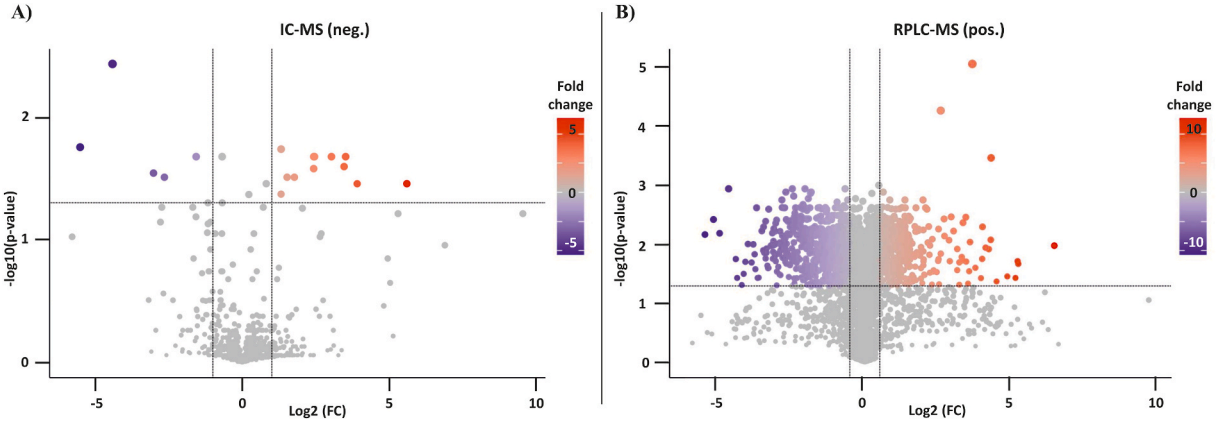

Fig. 8. Volcano plots showing the altered compound-features in the filtered and unfiltered samples comparing log 2 fold change (FC) of filtered/unfiltered samples and -log10 raw p-value (*t*-test, $p < 0.05$) (red: an increase in the MWCO-filtered samples) **(A)** IC-MS (neg. ionisation mode); **(B)** RPLC-MS (pos. ionisation mode). All extractions were repeated in sample triplicate. (For interpretation of the references to colour in this figure legend, the reader is referred to the Web version of this article.)

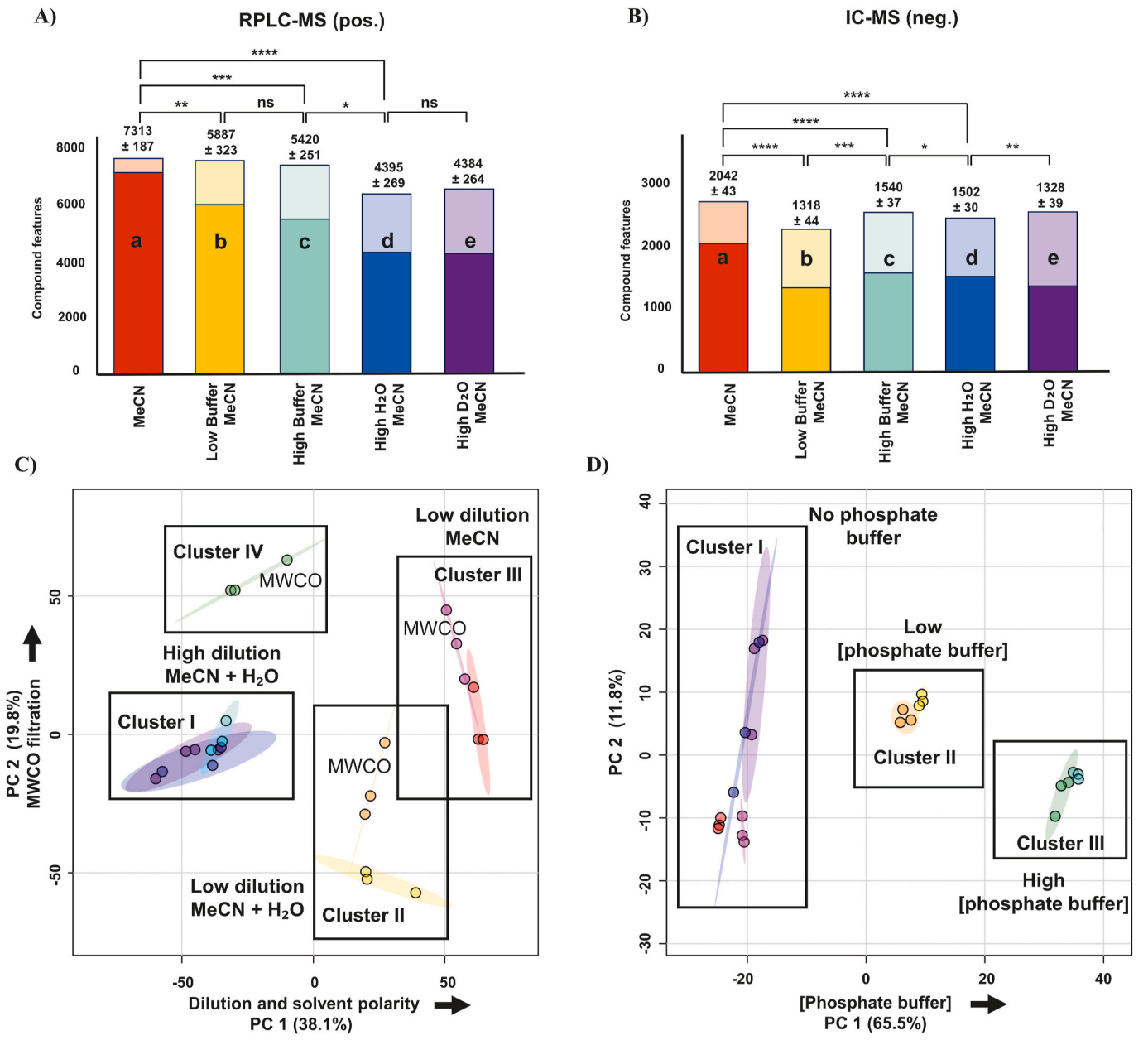

Fig. 9. A and B Bar chart showing the total number of detected compound-features for individual extraction methods (light colours) and the proportion of compound-features with a satisfactory CV value (%CV < 30; dark colours). CV values for individual features and absolute deviation values were determined based on the analysis of three sample replicates. For each method, the total number of features with a %CV < 30 is provided. The results of One-way ANOVA with selected results of Tukeý́s *post hoc* comparison tests are shown (the corrected significance levels are as follows: ns > 0.05; * >0.01; ** >0.001; *** >0.0001; **** <0.0001). For detailed ANOVA information and *post hoc* comparison tests for all groups, refer to the SI (SI Tables 6–15; SI Figs. 16–21). **(A)** RPLC-MS (pos. ionisation mode); **(B)** IC-MS (neg. ionisation mode). **C and D** PCA plot showing the different clustering patterns for the individual LC-MS platforms: **(C)** RPLC-MS (pos. ionisation mode) – a separate cluster (**I**) of high dilution unfiltered samples in Milli-Q water (blue), deuterated water (purple); phosphate buffer (turquoise), while MWCO-filtered phosphate buffer samples form an individual cluster (**IV**); a separate cluster (**II**) of low dilution samples in phosphate buffer with (orange) and without (yellow) MWCO filtration; a separate "control" cluster (**III**) of low-dilution unfiltered (red) and MWCO filtered samples (pink) **(D)** IC-MS (neg. ionisation mode) – a separate cluster (**I**) of samples without any added buffer, including serum controls (red and pink), Milli-Q water (blue) and deuterated water (purple) samples; a separate cluster (**II**) of low dilution samples with a small proportion of added phosphate buffer (relative to serum and MeCN) content; a separate cluster (**III**) of samples highly diluted with phosphate buffer. Note: All samples were extracted in MeCN. All extractions were repeated in sample triplicate. The colour-coding applied was as follows: *red* (serum control); *pink* (serum control, MWCO-filtered); *yellow* (high serum ratio in phosphate buffer); *orange* (high serum ratio in phosphate buffer, MWCO-filtered); *turquoise* (low serum ratio in phosphate buffer); *green* (low serum ratio in phosphate buffer, MWCO-filtered); *blue* (low serum ratio in Milli-Q water; dilution control); *purple* (low serum ratio in deuterated water; deuteration control). (For interpretation of the references to colour in this figure legend, the reader is referred to the Web version of this article.)

relative grouping of samples illustrates how the dilution factor and the polarity of the diluent (determined by the proportion of acetonitrile in the sample), and the inherent efficiency of protein precipitation influence the metabolite landscape (as indicated by distance along the *x*-axis; Fig. 9C). Notably, samples extracted solely in acetonitrile formed a distinct cluster (Fig. 9C cluster **III**), adjacent to those extracted using a combination of organic and aqueous solvents with the same dilution factor (Fig. 9C cluster **II**). Furthermore, samples with a high content of

Table 2
List of experimental groups for the aqueous phosphate buffer concentration experiment, including a brief overview of the experimental design and colour-coding for Fig. 9 and the complementary SI Figs. 16–21 (MWCO column: 0 corresponds to unfiltered samples, and 1 corresponds to MWCO-filtered samples; Buffer = deuterated aq. phosphate buffer). Each condition was analysed in sample triplicate, using IC-MS and RPLC-MS.

Group	Diluent	Serum *V*/μL	Diluent *V*/μL	MeCN *V*/μL	Serum dilution	MWCO	Colour	Purpose
Serum control	None	50	0	117	1 : 2.33	0	Red	No additives
Serum control	None	50	0	117	1 : 2.33	1	Pink	MWCO effect
Low buffer *V*	Buffer	50	12.5	105	1 : 2.33	0	Yellow	Buffer effect
Low buffer *V*	Buffer	50	12.5	105	1 : 2.33	1	Orange	MWCO effect
High buffer *V*	Buffer	50	117	85	1 : 4.04	0	Turquoise	Buffer effect
High buffer *V*	Buffer	50	117	85	1 : 4.04	1	Green	MWCO effect
High H_2O *V*	H_2O	50	117	85	1 : 4.04	0	Blue	Dilution ctrl
High D_2O *V*	D_2O	50	117	85	1 : 4.04	0	Purple	Deuteration ctrl

aqueous diluent clustered separately (Fig. 9C, clusters **I** and **IV**). Additionally, MWCO filtration influenced the positioning of samples in the PCA space significantly (as depicted by the separation along the *y*-axis; Fig. 9C), corroborating the information presented in the volcano plot (Fig. 8B). Similar PCA clustering patterns were observed for RPLC-MS in neg. ionisation mode (SI Fig. 22).

For the IC-MS results, the PCA clustering patterns indicate that sample dilution and diluent polarity, despite the relative decrease in well-characterised features (%CV < 30; as depicted in the bar chart (Fig. 9B) **a** relative to **d**), were not the primary factors influencing the overall metabolomic profile. This observation was supported by the consistent PCA clustering of serum control samples (final dilution 1 : 2.33) with highly diluted Milli-Q and deuterated water samples (final dilution 1 : 4.04; Fig. 9D cluster **I**). However, in line with the results illustrated in the bar chart (Fig. 9B), the IC-MS analysis was significantly impacted by the concentration of the added phosphate ions, which emerged as the primary factor separating sample groups (as reflected in the separation along the *x*-axis; Fig. 9D). MWCO filtration appears to have negligible effects on polar metabolites, as evidenced by the complete overlap of filtered and unfiltered samples in the PCA plot clusters (Fig. 9D).

3.5. Recommended workflow for sequential NMR and multi-LC-MS analysis

Our experimental findings have demonstrated that for untargeted metabolomics analysis of human serum samples, utilising a single aliquot for both NMR and multiple LC-MS platforms analyses, it is possible to: 1) utilise deuterated solvents; 2) incorporate phosphate buffer into samples up to 75 mM (higher concentrations were not investigated); and 3) employ protein precipitation with acetonitrile or MWCO filtration. Our experiments demonstrated that integrating NMR and LC-MS analysis, compared to using each method individually, did not significantly compromise sample analysis. Although there was a slight decrease in compound-features with %CV < 30, the combined approach offers significant benefits, including reduced time, cost, and sample volume, while allowing the same sample to be utilised across multiple platforms (Table 3). Moreover, we observed that implementing MWCO filtration yielded the most effective protein removal with minimal impact on the polar metabolome, although it was found to alter the abundance of more hydrophobic compounds. For NMR analysis, protein precipitation in acetonitrile emerged as a more suitable method than MWCO filtration, demonstrating subtle enhancements in certain signals without introducing glycerol contamination from the filter surface. However, considering the diagnostic potential of specific macromolecules such as lipoproteins, *N*-acetyl glycoproteins, and medium-chain fatty acids, preserving these signals might be advantageous. Therefore, implementing the protein removal step after NMR data acquisition could be beneficial. Based on our findings, we propose two alternative workflows, selectable depending on the study's objectives (outlined in Fig. 10 and Table 3). Workflow 1: When the focus is exclusively on low molecular weight metabolites and/or maintaining highly similar NMR and LC-MS sample composition is desired, protein removal should be performed prior to NMR analysis (Fig. 10A *blue pathway*). Workflow 2: When the study may benefit from additional protein and peptide analysis by NMR, the protein removal step can be performed after the NMR analysis (Fig. 10B *green pathway*).

Table 3
Summary of the advantages and disadvantages of the two proposed workflows for serum sample processing: one optimised for NMR studies targeting macromolecular signals, and the other utilising the same sample for both NMR and LC-MS analyses. A comparison with the "standard" procedure, which involves separate sample processing methods for NMR and LC-MS, is provided in row 1.

Workflow	Features LC-MS	Recommended Application	Advantages	Disadvantages
Standard workflow: NMR (phosphate D_2O buffer) and LC-MS (MeCN) individually	**RPLC (pos.)** 6918 (6295) **RPLC (neg.)** 2422 (2359) **IC (neg.)** 2257 (1534) **NMR** Full coverage	Clinical applications/ when sufficient sample volume is available	No interference of metabolites with the NMR buffer	Requires larger volumes and increases both cost and labour. Typically, different aliquots are used (potentially introducing bias)
NMR combined with LC-MS with initial protein removal *(the blue workflow in Fig. 10)*	**RPLC (pos.)** 6485 (5143) **RPLC (neg.)** 3034 (2065) **IC (neg.)** 1987 (1206) **NMR** Loss of lipoprotein signals	Studies focused exclusively on low molecular weight metabolites	The exact same sample is analysed using NMR and LC-MS	Loss of potentially diagnostic NMR signals; potential interference with phosphate ions
NMR combined with LC-MS with subsequent protein removal *(the green workflow in Fig. 10)*	**RPLC (pos.)** 7367 (5887) **RPLC (neg.)** 3184 (2242) **IC (neg.)** 2224 (1318) **NMR** Full coverage	Research (biomarker discovery)	Maximised coverage for both NMR and LC-MS; reduced buffer effect	Potential interference with phosphate ions

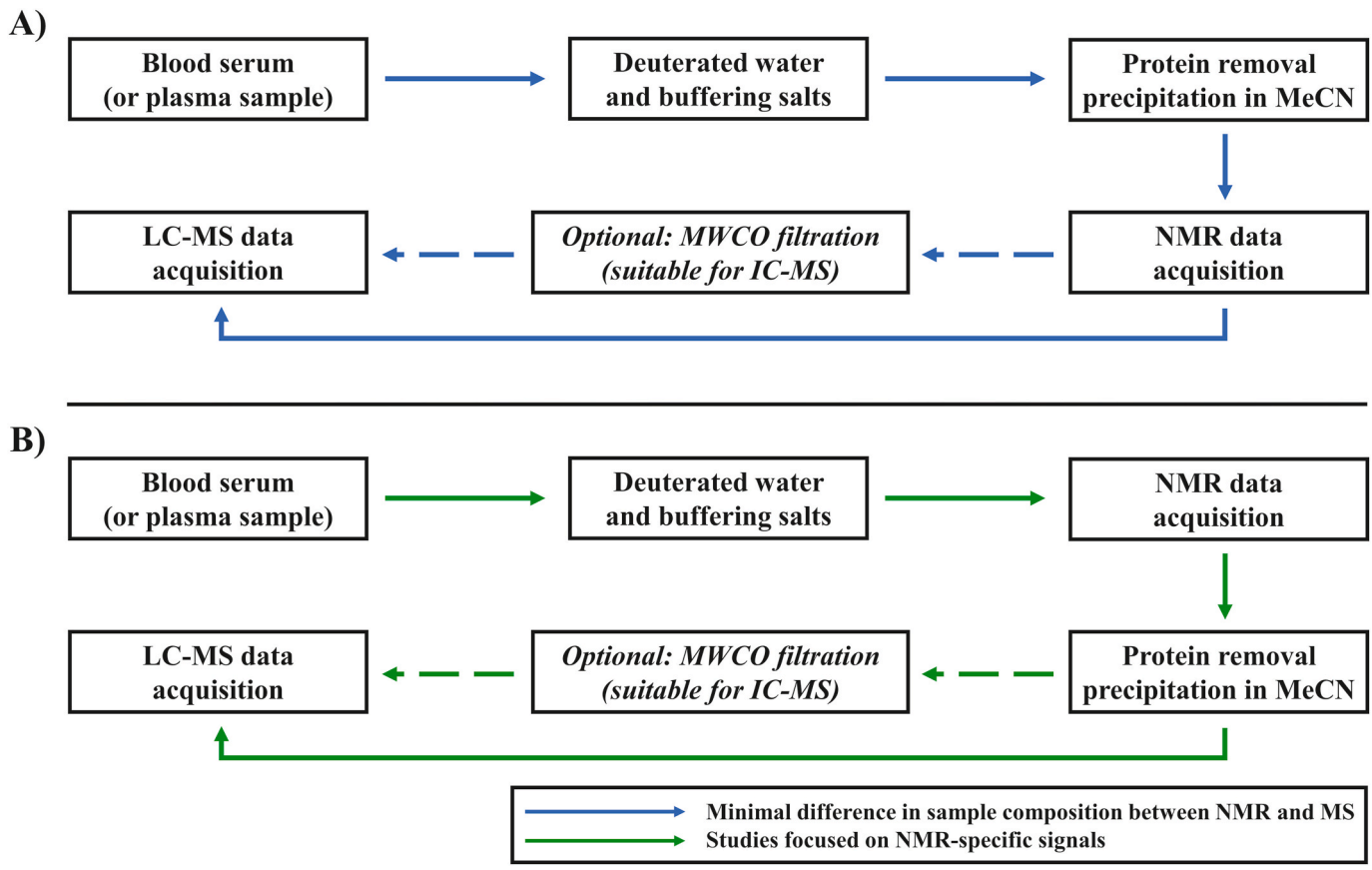

Fig. 10. The proposed workflows outlining the untargeted metabolomic analysis of human serum (or plasma) samples, involving sequential use of NMR and LC-MS. (**A**) Blue arrows illustrate a workflow characterised by minimal differences in the NMR and MS sample composition. (**B**) Green arrows represent a workflow tailored for studies, particularly focusing on NMR-detectable macromolecular signals (lipoproteins, *N*-acetyl glycoproteins and PUFAs). It is important to note that MWCO filtration is particularly suited for IC-MS analysis, as any residual protein was suspected to interfere with the electrolytic ion suppressor of the IC system [16]. (For interpretation of the references to colour in this figure legend, the reader is referred to the Web version of this article.)

4. Summary and conclusions

Our experiments have demonstrated that serum samples prepared for NMR metabolomics can be used for subsequent untargeted LC-MS metabolomic analysis. We have established that a single blood serum sample aliquot can be sequentially prepared for both NMR and multi-platform LC-MS-based untargeted metabolomics. Furthermore, our observations indicate minimal variations in the abundance of metabolites identified from our in-house database, thereby confirming the robustness of our preparation protocol for comprehensive metabolomic profiling. After protein removal, an NMR sample can be directly utilised for LC-MS analysis with multiple chromatographic methods, without the need to replace solvents, making this approach highly efficient and well-suited for research settings. Deuterated solvents and buffering salts required for NMR were well-tolerated in both RPLC-MS and IC-MS, with no evidence of metabolite deuteration, as demonstrated by the direct comparison of extractions using Milli-Q and deuterated water. While phosphate buffers have shown no adverse effects over two years of use, regular maintenance is recommended to mitigate the risk of salt accumulation in high-throughput workflows. We found that protein removal by acetonitrile precipitation and MWCO filtration significantly altered the NMR metabolome profile (e.g. by removing lipoprotein signals but also revealing some low-abundance molecule chemical shifts). We also demonstrated that there were differences in the metabolite profile obtained from acetonitrile-precipitated samples and those filtered by MWCO filtration, with the latter resulting in the loss of more lipophilic compounds.

We thus recommend two alternative workflows with the optimal approach dependent on research objectives. A notable advantage of these integrated NMR and LC-MS workflows lies in their efficiency, achieved through the utilisation of a single sample aliquot for all analytical platforms. This approach is particularly advantageous in research settings where retrospectively collected samples stored in biobanks with limited volumes are often used, and broad metabolite coverage is essential for metabolite discovery. Additionally, this method enables a more robust integration of NMR and MS results in untargeted metabolomics studies, enhancing metabolite coverage and providing internal validation of metabolite characterisations where overlap occurs. In conclusion, the described workflows support the routine integration of NMR and LC-MS analysis in metabolomics, facilitating efficient and comprehensive metabolite profiling.

CRediT authorship contribution statement

Tereza Kacerova: Writing – original draft, Visualization, Validation, Methodology, Investigation, Formal analysis, Conceptualization. **Elisabete Pires:** Writing – review & editing, Supervision, Formal analysis. **John Walsby-Tickle:** Writing – review & editing, Supervision, Formal analysis, Data curation. **Fay Probert:** Writing – review & editing, Supervision, Software, Resources, Project administration, Methodology, Funding acquisition, Conceptualization. **James S.O. McCullagh:** Writing – review & editing, Supervision, Software, Resources, Project administration, Funding acquisition, Conceptualization.

Declaration of competing interest

The authors declare the following financial interests/personal relationships which may be considered as potential competing interests: James McCullagh reports a relationship with Thermo Fisher Scientific Inc that includes funding grants. Other authors, declare that they have no known competing financial interests or personal relationships that could have appeared to influence the work reported in this paper.

Acknowledgements

FP is funded by a Dorothy Hodgkin Early Career Fellowship in Chemistry in association with Somerville College, University of Oxford (UK). TK is funded by an EPSRC Doctoral Training Partnership (EP/W524311/1), a UK research council and Numares AG (Am Biopark 9, 93053 Regensburg-Graß, Germany). We are grateful to the EPSRC (EP/V036408/1) and BBSRC (BB/R013829/1) for funding equipment used in this study. We are grateful to the Mass Spectrometry Research Facility (Department of Chemistry, University of Oxford) and NMR Research Facility (Department of Chemistry, University of Oxford) for use of equipment and advice.

Appendix A. Supplementary data

Supplementary data to this article can be found online at https://doi.org/10.1016/j.aca.2025.343979.

Data availability

Data will be made available on request.

References

[1] S. Alseekh, et al., Mass spectrometry-based metabolomics: a guide for annotation, quantification and best reporting practices, Nat. Methods 18 (7) (2021) 747–756.
[2] C.B. Clish, Metabolomics: an emerging but powerful tool for precision medicine, Cold Spring Harbor Molecular Case Studies 1 (1) (2015).
[3] C.H. Johnson, J. Ivanisevic, G. Siuzdak, Metabolomics: beyond biomarkers and towards mechanisms, Nat. Rev. Mol. Cell Biol. 17 (7) (2016) 451–459.
[4] S.P.M. Menacherry, et al., The impact of initial concentration of selected pharmaceuticals on their early stage of dissipation in soils, J. Soils Sediments 22 (2) (2022) 522–535.
[5] Q. Yang, et al., Metabolomics biotechnology, applications, and future trends: a systematic review, Rsc Advances 9 (64) (2019) 37245–37257.
[6] M. Kuzma, et al., Sequencing of new beauverolides by high-performance liquid chromatography and mass spectrometry, J. Mass Spectrom. 36 (10) (2001) 1108–1115.
[7] R. Abooshahab, et al., Metabolomics-A tool to find metabolism of endocrine cancer, Metabolites 12 (11) (2022).
[8] M.S. Kaspy, et al., Metabolomic profile of combined healthy lifestyle behaviours in humans: a systematic review, Proteomics 22 (18) (2022) e2100388.
[9] D. Pelclova, et al., NanoTiO sunscreen does not prevent systemic oxidative stress caused by UV radiation and a minor amount of NanoTiO is absorbed in humans, Nanomaterials 9 (6) (2019).
[10] J. Sotelo-Orozco, et al., A comparison of serum and plasma blood collection tubes for the integration of epidemiological and metabolomics data, Front. Mol. Biosci. 8 (2021).
[11] X.W. Zhang, et al., Mass spectrometry-based metabolomics in health and medical science: a systematic review, Rsc Advances 10 (6) (2020) 3092–3104.
[12] D. Pelclova, et al., Exhaled breath condensate biomarkers reflect systemic changes in patients with chronic dioxin intoxication, Monatshefte Fur Chemie 149 (9) (2018) 1579–1586.
[13] G.F. Zhang, et al., Metabolomics research with Tandem mass spectrometry, Tandem Mass Spectroscopy - Applications and Principles (2012) 309–330.
[14] X. Liu, et al., LC-MS-Based plasma metabolomics and lipidomics analyses for differential diagnosis of bladder cancer and renal cell carcinoma, Front. Oncol. 10 (2020) 717.
[15] L. Szczerbinski, et al., Untargeted metabolomics analysis of the serum metabolic signature of childhood obesity, Nutrients 14 (1) (2022).
[16] J.B. Ngere, et al., Ion-exchange chromatography coupled to mass spectrometry in life science, environmental, and medical research, Anal. Chem. 95 (1) (2023) 152–166.
[17] J. Walsby-Tickle, et al., Anion-exchange chromatography mass spectrometry provides extensive coverage of primary metabolic pathways revealing altered metabolism in IDH1 mutant cells, Commun. Biol. 3 (1) (2020) 247.
[18] K. Zhang, X. Liu, Mixed-mode chromatography in pharmaceutical and biopharmaceutical applications, J. Pharm. Biomed. Anal. 128 (2016) 73–88.
[19] P. Bosman, et al., Development of analytical methods to study the salivary metabolome: impact of the sampling, Anal. Bioanal. Chem. 414 (23) (2022) 6899–6909.
[20] D.Q. Tang, et al., HILIC-MS for metabolomics: an attractive and complementary approach to RPLC-MS, Mass Spectrom. Rev. 35 (5) (2016) 574–600.
[21] Z. Lewis, et al., Towards a generic method for ion chromatography/mass spectrometry of low-molecular-weight amines in pharmaceutical drug discovery and development, Rapid Commun. Mass Spectrom. 34 (Suppl 4) (2020) e8680.
[22] T.M. Quinn, et al., Randomised controlled trial of intravenous nafamostat mesylate in COVID pneumonitis: phase 1b/2a experimental study to investigate safety, pharmacokinetics and pharmacodynamics, EBioMedicine 76 (2022).
[23] T. Ghosh, et al., Reproducibility of mass spectrometry based metabolomics data, BMC Bioinf. 22 (1) (2021).
[24] F. Dieterle, et al., NMR and MS methods for metabonomics, Drug Safety Evaluation: Methods and Protocols 691 (2011) 385–415.
[25] A.S. Edison, et al., NMR: Unique strengths that enhance modern metabolomics research, Anal. Chem. 93 (1) (2021) 478–499.
[26] C. Ingallina, et al., Extra-virgin olive oils from nine Italian regions: an H-1 NMR-chemometric characterization, Metabolites 9 (4) (2019).
[27] E. Ralli, et al., NMR spectroscopy protocols for food metabolomics applications, Metabolic Profiling: Methods and Protocols 1738 (2018) 203–211.
[28] A. Vignoli, et al., High-throughput metabolomics by 1D NMR, Angewandte Chemie-International Edition 58 (4) (2019) 968–994.
[29] D.S. Wishart, et al., NMR and Metabolomics-A roadmap for the future, Metabolites 12 (8) (2022).
[30] N. Psychogios, et al., The human serum metabolome, PLoS One 6 (2) (2011).
[31] D.D. Marshall, et al., Combining DI-ESI-MS and NMR datasets for metabolic profiling, Metabolomics 11 (2) (2015) 391–402.
[32] D.D. Marshall, R. Powers, Beyond the paradigm: combining mass spectrometry and nuclear magnetic resonance for metabolomics, Prog. Nucl. Magn. Reson. Spectrosc. 100 (2017) 1–16.
[33] I. Perez-Victoria, J. Martin, F. Reyes, Combined LC/UV/MS and NMR strategies for the dereplication of marine natural products, Planta Med. 82 (9–10) (2016) 857–871.
[34] J. Teul, et al., LC-QTOF-MS and (1)H NMR metabolomics verifies potential use of greater omentum for Klebsiella pneumoniae biofilm eradication in rats, Pathogens 9 (5) (2020).
[35] D.Z. Wang, et al., NMR- and LC-MS/MS-based urine metabolomic investigation of the subacute effects of hexabromocyclododecane in mice, Environ. Sci. Pollut. Control Ser. 23 (9) (2016) 8500–8507.
[36] A. Capati, O.B. Ijare, T. Bezabeh, Diagnostic applications of nuclear magnetic resonance-based urinary metabolomics, Magn. Reson. Insights 10 (2017) 1178623X17694346.
[37] T. Hamerly, et al., Untargeted metabolomics studies employing NMR and LC-MS reveal metabolic coupling between nanoarcheum equitans and its archaeal host Ignicoccus hospitalis, Metabolomics 11 (4) (2015) 895–907.
[38] F. Probert, et al., Diagnosis and staging of multiple sclerosis using a metabolomics-based blood test: a simple method for monitoring progression independently of EDSS, Multiple Sclerosis Journal 25 (2019) 500–501.
[39] F. Probert, et al., Determination of CSF GFAP, CCN5, and vWF levels enhances the diagnostic accuracy of clinically defined MS from Non-MS patients with CSF oligoclonal bands, Front. Immunol. 12 (2022).
[40] K. Segers, et al., Analytical techniques for metabolomic studies: a review, Bioanalysis 11 (24) (2019) 2297–2318.
[41] K. Bingol, et al., Metabolomics beyond spectroscopic databases: a combined MS/NMR strategy for the rapid identification of new metabolites in complex mixtures, Anal. Chem. 87 (7) (2015) 3864–3870.
[42] C. Martias, et al., Optimization of sample preparation for metabolomics exploration of urine, feces, blood and saliva in humans using combined NMR and UHPLC-HRMS platforms, Molecules 26 (14) (2021).
[43] A. Beltran, et al., Assessment of compatibility between extraction methods for NMR- and LC/MS-Based metabolomics, Anal. Chem. 84 (14) (2012) 5838–5844.
[44] R. Powers, et al., Metabolic investigations of the molecular mechanisms associated with parkinson's disease, Metabolites 7 (2) (2017).
[45] M.S.A. Bustamam, et al., Complementary analytical platforms of NMR spectroscopy and LCMS analysis in the metabolite profiling of Isochrysis galbana, Mar. Drugs 19 (3) (2021).
[46] G. Petrella, et al., Personalized metabolic profile by synergic use of NMR and HRMS, Molecules 26 (14) (2021).
[47] A.C. Zanatta, et al., Understanding the seasonal effect of metabolite production in Terminalia catappa L. leaves through a concatenated MS- and NMR-based metabolomics approach, Metabolites 13 (3) (2023).
[48] D. Vuckovic, Current trends and challenges in sample preparation for global metabolomics using liquid chromatography-mass spectrometry, Anal. Bioanal. Chem. 403 (6) (2012) 1523–1548.
[49] P.G. Takis, et al., SMolESY: an efficient and quantitative alternative to on-instrument macromolecular H-1-NMR signal suppression, Chem. Sci. 11 (23) (2020) 6000–6011.
[50] J.A. Aguilar, et al., Reliable, high-quality suppression of NMR signals arising from water and macromolecules: application to bio-fluid analysis, Analyst 144 (24) (2019) 7270–7277.
[51] N.G. Bliziotis, et al., A comparison of high-throughput plasma NMR protocols for comparative untargeted metabolomics, Metabolomics 16 (5) (2020).

[52] G.A.N. Gowda, D. Raftery, NMR spectroscopy-based metabolic profiling for detecting hepatobiliary diseases, Emerging Trends in Dietary Components for Preventing and Combating Disease 1093 (2012) 407–415.
[53] G.A.N. Gowda, et al., Metabolomics-based methods for early disease diagnostics, Expert Rev. Mol. Diagn. 8 (5) (2008) 617–633.
[54] N.N. Jarenwattananon, L.S. Bouchard, Breakdown of carr-purcell meiboom-gill spin echoes in inhomogeneous fields, J. Chem. Phys. 149 (8) (2018).
[55] M. Jurynczyk, et al., Metabolomics reveals distinct, antibody-independent, molecular signatures of MS, AQP4-antibody and MOG-Antibody disease, Acta Neuropathologica Communications 5 (2017).
[56] J. McCullagh, N. Oldham, *Mass Spectrometry*. Oxford Chemistry Primers, Oxford University Press, Oxford, 2023.
[57] Z.H. Alshehry, et al., An efficient single phase method for the extraction of plasma lipids, Metabolites 5 (2) (2015) 389–403.
[58] Z.Q. Pang, et al., MetaboAnalyst 5.0: narrowing the gap between raw spectra and functional insights, Nucleic Acids Res. 49 (W1) (2021) W388–W396.
[59] W. Haynes, Benjamini–hochberg method, in: W. Dubitzky, O. Wolkenhauer, K. H. Cho, H. Yokota (Eds.), Encyclopedia of Systems Biology, Springer, New York, NY, 2013, pp. 78–79.
[60] W.S. Noble, How does multiple testing correction work? Nat. Biotechnol. 27 (12) (2009) 1135–1137.
[61] C.E. McHugh, , et al.Reproducible Rapid, Quantifiable NMR metabolomics: methanol and methanol: Chloroform precipitation for removal of macromolecules in serum and whole blood, Metabolites 8 (4) (2018).
[62] Y.H. Yang, et al., New sample preparation approach for mass spectrometry-based profiling of plasma results in improved coverage of metabolome, J. Chromatogr. A 1300 (2013) 217–226.
[63] G.A.N. Gowda, D. Raftery, Quantitating metabolites in protein precipitated serum using NMR spectroscopy, Anal. Chem. 86 (11) (2014) 5433–5440.
[64] B. Zhang, et al., Nanoparticle-assisted removal of protein in human serum for metabolomics studies, Anal. Chem. 88 (1) (2016) 1003–1007.
[65] K.O. Boernsen, S. Gatzek, G. Imbert, Controlled protein precipitation in combination with chip-based nanospray infusion mass spectrometry. An approach for metabolomics profiling of plasma, Anal. Chem. 77 (22) (2005) 7255–7264.
[66] Z.R. He, Z.Q. Liu, L.Z. Gong, Systematic evaluation of sample preparation strategy for GC-MS-based plasma metabolomics and its application in osteoarthritis, Anal. Biochem. 621 (2021).
[67] E. Hidvegi, G.P. Somogyi, Determination of main tetrahydrocannabinoids by GC-MS: impact of protein precipitation by acetonitrile on solid phase extraction of cannabinoids from human serum, Pharmazie 69 (6) (2014) 417–419.
[68] A. Acharjee, et al., Integration of metabolomic and clinical data improves the prediction of intensive care unit length of stay following major traumatic injury, Metabolites 12 (1) (2022).
[69] C. Keller, et al., Extraction optimization for combined metabolomics, peptidomics, and proteomics analysis of gut microbiota samples, J. Mass Spectrom. 56 (4) (2021).
[70] R. Kay, et al., Enrichment of low molecular weight serum proteins using acetonitrile precipitation for mass spectrometry based proteomic analysis, Rapid Commun. Mass Spectrom. 22 (20) (2008) 3255–3260.
[71] D. Baumstark, et al., H NMR spectroscopy quantifies visibility of lipoproteins, subclasses, and lipids at varied temperatures and pressures[S], JLR (J. Lipid Res.) 60 (9) (2019) 1516–1534.
[72] G. Corona, et al., H-NMR plasma lipoproteins profile analysis reveals lipid metabolism alterations in HER2-Positive breast cancer patients, Cancers 13 (22) (2021).
[73] J. Gumà, et al., Altered serum metabolic profile assessed by advanced 1H-NMR in breast cancer patients, Cancers 13 (17) (2021).

The following statement was added to the Introduction of Chapter 2 (with the added text underlined in red; pp. 77, column 2, ll. 18):

A separate challenge is the need for buffered NMR samples. This is due to the pH-dependent nature of NMR spectral chemical shift values, necessitating samples to be buffered to maintain a constant sample pH. Buffers were prepared in D_2O, and pH was measured with a standard glass electrode calibrated for H_2O, which provides an apparent pH typically ~0.4 units lower than the true pD. For consistency with previous metabolomics studies, we report the direct pH-meter readings. However, the increased sample salt concentrations resulting from the use of such buffers could theoretically pose a challenge for MS-based analytical methods, as certain salts (e.g. phosphates) can affect ionisation efficiency and sensitivity [56].

Supplementary Information – Manuscript 1

Supplementary Information

Integrating NMR and Multi-LC-MS-Based Untargeted Metabolomics for Comprehensive Analysis of Blood Serum Samples

Tereza Kacerova[1], Elisabete Pires[1], John Walsby-Tickle[1], Fay Probert[1*] and James S.O. McCullagh[1*]

[1] Chemistry Research Laboratory, Department of Chemistry, University of Oxford, Oxford OX1 3TA, UK.

Corresponding author: James S.O. McCullagh james.mccullagh@chem.ox.ac.uk

Corresponding author: Fay Probert fay.probert@chem.ox.ac.uk

Supplementary Information – Manuscript 1

Deuterium in NMR samples does not produce deuterated metabolites in the MS spectrum

List of features detected exclusively in the Milli-Q water and deuterated water extractions in negative (neg.) and positive (pos.) ion modes.

SI Table 1 *List of features detected either exclusively in Milli-Q water extractions or exclusively in deuterated water extractions (0 = negative outcome; 1 = positive outcome, each condition was analysed in sample triplicate)s*

Platform	Nominal Mass	H_2O	D_2O	Evidence for deuteration
IC-MS (neg.)	561	0	1	0
IC-MS (neg.)	462	0	1	0
IC-MS (neg.)	410	0	1	0
IC-MS (neg.)	388	0	1	0
IC-MS (neg.)	364	0	1	0
IC-MS (neg.)	360	0	1	0
IC-MS (neg.)	285	0	1	0
IC-MS (neg.)	182	0	1	0
IC-MS (neg.)	154	0	1	0
IC-MS (neg.)	90	0	1	0
IC-MS (neg.)	83	0	1	0
IC-MS (neg.)	82	0	1	0
IC-MS (neg.)	79	0	1	0
IC-MS (neg.)	62	0	1	0
IC-MS (neg.)	683	1	0	0
IC-MS (neg.)	671	1	0	0
IC-MS (neg.)	521	1	0	0
IC-MS (neg.)	505	1	0	0
IC-MS (neg.)	396	1	0	0
IC-MS (neg.)	395	1	0	0
IC-MS (neg.)	376	1	0	0
IC-MS (neg.)	344	1	0	0
IC-MS (neg.)	315	1	0	0
IC-MS (neg.)	305	1	0	0
IC-MS (neg.)	304	1	0	0
IC-MS (neg.)	297	1	0	0
IC-MS (neg.)	296	1	0	0
IC-MS (neg.)	294	1	0	0
IC-MS (neg.)	276	1	0	0
IC-MS (neg.)	252	1	0	0
IC-MS (neg.)	236	1	0	0
IC-MS (neg.)	219	1	0	0
IC-MS (neg.)	218	1	0	0
IC-MS (neg.)	206	1	0	0
IC-MS (neg.)	186	1	0	0
IC-MS (neg.)	160	1	0	0
IC-MS (neg.)	152	1	0	0

IC-MS (neg.)	148	1	0	0
IC-MS (neg.)	147	1	0	0
IC-MS (neg.)	107	1	0	0
IC-MS (neg.)	104	1	0	0
IC-MS (neg.)	72	1	0	0
RPLC-MS (neg.)	879	0	1	0
RPLC-MS (neg.)	857	0	1	0
RPLC-MS (neg.)	795	0	1	0
RPLC-MS (neg.)	791	0	1	0
RPLC-MS (neg.)	788	0	1	0
RPLC-MS (neg.)	766	0	1	0
RPLC-MS (neg.)	732	0	1	0
RPLC-MS (neg.)	708	0	1	0
RPLC-MS (neg.)	616	0	1	0
RPLC-MS (neg.)	588	0	1	0
RPLC-MS (neg.)	562	0	1	0
RPLC-MS (neg.)	540	0	1	0
RPLC-MS (neg.)	532	0	1	0
RPLC-MS (neg.)	520	0	1	0
RPLC-MS (neg.)	400	0	1	0
RPLC-MS (neg.)	394	0	1	0
RPLC-MS (neg.)	386	0	1	0
RPLC-MS (neg.)	380	0	1	0
RPLC-MS (neg.)	344	0	1	0
RPLC-MS (neg.)	342	0	1	0
RPLC-MS (neg.)	296	0	1	0
RPLC-MS (neg.)	272	0	1	0
RPLC-MS (neg.)	260	0	1	0
RPLC-MS (neg.)	231	0	1	0
RPLC-MS (neg.)	220	0	1	0
RPLC-MS (neg.)	166	0	1	0
RPLC-MS (neg.)	132	0	1	0
RPLC-MS (neg.)	127	0	1	0
RPLC-MS (neg.)	83	0	1	0
RPLC-MS (neg.)	899	1	0	0
RPLC-MS (neg.)	894	1	0	0
RPLC-MS (neg.)	876	1	0	0
RPLC-MS (neg.)	867	1	0	0
RPLC-MS (neg.)	762	1	0	0
RPLC-MS (neg.)	738	1	0	0
RPLC-MS (neg.)	734	1	0	0
RPLC-MS (neg.)	716	1	0	0
RPLC-MS (neg.)	694	1	0	0
RPLC-MS (neg.)	662	1	0	0
RPLC-MS (neg.)	607	1	0	0
RPLC-MS (neg.)	596	1	0	0

RPLC-MS (neg.)	584	1	0	0
RPLC-MS (neg.)	546	1	0	0
RPLC-MS (neg.)	544	1	0	0
RPLC-MS (neg.)	510	1	0	0
RPLC-MS (neg.)	488	1	0	0
RPLC-MS (neg.)	420	1	0	0
RPLC-MS (neg.)	360	1	0	0
RPLC-MS (neg.)	348	1	0	0
RPLC-MS (neg.)	334	1	0	0
RPLC-MS (neg.)	330	1	0	0
RPLC-MS (neg.)	286	1	0	0
RPLC-MS (neg.)	264	1	0	0
RPLC-MS (neg.)	244	1	0	0
RPLC-MS (neg.)	233	1	0	0
RPLC-MS (neg.)	224	1	0	0
RPLC-MS (neg.)	125	1	0	0
RPLC-MS (neg.)	121	1	0	0
RPLC-MS (neg.)	109	1	0	0
RPLC-MS (neg.)	67	1	0	0
RPLC-MS (pos.)	849	0	1	0
RPLC-MS (pos.)	848	0	1	0
RPLC-MS (pos.)	826	0	1	0
RPLC-MS (pos.)	793	0	1	0
RPLC-MS (pos.)	792	0	1	0
RPLC-MS (pos.)	791	0	1	0
RPLC-MS (pos.)	781	0	1	0
RPLC-MS (pos.)	780	0	1	0
RPLC-MS (pos.)	521	0	1	0
RPLC-MS (pos.)	520	0	1	0
RPLC-MS (pos.)	495	0	1	0
RPLC-MS (pos.)	494	0	1	0
RPLC-MS (pos.)	469	0	1	0
RPLC-MS (pos.)	445	0	1	0
RPLC-MS (pos.)	444	0	1	0
RPLC-MS (pos.)	399	0	1	0
RPLC-MS (pos.)	84	0	1	0
RPLC-MS (pos.)	71	0	1	0
RPLC-MS (pos.)	895	1	0	0
RPLC-MS (pos.)	890	1	0	0
RPLC-MS (pos.)	889	1	0	0
RPLC-MS (pos.)	870	1	0	0
RPLC-MS (pos.)	798	1	0	0
RPLC-MS (pos.)	784	1	0	0
RPLC-MS (pos.)	783	1	0	0
RPLC-MS (pos.)	702	1	0	0
RPLC-MS (pos.)	695	1	0	0

RPLC-MS (pos.)	640	1	0	0
RPLC-MS (pos.)	639	1	0	0
RPLC-MS (pos.)	538	1	0	0
RPLC-MS (pos.)	523	1	0	0
RPLC-MS (pos.)	479	1	0	0
RPLC-MS (pos.)	478	1	0	0
RPLC-MS (pos.)	413	1	0	0
RPLC-MS (pos.)	412	1	0	0
RPLC-MS (pos.)	103	1	0	0
RPLC-MS (pos.)	93	1	0	0
RPLC-MS (pos.)	79	1	0	0
RPLC-MS (pos.)	57	1	0	0

Supplementary Information – Manuscript 1

Deuterium in NMR samples does not produce deuterated metabolites in the MS spectrum

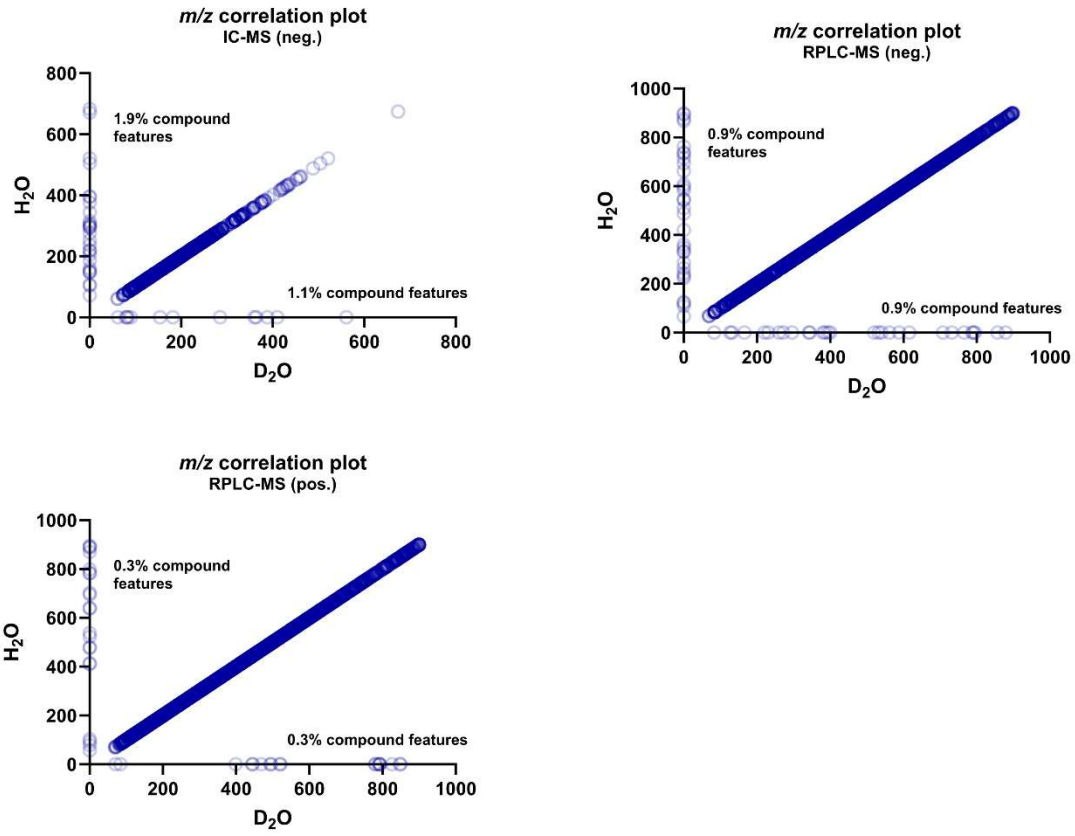

SI Fig. 1 *Comparison of features' m/z values (nominal mass) for Milli-Q and deuterated water analysed on the different platforms (IC-MS (neg. mode) and RPLC-MS (neg. mode; pos. mode). Each condition was analysed in sample triplicate.*

Supplementary Information – Manuscript 1

Deuterium in NMR samples does not produce deuterated metabolites in the MS spectrum

a) IC-MS data (negative ionisation mode)

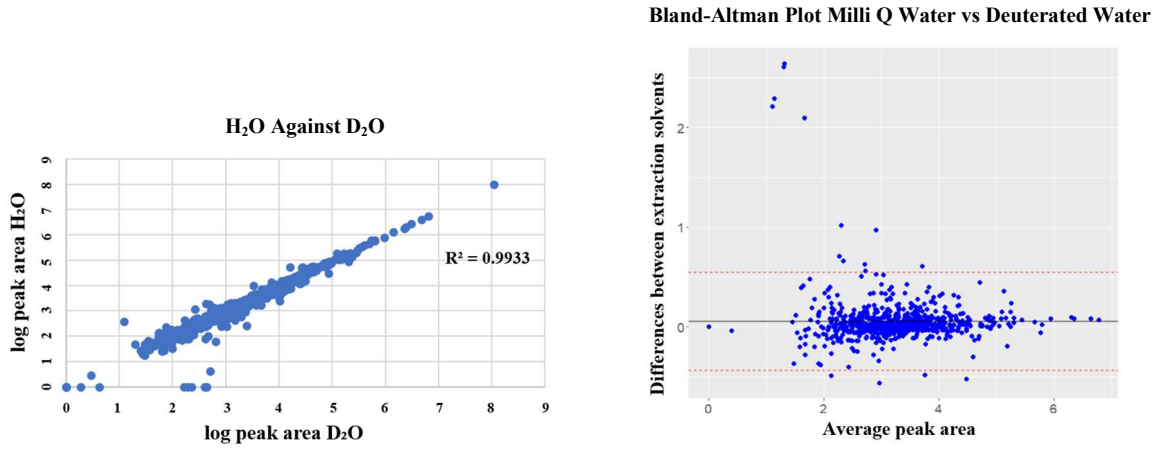

b) RPLC-MS data (negative ionisation mode)

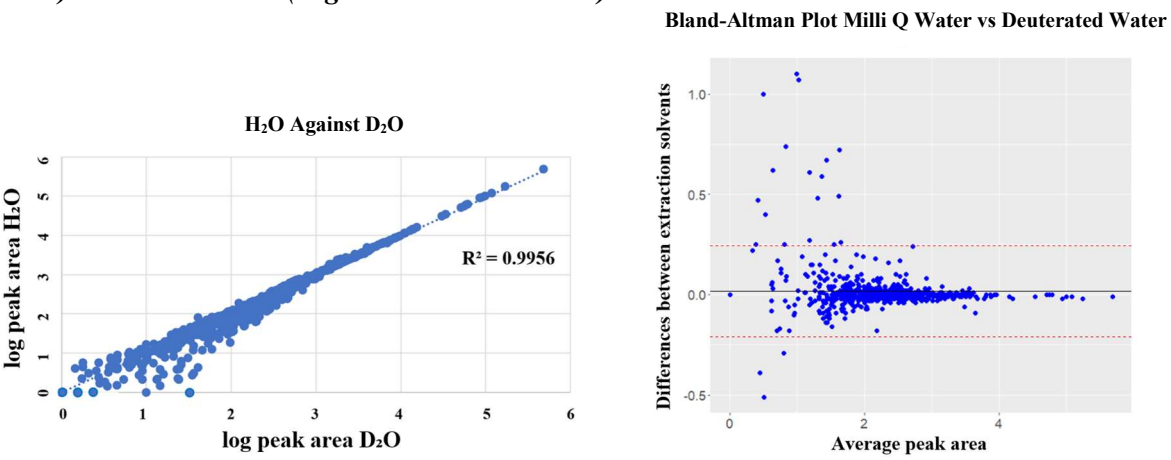

c) RPLC-MS data (positive ionisation mode)

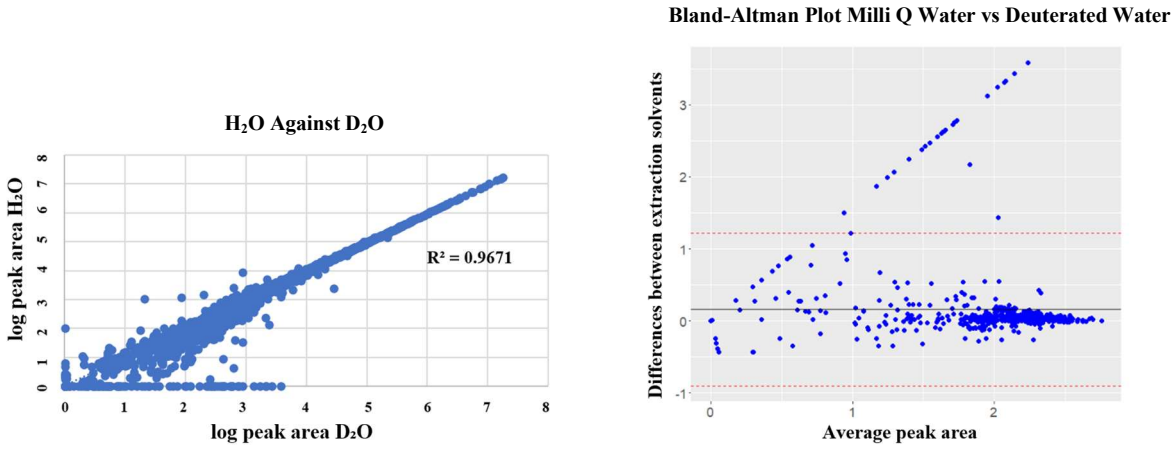

SI Fig. 2 *Comparison of features' peak areas (decimal log values) for Milli-Q and deuterated water analysed on the different platforms (IC-MS (neg. mode) and RPLC-MS (neg. mode; pos. mode)). The left side shows linear correlation plots (log); the right side shows Bland-Altman plots (log). a) IC-MS neg. mode; b) RPLC-MS neg. mode; c) RPLC-MS pos. mode. Note: Each data point was determined as an average of three sample replicates.*

Supplementary Information – Manuscript 1

Deuterium in NMR samples does not produce deuterated metabolites in the MS spectrum

SI Table 2 *List of compound features with significantly altered chromatographic peak intensity with their corresponding CV values. The colour coding corresponds to the CV values (all outlying compound features that were eluted within the void volume were omitted from this analysis). The CV value was determined based on the analysis of sample triplicate.*

Compound feature	CV value (%)	Platform
3.26_112.0525m/z	18.37	IC-MS neg.
3.26_72.02000m/z	11.5	IC-MS neg.
3.26_89.9942m/z	17.6	IC-MS neg.
3.26_97.9663m/z	19.5	IC-MS neg.
3.26_121.0483n	13.91	IC-MS neg.
5.27_686.5944 m/z	14.64	RPLC-MS neg.
11.07_540.3310 m/z	9.37	RPLC-MS neg.
11.06_867.2000 m/z	2.85	RPLC-MS pos.
10.92_313.0434 m/z	6.87	RPLC-MS pos.
10.89_309.6269 m/z	1.17	RPLC-MS pos.
12.56_321.3155 m/z	10.31	RPLC-MS pos.
11.81_538.4833 m/z	1.28	RPLC-MS pos.
3.02_539.2751 m/z	8.03	RPLC-MS pos.
11.76_524.9141 m/z	7.25	RPLC-MS pos.
12.37_121.0298 m/z	3.64	RPLC-MS pos.
10.18_401.8682 m/z	2.75	RPLC-MS pos.
2.49_289.0484 m/z	3.75	RPLC-MS pos.
9.68_431.6245 m/z	4.02	RPLC-MS pos.
9.98_244.1885 m/z	3.73	RPLC-MS pos.
1.29_199.0466 m/z	4.00	RPLC-MS pos.
13.18_765.1709 m/z	8.53	RPLC-MS pos.
7.66_459.9503 m/z	3.32	RPLC-MS pos.
7.97_94.0431 m/z	3.84	RPLC-MS pos.
12.67_254.2494 m/z	27.59	RPLC-MS pos.
2.56_740.2851 m/z	8.28	RPLC-MS pos.
16.09_301.9741 m/z	0.69	RPLC-MS pos.
10.46_425.1144 m/z	2.90	RPLC-MS pos.
8.08_209.1526 m/z	4.34	RPLC-MS pos.
4.46_521.9943 m/z	6.36	RPLC-MS pos.
10.06_315.5316 m/z	2.03	RPLC-MS pos.
16.01_627.5284 m/z	28.11	RPLC-MS pos.
15.22_416.2573 m/z	27.39	RPLC-MS pos.
12.22_344.7465 m/z	2.33	RPLC-MS pos.
2.42_758.2959 m/z	4.55	RPLC-MS pos.
10.58_699.4935 m/z	0.82	RPLC-MS pos.
16.06_207.8544 n	8.27	RPLC-MS pos.
10.37_403.2031 m/z	3.32	RPLC-MS pos.
9.27_288.2541 m/z	4.42	RPLC-MS pos.
13.71_445.0936 m/z	20.5	RPLC-MS pos.
11.90_463.1293 m/z	10.63	RPLC-MS pos.

4.12_427.6005 m/z	4.97	RPLC-MS pos.
13.73_519.1055 m/z	22.19	RPLC-MS pos.
4.12_640.3961 m/z	3.16	RPLC-MS pos.
8.09_339.2502 m/z	5.63	RPLC-MS pos.
9.92_487.0942 m/z	7.92	RPLC-MS pos.
10.82_104.1084 m/z	3.00	RPLC-MS pos.
9.80_297.0481 m/z	7.42	RPLC-MS pos.
11.06_104.1083 m/z	0.68	RPLC-MS pos.
13.73_638.2144 m/z	2.33	RPLC-MS pos.

CV 0-5%	CV 6-10%	CV 11-15%	CV 16-20%	CV 21-25%	CV 26-30%

Supplementary Information – Manuscript 1

NMR phosphate buffer induces subtle changes in the MS-detected features

a) IC-MS Milli-Q water compared to deuterated phosphate buffer

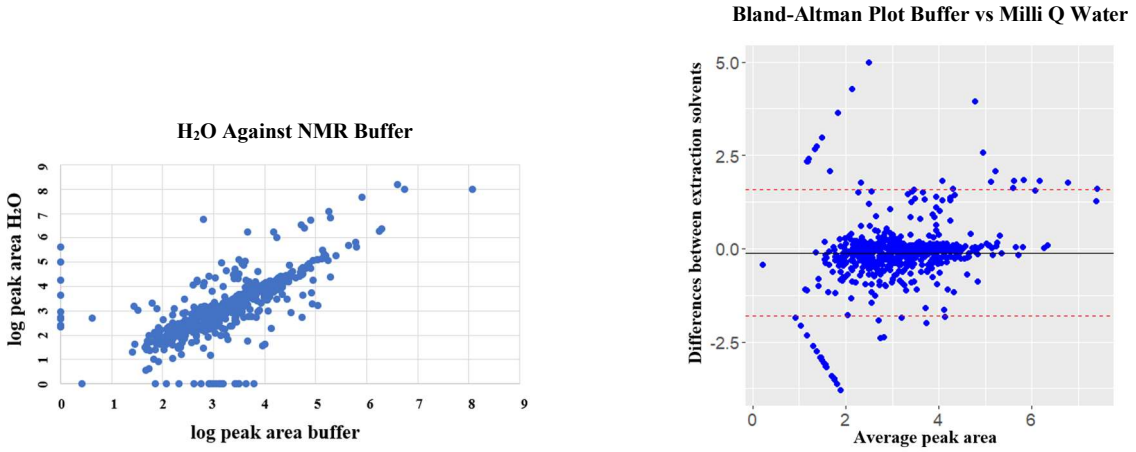

b) IC-MS deuterated water compared to deuterated phosphate buffer

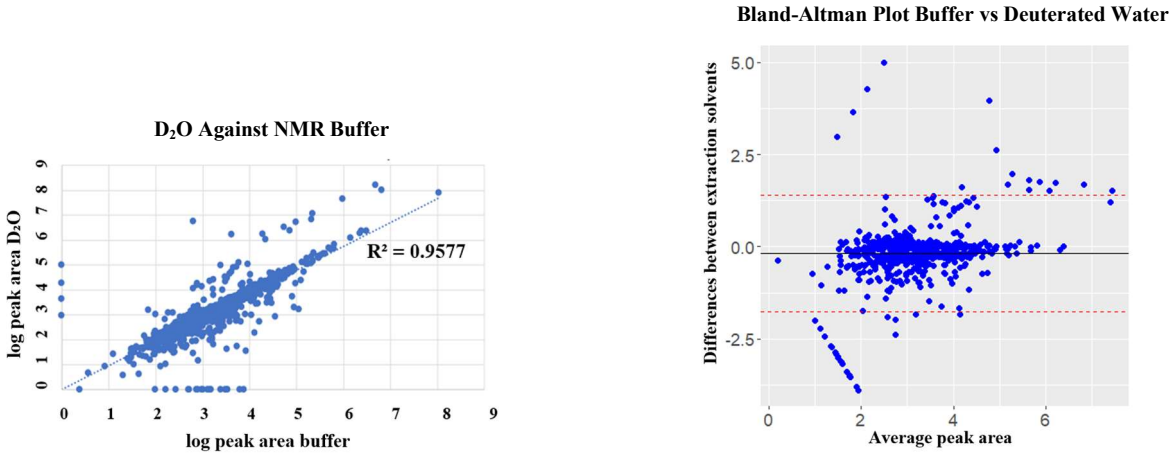

SI Fig. 3 *Comparison of features' peak areas (decimal log values) for Milli-Q water vs deuterated phosphate (NMR) buffer and deuterated water vs deuterated phosphate (NMR) buffer analysed on IC-MS (neg. mode). The left side shows linear correlation plots (log); the right side shows Bland-Altman plots (log). Note: Each data point was determined as an average of three sample replicates.*

Supplementary Information – Manuscript 1

NMR phosphate buffer induces subtle changes in the MS-detected features

a) RPLC-MS (neg.) Milli-Q water compared to deuterated phosphate buffer

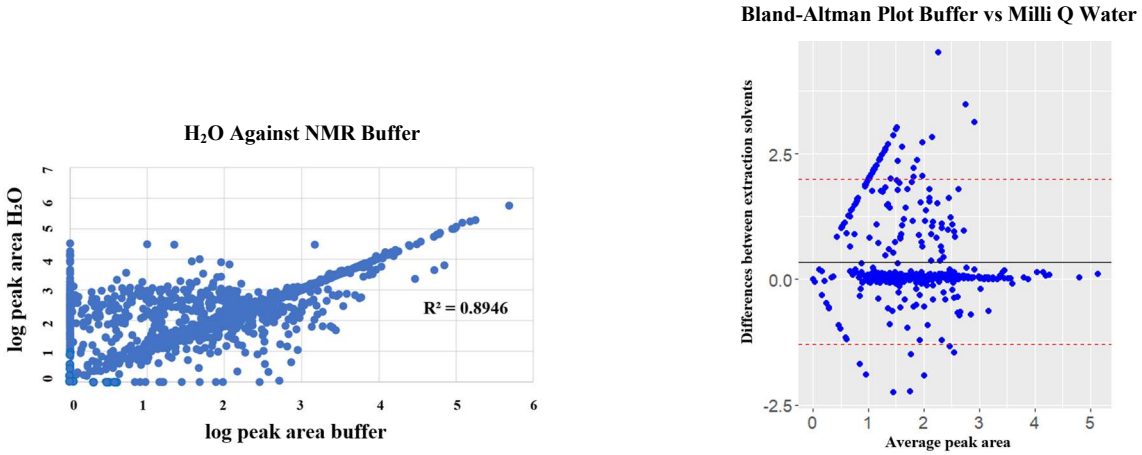

b) RPLC-MS (neg.) deuterated water compared to deuterated phosphate buffer

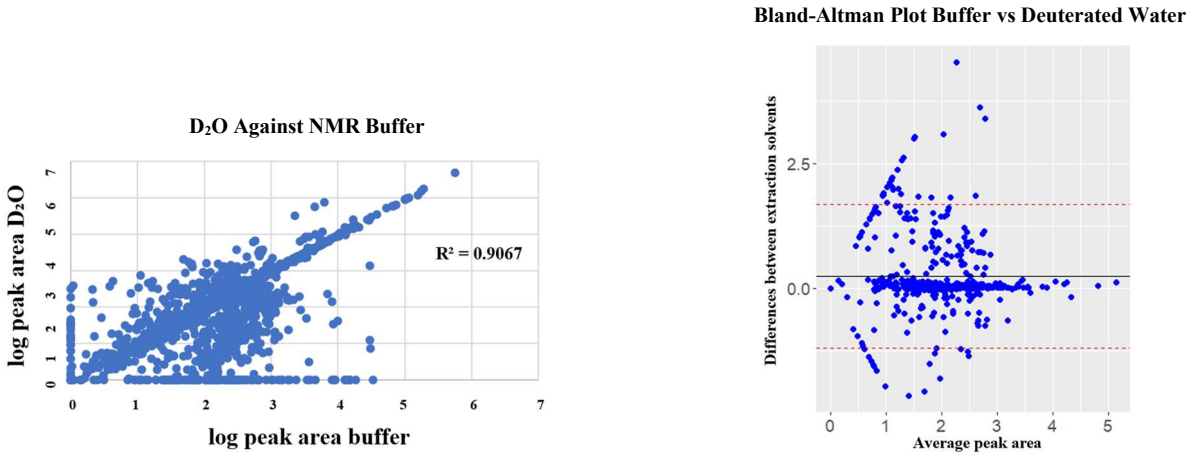

SI Fig. 4 *Comparison of features' peak areas (decimal log values) for Milli-Q water vs deuterated phosphate (NMR) buffer and deuterated water vs deuterated phosphate (NMR) buffer analysed on RPLC-MS (neg. mode). The left side shows linear correlation plots (log); the right side shows Bland-Altman plots (log). Note: Each data point was determined as an average of three sample replicates.*

Supplementary Information – Manuscript 1

NMR phosphate buffer induces subtle changes in the MS-detected features

a) RPLC-MS (pos.) Milli-Q water compared to deuterated phosphate buffer

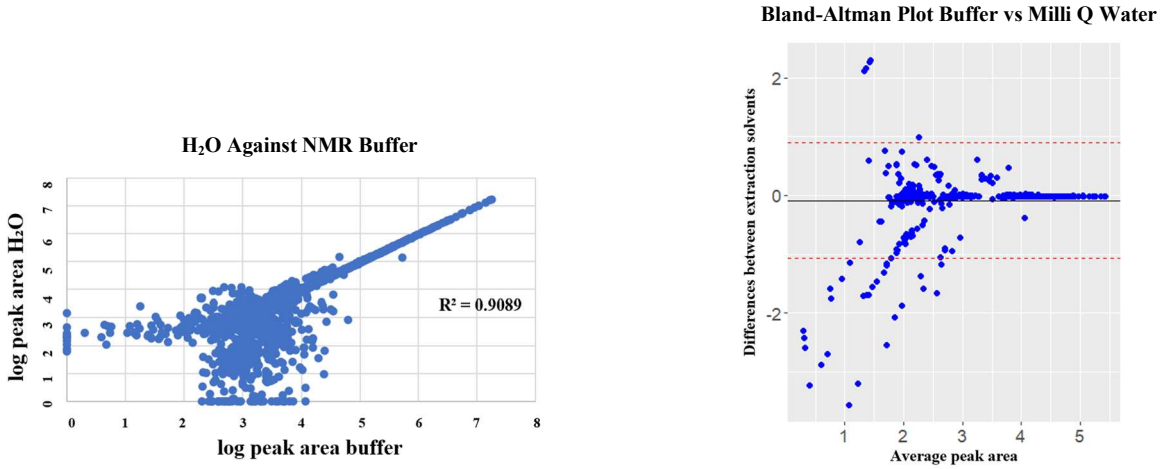

b) RPLC-MS (pos.) deuterated water compared to deuterated phosphate buffer

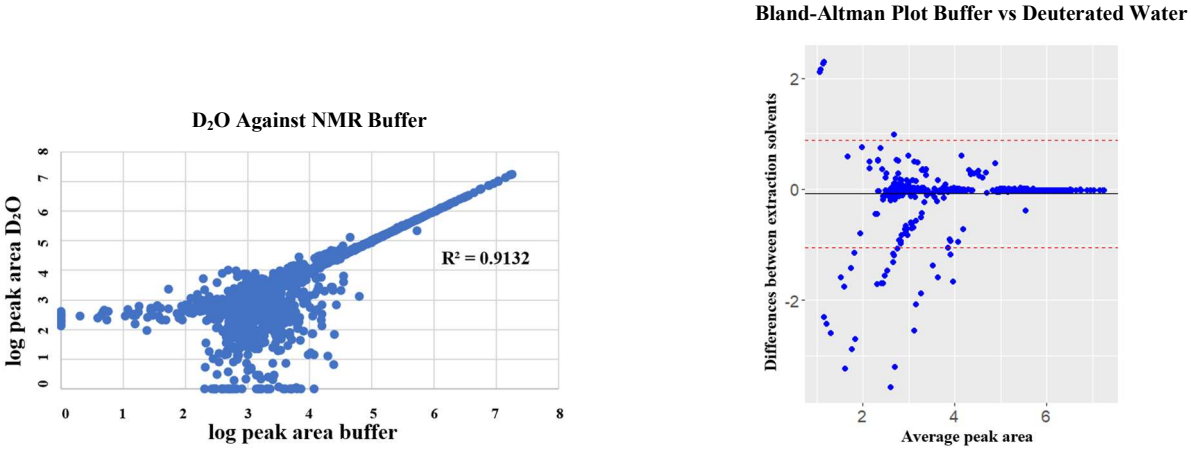

SI Fig. 5 *Comparison of features' peak area (decimal log values) for Milli-Q water vs deuterated phosphate (NMR) buffer and deuterated water vs deuterated phosphate (NMR) buffer analysed on RPLC-MS (pos. mode). The left side shows linear correlation plots (log); the right side shows Bland-Altman plots (log). Note: Each data point was determined as an average of three sample replicates.*

Supplementary Information – Manuscript 1

NMR phosphate buffer induces subtle changes in the MS-detected features

Correlation heatmaps showing the clustering between the individual groups (deuterated phosphate (NMR) buffer – green; deuterated water – purple and Milli-Q water – blue). Heatmap "a" shows all detected features, whereas each map "b" shows the distribution of the 50 most significant features, selected based on their lowest p-values from ANOVA. The overall pattern shows little difference between Milli-Q water and deuterated water; however, the phosphate addition is associated with specific changes.

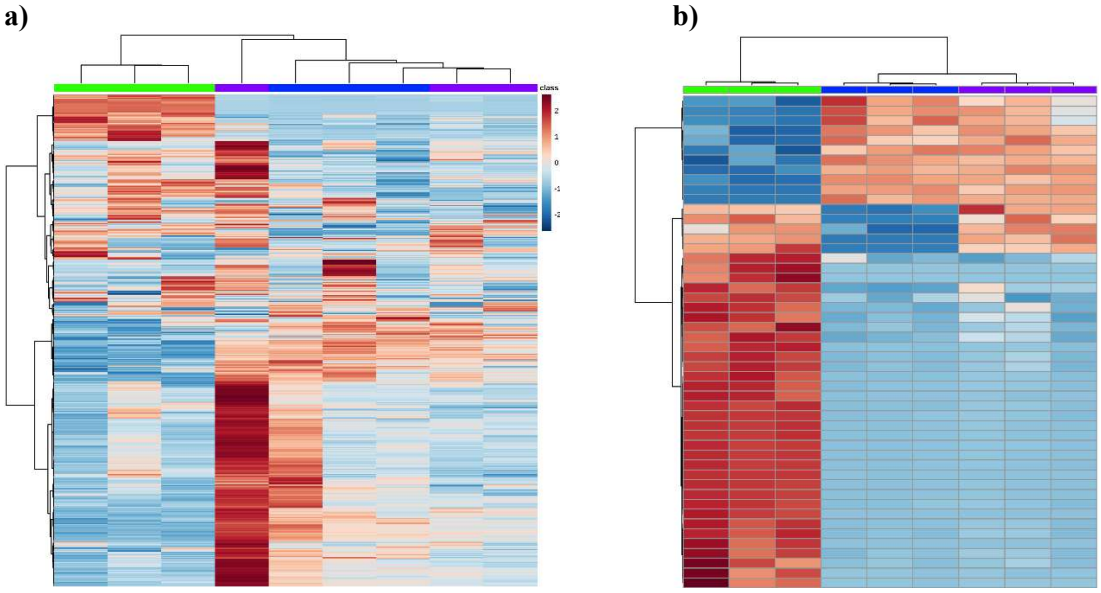

SI Fig. 6 *IC-MS (neg. mode) – Hierarchical clustering heatmap; a) all features; b) the most significantly changed 50 features (blue: H_2O; purple: D_2O; green: phosphate deuterated buffer) Each condition was analysed in sample triplicate.*

a) **b)**

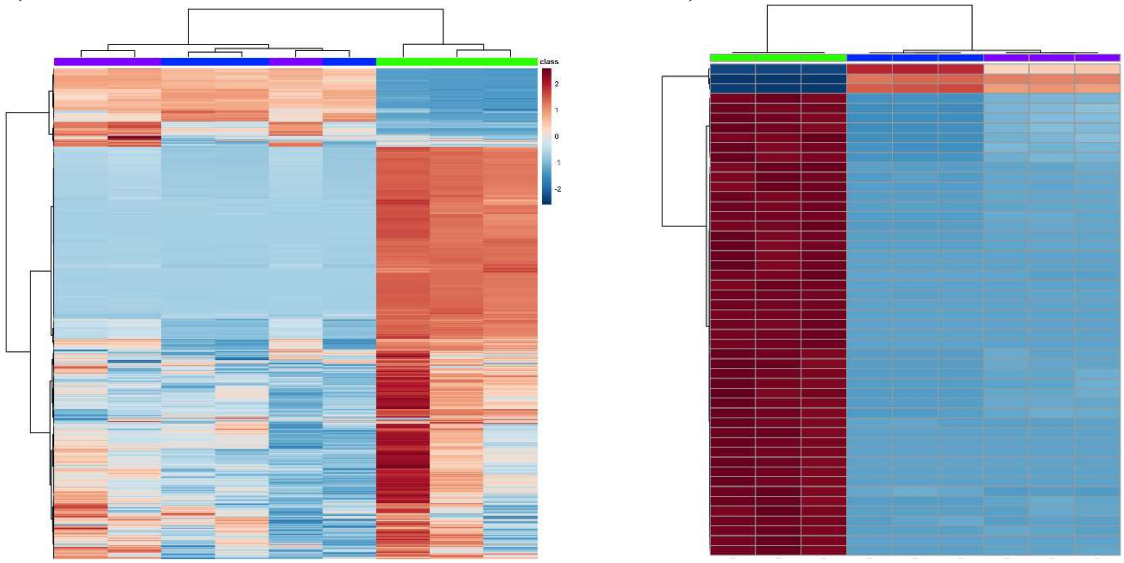

SI Fig. 7 *RPLC-MS (neg. mode) – Hierarchical clustering heatmap; a) all features; b) the most significantly changed 50 features (blue: H_2O; purple: D_2O; green: phosphate deuterated buffer). Each condition was analysed in sample triplicate.*

a) **b)**

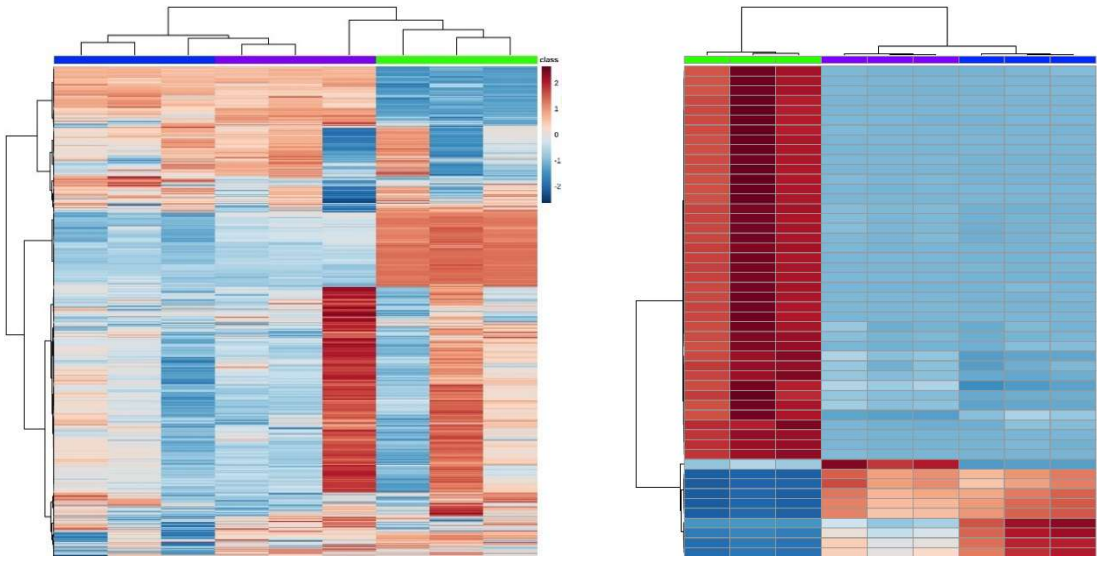

SI Fig. 8 *RPLC-MS (pos. mode) – Hierarchical clustering heatmap; a) all features; b) the most significantly changed 50 features (blue: H_2O; purple: D_2O; green: phosphate deuterated buffer). Each condition was analysed in sample triplicate.*

Supplementary Information – Manuscript 1

Multiple aqueous washes reduce the amount of glycerol released into the serum samples

SI Table 3 *MWCO filter washing – experiment design overview*

Wash solvent	*N* wash	Phosphate Buffer	Serum + MeCN
Methanol	1x	1	0
Methanol	2x	1	0
Methanol	2x	1	1
Methanol	3x	1	0
Ethanol	1x	1	0
Ethanol	2x	1	0
Ethanol	2x	1	1
Ethanol	3x	1	0
Acetonitrile	1x	1	0
Acetonitrile	2x	1	0
Acetonitrile	2x	1	1
Acetonitrile	3x	1	0
Milli-Q water	1x	1	0
Milli-Q water	2x	1	0
Milli-Q water	2x	1	1
Milli-Q water	3x	1	0
Milli-Q water Methanol Milli-Q water	1x 1x 1x	1	0
Milli-Q water Ethanol Milli-Q water	1x 1x 1x	1	0
Milli-Q water Acetonitrile Milli-Q water	1x 1x 1x	1	0

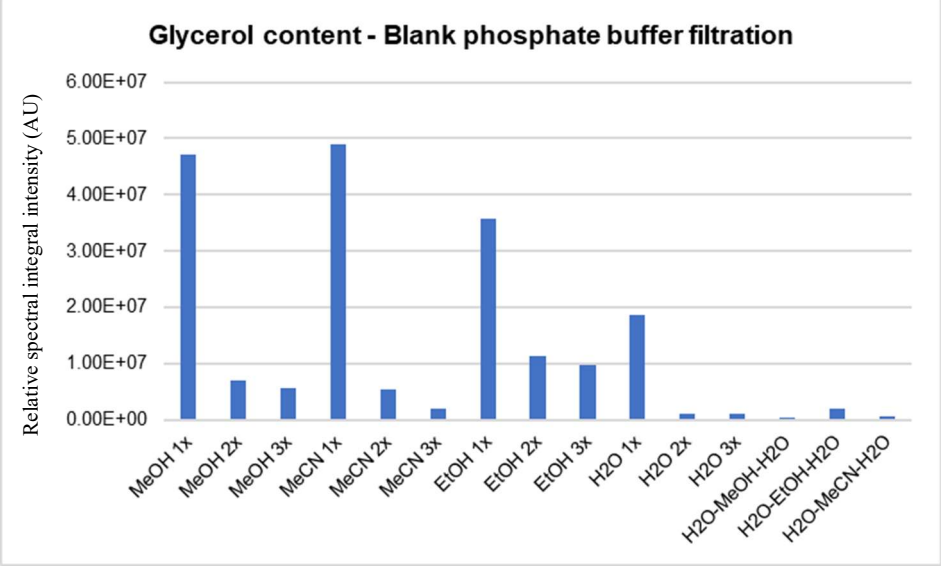

SI Fig. 9 *The intensity of glycerol peak (a contaminant) in blank phosphate buffer samples following the MWCO filter washes in different organic and aqueous solvents*

Multiple aqueous washes reduce the amount of glycerol released into the serum samples

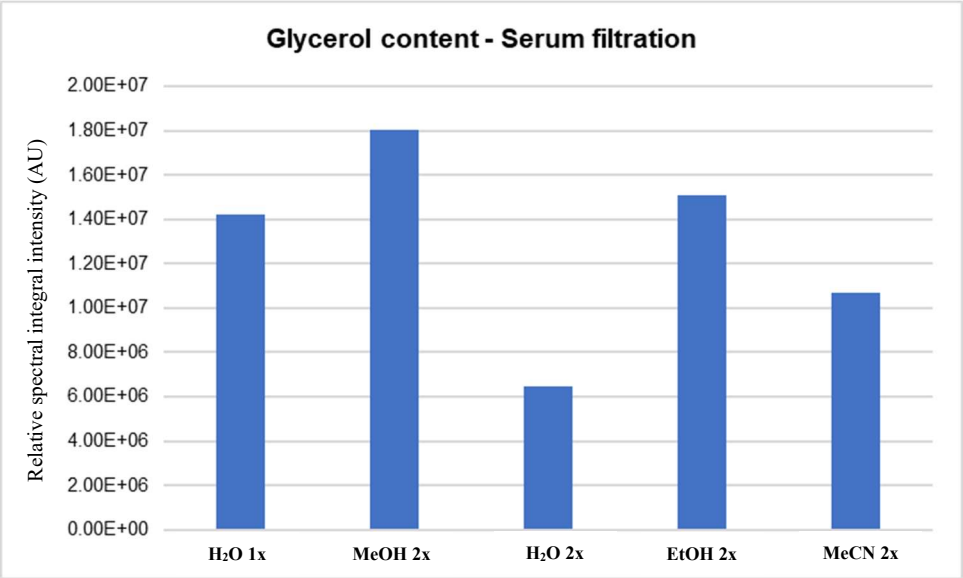

SI Fig. 10 *The intensity of glycerol peak (a contaminant) in serum samples in aqueous phosphate buffer following the MWCO filter washes in different organic and aqueous solvents*

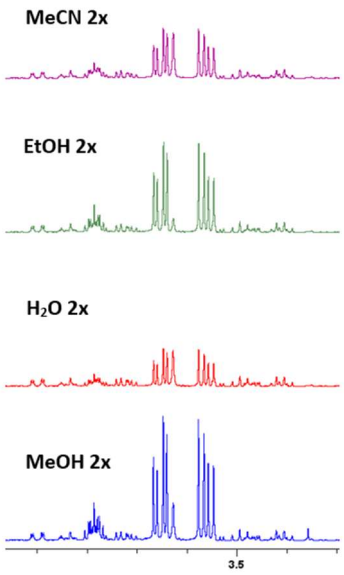

SI Fig. 11 *Detail of the glycerol peak in serum samples mixed with aqueous phosphate buffer and filtered with MWCO filters following the filters washing with different organic and aqueous solvents (2x). Although the two washes significantly reduce the released glycerol amount (SI Fig. 13), the glycerol peak is still more prominent than the metabolite peaks.*

Supplementary Information – Manuscript 1

MWCO filtration impedes the detection of some NMR-based metabolomics diagnostic features

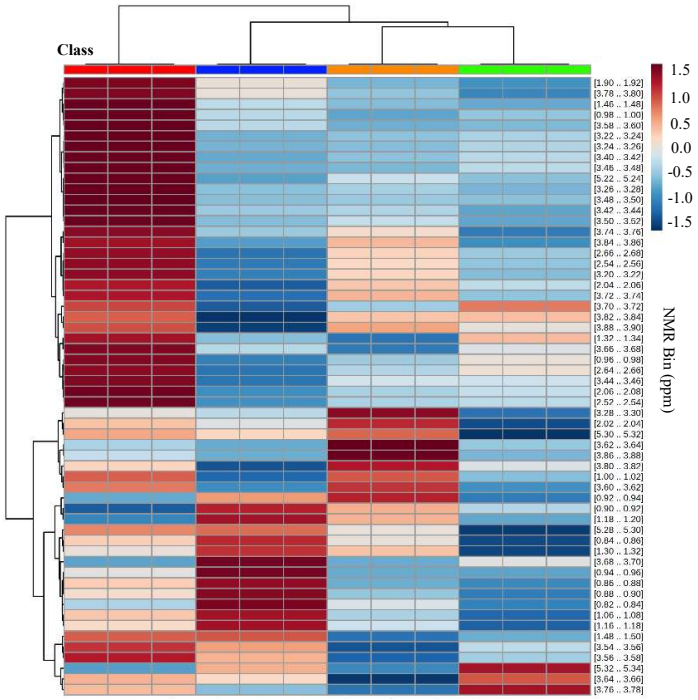

SI Fig. 12 *Hierarchically clustered heatmap showing the distribution of the relative standard deviations (RSD) for the individual bins for the four extraction methods i) aqueous phosphate buffer (green); ii) filtered in aqueous phosphate buffer (blue); iii) filtered in MeCN; MWCO-filtered and resuspended in aqueous phosphate buffer (red); iii) filtered in MeCN and resuspended in aqueous phosphate buffer (orange)). (CPMG NMR spectra; RSD were calculated based on the three sample replicates).*

Supplementary Information – Manuscript 1

MWCO filtration impedes the detection of some NMR-based metabolomics diagnostic features

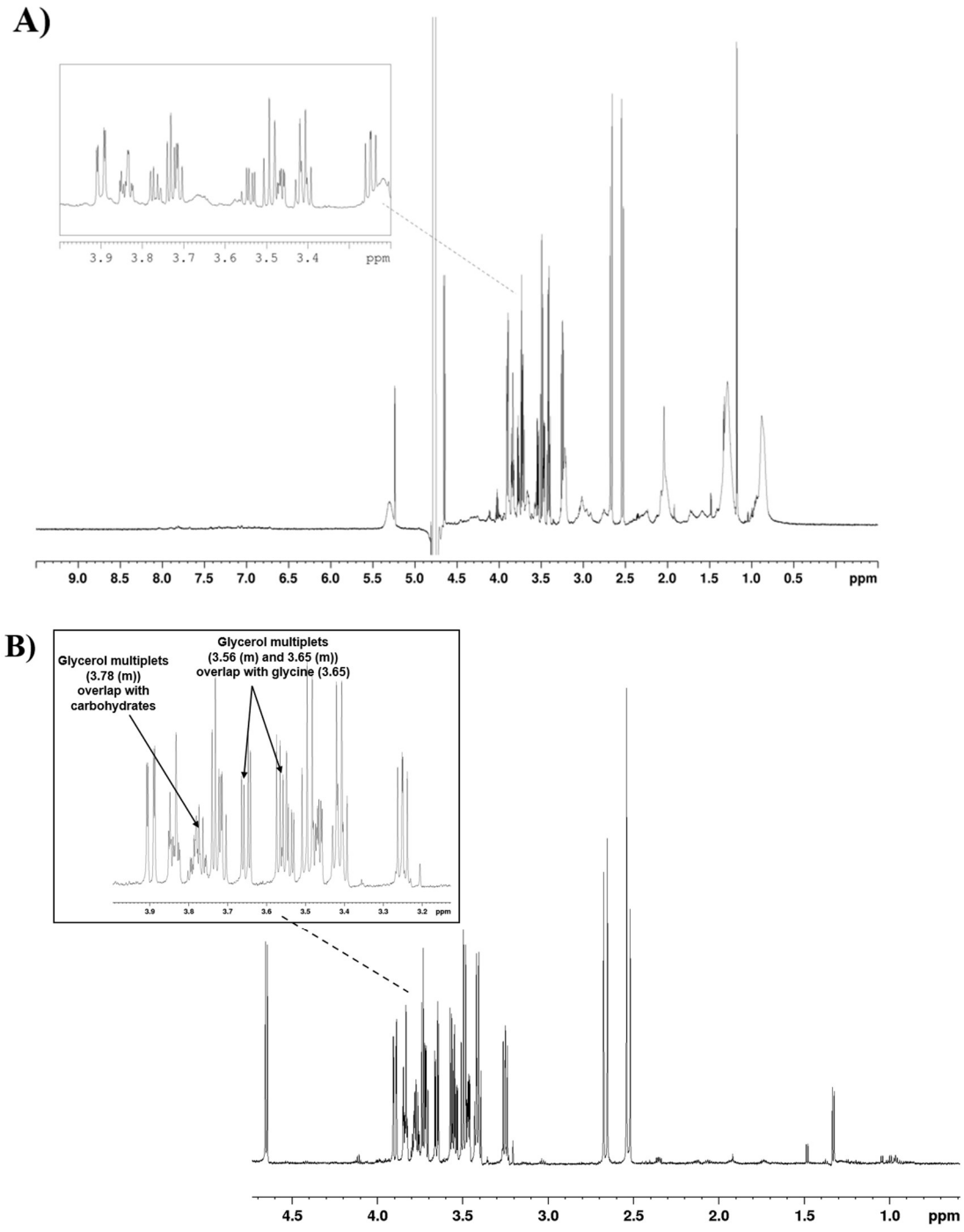

SI Fig. 13 *(**A**) NMR spectrum of an unfiltered serum sample (serum in deuterated phosphate buffer). The lipoproteins signals are visible at 0.86, 1.28 and 2.10 ppm. The spectrum also contains a propylene glycol contaminant from the blood collection tubes δ 1.17 (d), 3.50-3.59 (m), 3.9-3.72 (m)); Furthermore, no glycerol contaminants resulting from the MWCO filters are present at 3.56 ppm (tt), 3.65 ppm (tt), 3.74-3.80 ppm (m). (**B**) NMR spectrum of an filtered serum sample (serum in deuterated phosphate buffer; MWCO filtered). The lipoproteins signals at 0.86, 1.28 and 2.10 ppm are not present, as these were filtered out. Furthermore, the glycerol contamination signals (3.56 ppm (tt), 3.65 ppm (tt), 3.74-3.80 ppm (m)) are the most prominent peaks in the spectrum, impeding an accurate assignment and integration of the peaks in the sugar region (3.0-4.0 ppm) (refer to the magnification).*

Supplementary Information – Manuscript 1

MWCO filtration impedes the detection of some NMR-based metabolomics diagnostic features

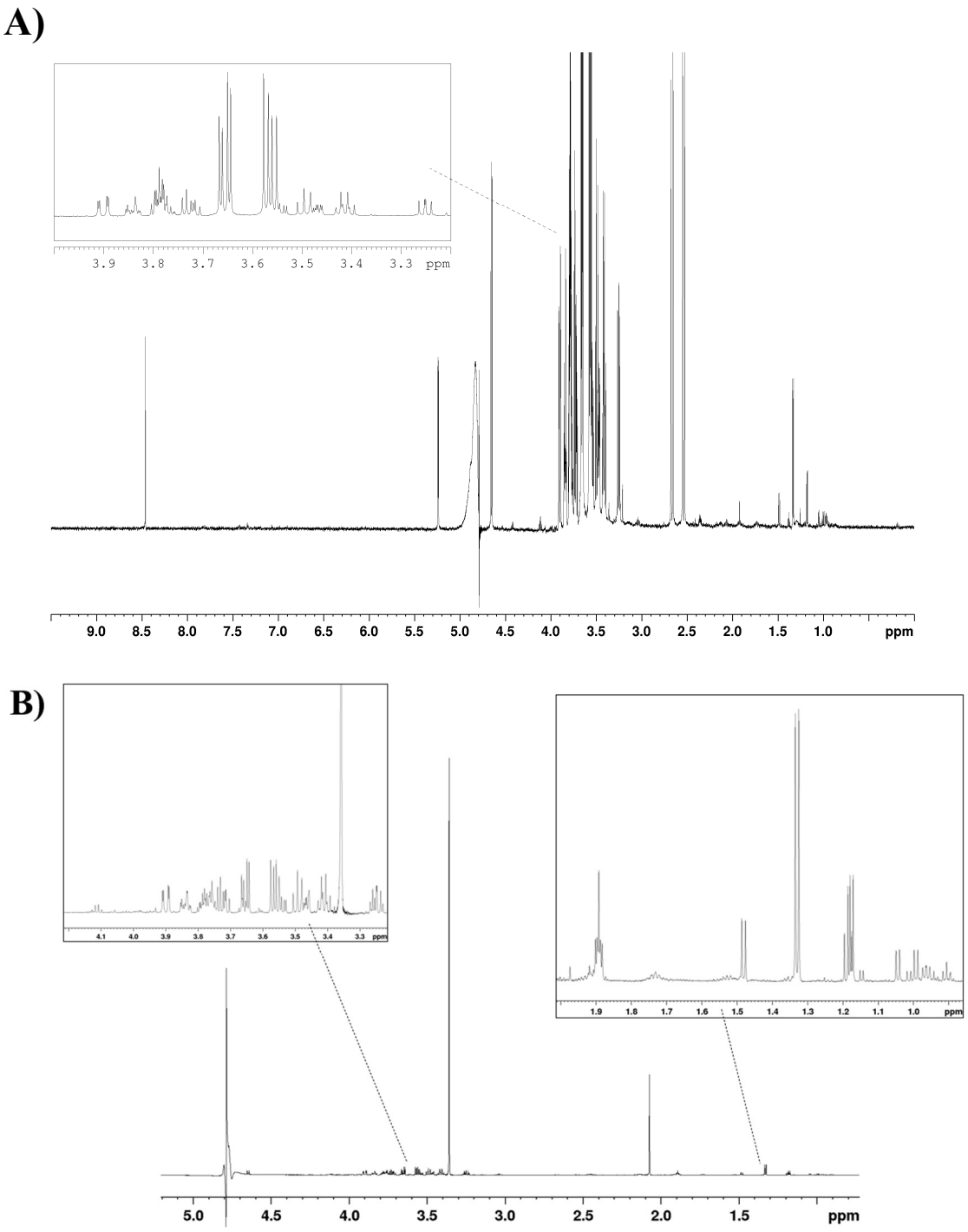

SI Fig. 14 A) *NMR spectrum of a filtered serum sample (serum filtered in acetonitrile and resuspended in deuterated phosphate buffer).* ***B)*** *NMR spectrum of a serum sample with proteins removed by precipitation in acetonitrile (without MWCO filtration). The lipoproteins signals at 0.86, 1.28 and 2.10 ppm are not present in both spectra. Furthermore, the glycerol contamination signals (3.56 ppm (tt), 3.65 ppm (tt), 3.74-3.80 ppm (m)) are the most prominent peaks in spectrum A, impeding an accurate assignment and integration of the peaks in the sugar region (3.0-4.0 ppm) (refer to the magnification). The singlet sat 8.5 ppm corresponds to the residual formate (introduced as an additive in the extraction procedure) contaminant.*

Supplementary Information – Manuscript 1

Identified compounds for Milli-Q water – deuterated water – phosphate buffer

SI Table 4 *List of all identified compounds (based on an in-house database) for the comparison of Milli-Q water, deuterated water, and deuterated phosphate (NMR) buffer. The table includes One-way ANOVA p-values with FDR multiple comparisons correction. (N.B. The FDR corrections could potentially lead to omitting some altered features; however, the FDR-corrected approach is the "gold standard" for untargeted metabolomics; therefore, we selected this method for all data analysis). Each condition was analysed in sample triplicate.*

Name	Platform	p-value	Significance
Acetylglycine	IC-MS neg.	0.8154	NS
Adenosine diphosphate	IC-MS neg.	0.1993	NS
Allantoin	IC-MS neg.	0.6689	NS
Arabinonic acid	IC-MS neg.	0.1646	NS
Arabinose	IC-MS neg.	0.4766	NS
Ascorbate	IC-MS neg.	0.3796	NS
Aspartate	IC-MS neg.	0.1091	NS
β-Citryl-*L*-glutamic acid	IC-MS neg.	0.4106	NS
Caffeic acid	IC-MS neg.	0.4294	NS
Citric acid	IC-MS neg.	0.3575	NS
Dihydroxyacetone	IC-MS neg.	0.0190	NS
Dihydroxyacetone phosphate	IC-MS neg.	0.3240	NS
Ferulic acid	IC-MS neg.	0.8030	NS
Galactaric acid	IC-MS neg.	0.0358	*
Galactose-6-phosphate	IC-MS neg.	0.3773	NS
Galacturonic acid	IC-MS neg.	0.2203	NS
Gluconate	IC-MS neg.	0.4712	NS
Gluconolactone	IC-MS neg.	0.0592	NS
Glucose	IC-MS neg.	0.1519	NS
Glucose-1-phosphate	IC-MS neg.	0.2783	NS
Glutaric acid	IC-MS neg.	0.3171	NS
Glycerol	IC-MS neg.	0.0637	NS
Glycerol-3phosphate	IC-MS neg.	0.1915	NS
Glycolic acid	IC-MS neg.	0.6984	NS
Homovanillic acid	IC-MS neg.	0.2809	NS
Hydroxyisoheptanoic acid	IC-MS neg.	0.2672	NS
Kojic acid	IC-MS neg.	0.0534	NS
Lactose	IC-MS neg.	0.1921	NS
Malic acid	IC-MS neg.	0.4000	NS
Mesaconic acid	IC-MS neg.	0.1422	NS
Methylglutaric acid	IC-MS neg.	0.7489	NS
Myoinositol	IC-MS neg.	0.4189	NS
N-Acetyl-aspartate	IC-MS neg.	0.4683	NS
N-Acetyl-*L*-alanine	IC-MS neg.	0.7732	NS
N-Acetylglutamate	IC-MS neg.	0.3746	NS
Nonate	IC-MS neg.	0.1861	NS
Pantothenic acid	IC-MS neg.	0.0807	NS
Pyroglutamic acid	IC-MS neg.	0.1294	NS

Raffinose	IC-MS neg.	0.0672	NS
Sorbitol	IC-MS neg.	0.0118	*
Succinic acid	IC-MS neg.	0.0676	NS
Succinyl homoserine	IC-MS neg.	0.7363	NS
Syringic acid	IC-MS neg.	0.0804	NS
Taurine	IC-MS neg.	0.8053	NS
Threitol	IC-MS neg.	3.11E-04	***
Vanillin	IC-MS neg.	0.0886	NS
Xylulose	IC-MS neg.	0.7081	NS
Citraconic acid	RPLC-MS neg.	0.0019	**
Citramalic acid	RPLC-MS neg.	0.3033	NS
Dodecanoic acid	RPLC-MS neg.	0.8418	NS
Linoleic acid	RPLC-MS neg.	0.1121	NS
Myristic acid	RPLC-MS neg.	0.2770	NS
Palmitic acid	RPLC-MS neg.	0.6671	NS
Phytanic acid	RPLC-MS neg.	0.6194	NS
Stearic acid	RPLC-MS neg.	0.1916	NS
2-aminocaprylic acid	RPLC-MS pos.	2.19E-04	***
Aspartame	RPLC-MS pos.	0.0533	NS
Aspirin	RPLC-MS pos.	0.8245	NS
Butyrylcarnitine	RPLC-MS pos.	0.1043	NS
Creatine	RPLC-MS pos.	0.0001	NS
Deoxycholic acid	RPLC-MS pos.	0.9022	NS
Epinephrine	RPLC-MS pos.	0.1248	NS
Indole-3-acetaldehyde	RPLC-MS pos.	0.3433	NS
Linoleic acid	RPLC-MS pos.	0.2144	NS
Myristic acid	RPLC-MS pos.	0.2448	NS
N-acetyl-L-methionine	RPLC-MS pos.	0.0287	NS
N-Acetylproline	RPLC-MS pos.	0.0013	NS
Oleic acid	RPLC-MS pos.	0.2548	NS
Palmitoleic Acid	RPLC-MS pos.	0.8305	NS
Phenyl acetate	RPLC-MS pos.	0.0711	NS
Phenyl-propionate	RPLC-MS pos.	0.2500	NS
Theobromine	RPLC-MS pos.	0.0008	***
Theophylline	RPLC-MS pos.	0.0902	NS
Urocanic acid	RPLC-MS pos.	0.0002	***

Supplementary Information – Manuscript 1

Lists of MS-identified compounds for Milli-Q water – deuterated water – phosphate buffer

SI Table 5 *List of all identified compounds (based on an in-house database) for the comparison of Milli-Q water, deuterated water, and deuterated phosphate (NMR) buffer. The table includes One-way ANOVA p-values with FDR multiple comparisons correction. Each condition was analysed in sample triplicate.*

Metabolite	Platform	CV (%) D_2O	CV (%) H_2O	CV (%) NMR	CV (%) MeCN
Acetylglycine	IC-MS neg.	27.57	8.09	15.64	9.47
Adenosine diphosphate	IC-MS neg.	8.54	6.85	15.40	3.87
Allantoin	IC-MS neg.	19.68	23.23	11.64	13.42
Arabinonic acid	IC-MS neg.	23.11	7.03	10.12	6.52
Arabinose	IC-MS neg.	6.79	7.13	11.66	4.90
Ascorbate	IC-MS neg.	9.18	11.12	11.13	7.11
Aspartate	IC-MS neg.	17.27	9.41	7.67	15.27
β-Citryl-*L*-glutamic acid	IC-MS neg.	31.68	30.13	30.76	23.71
Caffeic acid	IC-MS neg.	9.33	16.44	14.84	12.31
Citric acid	IC-MS neg.	17.72	10.97	14.52	7.82
Dihydroxyacetone	IC-MS neg.	9.27	7.32	6.06	4.71
Dihydroxyacetone phosphate	IC-MS neg.	13.87	12.90	13.23	10.89
Ferulic acid	IC-MS neg.	20.93	24.32	15.79	11.80
Galactaric acid	IC-MS neg.	24.90	29.31	30.30	16.73
Galactose-6-phosphate	IC-MS neg.	16.53	12.07	12.61	8.42
Galacturonic acid	IC-MS neg.	16.53	13.76	12.90	12.85
Gluconate	IC-MS neg.	12.76	13.54	8.84	8.48
Gluconolactone	IC-MS neg.	25.16	19.87	22.48	15.15
Glucose	IC-MS neg.	5.42	5.33	3.53	6.74
Glucose-1-phosphate	IC-MS neg.	16.53	9.47	4.18	11.89
Glutaric acid	IC-MS neg.	3.51	9.87	5.75	2.08
Glycerol	IC-MS neg.	13.22	7.36	18.44	11.74
Glycerol-3-phosphate	IC-MS neg.	12.12	12.05	10.98	8.23
Glycolic acid	IC-MS neg.	7.17	7.20	8.11	11.05
Homovanillic acid	IC-MS neg.	14.54	13.89	17.73	15.93
Hydroxyisoheptanoic acid	IC-MS neg.	10.98	11.39	13.07	4.76
Kojic acid	IC-MS neg.	4.92	3.56	7.58	5.25
Lactose	IC-MS neg.	19.87	12.93	21.41	32.13
Malic acid	IC-MS neg.	3.05	6.67	7.33	1.09
Mesaconic acid	IC-MS neg.	16.65	17.87	8.97	13.04
Methylglutaric acid	IC-MS neg.	11.77	10.48	14.98	5.91
Myoinositol	IC-MS neg.	3.28	3.11	2.87	5.34
N-Acetyl-aspartate	IC-MS neg.	12.15	13.12	12.32	15.46
N-Acetyl-*L*-alanine	IC-MS neg.	20.37	15.50	14.63	7.89
N-Acetylglutamate	IC-MS neg.	11.32	11.78	18.33	8.33
Nonate	IC-MS neg.	22.04	16.73	16.53	15.09
Pantothenic acid	IC-MS neg.	14.87	14.98	14.76	10.62
Pyroglutamic acid	IC-MS neg.	12.66	8.09	8.93	12.53

Raffinose	IC-MS neg.	17.98	19.07	20.05	7.94
Salicylic acid	IC-MS neg.	4.35	3.97	4.11	3.85
Sorbitol	IC-MS neg.	20.19	18.90	17.45	26.07
Succinic acid	IC-MS neg.	11.64	9.64	7.69	6.18
Succinyl homoserine	IC-MS neg.	16.76	13.76	11.89	13.43
Syringic acid	IC-MS neg.	11.65	8.64	10.02	7.27
Taurine	IC-MS neg.	4.56	2.11	4.14	6.02
Threitol	IC-MS neg.	12.98	10.79	9.33	3.93
Vanillin	IC-MS neg.	21.28	23.54	20.56	7.15
Xylulose	IC-MS neg.	13.45	10.58	18.44	10.21
Citraconic acid	RPLC-MS neg.	2.58	2.94	0.89	1.76
Citramalic acid	RPLC-MS neg.	4.09	3.96	0.96	5.98
Dodecanoic acid	RPLC-MS neg.	2.02	3.46	4.76	2.34
Linoleic acid	RPLC-MS neg.	5.71	5.33	2.34	0.82
Myristic acid	RPLC-MS neg.	3.35	3.16	4.45	4.92
Palmitic acid	RPLC-MS neg.	1.03	1.15	2.93	5.40
Phytanic acid	RPLC-MS neg.	7.78	6.17	21.53	30.81
Stearic acid	RPLC-MS neg.	3.87	0.93	8.91	2.71
2-aminocaprylic acid	RPLC-MS pos.	9.10	7.42	7.80	13.12
Aspartame	RPLC-MS pos.	7.16	9.02	6.39	10.87
Aspirin	RPLC-MS pos.	11.88	4.65	10.16	9.81
Butyrylcarnitine	RPLC-MS pos.	10.55	8.82	3.25	0.36
Creatine	RPLC-MS pos.	7.50	1.88	3.33	1.46
Deoxycholic acid	RPLC-MS pos.	5.13	4.03	4.23	3.15
Epinephrine	RPLC-MS pos.	15.66	13.76	10.83	5.82
Indole-3-acetaldehyde	RPLC-MS pos.	9.21	10.17	11.21	2.83
Linoleic acid	RPLC-MS pos.	7.42	7.57	3.35	2.01
Myristic acid	RPLC-MS pos.	2.66	6.13	5.40	0.87
N-acetyl-L-methionine	RPLC-MS pos.	6.42	5.11	5.59	10.02
N-Acetylproline	RPLC-MS pos.	6.78	5.73	4.35	4.21
Oleic acid	RPLC-MS pos.	11.23	9.33	8.22	6.98
Palmitoleic Acid	RPLC-MS pos.	7.74	8.12	8.23	8.87
Phenyl acetate	RPLC-MS pos.	11.35	12.79	9.93	7.47
Phenyl-propionate	RPLC-MS pos.	6.43	7.67	6.21	7.11
Theobromine	RPLC-MS pos.	7.65	3.20	7.24	3.13
Theophylline	RPLC-MS pos.	12.43	5.76	11.79	8.79
Urocanic acid	RPLC-MS pos.	9.85	10.79	12.96	1.61

Supplementary Information – Manuscript 1

Combining protein precipitation by acetonitrile and MWCO filtration shows a minimal effect on the polar metabolome but reduces hydrophobic compounds extraction reproducibility

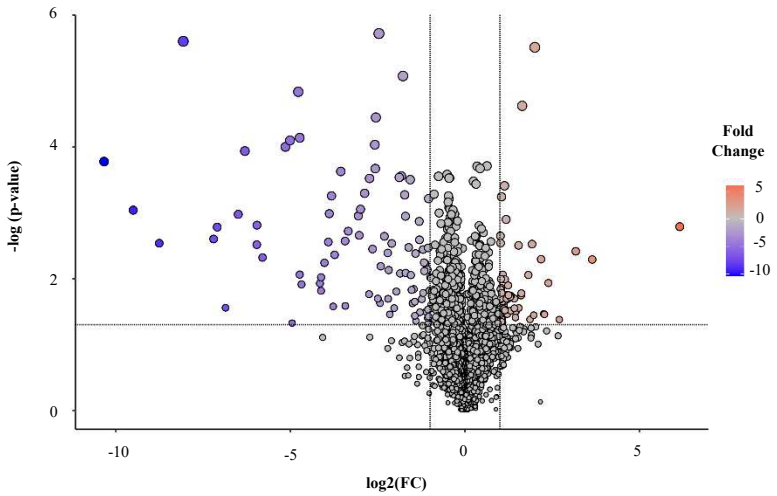

SI Fig. 15 A volcano plot showing the altered compound-features in the filtered and unfiltered samples comparing log 2 fold change (FC) of filtered/unfiltered samples and -log10 raw p value (t test, $p < 0.05$) (red: an increase in the MWCO-filtered samples (90 compound-features (4% of the total number); blue: a decrease in the MWCO-filtered samples (64 compound-features (3% of the total number)). RPLC-MS (neg. ion mode)

Supplementary Information – Manuscript 1

Sample dilution affects Serum LC-MS-detected metabolome profile

SI Table 6 *One-way ANOVA results with Dunnett test comparing the mean of every tested condition to the mean of the control set (serum extracted in MeCN without MWCO filtration). All compound-features with CV <30 were included. (IC-MS neg. ionisation mode; three sample replicates per group)*

Dunnett's multiple comparisons test	Mean Diff.	95.00% CI of diff.	Summary	Adjusted P Value
MeCN vs. MeCN MWCO	290.3	209.8 to 370.9	***	<0.0001
MeCN vs. Low Buffer MeCN	724.3	643.8 to 804.9	***	<0.0001
MeCN vs. Low Buffer MeCN MWCO	537.7	457.1 to 618.2	***	<0.0001
MeCN vs. High Buffer MeCN	502	421.4 to 582.6	***	<0.0001
MeCN vs. High Buffer MeCN MWCO	510	429.4 to 590.6	***	<0.0001
MeCN vs. High H_2O MeCN	540	459.4 to 620.6	***	<0.0001
MeCN vs. High D_2O MeCN	713.7	633.1 to 794.2	***	<0.0001

SI Table 7 *One-way ANOVA results with Tukey test comparing every mean with every other mean. All compound-features with CV <30 were included. (IC-MS neg. ionisation mode, three sample replicates per group)*

Tukey's multiple comparisons test	Mean Diff.	95.00% CI of diff.	Summary	Adjusted P Value
MeCN vs. MeCN MWCO	290.3	194.9 to 385.7	***	<0.0001
MeCN vs. Low Buffer MeCN	724.3	628.9 to 819.7	***	<0.0001
MeCN vs. Low Buffer MeCN MWCO	537.7	442.3 to 633.1	***	<0.0001
MeCN vs. High Buffer MeCN	502	406.6 to 597.4	***	<0.0001
MeCN vs. High Buffer MeCN MWCO	510	414.6 to 605.4	***	<0.0001
MeCN vs. High H_2O MeCN	540	444.6 to 635.4	***	<0.0001
MeCN vs. High D_2O MeCN	713.7	618.3 to 809.1	***	<0.0001
MeCN MWCO vs. Low Buffer MeCN	434	338.6 to 529.4	***	<0.0001
MeCN MWCO vs. Low Buffer MeCN MWCO	247.3	151.9 to 342.7	***	<0.0001
MeCN MWCO vs. High Buffer MeCN	211.7	116.3 to 307.1	***	<0.0001
MeCN MWCO vs. High Buffer MeCN MWCO	219.7	124.3 to 315.1	***	<0.0001
MeCN MWCO vs. High H_2O MeCN	249.7	154.3 to 345.1	***	<0.0001
MeCN MWCO vs. High D_2O MeCN	423.3	327.9 to 518.7	***	<0.0001
Low Buffer MeCN vs. Low Buffer MeCN MWCO	-186.7	-282.1 to -91.27	***	<0.0001
Low Buffer MeCN vs. High Buffer MeCN	-222.3	-317.7 to -126.9	***	<0.0001
Low Buffer MeCN vs. High Buffer MeCN MWCO	-214.3	-309.7 to -118.9	***	<0.0001
Low Buffer MeCN vs. High H_2O MeCN	-184.3	-279.7 to -88.93	***	0.0001
Low Buffer MeCN vs. High D_2O MeCN	-10.67	-106.1 to 84.73	ns	>0.9999
Low Buffer MeCN MWCO vs. High Buffer MeCN	-35.67	-131.1 to 59.73	ns	0.8883
Low Buffer MeCN MWCO vs. High Buffer MeCN MWCO	-27.67	-123.1 to 67.73	ns	0.9671
Low Buffer MeCN MWCO vs. High H_2O MeCN	2.333	-93.07 to 97.73	ns	>0.9999
Low Buffer MeCN MWCO vs. High D_2O MeCN	176	80.60 to 271.4	***	0.0002
High Buffer MeCN vs. High Buffer MeCN MWCO	8	-87.40 to 103.4	ns	>0.9999
High Buffer MeCN vs. High H_2O MeCN	38	-57.40 to 133.4	ns	0.8539
High Buffer MeCN vs. High D_2O MeCN	211.7	116.3 to 307.1	***	<0.0001
High Buffer MeCN MWCO vs. High H_2O MeCN	30	-65.40 to 125.4	ns	0.9503
High Buffer MeCN MWCO vs. High D_2O MeCN	203.7	108.3 to 299.1	***	<0.0001
High H_2O MeCN vs. High D_2O MeCN	173.7	78.27 to 269.1	***	0.0002

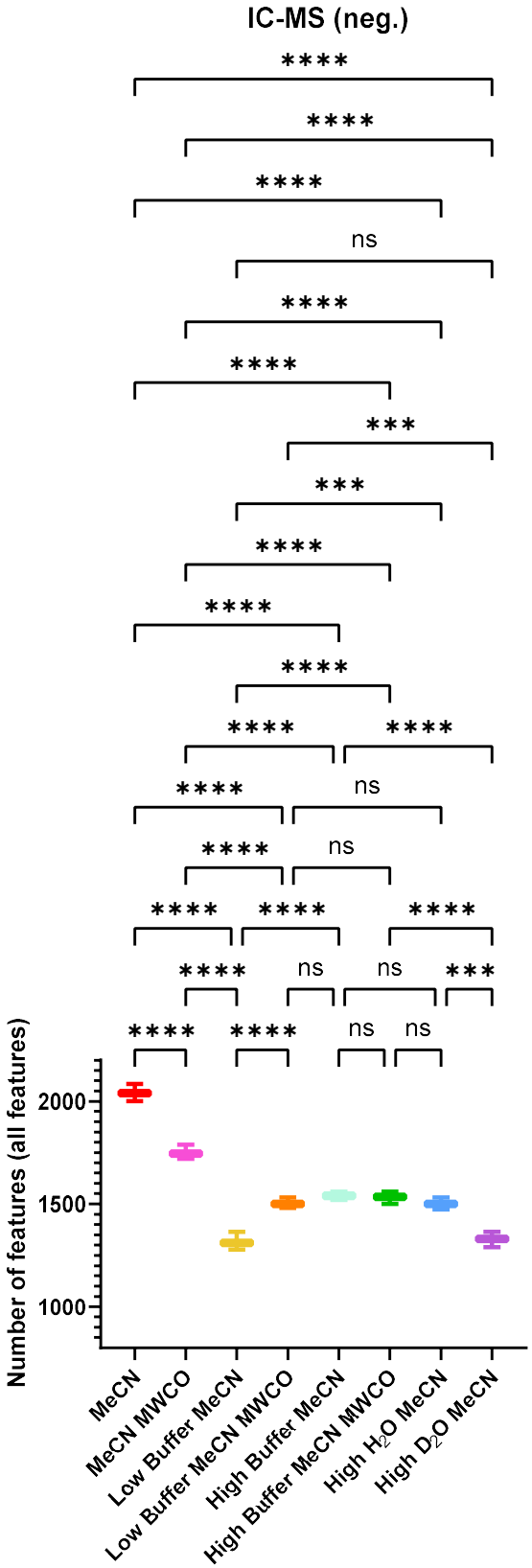

SI Fig. 16 *One-way ANOVA results with Tukey test comparing every mean with every other mean. All compound-features with CV <30 were included. (IC-MS neg. ionisation mode, three sample replicates per group)*

SI Table 8 *One-way ANOVA results with Dunnett test comparing the mean of every tested condition to the mean of the control set (serum extracted in MeCN without MWCO filtration). All compound-features with CV <30 were included. (RPLC-MS pos. ionisation mode, three sample replicates per group)*

Dunnett's multiple comparisons test	Mean Diff.	95.00% CI of diff.	Summary	Adjusted P Value
MeCN vs. MeCN MWCO	2272	1308 to 3237	***	<0.0001
MeCN vs. Low Buffer MeCN	1426	461.3 to 2391	**	0.003
MeCN vs. Low Buffer MeCN MWCO	2779	1814 to 3743	***	<0.0001
MeCN vs. High Buffer MeCN	1893	927.9 to 2857	***	0.0002
MeCN vs. High Buffer MeCN MWCO	2743	1778 to 3707	***	<0.0001
MeCN vs. High H_2O MeCN	2918	1953 to 3883	***	<0.0001
MeCN vs. High D_2O MeCN	2939	1974 to 3904	***	<0.0001

SI Table 9 *One-way ANOVA results with Tukey test comparing every mean with every other mean. All compound-features with CV <30 were included. (RPLC-MS pos. ionisation mode, three sample replicates per group)*

Tukey's multiple comparisons test	Mean Diff.	95.00% CI of diff.	Summary	Adjusted P Value
MeCN vs. MeCN MWCO	2272	1130 to 3415	***	<0.0001
MeCN vs. Low Buffer MeCN	1426	283.7 to 2568	**	0.0096
MeCN vs. Low Buffer MeCN MWCO	2779	1636 to 3921	***	<0.0001
MeCN vs. High Buffer MeCN	1893	750.4 to 3035	***	0.0006
MeCN vs. High Buffer MeCN MWCO	2743	1600 to 3885	***	<0.0001
MeCN vs. High H_2O MeCN	2918	1776 to 4060	***	<0.0001
MeCN vs. High D_2O MeCN	2939	1797 to 4081	***	<0.0001
MeCN MWCO vs. Low Buffer MeCN	-846.3	-1989 to 296.0	ns	0.2375
MeCN MWCO vs. Low Buffer MeCN MWCO	506.3	-636.0 to 1649	ns	0.7792
MeCN MWCO vs. High Buffer MeCN	-379.7	-1522 to 762.6	ns	0.9348
MeCN MWCO vs. High Buffer MeCN MWCO	470.3	-672.0 to 1613	ns	0.8331
MeCN MWCO vs. High H_2O MeCN	645.7	-496.6 to 1788	ns	0.5358
MeCN MWCO vs. High D_2O MeCN	666.7	-475.6 to 1809	ns	0.4989
Low Buffer MeCN vs. Low Buffer MeCN MWCO	1353	210.4 to 2495	*	0.0147
Low Buffer MeCN vs. High Buffer MeCN	466.7	-675.6 to 1609	ns	0.8382
Low Buffer MeCN vs. High Buffer MeCN MWCO	1317	174.4 to 2459	*	0.0182
Low Buffer MeCN vs. High H_2O MeCN	1492	349.7 to 2634	**	0.0065
Low Buffer MeCN vs. High D_2O MeCN	1513	370.7 to 2655	**	0.0057
Low Buffer MeCN MWCO vs. High Buffer MeCN	-886	-2028 to 256.3	ns	0.1965
Low Buffer MeCN MWCO vs. High Buffer MeCN MWCO	-36	-1178 to 1106	ns	>0.9999
Low Buffer MeCN MWCO vs. High H_2O MeCN	139.3	-1003 to 1282	ns	0.9998
Low Buffer MeCN MWCO vs. High D_2O MeCN	160.3	-982.0 to 1303	ns	0.9996
High Buffer MeCN vs. High Buffer MeCN MWCO	850	-292.3 to 1992	ns	0.2335
High Buffer MeCN vs. High H_2O MeCN	1025	-117.0 to 2168	ns	0.0957
High Buffer MeCN vs. High D_2O MeCN	1046	-95.98 to 2189	ns	0.0854
High Buffer MeCN MWCO vs. High H_2O MeCN	175.3	-967.0 to 1318	ns	0.9992
High Buffer MeCN MWCO vs. High D_2O MeCN	196.3	-946.0 to 1339	ns	0.9985
High H_2O MeCN vs. High D_2O MeCN	21	-1121 to 1163	ns	>0.9999

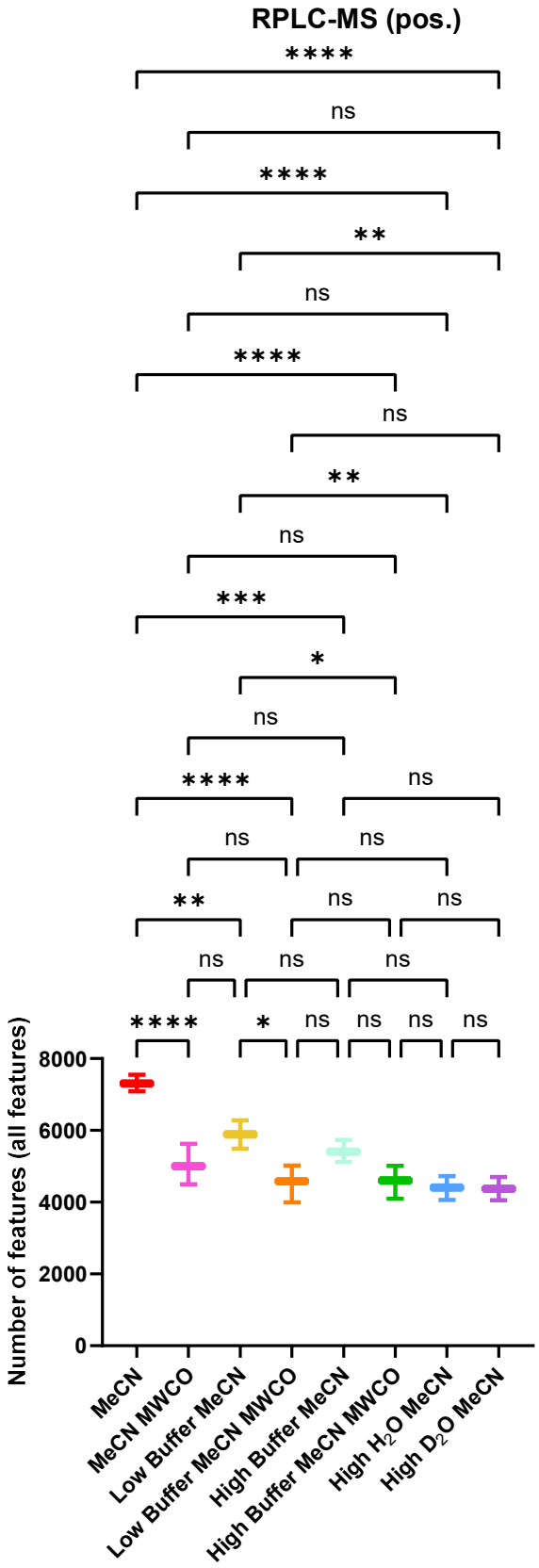

SI Fig. 17 *One-way ANOVA results with Tukey test comparing every mean with every other mean. All compound-features with CV <30 were included. (RPLC-MS pos. ionisation mode, three sample replicates per group)*

SI Table 10 *One-way ANOVA results with Dunnett test comparing the mean of every tested condition to the mean of the control set (serum extracted in MeCN without MWCO filtration). All compound-features were included. (IC-MS neg. ionisation mode, three sample replicates per group)*

Dunnett's multiple comparisons test	Mean Diff.	95.00% CI of diff.	Summary	Adjusted P Value
MeCN vs. MeCN MWCO	-141	-218.8 to -63.20	***	0.0004
MeCN vs. Low Buffer MeCN	440	362.2 to 517.8	***	<0.0001
MeCN vs. Low Buffer MeCN MWCO	33.67	-44.13 to 111.5	ns	0.6868
MeCN vs. High Buffer MeCN	160	82.20 to 237.8	***	0.0001
MeCN vs. High Buffer MeCN MWCO	418.3	340.5 to 496.1	***	<0.0001
MeCN vs. High H_2O MeCN	253.7	175.9 to 331.5	***	<0.0001
MeCN vs. High D_2O MeCN	189	111.2 to 266.8	***	<0.0001

SI Table 11 *One-way ANOVA results with Tukey test comparing every mean with every other mean. All compound-features were included. (IC-MS neg. ionisation mode, three sample replicates per group)*

Tukey's multiple comparisons test	Mean Diff.	95.00% CI of diff.	Summary	Adjusted P Value
MeCN vs. MeCN MWCO	-141	-233.1 to -48.88	**	0.0014
MeCN vs. Low Buffer MeCN	440	347.9 to 532.1	***	<0.0001
MeCN vs. Low Buffer MeCN MWCO	33.67	-58.46 to 125.8	ns	0.8989
MeCN vs. High Buffer MeCN	160	67.88 to 252.1	***	0.0004
MeCN vs. High Buffer MeCN MWCO	418.3	326.2 to 510.5	***	<0.0001
MeCN vs. High H_2O MeCN	253.7	161.5 to 345.8	***	<0.0001
MeCN vs. High D_2O MeCN	189	96.88 to 281.1	***	<0.0001
MeCN MWCO vs. Low Buffer MeCN	581	488.9 to 673.1	***	<0.0001
MeCN MWCO vs. Low Buffer MeCN MWCO	174.7	82.54 to 266.8	***	0.0001
MeCN MWCO vs. High Buffer MeCN	301	208.9 to 393.1	***	<0.0001
MeCN MWCO vs. High Buffer MeCN MWCO	559.3	467.2 to 651.5	***	<0.0001
MeCN MWCO vs. High H_2O MeCN	394.7	302.5 to 486.8	***	<0.0001
MeCN MWCO vs. High D_2O MeCN	330	237.9 to 422.1	***	<0.0001
Low Buffer MeCN vs. Low Buffer MeCN MWCO	-406.3	-498.5 to -314.2	***	<0.0001
Low Buffer MeCN vs. High Buffer MeCN	-280	-372.1 to -187.9	***	<0.0001
Low Buffer MeCN vs. High Buffer MeCN MWCO	-21.67	-113.8 to 70.46	ns	0.9896
Low Buffer MeCN vs. High H_2O MeCN	-186.3	-278.5 to -94.21	***	<0.0001
Low Buffer MeCN vs. High D_2O MeCN	-251	-343.1 to -158.9	***	<0.0001
Low Buffer MeCN MWCO vs. High Buffer MeCN	126.3	34.21 to 218.5	**	0.0042
Low Buffer MeCN MWCO vs. High Buffer MeCN MWCO	384.7	292.5 to 476.8	***	<0.0001
Low Buffer MeCN MWCO vs. High H_2O MeCN	220	127.9 to 312.1	***	<0.0001
Low Buffer MeCN MWCO vs. High D_2O MeCN	155.3	63.21 to 247.5	***	0.0005
High Buffer MeCN vs. High Buffer MeCN MWCO	258.3	166.2 to 350.5	***	<0.0001
High Buffer MeCN vs. High H_2O MeCN	93.67	1.545 to 185.8	*	0.0448
High Buffer MeCN vs. High D_2O MeCN	29	-63.12 to 121.1	ns	0.95
High Buffer MeCN MWCO vs. High H_2O MeCN	-164.7	-256.8 to -72.54	***	0.0003
High Buffer MeCN MWCO vs. High D_2O MeCN	-229.3	-321.5 to -137.2	***	<0.0001
High H_2O MeCN vs. High D_2O MeCN	-64.67	-156.8 to 27.46	ns	0.291

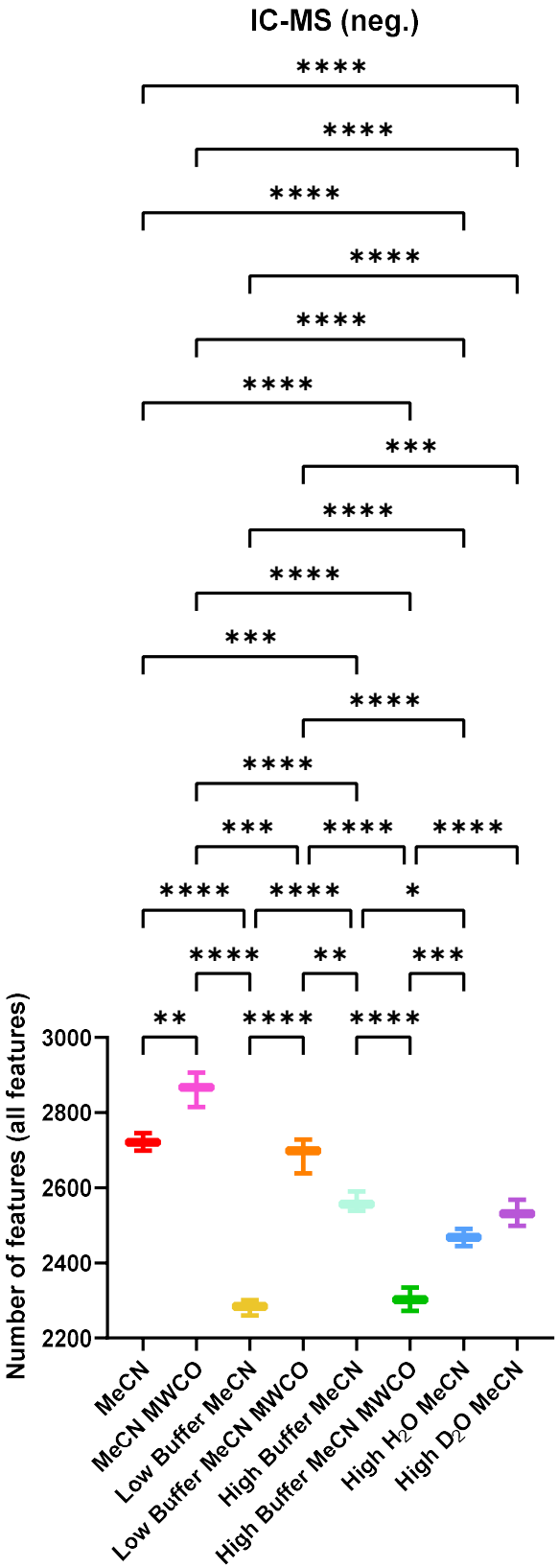

SI Fig. 18 *One-way ANOVA results with Tukey test comparing every mean with every other mean. All compound-features were included. (IC-MS neg. ionisation mode, three sample replicates per group)*

SI Table 12 *One-way ANOVA results with Dunnett test comparing the mean of every tested condition to the mean of the control set (serum extracted in MeCN without MWCO filtration). All compound-features were included. (RPLC-MS pos. ionisation mode, three sample replicates per group)*

Dunnett's multiple comparisons test	Mean Diff.	95.00% CI of diff.	Summary	Adjusted P Value
MeCN vs. MeCN MWCO	779.7	224.2 to 1335	**	0.0047
MeCN vs. Low Buffer MeCN	23.67	-531.8 to 579.1	ns	>0.9999
MeCN vs. Low Buffer MeCN MWCO	272	-283.4 to 827.4	ns	0.5748
MeCN vs. High Buffer MeCN	268.3	-287.1 to 823.8	ns	0.5877
MeCN vs. High Buffer MeCN MWCO	651.7	96.24 to 1207	*	0.0184
MeCN vs. High H_2O MeCN	1150	594.6 to 1705	***	0.0001
MeCN vs. High D_2O MeCN	1005	449.2 to 1560	***	0.0004

SI Table 13 *One-way ANOVA results with Tukey test comparing every mean with every other mean. All compound-features were included. (RPLC-MS pos. ionisation mode, three sample replicates per group)*

Tukey's multiple comparisons test	Mean Diff.	95.00% CI of diff.	Summary	Adjusted P Value
MeCN vs. MeCN MWCO	779.7	122.0 to 1437	*	0.0146
MeCN vs. Low Buffer MeCN	23.67	-634.0 to 681.3	ns	>0.9999
MeCN vs. Low Buffer MeCN MWCO	272	-385.7 to 929.7	ns	0.8301
MeCN vs. High Buffer MeCN	268.3	-389.3 to 926.0	ns	0.839
MeCN vs. High Buffer MeCN MWCO	651.7	-5.995 to 1309	ns	0.053
MeCN vs. High H_2O MeCN	1150	492.3 to 1808	***	0.0004
MeCN vs. High D_2O MeCN	1005	347.0 to 1662	**	0.0015
MeCN MWCO vs. Low Buffer MeCN	-756	-1414 to -98.34	*	0.0186
MeCN MWCO vs. Low Buffer MeCN MWCO	-507.7	-1165 to 150.0	ns	0.2005
MeCN MWCO vs. High Buffer MeCN	-511.3	-1169 to 146.3	ns	0.1944
MeCN MWCO vs. High Buffer MeCN MWCO	-128	-785.7 to 529.7	ns	0.9966
MeCN MWCO vs. High H_2O MeCN	370.3	-287.3 to 1028	ns	0.5401
MeCN MWCO vs. High D_2O MeCN	225	-432.7 to 882.7	ns	0.9252
Low Buffer MeCN vs. Low Buffer MeCN MWCO	248.3	-409.3 to 906.0	ns	0.8833
Low Buffer MeCN vs. High Buffer MeCN	244.7	-413.0 to 902.3	ns	0.8906
Low Buffer MeCN vs. High Buffer MeCN MWCO	628	-29.66 to 1286	ns	0.0668
Low Buffer MeCN vs. High H_2O MeCN	1126	468.7 to 1784	***	0.0004
Low Buffer MeCN vs. High D_2O MeCN	981	323.3 to 1639	**	0.0019
Low Buffer MeCN MWCO vs. High Buffer MeCN	-3.7	-661.3 to 654.0	ns	>0.9999
Low Buffer MeCN MWCO vs. High Buffer MeCN MWCO	379.7	-278.0 to 1037	ns	0.5115
Low Buffer MeCN MWCO vs. High H_2O MeCN	878	220.3 to 1536	**	0.0053
Low Buffer MeCN MWCO vs. High D_2O MeCN	732.7	75.00 to 1390	*	0.0236
High Buffer MeCN vs. High Buffer MeCN MWCO	383.3	-274.3 to 1041	ns	0.5003
High Buffer MeCN vs. High H_2O MeCN	881.7	224.0 to 1539	**	0.0051
High Buffer MeCN vs. High D_2O MeCN	736.3	78.67 to 1394	*	0.0227
High Buffer MeCN MWCO vs. High H_2O MeCN	498.3	-159.3 to 1156	ns	0.2168
High Buffer MeCN MWCO vs. High D_2O MeCN	353	-304.7 to 1011	ns	0.5941
High H_2O MeCN vs. High D_2O MeCN	-145.3	-803.0 to 512.3	ns	0.9928

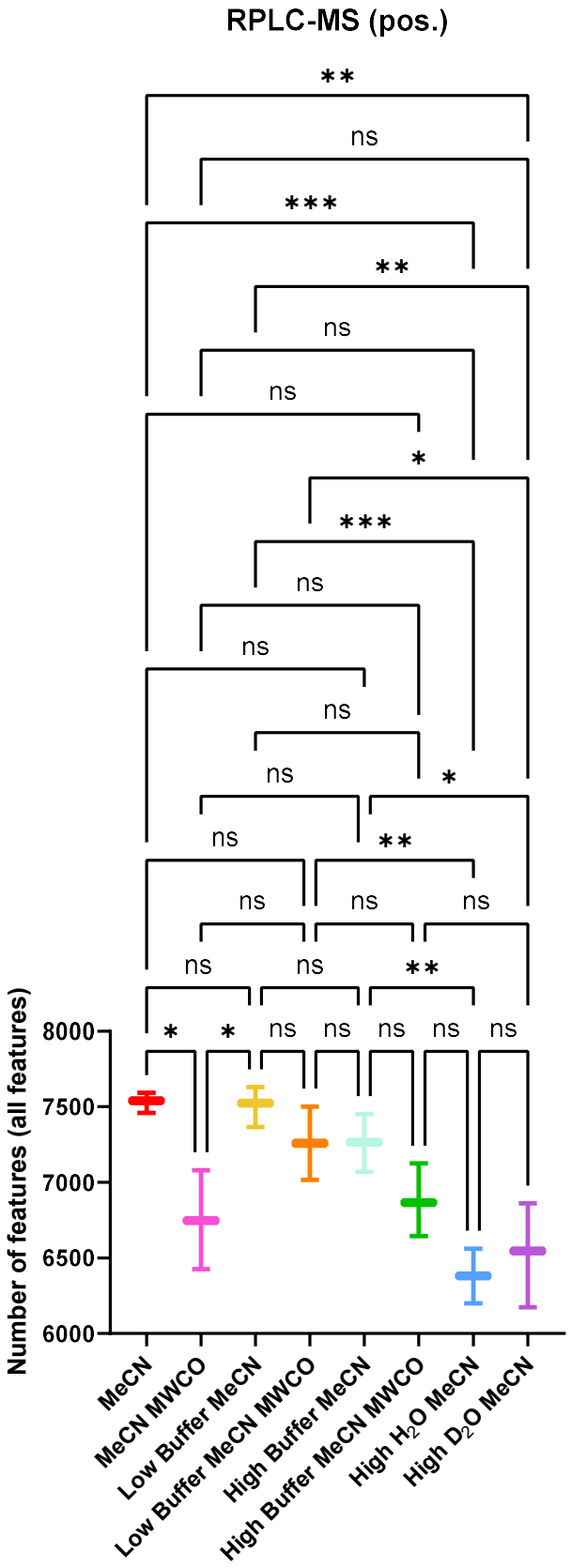

SI Fig. 19 *One-way ANOVA results with Tukey test comparing every mean with every other mean. All compound-features were included. (RPLC-MS pos. ionisation mode, three sample replicates per group)*

SI Table 14 *One-way ANOVA results with Tukey test comparing every mean with every other mean (excluding the MWCO filtration effect). All compound-features with CV <30 were included. (RPLC-MS pos. ionisation mode, three sample replicates per group)*

Tukey's multiple comparisons test	Mean Diff.	95.00% CI of diff.	Summary	Adjusted P Value
MeCN vs. Low Buffer MeCN	1426	563.2 to 2289	**	0.0021
MeCN vs. High Buffer MeCN	1893	1030 to 2755	***	0.0002
MeCN vs. High H_2O MeCN	2918	2055 to 3781	****	<0.0001
MeCN vs. High D_2O MeCN	2939	2076 to 3802	****	<0.0001
Low Buffer MeCN vs. High Buffer MeCN	466.7	-396.1 to 1329	ns	0.4338
Low Buffer MeCN vs. High H_2O MeCN	1492	629.2 to 2355	**	0.0015
Low Buffer MeCN vs. High D_2O MeCN	1513	650.2 to 2376	**	0.0013
High Buffer MeCN vs. High H_2O MeCN	1025	162.5 to 1888	*	0.0191
High Buffer MeCN vs. High D_2O MeCN	1046	183.5 to 1909	*	0.0169
High H_2O MeCN vs. High D_2O MeCN	21	-841.8 to 883.8	ns	>0.9999

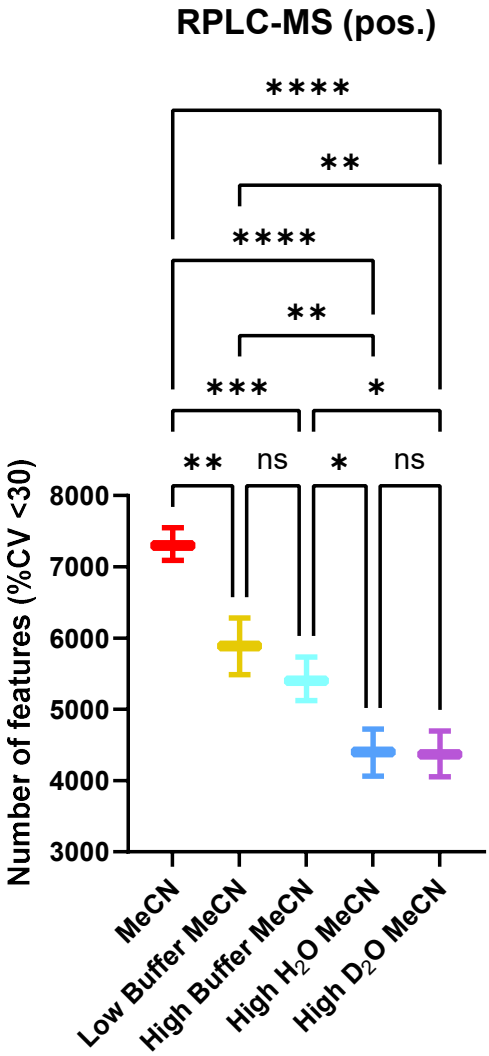

SI Fig. 20 *One-way ANOVA results with Tukey test comparing every mean with every other mean; excluding the MWCO filtration effect. All compound-features with CV <30 were included. (RPLC-MS pos. ionisation mode, three sample replicates per group)*

SI Table 15 *One-way ANOVA results with Tukey test comparing every mean with every other mean (excluding the MWCO filtration effect). All compound-features with CV <30 were included. (IC-MS neg. ionisation mode, three sample replicates per group)*

Tukey's multiple comparisons test	Mean Diff.	95.00% CI of diff.	Summary	Adjusted P Value
MeCN vs. Low Buffer MeCN	724	627.9 to 820.1	****	<0.0001
MeCN vs. High Buffer MeCN	501.7	405.6 to 597.8	****	<0.0001
MeCN vs. High H_2O MeCN	539.7	443.6 to 635.8	****	<0.0001
MeCN vs. High D_2O MeCN	713.3	617.2 to 809.4	****	<0.0001
Low Buffer MeCN vs. High Buffer MeCN	-222.3	-318.4 to -126.2	***	0.0001
Low Buffer MeCN vs. High H_2O MeCN	-184.3	-280.4 to -88.22	***	0.0006
Low Buffer MeCN vs. High D_2O MeCN	-10.67	-106.8 to 85.45	ns	0.9956
High Buffer MeCN vs. High H_2O MeCN	58	-88.12 to 134.1	*	0.0497
High Buffer MeCN vs. High D_2O MeCN	211.7	115.6 to 307.8	***	0.0002
High H_2O MeCN vs. High D_2O MeCN	173.7	77.55 to 269.8	**	0.001

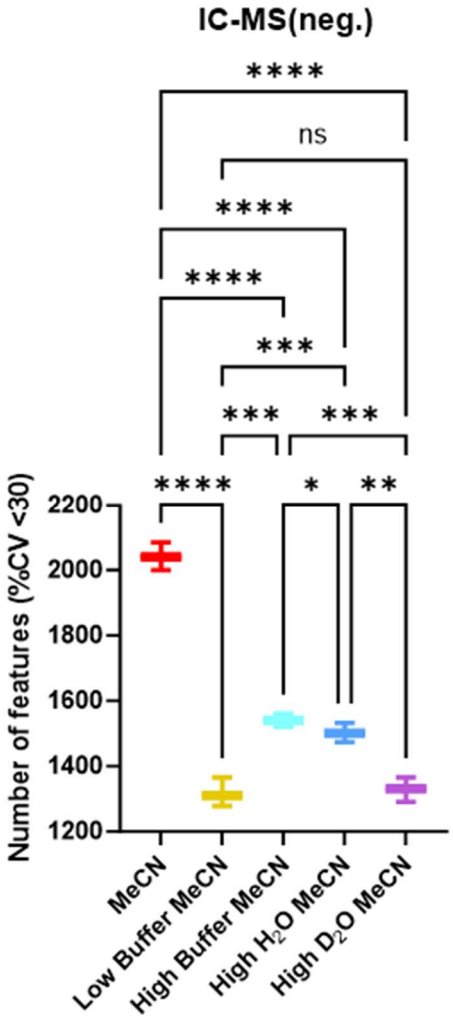

SI Fig. 21 *One-way ANOVA results with Tukey test comparing every mean with every other mean; excluding the MWCO filtration effect. All compound-features with CV <30 were included. (IC-MS neg. ionisation mode, three sample replicates per group)*

Effects of sample dilution on serum metabolite profiles analysed by LC-MS

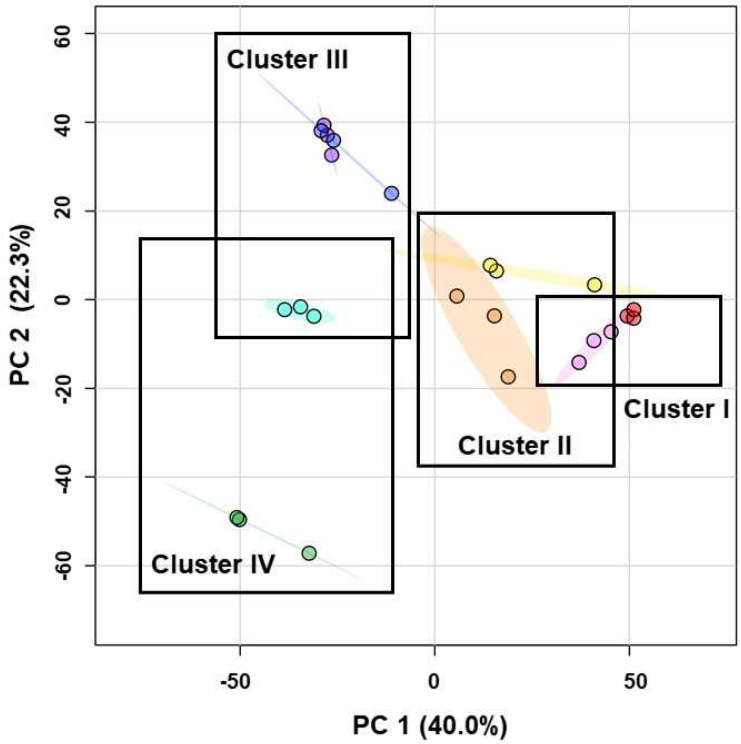

SI Fig. 22 PCA plot showing the clustering pattern for RPLC-MS in neg. ionisation mode. Cluster **I** contains low-dilution unfiltered serum samples (red) and MWCO-filtered serum samples (pink). Cluster **II** includes low-dilution samples in phosphate buffer, with MWCO filtration (orange) and without filtration (yellow). Cluster **III** contains high-dilution unfiltered samples in Milli-Q water (blue), deuterated water (purple), and phosphate buffer (turquoise), overlapping with Cluster **IV**, which primarily consists of MWCO-filtered phosphate buffer samples.

Supplementary Information – Manuscript 1

Sample processing workflows (including the applied colour-coding)

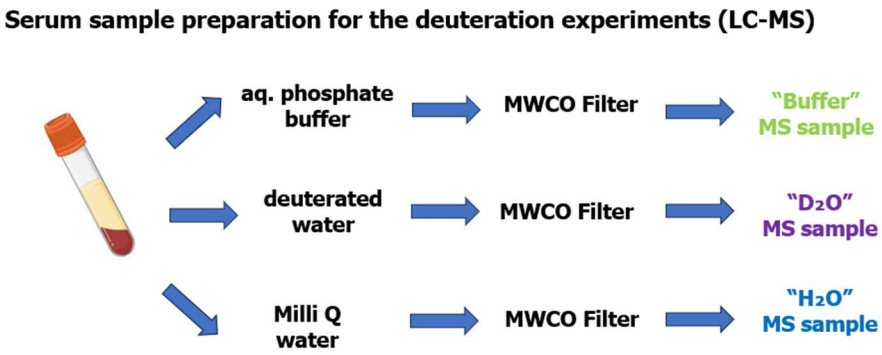

SI Methods 1 *Workflow for preparing serum samples for the deuteration experiments. The samples were analysed by IC-MS neg. mode and RPLC-MS pos. and neg. modes.*

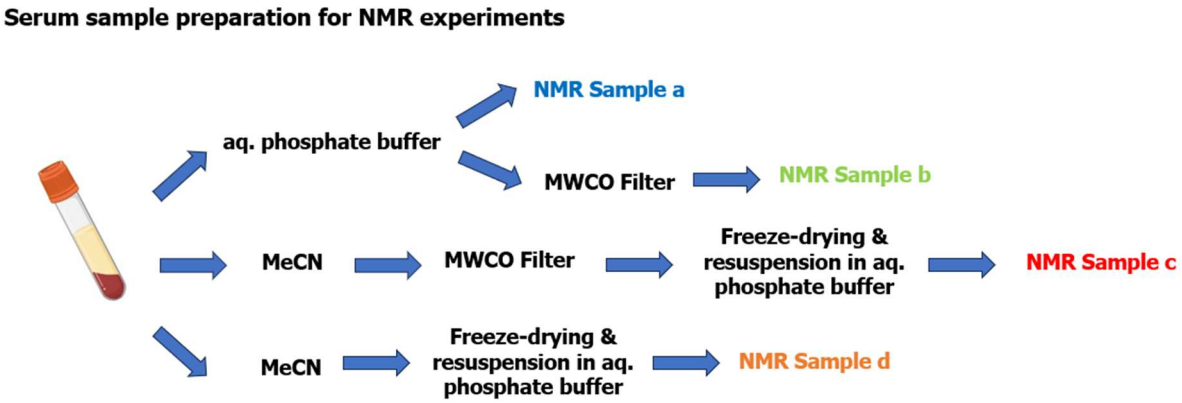

SI Methods 2 *Workflow for preparing serum samples for the NMR experiments.*

Supplementary Information – Manuscript 1

Sample processing workflows (including the applied colour-coding)

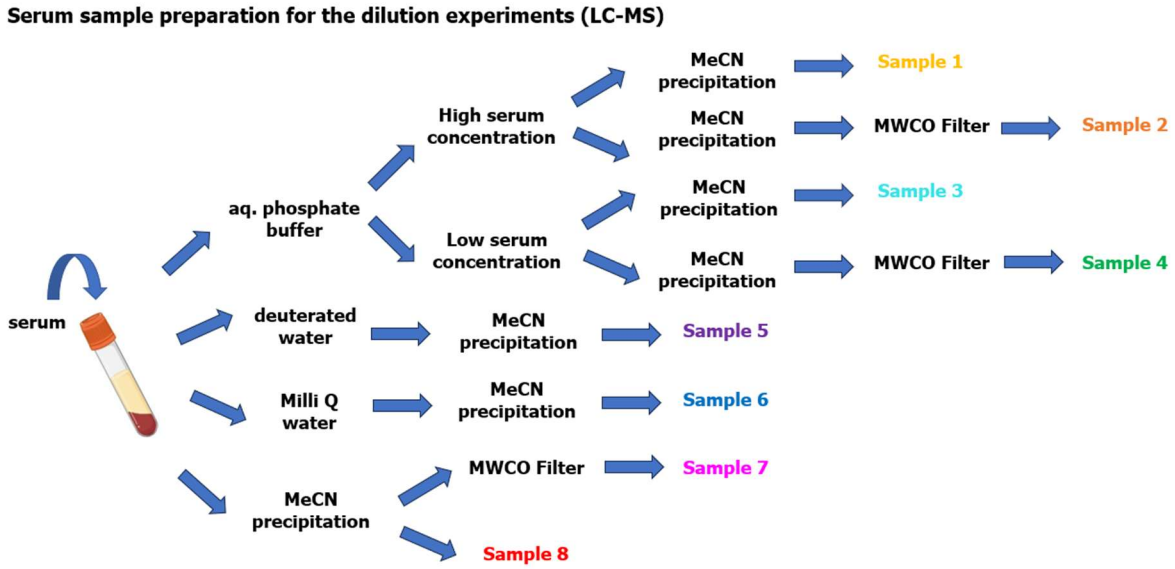

SI Methods 3 *Workflow for preparing serum samples for the dilution and MWCO-effect experiment and assessing the feasibility of using acetonitrile for protein precipitation. The samples were analysed by IC-MS neg.ionisation mode and RPLC-MS pos. and neg. ionisation mode.*

3. 4 Statement of Authorship

Title of paper	Refining Precision: Formic Acid Treatment Enhances Reproducibility in Untargeted Serum and Plasma Metabolomics
Publication status	Submitted
Publication details	Kacerova, T., Pires, E., Dixon, A., Williams, R., Legge, I., Hippisley, M., Yates, A. G., Smith, A. D., Anthony, D. C., Probert, F. & McCullagh, J.: **Refining Precision: Formic Acid Treatment Enhances Reproducibility in Untargeted Serum and Plasma Metabolomics**. Manuscript submitted to *Analytical Chemistry*.

Student confirmation

Student name	Tereza Kacerova
Contribution to the paper	T.K. Conceptualisation of the study, Test and clinical sample preparation, LC-MS analysis, Data analysis and interpretation, Manuscript writing; E.P. Test sample preparation, LC-MS analysis; A. D. and R. W. amino acid analysis; I. L. and M. H. Test sample preparation, LC-MS analysis; A. G. Y. selection of pilot clinical samples; A. D. S. was responsible for clinical trials oversight and patient recruitment; D. C. A. conceptualisation of the clinical samples analyses; F. P. and J. S. O. M. are the principal investigators/supervisors of the research described in the manuscript, contributed extensively to project/data conceptualisation and visualisation, and manuscript reviewing/editing.
Date	30/06/2025
Signature	

Supervisor confirmation

By signing the Statement of Authorship, you are certifying that the candidate made a substantial contribution to the publication, and that the description described above is accurate.

Supervisor name	Prof James S. O. McCullagh
Contribution to the paper	I am happy to state that the candidate made a major and substantial contribution this publication, and that the description above is accurate.
Date	29th June 2025
Signature	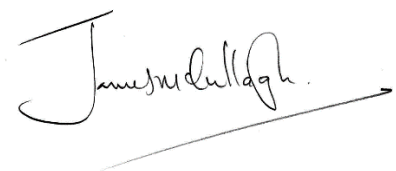

Chapter 3 Optimisation of Protein Removal Strategies for Reproducible LC-MS-Based Metabolomics

3.1 Project context and chapter overview

Untargeted plasma metabolomics by LC-MS has become a powerful tool for biomarker discovery in clinical and translational research. Yet, its performance remains highly sensitive to sample preparation protocols, with even subtle procedural variations capable of introducing significant shifts in analytical outcomes. Protein removal represents a critical step, essential for minimising matrix effects, reducing ion suppression, and enhancing both chromatographic performance and metabolite detectability.[1] Following the findings presented in **Chapter 2** - highlighting the potential for sample preparation artefacts, such as glycerol released from filter membranes, to influence spectral and statistical outputs - this chapter focuses on the systematic evaluation of protein removal strategies for LC-MS. Many studies have recognised the critical impact of sample preparation on the quality of untargeted metabolomics data, highlighting the need for optimised protocols, particularly when working with low-volume clinical samples.[1-5] Building on the findings presented in **Chapter 2**, this chapter focuses on optimising LC-MS sample preparation for low-volume, biobanked plasma samples. Specifically, we investigated the effect of pre-treating plasma and serum with 1% formic acid (FA) prior to protein precipitation with MeCN. This acidification step significantly improved extraction reproducibility and expanded the range of detectable compounds. Notably, it also enhanced the performance of supervised multivariate modelling.

To contextualise the evaluation of FA treatment, we first examine the practical performance of commonly used protein removal strategies in LC-MS-based metabolomics. Several approaches have been developed, each presenting distinct methodological advantages and performance trade-offs. Molecular weight cut-off (MWCO) filtration is frequently employed, often using regenerated cellulose membranes; however, these can exhibit hydrophobic interactions that retain lipophilic metabolites alongside proteins.[2] While hydrophilic alternatives may reduce unintended metabolite loss, they typically show lower protein depletion efficiency.[6] In contrast, protein precipitation using organic solvents, salts, or acids is a scalable and widely adopted alternative, offering effective protein removal and broad compatibility with diverse LC-MS platforms.[4-7]

To assess the efficiency and reproducibility of commonly employed protein depletion methods, we systematically compared MWCO filtration with two solvent-based precipitation strategies: MeCN and a 1:4 (v/v) mixture of *n*-butanol and methanol (BuOH/MeOH).[3] Both solvent-based approaches are extensively utilised in metabolomics workflows due to their robust protein-precipitating properties and compatibility with downstream LC-MS analyses.[4] MeCN and MeOH are widely regarded as benchmark extraction solvents, while the incorporation of BuOH has been reported to enhance the solubilisation of hydrophobic and amphiphilic metabolites.[8] Aqueous extractions were included as a control condition, given their alignment with LC-MS platforms designed for polar compound analysis, such as hydrophilic interaction liquid chromatography-MS (HILIC-MS) and ion-exchange MS (IC-MS).[9] Spectrophotometric quantification of residual protein revealed that MeCN precipitation was the most effective solvent-based strategy, depleting over threefold more protein compared to the BuOH/MeOH mixture. Although MWCO filtration resulted in the lowest overall protein content, MeCN-treated samples demonstrated both substantial protein removal and superior retention of hydrophobic metabolites, which are frequently lost during membrane-based filtration. These findings suggest that MeCN precipitation constitutes a practical and analytically favourable approach, particularly in workflows prioritising maximal compound recovery and reduced mechanical handling.

To evaluate the impact of different extraction methods on untargeted metabolite coverage and analytical reproducibility, each protocol was tested in triplicate using RPLC-MS in positive ionisation mode, which offers broad sensitivity for lipophilic and moderately polar metabolite. Among the methods tested, MeCN extraction resulted in the highest number of detected compound-features and the greatest proportion with CV below 30% (Fig. 3.1a). However, it was also associated with the highest inter-sample variability, indicated by an elevated median CV and greater dispersion of replicate measurements, as visualised by principal component analysis (PCA; Fig. 3.1b). These findings suggest that while MeCN enables effective protein depletion and broad metabolite recovery, its reduced reproducibility may limit its suitability for high-throughput or large-scale studies requiring stringent analytical consistency.

.

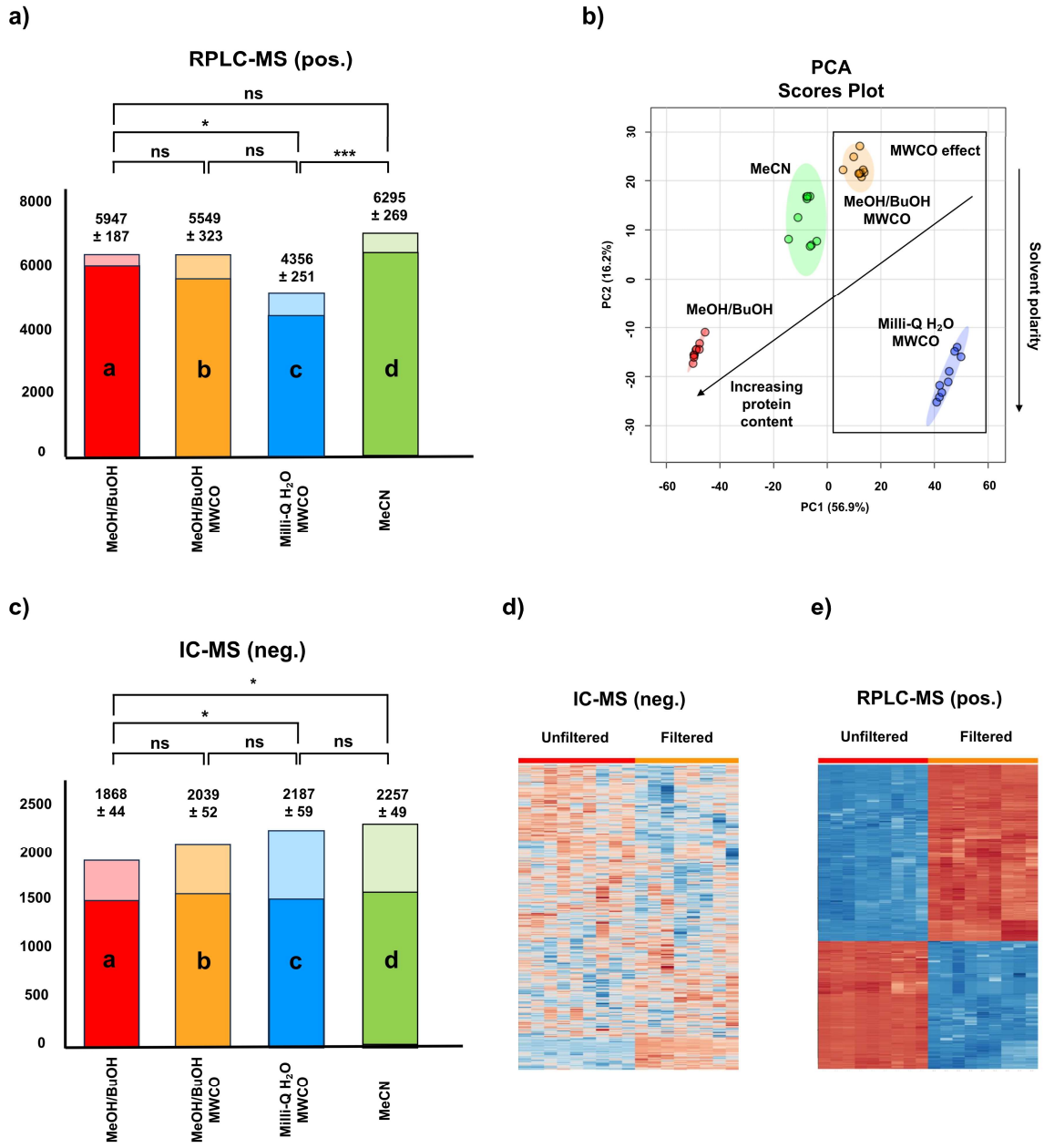

Figure 3.1. Evaluation of extraction methods for plasma metabolomics. **(a, c)** Total number of compound-features (light bars) and proportion with acceptable reproducibility (%CV < 30%; dark bars) detected using RPLC-MS (pos. ionisation mode) and IC-MS (neg. ionisation mode), respectively. Bars represent mean ± SD from three sample and three analytical replicates. Statistical significance assessed via one-way ANOVA with Tukey's *post hoc* test (ns > 0.05; * > 0.01; ** > 0.001; *** > 0.0001; **** < 0.0001). **(b)** PCA scores plot (RPLC-MS, pos. ionisation mode) showing clustering by extraction method. Arrows indicate trends driven by protein content and solvent polarity. **(d, e)** Hierarchically clustered heatmaps of the top 1000 features (based on IQR) comparing unfiltered and MWCO-filtered plasma extracts for **(d)** IC-MS (neg. ionisation mode) and **(e)** RPLC-MS (pos. ionisation mode).

In contrast, for IC-MS, used to profile highly polar metabolites, the choice of extraction solvent had minimal impact on reproducibility or the number of detected compound-features (Fig. 3.1c). Within this analytical context, MWCO filtration emerged as the preferred protein removal strategy, offering efficient removal of

macromolecules with minimal disruption to the polar metabolome (Fig. 3.1d). Importantly, effective protein removal is critical for maintaining the integrity of the electrolytic ion suppressor in the IC system.[9] Unlike in RPLC workflows, where filtration can result in the loss of hydrophobic analytes (Fig. 3.1e), MWCO filtration preserved the detection of highly polar compounds, ensuring both analytical stability and platform compatibility for IC-MS applications. Supporting this, conductivity measurements collected throughout the 37-minute analytical run showed that the most prominent conductivity peak, corresponding to an analyte eluting at 7.6 minutes, averaged 479 ± 42 μS in unfiltered MeCN-extracted samples, approximately threefold higher than in MWCO-filtered samples.

While MWCO filtration proved effective for IC-MS, addressing reproducibility challenges in RPLC-MS required a distinct optimisation strategy. To improve the consistency of MeCN-based extractions in RPLC-MS workflows, we investigated the addition of FA as a means to enhance extraction performance while maintaining efficient protein removal. FA has previously been shown to improve protein precipitation and analytical reproducibility in both proteomics and metabolomics contexts.[10-12] We therefore evaluated the impact of FA-modified MeCN on key performance parameters, including extraction reproducibility, protein removal efficiency, and metabolite coverage in RPLC-MS. Our findings demonstrate that pre-treatment of serum or plasma with FA enhances data quality across multiple metrics, including signal consistency, classification accuracy, and fold-change detection within supervised multivariate models. Given the positive impact of this protocol in two pilot clinical studies, the optimised extraction method is applied in **Chapter 6** to support biomarker discovery in a clinical trial of B vitamin supplementation in individuals with MCI.

3. 2 References

(1) Want, E. J.; O'Maille, G.; Smith, C. A.; Brandon, T. R.; Uritboonthai, W.; Qin, C.; Trauger, S. A.; Siuzdak, G. Solvent-dependent metabolite distribution, clustering, and protein extraction for serum profiling with mass spectrometry. *Anal Chem* **2006**, *78* (3), 743-752. DOI: 10.1021/ac051312t.
(2) Vuckovic, D. Current trends and challenges in sample preparation for global metabolomics using liquid chromatography-mass spectrometry. *Anal Bioanal Chem* **2012**, *403* (6), 1523-1548. DOI: 10.1007/s00216-012-6039-y.
(3) Bruce, S. J.; Tavazzi, I.; Parisod, V.; Rezzi, S.; Kochhar, S.; Guy, P. A. Investigation of Human Blood Plasma Sample Preparation for Performing Metabolomics Using Ultrahigh Performance Liquid Chromatography/Mass Spectrometry. *Anal Chem* **2009**, *81* (9), 3285-3296. DOI: 10.1021/ac8024569.
(4) Southam, A. D.; Haglington, L. D.; Najdekr, L.; Jankevics, A.; Weber, R. J. M.; Dunn, W. B. Assessment of human plasma and urine sample preparation for reproducible and high-throughput UHPLC-MS clinical metabolic phenotyping. *Analyst* **2020**, *145* (20), 6511-6523. DOI: 10.1039/d0an01319f.
(5) Dunn, W. B.; Broadhurst, D.; Begley, P.; Zelena, E.; Francis-McIntyre, S.; Anderson, N.; Brown, M.; Knowles, J. D.; Halsall, A.; Haselden, J. N.; et al. Procedures for large-scale metabolic profiling of serum and plasma using gas chromatography and liquid chromatography coupled to mass spectrometry. *Nat Protoc* **2011**, *6* (7), 1060-1083. DOI: 10.1038/nprot.2011.335 From NLM Medline.
(6) Solhi, L.; Guccini, V.; Heise, K.; Solala, I.; Niinivaara, E.; Xu, W.; Mihhels, K.; Kroger, M.; Meng, Z.; Wohlert, J.; et al. Understanding Nanocellulose-Water Interactions: Turning a Detriment into an Asset. *Chem Rev* **2023**, *123* (5), 1925-2015. DOI: 10.1021/acs.chemrev.2c00611 From NLM PubMed-not-MEDLINE.
(7) O'Connor, D.; Clarke, D. E.; Morrison, D.; Watt, A. P. Determination of drug concentrations in plasma by a highly automated, generic and flexible protein precipitation and liquid chromatography/tandem mass spectrometry method applicable to the drug discovery environment. *Rapid Commun Mass Sp* **2002**, *16* (11), 1065-1071. DOI: 10.1002/rcm.679.
(8) Cruz, M.; Wang, M.; Frisch-Daiello, J.; Han, X. L. Improved Butanol-Methanol (BUME) Method by Replacing Acetic Acid for Lipid Extraction of Biological Samples. *Lipids* **2016**, *51* (7), 887-896. DOI: 10.1007/s11745-016-4164-7.
(9) Ngere, J. B.; Ebrahimi, K. H.; Williams, R.; Pires, E.; Walsby-Tickle, J.; McCullagh, J. S. O. Ion-Exchange Chromatography Coupled to Mass Spectrometry in Life Science, Environmental, and Medical Research. *Anal Chem* **2023**, *95* (1), 152-166. DOI: 10.1021/acs.analchem.2c04298.
(10) Chen, D. X.; Song, J. W.; Yang, H.; Xiong, S. B.; Liu, Y. M.; Liu, R. Effects of Acid and Alkali Treatment on the Properties of Proteins Recovered from Whole Gutted Grass Carp (Ctenopharyngodon idellus) Using Isoelectric Solubilization/Precipitation. *J Food Quality* **2016**, *39* (6), 707-713. DOI: 10.1111/jfq.12236.
(11) Zhang, Z. Y.; He, S. D.; Liu, H. Y.; Sun, X. B.; Ye, Y. K.; Cao, X. D.; Wu, Z. Y.; Sun, H. J. Effect of pH regulation on the components and functional properties of proteins isolated from cold-pressed rapeseed meal through alkaline extraction and acid precipitation. *Food Chem* **2020**, *327*. DOI: ARTN 126998 10.1016/j.foodchem.2020.126998.
(12) Liu, A. P.; Pasquali, M. Acidified acetonitrile and methanol extractions for quantitative analysis of acylcarnitines in plasma by stable isotope dilution tandem mass spectrometry. *J Chromatogr B* **2005**, *827* (2), 193-198. DOI: 10.1016/j.jchromb.2005.09.004.

3. 3 Manuscript information

This chapter consists of a scientific letter submitted to *Analytical Chemistry* (20/06/2025).

Kacerova, T., Pires, E., Dixon, A., Williams, R., Mikhailov, V., Yates, A. G., Smith, A. D., Anthony, D. C., Probert, F. & McCullagh, J.: **Refining Precision: Formic Acid Treatment Enhances Reproducibility in Untargeted Serum and Plasma Metabolomics** *Analytical Chemistry*

Manuscript status: *Submitted*

Formic Acid Pre-treatment Enhances Untargeted Serum and Plasma Metabolomics

Tereza Kacerova[1], Elisabete Pires[1], Abigail Dixon[1], Rachel Williams[1], Isabelle Legge[1], Mia Hippisley[1], Abi G. Yates[1,2], A. David Smith[2], Daniel C. Anthony[2], Fay Probert[1], James S.O. McCullagh[1*]

[1]Chemistry Research Laboratory, Department of Chemistry, University of Oxford, Oxford, OX1 3TA, UK.
[2]Department of Pharmacology, University of Oxford, Oxford, OX1 3QT, UK.

*Corresponding author(s). E-mail(s): james.mccullagh@chem.ox.ac.uk;

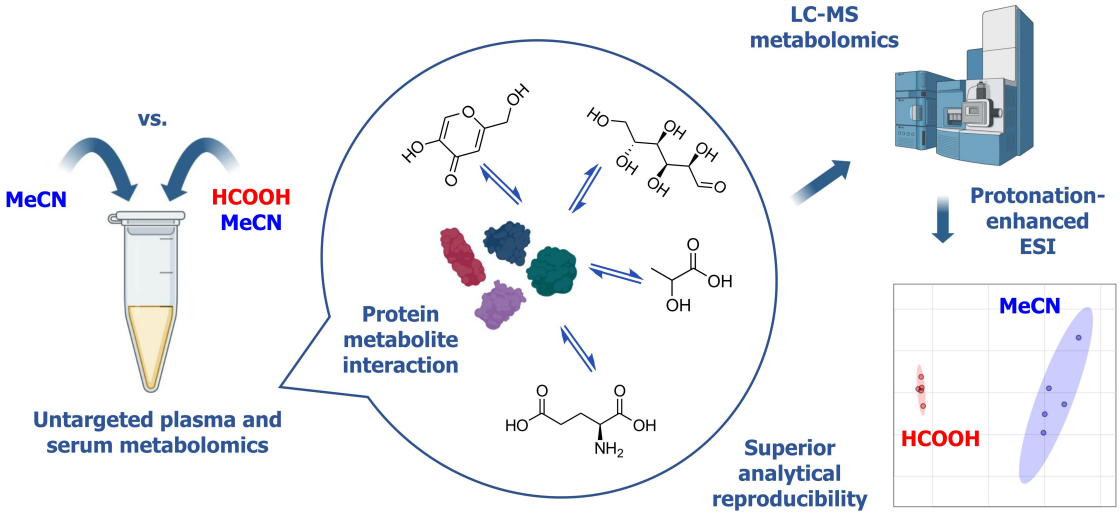

Abstract

Untargeted metabolic profiling of plasma and serum by liquid chromatography-mass spectrometry (LC-MS) is becoming increasingly important in clinical and translational research; however, sample preparation protocols can have a significant impact on study outcomes and there is currently a lack of standardised approaches.

In this study, we demonstrate that pre-treatment with 1% formic acid (FA, v/v) prior to acetonitrile (MeCN)-induced protein precipitation significantly enhances analytical performance in reversed-phase LC-MS (RPLC-MS). The FA-based protocol increased the number of reproducible compound-features and signal intensity across both positive and negative ionisation modes. In two independent dementia serum cohorts (OPTIMA and VITACOG), FA-based extraction improved multivariate modelling (orthogonal partial least squares discriminant analysis, OPLS-DA), with consistently higher classification accuracy, sensitivity, and specificity, alongside reduced variability and increased fold-changes in discriminatory compound-features. We investigated factors potentially involved in the enhanced performance and observed outcomes consistent with the disruption of non-covalent protein–metabolite interactions and the stabilisation of labile species. We found no correlation with either protein depletion or differential adduct formation. The results were also not attributable to pH lowering after metabolite extraction.

In this study, we demonstrate that FA pre-treatment of plasma and serum prior to protein precipitation significantly improves sample reproducibility and detection sensitivity in untargeted RPLC-MS metabolomics. This optimised sample preparation strategy offers clear advantages for clinical and translational metabolomics, with strong potential to enhance biomarker discovery and metabolic phenotyping.

Keywords: formic acid, LC-MS, metabolomics, plasma, serum, IC-MS, sample preparation, reproducibility, sensitivity

1 Background

Liquid chromatography-mass spectrometry (LC-MS)-based metabolomics is increasingly employed for biomarker discovery, disease stratification, and personalised medicine.[1-3] However, clinical studies are often challenged by substantial inter-individual biological variability, while disease-associated metabolic alterations are typically subtle, particularly in early or prodromal stages.[3-5] In this context, technical variation introduced during sample preparation can significantly compromise analytical sensitivity and reproducibility.[6] Rigorous optimisation of pre-analytical workflows is therefore essential to maximise metabolome coverage and ensure data robustness.

Protein precipitation using acetonitrile (MeCN) is the standard approach for preparing plasma and serum samples for LC-MS.[4,6-8] Although effective at protein removal, this approach introduces variability in the metabolite recovery profile, especially for low-abundance or protein-bound small molecules.[9,10] This is particularly relevant for circulating metabolites that exhibit partial or reversible binding to plasma proteins *in vivo*. These include lipophilic compounds, steroids, and organic acids, as their binding may impair extraction efficiency and reduce quantification precision.[11] Acid-assisted metabolite extraction protocols using low concentrations of formic acid (FA $\leq$ 0.3%) have been shown to improve stability in targeted assays.[12,13] However, the systematic evaluation of FA-assisted extraction for untargeted metabolomics, including optimal concentration ranges and analytical impact, has not been reported.

Here, we systematically evaluated the pre-treatment of serum and plasma samples with varying concentrations of FA (0.3-5% by volume) and found that 1% FA, when applied prior to MeCN precipitation, significantly enhanced metabolite recovery. This was reflected by increased feature detection and improved reproducibility in reversed-phase LC–MS (RPLC-MS) under both positive (pos.) and negative (neg.) ionisation modes. We further examined potential mechanisms underlying these improvements, including disruption of protein–metabolite interactions, pH modulation,

and alterations in ionisation efficiency. Comparative analyses in two clinical cohorts (OPTIMA and VITACOG),[14,15] designed to investigate cognitive decline, demonstrated that FA-treated samples consistently yielded superior multivariate model performance, greater fold change (FC) in discriminatory compound-features, and reduced technical variability. Collectively, these findings indicate that FA pre-treatment constitutes a simple yet effective optimisation for untargeted LC–MS metabolomics workflows in clinical research.

2 Experimental

2.1 Sample preparation and LC-MS analysis

Plasma and serum metabolites were extracted using MeCN with or without pre-treatment with FA (1%, final concentration). Samples were vortexed, centrifuged, and supernatants collected for LC-MS analysis (eMethods 1.1-1.2). RPLC-MS was performed on a Xevo G2-XS QTOF mass spectrometer coupled to an Acquity UPLC system under gradient elution (Waters Limited, Wilmslow, UK). Data processing was performed using Progenesis QI and *in-house* R scripts and MetaboAnalyst 6.0.[16] For detailed method description, including RPLC-MS (pos. and neg. ionisation modes), hydrophilic interaction liquid chromatography-MS (HILIC-MS), anion-exchange chromatography-MS (AEC-MS), and MALDI-TOF MS analyses, as well as complete experimental protocols, see (eMethods 1.3-1.6).[17]

2.2 Statistical analysis

Untargeted clinical LC-MS data were analysed using R software (v4.2.1) with *in-house* scripts (eMethods 1.7). Multivariate analysis was performed using orthogonal partial least squares discriminant analysis (OPLS-DA) with 10-fold cross-validation, repeated permutation testing, and variable importance in projection (VIP) scoring, as previously described (eMethods 1.8).[18,19] Full methodological details, statistical workflows, and clinical information for the OPTIMA and VITACOG cohorts are provided in the Supplementary Information (SI; eMethods 2.1-2.3). Univariate analysis involved fold change (FC) and t-test p-value calculations between extraction methods, visualised as volcano plots (FC > 2, $p < 0.05$). To maximise sensitivity, multiple testing corrections were not applied unless stated. Principal component analysis (PCA) assessed group variation. Remaining analyses were conducted in GraphPad Prism 9 (significance $p < 0.05$).

3 Results

3.1 Formic acid pre-treatment enhances sensitivity and reproducibility in metabolic profiling

Protein precipitation with MeCN is widely used in LC-MS-based metabolomics to remove residual protein, simplify the sample matrix, and minimise ion suppression. However, this approach also introduces variability in metabolite extraction efficiency, impacting reproducibility and sensitivity. To address this, we tested whether pre-treatment with different concentrations of FA prior to MeCN precipitation improved metabolite extraction performance. Initially, blood plasma samples ($n = 5$ replicates) were processed with MeCN alone or with FA pre-treatment across a range of concentrations (0.1-5%) and analysed by RPLC–MS in pos. and neg. ionisation modes. At 1% FA and above we observed a step-change in the reproducibility of metabolite extraction, an increase in the number of compound-features with a %CV< 30, and higher average metabolite intensities (Fig. 1a-d). The experiment was repeated multiple times using two separate Waters Xevo G2-XS QTOF instruments. Results were consistent across experiment replicates and platforms. Improvements in extraction performance were also observed using serum samples, although the magnitude of the increased reproducibility was reduced (SI Fig. 1).

The markedly tighter clustering of FA+MeCN extracts in pos. ion mode, indicated a reduction in technical variance (Fig. 1a). Interestingly, FA pre-treatment led to an increase in the number of compound-features with %CV < 30%, and substantially elevated the proportion with %CV $<$ 5% (Fig. 1b), despite a modest reduction in total compound-feature count ($p = 0.03$). Among the 50 most stable compound-features (%CV 0–1%), a strong positive correlation with FA concentration was observed, supporting a concentration-dependent effect (Fig. 1c). Pre-treatment with FA also resulted in a significant increase in the average ion intensity ($p < 0.0001$; Fig. 1d). This trend was consistent across both pos. and neg. ionisation modes (SI Fig. 2). Notably, no further gains in intensity or reproducibility were observed beyond 1% FA (SI Fig. 3), and total protein removal remained unaffected ($p = 0.2$), indicating that FA pre-treatment improved analytical performance without compromising precipitation efficiency.

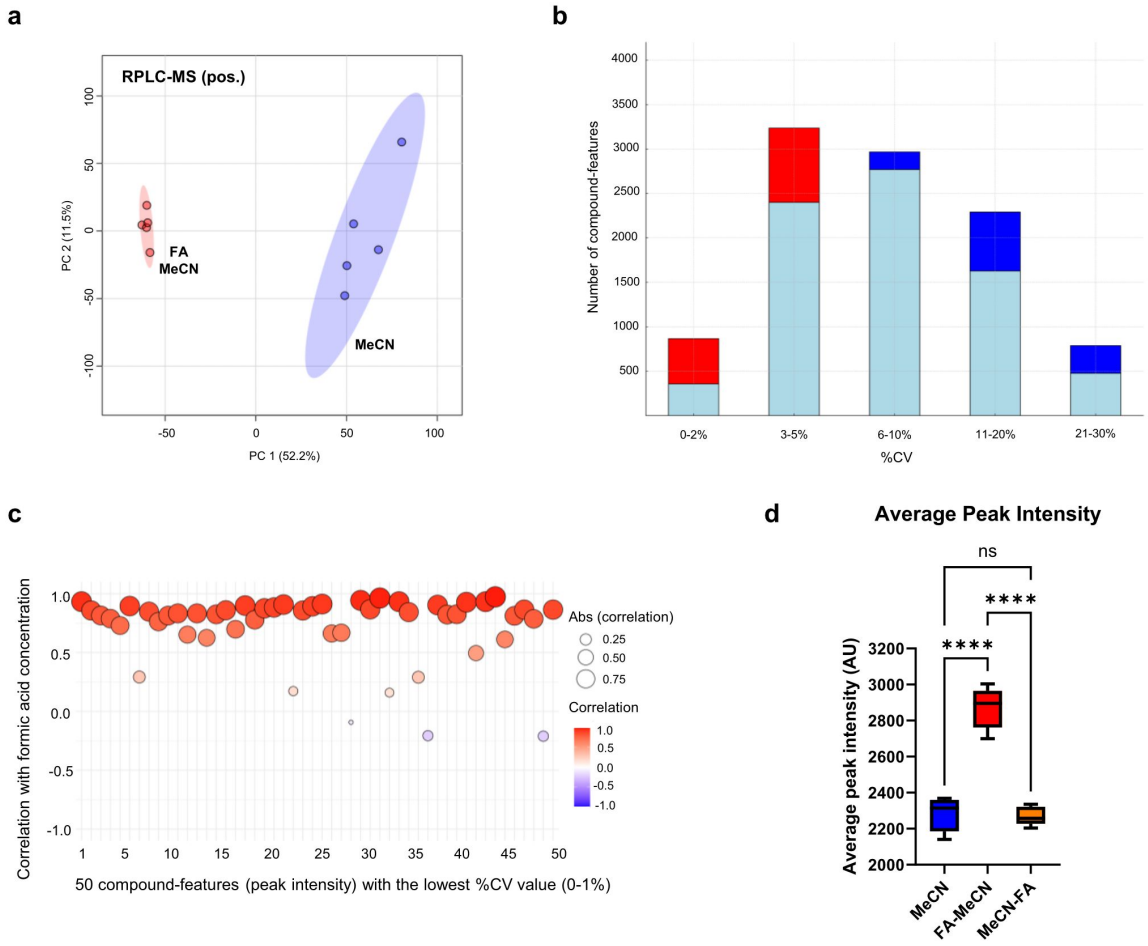

Fig. 1: **Impact of Formic Acid (FA) on Plasma Extraction Efficiency and Reproducibility.** **(a)** PCA plot shows tighter clustering of FA-treated extracts (shaded area = 95% confidence interval). **(b)** Histogram illustrating the distribution of %CV values for compound-features detected following extraction with 1% FA prior to MeCN (red) or MeCN only (dark blue). Overlapping features in each %CV bin are shown in light blue. **(c)** Correlation plot showing the relationship between FA concentration and normalised peak intensities for compound-features with low variability (%CV 0–1%, top 50 compound-features). Dot colour reflects the direction and strength of the Pearson correlation (blue = negative, red = positive), while dot size corresponds to the absolute correlation value, indicating the strength of association regardless of direction. **(d)** Box plots comparing average peak intensities (%CV < 30%) across three extraction strategies: MeCN alone, FA pre-treatment followed by MeCN extraction (FA–MeCN), and post-spiking with FA after MeCN extraction (MeCN–FA), (****$p < 0.0001$; ns = not significant; one-way ANOVA with *post hoc* test). All panels are based on $n = 5$ sample preparation replicates per condition. All analysis were conducted using RPLC-MS in pos. ionisation mode.

3.2 Lower pH alone does not explain FA-induced improvements

We hypothesised that increased proton availability in FA-treated samples could be enhancing ionisation efficiency, promoting $[M + H]^+$ formation resulting in higher, and more reproducible, metabolite abundances. To test this, we compared three extraction approaches using human plasma: (1) MeCN alone (control), (2) 1% FA pre-treatment followed by MeCN, and (3) MeCN extraction followed by post-spiking with 1% FA. Samples were analysed by RPLC-MS in both pos. and neg. ionisation modes, and using AEC-MS. The AEC-MS method incorporated an electrolytic ion suppressor that removed mobile phase cations - including protons - providing a control for FA-induced ionisation effects (in neg. ionisation mode only; eMethods 1.5).[20] Our results demonstrated that post-precipitation addition of FA led to improved replicate clustering compared

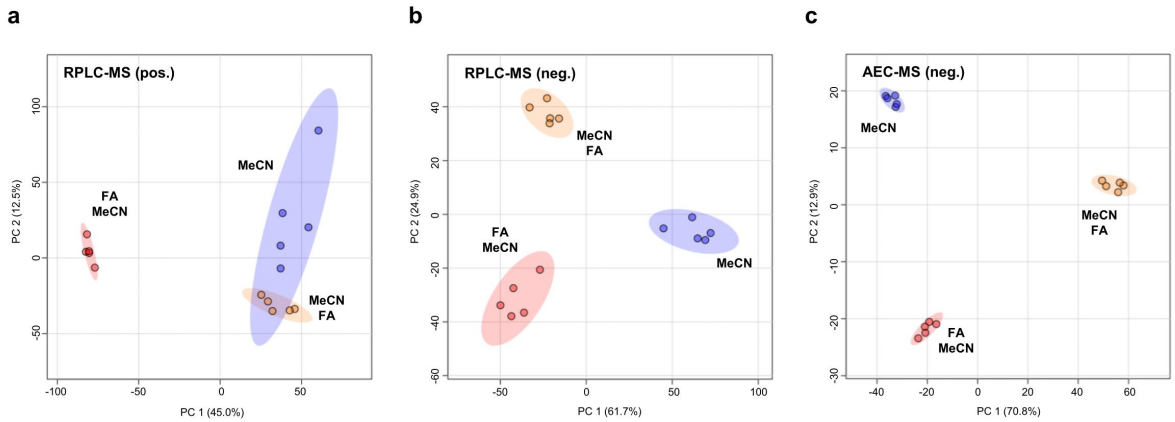

Fig. 2: **Reproducibility of Extraction Workflows Across LC–MS Platforms.** PCA plots of plasma metabolite extracts prepared using three workflows: MeCN-only (blue), FA pre-treatment followed by MeCN (FA-MeCN; red), and MeCN extraction followed by FA addition (MeCN-FA; orange). **(a)** RPLC-MS (pos. ionisation mode), **(b)** RPLC-MS (neg. ionisation mode), and **(c)** AEC-MS (neg. ionisation mode). Each panel shows $n = 5$ replicate extractions from the same plasma aliquot.

to MeCN-only extracts; however, the most consistent clustering was observed when FA was added prior to MeCN precipitation (Fig. 2a). Notably, while both FA-based methods reached the same final pH, only pre-treatment with FA (FA–MeCN) resulted in significantly higher average ion intensity in RPLC-MS pos. ionisation mode ($p < 0.0001$; Fig. 1d), whereas no significant difference was detected between MeCN-only and post-FA-spiked samples ($p = 0.98$; Fig. 1d). These findings suggest that the improvements in reproducibility and signal intensity are unlikely to be driven solely by pH reduction or enhanced proton availability affecting ionisation efficiency. Importantly, no detrimental impact on ion intensity was observed in the neg. ionisation mode following 1% FA pre-treatment (SI Fig. 2), indicating that the protocol is broadly compatible across ionisation conditions.

In RPLC-MS neg. mode, FA pre-treatment (FA+MeCN) exerted minimal effect on sample clustering (Fig. 2b); however, the average ion intensity profile mirrored that of pos. ionisation mode, with FA added prior to MeCN yielding significantly higher ion intensities than MeCN alone or MeCN+FA (SI Fig. 2). This pattern was also observed in AEC-MS (neg. ionisation mode), where all extraction groups showed tighter replicate clustering, likely reflecting improved retention and separation of ionic and polar metabolites (Fig. 2c). Although FA addition during sample preparation substantially lowered pH (∼2.5), it is unlikely that pH remained significantly different during ionisation due to dilution by the mobile phase. Notably, in neg. mode, all three extraction methods (MeCN, FA-MeCN, and post-FA) formed distinct PCA clusters, despite comparable average ion intensities between MeCN-only and post-FA extracts. These findings suggest that FA addition prior to precipitation alters the physicochemical properties of the extract in a way that impacts ionisation behaviour and multivariate clustering.

3.3 Addition of FA did not affect the adduct profile for the majority of metabolites in plasma and serum

To assess whether addition of FA altered adduct formation, we examined FA and MeCN adducts in both pos. and neg. ionisation modes across both chromatographic methods (SI Tables 1-3). Adducts were annotated using the peak picking and deconvolution workflow in Progenesis QI. No notable differences in adduct profiles were observed between FA-treated and untreated samples. As the mobile phase already contained 0.1% FA, formate-related adducts were present in all experimental groups, but the additional FA introduced during extraction, did not significantly alter the adduct profile ($p > 0.05$). It was also observed that addition of FA (before or after MeCN precipitation) had no detectable effect on sodium or potassium adduct formation, indicating that alkali metal ion clustering remains unaffected. Together, these results confirmed that FA treatment did not systematically alter adduct behaviour under the tested conditions.

3.4 Disrupting protein-metabolite interactions

Our experiments consistently revealed enhanced sample clustering and increased total ion abundance in plasma samples treated with

FA prior to MeCN extraction. At physiological pH, plasma proteins maintain native structures and readily form non-covalent complexes with small molecules. Endogenous proteins such as serum albumin and lipoproteins are known to play a physiological role as metabolite carriers, binding a range of hydrophobic compounds, including hormones, fatty acids, lipids, and drugs in circulation.[8,21] We hypothesised that during protein precipitation, these non-covalent interactions may sequester protein-bound metabolites, impacting extraction efficiency and that FA pre-treatment may disrupt these interactions prior to precipitation, leading to an improvement in metabolite release and extraction efficiency.

To test this hypothesis, plasma samples were incubated with additional bovine serum albumin (BSA, 150 μM) and extracted with or without prior FA treatment (eMethods 1.1). In RPLC-MS pos. ionisation mode, BSA addition led to a marked increase in the number of compound-features in FA-treated samples (Fig. 3a), supporting the hypothesis that FA disrupts protein-metabolite interactions. A similar trend was observed in RPLC-MS neg. mode (SI Fig. 5a), whereas no corresponding increase was seen in AEC-MS (SI Fig. 5b). As AEC-MS selectively detects small, highly polar and ionic compounds, the absence of an effect suggests that the released metabolites are more hydrophobic and possibly of higher molecular mass - consistent with the physicochemical characteristics of compounds typically bound to proteins *in vivo*, such as lipids and fatty acids. This interpretation is further supported by Student's t-test results from the plasma extraction comparison, which showed that the most significantly altered compound-features were predominantly increased in FA-treated samples (SI Table 4). Although not identified, their m/z values and retention times (SI Table 4) suggest they are primarily lipid-like species, consistent with the release of hydrophobic compounds from protein binding sites. To assess whether the observed effects were influenced by differences in protein removal, potentially impacting ion suppression and signal-to-noise ratios, we compared residual protein content between MeCN-only and FA pre-treated samples; however, no significant difference was observed (150 ± 30 μg/mL vs. 170 ± 20 μg/mL; $p = 0.2$).

Finally, to evaluate whether FA treatment prior to protein precipitation could lead to protein degradation, we analysed the protein content of the post-extraction pellets. Plasma and aqueous albumin solutions were extracted using MeCN or FA+MeCN and the resulting pellets were reconstituted and analysed by MALDI-MS. In both cases, intact serum albumin was observed and while no major differences in protein profiles were detected, the MALDI spectra suggest that FA may slightly enhance albumin denaturation, as indicated by subtle shifts in both high (30–200 kDa; Fig. 3b, SI Fig. 6) and low (4–20 kDa; SI Fig. 7,8) molecular weight ranges. MALDI analysis of the corresponding supernatants confirmed the absence of detectable peptide or protein signals in both extraction conditions, indicating that degradation products are not present in the analysed supernatant.

To confirm that FA pre-treatment did not lead to the release of proteinogenic amino acids via protein hydrolysis, we performed HILIC–MS analysis on MeCN-only and FA–MeCN extracts to compare free amino acid levels. Of the 20 main proteinogenic amino acids, 15 were detected (aspartic acid, glutamic acid, threonine, cysteine, and asparagine were not observed; SI Table 5). For most amino acids, FA pre-treatment had no significant effect on the levels detected. Interestingly, levels of glycine ($p = 0.02$; Fig. 3c), phenylalanine ($p = 0.01$; Fig. 3d), tryptophan ($p = 0.01$; Fig. 3e), and glutamine ($p = 0.02$; Fig. 3f) were significantly lower in FA-treated samples, with tyrosine showing borderline significance ($p = 0.09$). These findings provide no indication that FA pre-treatment promotes the release of free amino acids via protein hydrolysis or related mechanisms.

3.5 Case Study 1: OPTIMA

To evaluate the translational potential of FA-enhanced extraction in clinical samples, we applied both MeCN-only and FA-MeCN protocols to serum samples from the OPTIMA cohort, a dementia case-control study.[14,22] While method development was performed in plasma, comparable improvements in reproducibility and PCA clustering with FA pre-treatment were also observed in both standard serum and deuterated phosphate-buffered serum matrices (SI Fig. 1).[23] The OPTIMA analysis focused on a subset of 63 patients with mild to moderate cognitive impairment, comprising 34 individuals who later developed vascular dementia (VaD) and 29 who progressed to Alzheimer's disease (AD). Samples were analysed using RPLC-MS in pos. ionisation mode, and group separation was assessed using OPLS-DA models comparing AD and VaD outcomes. As expected for early-stage differentiation, the overall model performance was modest. Using MeCN-only extraction, the classification accuracy reached 53.5±7.3% (Fig. 4a), which was nonetheless significantly above the accuracy of a random model ensemble ($p < 0.0001$). Notably, the pre-treatment

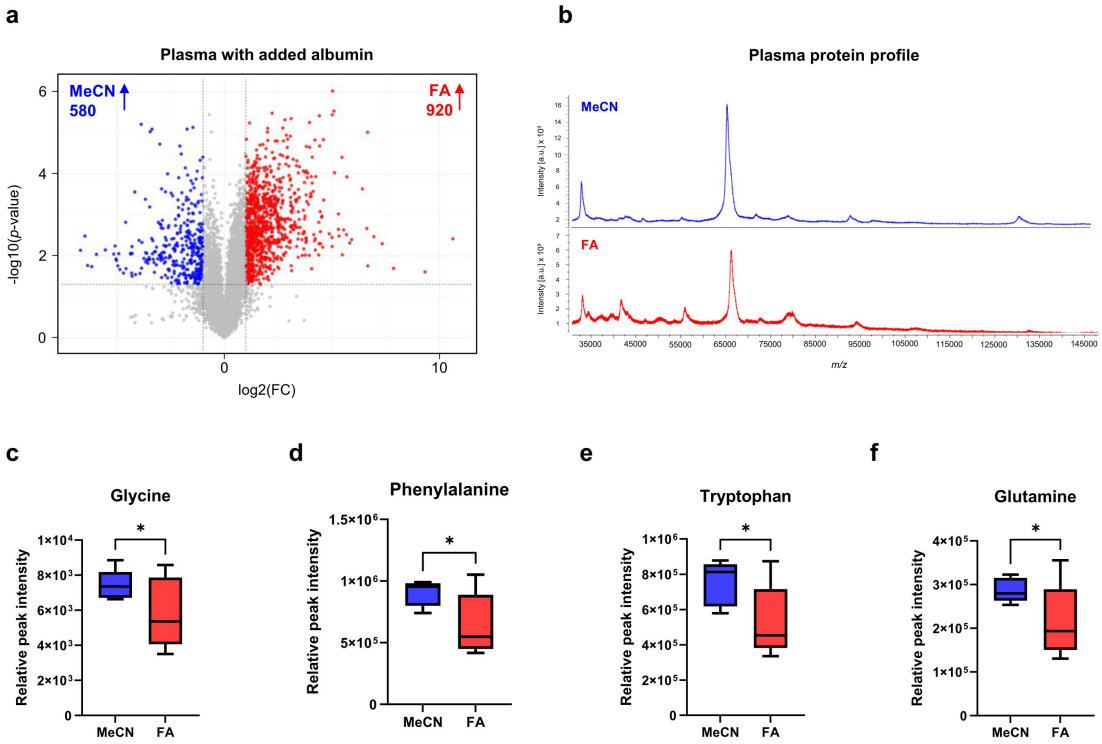

Fig. 3: **Effects of Formic Acid–Protein Interactions on Metabolite Extraction Efficiency. (a)** Volcano plot showing altered compound-features between acidified and unacidified plasma with additional albumin (c = 7.0 g/dL) extractions (t-test, $p < 0.05$, uncorrected; RPLC-MS (pos. ionisation mode)). **(b)** MALDI-MS spectra of the resuspended plasma protein pellet following extraction with acetonitrile (MeCN, blue) and formic acid–acetonitrile (FA-MeCN, red). Both spectra are dominated by albumin peaks, with no significant differences observed **(c-f)** Amino acids significantly altered between MeCN and FA-MeCN plasma extracts (HILIC-MS data): **(c)** glycine ($p = 0.02$), **(d)** phenylalanine ($p = 0.01$), **(e)** tryptophan ($p = 0.01$), and **(g)** glutamine ($p = 0.02$). All extractions correspond to $n = 5$ samples from the same plasma aliquot.

with FA prior to MeCN extraction improved classification accuracy to 58.6±6.0% (Fig. 4b). These results were based on 1000 cross-validated models per condition, with the improvement in classification accuracy reaching statistical significance ($p = 4.31 \times 10^{-6}$, Fig. 4c). Similar improvements were observed in sensitivity ($p = 4.7 \times 10^{-4}$) and specificity ($p = 9.25 \times 10^{-6}$, SI Fig. 9). These findings align with our earlier observations that FA pre-treatment enhances reproducibility, increases metabolite signal intensity, and improves the detection of low-variance features across the metabolome.

3.6 Case Study 2: VITACOG

To demonstrate the consistency of improvements observed in multivariate models, the two extraction methods were further evaluated in a more clearly defined cohort from a different clinical study focussed on mild cognitive impairment - the VITACOG study, where more pronounced metabolic differences were anticipated.[15,24] The analysis used serum samples prepared in deuterated phosphate buffer from 30 individuals with mild cognitive impairment who had received B vitamin supplementation (previously identified as treatment responders), alongside 30 placebo-treated controls. Consistent with the OPTIMA findings, FA-enhanced extraction outperformed MeCN-only (Fig. 4d,e), yielding significantly higher classification accuracy (77.9 ± 3.7% vs. 66.4 ± 4.0%, $p = 1.45 \times 10^{-52}$, Fig. 4f), sensitivity (80.2 ± 5.0% vs. 70.3 ± 6.1%, $p = 4.18 \times 10^{-52}$), and specificity (78.2 ± 5.6% vs. 67.2 ± 6.3%, $p = 2.13 \times 10^{-27}$, SI Fig. 9).

In both cohorts, VIP-ranked features showed minimal overlap between extraction methods, indicating that each captures distinct regions of the serum metabolome (SI Tables 6-9). The FA-based protocol, which consistently achieved higher classification accuracy, yielded a smaller but more

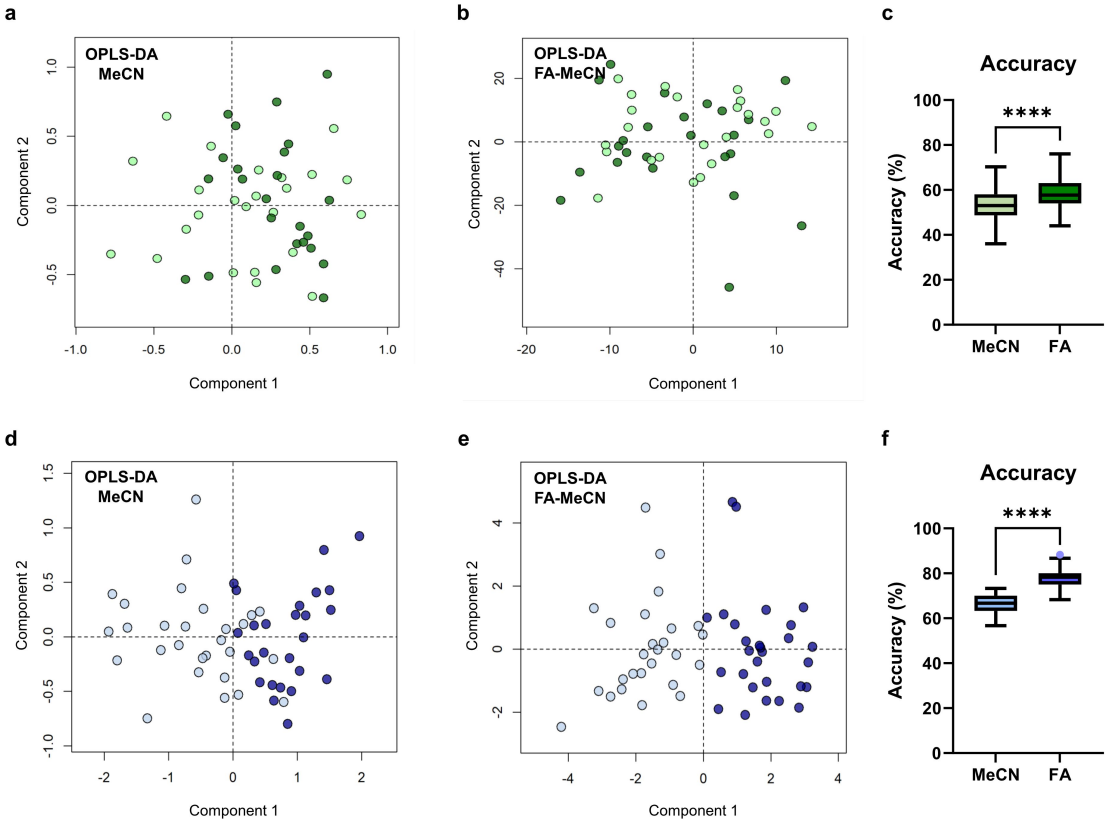

Fig. 4: **Comparison of Extraction Methods Across Two Independent Clinical Cohorts.** Serum samples from the OPTIMA **(a–c)** and VITACOG **(d–f)** studies were extracted using either MeCN **(a, d)** or FA-enhanced **(b, e)** workflows. **(a, b)** OPLS-DA scores plots for OPTIMA (light green: Alzheimer's disease; dark green: vascular dementia). **(d, e)** OPLS-DA scores plots for VITACOG (light blue: B vitamin treatment; dark blue: placebo). **(c, f)** Classification accuracy from 1000 cross-validated models. In both cohorts, FA-based extraction consistently improved classification performance (****$p < 0.0001$, Kolmogorov-Smirnov test).

consistently selected set of discriminative features. In contrast, MeCN-only extraction identified a broader array of features with lower individual contributions to group separation, suggesting a more diffuse, noisy signal. Notably, some features were uniquely detectable with FA+MeCN extraction, indicating method-specific enrichment (SI Tables 10-12) likely driven by metabolite class–dependent responses influenced by polarity, stability, and matrix interactions. The FA+MeCN approach also yielded significantly larger FC between groups ($p = 0.007$; SI Table 10, 12), reflecting improved biological resolution and enhanced detection of treatment-related metabolites. These findings align with our pooled plasma and serum experiments, where MeCN-only extraction yielded a slightly higher total number of compound-features ($p = 0.03$) but with lower reproducibility and signal intensity. In contrast, FA pre-treatment enabled more consistent recovery of analytically robust features, including compounds undetectable with MeCN alone. The improved performance may result from greater matrix stabilisation, as acidification standardises sample pH, reducing chemical reactivity, degradation, and adduct formation. Collectively, these results support the incorporation of FA pre-treatment as a simple and scalable optimisation for clinical LC-MS sample preparation protocols.

4 Limitations and conclusions

This observational study has demonstrated that pre-treatment of plasma and serum with 1% FA prior to MeCN extraction consistently enhances analytical performance in untargeted metabolomics, particularly using RPLC-MS in pos. ionisation mode. FA pre-treatment consistently led to increased compound abundances, improved

sample clustering in both supervised and unsupervised models, and reduced %CV values across detected compound-features. These improvements translated into greater classification accuracy in two independent clinical studies, supporting the translational potential of this simple, low-cost method optimisation.

While the specific mechanisms underlying the observed effects remain to be fully elucidated, experiments using multiple analytical platforms and sample preparation controls suggest that several physiochemical processes may contribute to the metabolome-wide changes observed. These include matrix pH standardisation, stabilisation of labile metabolites, and disruption of protein–metabolite interactions. However, it is important to note that FA may differentially affect individual analytes by influencing their stability, ionisation efficiency, or physicochemical properties. Such effects could be both analyte- and/or platform-dependent, and targeted validation is recommended if applying this sample preparation approach to alternative matrices or compound-classes.

Collectively, our findings demonstrate the utility of FA pre-treatment as a robust and scalable approach to improve reproducibility, sensitivity, and discriminatory power using untargeted metabolomics workflows, particularly in the context of clinical research, personalised medicine, and biomarker discovery, where metabolic changes can be subtle and challenging to detect, and improved sensitivity and reproducibility can have a significant impact on clinical outcomes.

5 References

1. Dunn WB, Bailey NJ, Johnson HE. Measuring the metabolome: current analytical technologies. Analyst. May 2005;130(5):606-25. doi:10.1039/b418288j

2. Dunn WB, Broadhurst D, Begley P, et al. Procedures for large-scale metabolic profiling of serum and plasma using gas chromatography and liquid chromatography coupled to mass spectrometry. Nat Protoc. Jun 30 2011;6(7):1060-83. doi:10.1038/nprot.2011.335

3. Kohler I, Verhoeven A, Derks RJE, Giera M. Analytical pitfalls and challenges in clinical metabolomics. Bioanalysis. Jul 2016;8(14):1509-1532. doi:10.4155/bio-2016-0090

4. Southam AD, Haglington LD, Najdekr L, Jankevics A, Weber RJM, Dunn WB. Assessment of human plasma and urine sample preparation for reproducible and high-throughput UHPLC-MS clinical metabolic phenotyping. Analyst. Oct 21 2020;145(20):6511-6523. doi:10.1039/d0an01319f

5. Want EJ, O'Maille G, Smith CA, et al. Solvent-dependent metabolite distribution, clustering, and protein extraction for serum profiling with mass spectrometry. Anal Chem. Feb 1 2006;78(3):743-752. doi:10.1021/ac051312t

6. Lepoittevin M, Blancart-Remaury Q, Kerforne T, Pellerin L, Hauet T, Thuillier R. Comparison between 5 extractions methods in either plasma or serum to determine the optimal extraction and matrix combination for human metabolomics. Cell Mol Biol Lett. May 20 2023;28(1):43. doi:10.1186/s11658-023-00452-x

7. Polson C, Sarkar P, Incledon B, Raguvaran V, Grant R. Optimization of protein precipitation based upon effectiveness of protein removal and ionization effect in liquid chromatography-tandem mass spectrometry. J Chromatogr B. Mar 5 2003;785(2):263-275. doi:Pii S1570-0232(02)00914-5 Doi 10.1016/S1570-0232(02)00914-5

8. Wawrzyniak R, Kosnowska A, Macioszek S, Bartoszewski R, Jan Markuszewski M. New plasma preparation approach to enrich metabolome coverage in untargeted metabolomics: plasma protein bound hydrophobic metabolite release with proteinase K. Sci Rep. Jun 22 2018;8(1):9541. doi:10.1038/s41598-018-27983-0

9. A J, Trygg J, Gullberg J, et al. Extraction and GC/MS analysis of the human blood plasma metabolome. Anal Chem. Dec 15 2005;77(24):8086-94. doi:10.1021/ac051211v

10. Satomi Y, Hirayama M, Kobayashi H. One-step lipid extraction for plasma lipidomics analysis by liquid chromatography mass spectrometry. J Chromatogr B Analyt Technol Biomed Life Sci. Sep 15 2017;1063:93-100. doi:10.1016/j.jchromb.2017.08.020

11. Skov K, Hadrup N, Smedsgaard J, Frandsen H. LC-MS analysis of the plasma metabolome–a novel sample preparation strategy. J Chromatogr B Analyt Technol Biomed Life Sci. Jan 26 2015;978-979:83-8. doi:10.1016/j.jchromb.2014.11.033

12. Sun LN, Zhao Y, Gao HY, et al. LC-MS/MS methods for determination of unstable pivmecillinam and mecillinam in acidified human plasma: Application to a pharmacokinetic study. J Sep Sci. Jul 2022;45(14):2543-2554. doi:10.1002/jssc.202200070

13. Liu AP, Pasquali M. Acidified acetonitrile and methanol extractions for quantitative analysis of acylcarnitines in plasma by stable isotope dilution tandem mass spectrometry. J Chromatogr B. Dec 5 2005;827(2):193-198. doi:10.1016/j.jchromb.2005.09.004

14. Seeburger JL, Holder DJ, Combrinck M, et al. Cerebrospinal Fluid Biomarkers Distinguish Postmortem-Confirmed Alzheimer's Disease from Other Dementias and Healthy Controls in the OPTIMA Cohort. Journal of Alzheimers Disease. 2015;44(2):525-539. doi:10.3233/Jad-141725

15. Smith AD, Smith SM, de Jager CA, et al. Homocysteine-lowering by B vitamins slows the rate of accelerated brain atrophy in mild cognitive impairment: a randomized controlled trial. Plos One. Sep 8 2010;5(9):e12244. doi:10.1371/journal.pone.0012244

16. Pang Z, Lu Y, Zhou G, et al. MetaboAnalyst 6.0: towards a unified platform for metabolomics data processing, analysis and interpretation. Nucleic Acids Res. Jul 5 2024;52(W1):W398-W406. doi:10.1093/nar/gkae253

17. Walsby-Tickle J, Gannon J, Hvinden I, et al. Anion-exchange chromatography mass spectrometry provides extensive coverage of primary metabolic pathways revealing altered metabolism in IDH1 mutant cells. Commun Biol. May 20 2020;3(1):247. doi:10.1038/s42003-020-0957-6

18. Yeo T, Probert F, Sealey M, et al. Objective biomarkers for clinical relapse in multiple sclerosis: a metabolomics approach. Brain Commun. 2021;3(4):fcab240. doi:10.1093/braincomms/fcab240

19. Yeo T, Sealey M, Zhou Y, et al. A blood-based metabolomics test to distinguish relapsing-remitting and secondary progressive multiple sclerosis: addressing practical considerations for clinical application. Sci Rep. Jul 24 2020;10(1):12381. doi:10.1038/s41598-020-69119-3

20. Ngere JB, Ebrahimi KH, Williams R, Pires E, Walsby-Tickle J, McCullagh JSO. Ion-Exchange Chromatography Coupled to Mass Spectrometry in Life Science, Environmental, and Medical Research. Anal Chem. Jan 10 2023;95(1):152-166. doi:10.1021/acs.analchem.2c04298

21. Li X, Gianoulis TA, Yip KY, Gerstein M, Snyder M. Extensive in vivo metabolite-protein interactions revealed by large-scale systematic analyses. Cell. Nov 12 2010;143(4):639-50. doi:10.1016/j.cell.2010.09.048

22. Razay G, Williams J, King E, Smith AD, Wilcock G. Blood pressure, dementia and Alzheimer's disease: the OPTIMA longitudinal study. Dement Geriatr Cogn Disord. 2009;28(1):70-4. doi:10.1159/000230877

23. Kacerova T, Pires E, Walsby-Tickle J, Probert F, McCullagh JSO. Integrating NMR and Multi-LC-MS-Based Untargeted Metabolomics for Comprehensive Analysis of Blood Serum Samples. Anal Chim Acta. 2025;1356doi:10.1016/j.aca.2025.343979

24. de Jager CA, Oulhaj A, Jacoby R, Refsum H, Smith AD. Cognitive and clinical outcomes of homocysteine-lowering B-vitamin treatment in mild cognitive impairment: a randomized controlled trial. Int J Geriatr Psychiatry. Jun 2012;27(6):592-600. doi:10.1002/gps.2758

Contribution statement

J.S.O.M., T.K., and E.P. conceived and designed the study. T.K., E.P., A.D., R.W., I.L., and M.H. performed the experiments. E.P. and T.K. developed and optimised the sample processing methods. T.K. processed and analysed the data. A.D.S. was responsible for clinical trials oversight and patient recruitment. A.G., F.P. and D.C.A. selected the clinical pilot samples. J.S.O.M, F.P., and D.C.A. provided supervision. T.K. drafted the manuscript. E.P., F.P., and J.S.O.M., provided critical feedback and guidance for experimental and analysis design. All authors provided input on the manuscript.

Declaration of competing interest

A.D.S. is named as an inventor on two patents held by the University of Oxford on the use of B-vitamins to treat cognitive disorders (US9364497 and US10966947). These patents have been licensed to Elysium Health, NY. J.S.O.M. has a research contract and equipment loan from ThermoFisher Scientific, which manufactures IC-MS systems. All other authors report no conflicts of interest.

Funding

F.P. is funded by a Dorothy Hodgkin Early Career Fellowship in Chemistry in association with Somerville College. T.K. is funded by an EPSRC Doctoral Training Partnership (EP/W524311/1) and Numares AG (Am Biopark 9, 93053 Regensburg-Graß, Germany). The original VITACOG trial was supported by grants from Charles Wolfson Charitable Trust, Medical Research Council, Alzheimer's Research Trust, Henry Smith Charity, John Coates Charitable Trust, Thames Valley Dementias and Neurodegenerative Diseases Research Network of the National Institute for Health Research, UK, and the Sidney and Elizabeth Corob Charitable Trust. The original OPTIMA cohort was supported by grants from Bristol-Myers Squibb, Medical Research Council and the Charles Wolfson Charitable Trust.

Ethics approval and consent to participate

The trial, registered as VITACOG under the title "*Homocysteine and B Vitamins in Cognitive Impairment*" (ISRCTN 94410159), was conducted in accordance with the principles outlined in the Declaration of Helsinki. Ethical approval was granted by the local NHS research ethics committee (COREC 04/Q1604/100). For OPTIMA, protocols were approved by the Central Oxford Ethics Committee, number 1656. All participants provided written consent after information regarding the study protocol was provided to the participants and in cases of moderate- to severe dementia, also to a caregiver.

Data access and availability

Anonymised data will be made available by request from any qualified investigator.

Acknowledgement

The authors thank all patients participating in this study and the NMR and MS Research Facility (Department of Chemistry, University of Oxford) for use of equipment and advice.

Supplementary Information – Manuscript 2

Supplementary Information

Formic Acid pre-treatment Enhances Untargeted Serum and Plasma Metabolomics

Tereza Kacerova[1], Elisabete Pires[1], Abigail Dixon[1], Rachel Williams[1], Isabelle Legge[1], Mia Hippisley[1], Abi G. Yates[1,2], A. David Smith[2], Daniel C. Anthony[2], Fay Probert[1], James S. O. McCullagh[1]*

[1] Chemistry Research Laboratory, Department of Chemistry, University of Oxford, Oxford OX1 3TA, UK

[2] Department of Pharmacology, University of Oxford, Oxford OX1 3QT, UK

Corresponding author: James S. O. McCullagh james.mccullagh@chem.ox.ac.uk

Supplementary Information – Manuscript 2

1 eMethods

1. 1 Plasma metabolite extraction

For all experiments, fresh human plasma from Research Donors (Cambridge Bioscience, UK) was used. The plasma aliquots were thawed at 4°C. All samples were prepared in replicates of five and each MS injection was repeated twice in random order. Metabolites from human plasma were extracted by adding formic acid (Merck, ≥95%) to achieve the required concentration (0.01-5.00% were tested). The samples were then vortexed, extracted in acetonitrile (1 : 2.33 (v/v)), and centrifuged (16 000 x g; 15 min, 4°C). The supernatant was transferred into the total-recovery MS vials. For albumin experiments, bovine serum albumin (Merck, ≥98%) was either dissolved in Milli Q water or added to plasma (incubation time 3h) to achieve a final concentration of 150 µM in plasma.

1. 2 Clinical serum samples (VITACOG and OPTIMA) metabolite extraction

The serum aliquots were thawed at 4°C and the samples were visually checked for any protein precipitation. All serum samples were processed for a parallel NMR and multi-LC-MS analysis, according to well-established protocol. 405 µL of the sample was then diluted with 50 µL of 75 mM sodium phosphate buffer prepared in D_2O (pH 7.4). For the first sample set (acetonitrile) 75 µL of the resulting sample was mixed with 200 µL of acetonitrile to precipitate any residual protein. The samples were vortexed for 1 min, centrifuged (16 000 x g; 15 min, 4°C), and the supernatant was transferred into total-recovery MS vials. For the second sample set; 0.78 µL of formic acid was added to the mixture of serum and deuterated phosphate buffer. The samples were vortexed for 1 min and the resulting sample was mixed with 200 µL of acetonitrile to precipitate any residual protein. The samples were vortexed for 1 min, centrifuged (16 000 x g; 15 min, 4°C), and the supernatant was transferred into total-recovery MS vials.

1. 3 Total protein content measurement

Total protein concentrations for each extraction method were quantified using the Pierce™ Rapid Gold BCA Protein Assay Kit-1 (Thermo Fisher Scientific, UK). Supernatants (µg μL^{-1}) were mixed with working reagent in a 1:20 ratio (sample:reagent), and absorbance at 480 nm was measured using a ClarioStar Plus microplate reader (BMG LABTECH, Germany) with an LVis plate.

1.4 Reversed-Phase Ultra Performance Liquid Chromatography (RPLC)-MS Analysis

C18 reversed-phase analysis was performed using an Acquity UPLC liquid chromatograph (produced by Waters, UK) system with a gradient elution program coupled directly to a high-resolution tandem mass spectrometer, Xevo G2-XS QTOF. A 5 µL partial loop injection was used for all analyses with pre- and post-injection wash programs. The technical details have been previously published in [Kacerova *et al., Anal Chim Acta*, 2025, PMID 40288864].

1.5 Anion-Exchange Chromatography (AEC)-MS Analysis

Anion-exchange chromatography-MS (AEC-MS) analysis was carried out using a Dionex ICS-5000+ high-pressure ion chromatography system with a continuously regenerated trap column, Dionex ERS 500e suppressor and AS11-HC (2 × 250 mm, 4 µm) column, all from Dionex (Sunnyvale, CA, USA). The technical details have been previously published in [Walsby-Tickle *et al., Commun Biol.,* 2020, PMID 32433536].

1.6 Hydrophilic Interaction Liquid Chromatography (HILIC)-MS Analysis

The samples were analysed using an Atlantis Premier BEH Z-HILIC column (1.7µm, 2.1 x 150 mm) on an Ultimate 3000 LC system coupled to an Orbitrap Exploris™ 240 mass spectrometer in H-ESI mode. Eluent A was 100% Acetonitrile and Eluent B was 5mM Ammonium Formate in Type-1 water. A gradient program was used as follows: 0 mins – 5% B; 2 mins – 5% B; 6 mins – 15% B; 14 mins – 60% B; 15 mins – 60% B; 16 mins – 5% B; 30 mins – 5% B at a flow rate of 0.4 mL/min. The column temperature was 50 °C and the autosampler was kept at 4 °C with an injection volume of 5 µL.

The samples were analysed in positive ion mode with a top 10 data dependent acquisition MS2 approach. The spray voltage was 3500 V and the gas flow rates were 25, 8, and 0 for the sheath gas, aux gas, and sweep gas respectively. The ion transfer tube and vapouriser temperatures were both 300 °C. The full scan resolution was 60,000 with a scan range of 60-900 *m/z*. The microscans were set to two with the AGC target set to 5e6 and the maximum injection time set to 120 ms. The ddMS2 resolution was 15,000 with an isolation window of 2 *m/z* and the normalised HCD collision energy was 35%. 2 microscans were used with the AGC target set to 1e5 and the maximum injection time set to 80 ms.

1.7 MALDI-TOF MS Analysis

Sinapinic acid (SA) was prepared at a concentration of 10 mg/mL in a solvent mixture comprising 50% (v/v) acetonitrile, 50% (v/v) water, and 0.3% (v/v) trifluoroacetic acid (TFA). The solution was vortexed for 1 minute, sonicated for 15 minutes, and vortexed again for 1 minute to ensure complete dissolution.

For MALDI-TOF MS analysis, 3 µL of each sample was mixed with 3 µL of the SA matrix solution. A volume of 1.5 µL of the resulting mixture was spotted onto a 384-position ground steel MALDI target plate and air-dried at room temperature. Calibration spots containing bovine serum albumin (BSA, 66,414 Da) were prepared using the same protocol. Mass spectra were acquired using a MALDI Autoflex Speed mass spectrometer (Bruker Daltonics, Bremen, Germany), equipped with an Nd:YAG laser (355 nm) operating at a repetition rate of up to 2 kHz. The instrument was operated in linear positive ion mode under the following settings: mass range 30–210 kDa, sampling rate 0.16 GS/s, 1000 laser shots per spectrum, 100% laser power, 100 Hz laser frequency, and 25 kV detector gain. External mass calibration was performed using BSA. Spectral data were processed using FlexAnalysis software (Bruker Daltonics).

1.8 Data Processing

The untargeted metabolomics data were processed in Progenesis QI (Nonlinear Dynamics, Waters, Elstree, UK), and the detected compound-features were compared between the different extraction methods, primarily focusing on the total number of detected compound-features and their associated % coefficient of variance (%CV) for evaluating the efficacy of sample preparation efficiency across independent datasets.

Metabolite identification was based on matching multiple experimental data to metabolite databases. In-house libraries of over 450 (IC-MS) and 150 (RPLC-MS) authentic metabolite standards with matching of multiple independent measurements under the same experimental conditions to provide Level 1 identifications (e.g. retention time (Rt error < 2 min; accurate-mass < 5 ppm (IC-MS) and 20 ppm (RPLC-MS); isotope and fragmentation patterns > 90%).

1.9 Statistical analysis

The %CV filtered (30% cut-off) data exported from Progenesis were processed in MetaboAnalyst 6.0 and R software 4.2.1 (R Foundation for Statistical Computing, Vienna, Austria), using the *corrr*, *ggplot2*, *ggpubr*, and *dplyr* packages. The datasets were median normalised, Pareto scaled and log transformed. Univariate statistical analysis included determining fold change (FC) and *t* test *p* values between different extraction methods for compound-features and combined in volcano plots. The FC threshold was set to 2 and the *p* value cut-off was set to 0.05 to determine significance. The data were projected using an unsupervised principal component analysis (PCA), which allowed the similarities within the individual datasets to be shown. The significance cut-off was set at $p < 0.05$ for all data sets. To maximise the likelihood of identifying potential differences between extraction methods, multiple testing corrections such as false discovery rate (FDR) were generally not applied.

To assess metabolomic differences between treated individuals and placebo controls, we applied logistic regression with elastic net regularisation and orthogonal partial least squares discriminant analysis (OPLS-DA), adapted from previously published work. Each data point in the resulting multivariate plots represents the serum metabolomic profile of a specific individual with mild cognitive impairment (MCI). The dataset was split into two classes, and feature selection was performed on the training set during each fold. Elastic net regularisation ($\alpha = 0.5$) with cross-validation was used to determine the optimal regularisation parameter (λ), and features were selected based on non-zero coefficients from the regularised logistic regression model.

For OPLS-DA, 10-fold cross-validation with repetition and permutation testing was used to mitigate overfitting. Each model was tested using an independent subset of samples excluded from the training set, allowing for the assessment of model accuracy, sensitivity, and specificity. To validate feature selection and classification performance, randomised null models were generated by shuffling class labels. If the final model ensemble significantly outperformed 1000 null models (two-sided Kolmogorov–Smirnov test, $p < 0.05$), discriminatory compound-features were extracted by averaging Variable Importance in Projection (VIP) scores across models. Features were ranked within each model, and their overall importance was calculated as the frequency of selection divided by the average rank, prioritising variables that were consistently selected and highly ranked across iterations.

Supplementary Information – Manuscript 2

2 eMethods – The description of clinical cohorts

2.1 OPTIMA

The Oxford Project to Investigate Memory and Ageing (OPTIMA) is a longitudinal study of cognitive decline in ageing individuals. For this analysis, we used a subset of 29 Alzheimer's disease (AD) and 34 vascular dementia (VaD) patients from the OPTIMA cohort, matched for Mini-Mental State Examination (MMSE) scores above 20, indicating mild to moderate cognitive impairment. These were archived serum samples from a subsample previously selected for omics analyses, used here as a proof-of-concept to evaluate and optimise the extraction protocols.

2.2 VITACOG

The VITACOG trial was a randomised, placebo-controlled study investigating the effects of B-vitamin supplementation on brain atrophy in individuals with mild cognitive impairment. For this analysis, we selected stored serum samples from 30 participants who received B-vitamin treatment and showed a slowed rate of brain atrophy, and 30 placebo-treated individuals who exhibited accelerated atrophy over the study period. These represent extreme phenotypes within the trial population and were used to explore the performance of the extraction protocols under contrasting biological conditions.

2.3 Participants consent and trials registration

The VITACOG trial was conducted according to the principles described in the Declaration of Helsinki. The study was approved by a local NHS research ethics committee (COREC 04/Q1604/100). Each involved individual provided written consent for their participation. For OPTIMA, full ethics committee approval was obtained for collection of clinical data (Frenchay REC Ref 09/H0107/9) and for use of brain tissue for research (Oxford REC 07/H0606/85 for use of tissue in the Thomas Willis Oxford Brain Collection).

Supplementary Information – Manuscript 2

3 Results

3.1 FA pre-treatment improves extraction reproducibility and efficiency in serum and phosphate-buffered serum

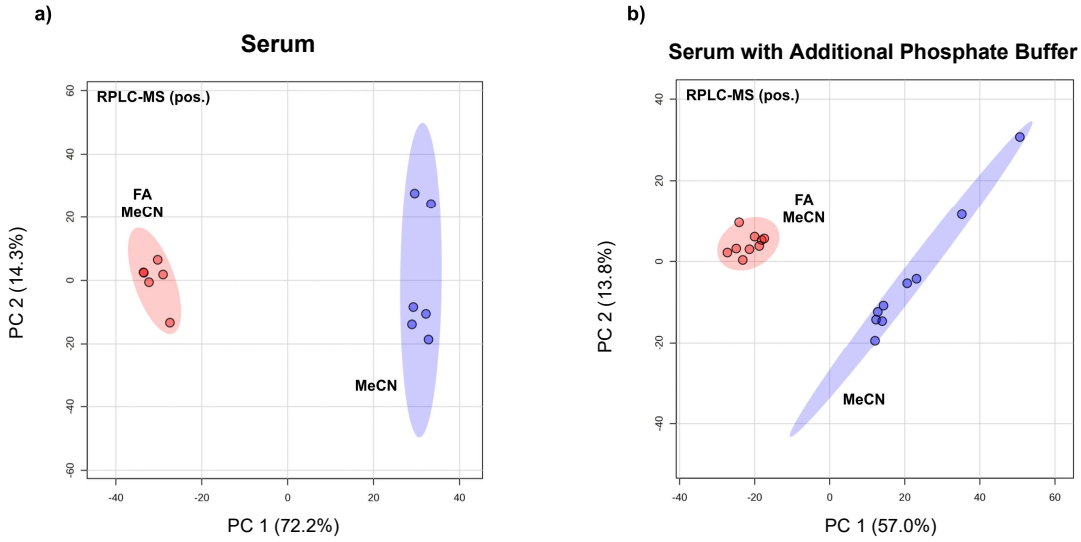

SI Figure 1. PCA analysis of FA–MeCN versus MeCN-only extraction in serum and phosphate-buffered serum. PCA plots showing the effect of extraction method on sample clustering in **(a)** unmodified serum and **(b)** serum supplemented with deuterated phosphate buffer. Samples were extracted using either MeCN-only (blue) or FA pre-treatment followed by MeCN (FA–MeCN; red) and analysed by RPLC-MS in pos. ionisation mode. Each panel represents $n = 5$ replicate extractions from the same serum pool.

3.2 Mechanistic insights: extraction effects

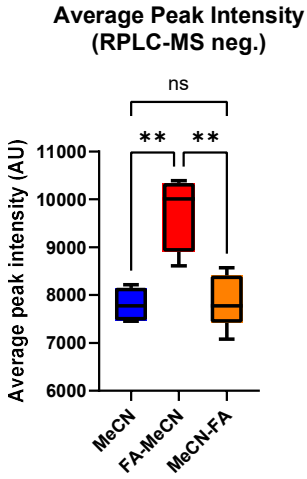

SI Figure 2. Box plots comparing average peak intensities (%CV < 30) across three extraction strategies: MeCN alone, FA pre-treatment followed by MeCN extraction (FA–MeCN), and post-spiking with FA after MeCN extraction (MeCN–FA), (**p < 0.01; ns = not significant; one-way ANOVA with *post hoc* test). The panel is based on $n = 5$ sample preparation replicates per condition. The analysis was conducted using RPLC-MS in neg. ionisation mode.

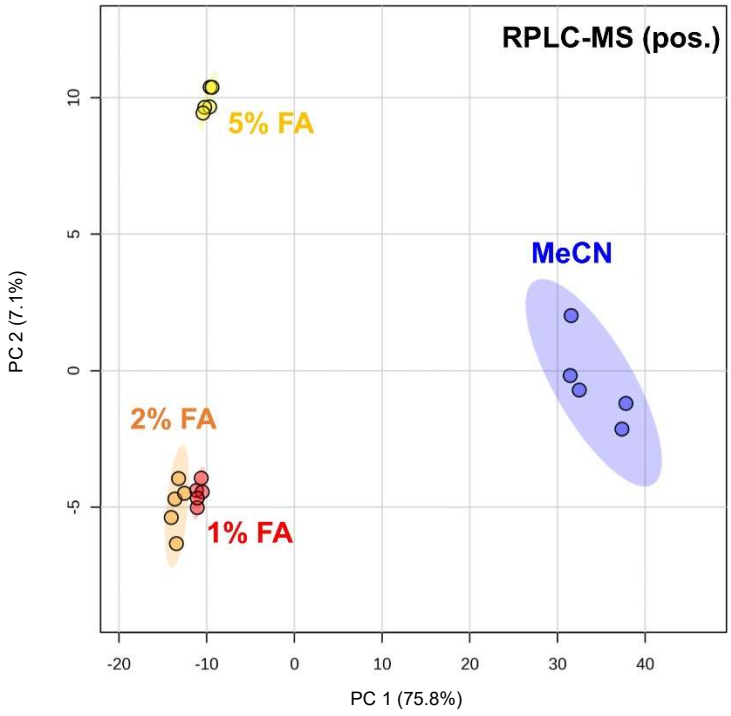

SI Figure 3. PCA plot of RPLC–MS (pos. ionisation mode) data comparing protein precipitation using MeCN alone versus FA pre-treatment at increasing concentrations (1%, 2%, and 5% v/v). While FA pre-treatment markedly improves clustering compared to MeCN alone, higher concentrations (>1%) do not result in further gains in reproducibility. Based on these findings, 1% FA was selected as the optimal concentration (considering also instrument compatibility, as FA is further diluted in the mobile phase prior to entering the ion source).

3.3 Mechanistic insights: extraction effects

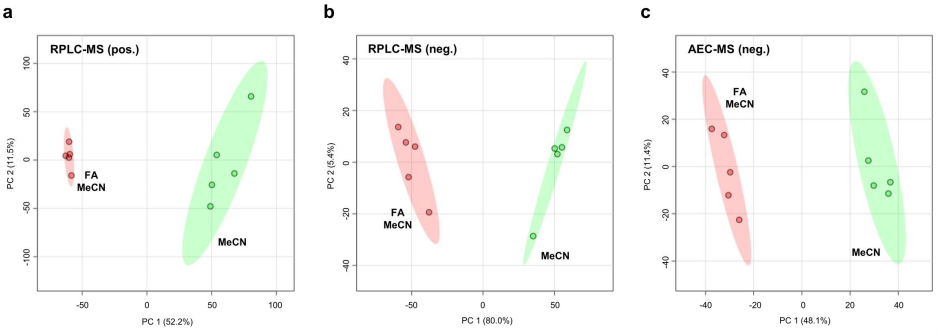

SI Figure 4. Impact of Formic Acid on Plasma Extraction Efficiency and Reproducibility. (a–c) PCA plots highlighting clustering patterns between acetonitrile (MeCN, green) and FA and acetonitrile (FA-MeCN; red) extractions. **(a)** RPLC-MS (pos. ionisation mode), a significant impact of FA treatment on the extraction reproducibility; **(b)** RPLC-MS (neg. ionisation mode); **(c)** AEC-MS (neg. ionisation mode). All extractions were prepared in five replicates.

3.4 Assessment of Adduct Formation Following Formic Acid Extraction

Adduct profiles were evaluated using the *Progenesis QI* software (Nonlinear Dynamics, Waters, Elstree, UK), which applies automated peak picking followed by adduct deconvolution based on accurate mass differences and isotope pattern matching. The analysis included typical adducts observed in electrospray ionisation, and the assignment was carried out with the default adduct library for both positive and negative ion modes, with tolerance settings of 5 ppm for precursor mass and 20 ppm for fragment ions. Only features consistently detected across replicates (%CV<30) were included in the final comparison.

SI Table 1. Summary of common adducts detected in **RPLC-MS (positive ion mode)** following extraction with either MeCN alone or 1% formic acid (FA) followed by MeCN. The table includes the theoretical mass shifts ($\Delta m/z$) for each adduct relative to the neutral monoisotopic mass (M), along with the number of features assigned to each adduct using Progenesis QI. Adducts were automatically annotated based on accurate mass and isotope pattern matching within a 5 ppm tolerance. Dimeric adducts and multiply charged species are also included.

Adduct	$\Delta m/z$ (Da)	MeCN (Count)	FA (Count)
M+Na	+22.989218	712	726
M+K	+38.963158	429	445
M+MeCN+H	+42.033823	275	286
M+MeCN+Na	+64.022842	114	121
M+Na+H	+23.997037	179	180
M+FA+H	+46.005479	370	384
M+H-H_2O	–18.010565	381	401
M+2H	+2.014552 ($z = 2 \rightarrow m/z = (M + 2H)/2$)	164	163
2M+H	+M + 1.007276	58	57
2M+Na	+M + 22.989218	86	87
2M+K	+M + 38.963158	70	74

SI Table 2. Summary of common adducts detected in **RPLC-MS (negative ion mode)** following extraction with either MeCN alone or 1% formic acid (FA) followed by MeCN. The table lists theoretical mass shifts ($\Delta m/z$) for each adduct relative to the neutral monoisotopic mass (M), along with the number of features annotated using Progenesis QI. Adducts were identified using accurate mass and isotope pattern matching with a 5 ppm mass tolerance. Deprotonated species, water loss, chloride adducts, and dimeric ions are included.

Adduct	$\Delta m/z$ (Da)	MeCN (Count)	FA (Count)
M-H-H_2O	–19.017841	180	157
M+FA-H	+44.998203	223	212
M+Na-2H	+20.974666	304	288
M+K-2H	+36.948606	232	209
M+Cl	+34.969402	330	302
2M+FA-H	+M + 44.998203	21	31
2M-H	**+M – 1.007276**	27	25

SI Table S3. Summary of common adducts detected in **AEC-MS (negative ion mode)** following extraction with either MeCN alone or 1% formic acid (FA) followed by MeCN. The table lists theoretical mass shifts (Δ*m/z*) for each adduct relative to the neutral monoisotopic mass (*M*), along with the number of features annotated using Progenesis QI. Adducts were identified using accurate mass and isotope pattern matching with a 5 ppm mass tolerance. Deprotonated species, water loss, chloride adducts, and dimeric ions are included.

Adduct	Δ*m/z* (Da)	MeCN (Count)	FA (Count)
M-H-H_2O	–19.017841	50	50
M+FA-H	+44.998203	27	25
M+Na-2H	+20.974666	14	17
M+K-2H	+36.948606	18	18
M+Cl	+34.969402	27	22
2*M*+FA-H	+*M* + 44.998203	3	3
2*M*-H	**+*M* – 1.007276**	31	29

3.5 Mechanistic insights: protein-metabolite interactions

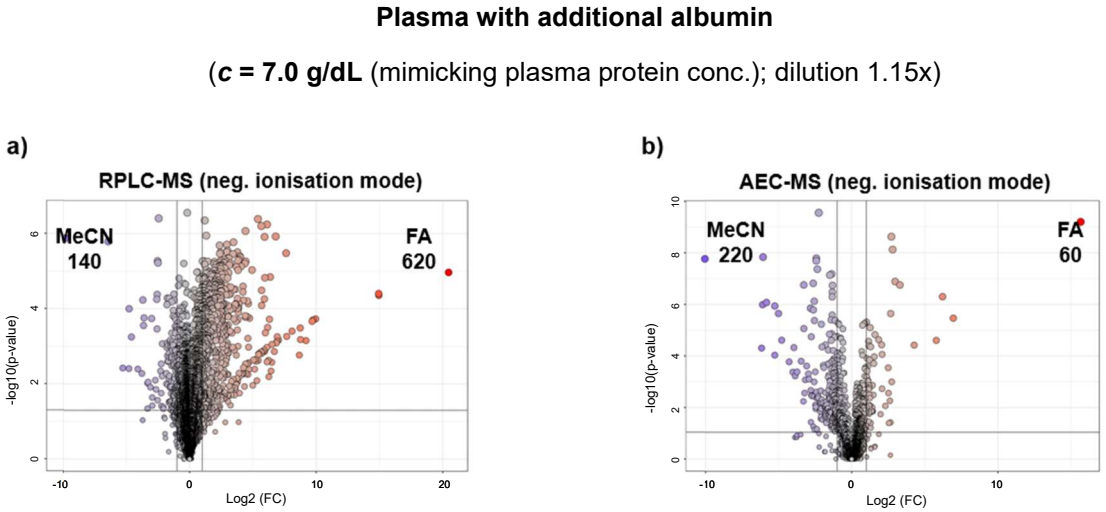

SI Figure 5. Effects of Formic Acid–Protein Interactions on Metabolite Extraction Efficiency. Volcano plots showing differences in compound features between acidified and unacidified plasma samples with additional albumin (c = 7.0 g/dL) (t-test, $p < 0.05$). **(a)** RPLC-MS (neg. ionisation mode). **(b)** AEC-MS (neg. ionisation mode). Each extraction for repeated in five sample replicates.

3.5 Mechanistic insights: protein-metabolite interactions

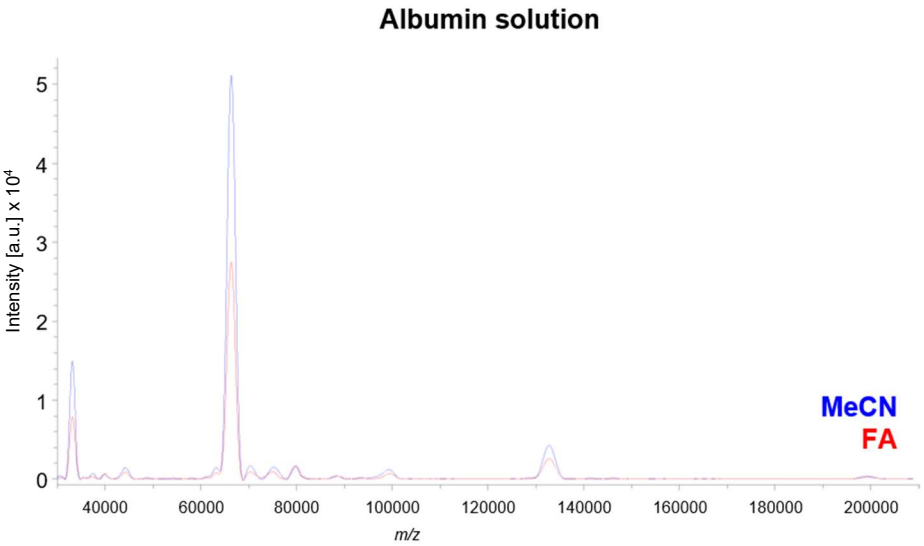

SI Figure 6. MALDI-MS spectra of the albumin protein pellet (aqueous bovine serum albumin (BSA); *c* = 7.0 g/dL) after extraction with MeCN (blue) and FA-MeCN (red). Spectra for the high mass range: 40-200kDa.

3.5.1 MALDI-MS Spectra for lower molecular masses (plasma)

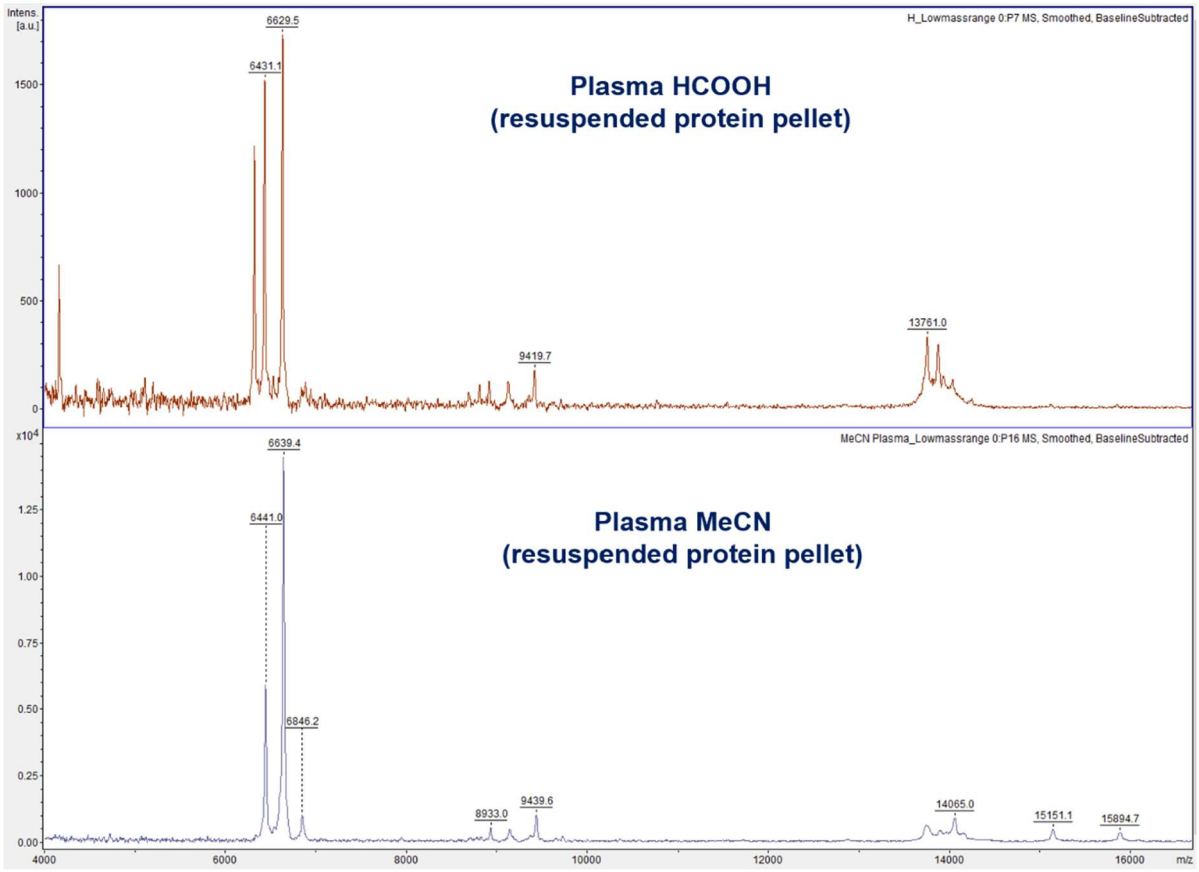

SI Figure 7. MALDI-MS spectra of the plasma protein pellet after extraction with MeCN (top) and FA-MeCN (bottom). Spectra for the low mass range: 4-16kDa.

3.5.2 MALDI-MS Spectra for lower molecular masses (albumin aqueous solution; *c* = 7.0 g/dL)

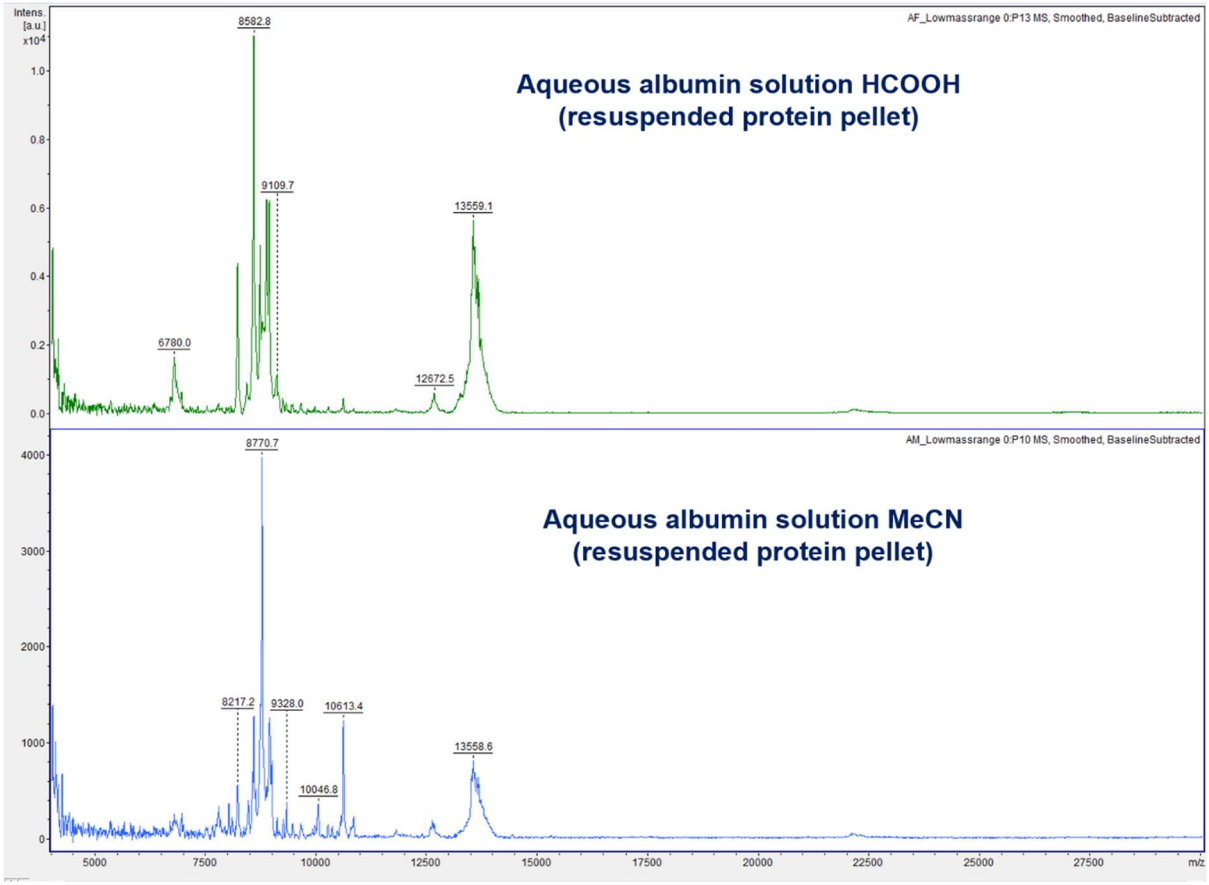

SI Figure 8. MALDI-MS spectra of the albumin protein pellet (aqueous bovine serum albumin (BSA); *c* = 7.0 g/dL) after extraction with MeCN (top) and FA-MeCN (bottom). Spectra for the low mass range: 4-16kDa.

3.5 Mechanistic insights: protein-metabolite interactions

SI Table 4. Compound-features with the lowest *p*-values in unpaired Student's t-tests comparing plasma extracts prepared with FA+MeCN versus MeCN alone (n = 5 replicates per group) in RPLC-MS positive ionisation mode. Positive t-statistic values indicate features more abundant in FA-treated samples. While the compound-features have not been definitively identified, their relatively high m/z values (approximately 280–780 *m/z*) and retention times (predominantly 10–12 minutes in an 18-minute gradient) suggest they are likely lipid-like metabolites, consistent with the enhanced recovery of hydrophobic compounds following disruption of protein–metabolite interactions by formic acid pre-treatment.

m/z	retention time (min)	t-statistic	*p*-value	FDR *p*-value
642.3703n	11.95	74.846	1.13E-12	6.53E-09
483.3255m/z	12.24	71.353	1.66E-12	6.53E-09
776.7881m/z	0.72	60.812	5.94E-12	1.56E-08
277.2128m/z	10.25	52.64	1.88E-11	3.71E-08
589.4303m/z	11.76	50.361	2.68E-11	3.84E-08
540.4470m/z	11.76	49.811	2.92E-11	3.84E-08
559.0890m/z	12.18	-47.559	4.23E-11	4.76E-08
588.2308n	9.44	44.415	7.29E-11	7.18E-08
406.3112n	11.42	41.912	1.16E-10	9.57E-08
545.4071m/z	12.51	41.662	1.21E-10	9.57E-08
635.3883m/z	11.95	40.968	1.39E-10	9.94E-08
689.0338m/z	12.22	-39.52	1.85E-10	1.17E-07
545.7428m/z	14.26	-39.034	2.04E-10	1.17E-07
486.8645m/z	13.42	-38.76	2.16E-10	1.17E-07
567.0929m/z	12.42	-38.613	2.22E-10	1.17E-07
565.0940m/z	12.2	-38.151	2.45E-10	1.21E-07
421.3404m/z	10.83	37.773	2.65E-10	1.23E-07
619.3092m/z	11.5	37.32	2.92E-10	1.27E-07
567.2511m/z	9.44	37.082	3.07E-10	1.27E-07
663.4587m/z	12.61	36.667	3.36E-10	1.32E-07
623.0654m/z	12.17	-35.948	3.93E-10	1.43E-07
459.3251m/z	12.46	35.863	4.00E-10	1.43E-07
657.1246m/z	12.63	-35.393	4.45E-10	1.52E-07
473.3456m/z	11.04	35.14	4.71E-10	1.55E-07
510.3564m/z	11.52	34.341	5.65E-10	1.78E-07
485.3357m/z	11.09	34.085	6.00E-10	1.81E-07
551.4270m/z	11.95	33.919	6.24E-10	1.81E-07
631.0758m/z	12.24	-33.741	6.50E-10	1.81E-07
508.3752m/z	11.73	33.639	6.66E-10	1.81E-07
625.4655m/z	12.51	33.509	6.87E-10	1.81E-07

3.5 Mechanistic insights: protein-metabolite interactions

SI Table 5. Comparison of proteinogenic amino acid levels in acetonitrile and formic acid–spiked acetonitrile extracts (HILIC-MS data). A total of 15 proteinogenic amino acids were detected, of which 4 showed significant differences (uncorrected *p*-values; no FDR adjustment to maximise sensitivity). All significantly altered amino acids were decreased in the acidified extracts, suggesting that the addition of formic acid does not promote cleavage of protein–peptide bonds to release free amino acids.

Amino acid	*p*-value
Alanine	0.911
Arginine	0.320
Glutamine	0.022
Glycine	0.021
Histidine	0.247
Isoleucine	0.147
Leucine	0.496
Lysine	0.157
Methionine	0.332
Phenylalanine	0.013
Proline	0.624
Serine	0.764
Tryptophan	0.012
Tyrosine	0.095
Valine	0.441

3.6 Case Studies – OPTIMA and VITACOG

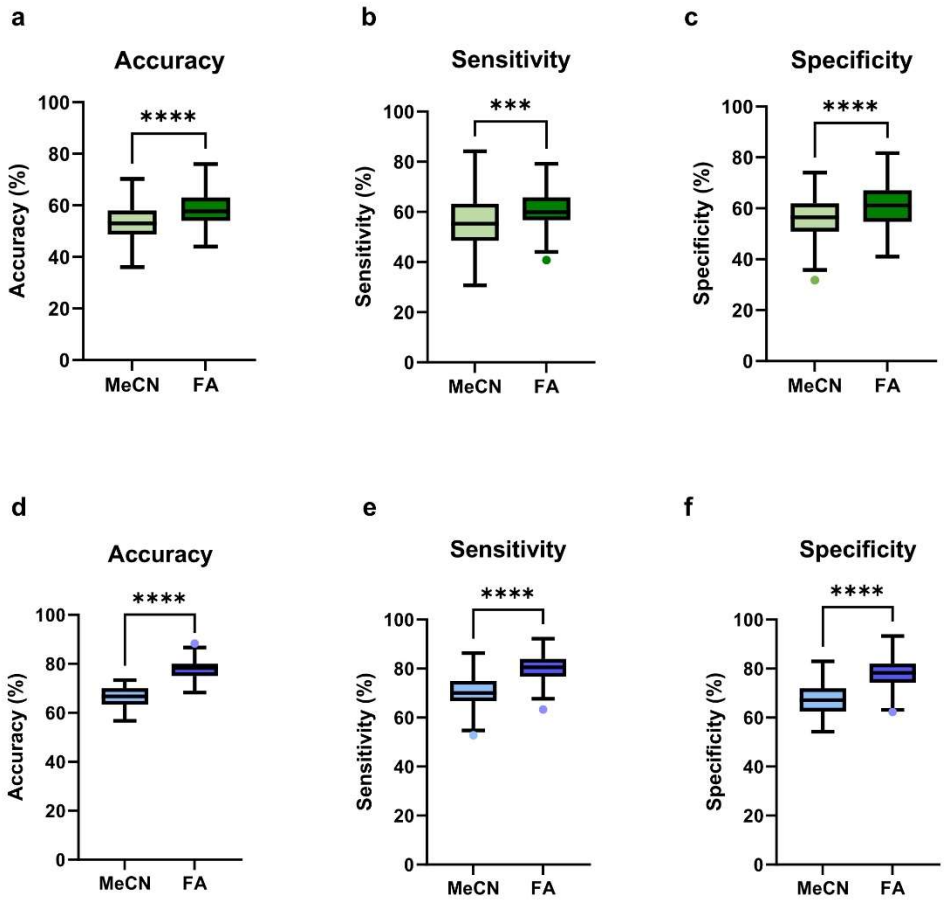

SI Figure 9. Formic acid–based extractions enhance the discriminatory capacity of supervised multivariate statistical models (orthogonal partial least squares discriminant analysis, OPLS-DA), as demonstrated in two independent cohorts: OPTIMA (early vascular dementia vs. early Alzheimer's disease) and VITACOG (vitamin B-treated patients vs. placebo controls). **(a–c)** Results for the OPTIMA cohort; **(d–f)** Results for the VITACOG cohort. Each panel compares accuracy, sensitivity, and specificity across 1000 diagnostic models constructed using either acetonitrile-based or formic acid–based extraction protocols.

- (a) OPTIMA accuracy ($p = 4.31\times10^{-6}$)
- (b) OPTIMA sensitivity ($p = 4.7\times10^{-4}$)
- (c) OPTIMA specificity ($p = 9.25\times10^{-6}$)
- (d) VITACOG accuracy ($p = 1.45\times10^{-52}$)
- (e) VITACOG sensitivity ($p = 4.18\times10^{-52}$)
- (f) VITACOG specificity ($p = 2.13\times10^{-27}$)

These results highlight the improved model performance achieved with formic acid–based extractions.

3.7 OPTIMA VIP Scores

SI Table 6. List of the variables importance in projection identified from the AD vs VaD model (OPTIMA) for the MeCN-based extractions.

Rank	Compound-feature	Frequency	Average rank	Overall score
1	13.66_615.1469 m/z	533	8.6	62.3
2	2.80_114.0921 m/z	367	6.4	57.7
3	13.66_610.1929 m/z	470	10.7	43.9
4	8.30_244.2634 m/z	567	13.3	42.7
5	0.88_218.1398 m/z	650	17.5	37.2
6	7.08_255.5784 m/z	256	7.2	35.7
7	7.10_155.5415 m/z	288	8.1	35.6
8	8.56_153.0574 m/z	655	18.7	35.1
9	10.34_375.2855 m/z	618	18.0	34.4
10	0.79_132.0787 m/z	622	18.2	34.2
11	0.77_114.0678 m/z	599	18.2	32.8
12	0.77_114.0678 m/z	601	18.4	32.6
13	12.20_400.3476 m/z	592	19.6	30.2
14	0.79_136.0497 m/z	584	19.5	30.0
15	8.30_579.6032 m/z	281	10.0	28.1
16	7.92_370.0968 m/z	248	10.0	24.9
17	4.61_218.2116 m/z	183	7.7	23.8
18	5.97_212.0201 m/z	330	14.1	23.4
19	10.87_256.0872 m/z	204	8.8	23.2
20	0.88_231.0862 m/z	227	10.6	21.5
21	6.84_475.1081 m/z	201	9.5	21.1
22	8.35_597.4737 m/z	194	9.4	20.6
23	7.10_169.0647 m/z	218	10.9	20.0
24	7.75_477.1235 m/z	224	11.5	19.4
25	5.44_221.0128 m/z	160	8.3	19.2

Supplementary Information – Manuscript 2

SI Table 7. List of the variables importance in projection identified from the AD vs VaD model (OPTIMA cohort) for the FA-MeCN-based extractions.

Rank	Compound-feature	Frequency	Average rank	Overall score
1	9.12_316.3179 m/z	701	10.1	69.2
2	11.74_561.4805 m/z	362	6.0	60.6
3	11.50_281.2698 n	723	13.6	53.2
4	4.55_715.0295 m/z	446	9.8	45.6
5	4.55_856.8306 m/z	437	11.0	39.6
6	11.28_737.2232 m/z	334	9.2	36.3
7	7.49_249.1125 m/z	363	10.3	35.4
8	8.56_219.0681 m/z	289	8.6	33.7
9	12.46_662.6014 m/z	290	9.9	29.2
10	13.56_782.5610 m/z	600	20.8	28.8
11	13.51_806.5595 m/z	571	22.2	25.8
12	13.70_806.5598 m/z	570	22.3	25.5
13	11.21_521.3447 n	559	23.2	24.1
14	11.69_523.3588 n	562	23.6	23.8
15	11.02_495.3289 n	549	23.6	23.3
16	14.83_674.5643 m/z	551	23.7	23.2
17	4.68_269.9842 m/z	194	8.4	23.1
18	4.56_868.0168 m/z	298	13.2	22.6
19	10.32_270.6484 m/z	434	20.3	21.4
20	3.70_340.2595 m/z	227	10.8	21.1
21	4.68_237.9590 m/z	230	12.2	18.9
22	6.29_796.9330 m/z	227	12.1	18.8
23	2.80_114.0928 m/z	190	10.4	18.3
24	6.55_182.1191 m/z	311	18.8	16.6
25	6.31_797.2667 m/z	159	9.6	16.6

3.8 VITACOG VIP Scores

SI Table 8. List of the variables importance in projection identified from the B vitamin-treated vs placebo model (VITACOG cohort) for the MeCN-based extractions.

Rank	Compound-feature	Frequency	Average rank	Overall score
1	11.90_514.3414 m/z	900	4.3	208.7
2	12.12_559.4056 m/z	460	3.3	138.6
3	10.51_271.1641 m/z	997	7.3	136.7
4	12.43_552.3962 m/z	397	3.3	122.0
5	10.71_417.7710 m/z	1000	9.8	102.0
6	9.89_293.2102 m/z	951	11.2	85.3
7	10.53_841.5444 m/z	366	5.0	73.2
8	11.47_839.5645 m/z	285	4.0	71.9
9	4.12_481.2622 m/z	662	9.4	70.2
10	10.54_885.5721 m/z	731	11.4	64.3
11	10.51_270.6550 m/z	738	12.2	60.3
12	11.01_519.8367 m/z	108	1.8	60.1
13	3.76_467.0084 m/z	284	5.0	56.7
14	5.90_236.1049 n	527	9.5	55.5
15	12.68_871.5632 m/z	112	2.1	53.6
16	0.65_127.0129 n	654	12.3	53.0
17	10.51_410.7730 m/z	129	2.7	48.1
18	18.00_123.0574 m/z	613	12.8	47.8
19	15.87_149.9562 m/z	112	2.4	45.8
20	3.28_484.5266 m/z	785	17.6	44.6
21	0.64_96.9622 m/z	981	22.4	43.8
22	8.66_250.1221 n	539	13.0	41.5
23	3.28_484.2760 m/z	757	18.7	40.5
24	11.42_783.9943 m/z	934	23.5	39.8
25	7.25_247.1219 m/z	753	19.2	39.2

SI Table 9. List of the variables importance in projection identified from the B vitamin-treated vs placebo model (VITACOG cohort) for the FA-MeCN-based extractions.

Rank	Compound-feature	Frequency	Average rank	Overall score
1	9.68_261.1482	1000	1.8	370.8
2	9.66_239.1683	310	1.1	287.6
3	7.18_837.6481	910	3.5	157.2
4	4.60_247.0146	1000	4.7	152.2
5	4.65_682.2554	935	5.6	139.6
6	7.18_838.2505	489	3.2	119.6
7	9.27_553.2105	228	1.7	110.4
8	7.18_838.4518	991	8.1	104.0
9	7.44_398.2472	995	10.4	95.9
10	9.53_410.2644	812	9.0	80.3
11	11.52_286.2388	182	2.4	76.3
12	7.75_166.0669 n	807	11.3	73.6
13	9.98_373.2453	959	13.4	64.5
14	10.87_796.9837	852	14.3	58.2
15	4.60_199.1359	978	17.0	56.7
16	4.65_685.2611	1000	18.7	49.6
17	0.73_218.9237	379	7.6	47.0
18	4.53_742.3158	67	1.3	43.7
19	7.44_376.2652	1000	22.3	42.4
20	4.44_472.2446	989	22.3	40.4
21	12.85_843.5655	626	14.3	38.5
22	8.97_365.1435	286	7.2	33.7
23	7.89_684.1699	581	15.6	31.8
24	12.96_603.5229	287	7.8	30.6
25	12.65_848.5702	944	27.7	30.2

SI Table 10. Comparison of compound-features extracted using FA-based and pure acetonitrile-based protocols. The compound-features were selected based on their associated VIP scores for the vitamin B-treated individuals (VB) vs placebo controls (P) model constructed using the FA-based extraction data. The table includes the median %CV (calculated from pooled QC samples), mean fold change (VB/P) for both extraction methods, and significance levels from unpaired two-sample t-tests comparing VB and P abundance (p-values: ***$p < 0.001$, **$p < 0.01$, *$p < 0.05$). Additionally, it reports the FA/MeCN mean abundance ratio, with associated t-test results (same p-value thresholds). Curation criteria for matching compound features between datasets included: retention time (Rt) error < 60 s, accurate mass error < 20 ppm, and isotope/fragmentation patterns match > 90%. Annotations: NA = compound-feature not detected; NA† = compound-feature not detected in any other analysed dataset; NA‡ = compound-feature not detected in acetonitrile-extracted clinical samples but detected in FA-based serum standards. For detailed t-test results, abundance and %CV data (for individual analytical subgroups), refer to SI Tables 7 and 8.

FA Protocol					MeCN Protocol	
Variable *Rt_m/z*	VIP Score	%CV	FC (VB/P)	Abundance ratio (FA/MeCN)	%CV	FC (VB/P)
9.68_261.1482	370.8	10.41	3.397***	0.79***	12.83	1.628***
9.66_239.1683	287.6	10.53	3.448***	0.74***	13.59	1.630***
7.18_837.6481	157.2	14.64	2.005*	NA†	NA†	NA†
4.60_247.0146	152.2	12.65	0.521*	NA‡	NA‡	NA‡
4.65_682.2554	139.6	16.22	1.444**	0.72***	7.70	1.262ns
7.18_838.2505	119.6	12.77	0.255***	3.02***	11.23	0.819ns
9.27_553.2105	110.4	13.65	0.599*	NA‡	NA‡	NA‡
7.18_838.4518	104.0	13.81	0.284***	1.93***	11.20	0.777**
7.44_398.2472	95.9	10.74	2.863***	0.80**	7.90	1.627***
9.53_410.2644	80.3	10.28	3.091***	1.04***	10.72	1.586***
11.52_286.2388	76.3	10.57	1.961***	4.58***	17.48	0.911ns
7.75_166.0669 n	73.6	21.37	0.567***	0.46***	6.74	0.775**
9.98_373.2453	64.5	14.71	0.514***	NA‡	NA‡	NA‡
10.87_796.9837	58.2	10.34	0.695**	0.33***	5.73	0.715***
4.60_199.1359	56.7	10.73	0.843ns	0.86ns	9.29	1.551**
4.65_685.2611	49.6	21.07	0.336*	1.96***	24.52	0.922ns
0.73_218.9237	47.0	17.46	0.848**	0.08***	6.46	0.675***
4.53_742.3158	43.7	10.36	0.818ns	0.13***	6.34	0.674ns
7.44_376.2652	42.4	19.67	5.967***	0.59***	9.12	1.963***
4.44_472.2446	40.4	16.33	0.756*	0.28***	4.14	1.003ns
12.85_843.5655	38.5	10.37	0.893*	0.30***	11.10	0.777***
8.97_365.1435	33.7	16.74	1.749***	5.18***	17.97	0.524***
7.89_684.1699	31.8	15.65	2.143ns	NA‡	NA‡	NA‡
12.96_603.5229	30.6	14.61	0.837**	0.98*	15.31	0.616***
12.65_848.5702	30.2	10.65	1.008ns	1.92***	9.60	0.634ns

We compared the top 20 compound-features (by VIP score) detected in both FA- and MeCN-extracted datasets. No consistent pattern was observed in their abundance or %CV, with FA treatment leading to both increases and decreases depending on the compound-feature. The average %CV in QC samples was significantly lower in MeCN extracts ($p = 0.026$), and 12 of the 20 features showed higher abundance in MeCN. However, OPLS-DA separation is likely driven more by relative differences and reduced background noise than absolute abundance. Fold-changes between treated and placebo groups were enhanced in FA-treated samples (Table 6, SI Table 8), suggesting improved capture of biologically relevant variation through this extraction protocol (FC $p = 0.007$ (for FC < 1; the reversed value (1/FC) was used for p value calculations).

Supplementary Information – Manuscript 2

SI Table 11. Compound-features with the highest VIP scores in the comparison between the vitamin B-treated (VB) and placebo (P) groups, based on FA-extracted data. The table includes the coefficient of variance (%CV) for the pooled QC samples, as well as for two sets of analytical samples: one set consisting only of vitamin B-treated individuals and another consisting only of placebo controls. The %CV values are provided for both FA-based and pure acetonitrile extractions. Curation criteria for matching compound features between datasets included: retention time (Rt) error < 60 s, accurate mass error < 20 ppm, and isotope/fragmentation patterns match > 90%. Annotations: NA = feature not detected; NA† = feature not detected in any other analysed dataset; NA‡ = feature not detected in acetonitrile-extracted clinical samples but detected in FA-based serum standards.

Variable *Rt_m/z*	FA			MeCN		
	%CV QC	%CV VB	%CV Placebo	%CV QC	%CV VB	%CV Placebo
9.68_261.1482	10.41	59.25	124.13	12.83	83.89	32.61
9.66_239.1683	10.53	52.33	103.73	13.59	79.75	49.98
7.18_837.6481	14.64	50.01	68.37	NA†	NA†	NA†
4.60_247.0146	12.65	109.35	92.42	NA‡	NA‡	NA‡
4.65_682.2554	16.22	211.9	181.88	7.70	63.78	48.37
7.18_838.2505	12.77	127.21	178.12	11.23	60.40	57.13
9.27_553.2105	13.65	74.11	81.11	NA‡	NA‡	NA‡
7.18_838.4518	13.81	133.01	175.72	11.20	55.91	48.14
7.44_398.2472	10.74	60.03	52.2	7.90	53.55	57.17
9.53_410.2644	10.28	82.07	79.48	10.72	40.94	34.92
11.52_286.2388	10.57	33.99	66.49	17.48	189.17	55.95
7.75_166.0669 n	21.37	85.93	57.12	6.74	73.69	57.33
9.98_373.2453	14.71	73.47	50.16	NA‡	NA‡	NA‡
10.87_796.9837	10.34	122.27	73.04	5.73	88.92	34.27
4.60_199.1359	10.73	46.31	81.64	9.29	32.57	80.21
4.65_685.2611	21.07	103.2	90.19	24.52	67.35	50.14
0.73_218.9237	17.46	131.2	137.48	6.46	14.82	20.82
4.53_742.3158	10.36	75.65	64.4	6.34	82.733	77.91
7.44_376.2652	19.67	126.68	125.36	9.12	47.95	67.18
4.44_472.2446	16.33	60.64	57.51	4.14	71.34	46.17
12.85_843.5655	10.37	52.71	32.76	11.1	38.56	44.30
8.97_365.1435	16.74	55.21	169.08	17.97	237.17	260.03
7.89_684.1699	15.65	75.23	104.52	NA‡	NA‡	NA‡
12.96_603.5229	14.61	49.59	25.28	15.31	27.00	33.82
12.65_848.5702	10.65	44.52	26.05	9.60	79.72	81.18

SI Table 12. Compound-features with the highest VIP scores in the comparison between the vitamin B-treated (VB) and placebo (P) groups, based on FA-extracted data. The table includes the mean fold change in compound features for VB vs P individuals in both acetonitrile and FA-based extracts. The corresponding *p*-values, based on a t-test comparing the mean abundances for each condition, are also provided. Additionally, the ratio of compound-feature abundance between acetonitrile and FA-based extracts is shown, along with p-values (from t-tests) for these comparisons. Curation criteria for matching compound features between datasets included: retention time (Rt) error < 60 s, accurate mass error < 20 ppm, and isotope/fragmentation patterns match > 90%. Annotations: NA = feature not detected; NA† = feature not detected in any other analysed dataset; NA‡ = feature not detected in acetonitrile-extracted clinical samples but detected in FA-based serum standards.

Variable *Rt_m/z*	FA		MeCN		QC FA vs MeCN	
	FC (VB/P)	*p*-value abundance	FC (VB/P)	*p*-value abundance	QC Abundance	*p*-value
9.68_261.1482	3.397	2.76E-06	1.628	1.64E-07	0.79	1.83E-07
9.66_239.1683	3.448	1.55E-06	1.630	1.99E-05	0.74	6.30E-13
7.18_837.6481	2.005	0.0415	NA†	NA†	NA†	NA†
4.60_247.0146	0.521	0.0131	NA‡	NA‡	NA‡	NA‡
4.65_682.2554	1.444	0.0070	1.262	0.6885	0.72	3.26E-18
7.18_838.2505	0.255	6.09E-05	0.819	0.0554	3.02	2.88E-14
9.27_553.2105	0.599	0.0281	NA‡	NA‡	NA‡	NA‡
7.18_838.4518	0.284	2.45E-04	0.777	0.0046	1.93	5.23E-12
7.44_398.2472	2.863	3.67E-07	1.627	5.38E-10	0.80	0.0070
9.53_410.2644	3.091	5.73E-08	1.586	1.33E-10	1.04	0.29840
11.52_286.2388	1.961	1.18E-04	0.911	0.0803	4.58	1.76E-11
7.75_166.0669 n	0.567	6.64E-04	0.775	0.0038	0.46	3.03E-21
9.98_373.2453	0.514	2.97E-09	NA‡	NA‡	NA‡	NA‡
10.87_796.9837	0.695	0.0016	0.715	1.51E-09	0.33	1.33E-20
4.60_199.1359	0.843	0.1087	1.512	0.0018	0.86	0.3965
4.65_685.2611	0.336	0.0216	0.922	0.6148	1.96	7.59E-23
0.73_218.9237	0.848	0.0063	0.675	6.24E-07	0.08	4.73E-10
4.53_742.3158	0.818	0.1036	0.674	0.1814	0.13	1.28E-20
7.44_376.2652	5.967	3.04E-04	1.963	1.37E-11	0.59	1.80E-08
4.44_472.2446	0.756	0.0399	1.003	0.7448	0.28	1.92E-14
12.85_843.5655	0.893	0.0414	0.777	4.54E-06	0.30	1.66E-11
8.97_365.1435	1.749	3.72E-04	0.524	0.0008	5.18	3.83E-10
7.89_684.1699	2.143	0.5635	NA‡	NA‡	NA‡	NA‡
12.96_603.5229	0.837	0.0067	0.616	1.16E-05	0.98	0.0260
12.65_848.5702	1.008	0.7637	0.634	0.3945	1.92	2.60E-19

4. 4 Statement of Authorship

Title of paper	Serum GFAP and NfL Augment a Metabolomics-Driven Strategy for Long-Term Prediction of Multiple Sclerosis Progression
Publication status	Submitted – under review
Publication details	Kacerova, T., Willemse, E., Oechtering, J., Radford-Smith, D.E., Xiong, W., Maleska Maceski, A., Yeo, T., De Luca, G., Palace, J., Leppert, D., Kuhle, J., Anthony, D. C., Probert. F.: **Serum GFAP and NfL Augment a Metabolomics-Driven Strategy for Long-Term Prediction of Multiple Sclerosis Progression**. Manuscript submitted (06/03/2025) to: *Communications Medicine*.

Student confirmation

Student name	Tereza Kacerova
Contribution to the paper	T.K. NMR sample preparation and analysis, Data analysis and interpretation, Manuscript writing; E. W., J. O. and A. M. M. performed GFAP and NfL measurements (University of Basel); D.E.R.S. and W.X. assisted with data analysis; D. L. and J. K. were responsible for clinical trial (Basel MS cohort) oversight and patient recruitment; A. Y., G. de L., J. P. and D. C. A. were responsible for clinical trial (Oxford MS cohort) oversight and patient recruitment; F. P. and D.C.A. are the principal investigators/supervisors of the research described in the manuscript, contributed extensively to project/data conceptualisation and visualisation, and manuscript reviewing/editing.
Date	30/06/2025
Signature	

Supervisor confirmation

By signing the Statement of Authorship, you are certifying that the candidate made a substantial contribution to the publication, and that the description described above is accurate.

Supervisor name	Prof James S. O. McCullagh
Contribution to the paper	I am happy to state that the candidate made a major and substantial contribution this publication, and that the description above is accurate.
Date	29th June 2025
Signature	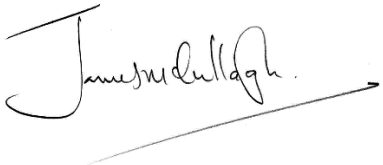

Chapter 4 Combining Serum NMR Metabolomics and Protein Biomarkers to Predict Disease Progression in Multiple Sclerosis

4. 1 Project context and chapter overview

Building on the analytical workflow optimisation described in **Chapters 2** and **3**, this chapter presents the first clinical application of omics in this thesis, using a validated NMR-based serum metabolomics platform to investigate disease progression in multiple sclerosis. This transition from method development to clinical application illustrates how robust omics workflows can be applied to investigate complex biological mechanisms and support translational research in neuroinflammatory disease.

Multiple sclerosis is a chronic, immune-mediated disorder of the CNS, characterised by pronounced inter-individual heterogeneity in clinical progression, radiological findings, and underlying pathology.[1] Despite advances in imagining techniques and diagnostic criteria, the ability to predict long-term disease trajectories, particularly the onset of irreversible progression, remains limited. Notably, this predictive gap constrains personalised treatment planning, impedes timely therapeutic intervention, and presents a major barrier to effective patient stratification in clinical trials.

Recent development in biomarker research has underscored the potential of biofluid-based measures for assessing disease severity and progression in multiple sclerosis. Among these, NfL, a marker of axonal injury, and GFAP, reflective of astrocytic activation, have emerged as sensitive indicators of neurodegeneration.[2-4] However, most biomarker studies to date have focused on CSF, which, despite providing direct access to CNS-derived biomarkers and offering high analytical sensitivity, is invasive and challenging to implement routinely, thereby limiting its utility for longitudinal and large-scale monitoring. As a result, there is growing interest in developing reliable serum-based biomarkers that provide a scalable, minimally invasive alternative suitable for longitudinal monitoring and broader clinical implementation.

To address this unmet clinical need, this chapter applies a high-throughput, quantitatively robust NMR-based serum metabolomics platform to investigate biological signatures associated with disease progression in multiple sclerosis. Moving beyond conventional classification systems based on clinical phenotypes such as relapsing-remitting MS (RRMS) and secondary-progressive MS (SPMS),[5, 6] the analysis outlined in

Chapter 4 adopts a biologically informed framework. The focus is on an 'extreme-phenotype' subset from the Swiss Multiple Sclerosis Cohort (SMSC), enabling comparison between patients with stable disease and those with pronounced progression. Importantly, untargeted metabolomic profiling is integrated with targeted proteomic markers of neuroinflammation and neuroaxonal damage, specifically serum GFAP and NfL.[7] By leveraging multi-omics data from baseline serum samples, the chapter explores the development of prognostic models that are clinically informative, scalable, and applicable across centres.

Together, these results underscore the translational potential of serum-based multi-omics analysis within a precision medicine framework for MS, offering a clinically relevant platform for disease monitoring and patient stratification. This chapter also marks a key transition in the thesis - from methodological development to disease-focused application - laying the groundwork for the prognostic modelling, diagnostic stratification, and treatment-response monitoring explored in subsequent chapters.

4. 2 References

(1) Dobson, R.; Giovannoni, G. Multiple sclerosis - a review. *Eur J Neurol* **2019**, *26* (1), 27-40. DOI: 10.1111/ene.13819 From NLM Medline.
(2) Disanto, G.; Barro, C.; Benkert, P.; Naegelin, Y.; Schadelin, S.; Giardiello, A.; Zecca, C.; Blennow, K.; Zetterberg, H.; Leppert, D.; et al. Serum Neurofilament light: A biomarker of neuronal damage in multiple sclerosis. *Ann Neurol* **2017**, *81* (6), 857-870. DOI: 10.1002/ana.24954 From NLM Medline.
(3) Cross, A. H.; Gelfand, J. M.; Thebault, S.; Bennett, J. L.; von Budingen, H. C.; Cameron, B.; Carruthers, R.; Edwards, K.; Fallis, R.; Gerstein, R.; et al. Emerging Cerebrospinal Fluid Biomarkers of Disease Activity and Progression in Multiple Sclerosis. *JAMA Neurol* **2024**, *81* (4), 373-383. DOI: 10.1001/jamaneurol.2024.0017 From NLM Publisher.
(4) Comabella, M.; Montalban, X. Body fluid biomarkers in multiple sclerosis. *Lancet Neurol* **2014**, *13* (1), 113-126. DOI: 10.1016/S1474-4422(13)70233-3 From NLM Medline.
(5) Yeo, T.; Probert, F.; Sealey, M.; Saldana, L.; Geraldes, R.; Hoeckner, S.; Schiffer, E.; Claridge, T. D. W.; Leppert, D.; DeLuca, G.; et al. Objective biomarkers for clinical relapse in multiple sclerosis: a metabolomics approach. *Brain Commun* **2021**, *3* (4), fcab240. DOI: 10.1093/braincomms/fcab240 From NLM PubMed-not-MEDLINE.
(6) Yeo, T.; Sealey, M.; Zhou, Y.; Saldana, L.; Loveless, S.; Claridge, T. D. W.; Robertson, N.; DeLuca, G.; Palace, J.; Anthony, D. C.; et al. A blood-based metabolomics test to distinguish relapsing-remitting and secondary progressive multiple sclerosis: addressing practical considerations for clinical application. *Sci Rep* **2020**, *10* (1), 12381. DOI: 10.1038/s41598-020-69119-3 From NLM Medline.
(7) Meier, S.; Willemse, E. A. J.; Schaedelin, S.; Oechtering, J.; Lorscheider, J.; Melie-Garcia, L.; Cagol, A.; Barakovic, M.; Galbusera, R.; Subramaniam, S.; et al. Serum Glial Fibrillary Acidic Protein Compared With Neurofilament Light Chain as a Biomarker for Disease Progression in Multiple Sclerosis. *JAMA Neurol* **2023**, *80* (3), 287-297. DOI: 10.1001/jamaneurol.2022.5250 From NLM Medline.

4. 3 Manuscript information

This chapter consists of a research article manuscript submitted to *Communications Medicine* (07/03/2025).

Kacerova, T., Willemse, E., Oechtering, J., Radford-Smith, D.E., Xiong, W., Maleska Maceski, A., Yeo, T., De Luca, G., Palace, J., Leppert, D., Kuhle, J., Anthony, D. C., Probert. F.: **Serum GFAP and NfL Augment a Metabolomics-Driven Strategy for Long-Term Prediction of Multiple Sclerosis Progression**

Manuscript status: *Under Review*

Serum GFAP and NfL Augment a Metabolomics-Driven Strategy for Long-Term Prediction of Multiple Sclerosis Progression

Tereza Kacerova[1], Eline Willemse[2,3], Johanna Oechtering[2,3], Daniel E. Radford-Smith[4], Wenzheng Xiong[4], Aleksandra Maleska Maceski[2,3], Tianrong Yeo[5,6,7], Gabriele De Luca[8], Jacqueline Palace[8], David Leppert[2,3], Jens Kuhle[2,3], Daniel C. Anthony[4*], Fay Probert[1]

[1]Chemistry Research Laboratory, Department of Chemistry, University of Oxford, Oxford, OX1 3TA, UK.
[2]Department of Neurology, University Hospital and University of Basel, Basel, Switzerland.
[3]Multiple Sclerosis Centre, Departments of Biomedicine and Clinical Research, University Hospital and University of Basel, Basel, Switzerland.
[4]Department of Pharmacology, University of Oxford, Oxford, OX1 3QT, UK.
[5]Department of Neurology, National Neuroscience Institute, 11 Jalan Tan Tock Seng, Singapore, 308433, Singapore.
[6]Duke-NUS Medical School, 8 College Road, Singapore, 169857, Singapore.
[7]Lee Kong Chian School of Medicine, Nanyang Technological University, 11 Mandalay Road, Singapore, 308232, Singapore.
[8]Nuffield Department of Clinical Neurosciences, John Radcliffe Hospital, University of Oxford, Oxford, OX3 9DU, UK.

*Corresponding author(s). E-mail(s): daniel.anthony@pharm.ox.ac.uk;

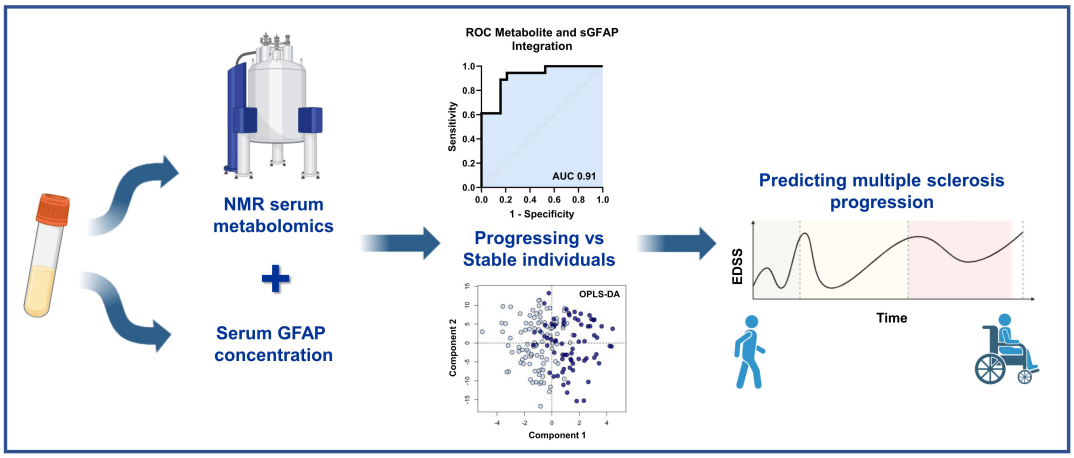

Abstract

Background: Reliable biomarkers for predicting disease progression in multiple sclerosis (MS) are crucial for advancing precision medicine and optimising treatment strategies. This study evaluates the predictive potential of serum nuclear magnetic resonance (NMR)-based metabolomics, individually and in combination with well-established biomarkers of neuroinflammation (serum glial fibrillary acidic protein, sGFAP) and axonal damage (neurofilament light chain, sNfL), in an extreme-phenotype subset of the Swiss Multiple Sclerosis Cohort (SMSC).
Methods: Serum samples were analysed using NMR-based metabolomics, along with quantification of sNfL and sGFAP. Supervised multivariate analysis was performed to differentiate MS phenotypes and identify future progressors. Multivariable receiver operating characteristic (ROC) analysis evaluated predictive performance, with key metabolite findings validated in an independent Oxford MS cohort.
Results: NMR-based metabolomics distinguished relapsing-remitting MS (RRMS) from secondary-progressive MS (SPMS) and predicted individual disease transitions. Key predictive metabolites - including lipoproteins, glutamine, alanine, valine, and glucose - were associated with progression independent of relapse activity (PIRA), a clinically relevant marker of sustained disability worsening. ROC analysis demonstrated strong predictive performance for disease progression (AUC = 0.81, $p = 0.001$), with external validation confirming its robustness. Integrating NMR-metabolomics with sGFAP and sNfL further improved predictive accuracy, achieving an AUC of 0.91 ($p < 0.0001$) for sGFAP and 0.87 ($p = 0.0002$) for sNfL, with independent cohort validation supporting these findings.
Discussion: The integration of metabolic and protein biomarkers enabled early, serum-based identification of MS progression, providing a clinically viable precision medicine tool for disease monitoring and therapeutic decision-making. These findings highlight the translational potential of an integrative biomarker approach to refine MS progression prediction and improve patient outcomes.

Keywords: multiple sclerosis progression, NMR-metabolomics, glial fibrillary acidic protein (GFAP), neurofilament light chain (NfL)

1 Background

Historically, patients with multiple sclerosis (MS) have been dichotomised into those in the relapsing-remitting MS (RRMS) stage or those who have transitioned to the secondary progressive MS (SPMS) stage.[1,2] Currently, this classification relies heavily on clinical assessment, typically through the expanded disability status scale, (EDSS)[3] in conjunction with magnetic resonance imaging (MRI).[4] However, despite the necessity for distinct treatment strategies at each stage, a standardised method for identifying the transition from RRMS to SPMS remains elusive.[1-3] This challenge likely stems from the somewhat arbitrary nature of the RR/SP classification, as some individuals exhibit stable disability while others experience deterioration independent of RR/SP staging.[2,5,6] Moreover, an increasing body of evidence highlights the limitations of this dichotomy, as progression independent of relapse activity (PIRA) is frequently observed even during the RR phase, underscoring the need to move beyond stage-based classifications and focus on factors driving disease progression at a more granular level. However, the absence of validated biomarkers of progression[2,7] and the variability of treatment responses complicate this endeavour.[1] Since subclinical neurodegenerative processes begin early in MS, relying solely on clinical markers to define disease progression may not fully capture the underlying molecular mechanisms. Therefore, identifying biomarkers capable of staging or predicting the rate of progression would offer valuable personalised prognostic insights, enabling timely and optimised treatment strategies.

Serum glial fibrillary acidic protein (sGFAP) is a proposed biomarker for neurological disorders,[8-12] demonstrating elevated levels in MS. A marked disparity in sGFAP concentrations was observed between SPMS and RRMS patients, with SPMS individuals demonstrating higher levels.[9,13,14] Moreover, recent studies have proposed a correlation between sGFAP

abundance and disease progression.[13-19] Conversely, concentrations of serum neurofilament light chain (sNfL) reflect neuroinflammatory activity,[20-23] neuroaxonal damage due to ongoing brain inflammation,[22,24,25] and responsiveness to treatment.[21,26-29] Elevated sNfL was found to be linked to relapse incidence in RRMS,[11,21,30-33] and to lesser degree with disease progression.[16,21]

We have previously demonstrated, that serum nuclear magnetic resonance (NMR)-metabolomics effectively discriminates between RRMS and SPMS[34,37] and identifies relapse activity in RRMS patients.[38] While NMR holds promise in identifying biomarkers for MS clinical stages,[34-36,39,40] studies utilising NMR-metabolomics to monitor MS progression are lacking.[39,41] Additionally, the lack of longitudinal studies with samples from the same individuals across different disease stages represents a critical gap, limiting the translation of findings into personalised medical application.

The Basel extreme phenotype cohort,[16] provides a unique platform for identifying progression biomarkers, with potential for future validation in larger cohorts. Despite its modest size, it enables the study of longitudinal biomarker dynamics and enhances understanding of the RRMS-to-SPMS transition. Here, we sought to: (1) validate previously identified NMR-detectable biomarkers of MS stages for monitoring the transition from RRMS to SPMS; (2) investigate whether the baseline serum NMR metabolome is predictive of MS progression and (3) explore whether integrating NMR metabolites with sGFAP and sNfL could enhance the prediction of progression.

2 Material and Methods

2.1 Study subjects and procedures

The study utilised clinical samples from the longitudinal Swiss MS Cohort (SMSC), consortium of tertiary referral hospitals. Patients with MS were included based on matched baseline EDSS scores, stability or worsening disability, and absence of relapses throughout follow-up. Non-progressors experienced no PIRA events, while progressors reported $\geq$ 1 PIRA event, defined as confirmed disability worsening (CDW) without relapse activity. CDW was classified as an EDSS increase of ≥ 1.5 points (baseline EDSS = 0), ≥ 1.0 points (EDSS 1.0–5.5), or $\geq$ 0.5 points (EDSS ≥ 6.0), confirmed after ≥ 6.0 months.[16]

The validation cohort was derived from the Oxford METabolomics MS cohort, with patients recruited from the John Radcliffe Hospital, Oxford University Hospitals NHS Foundation Trust.[36] Progressor and non-progressor subsets were selected based on extreme ambulatory trajectories, with groups matched for baseline EDSS. Non-progressors exhibited stable ambulatory function, maintaining unrestricted walking ability at both baseline and 2-year follow-up, whereas progressors experienced pronounced ambulatory decline, defined by a reduction in walking capacity to $\leq$ 500 meters. Based on these criteria, 19 progressors and 24 non-progressors were identified.

2.2 sGFAP and sNfL measurements

Blood samples were stored at $-80\,^{\circ}$C following standardised procedures.[42] Concentrations of sGFAP and sNfL were measured, as part of a previous study, in duplicate using ultrasensitive single molecule array (Simoa) technology (Quanterix) the singleplex Simoa GFAP Discovery Kit[16] and Simoa Nf-Light Kit,[21] respectively.

2.3 NMR sample preparation

Samples for ^{1}H NMR metabolomics analysis were prepared following a well-established.[35,38] Serum samples were thawed at room temperature and 150 μL was combined with 400 μL of 75 mM sodium phosphate buffer (in D2O, pH 7.4), then transferred to 5 mm NMR tubes (Norell^{TM}, Merck, UK).

2.4 ^{1}H NMR metabolomics data acquisition and processing

Global (untargeted) metabolomics encompasses the detection of all discernible metabolites within a given sample. All ^{1}H NMR metabolomics experiments were performed using a 700-MHz Bruker AVII spectrometer operating at 16.4 T equipped with a ^{1}H (^{13}C/^{15}N) TCI cryoprobe (Department of Chemistry, University of Oxford), as described previously.[35,36,38,43] ^{1}H NMR spectra were acquired using a 1D NOESY presaturation scheme and a spin-echo Carr-Purcell-Meiboom-Gill (CPMG) sequence. CPMG spectra were manually phased, baseline corrected, and chemical shifts referenced to lactate -CH_3 ($\delta = 1.33$ ppm) in Topspin 4.1.4 (Bruker, Germany). Next, in ACD/NMR processor academic edition 12.01 (Advanced Chemistry Development, Inc.), the 0.50–4.20 ppm and 5.20–8.50 ppm regions were divided into 0.02 ppm width bins and the sum-normalised integrals of each bin were exported for multivariate statistical analysis. The metabolite assignment was performed with reference to literature[35,38,41,44] and the Human Metabolome Database.[45] Additional confirmation was attained through the inspection of 1D total correlation spectroscopy (TOCSY) spectra.

2.5 Statistical analysis

Multivariate analysis was performed in R software 4.2.1 (R foundation for statistical computing, Vienna, Austria) using in-house R scripts and the *ropls* package.[46] Prior to analysis, all datasets were z-scored, with sGFAP and sNfL z-scored while adjusting for age and BMI.[21] "Orthogonal partial least square discriminant analysis" (OPLS-DA) was performed, employing 10-fold cross-validation in combination with repetition and permutation testing, as previously described.[41,43] Biomarker selection was based on variable importance in projection (VIP) scores derived from the OPLS-DA model, with the most discriminatory features identified at the inflection point of the VIP score distribution.[41,43] The analysis focused initially on the clinical stratification into RRMS and SPMS (for demographic details, refer to the Supplementary Information (SI) eTable 1). A subsequent multivariate model was constructed using a subset of non-transitioning RRMS patients ($N = 10$) and SPMS participants who were clinically diagnosed as SPMS at the time of baseline sampling ($N = 9$). Patients who transitioned from RRMS to SPMS during the study ($N = 8$) and an additional cohort of stable RRMS patients ($N = 10$) were excluded from the model as an independent validation set for leave-one-out cross-validation.

To validate our key findings, we used an independent Random Forest (RF) model with 500 trees, constructed using the *randomForest* R package,[47] to confirm the OPLS-DA-derived outcomes. A 10-fold cross-validation was applied and repeated 100 times. Feature selection was performed using t-tests, receiver operating characteristic (ROC) curve, area under the curve (AUC), and Cohen's D effect size. Model accuracy, sensitivity, specificity, and AUC were assessed and averaged across folds and repetitions, and permutation testing was performed to generate random classification baselines. The VIP scores and out-of-bag error rates were determined for the constructed model.

Predictor variables identified through VIP scores from OPLS-DA and RF models were evaluated for their diagnostic potential. Univariate data analysis was performed in GraphPad Prism 10 software. Student's t-test ($p < 0.05$) was used to compare metabolite concentrations between progressors and non-progressors. Quantitative data are shown as Tukey boxplots with IQR and whiskers (1.5× IQR). Benjamini-Hochberg FDR correction was applied where appropriate. The Pearson correlation analysis was conducted using the *corrplot* R package. The Kaplan-Meier curves utilised baseline levels of the identified discriminatory metabolites, standardised as z-scores. The "event" plotted on the curve was defined as the time point when the patient was clinically classified as SPMS or experienced an EDSS increase of ≥ 1.5 units (for EDSS ≥ 6.0, a 0.5-unit increment was counted as 1 unit) relative to baseline. The identified metabolites were evaluated using ROC curves, AUC, and optimal thresholds calculated with the *pROC* R package.[48] The AUC threshold was determined using the Youden Index, maximising the sum of sensitivity and specificity on the ROC curve. To capture complex relationships, two-way interaction terms between predictor variables were evaluated. A logistic regression model was then fitted to classify the binary outcome (progressors vs non-progressors). Given the limited sample size and the rigorous prior cross-validation of metabolites using OPLS-DA and RF the ROC curves were generated without additional cross-validation. The DeLong test was applied to assess the model discriminatory power, calculating the p-value for the ROC AUC to test the null hypothesis of no discrimination (AUC = 0.5).

3 Results

3.1 Patient characteristics

The cohort comprised 18 progressors ($\geq$ 1 PIRA event) and 19 non-progressors (absence of PIRA events). The groups were balanced for sex, age, BMI, and EDSS at the first sample (Table 1). As expected, progressors exhibited significantly higher EDSS scores at the last sample $p < 0.001$), greater number of PIRA events ($p < 0.001$), and a markedly higher prevalence of SPMS (SPMS; 44.4% vs 5.0%; $p < 0.001$) and transition from RRMS to SPMS (44.4% vs 0.0%; $p < 0.001$). Treatment patterns differed between groups. At baseline, progressors were more frequently treated with monoclonal antibodies, while non-progressors predominantly received oral therapies. By the last sample, monoclonal antibody use increased among progressors, whereas non-progressors largely remained on oral therapies.

3.2 Monitoring the transition from RRMS to SPMS at the individual level using NMR serum metabolomics

We first confirmed metabolome stability in patients who had a consistent diagnosis of RRMS ($N = 20$) or SPMS ($N = 9$) throughout the follow-up period (SI eTable 1). Our findings revealed a significant increase in high-density lipoproteins (HDLs, δ 0.86-0.88 ppm; region dominated by

Table 1: **Demographic characteristics of progressing and non-progressing MS individuals** (for more details on patient selection criteria, please refer to the original study[16]). The individual characteristics, presented as mean ± standard error of the mean (SEM), were compared using Fisher's exact test for categorical variables and the Wilcoxon test for continuous variables that were not normally distributed. Statistical significance was determined with the following thresholds: * $p < 0.05$, ** $p < 0.01$, *** $p < 0.001$. † Diagnosis remained stable from baseline to last follow-up. †† Diagnosis changed between baseline to follow-up.

Parameter	Progressor	Non-progressor	p-value
N	18	19	data NA
Female (%)	11 (61.1%)	12 (63.2%)	$p < 0.99$
Age first sample	46.8 ± 10.5	45.1 ± 9.7	0.63
Age last sample	52.9 ± 10.9	52.1 ± 9.9	0.82
Number of visits	10.6 ± 2.8	8.9 ± 1.6	0.13
Length of follow-up (months)	79.8 ± 20.8	82.4 ± 16.0	0.41
BMI (baseline)	25.3 ± 4.6	26.7 ± 4.7	0.40
EDSS first sample	3.9 ± 1.2	3.3 ± 1.2	0.11
EDSS last sample	6.3 ± 1.1	2.9 ± 1.5	$p < 0.001$ ***
T2w lesion volume	16.3	10.9	0.21
median (IQR), mL (baseline)	(12.8-44.7)	(2.7-19.7)	
No. of PIRA events			
0	0 (0)	19 (100)	
1	6 (33.3%)	0 (0%)	$p < 0.001$ ***
2	8 (44.4%)	0 (0%)	
3	4 (22.2%)	0 (0%)	
Disease course			
†RRMS	2 (16.6%)	18 (95.5%)	
†SPMS	8 (44.4%)	1 (5.0%)	$p < 0.001$ ***
††Transitioning RRMS to SPMS	8 (44.4%)	0 (0%)	
Therapy baseline			
Untreated	(7)	(3)	
Orals	fingolimod (4)	fingolimod (5)	
	dimethyl fumarate (1)	dimethyl fumarate (1)	
	azathioprine (1)	-	
Monoclonal antibodies	ocrelizumab (1)	-	$p < 0.001$ ***
	natalizumab (2)	natalizumab (5)	
	rituximab (1)	-	
Platform	(0)	glatiramer acetate (1)	
	-	interferon beta 1a (1)	
	-	interferon beta 1b (3)	
Therapy last sample			
Untreated	(4)	(1)	
Orals	(0)	fingolimod (8)	
		dimethyl fumarate (1)	
		ozanimod (1)	
		teriflunomide (1)	
Monoclonal antibodies	ocrelizumab (8)	ocrelizumab (1)	$p < 0.001$ ***
	natalizumab (6)	natalizumab (2)	
Platform	(0)	interferon beta 1a (1)	
	-	interferon beta 1b (2)	
	-	peginterferon beta 1a (1)	

HDLs mobile -CH_3; $p = 0.003$) and low-density lipoproteins (LDLs, δ 1.26-1.28 ppm; region dominated by LDLs mobile (-CH_2-)$_n$; $p = 0.023$), along with a significant decrease in N-acetylated glycoprotein (GlycA, δ 2.04-2.06 ppm region overlapping with mobile lipoprotein = CH–CH_2–CH_2– resonances, $p = 0.014$) and glucose (δ 3.76-3.78 ppm; $p = 0.032$) in RRMS compared to SPMS, consistent with findings from our previous work.[34-37]

To assess metabolome ability to capture the transition from RRMS to SPMS, we constructed an OPLS-DA model using the 9 SPMS individuals and a subset of 10 stable RRMS individuals who did not transition during the follow-up period (SI eTable 2). The model achieved an accuracy of 74.6 ± 2.3%, sensitivity of 73.9 ± 3.1%, specificity of 77.1 ± 6.2% (SI eFig. 1). Compared to previously reported studies focusing on dichotomising RRMS and SPMS,[34-36] glutamine (δ 2.12-2.2.14 ppm; $p = 0.0002$), alanine (δ 1.48-1.50 ppm; $p = 0.006$), and valine (δ 0.98-1.00 ppm; $p = 0.021$), all of which were elevated in SPMS participants, emerged as highly discriminatory metabolites (SI eTable 3). To corroborate the OPLS-DA-derived findings, we applied a RF algorithm to the same dataset, resulting in comparable performance metrics: an accuracy of 74.9 ± 2.6%, sensitivity of 74.4 ± 4.0%, and specificity of 76.7 ± 3.4%. Most discriminatory variables identified by OPLS-DA model also emerged as significant in the RF analysis, with the exception of glutamine and GlycA (SI eTable 4). This minor discrepancy suggests that glutamine and GlycA may have reduced relative importance in RF due to weaker classification contributions or redundancy with other metabolites. However, the consistency of key features across methods confirms model robustness.

The OPLS-DA model was used to predict the classification of samples from eight individuals who transitioned from RRMS to SPMS during follow-up, as determined by clinical examination (for demographic details, see SI eTable 5). As part of the validation process, the model predictive accuracy was tested on a separate cohort of 10 stable RRMS patients, which had been excluded from the initial model training (SI eFig. 2). Additionally, leave-one-out cross-validation was performed on the remaining individuals used to train the multivariate model, consisting of 10 RRMS and 9 SPMS cases (SI eFig. 3 and 4). The subsequent analysis of predictive component scores revealed that transitioning patients exhibited significantly greater metabolomic fluctuations (Fig. 1, cases 1–8) compared to stable RRMS ($N = 20$, SI eFig. 2, 3) and non-transitioning SPMS ($N = 9$, SI eFig. 4) individuals. Building on these results, we examined the alignment between conventional clinical staging and NMR metabolomics (Fig. 1, column 1; "Metabolomics"). Focusing on the pivotal transition point to SPMS, we observed perfect agreement between clinical and metabolomics-based diagnoses for two individuals (Fig. 1, cases 2 and 3). Conversely, for two individuals, the metabolomics-based model indicated an earlier transition than captured by the clinical diagnosis (Fig. 1, cases 1 and 7), while for four individuals, a later transition was indicated by metabolomics (Fig. 1, cases 4, 5, 6, 8). Analysing the general trend, as represented by the fluctuations in individual metabolomes, revealed overall agreement for five participants (Fig. 1, cases 1, 2, 4, 6, 8). In contrast, for two participants, the metabolome initially reached an "SPMS-apex" and gradually reverted to an RRMS-like composition, a pattern not reflected in the clinical assessment (Fig. 1, cases 3, 5). For one participant, the metabolomic profile suggested SPMS at the first sample (Fig. 1, case 7), while the clinical diagnosis indicated the transition at a later time point. Examining the EDSS scores associated with each sample did not reveal any direct correlation with the transition, in line with its known insensitivity to change.

Given recent progress in utilising sGFAP levels to monitor MS progression, we next assessed their agreement with clinical staging (using z-scores of sGFAP concentration; Fig. 1, column 2; "GFAP"). The metabolomics-based model demonstrated a higher degree of agreement with the clinical diagnosis compared to the sGFAP-based model. The agreement (within the 95% CI) with the metabolomics-based model allowed for a consistent classification of 19/27 RRMS samples (70%) and 47/64 SPMS samples (73%). Contrarily, for sGFAP alone, the overall agreement with the clinical examination-based diagnosis was observed for 15/27 RRMS samples (56%) and 45/64 SPMS samples (70%). Finally, we assessed whether the combination of NMR metabolomics and sGFAP yields improved agreement with the clinically defined diagnosis by incorporating sGFAP concentration into the OPLS-DA model (SI eFig. 5). Integrating untargeted metabolomics data with sGFAP concentrations (Fig. 1, column 3; "Metabolomics + GFAP") improved sample classification accuracy for RRMS and SPMS compared to metabolomics-only or sGFAP-only models, achieving agreement with clinical diagnosis in 22/27 (82%) RRMS and 57/64 (84%) SPMS samples.

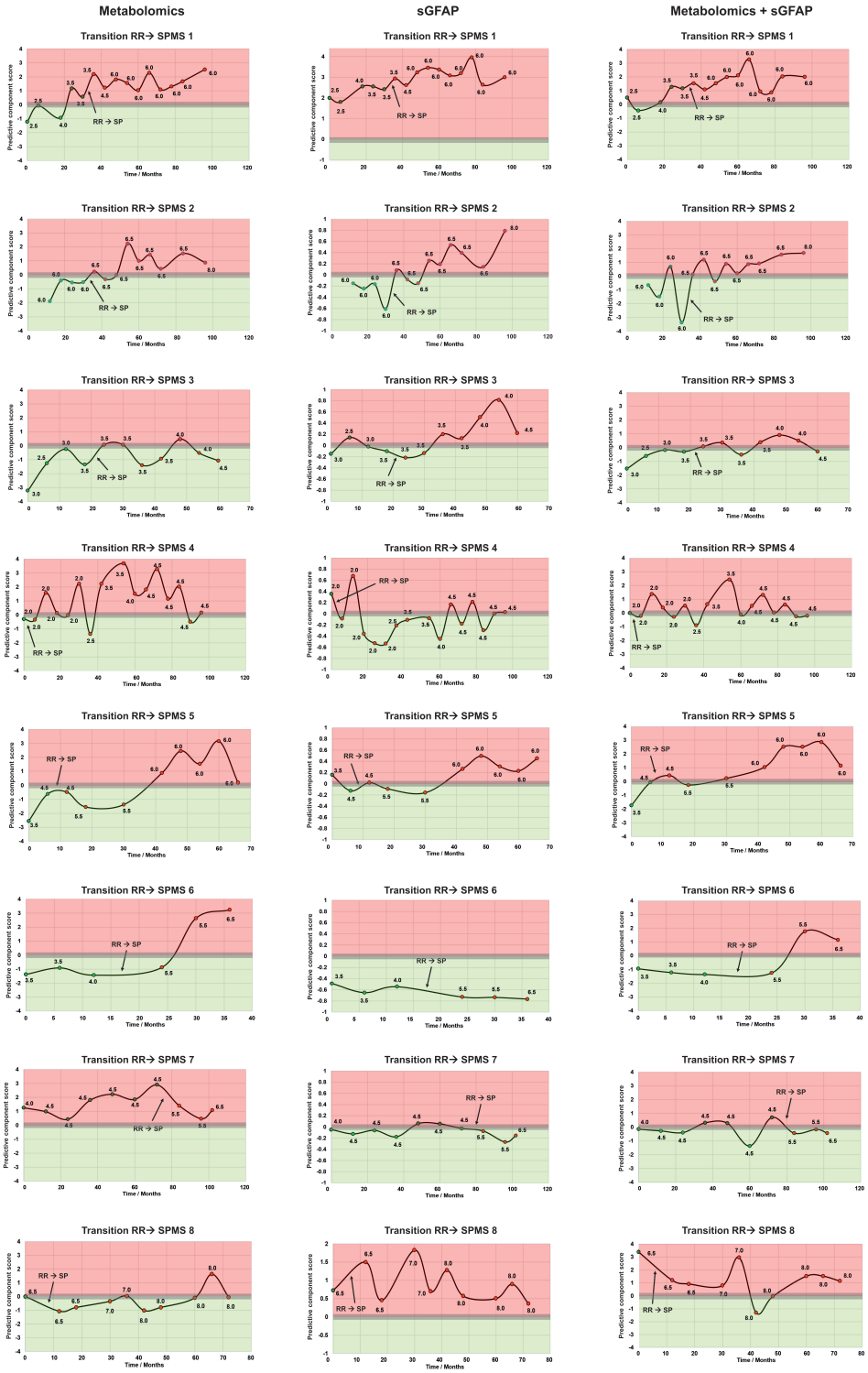

Fig. 1: **Serum metabolomics as an alternative approach to stage MS.** Predicted OPLS-DA scores of eight individuals undergoing the transition from RRMS to SPMS are illustrated. The red-shaded area represents the SPMS-like metabolome, while the green area corresponds to the RRMS-like metabolome, the grey area represents 95% CI. Each datapoint corresponds to a specific time point when the blood sample was collected, with red data points indicating clinical SPMS diagnosis and green points clinical RRMS diagnosis. Each datapoint is labelled with the corresponding EDSS score. The arrows emphasise the transition from RRMS to SPMS in each individual, according to the clinical examination results. **Column 1** - Metabolomics-based multivariate model; **column 2** - GFAP-based model (using z-scores of sGFAP concentration); **column 3** - Combination of metabolomics and GFAP (multivariate model; SI eFig. 5). For comparison, profiles of non-transitioning individuals are presented in the SI (RRMS SI eFig. 2, 3; SPMS SI eFig. 4).

3.3 The baseline NMR serum metabolome is an indicator of future transition to SPMS

Having demonstrated that the identified metabolites reflect disease stage at a given time point, we next evaluated the potential of baseline metabolites to predict the transition from RRMS to SPMS. Survival analysis was conducted using baseline samples from all stable RRMS (N = 20) and transitioning (N = 8) individuals. The "event" in the Kaplan-Meier curves was defined as the transition to SPMS (SI eFig. 6). The results indicated that the baseline metabolome partially predicted the RRMS-to-SPMS transition. Among the metabolites, lipoproteins emerged as the most predictive biomarkers ($p = 0.045$; SI eFig. 6a), with lower baseline lipoprotein levels associated with a higher likelihood of transitioning to SPMS. In contrast, baseline levels of alanine ($p = 0.171$; SI eFig. 6b), glutamine ($p = 0.183$; SI eFig. 6c), valine ($p = 0.234$; SI eFig. 6d), glucose ($p = 0.392$; SI eFig. 6e), and GlycA ($p = 0.303$; SI eFig. 6f) were not significantly associated with future transition to SPMS.

3.4 The baseline NMR serum metabolome predicts rate of progression independently of disease stage

Expanding on the capacity of baseline metabolite concentrations to forecast disease trajectory and the transition to SPMS, we aimed to ascertain whether the relative concentration of the discriminatory serum metabolites (HDLs, LDLs, alanine, glutamine, valine, GlycA, glucose) could differentiate between future progressors and non-progressors, irrespective of disease stage. We observed subtle yet significant alterations in the levels of these potential biomarkers in baseline samples matched for EDSS scores, highlighting their ability to distinguish between progressors and non-progressors (Fig. 2a-e). Additionally, ROC curve analysis indicated that most metabolites demonstrated a distinct ability to assess disease progression (Fig. 2f). The AUCs for each metabolite were as follows: HDLs (AUC 0.54 (95% CI: 0.34-0.73), t-test $p = 0.336$), GlycA (AUC 0.56 (95% CI: 0.37-0.73), t-test $p = 0.393$), LDLs (AUC 0.62 (95% CI: 0.43-0.81), t-test $p = 0.148$, Fig. 2a, f), glucose (AUC 0.66 (95% CI: 0.47-0.84), t-test p = 0.084, Fig. 2b, f), valine (AUC 0.63 (95% CI: 0.45-0.81), t-test $p = 0.056$, Fig. 2c, f), alanine (AUC 0.67 (95% CI: 0.49-0.84), t-test $p = 0.020$, Fig. 2d, f), and glutamine (AUC 0.68 (95% CI: 0.50-0.86), t-test $p = 0.024$, Fig. 2e, f).

The odds ratios (ORs; Fig. 2g) for baseline biomarker levels indicated moderate predictive capacity but, with the exception of glutamine, remained lower than those of GFAP z-scores (OR 2.02, 95% CI: 1.13–4.27) and NfL z-scores (OR 1.83, 95% CI: 1.00–3.93). Specifically, LDLs were associated with an OR of 0.52 (95% CI: 0.22-1.04), valine 1.35 (95% CI: 0.70-2.83), alanine 1.55 (95% CI: 0.79-3.30), glutamine 1.94 (95% CI: 0.96-4.49), and glucose 1.29 (95% CI: 0.66-2.60), while GlycA (OR 1.11 (95% CI: 0.47-2.24)) and HDLs (OR 0.97 (95% CI: 0.49-1.88)) exhibited minimal predictive capacity. Combining the identified predictor metabolites - LDLs, glutamine, alanine, valine, and glucose - each associated with a relatively high AUC and discriminatory OR, into a unified model significantly improved differentiation between future progressors and non-progressors, achieving an AUC of 0.81 (95% CI: 0.68-0.95, DeLong $p = 0.001$, Fig. 2h). This model accurately classified 78% of progressors (14/18) and 63% of non-progressors (12/19) based on baseline serum metabolomic profiles.

We then further validated whether the baseline concentration of the identified discriminatory metabolites could predict progression. To achieve this, we conducted Kaplan-Meier analysis, using metabolite baseline z-scored levels to define abundance (positive = high, negative = low), with an event defined as an EDSS increase ≥ 1.5 (Fig. 3). We compared these results to sGFAP and sNfL for reference. The Kaplan-Meier curves showed that individuals with lower baseline serum lipoprotein levels (δ 1.26-1.28 ppm for LDLs and δ 0.86-0.88 ppm for HDLs) were more likely to experience a significant increase in their EDSS score ($p = 0.146$, Fig. 3a). Specifically, 63% (95% CI: 30%-80%) of individuals with low baseline lipoprotein levels and 33% (95% CI: 10%-51%) with high baseline lipoprotein levels experienced an EDSS score increase ≥ 1.5 within five years. Similarly, participants with higher alanine levels at baseline were more likely to experience an EDSS score increase ≥ 1.5 over the follow-up ($p = 0.027$, Fig. 3b), with 58% (95% CI: 27%-73%) of individuals with high and 26% (95% CI: 4%-44%) with low baseline alanine levels projected to progress in the next five years. Similarly, 56% (95% CI: 26%-73%) of participants with high baseline glutamine levels and 28% (95% CI: 4%-42%) with low baseline levels were more likely to progress ($p = 0.052$, Fig. 3c). A similar trend was observed for valine, where 61% (95% CI: 31%-78%) of participants with high baseline valine concentrations and 32% (95% CI: 7%-49%) with low concentrations were likely to progress within five years ($p = 0.163$, Fig. 3d).

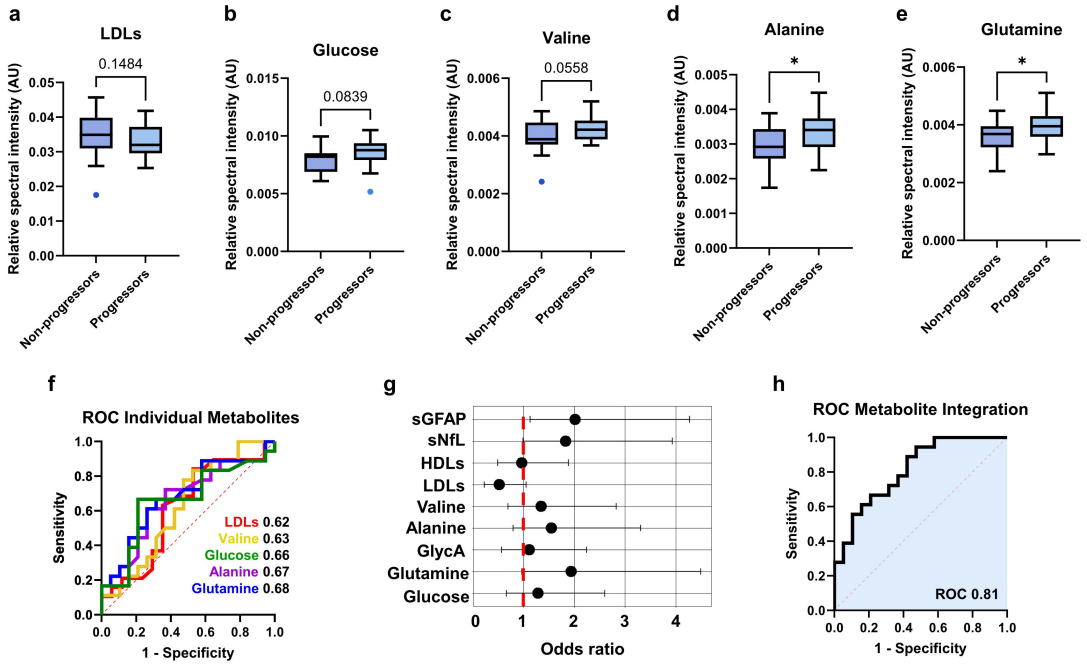

Fig. 2: **Combining individual serum metabolites substantially improves prediction of MS progression.** Baseline levels of the most predictor metabolites for progressors and non-progressors (*$p < 0.05$): **(a)** LDLs; $p = 0.148$, **(b)** glucose; $p = 0.084$, **(c)** valine; $p = 0.056$, **(d)** alanine; $p = 0.020$, **(e)** glutamine; $p = 0.024$. **(f)** ROC curves utilising the baseline concentrations of the five metabolites discriminating between progressors and non-progressors. **(g)** Odds ratios (log values of biomarker concentrations; given for progressors/non-progressors) for all potential NMR-identified biomarkers and sGFAP and sNfL z-scores. **(h)** ROC curve incorporating the most discriminatory metabolites - LDLs, glucose, valine, alanine, and glutamine - achieved an AUC of 0.81 (95% CI: 0.68–0.95, DeLong $p = 0.001$), using baseline concentrations to distinguish between progressors and non-progressors.

In contrast, glucose did not show any predictive power ($p = 0.336$, Fig. 3e), with 53% (95% CI: 27%-70%) of individuals with high baseline glucose concentrations and 36% (95% CI: 9%-54%) with low concentrations at greater risk of progression. Similarly, the GlycA signal ($p = 0.441$, Fig. 3f) did not show predictive value for, with 55% (95% CI: 26%-71%) of participants with high baseline GlycA levels and 37% (95% CI: 8%-55%) with low levels more likely to progress.

In comparison, sGFAP and sNfL concentrations revealed that individuals with higher levels were significantly more likely to progress. sNfL demonstrated similar predictive power to alanine ($p = 0.014$, Fig. 3g) with 68% (95% CI: 26%-87%) of individuals with high and 28% (95% CI: 8%-44%) with low baseline concentration predicted to progress. In contrast, sGFAP substantially correlated with disease progression ($p = 0.004$, Fig. 3h), as 69% (95% CI: 34%-85%) of individuals with high and 22% (95% CI: 3%-38%) with low sGFAP baseline concentration were identified as progressors.

3.5 Integration of sGFAP and NMR-metabolites enhances prediction of disease progression

Having previously established a correlation between sGFAP, and sNfL concentration levels and MS progression in the SMSC cohort,[16] our objective was to assess whether incorporating the NMR-derived biomarkers could enhance overall prediction accuracy. The Kaplan-Meier analysis for sNfL yielded results comparable to those for lipoprotein signals and alanine ($p = 0.014$, Fig. 3g), whereas the predictive power of sGFAP was significantly stronger ($p = 0.004$, Fig. 3h), consistent with previous studies.[16] Logistic regression comparing progressors and non-progressors showed that both sNfL (AUC 0.68 (95% CI: 0.52-0.84), t-test $p = 0.063$, Fig. 4a, b) and sGFAP z-scores (AUC 0.72 (95% CI: 0.55-0.88), t-test $p = 0.020$, Fig. 4a, c) demonstrated notable baseline discriminatory capacity.

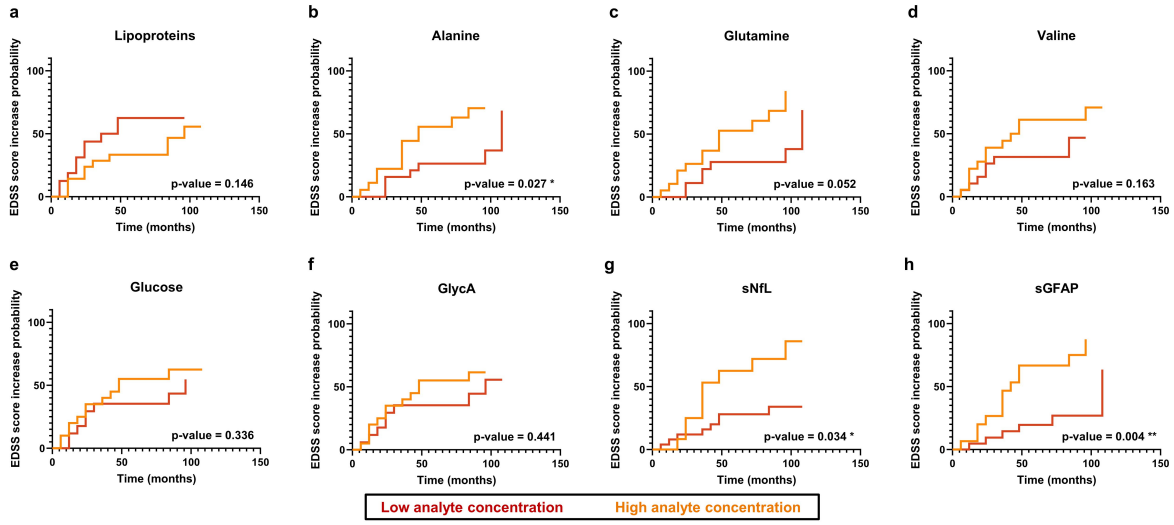

Fig. 3: **Prediction of an increase in EDSS score based on the baseline levels of serum metabolites** (HDLs, LDLs, alanine, glutamine, valine, glucose and GlycA), sGFAP and sNfL. Kaplan-Meier curves illustrate the predictive capacity of the most discriminatory analytes. The event was defined as an EDSS score increase by $\geq$ 1.5 units. Patients were stratified based on their baseline metabolite concentration, with low (negative z-scores) concentration depicted in red and high (positive z-scores) concentration depicted in yellow. **(a)** Lipoproteins - the trends for both LDLs and HDLs were similar, **(b)** alanine, **(c)** glutamine, **(d)** valine, **(e)** glucose, **(f)** GlycA, **(g)** sNfL, **(h)** sGFAP.

We further investigated the potential benefits of integrating sGFAP and sNfL with serum metabolites to improve the differentiation between future progressors and non-progressors. Incorporating the five previously identified metabolites with the highest discriminatory capacity – LDLs, alanine, glutamine, valine, and glucose – alongside sNfL and sGFAP z-scores, significantly enhanced the predictive performance. Specifically, the AUC values increased to 0.87 (95% CI: 0.76–0.98, DeLong p = 0.0002) for sNfL and 0.91 (95% CI: 0.83–0.99, DeLong $p < 0.0001$) for sGFAP (Fig. 4e and 4f, respectively), indicating a strong capacity to predict progression. These findings were further corroborated using a RF algorithm, which yielded an average ROC AUC of 0.86 and an accuracy of 76.2% for the integration with sGFAP, confirming the diagnostic potential of this biomarker constellation (SI eFig. 7a). Including the less discriminatory metabolites, GlycA and HDL signals, did not enhance model performance, likely due to their limited predictive value and potential collinearity with metabolites already incorporated in the model. Pearson correlation analysis (Fig. 4d) demonstrated a moderate positive correlation between sGFAP and most serum metabolites, excluding lipoproteins, which showed a negative correlation, and GlycA, which showed no correlation. Although correlations between sNfL and metabolites were moderate, integrating sNfL with the five key predictor metabolites - LDLs, alanine, glutamine, valine, and glucose - enabled the correct classification of 13 out of 18 (72%) progressors and 15 out of 19 (78%) non-progressors. Further improvement was achieved by incorporating sGFAP levels, which, when combined with these five metabolites, increased classification accuracy to 15 out of 18 (83%) progressors and 17 out of 19 (89%) non-progressors based on baseline metabolite levels.

3.6 Independent cohort validation confirms the metabolomic findings

To assess the reproducibility and generalisability of our findings, we performed an external validation using an independent cohort, a subset of the Oxford METabolomics cohort (SI eTable 6). Progressors (N = 19) and non-progressors (N = 24) were selected based on extreme ambulatory trajectories, with groups matched for baseline EDSS scores (p = 0.11).

Univariate and ROC curve analyses demonstrated that specific serum metabolites exhibited trends consistent with the Basel 'extreme phenotypes' cohort, with significantly decreased LDLs levels in progressing individuals (AUC 0.71 (95% CI: 0.55–0.87), t-test p = 0.027, Fig. 5a, g) and, conversely, elevated glucose (AUC 0.70 (95% CI: 0.54–0.86), t-test p = 0.025, Fig. 5b, g), valine (AUC 0.59 (95% CI: 0.41–0.77), t-test p = 0.235,

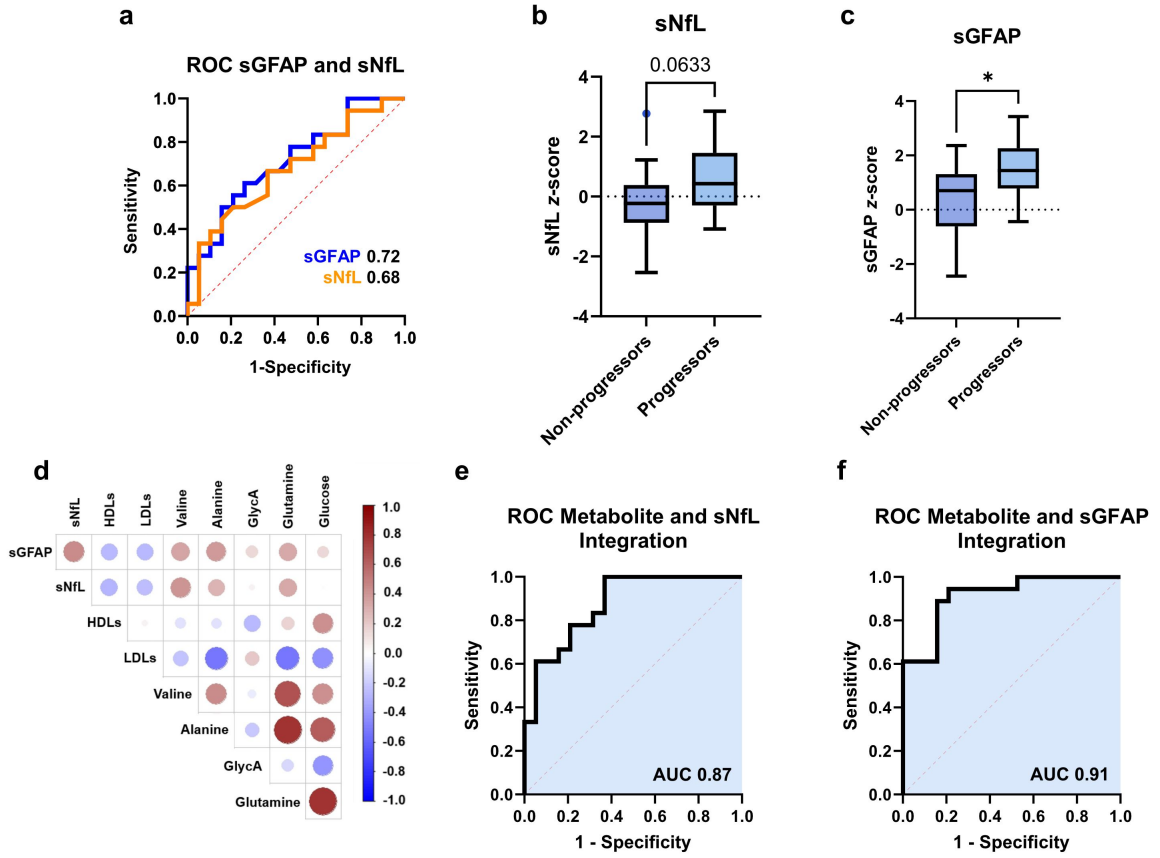

Fig. 4: Improved classification of future progressors and non-progressors was achieved through the combination of five metabolites (LDLs, glutamine, valine, alanine, glucose) with sGFAP or sNfL. **(a)** ROC curves utilising baseline sGFAP and sNfL z-scores to discriminate between progressors and non-progressors. **(b, c)** t-test results for baseline levels of sNfL and sGFAP z-scores for progressors and non-progressors; **(b)** sNfL; $p = 0.063$; **(c)** sGFAP; $p = 0.020$. **(d)** Correlation analysis of sGFAP, sNfL, and serum metabolites. **(e)** ROC curve for the integration of five serum metabolites (LDLs, alanine, glutamine, valine, glucose) and sNfL z-scores. **(f)** ROC curve for the integration of five serum metabolites and sGFAP z-scores.

Fig. 5c, g), alanine (AUC 0.72 (95% CI: 0.56–0.89), t-test $p = 0.061$, Fig. 5d, g), and glutamine (AUC 0.72 (95% CI: 0.57–0.88), t-test $p = 0.015$, Fig. 5e, g) in progressing MS individuals. Multiple logistic regression incorporating these metabolites further reinforced their association with MS progression, yielding an ROC AUC of 0.85 (95% CI: 0.71–0.96; DeLong $p = 0.0001$, Fig. 5h, grey ROC), surpassing the Basel model and highlighting their potential as predictive biomarkers.

In contrast to the Basel cohort, sNfL z-scored levels were not significantly different between progressors and non-progressors ($p = 0.667$; Fig. 5f) and did not demonstrate predictive utility for disease progression (AUC 0.52 (95% CI: 0.34–0.70), Fig. 5g). Despite the lack of significance, sNfL levels were elevated in progressors but exhibited substantial data variability (Fig. 5f). This variability, unlike in the Basel cohort, may reflect the shorter follow-up period, potentially limiting the ability to capture long-term progression patterns, or greater heterogeneity in disease course within the Oxford cohort, both of which would contribute to the reduced predictive effect observed. However, despite its limited predictive performance alone, integrating NfL with metabolite data significantly improved the model, achieving an ROC AUC of 0.89 (95% CI: 0.82–0.99), DeLong $p < 0.0001$, Fig. 5h), highlighting the advantages of combining diverse serum markers for more accurate disease trajectory prediction.

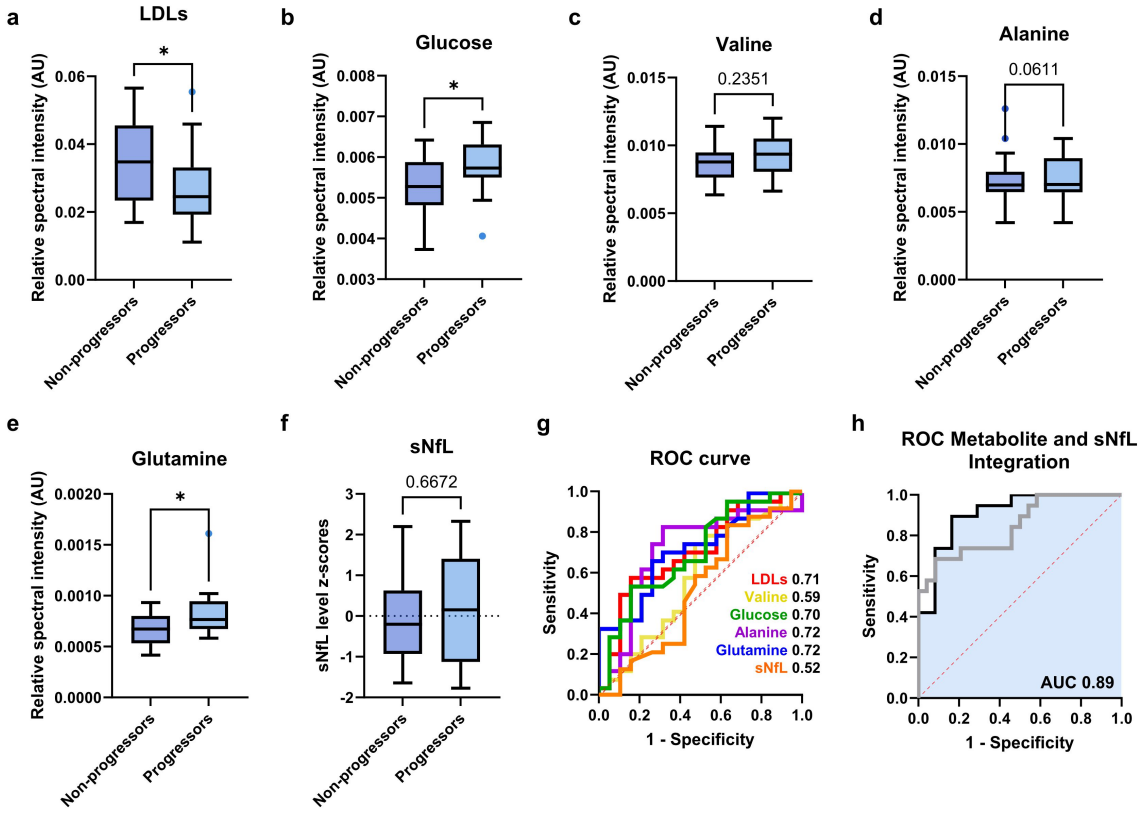

Fig. 5: **Validation of serum metabolite-based prediction of disease progression in an independent cohort.** Baseline levels of the most predictor metabolites in progressors and non-progressors: **(a)** LDLs; $p = 0.027$, **(b)** glucose; $p = 0.025$, **(c)** valine; $p = 0.235$, **(d)** alanine; $p = 0.061$, **(e)** glutamine; $p = 0.015$, **(f)** sNfL; $p = 0.667$. **(g)** ROC curve analysis using baseline concentrations of these analytes to discriminate between progressors and non-progressors. **(h)** A model incorporating the most discriminatory metabolites - LDLs, glucose, valine, alanine, and glutamine - achieved an AUC of 0.85 (95% CI: 0.71–0.96; DeLong $p = 0.0001$, grey ROC). When combined with NfL z-scores, the AUC increased to 0.89 (95% CI: 0.82–0.99; DeLong $p < 0.0001$), further improving the ability to distinguish between progressors and non-progressors based on baseline concentrations.

4 Discussion

In a rigorously defined extreme phenotype MS cohort of Swiss individuals, we identified distinct serum metabolite patterns associated with disease progression. Metabolites, sNfL, and particularly sGFAP correlated with both RRMS-to-SPMS transition and PIRA-defined progression, suggesting that baseline biomarkers can predict disease progression independently of disease stage and inflammatory activity. These findings further support the role of early neurodegenerative mechanisms in MS progression. Despite evidence of metabolic differences between RRMS and SPMS, the transition between these stages remains poorly understood.[34-36,39] While the RRMS-SPMS classification is becoming less favoured in research, it remains essential in clinical practice, necessitating reliable monitoring tools. Here, we show that metabolic signatures remain stable within RRMS and SPMS despite temporal variability and can effectively detect transitions. Integrating key NMR-identified metabolites with sGFAP[13-16] suggests that a composite biomarker panel could enhance clinical assessments and reduce misclassification risks in atypical cases.[4,7,49] Given the ambiguity in RRMS-SPMS classification,[1,4-6] this approach offers an orthogonal prognostic tool, providing insights beyond PIRA events while maintaining a strong association with disease progression. We identified seven serum metabolites distinctly altered between RRMS and SPMS, with alanine, glutamine, and - to a lesser extent - valine, glucose, and LDLs linked to both the RRMS-to-SPMS transition and disease progression. In contrast, while HDLs and GlycA differentiated RRMS from SPMS, their association was limited to disease stage rather than progression, suggesting they

primarily reflect inflammation related to disease status.

The association between inflammatory diseases and altered lipid metabolism, has been well-documented.[50-52] Building on this, our previous work demonstrated that lipoprotein NMR profiles can effectively distinguish RRMS from SPMS.[34-36] In this study, we further show that LDLs and HDLs may serve as progression biomarkers, as their serum levels reflect both disease staging and future worsening.

While the link between peripheral glucose levels and MS progression requires further investigation, the subtle glucose increase in progressors may indicate increased metabolic activity or dysregulation in active MS.[53] Similarly, the increased need for rapid energy sources could be attributed to elevated energy demands in the brain, driven by inflammation and demyelination as shown in experimental studies.[54] Previous studies have demonstrated that glucose levels can discriminate between RRMS and SPMS,[34] and it has also been hypothesised that there is a link between disease severity and insulin resistance.[55]

Amino acids play a pivotal role in the central nervous system, functioning as neurotransmitters, neuromodulators, and energy regulators.[56] Neurodegeneration and neuroinflammation disrupt amino acid homeostasis, driven by metabolic alterations, oxidative stress, and gastrointestinal protein malabsorption.[57-59] We propose that the elevated serum glutamine in progressing MS reflects increased glutamine efflux across the blood-brain barrier, likely driven by impaired neurotransmitter synthesis.[60-62] We further observed elevated serum valine in progressing MS individuals. While branched chain amino acids (BCAA) dysregulation has not been previously linked to MS,[38] altered BCAA levels have been reported in Parkinson's disease and amyotrophic lateral sclerosis.[63,64] Given the role of excessive glutamate release in neurodegeneration,[65,66] BCAA imbalance may contribute to MS pathophysiology. Additionally, evidence suggests a connection between neurodegeneration and disrupted alanine metabolism,[63,67] with one study reporting increased serum alanine in SPMS and its potential involvement in disease progression.[68]

Expanding on prior research linking MS progression to sGFAP,[13,15,16,41] our study integrates established biomarkers (sGFAP, sNfL) with serum metabolites, offering novel insights. Given the early onset of neurodegeneration,[1,4,5,69] this biomarker combination enables individualised prognostic assessment and early intervention.[70] The feasibility, non-invasiveness, and cost-effectiveness of measuring sGFAP and NMR-metabolites in blood samples make this approach a promising tool for personalised MS management. By integrating molecular biomarkers with clinical and MRI-based evaluations, this method enhances individualised disease monitoring and treatment optimisation.

4.1 Potential confounds

No baseline disparities were observed. Identified metabolites showed no significant correlations with age, disease duration, sex, or pharmacotherapy. Additionally, NMR metabolite levels did not differ between DMT-treated and untreated individuals, though the small subgroup sizes and treatment variability may have limited the assessment of DMT effects.

4.2 Limitations

The main limitation of this study is the relatively small sample size; however, this is partially offset by the long-term, consistent follow-up and the selection of extreme MS phenotypes, which provide a valuable framework for future research. The limited sample size constrains cross-validation using baseline samples alone; however, identified metabolites were validated through rigorous machine learning models (OPLS-DA, RF), and even successfully validated in an independent cohort. Additionally, in a separate MS cohort (Turku, Finland, unpublished data) focused on mild progression (ΔEDSS/year $\geq$ 0.5), elevated serum glutamine and glucose were observed in progressors, highlighting the potential for broader clinical application. Although sNfL exhibited lower discriminative power in the external validation cohort, this may reflect differences in follow-up duration and disease heterogeneity, potentially affecting predictive accuracy. These findings highlight the promise of this approach while underscoring the need for further validation in a larger cohort incorporating sGFAP and sNfL measurements.

5 Conclusion

This study, conducted in an extreme phenotype MS cohort with long-term follow-up, suggests that integrating serum NMR-detected metabolites with sGFAP and sNfL improves the prediction of MS progression over 5–8 years, enabling a more individualised and data-driven approach to disease management. Furthermore, findings from independent cohorts suggest the potential for translating these biomarkers into larger populations for broader disease progression prediction and monitoring.

6 References

1. Caseby, S.C.L., Woodhouse, F.A., Montgomery, S.M., Kroes, M.A. Duddy, M.E. Transition to secondary progressive multiple sclerosis: The consequences for patients and healthcare systems, a healthcare professional survey. Health Sci Rep-Us 5(2022).

2. Dobson, R. Giovannoni, G. Multiple sclerosis - a review. Eur J Neurol 26, 27-40 (2019).

3. Healy, B.C., Zurawski, J., Chitnis, T., Weiner, H.L. Glanz, B.I. Patient-reported outcomes associated with transition to secondary progressive multiple sclerosis. Qual Life Res 31, 1799-1805 (2022).

4. Ziemssen, T., et al. A mixed methods approach towards understanding key disease characteristics associated with the progression from RRMS to SPMS: Physicians' and patients' views. Mult Scler Relat Disord 38, 101861 (2020).

5. Tolley, C., et al. A Novel, Integrative Approach for Evaluating Progression in Multiple Sclerosis: Development of a Scoring Algorithm. JMIR Med Inform 8, e17592 (2020).

6. Ziemssen, T., et al. Secondary Progressive Multiple Sclerosis: A Review of Clinical Characteristics, Definition, Prognostic Tools, and Disease-Modifying Therapies. Neurol Neuroimmunol Neuroinflamm 10(2023).

7. McGinley, M.P., Goldschmidt, C.H. Rae-Grant, A.D. Diagnosis and Treatment of Multiple Sclerosis: A Review. JAMA 325, 765-779 (2021).

8. Sharquie, I.K., Gawwam, G.A. Abdullah, S.F. Serum Glial Fibrillary Acidic Protein: A Surrogate Marker of the Activity of Multiple Sclerosis. Medeni Med J 35, 212-218 (2020).

9. Abdelhak, A., et al. Blood GFAP as an emerging biomarker in brain and spinal cord disorders. Nat Rev Neurol 18, 158-172 (2022).

10. Magliozzi, R. Cross, A.H. Can CSF biomarkers predict future MS disease activity and severity? Mult Scler 26, 582-590 (2020).

11. Khalil, M., et al. Neurofilaments as biomarkers in neurological disorders. Nat Rev Neurol 14, 577-589 (2018).

12. Heimfarth, L., et al. Serum glial fibrillary acidic protein is a body fluid biomarker: A valuable prognostic for neurological disease - A systematic review. Int Immunopharmacol 107(2022).

13. Abdelhak, A., Huss, A., Kassubek, J., Tumani, H. Otto, M. Serum GFAP as a biomarker for disease severity in multiple sclerosis. Sci Rep-Uk 8(2018).

14. Hogel, H., et al. Serum glial fibrillary acidic protein correlates with multiple sclerosis disease severity. Mult Scler J 26, 210-219 (2020).

15. Barro, C., et al. Serum GFAP and NfL Levels Differentiate Subsequent Progression and Disease Activity in Patients With Progressive Multiple Sclerosis. Neurol Neuroimmunol Neuroinflamm 10(2023).

16. Meier, S., et al. Serum Glial Fibrillary Acidic Protein Compared With Neurofilament Light Chain as a Biomarker for Disease Progression in Multiple Sclerosis. JAMA Neurol 80, 287-297 (2023).

17. Monreal, E., et al. Serum biomarkers at disease onset for personalized therapy in multiple sclerosis. Brain (2024).

18. Madill, E., et al. Serum glial fibrillary acidic protein predicts disease progression in multiple sclerosis. Ann Clin Transl Neurol 11, 2719-2730 (2024).

19. Benkert, P., et al. Serum Glial Fibrillary Acidic Protein and Neurofilament Light Chain Levels Reflect Different Mechanisms of Disease Progression under B-Cell Depleting Treatment in Multiple Sclerosis. Ann Neurol (2024).

20. Ammitzboll, C., et al. NfL and GFAP in serum are associated with microstructural brain damage in progressive multiple sclerosis. Mult Scler Relat Dis 77(2023).

21. Benkert, P., et al. Serum neurofilament light chain for individual prognostication of disease activity in people with multiple sclerosis: a retrospective modelling and validation study. Lancet Neurol 21, 246-257 (2022).

22. Disanto, G., et al. Serum Neurofilament light: A biomarker of neuronal damage in multiple sclerosis. Ann Neurol 81, 857-870 (2017).

23. Varhaug, K.N., Torkildsen, O., Myhr, K.M. Vedeler, C.A. Neurofilament Light Chain as a Biomarker in Multiple Sclerosis. Frontiers in Neurology 10(2019).

24. Cantó, E., et al. Association Between Serum Neurofilament Light Chain Levels and Long-term Disease Course Among Patients With Multiple Sclerosis Followed up for 12 Years. Jama Neurology 76, 1359-1366 (2019).

25. Leppert, D., et al. Blood Neurofilament Light in Progressive Multiple Sclerosis: Post Hoc Analysis of 2 Randomized Controlled Trials. Neurology 98, e2120-e2131 (2022).

26. Bridel, C., et al. Serum Neurofilament Light Association With Progression in Natalizumab-Treated Patients With Relapsing-Remitting Multiple Sclerosis. Neurology 97, e1898-e1905 (2021).

27. Kuhle, J., et al. Sustained reduction of serum neurofilament light chain over 7 years by alemtuzumab in early relapsing-remitting MS. Mult Scler 28, 573-582 (2022).

28. Kuhle, J., et al. Fingolimod and CSF neurofilament light chain levels in relapsing-remitting multiple sclerosis. Neurology 84, 1639-1643 (2015).

29. Kuhle, J., et al. Blood neurofilament light chain as a biomarker of MS disease activity and treatment response. Neurology 92, e1007-e1015 (2019).

30. Manouchehrinia, A., et al. Plasma neurofilament light levels are associated with risk of disability in multiple sclerosis. Neurology 94, E2457-E2467 (2020).

31. Rival, M., Galoppin, M. Thouvenot, E. Biological Markers in Early Multiple Sclerosis: the Paved Way for Radiologically Isolated Syndrome. Front Immunol 13(2022).

32. Thebault, S., et al. High or increasing serum NfL is predictive of impending multiple sclerosis relapses. Mult Scler Relat Dis 59(2022).

33. Varhaug, K.N., et al. Neurofilament light chain predicts disease activity in relapsing-remitting MS. Neurol Neuroimmunol Neuroinflamm 5, e422 (2018).

34. Dickens, A.M., et al. A type 2 biomarker separates relapsing-remitting from secondary progressive multiple sclerosis. Neurology 83, 1492-1499 (2014).

35. Probert, F., et al. Diagnosis and staging of multiple sclerosis using a metabolomics-based blood test: a simple method for monitoring progression independently of EDSS. Mult Scler J 25, 500-501 (2019).

36. Yeo, T., et al. A blood-based metabolomics test to distinguish relapsing-remitting and secondary progressive multiple sclerosis: addressing practical considerations for clinical application. Sci Rep 10, 12381 (2020).

37. Aguilar, J.A., et al. Reliable, high-quality suppression of NMR signals arising from water and macromolecules: application to bio-fluid analysis. Analyst 144, 7270-7277 (2019).

38. Yeo, T., et al. Objective biomarkers for clinical relapse in multiple sclerosis: a metabolomics approach. Brain Commun 3, fcab240 (2021).

39. Bhargava, P. Anthony, D. Metabolomics in multiple sclerosis disease course and progression. Mult Scler J 26, 591-598 (2020).

40. Villoslada, P., et al. Metabolomic signatures associated with disease severity in multiple sclerosis. Neurol Neuroimmunol Neuroinflamm 4, e321 (2017).

41. Probert, F., et al. Determination of CSF GFAP, CCN5, and vWF Levels Enhances the Diagnostic Accuracy of Clinically Defined MS From Non-MS Patients With CSF Oligoclonal Bands. Front Immunol 12(2022).

42. Teunissen, C.E., et al. A consensus protocol for the standardization of cerebrospinal fluid collection and biobanking. Neurology 73, 1914-1922 (2009).

43. Probert, F., et al. Plasma Nuclear Magnetic Resonance Metabolomics Discriminates Between High and Low Endoscopic Activity and Predicts Progression in a Prospective Cohort of Patients With Ulcerative Colitis. J Crohns Colitis 12, 1326-1337 (2018).

44. Luo, Y.J., Zhu, J.Y. Gao, Y.Q. Metabolomic analysis of the plasma of patients with high-altitude pulmonary edema (HAPE) using H NMR. Mol Biosyst 8, 1783-1788 (2012).

45. Wishart, D.S., et al. HMDB 5.0: the Human Metabolome Database for 2022. Nucleic Acids Res 50, D622-D631 (2022).

46. Thevenot, E.A., Roux, A., Xu, Y., Ezan, E. Junot, C. Analysis of the Human Adult Urinary Metabolome Variations with Age, Body Mass Index, and Gender by Implementing a Comprehensive Workflow for Univariate and OPLS Statistical Analyses. J Proteome Res 14, 3322-3335 (2015).

47. Breiman, L. Random forests. Mach Learn 45, 5-32 (2001).

48. Robin, X., et al. pROC: an open-source package for R and S+ to analyze and compare ROC curves. Bmc Bioinformatics 12, 77 (2011).

49. Hemond, C.C. Bakshi, R. Magnetic Resonance Imaging in Multiple Sclerosis. Cold Spring Harb Perspect Med 8(2018).

50. Bogie, J.F.J., Haidar, M., Kooij, G. Hendriks, J.J.A. Fatty acid metabolism in the progression and resolution of CNS disorders. Adv Drug Deliv Rev 159, 198-213 (2020).

51. Pineda-Torra, I., Siddique, S., Waddington, K.E., Farrell, R. Jury, E.C. Disrupted Lipid Metabolism in Multiple Sclerosis: A Role for Liver X Receptors? Front Endocrinol (Lausanne) 12, 639757 (2021).

52. Tracey, T.J., Steyn, F.J., Wolvetang, E.J. Ngo, S.T. Neuronal Lipid Metabolism: Multiple Pathways Driving Functional Outcomes in Health and Disease. Front Mol Neurosci 11(2018).

53. Shi, J., Fan, J., Su, Q. Yang, Z. Cytokines and Abnormal Glucose and Lipid Metabolism. Front Endocrinol (Lausanne) 10, 703 (2019).

54. Yeo, T., et al. Metabolomics detects clinically silent neuroinflammatory lesions earlier than neurofilament-light chain in a focal multiple sclerosis animal model. J Neuroinflammation 19, 252 (2022).

55. Sepidarkish, M., Kalantari, N., Gorgani-Firouzjaee, T., Rostami-Mansoor, S. Shirafkan, H. Association between insulin resistance and multiple sclerosis: a systematic review and meta-analysis. Metab Brain Dis 39, 1015-1026 (2024).

56. Akyuz, E., Celik, B.R., Aslan, F.S., Sahin, H. Angelopoulou, E. Exploring the Role of Neurotransmitters in Multiple Sclerosis: An Expanded Review. Acs Chem Neurosci 14, 527-553 (2023).

57. Pegoretti, V., et al. Inflammation and Oxidative Stress in Multiple Sclerosis: Consequences for Therapy Development. Oxid Med Cell Longev 2020(2020).

58. Ohl, K., Tenbrock, K. Kipp, M. Oxidative stress in multiple sclerosis: Central and peripheral mode of action. Exp Neurol 277, 58-67 (2016).

59. Zakharov, S., et al. Neuroinflammation markers and methyl alcohol induced toxic brain damage. Toxicology Letters 298, 60-69 (2018).

60. Andersen, J.V. Schousboe, A. Glial Glutamine Homeostasis in Health and Disease. Neurochem Res 48, 1100-1128 (2023).

61. Kadry, H., Noorani, B. Cucullo, L. A blood-brain barrier overview on structure, function, impairment, and biomarkers of integrity. Fluids Barriers Cns 17(2020).

62. Kostic, M., Zivkovic, N. Stojanovic, I. Multiple sclerosis and glutamate excitotoxicity. Rev Neurosci 24, 71-88 (2013).

63. Trupp, M., et al. Metabolite and peptide levels in plasma and CSF differentiating healthy controls from patients with newly diagnosed Parkinson's disease. J Parkinsons Dis 4, 549-560 (2014).

64. Wuolikainen, A., et al. Multi-platform mass spectrometry analysis of the CSF and plasma metabolomes of rigorously matched amyotrophic lateral sclerosis, Parkinson's disease and control subjects. Mol Biosyst 12, 1287-1298 (2016).

65. Lewerenz, J. Maher, P. Chronic Glutamate Toxicity in Neurodegenerative Diseases-What is the Evidence? Front Neurosci-Switz 9(2015).

66. Sheldon, A.L. Robinson, M.B. The role of glutamate transporters in neurodegenerative diseases and potential opportunities for intervention. Neurochem Int 51, 333-355 (2007).

67. Hwangbo, N., et al. Predictive Modeling of Alzheimer's and Parkinson's Disease Using Metabolomic and Lipidomic Profiles from Cerebrospinal Fluid. Metabolites 12(2022).

68. Rzepinski, L., Koslinski, P., Gackowski, M., Koba, M. Maciejek, Z. Amino Acid Levels as Potential Biomarkers of Multiple Sclerosis in Elderly Patients: Preliminary Report. J Clin Neurol 18, 529-534 (2022).

69. Inojosa, H., Schriefer, D. Ziemssen, T. Clinical outcome measures in multiple sclerosis: A review. Autoimmun Rev 19, 102512 (2020).

70. Letertre, M.P.M., Giraudeau, P. de Tullio, P. Nuclear Magnetic Resonance Spectroscopy in Clinical Metabolomics and Personalized Medicine: Current Challenges and Perspectives. Front Mol Biosci 8(2021).

Contribution statement

J.K., D.C.A., F.P., and D.L. conceived and designed the study. T.K. and E.W. performed the experiments. T.K., D.E.R.S., and W.X. analysed the data. J.K., D.L., E.W., J.O., and A.M.M. oversaw the Swiss MS cohort. J.P., G.L., T.Y., F.P., and D.C.A. oversaw the Oxford MS cohort. J.K., D.C.A., F.P., D.L., and E.W. provided critical feedback and guidance for experimental and analysis design. T.K. drafted the manuscript with input from all authors. All authors reviewed and approved the manuscript.

Declaration of competing interest

The authors declare no competing interest.

Ethics approval and consent to participate

Swiss Multiple Sclerosis Cohort (SMSC; NCT02433028). John Radcliffe Hospital, Oxford University Hospital Trust (MET cohort; REC reference: 09/H0606/5 + 5). Participants provided written informed consent. This study followed the Strengthening the Reporting of Observational Studies in Epidemiology (STROBE) reporting guidelines.

Data access and availability

Anonymised data not published within this article will be made available by request from any qualified investigator.

Funding

This work is funded by EPSRC grant (EP/Y000420/1 (aquasynapse)). F.P. is funded by a Dorothy Hodgkin Early Career Fellowship in Chemistry in association with Somerville College. T.K. is funded by an EPSRC Doctoral Training Partnership (EP/W524311/1) and Numares AG (Am Biopark 9, 93053 Regensburg-Graß, Germany).

Acknowledgement

The authors thank all MS patients participating in this study and the NMR Research Facility (Department of Chemistry, University of Oxford) for use of equipment and advice.

Supplementary Information – Manuscript 3

Supplementary Information

Serum GFAP and NfL Augment a Metabolomics-Driven Strategy for Long-Term Prediction of Multiple Sclerosis Progression

Tereza Kacerova[1], Eline Willemse[2,3,4,5], Johanna Oechtering[2,3,4], Daniel E. Radford-Smith[6], Wenzheng Xiong[6], Aleksandra Maleska Maceski[2,3,4], Tianrong Yeo[7,8,9], Gabriele De Luca[10], Jacqueline Palace[10], David Leppert[2,3,4], Jens Kuhle[2,3,4], Daniel C. Anthony[6*], Fay Probert[1]

[1] Chemistry Research Laboratory, Department of Chemistry, University of Oxford, Oxford OX1 3TA, UK
[2] Department of Neurology, University Hospital and University of Basel, Basel, Switzerland
[3] Multiple Sclerosis Centre, Departments of Biomedicine and Clinical Research, University Hospital and University of Basel, Basel, Switzerland
[4] Research Center for Clinical Neuroimmunology and Neuroscience Basel, University Hospital and University of Basel, Switzerland
[5] Department of Clinical Research, University Hospital Basel, University of Basel, Basel, Switzerland
[6] Department of Pharmacology, University of Oxford, Oxford OX1 3QT, UK
[7] Department of Neurology, National Neuroscience Institute, 11 Jalan Tan Tock Seng, Singapore 308433, Singapore
[8] Duke-NUS Medical School, 8 College Road, Singapore 169857, Singapore
[9] Lee Kong Chian School of Medicine (Nanyang Technological University), 11 Mandalay Road, Singapore 308232, Singapore
[10] Nuffield Department of Clinical Neurosciences, John Radcliffe Hospital, University of Oxford, Oxford OX3 9DU, UK

Corresponding author: Daniel C. Anthony daniel.anthony@pharm.ox.ac.uk

Supplementary Information – Manuscript 3

Metabolomics discriminates between RRMS and SPMS

SI eTable 1 The demographic characteristics (all results are presented as mean ± standard error of the mean (SEM)) of stable RRMS and SPMS individuals involved in the initial multivariate model. In this analysis, all stable RRMS and stable SPMS individuals were incorporated (only individuals transitioning from RRMS to SPMS were deliberately excluded from the analysis).

Parameter	RRMS	SPMS
N	20	9
Female (%)	13 (65.0%)	3 (33.3%)
EDSS first sample	3.3 ± 1.1	4.1 ± 1.1
EDSS last sample	3.0 ± 1.6	6.4 ± 0.9
Age first sample	44.1 ± 9.4	50.9 ± 13.9
Age last sample	50.6 ± 9.6	57.8 ± 14.8
Treatment – baseline	Orals (6) Monoclonal antibodies (7) Platform (4) Untreated (3)	Orals (1) Monoclonal antibodies (1) Platform (1) Untreated (6)

OPLS-DA Model parameters:

Model accuracy: 68.7 ± 2.4%

Model sensitivity: 67.9 ± 3.8%

Model specificity: 70.6 ± 3.3%

Random Forest Model parameters:

Model accuracy: 68.9 ± 2.7%

Model sensitivity: 69.8 ± 3.9%

Model specificity: 69.2 ± 3.8%

Supplementary Information – Manuscript 3

Metabolomics discriminates between RRMS and SPMS

SI eTable 2 Demographic characteristics (all results are presented as mean ± SEM) of stable RRMS and SPMS individuals used for the RRMS vs SPMS multivariate model (a size-matched *sub*-cohort was selected)

Parameter	RRMS	SPMS
N	10	9
Female (%)	7 (70.0%)	3 (33.3%)
EDSS first sample	2.8 ± 0.7	4.1 ± 1.1
EDSS last sample	2.1 ± 1.1	6.4 ± 0.9
Age first sample	42.4 ± 8.6	50.9 ± 13.9
Age last sample	48.6 ± 8.7	57.8 ± 14.8
Treatment	Orals (3) Monoclonal antibodies (2) Platform (3) Untreated (2)	Orals (1) Monoclonal antibodies (1) Platform (1) Untreated (6)

OPLS-DA model discriminating between "pure" RRMS and SPMS individuals was constructed. The *sub*-cohort comprises 10 participants with stable RRMS (selected based on the baseline EDSS score) and 9 participants with SPMS. Note: multiple samples from each individual (collected at different time points over an 8-year period) were used to construct this multivariate model to ensure adequate statistical power.

OPLS-DA Model parameters:

Model accuracy: 74.6 ± 2.3%

Model sensitivity: 73.9 ± 3.1%

Model specificity: 77.1 ± 6.2%

AUC (multivariable ROC – metabolites): 0.886 (95% CI 0.834 – 0.957)

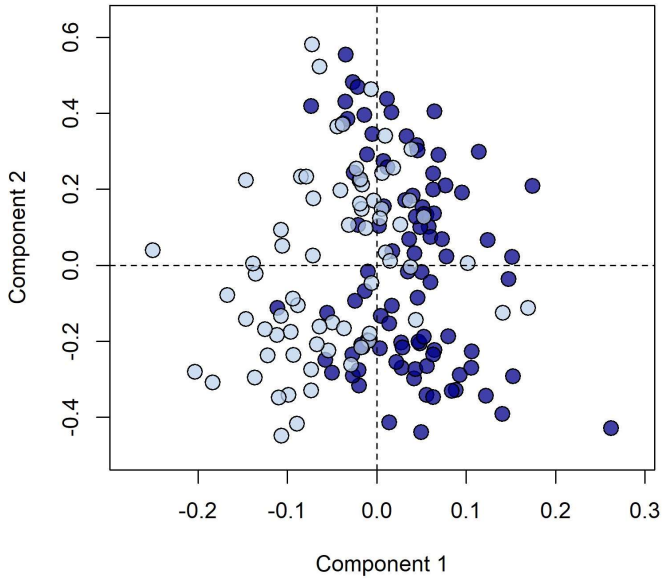

SI eFig. 1 OPLS-DA model discriminating between RRMS (dark blue) and SPMS (light blue) individuals

Supplementary Information – Manuscript 3

SI eTable 3 List of the twenty most discriminatory compounds for the RRMS vs SPMS model based on the OPLS-DA algorithm (the fold change is given for SPMS relative to RRMS (SPMS/RRMS))

Metabolite	NMR Bin	VIP Rank	VIP Score	Fold change
Mobile (–CH_2–)n (LDL dominated)	[1.28..1.30]	1	2.889	0.921
Mobile (–CH_2–)n (LDL dominated)	[1.30..1.32]	2	2.418	0.954
Mobile (–CH_2–)n (LDL dominated)	[1.26..1.28]	3	2.235	0.925
Valine	[0.98..1.00]	4	1.812	1.104
Glutamine	[2.12..2.14]	5	1.810	1.076
Glucose	[3.76..3.78]	6	1.762	1.048
Glutamine	[2.48..2.50]	7	1.683	1.128
Alanine	[1.48..1.50]	8	1.654	1.036
Mobile (–CH_3)n (HDL dominated)	[0.88..0.90]	9	1.621	0.936
GlycA	[3.66..3.68]	10	1.601	1.069
Glucose	[3.88..3.90]	11	1.589	1.046
GlycA/=CH–C**H_2**–CH_2–	[2.04..2.06]	12	1.543	1.024
Mobile (–CH_3)n (HDL dominated)	[0.86..0.88]	13	1.411	1.023
Valine	[1.02..1.04]	14	1.399	1.064
GlycA	[2.00..2.02]	15	1.345	0.963
Glutamine	[2.44..2.46]	16	1.339	1.123
Glucose	[3.70..3.72]	17	1.282	1.036
Glucose	[3.90..3.92]	18	1.235	1.032
Alanine	[1.46..1.48]	19	1.176	1.052
Glutamine	[2.46..2.48]	20	1.152	1.113

(*N.B.* the LDLs and HDLs regions were assigned based on previous signal deconvolution studies (Yeo *et al.* (2021) in *Brain Commun* 3, DOI: 10.1093/braincomms/fcab240).

Random Forest Model parameters:

Model accuracy: 74.9 ± 2.6%

Model sensitivity: 74.4 ± 4.0%

Model specificity: 76.7 ± 3.4%

Supplementary Information – Manuscript 3

SI eTable 4 List of the twenty most discriminatory compounds for the RRMS vs SPMS model based on the Random Forest algorithm

Metabolite	NMR Bin	VIP Rank	VIP Score
Mobile (–CH_3)n (HDL dominated)	[0.82....0.84]	1	3.221
Mobile (–CH_3)n (HDL dominated)	[0.84....0.86]	2	1.566
Mobile (–CH_3)n (HDL dominated)	[0.88....0.90]	3	1.423
Valine	[0.98....1.00]	4	1.367
Mobile (–CH_3)n (VLDL dominated)	[0.90....0.92]	5	1.366
Mobile (–CH_3)n (HDL dominated)	[0.86....0.88]	6	1.261
Valine	[1.04....1.06]	7	1.259
Valine	[1.02....1.04]	8	1.123
Mobile (–CH_2–)n (LDL dominated)	[1.22....1.24]	9	0.998
Mobile (–CH_2–)n (LDL dominated)	[1.24....1.26]	10	0.885
Mobile (–CH_2–)n (LDL dominated)	[1.26....1.28]	11	0.807
Mobile (–CH_2–)n (LDL dominated)	[1.28....1.30]	12	0.737
Mobile (–CH_2–)n (LDL dominated)/lactate	[1.30....1.32]	13	0.685
Alanine	[1.46....1.48]	14	0.641
Lactate	[4.12....4.14]	15	0.608
Glucose	[3.78....3.80]	16	0.607
Glucose	[3.76....3.78]	17	0.606

Supplementary Information – Manuscript 3

Metabolomics discriminates between RRMS and SPMS – Demographics of the eight individuals changing MS stage during the follow-up period

SI eTable 5 Demographic characteristics of individuals transitioning from RRMS to SPMS (the patient numbers correspond to the numbering in Fig. 1)

Patient	Class	Sex	Age sample 1	Age last sample	EDSS sample 1	EDSS last sample	Samples RRMS	Samples SPMS
1	Progressor	F	43.8	51.3	2.5	6.0	5	10
2	Progressor	F	47.5	55	6.0	8.0	4	9
3	Progressor	F	43.9	49.1	3.0	4.5	4	7
4	Progressor	F	40.8	48.9	2.0	4.5	1	15
5	Progressor	F	58.9	64.3	3.5	6.0	2	8
6	Progressor	F	41.7	44.5	3.5	6.5	3	3
7	Progressor	F	42.3	50.7	4.0	6.5	7	3
8	Progressor	M	40.6	47.7	6.5	8.0	1	9
Average	NA	NA	**44.9**	**51.4**	**3.9**	**6.3**		
St. dev.	NA	NA	**6.1**	**6.0**	**1.6**	**1.5**		

Supplementary Information – Manuscript 3

Metabolomics facilitates the staging of multiple sclerosis in an individual

Individuals diagnosed with RRMS who remained stable (classified as RRMS throughout the follow-up period) exhibited a metabolomic signature with minimal fluctuations compared to those who transitioned from RRMS to SPMS (refer to Fig. 1).

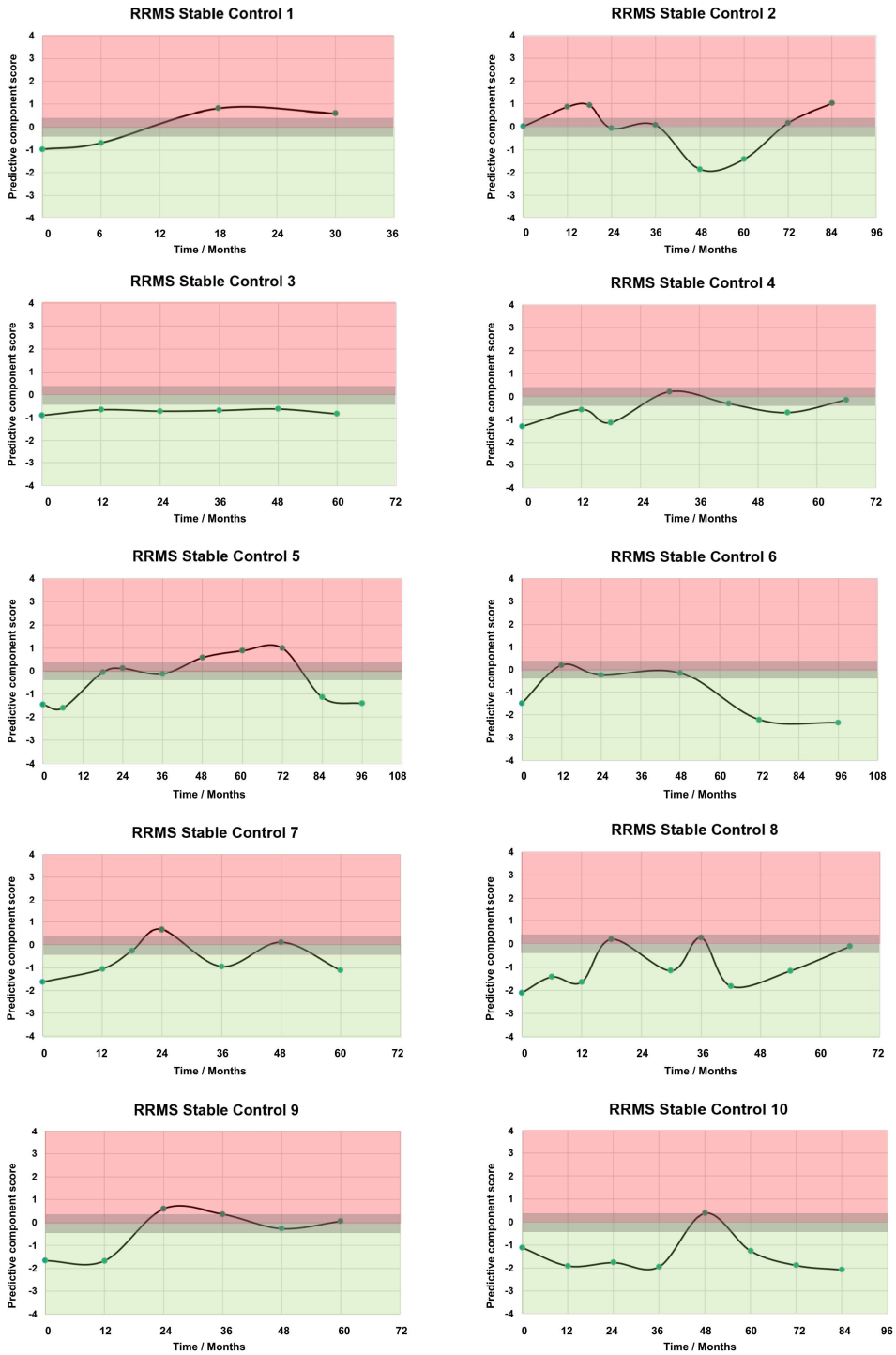

SI eFigure 2. Serum metabolomics as an alternative approach to stage MS. Predicted OPLS-DA scores of 10 control individuals (stable RRMS) that were not used to construct the reference multivariate model. The red-shaded area represents the SPMS-like metabolome, while the green area corresponds to the RRMS-like metabolome (grey-shaded area represents the 95% CI). Each datapoint corresponds to a specific time point when the blood sample was collected.

Supplementary Information – Manuscript 3

Metabolomics facilitates the staging of multiple sclerosis in an individual

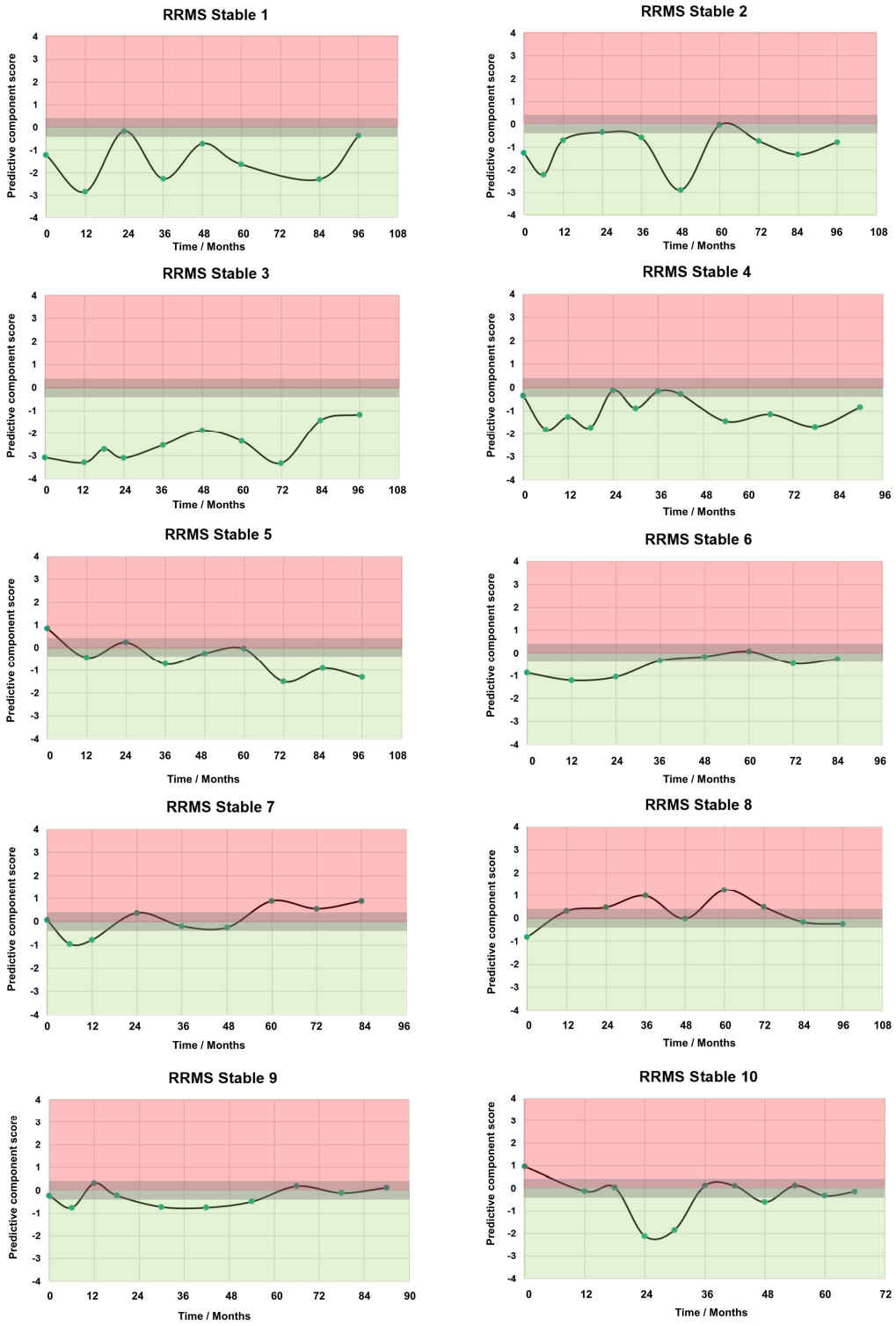

SI eFig. 3 Profile of ten stable RRMS (non-progressing) individuals, originally utilised to construct the reference multivariate model. Subsequently, each of these individuals was excluded from the original model, and a new diagnostic model was constructed to predict the position of the excluded individual. The red-shaded area represents the SPMS-like metabolome, while the green area corresponds to the RRMS-like metabolome (grey-shaded area represents the 95% CI). Each data point corresponds to a specific time point when the blood sample was collected. The predictive component score of each point represents the metabolomics profile at a given time point and was then plotted.

Supplementary Information – Manuscript 3

Metabolomics facilitates the staging of multiple sclerosis in an individual

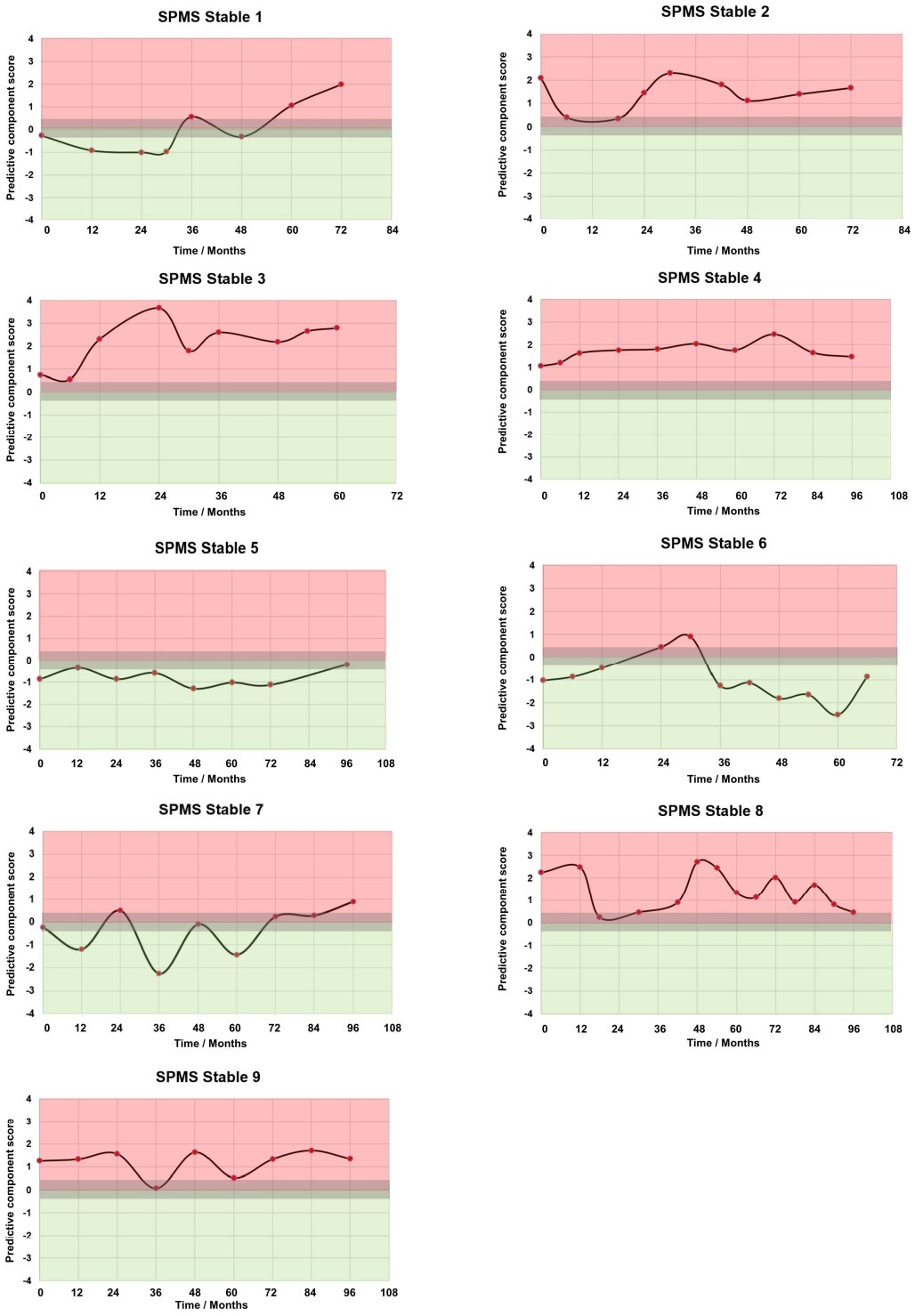

SI eFig. 4 Profile of ten non-transitioning SPMS (slow progressing) individuals, originally utilised to construct the reference multivariate model. Subsequently, each of these individuals was excluded from the original model, and a new diagnostic model was constructed to predict the position of the excluded individual. The red-shaded area represents the SPMS-like metabolome, while the green area corresponds to the RRMS-like metabolome (grey-shaded area corresponds to the 95% CI). Each data point corresponds to a specific time point when the blood sample was collected. The predictive component score of each point represents the metabolomics profile at a given time point and was then plotted.

Supplementary Information – Manuscript 3

Metabolomics integrated with sGFAP allows MS staging in an individual

An OPLS-DA model discriminating between "pure" RRMS and SPMS individuals, involving sGFAP serum concentrations as an additional variable, was constructed. The *sub*-cohort consisted of 10 participants with stable RRMS and 9 participants with SPMS – for patient demographics, refer to SI eTable 2. Note: multiple samples from each individual (collected at different time points over an 8-year period) were used to construct this multivariate model to ensure adequate statistical power.

The integration of NMR metabolomics with serum concentrations of sGFAP augmented the discriminatory capacity of the multivariate model, thereby enhancing accuracy, sensitivity, and specificity parameters.

OPLS-DA Model parameters:

Model accuracy: 78.6 ± 1.8%

Model sensitivity: 79.5 ± 3.1%

Model specificity: 77.1 ± 2.4%

AUC (multivariable ROC – metabolites): 0.912 (95% CI 0.868-0.955)

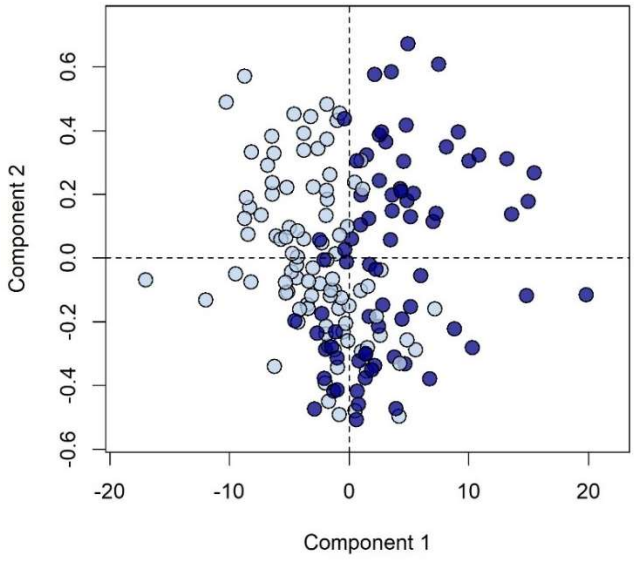

SI eFig. 5 OPLS-DA model discriminating between RRMS (dark blue) and SPMS (light blue) individuals (sGFAP was included as an additional variable in the original NMR metabolomics-based model)

Random Forest Model parameters:

Model accuracy: 82.1 ± 2.0%

Model sensitivity: 85.1 ± 2.6%

Model specificity: 81.2 ± 3.4%

Supplementary Information – Manuscript 3

The baseline concentrations of five serum metabolites and sGFAP and sNfL predict the likelihood of MS disease stage change (transition from RRMS to SPMS)

The Kaplan-Meier analysis revealed that baseline serum metabolites, along with sGFAP and sNfL concentration levels, have predictive capabilities for an individual's transition from RRMS to SPMS.

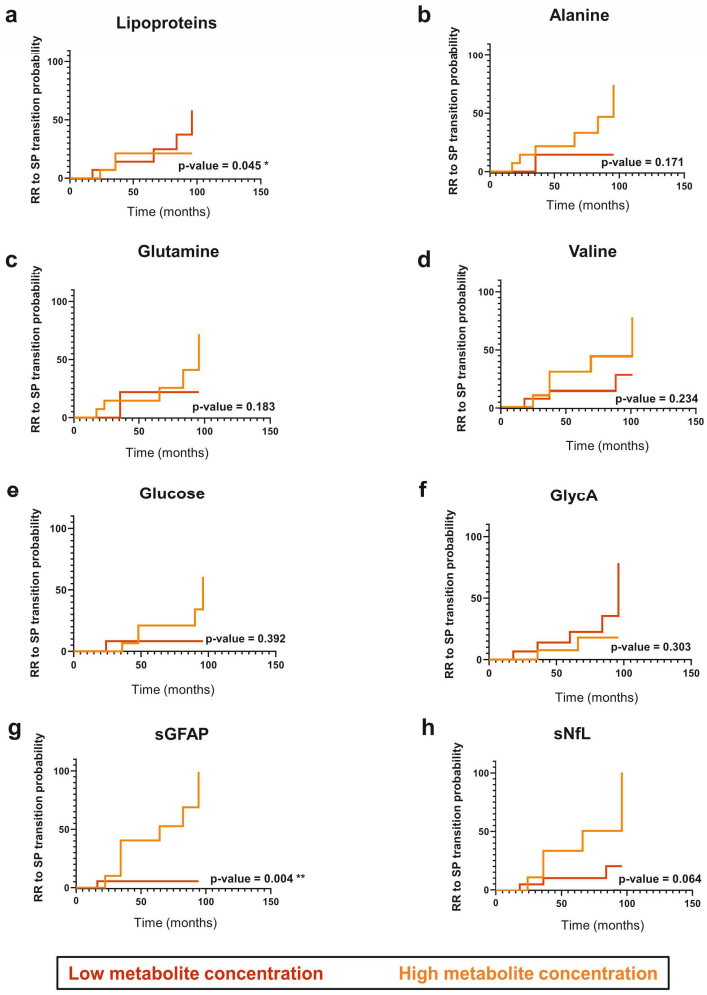

SI eFig. 6 Kaplan-Meier curves for the most discriminatory serum metabolites, sGFAP, and sNfL. The baseline concentrations of potential biomarkers were utilised, and the transition from RRMS to SPMS was defined as the event of interest, as depicted in the Kaplan-Meier curves. High baseline serum levels of the specified metabolite (using *z*-scores of each metabolite concentration) are depicted in yellow, while low baseline metabolite levels are represented in red.

Supplementary Information – Manuscript 3

Integration of sGFAP and NMR-metabolites enhances prediction of disease progression

The predictive accuracy of the different biomarker combinations was assessed by repeating the Random Forest analysis using only the identified discriminatory variables. The mean AUC was calculated across all folds and repetitions to provide an average measure of model discrimination performance. To validate the significance of the model's AUC, a permutation test was performed where class labels were randomly shuffled to create a null distribution of AUC values. The model's AUC was compared against this distribution to confirm it performed better than random chance. The reported AUC represents the mean AUC obtained from the full dataset (all available samples; *i.e.,* not exclusively baseline samples) across all cross-validation runs. The reported ROC curves are the aggregate ROC curves generated by combining true labels and predicted probabilities from all cross-validation folds.

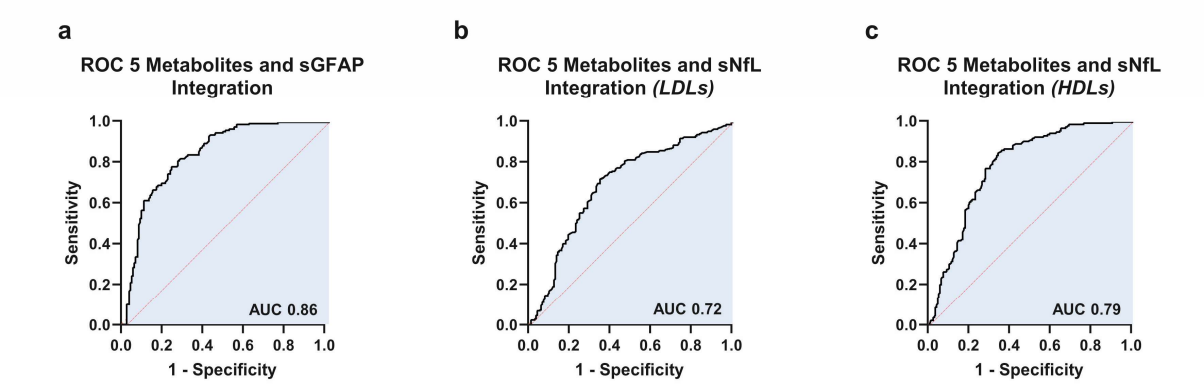

SI eFig 7. Improved classification of future progressors and non-progressors was achieved through the combination of five metabolites (LDLs, glutamine, valine, alanine, glucose) with sGFAP and sNfL. (a) ROC curve for the integration of five serum metabolites (LDLs, alanine, glutamine, valine, glucose) and sGFAP. (b) ROC curve for the integration of five serum metabolites (***LDLs***, alanine, glutamine, valine, glucose) and sNfL.(c) ROC curve for the integration of five serum metabolites (***HDLs***, alanine, glutamine, valine, glucose) and sNfL.

ROC curve eFig. 7a LDLs, alanine, glutamine, valine, glucose and sGFAP

AUC: 0.86 (95% CI 0.80 - 0.90)
Accuracy: 76.2 ± 1.1%
Sensitivity: 74.9 ± 1.6%
Specificity: 77.8 ± 1.5%

Supplementary Information – Manuscript 3

ROC curve eFig. 7b *LDLs*, alanine, glutamine, valine, glucose and sNfL

AUC: 0.72 (95% CI 0.65 - 0.79)
Accuracy: 66.6 ± 1.4%
Sensitivity: 68.0 ± 1.8%
Specificity: 65.8 ± 2.4%

ROC curve eFig. 7c *HDLs*, alanine, glutamine, valine, glucose and sNfL

AUC: 0.79 (95% CI 0.74 - 0.84)
Accuracy: 71.9 ± 1.5%
Sensitivity: 72.1 ± 1.8%
Specificity: 72.2 ± 2.3%

Interestingly, replacing LDLs with HDLs increased the ROC AUC to 0.79; however, this effect was not observed at baseline. This improvement might be attributed to collinearity between NfL and LDLs, with HDLs potentially capturing complementary information that the other variables do not provide.

Supplementary Information – Manuscript 3

Independent cohort validation confirms the metabolomic findings

SI eTable 6 *Demographic characteristics of progressing and non-progressing MS individuals for the validation cohort (Oxford MET cohort). Non-progressors exhibited stable ambulatory function, maintaining unrestricted walking ability at both baseline and 3-year follow-up, whereas progressors experienced pronounced ambulatory decline, defined by a reduction in walking capacity to ≤500 meters. The individual characteristics, presented as mean ± standard error of the mean (SEM), were compared using Fisher's exact test for categorical variables and the Wilcoxon test for continuous variables that were not normally distributed. Statistical significance was determined with the following thresholds: *p < 0.05, **p < 0.01, ***p < 0.001.*

Parameter	Progressors	Non-progressors	p-value
N	19	24	NA
Female (%)	13 (68.4%)	13 (54.2%)	0.37
Age first sample	46.6 ± 10.8	43.4 ± 8.9	0.30
BMI (baseline)	25.8 ± 5.0	25.6 ± 4.9	0.92
EDSS first sample	3.5 ± 1.1	2.9 ± 1.1	0.11
Disease course			
RRMS	14 (73.7%)	23 (95.8%)	
SPMS	3 (15.8%)	0 (0.0%)	0.13
PPMS	1 (5.3%)	0 (0.0%)	
CIS	1 (5.3%)	1 (4.2%)	
Therapy - baseline			
Untreated	**7**	**9**	
Orals	**7**	**8**	
	dimethyl fumarate (5)	dimethyl fumarate (7)	
	fingolimod (1)	fingolimod (1)	
	teriflunomide (1)	-	0.43
Monoclonal antibodies	**3**	**1**	
	natalizumab (3)	natalizumab (1)	
Platform	**2**	**6**	
	interferon-beta-1a (1)	interferon-beta-1a (1)	
	glatiramer acetate (1)	glatiramer acetate (5)	

5. 4 Statement of Authorship

Title of paper	Plasma *N*-Glycan Profiling Enhances Diagnostic Precision in Multiple Sclerosis, AQP4-Ab NMOSD, and MOGAD
Publication status	Submitted – revised manuscript submitted
Publication details	Kacerova, T., Sealey, M., Saldana, L., Xiong, W., Woodhall, M., Waters, P., Sénard, T., Cheeseman, J., Urbanowicz, P., Elgood Hunt, G., Spencer, D.I.R., McCullagh, J.S.O., Leite, M.I., DeLuca, G., Palace, J., Anthony, D.C., Yeo, T., Probert, F.: **Plasma *N*-Glycan Profiling Enhances Diagnostic Precision in Multiple Sclerosis, AQP4-Ab NMOSD, and MOGAD.** Manuscript submitted (17/03/2025) to: *Neurology: Neuroimmunology and Neuroinflammation*)

Student confirmation

Student name	Tereza Kacerova
Contribution to the paper	T.K. Data analysis and interpretation, Manuscript writing; T. S. provided data processing software training; W. X. provided assistance with data processing; P. S., J. C., P. U., G. E. H., D. I. R. S. (Ludger Ltd.) performed the UHPLC-MS analysis; M. S. and L. S. were involved in the clinical sample collection. M. I. L., J. P., G. de L., T. Y., F. P., and D. C. A. were responsible for clinical trial oversight and patient recruitment; F. P., T. Y., and D. C. A. conceptualisation of the clinical samples analyses; F. P., J. S. O. M., T. Y., and D. C. A. are the principal investigators/supervisors of the research described in the manuscript, contributed extensively to project/data conceptualisation and visualisation, and manuscript reviewing/editing.
Date	30/06/2025
Signature	

Supervisor confirmation

By signing the Statement of Authorship, you are certifying that the candidate made a substantial contribution to the publication, and that the description described above is accurate.

Supervisor name	Prof James S. O. McCullagh
Contribution to the paper	I am happy to state that the candidate made a major and substantial contribution this publication, and that the description above is accurate.
Date	29th June 2025
Signature	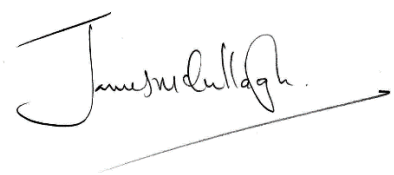

Chapter 5 Plasma *N*-Glycomics as a Diagnostic Tool in Demyelinating Neuroinflammatory Disorders

5. 1 Project context and chapter overview

Building on the prognostic modelling of multiple sclerosis progression using serum metabolomics (**Chapter 4**), this chapter expands the multi-omics framework to address a distinct but complementary clinical challenge: differential diagnosis of CNS demyelinating diseases. Accurate discrimination between multiple sclerosis, AQP4-Ab NMOSD, and MOGAD remains difficult, particularly in seronegative cases or early disease stages when clinical and radiological features often overlap.[1, 2] Misclassification may result in detrimental therapeutic decisions, as disease-modifying treatments indicated for multiple sclerosis, particularly B cell-depleting agents, have been shown to exacerbate disease activity in Ab-mediated disorders such as AQP4-Ab NMOSD.[3, 4] Furthermore, the increasing availability of high-efficacy, disease-specific treatments underscores the need for reliable, minimally invasive tools that can support early and accurate diagnosis.[5, 6, 7]

While metabolomics offers insight into broader biochemical perturbations, glycosylation, a fundamental post-translational modification involved in immune regulation, remains underexplored in this context. Notably, prior analyses in the Oxford MS cohort (**Chapter 4**) identified the GlycA signal (2.00 ppm) in serum NMR spectra as a potentially discriminatory feature,[8] raising the possibility that blood glycan profiles might capture disease-specific immunopathological differences.

In this chapter, we apply a targeted plasma *N*-glycomics approach to explore this hypothesis. Using ultra-high-performance hydrophilic interaction liquid chromatography (UHPLC–HILIC) coupled with high-resolution mass spectrometry (HRMS), we characterised glycosylation patterns in a clinically stratified cohort spanning multiple sclerosis (RRMS and SPMS), AQP4-Ab NMOSD, and MOGAD. This platform enables the high-resolution profiling of structurally diverse *N*-glycans, including isomers typically unresolved by conventional methods. Data acquisition was carried out in collaboration with Ludger Ltd. (UK), with rigorous quality control and multivariate analysis applied to identify diagnostic signatures.

By situating glycomics within a broader multi-omics diagnostic framework, this study aims to enhance disease classification strategies and support future integrative approaches. Crucially, it also explores whether plasma *N*-glycan signatures reflect underlying disease biology rather than transient serological markers, thereby supporting their application in routine diagnostic workflows, particularly when Ab status is inconclusive.

5. 2 References

(1) Jurynczyk, M.; Geraldes, R.; Probert, F.; Woodhall, M. R.; Waters, P.; Tackley, G.; DeLuca, G.; Chandratre, S.; Leite, M. I.; Vincent, A.; et al. Distinct brain imaging characteristics of autoantibody-mediated CNS conditions and multiple sclerosis. *Brain* **2017**, *140*, 617-627. DOI: 10.1093/brain/aww350.
(2) Yeo, T. R.; Probert, F.; Jurynczyk, M.; Sealey, M.; Cavey, A.; Claridge, T. D. W.; Woodhall, M.; Waters, P.; Leite, M. I.; Anthony, D. C.; et al. Classifying the antibody-negative NMO syndromes Clinical, imaging and metabolomic modeling. *Neurol-Neuroimmunol* **2019**, *6* (6). DOI: ARTN e62610.1212/NXI.0000000000000626.
(3) Palace, J.; Lin, D. Y.; Zeng, D.; Majed, M.; Elsone, L.; Hamid, S.; Messina, S.; Misu, T.; Sagen, J.; Whittam, D.; et al. Outcome prediction models in AQP4-IgG positive neuromyelitis optica spectrum disorders. *Brain* **2019**, *142* (5), 1310-1323. DOI: 10.1093/brain/awz054 From NLM Medline.
(4) Traub, J.; Hausser-Kinzel, S.; Weber, M. S. Differential Effects of MS Therapeutics on B Cells-Implications for Their Use and Failure in AQP4-Positive NMOSD Patients. *Int J Mol Sci* **2020**, *21* (14). DOI: 10.3390/ijms21145021 From NLM Medline.
(5) Cree, B. A. C.; Bennett, J. L.; Kim, H. J.; Weinshenker, B. G.; Pittock, S. J.; Wingerchuk, D. M.; Fujihara, K.; Paul, F.; Cutter, G. R.; Marignier, R.; et al. Inebilizumab for the treatment of neuromyelitis optica spectrum disorder (N-MOmentum): a double-blind, randomised placebo-controlled phase 2/3 trial. *Lancet* **2019**, *394* (10206), 1352-1363. DOI: 10.1016/S0140-6736(19)31817-3.
(6) Pittock, S. J.; Barnett, M.; Bennett, J. L.; Berthele, A.; de Seze, J.; Levy, M.; Nakashima, I.; Oreja-Guevara, C.; Palace, J.; Paul, F.; et al. Ravulizumab in Aquaporin-4-Positive Neuromyelitis Optica Spectrum Disorder. *Ann Neurol* **2023**, *93* (6), 1053-1068. DOI: 10.1002/ana.26626.
(7) Probert, F.; Yeo, T. R.; Zhou, Y. F.; Sealey, M.; Arora, S.; Palace, J.; Claridge, T. D. W.; Hillenbrand, R.; Oechtering, J.; Kuhle, J.; et al. Determination of CSF GFAP, CCN5, and vWF Levels Enhances the Diagnostic Accuracy of Clinically Defined MS From Non-MS Patients With CSF Oligoclonal Bands. *Front Immunol* **2022**, *12*. DOI: ARTN 81135110.3389/fimmu.2021.811351.
(8) Jurynczyk, M.; Probert, F.; Yeo, T.; Tackley, G.; Claridge, T. D. W.; Cavey, A.; Woodhall, M. R.; Arora, S.; Winkler, T.; Schiffer, E.; et al. Metabolomics reveals distinct, antibody-independent, molecular signatures of MS, AQP4-antibody and MOG-antibody disease. *Acta Neuropathol Com* **2017**, *5*. DOI: ARTN 9510.1186/s40478-017-0495-8.

5. 3 Manuscript information

This chapter consists of a research article manuscript submitted to *Neurology: Neuroimmunology and Neuroinflammation* (17/03/2025).

Kacerova, T., Sealey, M., Saldana, L., Xiong, W., Woodhall, M., Waters, P., Sénard, T., Cheeseman, J., Urbanowicz, P., Elgood Hunt, G., Spencer, D.I.R., McCullagh, J.S.O., Leite, M.I., DeLuca, G., Palace, J., Anthony, D.C., Yeo, T., Probert, F.: **Plasma *N*-Glycan Profiling Enhances Diagnostic Precision in Multiple Sclerosis, AQP4-Ab NMOSD and MOGAD.**

Manuscript status: *Revisions submitted; awaiting editorial decision.*

Plasma *N*-Glycan Profiling Enhances Diagnostic Precision in Multiple Sclerosis, AQP4-Ab NMOSD, and MOGAD

Tereza Kacerova[1], Megan Sealey[2], Luisa Saldana[3], Wenzheng Xiong[2], Mark Woodhall[3], Patrick Waters[3], Thomas Sénard[4,5], Jack Cheeseman[4], Paulina Urbanowicz[4], Georgia Elgood Hunt[4], Daniel I.R. Spencer[4], James S.O. McCullagh[1], Maria Isabel Leite[3], Gabriele DeLuca[3], Jacqueline Palace[3], Daniel C. Anthony[2], Tianrong Yeo[6,7,8*], Fay Probert[1]

[1]Department of Chemistry, University of Oxford, Chemistry Research Laboratory, Mansfield Road, Oxford, OX1 3TA, UK.
[2]Department of Pharmacology, University of Oxford, Oxford, OX1 3QT, UK.
[3]Nuffield Department of Clinical Neurosciences, John Radcliffe Hospital, University of Oxford, Oxford, OX3 9DU, UK.
[4]Ludger Ltd, Culham Science Centre, Abingdon, UK.
[5]Division of Endocrinology and Diabetes Prevention and Care, IRCCS Azienda Ospedaliero-Universitaria di Bologna, Bologna, 40138, Italy.
[6]Department of Neurology, National Neuroscience Institute, 11 Jalan Tan Tock Seng, Singapore, 308433, Singapore.
[7]Duke-NUS Medical School, 8 College Road, Singapore, 169857, Singapore.
[8]Lee Kong Chian School of Medicine, Nanyang Technological University, 11 Mandalay Road, Singapore, 308232, Singapore.

*Corresponding author(s). E-mail(s): yeo.tianrong@singhealth.com.sg;

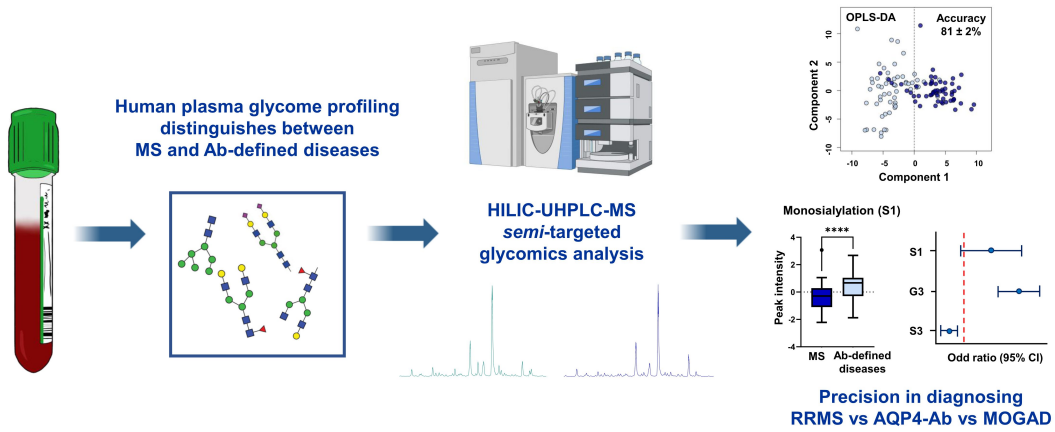

Abstract

Background and Objectives: Differentiating multiple sclerosis (MS) from antibody (Ab)-defined diseases, such as neuromyelitis optica spectrum disorders (NMOSDs) remains challenging, particularly as Ab levels decline. *N*-glycans play a key role in immunity, with changes in branching and fucosylation linked to T/B cell function and MS onset, while increased *N*-acetylglucosamine residues correlate with disease progression. Despite growing recognition of glycosylation in neuroinflammation, direct comparisons of the *N*-glycome between MS and Ab-defined diseases are lacking. This study is the first to assess whether plasma *N*-glycome profiling can effectively differentiate these conditions and their subtypes.
Methods: This cohort study included 120 participants: 30 relapsing-remitting MS (RRMS), 30 secondary progressive MS (SPMS), 30 myelin oligodendrocyte glycoprotein Ab-associated disease (MOGAD), and 30 aquaporin-4 (AQP4)-Ab NMOSD patients, recruited from the John Radcliffe Hospital, Oxford University Hospitals NHS Trust. Plasma *N*-glycans were analysed using ultra-high-performance (UHPLC) hydrophilic interaction liquid chromatography (HILIC) coupled with high-resolution mass spectrometry (HRMS). Orthogonal partial least squares discriminant analysis (OPLS-DA) was applied to identify disease-specific glycomic patterns.
Results: Distinct *N*-glycome profiles were identified across diseases and phenotypes. Plasma *N*-glycans differentiated MS from Ab-defined diseases with 80.5% (±1.5%) accuracy, MOGAD from AQP4-Ab NMOSD with 77.8% (±3.1%) accuracy, and RRMS from SPMS with 75.2% (±3.6%) accuracy. Key discriminatory features included increased monosialylation (S1; OR = 2.57, $p < 0.0001$), trigalactosylation (G3; OR = 2.70, $p < 0.0001$), highly branched *N*-glycans (HB; OR = 2.32, $p = 0.0002$), and antennary fucosylation (AF; OR = 2.89, $p < 0.0001$), effectively distinguishing Ab-defined diseases from MS, independent of Ab serostatus at the time of sampling.
Discussion: These findings underscore the potential of plasma *N*-glycomics as a diagnostic tool for neuroinflammatory diseases. While further research is needed to clarify the mechanistic links between glycomic alterations and disease pathology, our results suggest that plasma *N*-glycan profiling could improve disease classification. Given its non-invasive and cost-effective nature, this approach holds promise as a complementary diagnostic tool for CNS demyelinating diseases in clinical practice.

Keywords: *N*-glycomics, HILIC-UHPLC-MS, multiple sclerosis, neuromyelitis optica spectrum disorders

1 Background

The clinical and MRI overlap between multiple sclerosis (MS), aquaporin-4 (AQP4)-antibody (Ab) neuromyelitis optica spectrum disorders (NMOSDs), and myelin oligodendrocyte glycoprotein Ab-associated disease (MOGAD) poses a diagnostic challenge, particularly at onset or when Ab titre has diminished.[1,2] While brain MRI can differentiate MS from AQP4-Ab NMOSD and MOGAD with high sensitivity and specificity, a significant proportion of patients with AQP4-Ab NMOSD or MOGAD exhibit no detectable brain lesions. Consequently, MRI may be indistinct especially if it is performed outside of an attack.[1,3,4] Ab testing remains the gold standard; however, Ab levels may fall below detection limits during remission or following immunotherapy,[1,4] highlighting the need for reliable biomarkers to distinguish MS from Ab-defined diseases.[5] Accurate diagnosis is crucial, as MS-specific therapies can trigger relapses in Ab-defined diseases,[6] while the availability of early high-efficacy MS treatments,[7] along with emerging monoclonal Ab therapies for AQP4-Ab NMOSD, further emphasise this need.[8-10] Traditionally, distinguishing relapsing-remitting MS (RRMS) from secondary progressive MS (SPMS) relies on clinical evaluation and disability indices like the Expanded Disability Status Scale (EDSS). However, early SPMS diagnosis lacks consensus on clinical thresholds and rely on long-term observation of irreversible disability progression. While emerging biofluid markers show promise for detecting MS progression, further validation is required before clinical integration.[11-13]

Nuclear magnetic resonance (NMR)-metabolomics of human blood has been shown to accurately distinguish RRMS from AQP4-Ab

NMOSD, MOGAD, and SPMS.[12-18] Notably, glycoprotein A (GlycA), an NMR-specific marker of *N*-acetylglucosamine glycan residues linked to inflammation,[19] shows elevated levels in SPMS,[12,13] suggesting that *N*-glycan structures may serve as markers of transition to SPMS. In line with these findings, increased complex glycans, characterised by multiple galactose and sialic acid residues, as well as antennary fucosylation (AF), have been observed in MS patient plasma compared to healthy controls.[20] Similarly, a higher abundance of bisected and monogalactosylated (G1) glycans has been reported in the cerebrospinal fluid (CSF) of MS patients.[21] However, no studies have investigated *N*-glycome alterations in relation to MS progression. Likewise, despite distinct mechanisms of Ab-mediated and cell-mediated diseases and the established role of *N*-glycans in T and B cell function, direct comparisons of *N*-glycome profiles between MS and Ab-defined diseases are lacking. *N*-glycans modulate immune responses through Fcγ receptor IIIa (FcγRIIIa), with glycan modifications influencing inflammation.[22] Reduced *N*-glycan branching has been shown to trigger autoimmunity and promote demyelination in murine models,[23] highlighting the potential of plasma *N*-glycome profiling to provide novel insights into disease mechanisms, onset, and progression.

Using ultra-high-performance (UHPLC) hydrophilic interaction liquid chromatography (HILIC) coupled with high-resolution mass spectrometry (HRMS), we analysed samples from a cohort of 30 RRMS, 30 SPMS, 30 MOGAD, and 30 AQP4-Ab NMOSD patients to identify novel *N*-glycan biomarkers and glycan traits for distinguishing MS from Ab-defined diseases, differentiating RRMS from SPMS, and classifying MOGAD from AQP4-Ab NMOSD.

2 Material and Methods

2.1 Study subjects and procedures

Patients were recruited from the John Radcliffe Hospital, Oxford University Hospital Trust, as part of the Oxford METabolomics cohort, with consent under the Oxford Radcliffe Biobank and ethical approval from the NRES Committee South Central - Oxford C (REC reference: 09/H0606/5+5). MS patients met the 2017 McDonald diagnostic criteria, while SPMS was diagnosed in individuals with prior RRMS diagnosis and at least one year of disability progression without relapses.[24] AQP4-Ab NMOSD was diagnosed using the 2015 IPND criteria, with AQP4 Ab confirmed via live cell-based assay.[25] MOGAD was diagnosed with MOG Ab positivity on live cell-based assay in patients with at least one inflammatory demyelinating event compatible with MOGAD.[26] Blood samples were collected in lithium-heparin tubes (Becton Dickinson 367375), left at room temperature for 30 minutes, then centrifuged at 1,300g for 10 minutes, as previously described.[13] Plasma was aliquoted and stored at $-80\,^{\circ}$C. A random subset of MS samples collected before April 2019 and Ab-defined disease samples collected before February 2018, with no prior freeze-thaw cycles, were selected for glycomics analysis.

2.2 HILIC-HRMS analysis of glycans

The HILIC-UHPLC-MS analysis was carried out by Ludger Ltd., UK. A volume of $5\,\mu$L of either plasma (single aliquot), plasma standard (triplicate aliquot), or immunoglobulin G (IgG) standard (triplicate aliquot) was added to each well of a skirted $180\,\mu$L volume 96-well plate (4titide Ltd., UK). The plate was transferred to a liquid handling robot (Hamilton, Birmingham, UK) for a semi-automatic processing. Recombinant PNGase F (P0709, New England Biolabs, UK) was used to release *N*-glycans from glycoproteins. Each sample was adjusted to a total volume of $9\,\mu$L by adding $4\,\mu$L of water, followed by the addition of $1\,\mu$L of denaturation buffer. The samples were vortexed and centrifuged before incubation at 37 °C for 16 hours. The resulting sample mixtures were dried using a vacuum centrifuge (Thermo Fisher Scientific, UK) for 2 hours at RT. The glycans were converted to aldoses by addition of $20\,\mu$L 1% formic acid solution (Sigma Aldrich, UK). The samples were vortexed and centrifuged before incubation for 45 minutes at room temperature. The samples were filtered through a LudgerClean (LC-PBM-96, Ludger Ltd., UK) 96-well protein binding membrane plate with water (2 x $100\,\mu$L) to remove excess protein. The resulting $200\,\mu$L solutions were transferred to a non-skirted $300\,\mu$L volume 96-well plate (4titude Ltd, UK) and dried down in a vacuum centrifuge for 9 hours at RT. The dried glycans were subjected to fluorescent labelling by reductive amination with $20\,\mu$L procainamide labelling solution (LT-KPROC-96, Ludger Ltd., UK). The samples were vortexed and briefly centrifuged before incubation for 1 hour at 65 °C. The samples were mixed with $80\,\mu$L acetonitrile (Romil Ltd., UK) before being transferred to a LudgerClean procainamide clean-up plate (LC-PROC-96, Ludger Ltd., UK) and washed with acetonitrile (3 x $100\,\mu$L) to remove excess labelling solution. The labelled glycans were recovered by washing with water (2 x $100\,\mu$L). For LC-MS/MS analysis, $100\,\mu$L of each sample was

added to 300 μL of acetonitrile. System suitability standards (plasma, IgG, Glucose Homopolymer (GHP, Ludger Ltd., UK)) and blanks were prepared by adding 25 μL of each standard to 75 μL acetonitrile. All samples were analysed by HILIC-HRMS with florescence detection. A volume of 20 μL of each standard and sample was injected onto an ACQUITY UPLC BEH-Glycan 1.7 μm, 2.1 mm×150 mm column (Waters, UK) at 40 °C on a Thermo Fisher Scientific Vanquish UHPLC instrument with a fluorescence detector (λex= 310, λem=370 nm), coupled to a Thermo Fisher Scientific Orbitrap Exploris 120 mass spectrometer. The chromatography conditions were: Solvent A 50 mM ammonium formate pH 4.4 made from LudgerSep N-Buffer (Ludger Ltd., UK), and solvent B acetonitrile. Gradient conditions were 0 to 53.5 min, 76 to 51% B, 0.4 mL/min; 53.5 to 55.5 min, 51% to 0% B, 0.4 mL/min to 0.2 mL/min; 55.5 to 57.5 min, 0% B at a flow rate of 0.2 mL/min; 57.5 to 59.5 min, 0 to 76% B, 0.2 mL/min; 59.5 to 65.5 min, 76% B, 0.2 mL/min; 65.5 to 66.5 min, 76% B, 0.2 mL/min to 0.4 mL/min; 66.5 to 70.0 min, 76% B, 0.4 mL/min. The Exploris 120 settings were source vaporisation temperature, 350 °C; ion transfer tube temperature, 325 °C; sheath gas, 50 arbitrary units (Arb); auxiliary gas, 10 Arb; sweep gas, 1 Arb; capillary voltage, 3500 V; pos. ion mode. MS spectra were recorded in the mass range, 500–2500 m/z; resolution, 1.5×104; data dependent acquisition mode; RF level, 70%.

2.3 HILIC-HRMS data processing

Fluorescence data was quantified using HappyTools (v0.1-beta1), based on peak area.[27] MS data was processed with LaCyTools (v1.1.0-alpha), using extracted ion chromatogram peak areas.[28] Signals meeting the criteria for mass accuracy (±10 ppm), isotopic pattern quality (IPQ < 0.15), and signal-to-noise ratio ($S/N > 0.27$) were analysed.

2.4 *N*-glycans nomenclature

The standard Oxford Glycan Notation was followed.[29] *N*-glycans comprise two linked *N*-acetylglucosamines (GlcNAc) and three mannose residues, which may be modified by fucose (F), core mannose (M), galactose (G), sialic acid (S), bisecting GlcNAc (B), and branching patterns (antenna - A), with numeric notation indicating residue counts.[29] Isomeric glycans were named by elution order (e.g. FA3G3S2, FA3G3S2.1, etc.). *N*-galactosylation traits were calculated as the ratio of specific glycan peaks to the total glycan integral (e.g. G2/total*100).[20, 30] A list of traits is provided in SI Table 1.

2.5 Statistical analysis

Curated LaCyTools-derived features were imported into R (v4.2.1), sum normalised, standardised (mean-centred and scaled to unit variance), and analysed using *in-house* R scripts and the *ropls* package.[31] To evaluate differences between groups, orthogonal partial least square discriminant analysis (OPLS-DA) was performed, initially using individual glycan signals and subsequently the derived glycan traits, with 10-fold cross-validation, 100 repetitions, and permutation testing.[13] Accuracy, sensitivity, and specificity were reported for independent test data not used in model training. For significant models (Kolmogorov–Smirnov $p < 0.05$), discriminatory variables were identified separately for glycans and glycan traits. The average Variable Importance in Projection (VIP) scores were assessed to quantify each variable contribution to the model. Glycans and traits above the VIP inflection point were subjected to univariate analysis.

Odds ratios (ORs) were calculated in R (v4.2.1) to assess the change in diagnosis probability per unit increase in glycan traits. Binary classification models evaluated trait-outcome relationships, and results were visualised as forest plots with 95% confidence intervals (CIs). Remaining univariate analyses were conducted in GraphPad Prism 10. Continuous variables were compared using unpaired two-sample t-tests with false discovery rate (FDR) correction (Benjamini-Hochberg, $p < 0.05$), while categorical variables were analysed using the Chi-square test. Data are presented as Tukey boxplots (IQR with whiskers at 1.5×IQR). For multiple group comparisons, one-way ANOVA with Tukey's *post hoc* test was applied, controlling for multiple comparisons ($p < 0.05$).

3 Results

3.1 Patient characteristics

A total of 120 patients were included: RRMS ($n = 30$), SPMS ($n = 30$), MOGAD ($n = 30$), and AQP4-Ab NMOSD ($n = 30$). Demographic characteristics are summarised in Table 1. Consistent with prevailing knowledge, females predominated across groups: RRMS (60%), SPMS (90%), MOGAD (63%), and AQP4-Ab NMOSD (90%) ($p = 0.0016$).[32-34] Mean ages were: AQP4-Ab NMOSD, 52 years; MOGAD, 38 years; RRMS, 45 years; SPMS, 60 years ($p = 0.0002$), consistent with later onset in AQP4-Ab NMOSD and SPMS. Despite significant demographic differences (Table 1, SI Fig. 1A-E), multivariate analysis showed that gender, age, disease duration, relapse

Table 1: Demographic characteristics of RRMS, SPMS, MOGAD, AQP4-Ab NMOSD individuals. Chi-squared and One-way ANOVA p-values are reported for categorical and continuous variables, respectively. Tukey's *post hoc* p-values < 0.05, 0.01, and 0.001 relative to RRMS are represented by *, **, and *** while significant differences relative to MOGAD are represented by †, ††, and †††. For a summary of all post hoc results, refer to SI Fig. 1A-D. Age, BMI, EDSS, and time from last relapse are given as mean ± standard deviation (SD). ‡The indicated values are recorded at the sampling point. ‡‡Seronegative MOGAD patients had previously tested positive for MOG Ab but were seronegative at the time of sampling, consistent with the fluctuating serostatus observed in MOGAD. AQP4-Ab NMOSD patients who were previously positive for AQP4 Ab but with Ab titres ≤ 1:20 at time of sampling were classified as seronegative. ‡‡‡ Of the 11 MOGAD patients receiving corticosteroid therapy, 6 also received immunosuppressive treatment (Azathioprine: 4, Methotrexate: 2).

	RRMS	SPMS	MOGAD	AQP4-Ab NMOSD	p-value
N	30	30	30	30	NA
Female (%)	18 (60%)	27 (90%)*	19 (63%)	27 (90%)*, †	0.0016
Age (years)‡	45.18±10.12	59.86±9.90***, †††	37.52±11.93	51.67±17.05 †††	0.0002
BMI (kg/m^2)‡	27.95±7.64	25.81±7.07	27.72±5.55	28.89±8.05	0.429
EDSS‡	3.38±1.75††	6.67±1.04***, †††	1.92±1.34	3.78±2.22†††	$p < 0.0001$
Time from last relapse (yrs)‡	3.69±3.18	11.67±6.67***, †††	2.12±2.41	3.13±2.31	$p < 0.0001$
Ab-positivity status‡	NA	NA	22/30‡‡	24/30‡‡	NA
Therapy - sampling					
Orals, n (%)	22 (73%)	2 (7%)	0 (0%)	0 (0%)	NA
	Interferon beta-1a (4)	Interferon beta-1a (1)	-	-	
	Glatiramer acetate (10)	Peginterferon beta-1a (1)	-	-	
	Alemtuzumab (2)	-	-	-	
	Dimethyl fumarate (3)	-	-	-	
	Natalizumab (2)	-	-	-	
	Fingolimod (1)	-	-	-	
Corticosteroids, n (%)	1 (3%)	1 (3%)	11 (37%)‡‡‡	0 (0%)	NA
	Prednisolone (1)	Betamethasone (1)	Prednisolone (11)	-	NA
Immunosuppression, n (%)	0 (0%)	0 (%)	11 (37%)	30 (100%)	NA
	-	-	Azathioprine (6)	Mycophenolate mofetil (9)	
	-	-	Methotrexate (2)	Azathioprine (10)	
	-	-	Tocilizumab (1)	Methotrexate (5)	
	-	-	Mycophenolate mofetil (2)	Rituximab (4)	

timing, or medication did not enhance OPLS-DA model accuracy. Moreover, no strong correlations were found between discriminatory glycans and clinical variables ($R^2 < 0.20$, Spearman's $\rho < 0.30$). All AQP4-Ab NMOSD patients received immunosuppression, while 73% of RRMS patients were on disease-modifying therapies (DMTs). MOGAD treatments included steroids (17%), immunosuppressants (17%), or both (20%). OPLS-DA score plots (SI Fig. 2-4) showed no clustering by medication, suggesting minimal impact of pharmacotherapy on glycomic profiles.

3.2 *N*-glycomics enables accurate discrimination between MS and Ab-defined diseases

To assess the discriminatory potential of the human plasma N-glycome, we analysed 120 HILIC-HRMS spectra (30 per condition – RRMS, SPMS, AQP4-Ab NMOSD, MOGAD). We initially focused on discerning between participants diagnosed with MS (combining RRMS and SPMS) from those diagnosed with Ab-defined diseases (AQP4-Ab NMOSD and MOGAD). The ensemble of OPLS-DA models achieved a mean predictive accuracy of 80.5±1.5% for MS vs Ab-defined diseases (Fig. 1A-i), significantly outperforming the randomly permuted ensemble (50.1±6.5%, $p < 0.0001$; Fig. 1A-ii), highlighting the discriminatory potential of the plasma N-glycome in discriminating between MS and Ab-defined diseases.

3.3 Plasma *N*-glycomics as a discriminatory tool for RRMS, SPMS, MOGAD, and AQP4-Ab NMOSD

Given that the plasma N-glycome demonstrated robust discriminatory capacity in distinguishing MS from Ab-defined diseases, we assessed its ability to differentiate individual conditions. OPLS-DA models were built for pairwise comparisons (RRMS, SPMS, MOGAD, AQP4-Ab NMOSD), achieving consistently higher predictive accuracy than random class ensembles (Fig. 1B-G). OPLS-DA successfully separated RRMS and SPMS from AQP4-Ab NMOSD, with accuracies of 92.7±1.4% (Fig. 1B) and 96.7±0.8% (Fig. 1C), respectively. Significant differences were also observed between SPMS and MOGAD, achieving an accuracy of 75.8±2.4% (Fig. 1D). The model distinguishing RRMS from MOGAD showed a separation accuracy of 57.3±4.1% (Fig. 1E), while distinguishing between RRMS and SPMS

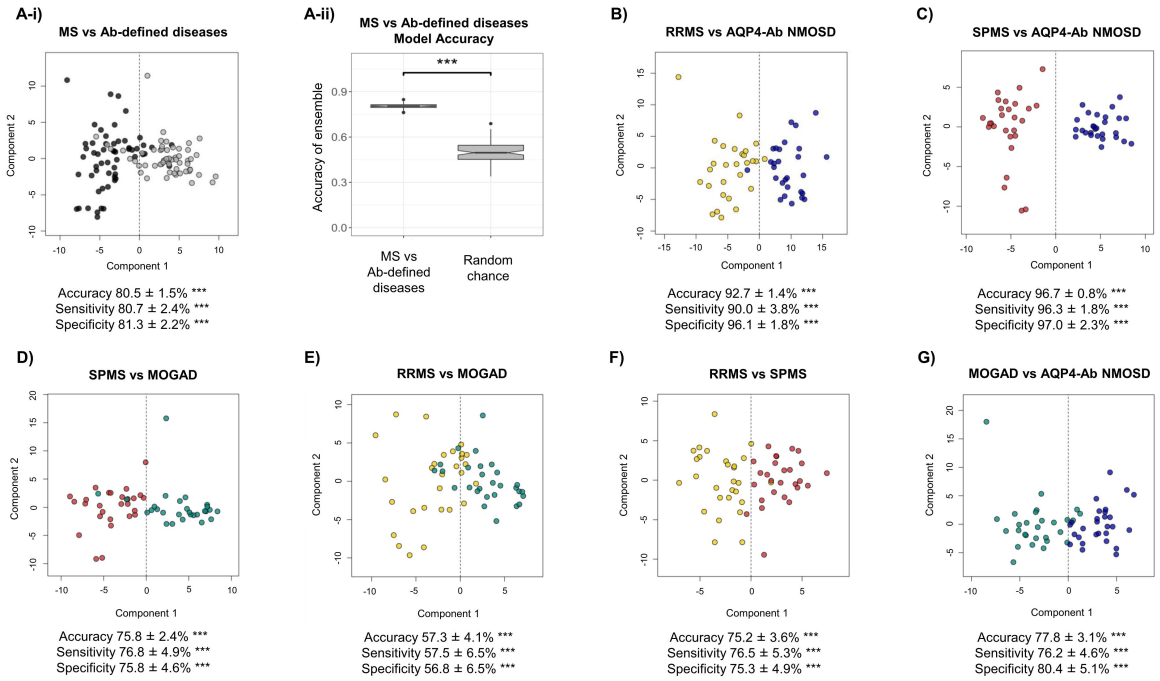

Fig. 1: ***N*-glycome discriminates between MS, Ab-defined diseases, and their phenotypes.** **(A-i)** OPLS-DA scores plot illustrating distinct separation of MS (RRMS and SPMS combined, $n = 60$, black) and Ab-defined diseases (MOGAD and AQP4-Ab NMOSD combined, $n = 60$, grey) plasma *N*-glycomes (model accuracy: 80.5±1.5%, specificity: 81.3±2.2%, sensitivity: 80.7±2.4%). **(A-ii)** The accuracy of the ensemble comprising 1000 MS vs Ab-defined diseases models, assessed through an independent test set classification, significantly surpassing that of the 1000 randomly permuted models. Significance was determined by Kolmogorov-Smirnov test $p < 0.0001$ (***). **(B-G)** OPLS-DA scores plots demonstrating patient differentiation based on plasma glycomics profiles for RRMS (yellow), SPMS (red), MOGAD (teal), and AQP4-Ab NMOSD (blue) across all permutations. Each model includes accuracy, sensitivity, and specificity parameters derived from cross-validation. Significance relative to a random class ensemble was determined by Kolmogorov-Smirnov test p-values $p < 0.0001$ (***). **(B)** RRMS vs AQP4-Ab NMOSD; **(C)** SPMS vs AQP4-Ab NMOSD; **(D)** SPMS vs MOGAD; **(E)** RRMS vs MOGAD; **(F)** RRMS vs SPMS; **(G)** MOGAD vs AQP4-Ab NMOSD.

demonstrated an accuracy of 75.2±3.6% (Fig. 1F). Furthermore, the plasma *N*-glycome effectively differentiated between Ab-defined diseases based on Ab profiles, achieving an accuracy of 77.8±3.1% for MOGAD vs AQP4-Ab NMOSD (Fig. 1G). All OPLS-DA models - with the exception of MOGAD vs RRMS - demonstrated high accuracy, sensitivity, and specificity, underscoring the diagnostic potential of glycan analysis. Notably, the separation among AQP4-Ab NMOSD, MOGAD, and MS was achieved independently of Ab serostatus at the time of sampling, with the majority of seronegative AQP4-Ab NMOSD and MOGAD patients accurately classified (SI Fig. 5A-E), supporting plasma *N*-glycome profiling as a robust, complementary diagnostic tool beyond traditional Ab markers. The most discriminatory 25 glycans for each model are summarised in SI Table 2. Fig. 2 displays chromatograms for each condition, highlighting the three glycan signals with the highest VIP score for each diagnostically relevant comparison.

The analysis of glycan signals with the highest VIP scores revealed that highly branched, complex glycans with multiple modifications - such as antennae structures, sialylation, and galactosylation - were consistently the most discriminatory across all comparisons. In the RRMS vs AQP4-Ab NMOSD model, the most distinctive glycans included A3G3S1.3 (1W-ANOVA $p < 0.0001$, SI Fig. 6A), which was markedly elevated in AQP4-Ab NMOSD, as well as FA2BG2S1.1 (1W-ANOVA $p < 0.0001$, SI Fig. 6B) and FA3G3S3.3 (1W-ANOVA $p = 0.001$, SI Fig. 6C), both of which were significantly reduced in AQP4-Ab NMOSD compared to the other groups. In the RRMS vs MOGAD model, the primary discriminatory features were unresolved chromatographic peaks (SI Table 2). Among the assigned glycans, the most distinctive were A3G3S1.4 (1W-ANOVA $p =$

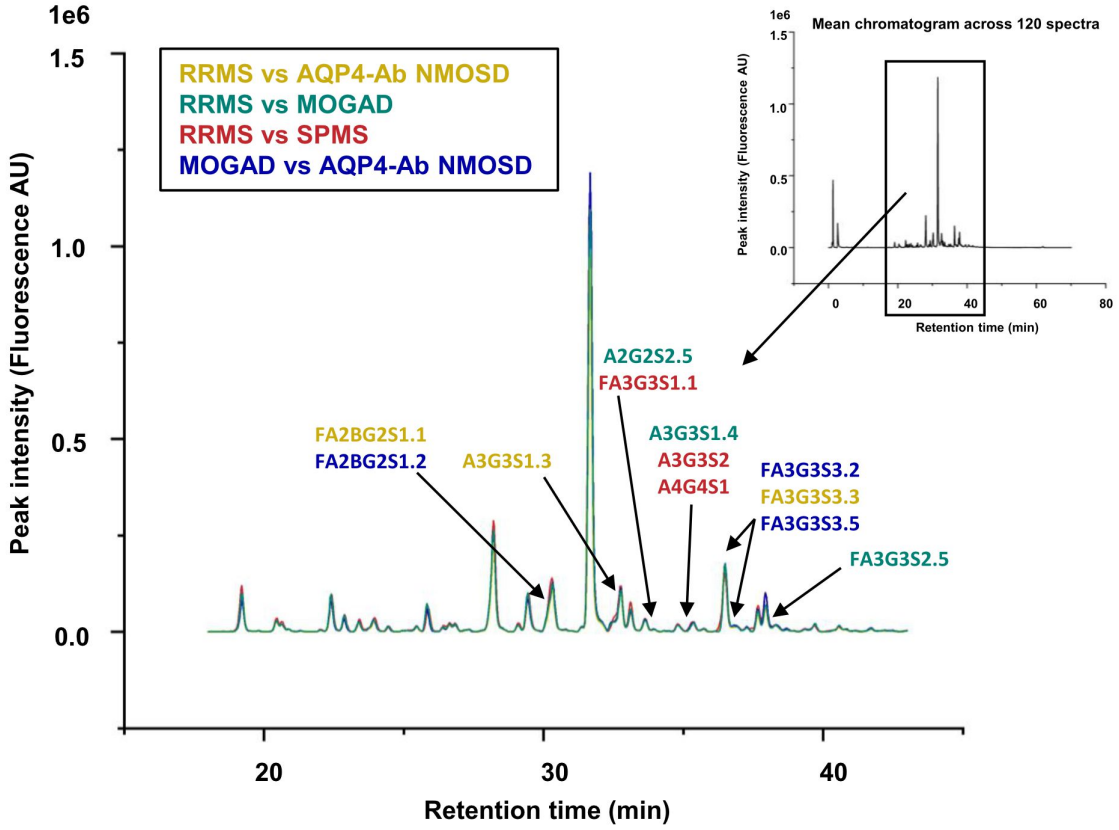

Fig. 2: **Representative HILIC-HRMS fluorescence profiles of individuals with RRMS, SPMS, MOGAD, and AQP4-Ab NMOSD.** The complete chromatogram is displayed in the top right corner, with a magnified view of the elution region (18-43 min), where most glycan species are identified. Each chromatogram represents the average of 30 samples per condition (RRMS yellow; SPMS red; MOGAD teal; AQP4-Ab NMOSD blue) for each condition. Three glycan signals (*note*: some co-elute within a multiple glycan peak) with the highest VIP score are highlighted for each diagnostically relevant comparison: RRMS vs AQP4-Ab NMOSD (yellow); MOGAD vs RRMS (teal); SPMS vs RRMS (red); AQP4-Ab NMOSD vs MOGAD (blue). The inset shows the overlay of the averaged chromatogram across all 120 spectra.

0.001, SI Fig. 6D), A2G2S2.5 (1W-ANOVA $p = 0.008$, SI Fig. 6E), and FA3G3S2.5 (1W-ANOVA $p < 0.0001$, SI Fig. 6F). For the RRMS vs SPMS model, glycan abundance changes were less pronounced, with A4G4S1 (1W-ANOVA $p = 0.14$, SI Fig. 6G), A3G3S2 (1W-ANOVA $p = 0.003$, SI Fig. 6H), and FA3G3S1.1 (1W-ANOVA $p = 0.002$, SI Fig. 6I) being the most discriminatory. The AQP4-Ab NMOSD vs MOGAD model was primarily driven by highly modified, fucosylated glycans, such as FA3G3S3.5 (1W-ANOVA $p < 0.0001$, SI Fig. 6J), FA3G3S3.2 (1W-ANOVA $p < 0.0001$, SI Fig. 6K), and FA2BG2S1.2 (1W-ANOVA $p < 0.0001$, Fig. SI 6L). Notably, 1W-ANOVA (particularly SI Fig. 6J,K) revealed significant differences in abundance for AQP4-Ab NMOSD compared to the other three groups. This suggests that AQP4-Ab NMOSD is the primary driver of separation in the MS vs Ab-defined diseases model (Fig. 1A-i), a conclusion supported by the high accuracy of the AQP4-Ab NMOSD vs SPMS and AQP4-Ab NMOSD vs RRMS models (Fig. 1B-C).

3.4 Plasma *N*-glycan traits differentiate MS from Ab-defined diseases, highlighting branching and sialylation patterns

To further understand the observed changes in the glycomics profiles, OPLS-DA was applied to *N*-glycosylation-derived traits (SI Table 1). While the accuracy of these models decreased by an average

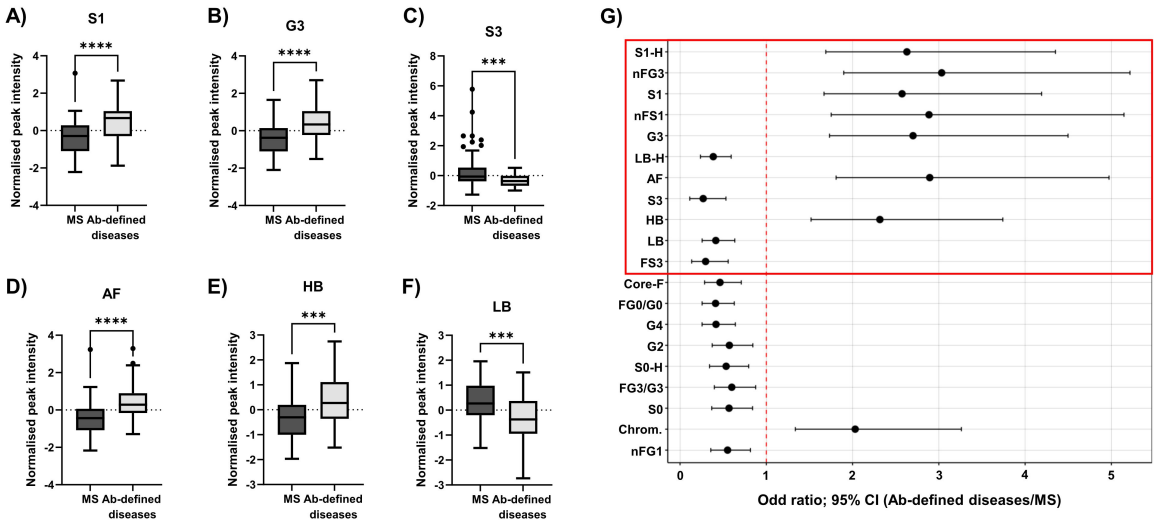

Fig. 3: **Key glycan traits driving separation between MS and Ab-defined diseases based on OPLS-DA VIP scores and statistical significance.** Results from unpaired two-sample t-test (FDR-corrected) are provided with significance level indicated ($p < 0.001$ ***; $p < 0.0001$ ****). **(A)** S1 ($p < 0.0001$); **(B)** G3 ($p < 0.0001$); **(C)** S3 ($p = 0.0004$); **(D)** AF ($p < 0.0001$); **(E)** HB ($p = 0.0002$); **(F)** LB ($p = 0.0001$). **(G)** Calculated OR (given for Ab-defined diseases / MS) for each glycan trait along with 95% CI. The red box highlights traits with the highest VIP scores, determined by the inflection point cut-off and ranked accordingly. AF (antennary fucosylation), G2–G4 (di- to tetragalactosylation), H (hybrids), HB (high branching glycans), LB (low branching glycans), nFG1 (monogalactosylation in non-fucosylated glycans), nFG3 (trigalactosylation in non-fucosylated glycans), nFS1 (monosialylation of non-fucosylated glycans), S0 (neutral glycans), S1 (monosialylation), S3 (trisialylation), and chrom. (sum of unresolved chromatographic peaks).

of 5-10% compared to those trained on all glycan signatures - except for the RRMS vs MOGAD model, where the accuracy of the glycan trait-based model increased - this decline was likely due to the reduced number of variables and the loss of diagnostically relevant information when consolidating individual signals (SI Table 3). Nevertheless, all models outperformed the random class ensemble, allowing for a detailed examination of the discriminatory traits identified through the VIP scores (SI Tables 4-8).

OPLS-DA successfully distinguished MS from Ab-defined diseases based solely on *N*-glycan traits, achieving an accuracy of 71.5±2.5%, sensitivity of 71.7±3.3%, and specificity of 72.4±3.4% (SI Table 4). The most discriminatory traits were primarily associated with variations in galactosylation, and fucosylation, specifically: monosialylation excluding hybrids (S1-H, $p < 0.0001$; OR = 2.63), trigalactosylation in non-fucosylated glycans (nFG3, $p < 0.0001$; OR = 3.03; Fig. 3G), monosialylation (S1, $p < 0.0001$; OR = 2.57; Fig. 3A, G), monosialylation in non-fucosylated glycans (nFS1, $p < 0.0001$; OR = 2.89; Fig. G); trigalactosylation (G3, $p < 0.0001$ OR = 2.70; Fig. 3B, G), and AF ($p < 0.0001$; OR = 2.89; Fig. 3D, G) were decreased in MS compared to Ab-defined diseases while trisialylation (S3, $p = 0.0004$; OR = 0.27; Fig. 3C, G) and trisialylation of fucosylated glycans (FS3, $p = 0.0005$; OR = 0.14; Fig. 3G) were elevated in MS. Notably, the complexity of glycan branching emerged as one of the key discriminatory features, with MS characterised by higher levels of low branching (LB) glycans ($p = 0.0001$; OR = 0.41; Fig. 3F, G) and LB excluding hybrids (LB-H; $p < 0.0001$; OR = 0.39; Fig. 3G), and lower levels of high branching (HB) glycans ($p = 0.0002$; OR = 2.32; Fig. 3E, G) relative to Ab-defined diseases.

We then focused on identifying glycan traits that differentiate the individual conditions. As SPMS is a distinct progressive stage, the key comparisons centred on differentiating RRMS from MOGAD and AQP4-Ab NMOSD, which is particularly relevant for early disease classification. The OPLS-DA model, based exclusively on glycan traits, demonstrated significant differentiation between RRMS and AQP4-Ab NMOSD, achieving an accuracy of 86.3±2.2% (SI Table 5). Notably, most of the discriminatory traits (Fig. 4A) overlapped with those identified in the MS vs Ab-defined diseases model (Fig. 3G). AF ($p = 0.0004$; OR = 3.63, Fig. 5B) and G3 ($p = 0.0004$; OR

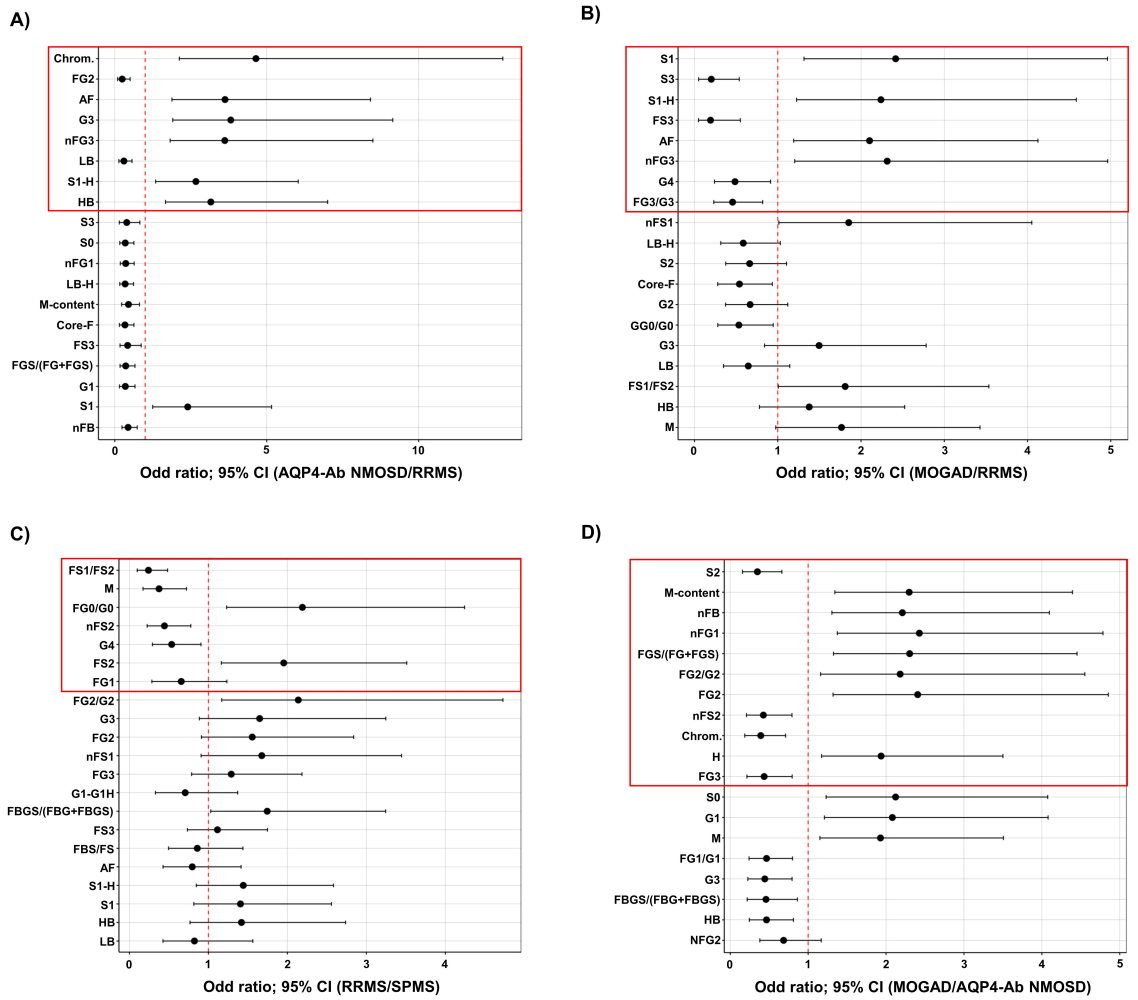

Fig. 4: **Odds ratios (OR) for key glycan traits distinguishing MS and Ab-defined disease phenotypes.** OR (given as AQP4-Ab NMOSD/RRMS in **A**; MOGAD/RRMS in **B**; RRMS/SPMS in **C**; MOGAD/AQP4-Ab NMOSD in **D**) for the individual traits along with 95% CI. The red box highlights the traits with the highest VIP scores (based on the inflection point cut-off; the individual traits are ordered based on the corresponding VIP score). *Note*: In Figs. A and C, the FG0/G0 trait was excluded due to high variability (see the forest plots in SI Figs. 7,8). AF (antennary fucosylation), FG0/G0 (fucosylated to non-fucosylated glycans ratio), FG1–FG2 (mono- and digalactosylation in fucosylated glycans), FG2/G2 (fucosylated to non-fucosylated digalactosylated glycans ratio), FGS/(FG+FGS) (sialylation of fucosylated galactosylated structures), FS1/FS2 (ratio of fucosylated monosialylated to disialylated glycans), FS2–FS3 (di- to trisialylation of fucosylated glycans), G1–G4 (mono- to tetragalactosylation), H (hybrids), HB (high branching glycans), LB (low branching glycans), M (high mannose glycans), M-content (high mannose glycans including hybrids), nFB (bisecting non-fucosylated glycans), nFG1–nFG3 (mono- to trigalactosylation in non-fucosylated glycans), nFS2 (disialylation of non-fucosylated glycans), S0–S3 (neutral to trisialylated glycans), and chrom. (sum of unresolved chromatographic peaks).

= 3.82; Fig. 5C) were significantly decreased in RRMS compared to AQP4-Ab NMOSD (SI Fig. 7). Furthermore, the inverse relationship between HB and LB glycans was conserved, with HB decreased (p = 0.001; OR = 3.16) and LB increased (p = 0.001; OR = 0.30) in RRMS. S3, previously identified as a discriminatory trait between MS and Ab-defined diseases, was elevated in RRMS, though the OR was relatively modest (p = 0.03; OR = 0.39). Similarly, although S1, identified as discriminatory in the MS vs Ab-defined diseases model, did not feature among the top VIP scores in the RRMS and AQP4-Ab NMOSD model, it exhibited the same trend (p = 0.02; OR = 1.25). Importantly, assessing S1 for non-hybrid structures only (S1-H) significantly increased the OR (p =

0.01; OR = 2.67). Conversely, digalactosylation in fucosylated glycans (FG2), which was not a discriminatory trait in the MS vs Ab-defined diseases model, was highly discriminatory in this comparison ($p = 0.0004$; OR = 0.24, Fig. 5A). Finally, the ratio of fucoyslated to non-fucosylated agalactosylated glycans (FG0/G0) was significantly increased in RRMS, despite being associated with high variability ($p = 2.03E-07$; OR = 24.57; SI Fig. 7).

The OPLS-DA model for RRMS vs MOGAD was the only comparison where accuracy increased when using glycan traits alone, achieving an accuracy of 67.6±2.9% (SI Table 6). The identified discriminatory glycan traits (Fig. 4B) were consistent with the findings from the RRMS vs AQP4-Ab NMOSD model and closely mirrored the results from the general MS vs Ab-defined diseases model (Fig. 3G). The most discriminatory glycan traits were identified as S1 ($p = 0.05$; OR = 2.42, Fig. 5D), S1-H ($p = 0.03$; OR = 2.24, Fig. 5F), AF ($p = 0.07$; OR = 2.10), and nFG3 ($p = 0.07$; OR = 2.31), all of which were decreased in RRMS relative to MOGAD. Conversely, S3 ($p = 0.03$; OR = 0.20, Fig. 5E), FS3 ($p = 0.07$; OR = 0.19), tetragalactosylation (G4, $p = 0.14$; OR = 0.49), and the ratio of fucosylated to non-fucosylated trigalactosylated glycans (FG3/G3, $p = 0.07$; OR = 0.46) were all significantly elevated in RRMS (Fig. 4B).

We further aimed to identify key glycan traits associated with MS, with a specific focus on distinguishing between RRMS and SPMS profiles (Fig. 4C). Compared to Ab-defined diseases, MS patients - particularly those with SPMS - were characterised by elevated levels of high mannose-content glycans (M, $p = 0.04$; OR = 0.38, Fig. 5H), with higher concentrations observed in SPMS. Although the RRMS vs SPMS model showed relatively high discriminatory capacity using all glycan signals (accuracy 75.8±2.4%; Fig. 1F), the accuracy decreased to 62.2±3.8% when only glycan traits were considered. This decline in accuracy corresponded to a smaller number of significantly altered glycan traits (Fig. 4C, SI Table 7). Among the glycan traits highlighted by the VIP scores, significant changes were observed in the ratio between mono- to disialylated fucosylated glycans, which was elevated in SPMS (FS1/FS2; $p = 0.0004$; OR = 0.38, Fig. 5G). Other discriminatory traits included FG0/G0 ($p = 0.04$; OR = 2.19, Fig. 5I) and disialylation in fucosylated glycans (FS2, $p = 0.11$; OR = 1.95), which were elevated in RRMS, while disialylation in non-fucosylated glycans (nFS2, $p = 0.04$; OR = 0.44), G4 ($p = 0.14$; OR = 0.54), and monogalactosylation in fucosylated glycans (FG1, $p = 0.72$; OR = 0.66) were increased in SPMS.

For discrimination between MOGAD and AQP4-Ab NMOSD, model accuracy decreased to 74.5±3.0% when only traits-derived information was used (SI Table 8). Examination of glycan traits with the highest VIP scores (Fig. 4D) revealed that disialylation was among the most discriminatory features, with both S2 ($p = 0.02$; OR = 0.35, Fig. 5J) and nFS2 ($p = 0.02$; OR = 0.43) significantly increased in AQP4-Ab NMOSD compared to MOGAD. Other prominent glycan traits included FG0/G0 ($p < 0.0001$; OR = 24.57, SI Fig. 8) and sialylation of fucosylated galactosylated glycans (FGS/(FG+FGS), $p = 0.02$; OR = 2.30) that were elevated in MOGAD individuals.

A similar trend was observed for FG2 ($p = 0.02$; OR = 2.41), while an inverse trend was noted for the related trigalactosylation in fucosylated glycans (FG3, $p = 0.02$; OR = 0.44). Additionally, monogalactosylation in non-fucosylated glycans (nFG1, $p = 0.02$; OR = 2.43) and the incidence of bisecting GlcNAc in non-fucosylated glycans (nFB, $p = 0.02$; OR = 2.21, Fig. 5L) were significantly decreased in AQP4-Ab NMOSD. In contrast to models focusing on MS vs Ab-defined diseases, the model centred solely on Ab-defined diseases identified mannose-containing (M-content) glycans and hybrids (H) as highly discriminatory, both of which were elevated in MOGAD (M-content ($p = 0.02$; OR = 2.30, Fig. 5K) and H ($p = 0.03$; OR = 1.94)).

These results indicate that specific glycan species are more abundantly expressed on plasma glycoproteins in MS patients compared to Ab-defined diseases. Fig. 6 comprehensively illustrates the overlap of individual glycan traits and summarises the significantly altered profiles across conditions, as determined by VIP scores from the multivariate models.

4 Discussion

Current diagnostic techniques for MS, MOGAD, and AQP4-Ab NMOSD rely on clinical evaluation, Ab detection, and imaging.[1,2,35-37] While effective, these approaches may be limited by accuracy, cost, and availability. Our previous studies across multiple independent cohorts demonstrated that NMR-based blood metabolomics can reliably distinguish MS from Ab-defined diseases and differentiate RRMS from SPMS, with significant differences also observed in *N*-glycan side-chain resonances between RRMS and SPMS.[13,16,18] Given the established link between altered glycosylation and neuroinflammation,[38,39] we investigated the diagnostic potential of *N*-glycans in MS and Ab-defined diseases.

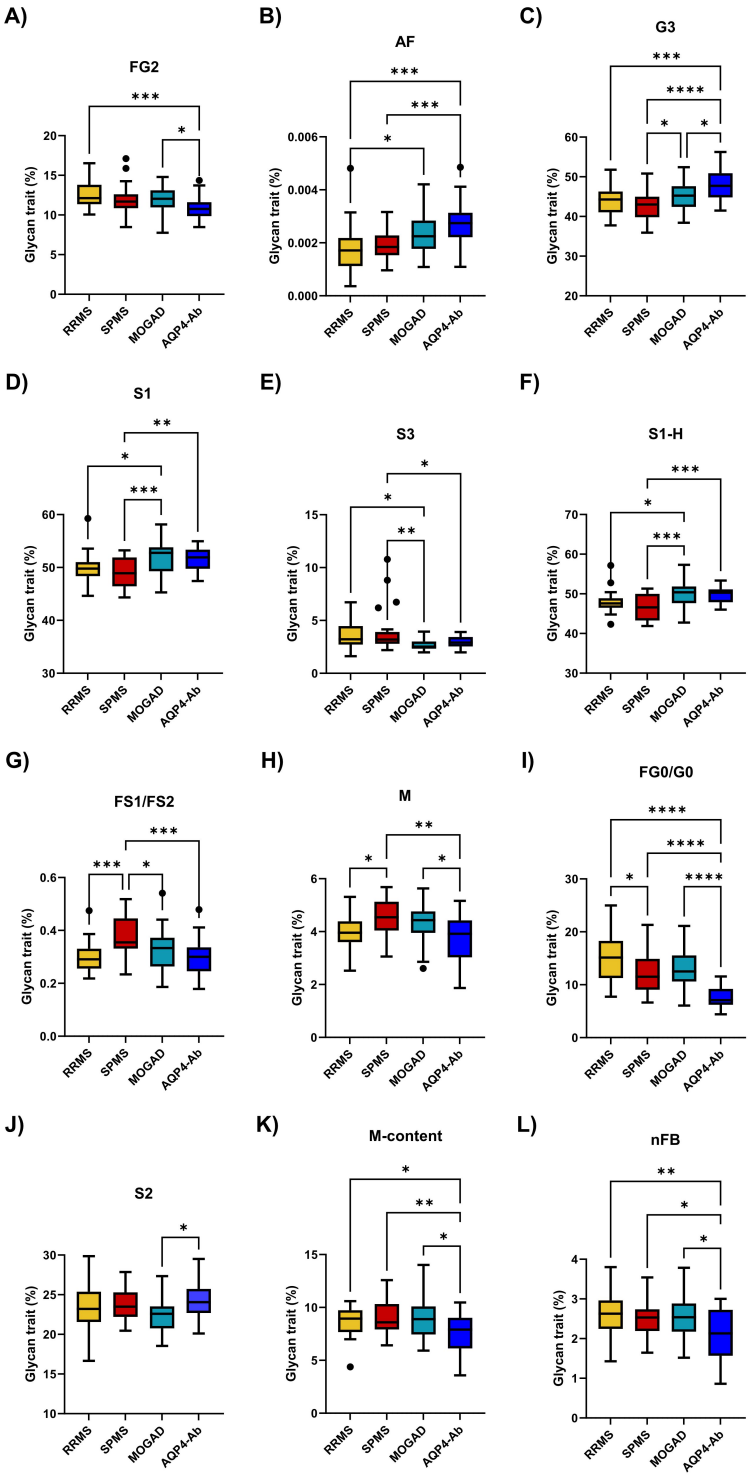

Fig. 5: **1W-ANOVA results (FDR-corrected) with Tukey's *post hoc*, adjusted for multiple comparisons (results detailed in SI Table 9), for the three glycan traits with the highest VIP scores in each of the four diagnostically relevant models**: **(A-C)** AQP4-Ab NMOSD vs RRMS; **(D-F)** MOGAD vs RRMS; **(G-I)** RRMS vs SPMS; **(J-L)** AQP4-Ab NMOSD vs MOGAD. **(A)** Digalactosylation in fucosylated glycans (FG2; $p = 0.002$); **(B)** antennary fucosylation (AF; $p < 0.0001$); **(C)** trigalactosylation (G3; $p < 0.0001$); **(D)** monosialylation (S1; $p = 0.0003$); **(E)** trisialylation (S3; $p = 0.003$); **(F)** monosialylation excluding hybrids (S1-H; $p = 0.0003$); **(G)** ratio of fucosylated monosialylated to disialylated glycans (FS1/FS2; $p < 0.0001$); **(H)** high mannose glycans (M; $p = 0.002$); **(I)** ratio of fucosylated to non-fucosylated agalactosylated glycans (FG0/G0; $p < 0.0001$); **(J)** disialylation (S2; $p = 0.02$); **(K)** all glycans containing mannose (M-content; $p = 0.003$); **(L)** incidence of bisecting non-fucosylated glycans (nFB; $p = 0.003$).

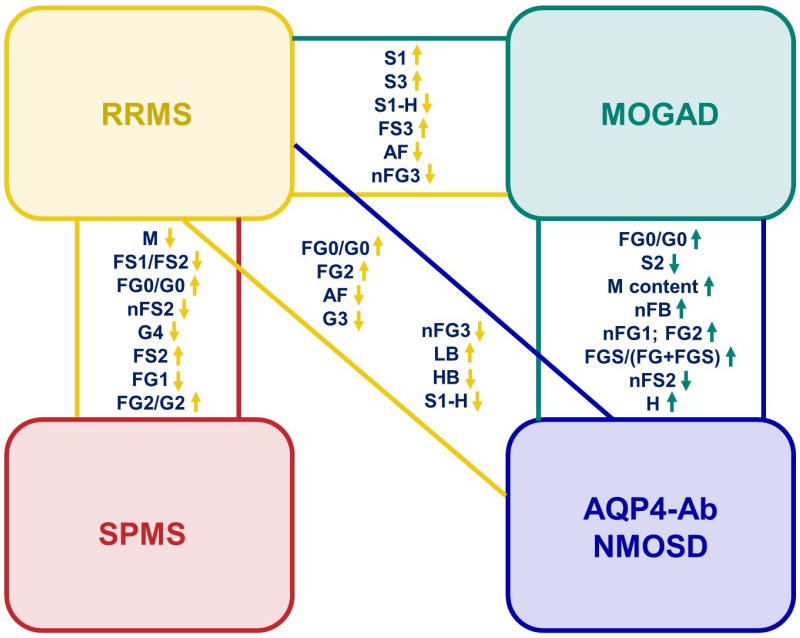

Fig. 6: **Summary of the discriminatory glycan traits identified by OPLS-DA for RRMS (yellow), SPMS (red), MOGAD (teal), and AQP4-Ab NMOSD (blue).** Arrows indicate increases (↑) or decreases (↓) in specific glycan traits within the patient group represented by the corresponding colour. Lines connecting groups illustrate how glycan traits change when comparing groups, with the arrow's direction indicating the change with respect to the starting group (e.g., the yellow arrow on the yellow-to-red line shows glycan trait changes between RRMS and SPMS, relative to RRMS). Glycan traits distinguishing SPMS from Ab-defined diseases (MOGAD and AQP4-Ab NMOSD) are omitted for clarity, as these are less relevant for clinical diagnostic purposes. The individual glycan traits abbreviations stand for: AF (antennary fucosylation), FG0/G0 (fucosylated to non-fucosylated glycans ratio), FG1–FG2 (mono- and digalactosylation in fucosylated glycans), FG2/G2 (fucosylated to non-fucosylated digalactosylated glycans ratio), FGS/(FG+FGS) (sialylation of fucosylated galactosylated structures), FS1/FS2 (fucosylated monosialylated-to-disialylated glycans ratio), FS2–FS3 (di- to trisialylation of fucosylated glycans), G3–G4 (tri- to tetragalactosylation), H (hybrids), HB (high branching glycans), LB (low branching glycans), M (high mannose glycans), M-content (high mannose glycans including hybrids), nFB (bisecting non-fucosylated glycans), nFG1–nFG3 (mono- to trigalactosylation in non-fucosylated glycans), nFS2 (disialylation of non-fucosylated glycans), S1–S3 (mono- to trisialylation).

Plasma *N*-glycome profiling effectively differentiates MS from Ab-defined diseases with 81% accuracy. Key discriminatory features include sialylation (S1, S1-H, S3), galactosylation, and AF, with the most pronounced alterations observed in AQP4-Ab NMOSD. Glycan branching also emerged as a distinguishing factor, with HB glycans significantly elevated in Ab-defined diseases, particularly in RRMS compared to AQP4-Ab NMOSD. However, limited clinical research on glycosylation in MS[17, 20, 21, 40] and even scarcer data on MOGAD and AQP4-Ab NMOSD[41] present challenges for direct comparisons. Existing studies often involve mixed cohorts, complicating subtype-specific analyses. Cvetko *et al.* reported increased HB glycans in MS compared to healthy controls, but no differences across MS stages, partially aligning with our findings.[20] Although glycan branching patterns effectively distinguished MS from Ab-defined diseases, with elevated HB glycans in the latter, no significant differences were detected between MS subtypes. The elevated levels of HB glycans in Ab-defined diseases may appear counterintuitive, considering recent studies in rodent models showing that *N*-glycan branching can reduce B cell-mediated inflammation and demyelination.[23] Similarly, *N*-glycan branching on antigen-presenting cell (APC) surface has been shown to modulate APC function, leading to reduced B cell APC-induced proinflammatory responses and cytokine release.[23] Furthermore, a recent study by Sy *et al.* reported that oral GlcNAc supplementation in MS patients led to

increased *N*-glycan branching, along with a reduction in serum levels of pro-inflammatory cytokines and neurofilament light chain (NfL).[22] The discrepancies between experimental and clinical findings highlight the complexity of these conditions and the challenges of comparing diverse cohorts and glycosylation analyses. Our findings reveal subtype-specific patterns, but validation in larger, standardised cohorts is needed to enhance clinical applicability.

G3 structures (independent of fucosylation) were significantly increased in Ab-defined diseases, particularly in AQP4-Ab NMOSD, whereas G1, G2, and G4 showed an opposite trend. Mono-, di- and trigalactosylated glycans have been shown to reduce inflammation via NK cell FcγRIIIa and complement component C5a inhibition,[42] yet some may also act as inflammatory markers, though their roles remain unclear.[42]

Sialylation patterns, including S1 and S3, demonstrated discriminatory potential, with S1 and S1-H elevated in MOGAD compared to RRMS, while S3 traits were decreased in MOGAD, independent of fucosylation. Notably, S2 distinguished AQP4-Ab NMOSD from MOGAD, with lower levels in MOGAD. Sialylation plays a key role in modulating inflammation, as hyposialylated IgG is associated with chronic inflammation, whereas highly sialylated IgG exerts anti-inflammatory effects via FcγRIIIa.[42,43]

Fucosylation, in combination with galactosylation and sialylation, emerged as one of the most discriminatory glycan traits across multiple models. Cvetko *et al.* reported increased core fucosylation in MS vs healthy controls,[20] while we observed significant fucosylation changes, with reduced AF in MS distinguishing it from Ab-defined diseases and differentiating RRMS from MOGAD and AQP4-Ab NMOSD. The FG0/G0 ratio separated RRMS from SPMS, whereas FG2/G2 distinguished MOGAD from AQP4-Ab NMOSD. Fucosylation is a key post-translational modification linked to inflammation.[42] Sakae *et al.* demonstrated that increased core fucosylation of IgG1-Fc inhibits FcγRIIIa interaction, reducing Ab-dependent cytotoxicity and promoting anti-inflammatory effects.[44] Conversely, Li *et al.* found that reduced fucosylation in M1 macrophages facilitates inflammation resolution in rheumatoid arthritis.[45] Although fucosylation-derived traits are emerging as markers in CNS diseases, their precise role warrants further investigation.

While elevated mannose levels have been reported in the *N*-glycome of MS patients compared to healthy controls,[20] mannose was not among the most discriminatory features distinguishing MS from Ab-defined diseases. However, M structures strongly differentiated RRMS from SPMS, with higher levels in SPMS. Additionally, total mannose, including M-based hybrids, effectively distinguished MOGAD from AQP4-Ab NMOSD, with lower levels observed in the latter. Mannose-rich glycans activate complement via mannose-binding lectin,[46] and complement overactivation has been linked to microglia-driven pathology in progressive MS.[47] Given this association, our findings suggest that M glycans may play a role in distinct inflammatory pathways in Ab-defined diseases.

The limited consideration of disease phenotypes in previous studies has contributed to gaps in blood glycome data for MS and Ab-defined diseases, making direct comparisons challenging. While we observed no significant effects of DMTs, small sample sizes may have masked subtle influences. Nonetheless, this study represents a unique investigation by using well-defined groups of CNS demyelinating diseases to highlight the potential of blood glycomics for disease diagnosis and providing novel insights into neuroinflammatory mechanisms. Future validation in larger, independent cohorts is essential to confirm clinical relevance.

In conclusion, our study demonstrates the potential of plasma *N*-glycomics to differentiate MS, Ab-defined diseases, and their respective phenotypes by revealing distinct glycosylation profiles and offering insights into underlying immune mechanisms which could shape future targeted therapeutic strategies.

5 References

1. Jurynczyk M, Probert F, Yeo T, et al. Metabolomics reveals distinct, antibody-independent, molecular signatures of MS, AQP4-antibody and MOG-antibody disease. Acta Neuropathol Com 2017;5.

2. Matthews L, Marasco R, Jenkinson M, et al. Distinction of seropositive NMO spectrum disorder and MS brain lesion distribution. Neurology 2013;80:1330-1337.

3. Jurynczyk M, Geraldes R, Probert F, et al. Distinct brain imaging characteristics of autoantibody-mediated CNS conditions and multiple sclerosis. Brain 2017;140:617-627.

4. Yeo TR, Probert F, Jurynczyk M, et al. Classifying the antibody-negative NMO syndromes Clinical, imaging and metabolomic modeling. Neurol-Neuroimmunol 2019;6.

5. Traub J, Hausser-Kinzel S, Weber MS. Differential Effects of MS Therapeutics on B Cells-Implications for Their Use and Failure in AQP4-Positive NMOSD Patients. Int J Mol Sci 2020;21.

6. Palace J, Lin DY, Zeng D, et al. Outcome prediction models in AQP4-IgG positive neuromyelitis optica spectrum disorders. Brain 2019;142:1310-1323.

7. Selmaj K, Cree BAC, Barnett M, Thompson A, Hartung HP. Multiple sclerosis: time for early treatment with high-efficacy drugs. J Neurol 2024;271:105-115.

8. Yamamura T, Kleiter I, Fujihara K, et al. Trial of Satralizumab in Neuromyelitis Optica Spectrum Disorder. New Engl J Med 2019;381:2114-2124.

9. Cree BAC, Bennett JL, Kim HJ, et al. Inebilizumab for the treatment of neuromyelitis optica spectrum disorder (N-MOmentum): a double-blind, randomised placebo-controlled phase 2/3 trial. Lancet 2019;394:1352-1363.

10. Pittock SJ, Barnett M, Bennett JL, et al. Ravulizumab in Aquaporin-4-Positive Neuromyelitis Optica Spectrum Disorder. Ann Neurol 2023;93:1053-1068.

11. Meier S, Willemse EAJ, Schaedelin S, et al. Serum Glial Fibrillary Acidic Protein Compared With Neurofilament Light Chain as a Biomarker for Disease Progression in Multiple Sclerosis. JAMA Neurol 2023;80:287-297.

12. Probert F, Yeo T, Jurynczyk M, et al. Diagnosis and staging of multiple sclerosis using a metabolomics-based blood test: a simple method for monitoring progression independently of EDSS. Mult Scler J 2019;25:500-501.

13. Yeo T, Sealey M, Zhou Y, et al. A blood-based metabolomics test to distinguish relapsing-remitting and secondary progressive multiple sclerosis: addressing practical considerations for clinical application. Sci Rep 2020;10:12381.

14. Oppong AE, Coelewij L, Robertson G, et al. Blood metabolomic and transcriptomic signatures stratify patient subgroups in multiple sclerosis according to disease severity. iScience 2024;27:109225.

15. Alwahsh M, Nimer RM, Dahabiyeh LA, et al. NMR-based metabolomics identification of potential serum biomarkers of disease progression in patients with multiple sclerosis. Sci Rep 2024;14:14806.

16. Dickens AM, Larkin JR, Griffin JL, et al. A type 2 biomarker separates relapsing-remitting from secondary progressive multiple sclerosis. Neurology 2014;83:1492-1499.

17. Wuhrer M, Selman MH, McDonnell LA, et al. Pro-inflammatory pattern of IgG1 Fc glycosylation in multiple sclerosis cerebrospinal fluid. J Neuroinflammation 2015;12:235.

18. Yeo T, Probert F, Sealey M, et al. Objective biomarkers for clinical relapse in multiple sclerosis: a metabolomics approach. Brain Commun 2021;3:fcab240.

19. Mallagaray A, Rudolph L, Lindloge M, et al. Towards a Precise NMR Quantification of Acute Phase Inflammation Proteins from Human Serum. Angew Chem Int Ed Engl 2023;62:e202306154.

20. Cvetko A, Kifer D, Gornik O, et al. Glycosylation Alterations in Multiple Sclerosis Show Increased Proinflammatory Potential. Biomedicines 2020;8.

21. Turcic A, Radovani B, Vogrinc Z, et al. Higher MRI lesion load in multiple sclerosis is related to the N-glycosylation changes of cerebrospinal fluid immunoglobulin G. Mult Scler Relat Dis 2023;79.

22. Sy M, Newton BL, Pawling J, et al. N-acetylglucosamine inhibits inflammation and neurodegeneration markers in multiple sclerosis: a mechanistic trial. J Neuroinflamm 2023;20.

23. Mortales CL, Lee SU, Manousadjian A, Hayama KL, Demetriou M. N-Glycan Branching Decouples B Cell Innate and Adaptive Immunity to Control Inflammatory Demyelination. iScience 2020;23:101380.

24. Thompson AJ, Banwell BL, Barkhof F, et al. Diagnosis of multiple sclerosis: 2017 revisions of the McDonald criteria. Lancet Neurol 2018;17:162-173.

25. Wingerchuk DM, Banwell B, Bennett JL, et al. International consensus diagnostic criteria for neuromyelitis optica spectrum disorders. Neurology 2015;85:177-189. 26. Banwell B, Bennett JL, Marignier R, et al. Diagnosis of myelin oligodendrocyte glycoprotein antibody-associated disease: International MOGAD Panel proposed criteria. Lancet Neurol 2023;22:268-282.

27. Jansen BC, Hafkenscheid L, Bondt A, et al. HappyTools: A software for high-throughput HPLC data processing and quantitation. Plos One 2018;13:e0200280.

28. Jansen BC, Falck D, de Haan N, et al. LaCyTools: A Targeted Liquid Chromatography-Mass Spectrometry Data Processing Package for Relative Quantitation of Glycopeptides. J Proteome Res 2016;15:2198-2210.

29. Neelamegham S, Aoki-Kinoshita K, Bolton E, et al. Updates to the Symbol Nomenclature for Glycans guidelines. Glycobiology 2019;29:620-624.

30. Pucic M, Knezevic A, Vidic J, et al. High Throughput Isolation and Glycosylation Analysis of IgG-Variability and Heritability of the IgG Glycome in Three Isolated Human Populations. Mol Cell Proteomics 2011;10.

31. Thevenot EA, Roux A, Xu Y, Ezan E, Junot C. Analysis of the Human Adult Urinary Metabolome Variations with Age, Body Mass Index, and Gender by Implementing a Comprehensive Workflow for Univariate and OPLS Statistical Analyses. J Proteome Res 2015;14:3322-3335.

32. Duquette P, Pleines J, Girard M, Charest L, Senecal-Quevillon M, Masse C. The increased susceptibility of women to multiple sclerosis. Can J Neurol Sci 1992;19:466-471.

33. Papp V, Illes Z, Magyari M, et al. Nationwide prevalence and incidence study of neuromyelitis optica spectrum disorder in Denmark. Neurology 2018;91:e2265-e2275.

34. Miclea A, Salmen A, Zoehner G, et al. Age-dependent variation of female preponderance across different phenotypes of multiple sclerosis: A retrospective cross-sectional study. CNS Neurosci Ther 2019;25:527-531.

35. Carnero Contentti E, Correale J. Neuromyelitis optica spectrum disorders: from pathophysiology to therapeutic strategies. J Neuroinflammation 2021;18:208.

36. Filippi M, Rocca MA, Ciccarelli O, et al. MRI criteria for the diagnosis of multiple sclerosis: MAGNIMS consensus guidelines. Lancet Neurol 2016;15:292-303.

37. Inojosa H, Schriefer D, Ziemssen T. Clinical outcome measures in multiple sclerosis: A review. Autoimmun Rev 2020;19:102512.

38. Conroy LR, Hawkinson TR, Young LEA, Gentry MS, Sun RC. Emerging roles of N-linked glycosylation in brain physiology and disorders. Trends Endocrinol Metab 2021;32:980-993.

39. Pradeep P, Kang H, Lee B. Glycosylation and behavioral symptoms in neurological disorders. Transl Psychiatry 2023;13:154.

40. Dojcsák D, Ilosvai AM, Vanyorek L, et al. NH-Functionalized Magnetic Nanoparticles for the -Glycomic Analysis of Patients with Multiple Sclerosis. Int J Mol Sci 2022;23.

41. Sharma G, Gopinath S, Narasimhan RL. Exploring the Molecular Aspects of Glycosylation in MOG Antibody Disease (MOGAD). Curr Protein Pept Sc 2022;23:384-394.

42. Radovani B, Gudelj I. N-Glycosylation and Inflammation; the Not-So-Sweet Relation. Front Immunol 2022;13:893365.

43. Kaneko Y, Nimmerjahn F, Ravetch EV. Anti-inflammatory activity of immunoglobulin G resulting from Fc sialylation. Science 2006;313:670-673.

44. Sakae Y, Satoh T, Yagi H, et al. Conformational effects of -glycan core fucosylation of immunoglobulin G Fc region on its interaction with Fc receptor IIIa. Sci Rep-Uk 2017;7.

45. Li J, Hsu HC, Ding Y, et al. Inhibition of fucosylation reshapes inflammatory macrophages and suppresses type II collagen-induced arthritis. Arthritis Rheumatol 2014;66:2368-2379.

46. Gupta A, Gupta GS. Status of mannose-binding lectin (MBL) and complement system in COVID-19 patients and therapeutic applications of antiviral plant MBLs. Mol Cell Biochem 2021;476:2917-2942.

47. Watkins LM, Neal JW, Loveless S, et al. Complement is activated in progressive multiple sclerosis cortical grey matter lesions. J Neuroinflamm 2016;13.

Contribution statement

T. Yeo, and F. Probert conceived and designed the study. T. Yeo., F. Probert., M.I. Leite, G. DeLuca, J. Palace, D.C. Anthony were responsible for study oversight and patient recruitment. M. Sealey, L. Saldana T. Yeo, and F. Probert were involved in sample collection and processing. M. Woodhall and P. Waters. were responsible for antibody testing. T. Sénard, J. Chessman., P. Urbanowicz, and G.E. Hunt performed experiments and data processing. T. Kacerova and W. Xiong analysed the data. T. Kacerova drafted the manuscript. T. Yeo, F. Probert, D.I.R. Spencer, J. McCullagh, and D.C. Anthony. provided critical feedback and guidance for experimental and analysis design. All authors provided input on the manuscript.

Declaration

P. Waters is a named inventor on patents for antibody assays and has received royalties. He has

received honoraria from Biogen Idec, Mereo Biopharma, Retrogenix, UBC, Euroimmun AG, UCB, F. Hoffmann La-Roche and Alexion; travel grants from the Guthy-Jackson Charitable Foundation (GJCF); and research funding from Euroimmun AG and the GJCF. His work in the Autoimmune Neurology Diagnostic Laboratory is supported by the NHS Commissioning service for NMOSD. T. Yeo has received honoraria from ASNA, Edanz Pharma, Euroimmun AG, Merck, Novartis, Roche, Terumo BCT for consulting services and speaker's fees, and research grants from the National Medical Research Council (NMRC Singapore), AstraZeneca and Roche. He has also received travel grants and awards from PACTRIMS, ACTRIMS, ECTRIMS, Orebro University, UCB, and Merck.

Funding

T. Kacerova is funded by an EPSRC Doctoral Training Partnership (EP/W524311/1) and Numares AG (Am Biopark 9, 93053 Regensburg-Graß, Germany). T.Yeo is funded by the Singapore Ministry of Health's National Medical Research Council Transition and Clinician Scientist Awards (TA20nov-002, CSAINV24jul-0004). F.Probert is funded by the Dorothy Hodgkin Early Career Fellowship in Chemistry in association with Somerville College.

Disclosures

T. Kacerova is funded by an EPSRC Doctoral Training Partnership (EP/W524311/1) and Numares AG (Am Biopark 9, 93053 Regensburg, Germany); T. Sénard was an employee of Ludger Ltd, UK; J. Cheeseman is an employee of Ludger Ltd, UK; P. Urbanowicz is an employee of Ludger Ltd, UK; G.E. Hunt is an employee of Ludger Ltd, UK; D.I.R. Spencer is an employee of Ludger Ltd, UK; T. Yeo is funded by the Singapore Ministry of Health's National Medical Research Council Transition and Clinician Scientist Awards (TA20nov-002, CSAINV24jul-0004); F. Probert is funded by the Dorothy Hodgkin Early Career Fellowship in Chemistry in association with Somerville College.

Ethics approval and consent to participate

John Radcliffe Hospital, Oxford University Hospital Trust (MET cohort; REC reference: 09/H0606/5 + 5). Participants provided written informed consent. This study followed the Strengthening the Reporting of Observational Studies in Epidemiology (STROBE) reporting guidelines.

Data access and availability

Anonymised data not published within this article will be made available by request to the corresponding authors from any qualified investigator.

Acknowledgement

The authors thank all patients who participated in this study.

Supplementary Information – Manuscript 4

Supplementary Information

Plasma *N*-Glycan Profiling Enhances Diagnostic Precision in Multiple Sclerosis, AQP4-Ab NMOSD, and MOGAD

Tereza Kacerova[1], Megan Sealey[2], Luisa Saldana[3], Wenzheng Xiong[2], Mark Woodhall[3], Patrick Waters[3], Thomas Sénard[4,5], Jack Cheeseman[4], Paulina Urbanowicz[4], Georgia Elgood Hunt[4], Daniel I. R. Spencer[4], James S.O. McCullagh[1], Maria Isabel Leite[3], Gabriele DeLuca[3], Jacqueline Palace[3], Daniel C. Anthony[2], Tianrong Yeo[6,7,8*], Fay Probert[1]

[1] Chemistry Research Laboratory, Department of Chemistry, University of Oxford, Oxford OX1 3TA, UK.
[2] Department of Pharmacology, University of Oxford, Oxford OX1 3QT, UK.
[3] Nuffield Department of Clinical Neurosciences, John Radcliffe Hospital, University of Oxford, Oxford OX3 9DU, UK.
[4] Ludger Ltd, Culham Science Centre, Abingdon, UK.
[5] Division of Endocrinology and Diabetes Prevention and Care, IRCCS Azienda Ospedaliero-Universitaria di Bologna, Bologna 40138, Italy.
[6] Department of Neurology, National Neuroscience Institute, 11 Jalan Tan Tock Seng, Singapore 308433, Singapore.
[7] Duke-NUS Medical School, 8 College Road, Singapore 169857, Singapore.
[8] Lee Kong Chian School of Medicine (Nanyang Technological University), 11 Mandalay Road, Singapore 308232, Singapore.

Corresponding author: Tianrong Yeo yeo.tianrong@singhealth.com.sg

Supplementary Information – Manuscript 4

_N_-glycan traits discriminate between MS and Ab-defined diseases

SI Table 1 List of calculated glycan traits. The table provides a description of each trait, the formula used for its calculation, and the abbreviation of the trait that is used throughout the study.

Glycan Trait Description	Formula	Abbreviation
contain mannose (high mannose structures (M) and hybrids (H))	(M+H)/total*100	M-content
High mannose glycans	M/total*100	M
Core fucosylation (CF)	CF/AF*100	core-F
sialylation of fucosylated galactosylated structures without bisecting GlcNAc	FGS/(FG+FGS)*100	FGS/(FG+FGS)
Trisialylation (S3) of fucosylated glycans (excluding M-content)	FS3/total*100	FS3
Antennary fucosylation (AF)	AF/total*100	AF
Monogalactosylation (G1) in non-fucosylated	nFG1/total*100	nFG1
Monogalactosylation (G1) in fucosylated	FG1/total*100	FG1
Monogalactosylation (G1)	G1/total*100	G1
Agalactosylation (G0)	G0/total*100	G0
Digalactosylation (G2) in non-fucosylated	nFG2/total*100	nFG2
Digalactosylation (G2) in fucosylated	FG2/total*100	FG2
Digalactosylation (G2)	G2/total*100	G2
Monogalactosylation (G1) all excluding mannose hybrids	(G1-H)/total*100	G1-H
Hybrids (H)	H/total*100	H
Trigalactosylation (G3) in non fucosylated (no mannose hybrids)	nFG3/total*100	nFG3
Trigalactosylation (G3) in fucosylated (no mannose hybrids)	FG3/total*100	FG3
Trigalactosylation (G3)	G3/total*100	G3
Tetragalactosylation (G4)	G4/total*100	G4
Neutral glycans (S0) (excluding high mannose structure but including hybrids)	S0/total*100	S0
Neutral glycans (S0) (excluding high mannose structure and excluding hybrids)	(S0-H)/total*100	S0-H
Monosialylation (S1) (excluding high mannose structure but including hybrids)	S1/total*100	S1
Monosialylation (S1) (excluding high mannose structure and excluding hybrids)	(S1-H)/total*100	S1-H
Monosialylation (S1) non-fucosylated only (excluding high mannose structure and excluding hybrids)	nFS1/total*100	nFS1
Monosialylation (S1) fucosylated only (excluding high mannose structure and excluding hybrids)	FS1/total*100	FS1
Disialylation (S2) (excluding high mannose structure but including hybrids)	S2/total*100	S2
Disialylation (S2) non-fucosylated only (excluding high mannose structure but including hybrids)	nFS2/total*100	nFS2
Disialylation (S2) fucosylated only (excluding high mannose structure but including hybrids)	FS2/total*100	FS2
Trisialylation (S3) (excluding high mannose structure but including hybrids)	S3/total*100	S3
Trisialylation (S3) non-fucosylated only (excluding high mannose structure but including hybrids)	nFS3/total*100	nFS3

Incidence of bisecting GlcNAc (B)	B/total*100	B
Incidence of bisecting GlcNAc (B) (excluding hybrids)	(B-BH)/total*100	B-BH
Incidence of bisecting GlcNAc (B) non-fucosylated only (excluding hybrids)	nFB/total*100	nFB
Incidence of bisecting GlcNAc (B) fucosylated only (excluding hybrids)	FB/total*100	FB
Unresolved chromatographic peaks	chrom. integral/total*100	Chrom.
Low branching (mono- and biantennary glycans)	LB/total*100	LB
Low branching (mono- and biantennary glycans) no hybrids	(LB-H)/total*100	LB-H
High branching (tri- and tetraannary glycans)	HB/total*100	HB
The percentage of sialylation of fucosylated galactosylated structures with bisecting GlcNAc	FBGS/(FBG+FBGS)*100	FBGS/(FBG+FBGS)
Ratio of fucosylated (without bisecting GlcNAc) monosialylated and disialylated structures	FS1/FS2*100	FS1/FS2
Ratio of fucosylated (with bisecting GlcNAc) monosialylated and disialylated structures	FBS1/FBS2*100	FBS1/FBS2
Ratio of all fucosylated sialylated structures with and without bisecting GlcNAc	FBS/FS*100	FBS/FS
Ratio of fucosylated and non-fucosylated agalactosylated structures	FG0/G0*100	FG0/G0
Ratio of fucosylated and non-fucosylated monogalactosylated structures	FG1/G1*100	FG1/G1
Ratio of fucosylated and non-fucosylated digalactosylated structures	FG2/G2*100	FG2/G2
Ratio of fucosylated and non-fucosylated trigalactosylated structures	FG3/G3*100	FG3/G3

Supplementary Information – Manuscript 4

One-Way ANOVA Results: Age, BMI, EDSS, disease duration, time since last relapse

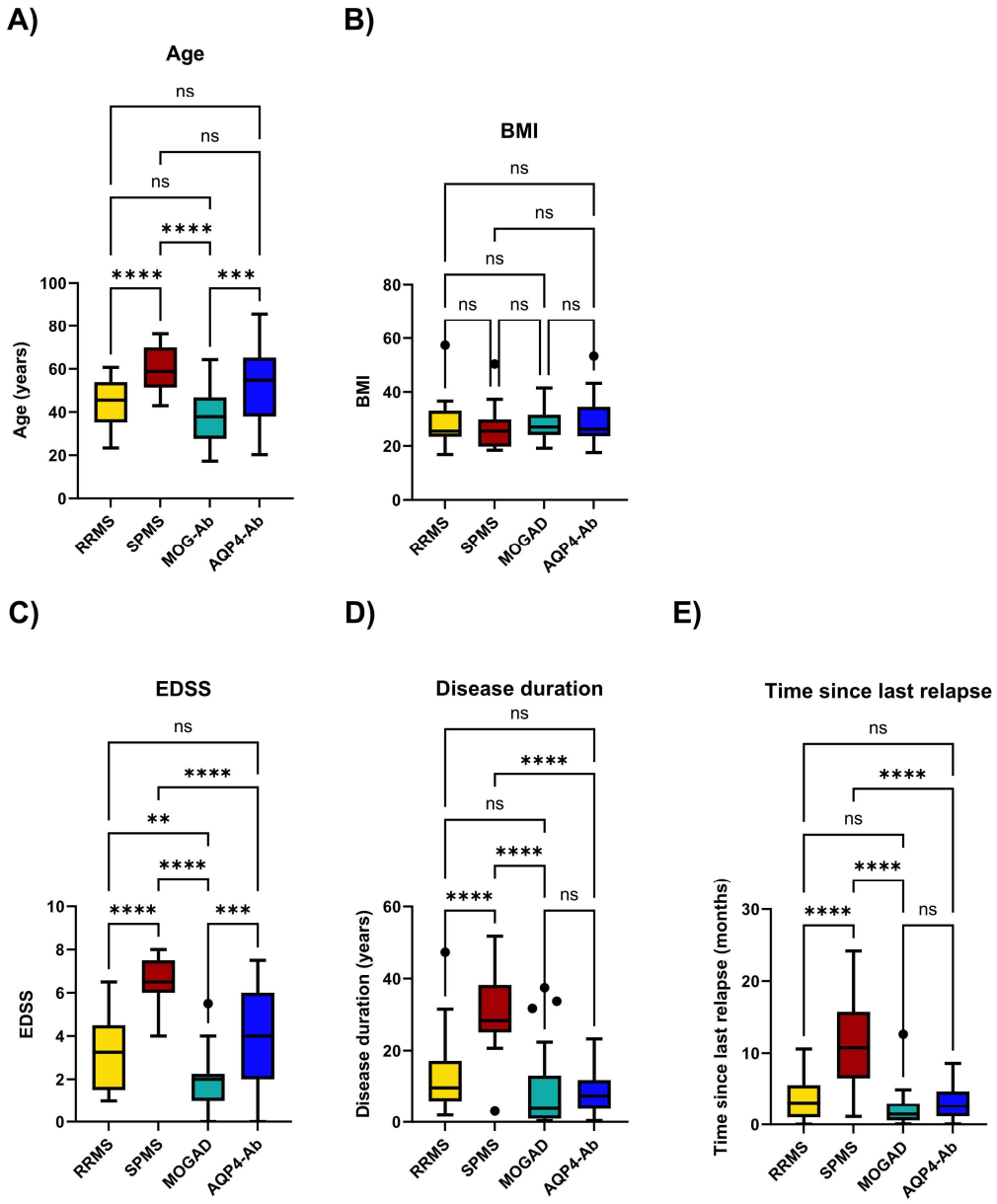

SI Figure 1 Results of a 1W- ANOVA with *post hoc* Tukey's test for multiple comparisons for: **(A)** age; **(B)** BMI; **(C)** Expanded Disability Status Scale (EDSS) score; **(D)** disease duration, and **(E)** time since the last relapse. The boxplots show the distribution across the four conditions: RRMS, SPMS, MOGAD, and AQP4-Ab NMOSD.

Supplementary Information – Manuscript 4

Assessment of potential confounders

DMT effect

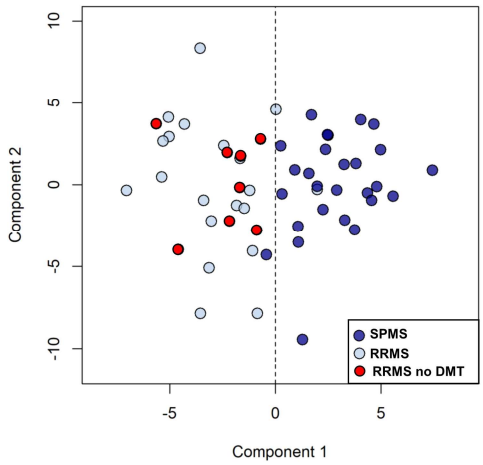

SI Figure 2 Scores plot of the RRMS vs SPMS OPLS-DA model shaded according to the potential confounder shows that the red circles (untreated (DMTs) RRMS individuals) are evenly distributed within the RRMS cluster and do not overlap with the SPMS cluster. This distribution suggests that the separation observed in the model is primarily driven by disease status rather than the absence of DMT, indicating a minimal influence of pharmacotherapy on the glycomic profile.

Immunosuppression effect

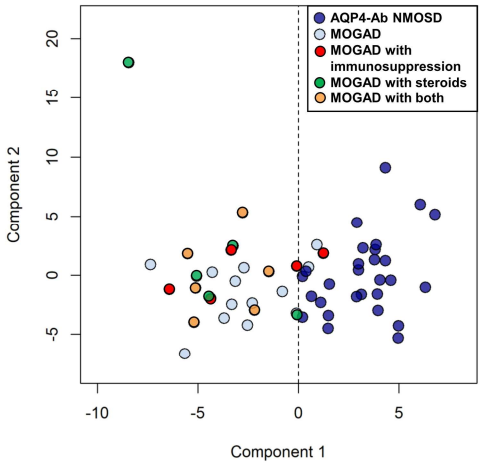

SI Figure 3 Scores plot of the MOGAD vs AQP4-Ab NMOSD OPLS-DA model shaded according to the potential confounder (red circles correspond to MOGAD individuals treated with immunosuppression and green circles to MOGAD individuals treated with steroids). The data points representing the treated participants are uniformly distributed across the disease classification, indicating minimal or negligible effect of the different pharmacotherapy on the multivariate model.

Steroid effect

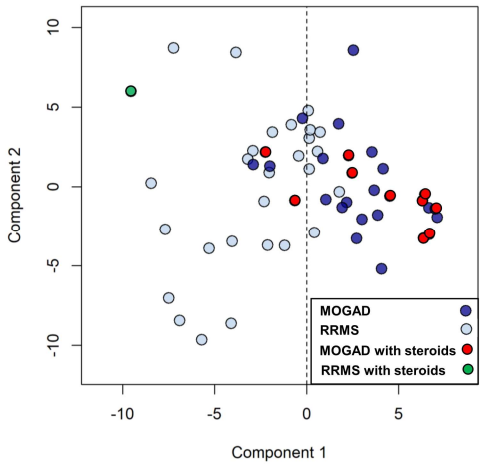

SI Figure 4 Scores plot of the MOGAD vs RRMS OPLS-DA model shaded according to the potential confounder (red circles correspond to MOGAD individuals treated with steroids and green circles to RRMS individuals treated with steroids). The data points representing the treated participants are uniformly distributed across the disease classification, indicating minimal or negligible effect of pharmacotherapy on the multivariate model.

Supplementary Information – Manuscript 4

Glycomic profiling discriminates AQP4-Ab NMOSD, MOGAD and MS independent of Ab serostatus at sampling

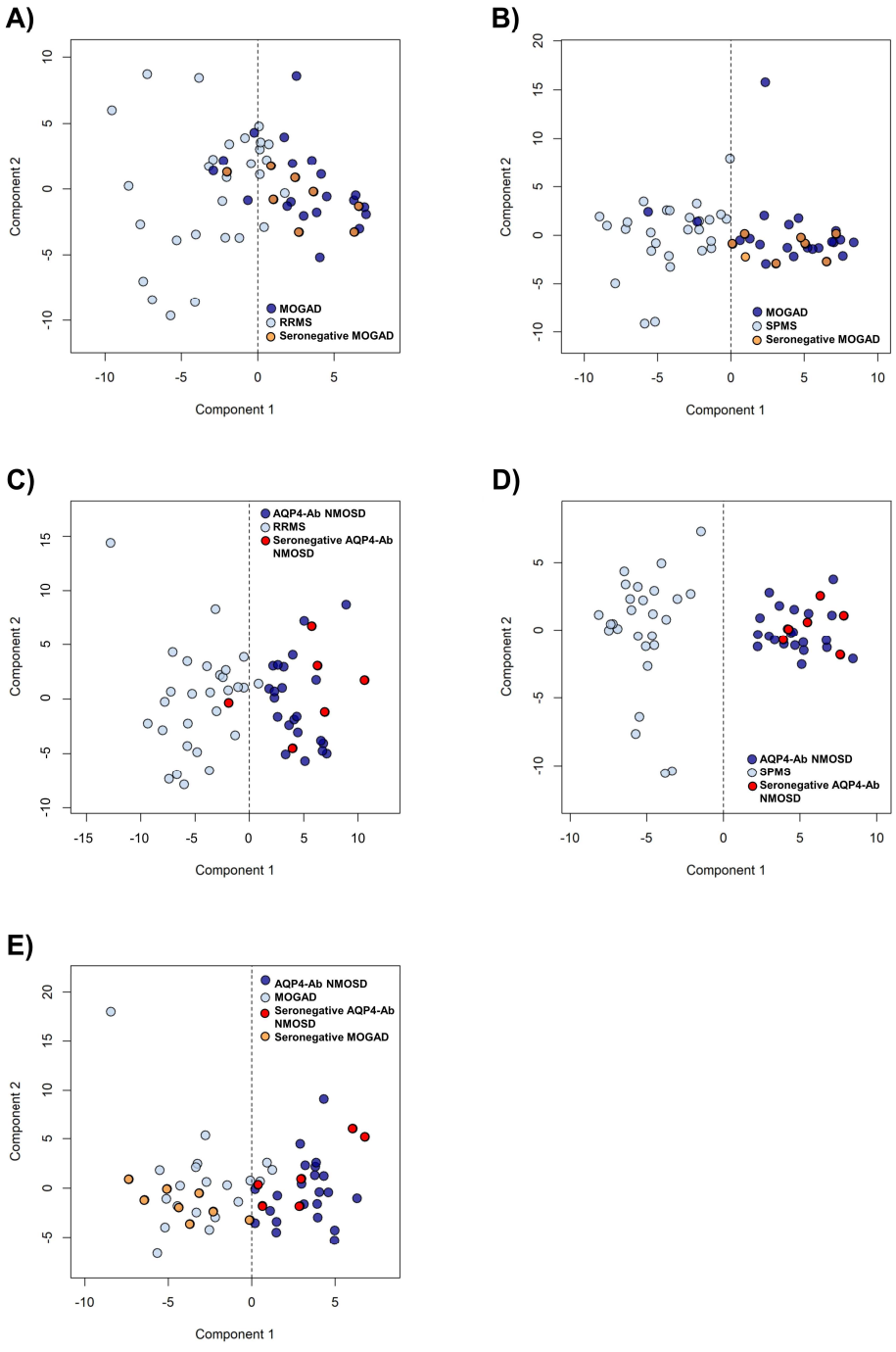

SI Figure 5 A) Scores plot of the MOGAD vs RRMS OPLS-DA model, with MOGAD seronegative patients highlighted in orange. **B)** Scores plot of the MOGAD vs SPMS OPLS-DA model, with MOGAD seronegative patients highlighted in orange. **C)** Scores plot of the AQP4-Ab NMOSD vs RRMS OPLS-DA model, with AQP4-Ab NMOSD seronegative patients highlighted in red. **D)** Scores plot of the AQP4-Ab NMOSD vs SPMS OPLS-DA model, with AQP4-Ab NMOSD seronegative patients highlighted in red. **E)** Scores plot of the AQP4-Ab NMOSD vs MOGAD OPLS-DA model, with AQP4-Ab NMOSD seronegative patients highlighted in red and MOGAD seronegative patients highlighted in orange. The even distribution of seronegative patients across all plots suggests that Ab serostatus at the time of sampling does not impact the accuracy of classification.

Supplementary Information – Manuscript 4

Plasma N-glycomics is a highly discriminatory tool for distinguishing RRMS, SPMS, MOGAD and AQP4-Ab NMOSD

SI Table 2 List of glycan signals characterised by the highest VIP scores. Four diagnostically relevant multivariate models are provided (refer to Figure 2). Twenty-five glycans are listed for each model in the format: glycan signal (VIP rank; VIP score). The signals follow the notation as described in the Methods section. *The X signals represent unresolved chromatographic peaks, with the assignment given as X_retention_time (in minutes).

RRMS vs AQP4	RRMS vs MOGAD	MOGAD vs AQP4	RRMS vs SPMS
A3G3S1.3 (1; 6.47)	A3G3S1.3 (18; 1.73)		
FA2BG2S1.1 (2; 3.79)		FA2BG2S1.1 (1; 2.33)	
FA3G3S3.3 (3; 2.61)			
A3G3S2.7 (4; 2.61)		FA3G3S3.3 (21; 1.45)	
FA3G3S2.4 (5; 2.54)			FA3G3S2.4 (22; 1.48)
FA2G2S2.3 (6; 2.54)			
A2BG1.1 (7; 2.32)		A2BG1.1 (9; 1.77)	
FA2G1.2 (8; 2.30)		FA2G1.2 (8; 1.80)	
*X_39.73 (9; 2.14)			*X_39.73 (12; 1.68)
A4G4S2 (10; 2.06)			A4G4S2 (25; 1.38)
M5A1G1 (11; 2.03)		M5A1G1 (15; 1.59)	
FA2 (12; 1.97)			
A2G2S2.1 (13; 1.80)			
M4A1G1 (14; 1.74)		M4A1G1 (24; 1.44)	
*X_32.08 (15; 1.70)	*X_32.08 (2; 2.13)		
FA3G3S2.2 (16; 1.58)	FA3G3S2.2 (17; 1.75)		
*X_40.56 (17; 1.54)			
*X_41.72 (18; 1.40)		*X_41.72 (19; 1.48)	
FA3G3S2.5 (19; 1.33)	FA3G3S2.5 (5; 1.99)		
*X_40.84 (20; 1.25)			
FA3G3S3.8 (21; 1.20)		FA3G3S3.8 (20; 1.47)	
M8.2 (22; 1.18)			M8 (17; 1.57)
*X_39.50 (23; 1.18)	*X_39.50 (7; 1.83)		
FA2G2S2.4 (24; 1.16)			
FA2BG2S1.3 (25; 1.15)			
	A3G3S1.4 (1; 2.18)		
	*X_40.17 (3; 2.12)		
	A2G2S2.5 (4; 2.05)		
	*X_40.34 (6; 1.95)		
	*X_27.10 (7; 1.82)	*X_27.10 (4; 2.06)	
	M5BG1S1.1 (8; 1.79)		
	A3G3S3.2 (9; 1.77)		
	FA3G3S1.4 (10; 1.76)		
	FA3G3S1.5 (11; 1.76)		
	A3G3S2.4 (12; 1.76)		
	A3G3S3.4 (13; 1.76)		

	A3G3S3.5 (14; 1.76)	A3G3S3.5 (12; 1.67)	
	*X_39.28 (16; 1.75)		
	M8 (19; 1.72)		
	FA3G3S2 (20; 1.70)		
	FA2BG1.1 (21; 1.66)		
	*X_41.45 (22; 1.63)		*X_41.45 (5; 1.91)
	A2G2S2.3 (23; 1.57)		
	FA2BG2S2 (24; 1.56)		
	A3G3S2.6 (25; 1.56)		
		FA3G3S3.5 (2; 2.29)	
		FA3G3S3.2 (3; 2.22)	
		FA2BG2S1.2 (5; 2.01)	
		M5 (6; 1.81)	
		A2G2S2 (7; 1.81)	A2G2S2 (15; 1.60)
		A2BG1S1 (10; 1.75)	
		A2G1 (11; 1.69)	
		A4G4S2.3 (13; 1.64)	
		FA2BG1.2 (14; 1.59)	
		*X_41.16 (16; 1.53)	
		FA2G2S1.1 (17; 1.53)	
		A2BG1 (18; 1.48)	A2BG1 (18; 1.54)
		A2BG2 (22; 1.44)	
		FA3G3S2.6 (23; 1.44)	
		A2G1S1.1 (25; 1.41)	
			A4G4S1 (1; 2.03)
			A3G3S2 (2; 1.97)
			FA3G3S1.1 (3; 1.97)
			A2G1.2 (4; 1.96)
			A2BG2S1.1 (6; 1.87)
			A3G3S2.5 (7; 1.88)
			A3G3S3.6 (8; 1.78)
			A2.1 (9; 1.78)
			FA3G3S1 (10; 1.77)
			M8.1 (11; 1.73)
			A2B (13; 1.66)
			FA1G1.1 (14; 1.65)
			A3G3S1.2 (16; 1.60)
			FA2G2S1 (19; 1.54)
			A2G2 (20; 1.52)
			FA3G3S1.2 (21; 1.51)
			A4G4S1.1 (23; 1.41)
			FA3G3S3 (24; 1.38)

Supplementary Information – Manuscript 4

Plasma *N*-glycomics as a discriminatory tool for RRMS, SPMS, MOGAD, and AQP4-Ab NMOSD

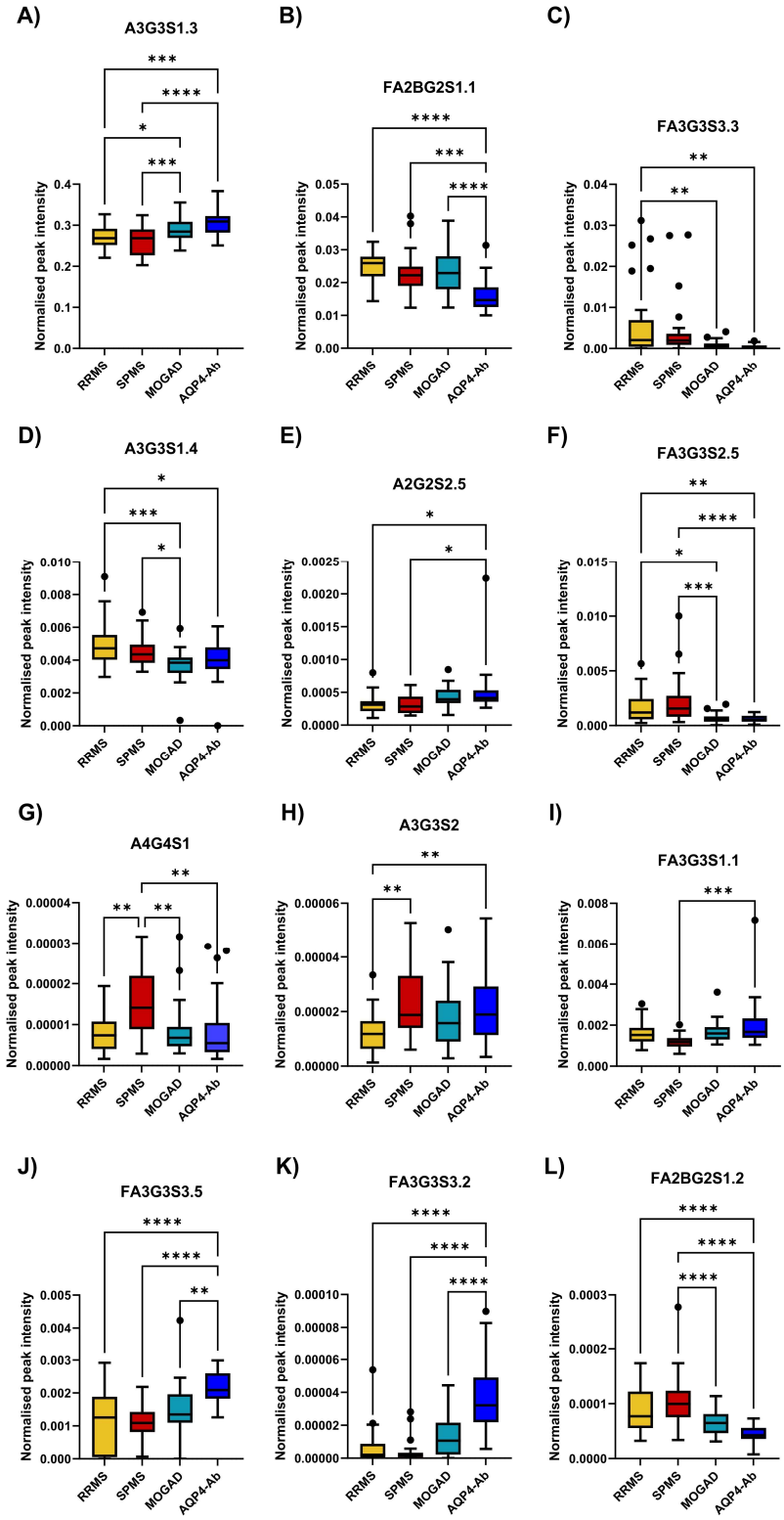

SI Figure 6 1W-ANOVA results (FDR-corrected) with Tukey`s *post hoc*, adjusted for multiple comparisons, for the three glycans with the highest VIP scores in each of the four diagnostically relevant models: **A-C)** AQP4-Ab NMOSD vs RRMS; **D-F)** MOGAD vs RRMS; **G-I)** RRMS vs SPMS; **J-L)** AQP4-Ab NMOSD vs MOGAD. **A)** A3G3S1.3 ($p < 0.0001$); **B)** FA2BG2S1.1 ($p < 0.0001$); **C)** FA3G3S3.3 ($p = 0.001$); **D)** A3G3S1.4 ($p = 0.001$); **E)** A2G2S2.5 ($p = 0.008$); **F)** FA3G3S2.5 ($p < 0.0001$); **G)** A4G4S1 ($p = 0.40$); **H)** A3G3S2 ($p = 0.003$); **I)** FA3G3S1.1 ($p = 0.002$); **J)** FA3G3S3.5 ($p < 0.0001$); **K)** FA3G3S3.2 ($p < 0.0001$); **L)** FA2BG2S1.2 ($p < 0.0001$).

Supplementary Information – Manuscript 4

_N_-glycan traits discriminate between MS and Ab-defined diseases

SI Table 3 Overview of the individual multivariate OPLS-DA models constructed, along with the corresponding accuracy, sensitivity, and specificity values for: 1) all detected glycan signals, and 2) all calculated glycan traits.

Model	Features	Accuracy	Sensitivity	Specificity
MS vs Ab-defined diseases	All signals	80.5±1.5	80.7±2.4	81.3±2.2
MS vs Ab-defined diseases	Traits	71.5±2.5	71.7±3.3	72.4±3.4
AQP4-Ab NMOSD vs MOGAD	All signals	77.8±3.1	76.2±4.6	80.4±5.1
AQP4-Ab NMOSD vs MOGAD	Traits	74.5±3.0	73.7±4.9	76.8±5.1
RRMS vs AQP4-Ab NMOSD	All signals	92.7±1.4	90.0±3.8	96.1±1.8
RRMS vs AQP4-Ab NMOSD	Traits	86.3±2.2	83.1±3.5	90.7±4.4
RRMS vs MOGAD	All signals	57.3±4.1	57.5±6.5	56.8±6.5
RRMS vs MOGAD	Traits	67.6±2.9	66.2±4.8	70.6±5.4
RRMS vs SPMS	All signals	75.2±3.6	76.5±5.3	75.3±4.9
RRMS vs SPMS	Traits	62.2±3.8	63.9±6.1	63.0±5.3
SPMS vs AQP4-Ab NMOSD	All signals	96.7±0.8	96.3±1.8	97.0±2.3
SPMS vs AQP4-Ab NMOSD	Traits	90.7±2.4	92.0±3.8	89.9±3.6
SPMS vs MOGAD	All signals	75.8±2.4	76.8±4.9	75.8±4.6
SPMS vs MOGAD	Traits	62.8±3.0	64.5±5.9	63.0±4.9

Supplementary Information – Manuscript 4

_N_-glycan traits discriminate between MS and Ab-defined diseases

SI Table 4 The list of glycan traits identified as particularly discriminatory in the MS vs Ab-defined diseases model. VIP scores, raw p-values, and FDR-corrected p-values determined from unpaired t-tests are provided. The direction of change is indicated relative to the MS group. The odds ratio (OR) is also provided, along with the corresponding lower and upper 95% confidence intervals (CI).

Glycan Trait	VIP score	p-value	FDR	MS	OR	Lower 95% CI	Upper 95% CI
S1-H	1.701	6.60E-06	5.56E-05	down	2.630	1.690	4.352
nFG3	1.685	6.21E-07	2.86E-05	down	3.033	1.898	5.216
S1	1.676	7.26E-06	5.56E-05	down	2.574	1.669	4.191
nFS1	1.557	1.51E-05	9.95E-05	down	2.886	1.752	5.146
G3	1.520	3.35E-06	5.13E-05	down	2.701	1.733	4.498
LB-H	1.487	2.51E-05	1.28E-04	up	0.385	0.237	0.593
AF	1.462	2.61E-06	5.13E-05	down	2.894	1.809	4.973
S3	1.412	1.14E-04	4.36E-04	up	0.268	0.113	0.532
HB	1.389	5.37E-05	2.25E-04	down	2.317	1.519	3.742
LB	1.386	2.51E-05	1.28E-04	up	0.414	0.256	0.635
FS3	1.371	1.45E-04	5.12E-04	up	0.296	0.135	0.558
Core-F	1.176	3.09E-04	1.02E-03	up	0.463	0.284	0.710
FG0/G0	1.173	1.81E-05	1.04E-04	up	0.412	0.256	0.629
G4	1.086	3.46E-05	1.59E-04	up	0.417	0.255	0.641
G2	1.030	4.88E-03	1.07E-02	up	0.572	0.372	0.844
S0.H	1.007	1.90E-03	5.46E-03	up	0.534	0.342	0.796
FG3/G3	1.007	8.36E-03	1.75E-02	up	0.600	0.397	0.877
S0	0.898	4.70E-03	1.07E-02	up	0.568	0.368	0.841
Chrom.	0.868	7.94E-04	2.44E-03	down	2.030	1.336	3.261
nFG1	0.806	2.82E-03	6.84E-03	up	0.551	0.357	0.816

SI Table 5 The list of glycan traits identified as particularly discriminatory in the AQP4-Ab NMOSD vs RRMS model. VIP scores, raw p-values, and FDR-corrected p-values determined from unpaired t-tests are provided. The direction of change is indicated relative to the RRMS group. The odds ratio (OR) is also provided, along with the corresponding lower and upper 95% confidence intervals (CI).

Glycan Trait	VIP score	p-value	FDR	RRMS	OR	Lower 95% CI	Upper 95% CI
FG0/G0	1.876	1.26E-11	5.81E-10	up	0.015	0.001	0.097
Chrom.	1.444	3.51E-05	4.32E-04	down	4.645	2.124	12.769
FG2	1.414	3.84E-05	4.32E-04	up	0.243	0.095	0.504
AF	1.398	3.12E-05	4.32E-04	down	3.627	1.881	8.413
G3	1.348	4.70E-05	4.32E-04	down	3.818	1.907	9.149
nFG3	1.289	9.70E-05	6.38E-04	down	3.619	1.822	8.493
LB	1.251	1.96E-04	0.0010203	up	0.300	0.135	0.567
S1-H	1.248	0.0042	0.010131	down	2.669	1.343	6.036

HB	1.242	0.0002	0.0010203	down	3.161	1.670	7.005
S3	1.181	0.0153	0.027022	up	0.394	0.149	0.825
S0	1.179	0.0072	0.023577	up	0.344	0.164	0.629
nFG1	1.166	0.0002	0.0011452	up	0.360	0.181	0.637
LB-H	1.146	0.0002	0.0010203	up	0.340	0.164	0.617
M-content	1.133	0.0082	0.015667	up	0.450	0.225	0.812
Core-F	1.130	0.0004	0.0016137	up	0.335	0.152	0.630
FS3	1.129	0.0214	0.036537	up	0.423	0.172	0.869
FGS/(FG+FGS)	1.121	0.0008	0.0027217	up	0.359	0.174	0.664
G1	1.102	0.0011	0.0036817	up	0.347	0.155	0.665
S1	1.099	0.0093	0.017252	down	2.399	1.247	5.158
nFB	1.067	0.0016	0.0047701	up	0.437	0.237	0.737

SI Table 6 The list of glycan traits identified as particularly discriminatory in the MOGAD vs RRMS model. VIP scores, raw p-values, and FDR-corrected p-values determined from unpaired t-tests are provided. The direction of change is indicated relative to the RRMS group. The odds ratio (OR) is also provided, along with the corresponding lower and upper 95% confidence intervals (CI).

Glycan Trait	VIP score	p-value	FDR	RRMS	OR	Lower 95% CI	Upper 95% CI
S1	2.027	0.0044	0.0503	up	2.416	1.315	4.961
S3	1.914	7.73E-04	0.0331	up	0.202	0.050	0.538
S1-H	1.896	0.0014	0.0331	down	2.239	1.227	4.586
FS3	1.823	0.0092	0.0704	up	0.192	0.048	0.550
AF	1.800	0.0112	0.0720	down	2.102	1.191	4.125
nFG3	1.491	0.0125	0.0720	down	2.314	1.203	4.963
G4	1.384	0.0269	0.1374	up	0.487	0.240	0.914
FG3/G3	1.360	0.0088	0.0704	up	0.457	0.231	0.819
FBS1/FBS2	1.357	0.0462	0.17712	down	8.187	1.086	84.553
nFS1	1.161	0.0584	0.1918	down	1.852	1.013	4.051
LB.H	1.068	0.0686	0.1974	up	0.585	0.315	1.031
S2	1.033	0.1251	0.3196	up	0.662	0.375	1.105
Core-F	0.960	0.0321	0.1419	up	0.540	0.279	0.934
G2	0.948	0.1385	0.3297	up	0.668	0.373	1.120
FG0/G0n	0.938	0.0339	0.1419	up	0.533	0.280	0.945
G3	0.930	0.1811	0.3966	down	1.496	0.841	2.782
LB	0.881	0.1434	0.3297	up	0.646	0.348	1.144
FS1/FS2	0.839	0.0532	0.1882	down	1.810	1.007	3.535
HB	0.758	0.2821	0.5407	down	1.377	0.780	2.525

Supplementary Information – Manuscript 4

SI Table 7 The list of glycan traits identified as particularly discriminatory in the SPMS vs RRMS model. VIP scores, raw p-values, and FDR-corrected p-values determined from unpaired t-tests are provided. The direction of change is indicated relative to the RRMS group. The odds ratio (OR) is also provided, along with the corresponding lower and upper 95% confidence intervals (CI).

Glycan Trait	VIP score	p-value	FDR	RRMS	OR	Lower 95% CI	Upper 95% CI
FS1/FS2	2.569	9.05E-06	0.0004	down	0.241	0.098	0.483
M	2.149	0.0030	0.0473	down	0.375	0.172	0.722
FG0/G0	1.951	0.0077	0.0473	up	2.190	1.231	4.244
nFS2	1.876	0.0044	0.0473	down	0.443	0.224	0.777
G4	1.578	0.0215	0.1413	down	0.535	0.291	0.906
FS2	1.573	0.0116	0.1067	up	1.954	1.164	3.512
FG1	1.155	0.2303	0.7231	down	0.656	0.284	1.234
FG2/G2	1.121	0.0175	0.1338	up	2.138	1.169	4.729
G3	1.090	0.1237	0.4978	up	1.649	0.886	3.247
FG2	1.079	0.1155	0.4978	up	1.555	0.912	2.839
nFS1	1.057	0.1162	0.4978	up	1.676	0.907	3.446
FG3	1.045	0.3255	0.7580	up	1.290	0.787	2.185
G1/G1H	1.038	0.3244	0.7580	down	0.706	0.330	1.371
(FBGS/(FBG+FBGS)	0.876	0.0444	0.2553	up	1.745	1.030	3.244
FS3	0.841	0.6175	0.8115	up	1.115	0.734	1.749
FBS/FS	0.841	0.5719	0.7890	down	0.859	0.496	1.437
AF	0.832	0.4476	0.7890	down	0.795	0.425	1.414
S1-H	0.826	0.1911	0.6761	up	1.441	0.847	2.584
S1	0.809	0.2358	0.7231	up	1.406	0.815	2.558
HB	0.801	0.2774	0.7580	up	1.419	0.767	2.737

SI Table 8 The list of glycan traits identified as particularly discriminatory in the AQP4-Ab NMOSD vs MOGAD model. VIP scores, raw p-values, and FDR-corrected p-values determined from unpaired t-tests are provided. The direction of change is indicated relative to the AQP4-Ab NMOSD group. The odds ratio (OR) is also provided, along with the corresponding lower and upper 95% confidence intervals (CI).

Glycan Trait	VIP	p-value	FDR	AQP	OR	Lower 95% CI	Upper 95% CI
FG0/G0	1.980	4.41E-09	2.03E-07	down	24.568	6.366	156.496
S2	1.530	0.0009	0.0188	up	0.349	0.157	0.663
M-content	1.430	0.0021	0.0188	down	2.297	1.343	4.393
nFB	1.390	0.0028	0.0188	down	2.209	1.305	4.096
nFG1	1.370	0.0019	0.0188	down	2.427	1.375	4.785
FGS/(FG+FGS)	1.330	0.0029	0.0188	down	2.303	1.326	4.452
FG2/G2	1.320	0.0169	0.0354	down	2.181	1.160	4.552
FG2	1.300	0.0039	0.0222	down	2.406	1.320	4.853
nFS2	1.290	0.007	0.0236	up	0.425	0.208	0.792
Chrom.	1.260	0.0018	0.0188	up	0.391	0.186	0.710
H	1.240	0.0102	0.0276	down	1.936	1.173	3.500
FG3	1.220	0.0068	0.0236	up	0.435	0.214	0.795

S0	1.146	0.0072	0.023577	down	2.122	1.231	4.075
G1	1.146	0.0089	0.02643	down	2.081	1.209	4.080
M	1.105	0.0133	0.03389	down	1.928	1.151	3.507
FG1/G1	1.103	0.0057	0.023577	up	0.466	0.241	0.799
G3	1.068	0.0060	0.023577	up	0.444	0.226	0.794
FBGS/(FBG+FBGS)	1.035	0.0168	0.035385	up	0.459	0.218	0.861
HB	1.027	0.0069	0.023577	up	0.465	0.244	0.811
NFG2	0.992	0.1771	0.21619	up	0.685	0.380	1.168

Supplementary Information – Manuscript 4

_N_-glycan traits discriminate between MS and Ab-defined diseases

SI Table 9 The results of the 1W-ANOVA comparing the normalised abundance of specific glycan traits among individuals with RRMS, SPMS, MOGAD, and AQP4-Ab NMOSD. The results of the *post hoc* Tukey's test, corrected for multiple comparisons, are also provided.

Glycan Trait	f-value	p-value	(-log)p	FDR	Tukey's HSD
FG0/G0	22.74	1.25E-11	10.904	5.74E-10	MOGAD-AQP4+; RRMS-AQP4+; SPMS-AQP4+; SPMS-RRMS
G3	12.27	5.07E-07	6.295	1.17E-05	MOGAD-AQP4+; RRMS-AQP4+; SPMS-AQP4+; SPMS-MOGAD
nFG3	10.90	2.34E-06	5.630	3.59E-05	RRMS-AQP4+; SPMS-AQP4+; SPMS-MOGAD
AF	10.17	5.41E-06	5.267	5.97E-05	RRMS-AQP4+; SPMS-AQP4+; RRMS-MOGAD
LB-H	10.01	6.49E-06	5.188	5.97E-05	RRMS-AQP4+; SPMS-AQP4+; SPMS-MOGAD
LB	9.78	8.51E-06	5.070	6.53E-05	MOGAD-AQP4+; RRMS-AQP4+; SPMS-AQP4+
HB	9.55	1.10E-05	4.958	7.23E-05	MOGAD-AQP4+; RRMS-AQP4+; SPMS-AQP4+
FS1/FS2	9.22	1.63E-05	4.789	9.36E-05	SPMS-AQP4+; SPMS-MOGAD; SPMS-RRMS
G4	8.85	2.52E-05	4.599	0.0001	SPMS-AQP4+; SPMS-MOGAD; SPMS-RRMS
Chrom.	8.80	2.65E-05	4.576	0.0001	MOGAD-AQP4+; RRMS-AQP4+; SPMS-AQP4+
S1-H	8.10	6.13E-05	4.213	0.0003	SPMS-AQP4+; RRMS-MOGAD; SPMS-MOGAD
S1	7.94	7.35E-05	4.134	0.0003	SPMS-AQP4+; RRMS-MOGAD; SPMS-MOGAD
nFS1	7.88	7.91E-05	4.102	0.0003	RRMS-AQP4+; SPMS-AQP4+; SPMS-MOGAD
nFG1	7.46	0.0001	3.881	0.0004	MOGAD-AQP4+; RRMS-AQP4+; SPMS-AQP4+
S0	6.25	0.0006	3.242	0.0017	MOGAD-AQP4+; RRMS-AQP4+; SPMS-AQP4+
nFS2	6.21	0.0006	3.222	0.0017	SPMS-MOGAD; SPMS-RRMS
FGS/(FG+FGS)	6.16	0.0006	3.195	0.0017	MOGAD-AQP4+; RRMS-AQP4+; SPMS-AQP4+
FG2	6.04	0.0007	3.128	0.0019	MOGAD-AQP4+; RRMS-AQP4+
M	5.85	0.0009	3.030	0.0023	MOGAD-AQP4+; SPMS-AQP4+; SPMS-RRMS
nFB	5.73	0.0011	2.965	0.0025	MOGAD-AQP4+; RRMS-AQP4+; SPMS-AQP4+
S3	5.65	0.0012	2.921	0.0025	SPMS-AQP4+; RRMS-MOGAD; SPMS-MOGAD
FS3	5.61	0.0013	2.901	0.0025	SPMS-AQP4+; RRMS-MOGAD; SPMS-MOGAD
G1-G1H	5.60	0.0013	2.895	0.0025	RRMS-AQP4+; SPMS-AQP4+
core-F	5.53	0.0014	2.855	0.0027	RRMS-AQP4+; SPMS-AQP4+
G1	5.47	0.0015	2.821	0.0028	MOGAD-AQP4+; RRMS-AQP4+; SPMS-AQP4+
M-content	5.36	0.0017	2.765	0.0030	MOGAD-AQP4+; RRMS-AQP4+; SPMS-AQP4+
S0-H	5.28	0.0019	2.721	0.0032	RRMS-AQP4+; SPMS-AQP4+

FG1/G1	5.04	0.0026	2.588	0.0042	MOGAD-AQP4+; RRMS-AQP4+
FBGS/(FBG+FBGS)	4.77	0.0036	2.444	0.0057	SPMS-AQP4+
FG2/G2	4.04	0.0090	2.046	0.0134	RRMS-AQP4+; SPMS-RRMS
B	4.02	0.0093	2.033	0.0134	RRMS-AQP4+; SPMS-AQP4+
B-BH	4.01	0.0093	2.031	0.0134	RRMS-AQP4+; SPMS-AQP4+
S2	3.75	0.0131	1.884	0.0182	MOGAD-AQP4+
H	3.61	0.0154	1.812	0.0209	MOGAD-AQP4+; RRMS-AQP4+
nFS3	3.53	0.0170	1.769	0.0224	RRMS-MOGAD
FS2	3.19	0.0264	1.578	0.0329	SPMS-RRMS
FG1	3.19	0.0264	1.578	0.0329	SPMS-AQP4+
G2	2.91	0.0376	1.424	0.0453	-
FG3/G3	2.89	0.0384	1.415	0.0453	-
FG3	2.62	0.0540	1.268	0.0620	-
FB	2.23	0.0880	1.056	0.0987	-
nFG2	2.09	0.1057	0.976	0.1158	-
FBS/FS	1.99	0.1200	0.921	0.1283	-
FS1	1.79	0.1527	0.816	0.1596	-
G0	1.62	0.1880	0.726	0.1922	-
FBS1/FBS2	1.10	0.3502	0.456	0.3502	-

_N_-glycan traits discriminate between MS and Ab-defined diseases

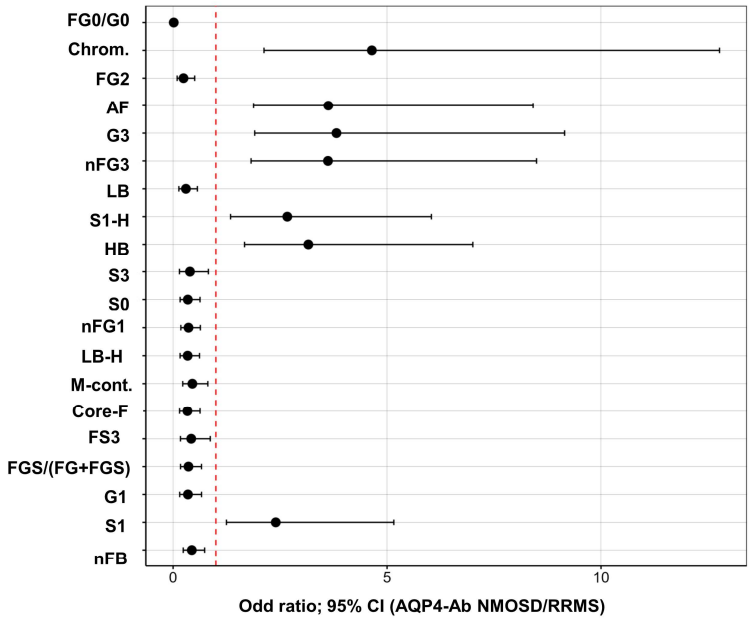

SI Figure 7 OR calculated for the most discriminatory glycan traits identified from the VIP scores for the OPLS-DA model differentiating between AQP4-Ab NMOSD and RRMS, along with 95% CI. This forest plot includes the highly variable FG0/G0 trait (OR = 0.015 (95% CI (0.001-0.097)).

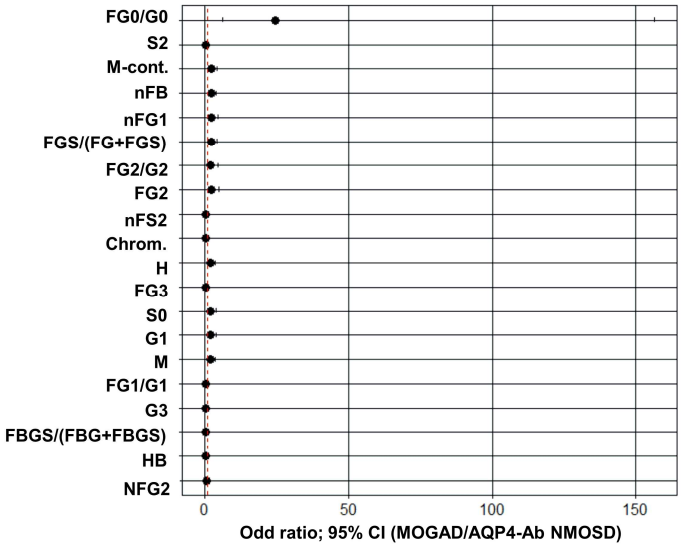

SI Figure 8 OR calculated for the most discriminatory glycan traits identified from the VIP scores for the OPLS-DA model differentiating between AQP4-Ab NMOSD and MOGAD, along with 95% CI. This forest plot includes the highly variable FG0/G0 trait (OR = 24.57 (95% CI (6.37-156.50)).

6. 4 Statement of Authorship

Title of paper	Role of B vitamins in modulating homocysteine and metabolic pathways linked to brain atrophy: metabolomics insights from the VITACOG trial
Publication status	Accepted
Publication details	Kacerova, T., Yates, A.G., Dai, J., Shepherd, D., Pires, E., de Jel, S., Gong, Q., Schiffer, E., Jernerén, F., Olsen, T., De Jager Loots, C.A., Refsum, H., Smith, A.D., McCullagh, J.S.O., Anthony, D.C., Probert, F.: **Role of B vitamins in modulating homocysteine and metabolic pathways linked to brain atrophy: metabolomics insights from the VITACOG trial**. Manuscript accepted (26/06/2025) by: *Alzheimer's & Dementia*

Student confirmation

Student name	Tereza Kacerova
Contribution to the paper	T.K. Sample preparation, NMR, and LC-MS data acquisition, Data analysis and interpretation, Manuscript writing; A. G. Y. NMR sample preparation and data acquisition; J. D. LC-MS biomarker validation; D. S. Oversaw the biobank management; E. P. LC-MS method optimisation; S. de J., Q. G., E. S. NMR data acquisition provider (Numares AG); F. J., T. O., C.A. de J. L., H. R., D. A. S. conceived and oversaw the original VITACOG trial; F. P., J. S. O. M., and D. C. A. are the principal investigators/supervisors of the research described in the manuscript, contributed extensively to project/data conceptualisation and visualisation, and manuscript reviewing/editing.
Date	30/06/2025
Signature	

Supervisor confirmation

By signing the Statement of Authorship, you are certifying that the candidate made a substantial contribution to the publication, and that the description described above is accurate.

Supervisor name	Prof James S. O. McCullagh
Contribution to the paper	I am happy to state that the candidate made a major and substantial contribution this publication, and that the description above is accurate.
Date	29th June 2025
Signature	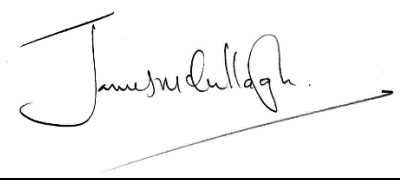

Chapter 6 Multi-Platform Serum Metabolomics Reveals B Vitamin-Induced Metabolic Reprogramming in Mild Cognitive Impairment

6.1 Project context and chapter overview

While the preceding chapters focused on demyelinating disorders, this final chapter addresses neurodegeneration, with a particular emphasis on MCI as a prodromal phase of AD. As the most prevalent neurodegenerative disorder and leading cause of dementia globally, AD is characterised by progressive cognitive decline associated with the accumulation of amyloid-β plaques and neurofibrillary tangles composed of hyperphosphorylated tau protein.[1] MCI represents an intermediate state between normal ageing and dementia, marked by measurable cognitive deficits, particularly in memory, without significant impairment in daily functioning.[2] While MCI can result from a range of underlying causes, it frequently precedes AD, particularly in individuals with biomarker evidence of Alzheimer-type pathology, and is increasingly recognised as a critical window for therapeutic intervention.

The identification of accessible, reliable biomarkers for early-stage AD remains a critical challenge in both research and clinical practice. Although PET and CSF analyses can quantify amyloid-β and tau pathology with high specificity, their clinical utility is limited by cost, invasiveness, and logistical constraints.[3, 4] Consequently, considerable efforts are now directed toward the development of blood-based biomarkers capable of capturing early neurodegenerative processes and enabling large-scale screening and longitudinal monitoring. Such tools are increasingly recognised as essential for the timely initiation of disease-modifying interventions, particularly in individuals with MCI or preclinical AD, where therapeutic strategies may have the greatest potential to preserve cognitive function.

Among several biochemical risk factors implicated in cognitive decline, elevated plasma total homocysteine (tHcy) has been consistently associated with brain atrophy and increased risk of progression to dementia.[5, 6] tHcy is an intermediate in the one-carbon metabolism pathway, and elevated levels have been linked to hippocampal atrophy and cognitive impairment in both observational and neuroimaging studies.[5] Supplementation with high-dose B vitamins (folic acid, B6, and B12) has been shown to lower tHcy concentrations by enhancing remethylation and trans-sulphuration pathways, in which these vitamins act as

essential cofactors.[6] While this biochemical relationship is well established, the broader metabolic and mechanistic consequences of tHcy reduction - and their relevance to neuroprotection - remain incompletely understood.

To address this gap, we applied a multi-platform untargeted metabolomics approach, combining NMR spectroscopy with complementary LC-MS platforms (RPLC-MS and IC-MS), to characterise the systemic metabolic effects of B vitamin supplementation. In addition to evaluating treatment-induced metabolic changes, we also explored the potential of serum-based metabolite profiles as biomarkers of cognitive decline or resilience. The VITACOG cohort offered a unique opportunity to investigate these questions, given its two-year longitudinal design, detailed clinical and neuroimaging characterisation, and specific relevance to early neurodegenerative processes.[6]

Despite the analytical potential of the VITACOG cohort, the limited serum aliquot volume available for each participant - due to long-term biobanking and prior use in other studies - posed a significant methodological challenge. This constraint necessitated a highly efficient analytical strategy capable of extracting maximal information from minimal sample input. To address this, we employed an integrative workflow in which NMR-prepared samples were subsequently recovered and repurposed for LC-MS analysis, using the sample preparation protocols developed in **Chapters 2 and 3**. Additionally, extraction procedures were tailored for different LC-MS platforms, including RPLC-MS and IC-MS, to optimise metabolite coverage across diverse chemical classes. This approach enabled comprehensive metabolomic profiling from single small-volume aliquots, supporting both mechanistic insight into B vitamin effects and the identification of candidate biomarkers for monitoring cognitive decline in MCI.

Notably, B vitamin treatment was found to induce substantial metabolic alterations, particularly within pathways related to energy metabolism, amino acid turnover, and the glutamine–glutamate cycle. These changes extend beyond the expected reduction in tHcy and offer mechanistic insight into the potential neuroprotective effects observed in the original trial. Moreover, this work highlights the utility of robust multi-omics workflows for extracting biologically meaningful information from biobanked clinical samples, enabling concurrent evaluation of treatment effects and the identification of candidate biomarkers for cognitive impairment.

6. 2 References

(1) DeTure, M. A.; Dickson, D. W. The neuropathological diagnosis of Alzheimer's disease. *Mol Neurodegener* **2019**, *14* (1), 32. DOI: 10.1186/s13024-019-0333-5 From NLM Medline.
(2) Horvath, A. A.; Berente, D. B.; Vertes, B.; Farkas, D.; Csukly, G.; Werber, T.; Zsuffa, J. A.; Kiss, M.; Kamondi, A. Differentiation of patients with mild cognitive impairment and healthy controls based on computer assisted hand movement analysis: a proof-of-concept study. *Sci Rep* **2022**, *12* (1), 19128. DOI: 10.1038/s41598-022-21445-4 From NLM Medline.
(3) Chouliaras, L.; O'Brien, J. T. The use of neuroimaging techniques in the early and differential diagnosis of dementia. *Mol Psychiatry* **2023**, *28* (10), 4084-4097. DOI: 10.1038/s41380-023-02215-8 From NLM Medline.
(4) Panyard, D. J.; McKetney, J.; Deming, Y. K.; Morrow, A. R.; Ennis, G. E.; Jonaitis, E. M.; Van Hulle, C. A.; Yang, C.; Sung, Y. J.; Ali, M.; et al. Large-scale proteome and metabolome analysis of CSF implicates altered glucose and carbon metabolism and succinylcarnitine in Alzheimer's disease. *Alzheimers Dement* **2023**, *19* (12), 5447-5470. DOI: 10.1002/alz.13130 From NLM Medline.
(5) Smith, A. D.; Refsum, H.; Bottiglieri, T.; Fenech, M.; Hooshmand, B.; McCaddon, A.; Miller, J. W.; Rosenberg, I. H.; Obeid, R. Homocysteine and Dementia: An International Consensus Statement. *J Alzheimers Dis* **2018**, *62* (2), 561-570. DOI: 10.3233/JAD-171042 From NLM Medline.
(6) Smith, A. D.; Smith, S. M.; de Jager, C. A.; Whitbread, P.; Johnston, C.; Agacinski, G.; Oulhaj, A.; Bradley, K. M.; Jacoby, R.; Refsum, H. Homocysteine-lowering by B vitamins slows the rate of accelerated brain atrophy in mild cognitive impairment: a randomized controlled trial. *Plos One* **2010**, *5* (9), e12244. DOI: 10.1371/journal.pone.0012244 From NLM Medline.

6. 3 Manuscript information

This chapter consists of a research article manuscript accepted by *Alzheimer's and Dementia* (26/06/2026).

Kacerova, T., Yates, A.G., Dai, J., Shepherd, D., Pires, E., de Jel, S., Gong, Q., Schiffer, E., Jernerén, F., Olsen, T., De Jager Loots, C.A., Refsum, H., Smith, A.D., McCullagh, J.S.O., Anthony, D.C., Probert, F. **Role of B vitamins in modulating homocysteine and metabolic pathways linked to brain atrophy: metabolomics insights from the VITACOG trial**

Manuscript status: *accepted*

Role of B vitamins in modulating homocysteine and metabolic pathways linked to brain atrophy: metabolomics insights from the VITACOG trial

Tereza Kacerova[1], Abi G. Yates[1,2], Jiayi Dai[1], Dawn Shepherd[2], Elisabete Pires[1], Sebastian de Jel[3], Qingxia Gong[3], Eric Schiffer[3], Fredrik Jernerén[4], Thomas Olsen[5], Celeste A. De Jager Loots[6], Helga Refsum[2,5], A. David Smith[2], James S.O. McCullagh[1*], Daniel C. Anthony[2*], Fay Probert[1]

[1]Department of Chemistry, University of Oxford, Mansfield Road, Oxford, OX1 3TA, UK.
[2]Department of Pharmacology, University of Oxford, Mansfield Road, Oxford, OX1 3QT, UK.
[3]numares AG, Am Biopark 9, Regensburg, 93053, Germany.
[4]Department of Pharmaceutical Biosciences, Uppsala University, Husargatan 3, Uppsala, 752 37, Sweden.
[5]Department of Nutrition, Institute of Basic Medical Sciences, Faculty of Medicine, University of Oslo, Postboks 1046 Blindern, Oslo, 0317, Norway.
[6]The Ageing Epidemiology Research Unit, School of Public Health, Imperial College London, Charing Cross Hospital, St Dunstan's Road, London, W6 8RP, UK.

*Corresponding author(s). E-mail(s): james.mccullagh@chem.ox.ac.uk; daniel.anthony@pharm.ox.ac.uk;

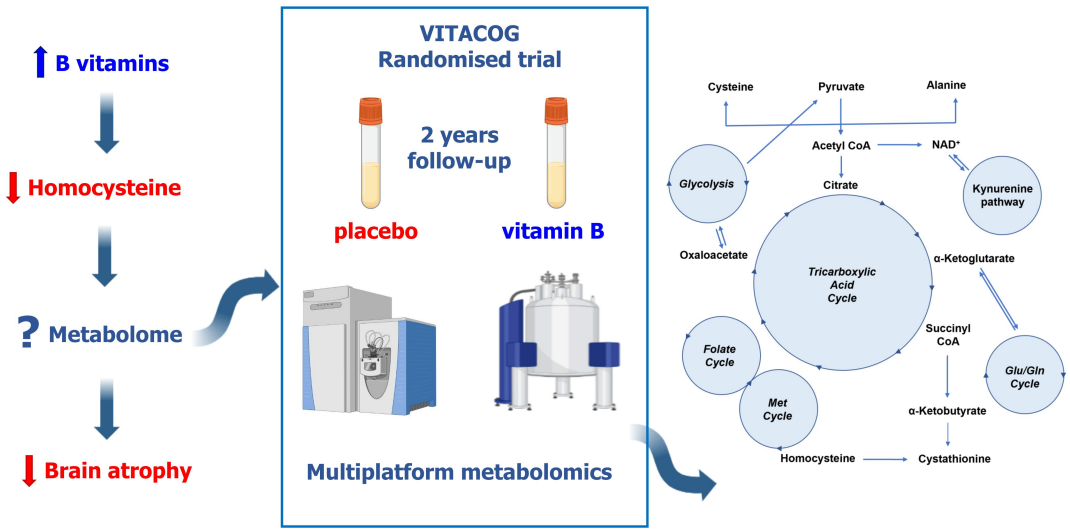

Abstract

Background and Objectives: Elevated total homocysteine (tHcy) is a major predictor of brain atrophy, cognitive decline, and Alzheimer's disease (AD) progression. The VITACOG trial, a randomised, placebo-controlled study in mild cognitive impairment (MCI), previously showed that B vitamin supplementation lowered tHcy, slowing brain atrophy and cognitive decline; however, the underlying mechanisms remained unclear.
Methods: We employed untargeted, multi-platform metabolomics, utilising nuclear magnetic resonance and liquid chromatography-mass spectrometry to analyse serum samples from 89 B-vitamin-treated and 84 placebo-treated MCI participants over a 2-year follow-up period.
Results: Multivariate modelling distinguished treated from placebo groups with 91.2±1.8% accuracy. B vitamin supplementation induced significant metabolic reprogramming, lowering quinolinic acid, α-ketoglutarate, α-ketobutyrate, glucose, and glutamate.
Discussion: These findings reveal that B vitamins influence metabolic pathways beyond tHcy reduction, particularly the tricarboxylic acid cycle and glutamine–glutamate cycling, critical for brain energy homeostasis and neurotransmission. This metabolic signature supports B vitamin supplementation as a strategy for slowing MCI progression.

Keywords:cognitive impairment, B vitamins, homocysteine, untargeted metabolomics, nuclear magnetic resonance, mass spectrometry

1 Background

Individuals with mild cognitive impairment (MCI) exhibit accelerated rate of brain atrophy, which correlates with an increased risk of developing Alzheimer's disease (AD).[1-3] The VITACOG trial demonstrated that B vitamin supplementation reduces plasma total homocysteine (tHcy) and slows brain atrophy progression in older adults with MCI.[4,5] However, the mechanisms underlying this neuroprotective effect remain incompletely understood. Elevated tHcy is associated with greater cerebral atrophy and cognitive decline, but it is unclear whether tHcy directly contributes to neurodegeneration or reflects broader metabolic dysfunction, such as subclinical B vitamin insufficiency.[6-9] This distinction has clinical relevance, as identifying the metabolic pathways responsive to B vitamin supplementation could clarify whether lowering tHcy has a mechanistic effect or merely serves as a surrogate marker of improved nutritional status.

Hcy is a sulphur-containing amino acid derived from methionine and metabolised via two B vitamin-dependent pathways: remethylation to methionine (requiring folate and vitamin B12) and trans-sulphuration to cysteine (requiring vitamin B6).[10] Deficiencies in these B vitamins have been reported to increase tHcy, which may exert direct neurotoxic effects through mechanisms including oxidative stress, excitotoxicity, and NAD^+ depletion.[11] Experimental models have demonstrated that Hcy inhibits neurite outgrowth in cerebellar Purkinje neurons[6,7]and induces apoptotic cell death in hippocampal neurons via DNA damage, activation of poly(ADP-ribose) polymerase (PARP), and NAD^+ depletion.[11,12] Notably, elevated tHcy can also result from factors beyond vitamin deficiency, such as renal dysfunction, genetic variation, and lifestyle,[13,14] raising the question of whether Hcy functions as a causal mediator of neurodegeneration or reflects broader systemic and metabolic alterations. While B vitamins are essential for Hcy metabolism, they also support a range of other biochemical pathways, including DNA methylation, neurotransmitter synthesis, and mitochondrial function.[15,16] The extent to which B vitamin supplementation modulates these broader metabolic networks *in vivo*, and whether such changes contribute to reduced brain atrophy, remains to be determined.

To investigate the metabolic effects of B vitamin supplementation and its relationship to Hcy lowering, we applied an untargeted metabolomics approach to serum samples from the VITACOG trial.[4] This randomised controlled trial assessed the impact of high-dose folic acid, vitamin B6, and vitamin B12 on plasma tHcy levels and cerebral atrophy in older adults.[4,5] Over 24 months, B vitamins supplementation significantly reduced tHcy and was associated with a 29.6% reduction in the rate of brain atrophy compared to placebo.[4,17] In

the placebo group, baseline tHcy positively correlated with atrophy rate, whereas this association was absent in the treatment group.[4] Although the trial also reported cognitive benefits in specific domains,[18,19] findings across studies remain inconsistent, highlighting the complexity of the relationship between tHcy metabolism, micronutrient status, and cognitive outcomes.[20-22]

Recent metabolomics studies have provided initial evidence linking B vitamin supplementation and tHcy reduction to metabolic alterations such as enhanced gluconeogenesis[23] and decreased oxidative stress.[24] However, the broader metabolic impact of B vitamins is poorly characterised. Untargeted (global) metabolomics enables comprehensive and unbiased profiling of the metabolome, allowing simultaneous assessment of a wide range of biochemical processes.[25] This approach facilitates both pathway-level interpretation and the identification of novel biomarkers, offering a robust framework to investigate the metabolic effects of B vitamins and their potential mechanistic links to Hcy metabolism and cerebral atrophy.

Here, we employed nuclear magnetic resonance (NMR) spectroscopy and mass spectrometry (MS) across two complementary platforms: reversed-phase liquid chromatography-MS (RPLC-MS), targeting low- to medium-polarity compounds, and anion-exchange chromatography-MS (AEC-MS), which extends coverage to charged, polar metabolites relevant to B vitamin-dependent pathways.[26] This combination - particularly the inclusion of AEC-MS, which remains uncommon in serum-based studies - provides broader analyte coverage and improved resolution of physicochemically diverse metabolites. The primary objective was to identify metabolites and pathways altered by B vitamin supplementation and the associated reduction in tHcy. By characterising these changes within a functional biochemical framework (as outlined in the graphical abstract), we aimed to elucidate the metabolic mechanisms underlying the neuroprotective effects of B vitamins in MCI and inform the optimisation of future interventions.

2 Methods

2.1 Participants and study design

The study utilised biobanked serum samples obtained from clinical trial VITACOG, conducted in the Oxford area between April 2004 and November 2006.[4] The patient inclusion criteria were defined by age $>$ 70 years and diagnosis of amnestic or non-amnestic MCI according to Petersen's criteria.[27] Additionally, the exclusion criteria included a diagnosis of dementia or treatment with anti-dementia drugs; active cancer; major stroke within past three months; treatment with methotrexate, anti-cancer or anti-epileptic drugs, or taking folic acid $>$ 300 μg/d, pyridoxine $>$ 3 μg/d or vitamin B12 $>$ 1.5 μg/d either per orally or any dose by injection.[4] Individuals fulfilling entry criteria were randomised to either a treatment group or a placebo group. Randomisation was conducted by an independent statistician using allocation concealment and minimisation, accounting for age, gender, baseline Modified Telephone Interview for Cognitive Status (TICS-M) score, and MRI consent. The treatment group received oral TrioBe Plus (Meda AB/Recip AB, Sweden) containing 0.8 mg folic acid, 0.5 mg cyanocobalamin and 20 mg pyridoxine HCl, or a placebo tablet.[4] The treatment lasted two years. For a complete description of the study protocol, refer to the original study reports.[4,18] In this study, we focused on biologically compliant individuals, as described by Smith *et al.*[4] Biological compliance was assessed based on changes in plasma B vitamin concentrations over a two-year period, with specific cut-off values used to categorise participants. In the treatment group, subjects were considered biologically compliant if they exhibited an increase in plasma folate of more than 10 nmol/L and an increase in vitamin B12 of more than 150 pmol/L from baseline to follow-up. In the placebo group, compliance was defined as an increase of 10 nmol/L or less in folate and 150 pmol/L or less in vitamin B12.[4] Participants who did not meet these criteria were classified as biologically non-compliant, and were excluded from the present analysis.

2.2 Protocol approvals, patient consent

The VITACOG trial was conducted according to the principles described in the Declaration of Helsinki. The study approved by a local NHS research ethics committee (COREC 04/Q1604/100). Each involved individual provided written consent for their participation. The Trial Protocol and the CONSORT checklist are available in the original study by Smith *et al.*[4] while the updated CONSORT flowchart is available in the Supplementary Information (SI Fig.1). As a secondary analysis of biobanked samples from a completed clinical trial, this study adheres to STROBE guidelines, and the STROBE checklist for retrospective studies is available in the electronic clinical trial material.

2.3 MRI acquisition and atrophy rate calculation

Volumetric cranial MRI scans were performed at baseline and after two years using a 1.5T MRI system (Siemens Sonata) at the Oxford Centre for Clinical Magnetic Resonance Research.[4] The T1-weighted 3D gradient echo (FLASH) protocol employed 1 mm isotropic voxels, a 19° flip angle, TR = 12 ms, and TE = 5.65 ms, with 208 coronal slices per slab.[4] Scans were repeated three times, averaged, and aligned. Brain atrophy rate was calculated using SIENA,[28] an automated method, which estimates atrophy per year based on two scans taken two years apart. Z-scores for the annual atrophy rate were calculated to classify participants with high-quality MRI scans into two groups: progressors (positive z-scores, atrophy rate: 0.899-3.324) and stable individuals (negative z-scores, atrophy rate: -0.585 to 0.890). Additional voxelwise analyses of grey matter loss in this cohort, particularly in medial temporal and prefrontal regions, have been reported previously.[29]

2.4 NMR sample preparation and analytical methodology

The serum aliquots were thawed at 4°C and the samples were visually checked for any protein precipitation. All samples were processed according to a standardised protocol applied by Numares AG, Regensburg, Germany.[30] 405 μL of the serum sample was diluted with 45 μL of D_2O-based buffer.[30,31] Following NMR analysis, the processed NMR samples were recovered and stored at −80°C until the day of LC-MS analysis.

All ^{1}H NMR metabolomics experiments were performed at Numares AG, Regensburg, Germany, using a 600-MHz Bruker AVIII ^{1}H NMR spectrometer. For spectra acquisition, the zgpr30 pulse sequence with pre-saturation to suppress water signal was used, as previously described.[30] The NMR spectra were manually phased, baseline corrected, and chemical shifts referenced to lactate –CH_3 doublet signal (δ = 1.33 ppm) in Topspin 4.1.4 (Bruker, Germany). The processed spectra were then uploaded in ACD/NMR processor academic edition 12.01 software (Advanced Chemistry Development, Inc.).[30] The spectral regions between the 0.55–4.25 ppm and 5.20–8.50 ppm were divided into 0.02 ppm width bins and the bins were sum-normalised. The integrals of each bin were then exported for multivariate statistical analysis. The metabolite assignment was performed with reference to previous experiments, literature[31-34] and the Human Metabolome Database.[35]

2.5 Serum sample preparation for LC-MS analyses

The recovered NMR samples were thawed at 4°C and prepared for LC-MS analysis. For RPLC-MS analysis, metabolites from the recovered NMR samples were extracted by the addition of excess of acetonitrile (1:2.33 (v/v)). The samples were vortexed for 1 min and centrifuged (16 000 × g; 15 min, 4°C). The supernatant was transferred into a clean microcentrifuge tube and centrifuged (16 000 × g; 15 min, 4°C). The supernatant was transferred into a total-recovery MS autosampler vial.[36]

For AEC-MS analysis, metabolites from the recovered NMR samples were extracted using a BuOH/MeOH mixture (1:4, v/v), added in excess to the NMR-recovered serum at a ratio of 1:2.33 (v/v). The samples were vortexed for 1 min and centrifuged (16 000 × g; 15 min, 4°C). The supernatant was transferred into pre-washed Molecular Weight Cut-Off (MWCO) filtration columns (10 kDa MWCO filter; Amicon Ultra 0.5 mL centrifugal filters) and centrifuged (16 000 × g; 30 min, 4°C). The filtrate was transferred into a total-recovery MS autosampler vial.

A quality control (QC) sample for each extraction method was prepared by pooling 5 μL from each biological sample into a single total-recovery MS autosampler vial. This QC sample was injected at the start of each LC-MS sequence and after every ten biological samples to evaluate data quality and ensure analytical consistency throughout the sequence. To further monitor overall system performance and retention time stability across platforms, a mixture of over 200 authentic metabolite standards was analysed at both the beginning and end of the experimental sample sequence.

To exclude B vitamins and their direct metabolites from the results, we first identified these compounds by spiking serum samples (human serum derived from male AB plasma; Merck, UK) with selected B vitamin-related metabolites. A comprehensive list of the assessed compounds is provided in SI Tables 1–3. This approach enabled the positive identification of these signals in the VITACOG study samples, ensuring their exclusion from statistical models and minimising the risk of bias in the results.

2.6 Anion-Exchange Chromatography-MS Analysis

AEC-MS analysis was performed using a Dionex ICS-5000+ high-pressure ion chromatography system equipped with a continuously regenerated trap column, Dionex ERS 500e suppressor and AS11-HC (2×250mm, 4 μm) column, all from

Dionex (Sunnyvale, CA, USA), coupled to a Q-Exactive hybrid quadrupole-Orbitrap MS via a HESI II probe (Thermo Fisher, 229 San Jose, CA, USA). The technical details of the AEC-MS-based analysis have been previously described.[37,38]

2.7 Reversed-Phase Ultra Performance Liquid Chromatography-MS Analysis

C18 RPLC-MS analysis was performed using an Acquity Ultra Performance Liquid Chromatography (UPLC) system (Waters, UK) operating under a gradient elution protocol, directly interfaced with a high-resolution quadrupole time-of-flight mass spectrometer (Xevo G2-XS QTOF, Waters, UK). Sample injection was carried out using a 5 μL partial-loop mode, with automated pre- and post-injection needle wash steps included to minimise sample carryover. Full technical details of the RPLC-MS analysis have been reported previously.[36]

2.8 Data Processing

The untargeted metabolomics data (both for RPLC-MS and AEC-MS) were processed using Progenesis QI (Nonlinear Dynamics, Waters, Elstree, UK). The spectra were aligned and corrected for drift in the retention time. Data processing included peak picking, identification of natural abundance isotope peaks, detection of characteristic adducts (for all methods, $[\pm\ H^+]$ and $[\pm\ H^+ - H_2O]$ were applied), and metabolite identification using an *in-house* database of standards. Metabolite identification was performed by matching multiple experimental parameters to the database of authentic standards, as previously described.[38] The library comprised over 450 standards for AEC-MS and 150 for RPLC-MS. Level 1 identifications, as defined by the Metabolomics Standards Initiative (MSI), were assigned based on retention time (Rt error $<$ 2 min), accurate mass ($<$ 5 ppm for AEC-MS and $<$ 20 ppm for RPLC-MS), and isotope and fragmentation pattern similarity ($>$ 90%).[39] All metabolites reported in the results section were further validated by co-analysing authentic standards alongside quality control (QC) samples to ensure precise retention time alignment. The AEC-MS method does not precisely resolve individual monosaccharides but reliably detects changes in C6 monosaccharides as a collective group. The most intense signal, represented by the overall chromatographic response, was primarily attributed to glucose due to its high abundance in serum. However, this signal likely also includes contributions from other hexose sugars present at lower abundances. Compound-features and the identified metabolite list were filtered based on a coefficient of variance (%CV) threshold of $<$ 30% in QC samples. Metabolites or compound-features with a %CV $>$ 30% in QC samples were excluded from further analysis. Ion intensity drift was corrected using the LOESS correction ($\alpha = 0.5$) feature in MetaboDrift, with QC samples employed to correct for within-batch drift.[40]

2.9 Multivariate statistical analysis

The MetaboDrift corrected data were imported into R software 4.2.1 (R Foundation for Statistical Computing, Vienna, Austria). Multivariate analysis was performed using *in-house* R scripts and the *ropls* package.[41] The NMR data were sum-normalised and standardised using z-scores, while the LC-MS data were sum-normalised, log-transformed, and standardised using z-scores. For NMR datasets, orthogonal partial least square discriminant analysis (OPLS-DA) with 10-fold cross-validation, 100 repetitions, and permutation testing was performed, as previously described, to characterise the metabolomic differences between the B vitamins-treated individuals and placebo controls.[42] For all models the reported accuracy, sensitivity, and specificity corresponds to the OPLS-DA on test data (the model was trained blinded from this test set). The generated model ensemble was tested against 1000 randomly permuted models to determine its discriminatory capacity compared to random chance (as determined by a two-sided Kolmogorov–Smirnov test, with a p-value significance cut-off of 0.05). The discriminatory metabolites and/or compound-features were identified based on the average Variable Importance in Projection (VIP) scores, representing the overall contribution of each variable to the OPLS-DA model. For LC-MS datasets and the models combining multiple metabolomic platforms, the assessment of metabolomic differences between treated individuals and placebo controls was conducted by a slightly altered version of the above-described method. To prevent a drop in accuracy due to the input of a large number of variables, OPLS-DA was combined with elastic net regularisation. Elastic net regularisation ($\alpha = 0.5$) was applied, with cross-validation to determine the optimal regularisation parameter λ. Features were selected based on non-zero coefficients from the regularised logistic regression model. Randomised null models were generated by shuffling classes to validate the robustness of the feature selection and classification performance. The OPLS-DA was then performed as described above. For VIP scores,

the overall score for a particular variable was determined as the frequency of selection divided by the average rank. Due to the large number of unidentified compound-features in the LC-MS datasets, complementary OPLS-DA models were reconstructed using only identified metabolites. Metabolites with the highest VIP scores, particularly endogenous ones, were then subjected to univariate analysis.

2.10 Univariate statistical analysis

Univariate analysis was performed in R software 4.2.1 (R Foundation for Statistical Computing, Vienna, Austria) using the *ggplot2*, *ggpubr*, *effects*, and *dplyr* packages. An unpaired two-sample t-test was applied for continuous variables, while the Chi-square test was performed for categorical variables. A three-way ANOVA was performed to assess the effects of treatment, atrophy progression, and time point on each metabolite, followed by pairwise comparisons using Tukey's *post-hoc* test. Subsequently, a two-way ANOVA was conducted to evaluate the effects of treatment, atrophy progression, and their interaction on each metabolite (follow-up levels adjusted for baseline levels), followed by pairwise comparisons using Tukey's *post-hoc* test. The significance cut-off was set at $p < 0.05$ for all data sets; the False Discovery Rate (FDR) corrections (Benjamini-Hochberg) were applied as appropriate (if not indicated otherwise). Quantitative data are shown as Tukey boxplots (GraphPad Prism 10 software), with whiskers extending to the furthest values within 1.5 times the interquartile range (IQR). Outliers exceeding 3 times the IQR were identified and removed from the boxplot visualisation to enhance interpretability. These extreme values were retained in the dataset for subsequent statistical analysis to assess their impact on the overall results.

A Pearson correlation analysis was performed using the *corrplot* R package to assess linear relationships among significantly altered metabolites, tHcy, folate, and vitamin B12 (all measured at follow-up), as well as atrophy rate and cognitive test scores (MMSE and TICS-M). A correlation matrix was calculated to assess the correlation coefficient (α) between pairs of variables.

2.11 Pathway analysis

Pathway topology enrichment analysis was performed using MetaboAnalyst 6.0,[43] based on the KEGG metabolite library specific to *Homo sapiens* and incorporated Global Analysis of Covariance (ANCOVA) enrichment analysis. The individual metabolites were allocated to metabolic pathways and an estimate of metabolite importance within a metabolic network was determined based relative betweenness centrality algorithm. To ensure robustness, only metabolites with MSI Level 1 identifications were included in the pathway analysis.[39]

3 Results

3.1 Patient characteristics

To investigate the effects of B vitamin-induced tHcy-lowering on the serum metabolome in the VITACOG cohort, we conducted a stratified analysis following the criteria established by Smith *et al.*[4] The demographic and clinical characteristics of biologically compliant individuals are summarised in Table 1, with no significant baseline differences observed between the placebo and treatment groups. Although baseline folate levels did not differ significantly between groups ($p = 0.173$), they exhibited considerable variability, with greater dispersion in the placebo group (31.3 ± 25.9 nmol/L) compared to the treatment group (24.4 ± 15.1 nmol/L). The Shapiro-Wilk normality test confirmed a right-skewed distribution, driven by two high outliers (> 90 nmol/L). Sensitivity analyses excluding these extreme values demonstrated no significant impact on metabolomic outcomes. To further assess group comparability, we also examined markers of kidney function, including estimated glomerular filtration rate (eGFR), which showed no significant differences between groups at baseline and follow-up (SI Fig. 2, 3), supporting the absence of renal confounding. To control for confounding factors, we evaluated correlations between metabolite abundance and a range of clinical and behavioural variables, including age, smoking status, alcohol intake, and nutritional supplement use, with no significant associations observed (all $R^2 < 0.2$, $p > 0.3$). Additionally, co-administered pharmacotherapies showed no discernible effect, as OPLS-DA score plots demonstrated an even distribution across medications without distinct clustering (SI Fig. 4–6). Given previous VITACOG findings indicating reduced treatment efficacy with aspirin,[4] signals corresponding to salicylic acid and acetylsalicylic acid were excluded from the analysis (SI Tables 1–3).

3.2 Polar metabolome discriminates between B vitamin-treated individuals and placebo controls

To confirm the absence of baseline differences in the metabolome between experimental groups, we first constructed a multivariate model that

Table 1: **Demographic and clinical characteristics of placebo controls and individuals receiving B vitamin treatment.** Mean ± standard deviation (SD) is reported for continuous variables. Chi-squared tests and unpaired two-sample t-tests were used to calculate p-values for categorical and continuous variables, respectively. Age, BMI, and systolic and diastolic blood pressure were recorded at baseline. Continuous variables are presented as mean ± standard deviation (SD). "Baseline" refers to pre-intervention, while "follow-up" denotes post-treatment assessments (2 years).

Characteristics	**Placebo ($N = 84$)**	**Treatment ($N = 89$)**	***p*-value**
Age (baseline)	76.4 ± 4.6	77.0 ± 5.1	0.471
Sex (% female)	54 (64%)	55 (62%)	0.735
Years of education	15.4 ± 3.9	14.1 ± 3.4	0.312
Body Mass Index, kg/m^2	26.1 ± 4.2	25.8 ± 3.5	0.471
Systolic blood pressure, mmHg	147 ± 18	145 ± 23	0.394
Diastolic blood pressure, mmHg	80 ± 10	79 ± 11	0.503
TICS-M (baseline)	24.95 ± 2.81	24.91 ± 2.76	0.921
TICS-M (follow-up)	26.83 ± 4.24	26.71 ± 5.03	0.871
MMSE (baseline)	28.26 ± 1.47	28.19 ± 1.82	0.699
MMSE (follow-up)	27.69 ± 2.23	27.81 ± 2.20	0.723
Initial brain volume (mL)*	1373.5 ± 67.4	1383.1 ± 87.2	0.482
Use of CVD drugs (anytime)	43 (51%)	56 (63%)	0.119
Use of CNS drugs (anytime)	27 (32%)	39 (44%)	0.114
Use of aspirin (anytime)	34 (40%)	35 (39%)	0.877
tHcy (baseline), µmol/L	11.49 ± 3.19	12.06 ± 3.56	0.885
tHcy (follow-up), µmol/L	13.01 ± 3.92	8.77 ± 1.90	< 0.0001
Folate (baseline), nmol/L	31.3 ± 25.9	24.4 ± 15.1	0.173
Folate (follow-up), nmol/L	23.6 ± 16.2	95.7 ± 38.9	< 0.0001
Δ Folate from baseline, nmol/L	-4.80 ± 13.88	70.53 ± 40.46	< 0.0001
Vitamin B12 (baseline), pmol/L	346.9 ± 95.8	342.1 ± 134.5	0.933
Vitamin B12 (follow-up), pmol/L	342.8 ± 99.6	749.1 ± 276.3	< 0.0001
Δ Vitamin B12 from baseline, pmol/L	5.72 ± 68.82	399.17 ± 232.90	< 0.0001
Atrophy rate*	2.46 ± 0.49	0.73 ± 0.66	0.007

*MRI data for atrophy rate determination were available for 62 individuals in the placebo group and 65 in the treatment group.

integrated data from all analytical platforms and methods (Fig. 1A). No statistically significant differences were observed at baseline, with the model achieving an accuracy of 49.6 ± 3.1%, which was not significantly different from the accuracy of a randomly permuted ensemble ($p = 0.502$). This established that any metabolomic differences observed post-intervention are attributable to B vitamin supplementation rather than pre-existing variability between the groups.

Having demonstrated a comparable baseline, we next evaluated the effects of B vitamins on the blood metabolome using untargeted metabolomic profiling of follow-up serum samples from 89 B vitamin-treated individuals and 84 placebo controls. A multi-platform approach combining NMR and LC-MS was employed, and multivariate OPLS-DA models were constructed to characterise metabolic differences and capture the biochemical impact of B vitamin supplementation.

Results from the NMR analysis indicated limited ability to detect metabolic changes directly attributable to B-vitamin supplementation, with model accuracy reaching 53.7 ± 2.9% (Fig. 1B). While this accuracy was significantly above random ($p = 2.4 \times 10^{-6}$), the observed metabolic differences between treatment groups were subtle, likely reflecting the relatively small effect size of B-vitamin supplementation on the high-abundance metabolites detectable by NMR. The only metabolite identified from the VIP scores as statistically significant was alanine (t-test $p = 0.03$), which was increased in B vitamin-treated individuals.

For LC-MS, the discriminatory power varied according to the polarity of the detected

metabolites. RPLC-MS analysis in positive ionisation mode demonstrated moderate discriminatory capacity, with an accuracy of 64.4 ± 2.4% (Fig. 1C). In contrast, RPLC-MS analysis in negative ionisation mode revealed no significant metabolomic differences, with model accuracy comparable to a random model ensemble (50.3 ± 3.2%; $p = 0.44$; Fig. 1D). In contrast, when the results from the AEC-MS analysis (negative ionisation mode) were modelled, an overall accuracy of 88.1 ± 1.6% was achieved. As AEC-MS specifically characterises highly polar and anionic compounds, this analysis highlighted the discriminatory potential of the polar metabolome in distinguishing B vitamin-treated individuals from placebo controls (Fig. 1E). To evaluate the impact of data integration on group discrimination, we first assessed all binary combinations of the analytical platforms. These analyses demonstrated that the AEC-MS dataset consistently provided the strongest discriminatory power, while the addition of other platforms yielded incremental gains in classification performance (SI Fig. 7). We then combined data from all platforms to generate a single OPLS-DA model, which achieved an accuracy of 91.2 ± 1.8% (Fig. 1F), representing a modest yet statistically significant improvement over the AEC-MS-based model alone ($p = 1.32 \times 10^{-5}$).

3.3 B vitamin supplementation alters central carbon metabolism

Next, we aimed to identify metabolites and compound-features significantly altered in the treatment group. Univariate analysis, in conjunction with multivariate models (SI Tables 4-5), was employed to delineate metabolomic changes driven by the treatment effect from those associated with brain atrophy progression. Consistent with findings from the original VITACOG study (Table 1),[4] B vitamin administration was associated with a significant reduction in the rate of brain atrophy. However, not all individuals receiving B vitamin treatment exhibited a reduced atrophy rate, while a subset of placebo-treated individuals showed minimal atrophy progression over the two-year follow-up period. To account for the potential confounding effects of brain atrophy, the cohort was stratified into four subgroups based on treatment allocation and atrophy rate, using MRI data from individuals with available scans ($N = 89$): B vitamin responders ($N = 51$), B vitamin non-responders ($N = 14$), stable individuals in the placebo group ($N = 31$), representing metabolomic changes attributable to natural ageing with MCI, and placebo individuals with worsening brain atrophy ($N = 31$), reflecting metabolomic changes associated with atrophy progression. Both baseline and follow-up samples were included for all subgroups to account for temporal effects.

A three-way ANOVA (SI Fig. 8 and SI Tables 6–8), incorporating treatment allocation (treatment vs. placebo), brain atrophy progression (stable vs. progressing), and timepoint (baseline vs. follow-up), identified treatment allocation as the primary factor influencing the majority of metabolites. The AEC-MS method identified statistically significant differences in the abundance of several exogenously-derived compounds between groups, including mannitol, arabitol, and sorbitol, as well as saccharides less commonly observed in human blood, such as mannose and ribulose (SI Table 6). These results suggest alterations in metabolites associated with energy and sugar metabolism. To specifically assess the effects of B vitamins on the intrinsic metabolome, subsequent analyses primarily focused on endogenous metabolites. Several metabolites identified through the three-way ANOVA exhibited significant treatment effects, while showing no significant associations with atrophy progression, timepoint effects, or their interactions, including: α-ketoglutaric acid (treatment effect $p < 0.0001$ (FDR $p = 0.002$), SI Fig. 8A), succinic acid (treatment effect $p = 0.002$ (FDR $p = 0.03$), SI Fig. 8C), malic acid (treatment effect $p = 0.0001$ (FDR $p = 0.008$), SI Fig. 8E), citramalic acid (treatment effect $p = 0.0002$ (FDR $p = 0.008$)), N-acetylaspartate (treatment effect $p = 0.0004$ (FDR $p = 0.01$)), glutaric acid (treatment effect $p = 0.0002$ (FDR $p = 0.009$), SI Fig. 8G), lactic acid (treatment effect $p = 0.0004$ (FDR $p = 0.01$), SI Fig. 8H), pyruvic acid (treatment effect $p = 0.001$ (FDR $p = 0.02$), SI Fig. 8I), and α-ketobutyric acid (treatment effect $p = 0.002$ (FDR $p = 0.03$), SI Fig. 8J).

Glutamic acid (treatment effect $p < 0.0001$ (FDR $p = 0.0004$), atrophy effect $p = 0.03$ (FDR $p = 0.21$), SI Fig. 8B), N-acetylglutamate (treatment effect $p = 0.0004$ (FDR $p = 0.01$), atrophy effect $p = 0.03$ (FDR $p = 0.25$), SI Fig. 8F), and the glucose signal (treatment effect $p = 0.0001$ ($p = 0.008$); atrophy effect $p = 0.07$ ($p = 0.39$), SI Fig. 8D) exhibited both significant treatment effects and moderate associations with atrophy progression. In contrast, quinolinic acid (treatment effect p =0.02 (FDR $p = 0.19$); atrophy effect $p = 0.03$ (FDR $p = 0.24$), SI Fig. 8K) was one of the few metabolites showing a notable relationship with atrophy progression, with an effect size comparable to that observed for treatment (SI Tables 6–8). These results suggest that quinolinic acid may be linked to both treatment response and atrophy

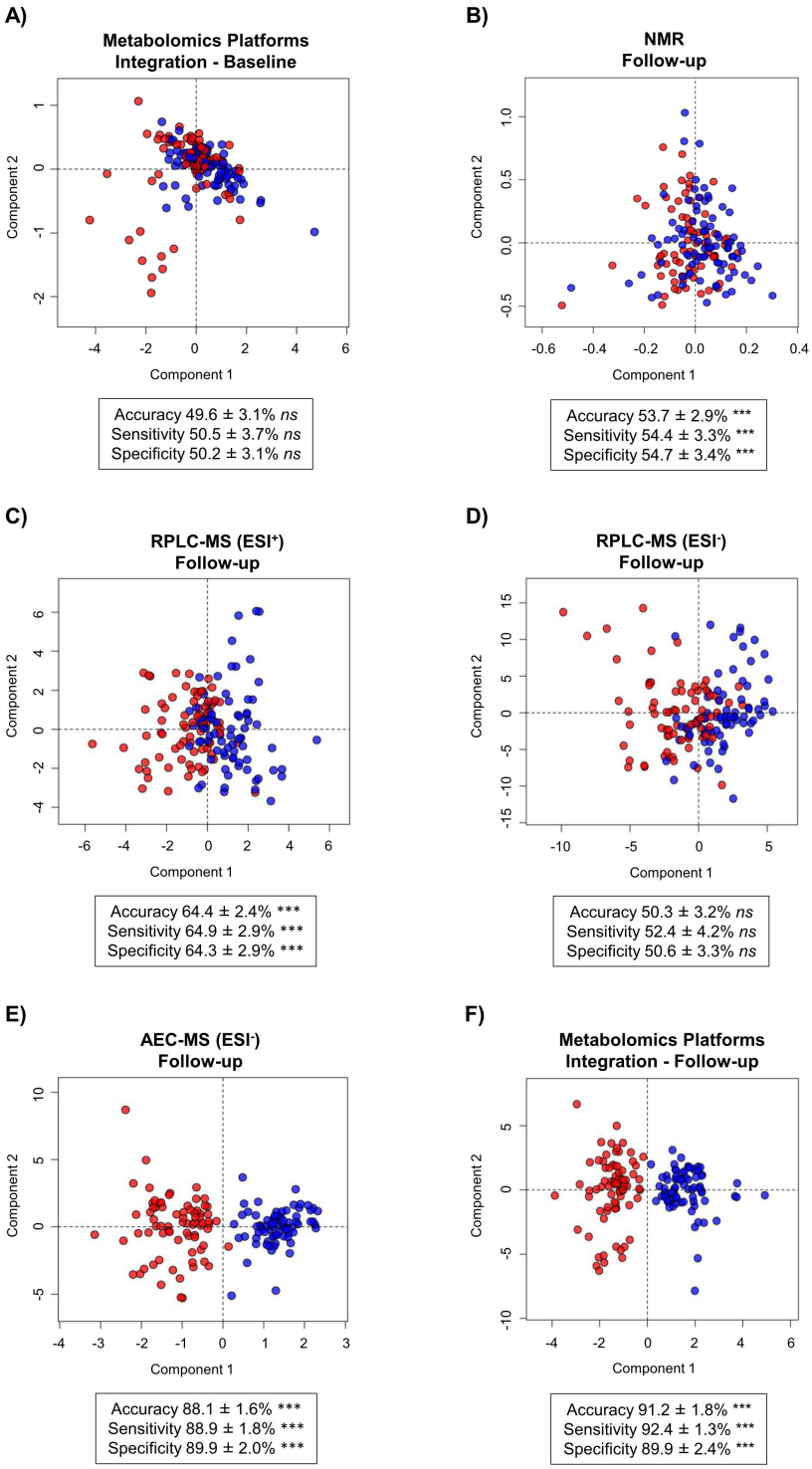

Fig. 1: **Orthogonal partial least squares discriminant analysis (OPLS-DA) score plots illustrating the separation between biologically compliant placebo controls (red data points) and B vitamin-treated individuals (blue data points) based on serum metabolomic profiling.** Results are presented for each individual metabolomic platform (follow-up time point) and for the integrated dataset (baseline and follow-up time points): **A)** Combination of all four platforms (baseline); **B)** NMR (follow-up); **C)** RPLC-MS (pos. ionisation mode; follow-up); **D)** RPLC-MS (neg. ionisation mode; follow-up); **E)** AEC-MS (neg. ionisation mode; follow-up); **F)** Combination of all four platforms (follow-up). "Baseline" refers to samples collected prior to any intervention, and "follow-up" refers to samples collected after two years of B vitamin supplementation or placebo administration. Each model includes accuracy, sensitivity, and specificity (mean ± SD) derived from cross-validation. Statistical significance ($p > 0.05$ ns; $p < 0.001$ $* **$) was assessed relative to a random class ensemble using the Kolmogorov–Smirnov test.

progression, whereas other metabolites exhibited stronger associations with treatment effects.

As evidenced by the multivariate OPLS-DA analysis, the NMR metabolome showed no clear discriminatory capacity between groups (Fig. 1B). The three-way ANOVA indicated that the only significantly altered metabolite was glutamine (SI Table 8), with a marginal treatment effect (p = 0.03 (FDR p = 0.38), SI Fig. 8L) and no significant temporal or atrophy effects. Alanine, which ranked highly among the VIPs in the NMR-based model, did not show a significant treatment effect (p = 0.13 (FDR p = 0.66)). Validation of NMR findings was limited by the LC-MS methods, which exhibited poor retention and characterisation of non-derivatised amino acids, except for glutamate and aspartate detected via AEC-MS.

To further account for potential temporal effects, a two-way ANOVA was performed on follow-up metabolite levels normalised to baseline, assessing the independent effects of treatment (B vitamins vs. placebo) and atrophy progression status (progressing vs. stable individuals). Consistent with the three-way ANOVA results, treatment emerged as the primary factor driving metabolic changes. Tukey's *post hoc* comparisons revealed that, for most metabolites, the most significant differences were observed between progressing individuals receiving placebo and those responding to B vitamin treatment, characterised by a stable rate of brain atrophy progression. These findings suggest that, while B vitamin administration exerts a primary influence on the metabolome, there may also be a modest additive effect associated with brain atrophy progression. The majority of metabolites, particularly intermediates of the TCA cycle, glutamic acid, glucose, and quinolinic acid, exhibited moderate treatment effects, with some displaying varying degrees of association with atrophy progression (Fig. 2, SI Table 9). Subtle differences were also observed within the B vitamin-treated group: for example, glutamine decreased (Fig. 2L) and glutaric acid increased (Fig. 2G) in non-responders relative to responders, although these trends require validation in larger cohorts due to the limited number of non-responders. Overall, metabolite levels decreased following B vitamin administration, especially in treatment responders, with the notable exception of glutamine (Fig. 2L), which significantly increased in abundance in the treatment group.

Based on the three-way ANOVA results, the following compounds were assessed (for details on the *post hoc* analysis, refer to SI Table 9): α-ketoglutaric acid (treatment effect p = 0.03; atrophy effect p = 0.32; Fig. 2A); glutamic acid (treatment effect p = 0.06; atrophy effect p = 0.53; Fig. 2B); succinic acid (treatment effect p = 0.03; atrophy effect p = 0.19; Fig. 2C); glucose (treatment effect p = 0.12; atrophy effect p = 0.11; Fig. 2D); malic acid (treatment effect p = 0.03; atrophy effect p = 0.48; Fig. 2E); N-acetylglutamate (treatment effect p = 0.20; atrophy effect p = 0.51; Fig. 2F); glutaric acid (treatment effect $p = 0.10$; atrophy effect $p = 0.36$; Fig. 2G); lactic acid (treatment effect p = 0.06; atrophy effect p = 0.41; Fig. 2H); pyruvic acid (treatment effect $p = 0.17$; atrophy effect $p = 0.66$; Fig. 2I); α-ketobutyric acid (treatment effect p = 0.03; atrophy effect p = 0.17; Fig. 2J); quinolinic acid (treatment effect p = 0.04; atrophy effect p = 0.15; Fig. 2K); glutamine (treatment effect p = 0.19; atrophy effect p = 0.38; Fig. 2L).

3.4 Metabolomics shows limited ability to distinguish atrophy progression, despite correlation with polar metabolites

Building on the modest yet statistically significant effects of atrophy progression identified in the two-way ANOVA *post hoc* analysis, further investigations were conducted to assess metabolic changes primarily associated with brain atrophy. OPLS-DA models were constructed for placebo controls stratified by atrophy rate, analysing stable and progressing individuals separately at both baseline (SI Fig. 9A) and follow-up (SI Fig. 9B). These models achieved similar accuracies of 64.3 ± 4.0% and 65.0 ± 4.4%, respectively, indicating only marginally detectable differences in the metabolome associated with brain atrophy. Furthermore, the results suggest that metabolic changes are present but remain relatively stable over the short follow-up period, in contrast to the more dynamic alterations observed in response to B vitamin treatment. Although classification performance was modest, permutation testing confirmed the statistical significance of both baseline and follow-up models ($p < 0.0001$), indicating that the metabolic differences between progressing and stable individuals were reproducible across timepoints. These findings align with univariate analyses, which also revealed metabolite-level associations with brain atrophy. The comparable performance of models at both timepoints suggests that the metabolic phenotype associated with atrophy progression remains relatively stable over the two-year follow-up, potentially reflecting persistent, low-grade metabolic dysregulation in this prodromal population. To further investigate the relationship between metabolite levels and atrophy

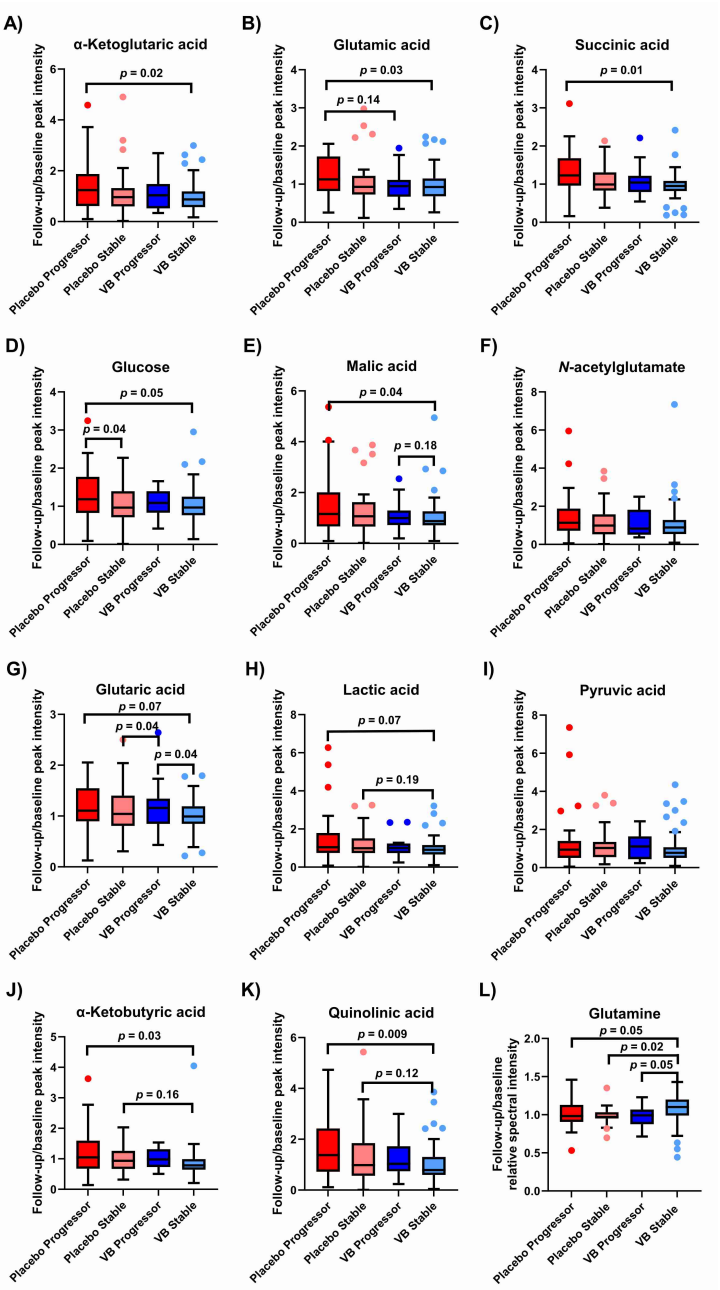

Fig. 2: **Results of two-way ANOVA comparing the relative serum abundance of individual metabolites across four groups, stratified by treatment status and brain atrophy progression as determined from MRI over the two-year follow-up period:** Placebo Progressors (dark red, $N = 31$), Placebo Stable (light red, $N = 31$), B vitamin Progressors (non-responders; dark blue, $N = 14$), and B vitamin Stable (responders; light blue, $N = 51$). The figure presents follow-up metabolite levels (adjusted for baseline) to enable interpretation of comparisons across treatment arms (placebo vs. B vitamins), progression status (progressors vs. stable), and within-group treatment response (responders vs. non-responders). Tukey's *post hoc* analysis was performed, with results summarised in SI Table 9. Significant and marginal p-values are displayed above the graphs; metabolites without displayed p-values were not associated with any significant pairwise comparisons. **A)** α-ketoglutaric acid (treatment $p = 0.03$; atrophy $p = 0.32$); **B)** glutamic acid (treatment $p = 0.06$; atrophy $p = 0.53$); **C)** succinic acid (treatment $p = 0.03$; atrophy $p = 0.19$); **D)** glucose (treatment $p = 0.12$; atrophy $p = 0.11$); **E)** malic acid (treatment $p = 0.03$; atrophy $p = 0.48$); **F)** N-acetylglutamate (treatment $p = 0.20$; atrophy $p = 0.51$); **G)** glutaric acid (treatment $p = 0.10$; atrophy $p = 0.36$); **H)** lactic acid (treatment $p = 0.06$; atrophy $p = 0.41$); **I)** pyruvic acid (treatment $p = 0.17$; atrophy $p = 0.66$); **J)** α-ketobutyric acid (treatment $p = 0.03$; atrophy $p = 0.17$); **K)** quinolinic acid (treatment $p = 0.04$; atrophy $p = 0.15$); **L)** glutamine (treatment effect $p = 0.19$; atrophy effect $p = 0.38$).

progression, MRI data were used to quantify the rate of brain atrophy over the two-year follow-up period. This analysis focused on follow-up samples from the subgroup of progressing individuals who received placebo ($N = 31$), thereby controlling for the potential confounding effects of treatment (Fig.3).

Pearson correlation analysis revealed a significant positive correlation between brain atrophy and tHcy (α = 0.47; Fig. 3), consistent with previous reports.[4] A strong negative correlation was observed between atrophy and cognitive scores at follow-up (α = -0.58 for MMSE and α = -0.64 for TICS-M; Fig. 3), which was more pronounced in this subset than in the full cohort. This correlation was absent in the treatment group (SI Fig. 10), potentially due to the treatment effect. Similarly, weak interactions between B vitamins and blood metabolites detected in the placebo group were not observed in the treatment group, except for glutaric acid, which positively correlated with both folate and vitamin B12 (SI Fig. 10).

TCA cycle-related metabolites exhibited moderate correlations with brain atrophy progression ($\alpha \approx 0.15$). Stronger associations were observed for glutamic acid ($\alpha = 0.18$) and quinolinic acid ($\alpha = 0.23$). The majority of metabolites demonstrated negative correlations with tHcy, with the exception of quinolinic acid ($\alpha = 0.55$), suggesting potential nonlinear or indirect pathway interactions between tHcy levels and atrophy progression. As expected, TCA cycle intermediates and their derivatives displayed strong intercorrelations ($\alpha > 0.5$). Similarly, glutamine exhibited strong negative correlations with TCA cycle intermediates, particularly pyruvic acid ($\alpha = -0.40$) and α-ketoglutaric acid ($\alpha = -0.33$). An inverse association between glutamic acid and glutamine was also identified ($\alpha = -0.24$). Quinolinic acid demonstrated weaker correlations with TCA cycle metabolites, glutamic acid, and glucose ($\alpha < 0.30$); however, these associations were stronger in the B vitamin responder group ($\alpha < 0.40$; SI Fig. 10). Interestingly, most metabolites exhibited weak correlations with cognitive scores (MMSE and TICS-M); however, in some cases, these correlations were unexpectedly stronger than those observed with atrophy. Notably, *N*-acetylglutamate ($\alpha = 0.20$) and glutamine ($\alpha = 0.15$) showed positive correlations with MMSE scores but not with atrophy (Fig. 3). The observed discrepancies between correlations with MMSE, TICS-M, and brain atrophy may reflect the limited sensitivity of standard cognitive assessments in detecting subtle metabolic alterations, particularly in individuals with MCI. These findings, derived from a relatively small sample size, should be interpreted as hypothesis-generating and require validation in larger, independent cohorts. Notably, although several correlations reached statistical significance, effect sizes were generally modest ($\alpha \approx$ 0.2–0.4), which is consistent with expectations in a clinically stable MCI population over a relatively short follow-up period. This likely reflects the heterogeneous and low-grade nature of peripheral metabolic changes in prodromal neurodegenerative states.

3.5 Metabolic pathway analysis revealed B vitamins effects on amino acid and central carbon metabolism

To explore the possible impact and functional significance of B vitamin administration on metabolic processes, we conducted metabolic pathways analysis using enrichment and topographical methods with organism specificity for *Homo sapiens*. The pathways affected by B vitamin treatment (treatment vs. placebo) are illustrated in Figure 4.

The most significantly altered pathways (Fig. 4, top; SI Table 10) included amino acid metabolism, particularly glycine, serine, and threonine, as well as arginine biosynthesis. Pathways linked to cysteine and methionine metabolism, both directly associated with Hcy metabolism, were identified by the analysis algorithm and exhibited a moderate impact. Although our methodology did not fully capture all aspects of fatty acid metabolism and biodegradation, we detected significant alterations in these pathways. Notably, lipoic acid and NAD^+ metabolism, both critical for the conversion of pyruvate to acetyl-CoA in the TCA cycle, were strongly affected (Fig. 4, 5). The TCA cycle and pyruvate metabolism showed moderate but impactful changes, while glycolysis emerged as a key altered pathway, connecting to the TCA cycle via NAD^+ and the conversion of phosphoenolpyruvate (PEP) to pyruvate (Fig. 5). Saccharide-involving pathways were also significantly altered, particularly pentose and galactose metabolism, with moderate changes observed in dietary saccharides such as starch and sucrose. Pathways involving glutamate and alanine metabolism showed alterations consistent with the three-way ANOVA results. Notably, alanine and α-ketoglutarate can be converted to pyruvate and glutamate via alanine aminotransferase (ALT), linking these pathways to the TCA cycle. Further pathways with high metabolic impact (Fig. 4, right) included ascorbate metabolism, which, intriguingly, is not directly related to B-vitamin metabolism. Taurine metabolism, a downstream product of the

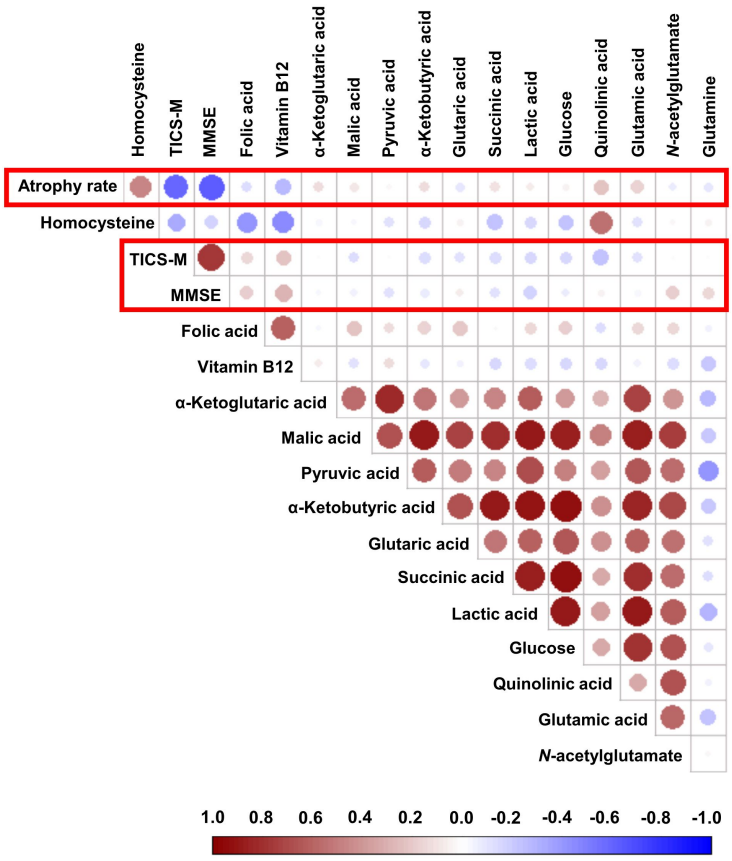

Fig. 3: **Pearson correlation analysis of follow-up levels of significantly altered metabolites, homocysteine (total homocysteine; tHcy), folate, and vitamin B12, along with atrophy rate and cognitive test scores** (MMSE and TICS-M, highlighted in the red box). Data from all compliant individuals with available MRI scans at the follow-up time point, receiving placebo and characterised by a fast rate of brain atrophy ("progressors"; $N = 31$). Colour intensity reflects the magnitude of the Pearson correlation coefficient, with red indicating positive correlations and blue indicating negative correlations.

Hcy-cysteine pathway,[44] did not exhibit significant metabolite-level alterations but was identified as a key pathway with notable impact in the enrichment analysis. These results suggest that the primary pathways influenced by B vitamins administration are central carbon metabolism and amino acid metabolism, likely due to the role of B vitamins as cofactors for several enzymes involved in these processes. Figure 5 provides a schematic representation of the metabolic pathways predicted to be modulated by treatment, illustrating their interconnections with B vitamins and Hcy metabolism, particularly the methionine and folate cycles.

4 Discussion

The VITACOG study previously reported that vitamins B6, B12, and folic acid significantly lowered tHcy and slowed cerebral atrophy in MCI.[4,5,8,17] While B6 and B12 act as cofactors and folate as a methyl donor in tHcy metabolism,[10] the broader metabolic effects remain unclear. We conducted untargeted metabolomic profiling of serum samples using NMR and multi-LC-MS. B vitamin supplementation significantly altered the polar metabolome, decreasing TCA cycle intermediates, glucose, glutamate, and quinolinic acid - metabolites interconnected with tHcy and folate metabolism. Although tHcy may be influenced by genetic, renal, or lifestyle factors, these were not associated with VITACOG outcomes.[4] Moreover, the randomised, placebo-controlled design, absence of baseline group differences, and minimal impact of multivariable adjustment support the attribution of the observed metabolic and neuroanatomical changes specifically to B vitamin supplementation. These broader metabolic effects were also reflected in brain atrophy, as quinolinic

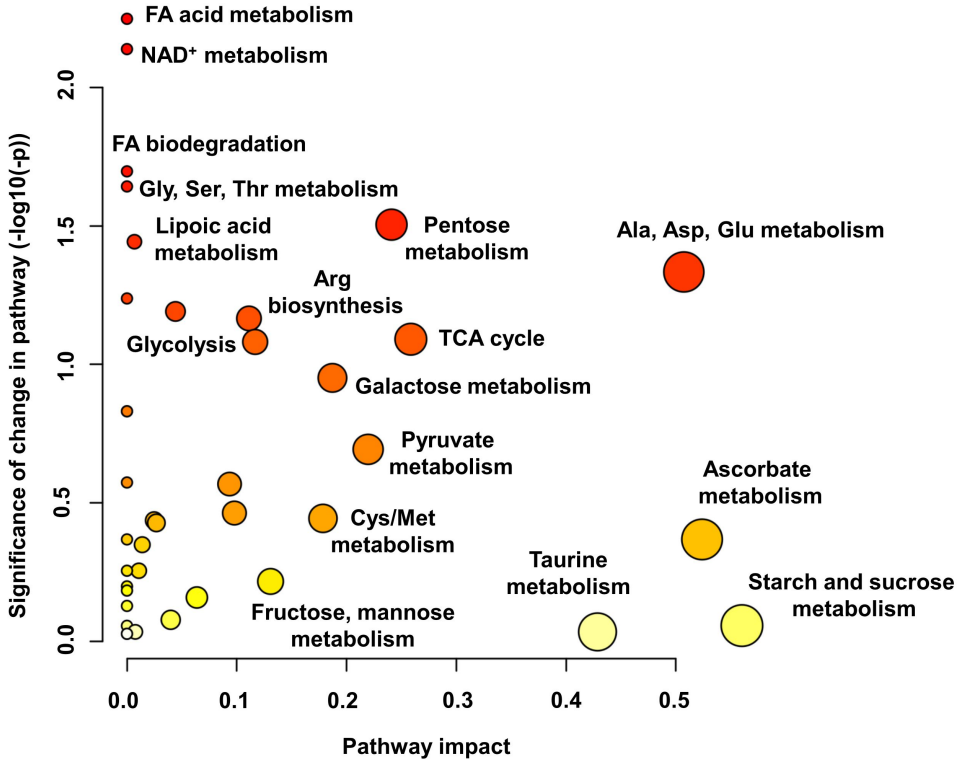

Fig. 4: **Metabolic pathway analysis of B vitamin-treated participants versus placebo controls.** Individual metabolic pathways are represented as nodes, with node size indicating pathway impact (based on topological analysis) and colour intensity (from white to red) reflecting pathway significance (based on enrichment analysis). A detailed description of the pathways, along with their associated significance and impact, is provided in SI Table 10. Fatty acids (FA) and amino acid metabolism (arginine, glycine, serine, threonine, alanine, aspartate, and glutamate) and central carbon metabolism (lipoic acid, NAD^+, pyruvate metabolism, glycolysis and the TCA cycle) were identified as the pathways most affected by B vitamin administration.

and glutamic acids correlated with its progression, supporting a potential mechanistic link between B vitamin–induced metabolic shifts and neuroprotection. To our knowledge, this is among the first studies to apply untargeted multi-platform metabolomics in a clinically well-characterised MCI cohort.

4.1 B vitamins lower serum glucose and TCA cycle intermediates

The primary metabolic changes in B vitamin-treated individuals included reduced serum glucose and altered TCA cycle intermediates. Impaired cerebral glucose metabolism, a hallmark of AD, results from defective insulin signalling and neuronal glucose accumulation.[45] Additionally, AD is associated with deficiencies in glucose transporters, such as GLUT3 in neurons and GLUT1 in astrocytes, which correlate with amyloid-β deposition.[46-48] Our study noted a weak negative correlation between serum glucose and B vitamins, but a strong association between peripheral glucose and cerebral atrophy progression. Furthermore, glycolysis emerged as one of the most significantly altered pathways in enrichment analysis, indicating that longitudinal increase in fasting plasma glucose is linked to higher brain tissue glucose concentrations in AD patients.[47,48] In the treatment group, we also observed significant decrease in lactate, a by-product of anaerobic glycolysis that is often upregulated with mitochondrial dysfunction. Moreover, Hcy is implicated in both chronic inflammation and oxidative stress, where it promotes formation of reactive oxygen species (ROS)[49] that can impair insulin signalling and increase glucose concentration.[50] Li *et al.* demonstrated that elevated Hcy may downregulate AMPKα/Sirt1 signalling, increasing oxidative stress.[50] This suggests that B vitamin-induced reduction in tHcy levels

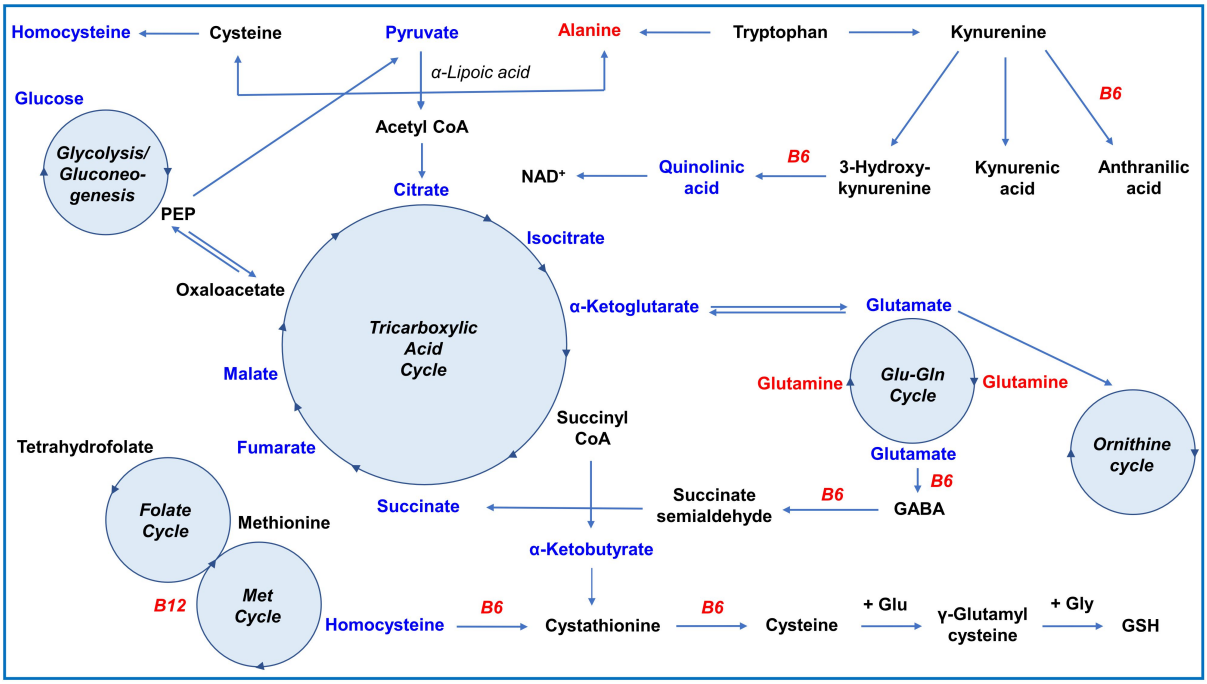

Fig. 5: **A simplified schematic of the metabolic networks related to and/or affected by B vitamin administration, as identified through multivariate, univariate, and pathway analyses.** The primary pathways include glycolysis, the TCA cycle, glutamine/glutamate/γ-aminobutyric acid (GABA) metabolism, the kynurenine pathway, and Hcy metabolism (including the folate and methionine cycles). Metabolites highlighted in blue exhibited decreased abundance following treatment, while those in red showed increased abundance. Metabolites shown in black were not detected by the analytical platforms employed in this study. This schematic was created by the authors based on established metabolic pathways.

may alleviate Hcy-triggered oxidative stress and inflammation, potentially contributing to reduced blood glucose levels.

Correlation analysis identified a strong association between glucose and TCA cycle intermediates. Recent studies examining TCA cycle-related enzyme expression in neuronal cells have consistently reported decreased levels in AD brains, leading to TCA cycle inhibition and increased ROS production, which is suspected to accelerate neurodegeneration.[51-53] However, peripheral alterations in TCA cycle enzymes or intermediates remain underexplored. As cofactors in synthesising several TCA cycle substrates, B vitamins are expected to impact TCA cycle function. Folic acid and vitamin B12 catalyse the conversion of Hcy to methionine, producing nucleotides and amino acids like glycine or serine that are converted into pyruvate and then acetyl coenzyme A (CoA), entering the TCA cycle.[54,55] Similarly, vitamin B6 facilitates amino acid transamination, such as alanine, to form pyruvate, linking amino acid metabolism with central carbon metabolism and providing substrates for gluconeogenesis and the TCA cycle. We hypothesise that the observed decrease in TCA cycle intermediates following B vitamin supplementation reflects enhanced peripheral TCA cycle efficiency, due to improved cofactor availability. This may facilitate a more rapid conversion of intermediates into downstream products, such as NADH and $FADH_2$, which are crucial for ATP production. Consequently, this could prevent the accumulation of TCA cycle intermediates, explaining their reduced serum levels after B vitamin administration. Furthermore, the enhanced TCA cycle activity may also relate to improved mitochondrial function,[55] suggesting that B vitamins counteract mitochondrial dysfunction in neurodegenerative conditions.

4.2 B vitamins indirectly affect glutamatergic and (GABA)ergic metabolism

A positive correlation was observed between glucose and glutamic acid, both of which significantly decreased following treatment. In the brain, glucose metabolism is crucial for energy production required for processes such as neurotransmitter release, reuptake, and recycling.[56,57] Impaired glucose metabolism and dysregulated

glutamatergic signalling can lead to excessive glutamate release and excitotoxicity, contributing to neuronal damage and astrocyte dysfunction.[58] The glutamate-glutamine cycle connects glutamate to the inhibitory neurotransmitter GABA. Among treatment responders, glutamine levels were significantly increased compared to placebo. An inverse correlation between glutamate and glutamine was observed in both groups, consistent with prior metabolomics findings.[59] Vitamin B6, a cofactor for glutamate decarboxylase (converting glutamate to GABA) and GABA transaminase (converting GABA to succinate semialdehyde), may enhance these metabolic pathways,[60] shifting equilibrium and contributing to reductions in glutamate, α-ketoglutarate, and succinate. While the balance between excitatory (glutamate) and inhibitory (GABA) neurotransmission involves complex regulations beyond metabolite availability, the significant decreases in GABA-associated metabolites following B vitamin treatment suggest an impact on neurotransmission.[61,62] Although GABA was not detected due to platform limitations, this pattern aligns with prior findings, which report contradictory GABA changes in AD - typically decreasing in the hippocampus and cortex, but increasing peripherally.[62]

4.3 B vitamins reduce quinolinic acid levels and modulate metabolic pathways linked to brain atrophy in MCI

Quinolinic acid levels were significantly reduced in individuals treated with B vitamins compared to placebo. Higher quinolinic acid levels were associated with greater brain atrophy, consistent with evidence linking elevated levels to poorer cognitive outcomes.[63] However, reports on the role of quinolinic acid in dementia are mixed, with some studies reporting lower levels in AD despite associations with cognitive impairment.[64,65] As a downstream metabolite of tryptophan in the kynurenine pathway, quinolinic acid acts as an *N*-methyl-*D*-aspartate (NMDA) receptor agonist, with overactivation linked to excitotoxicity and neuroinflammation in AD.[66,67] Hcy also activates NMDA receptors, sustaining their activity via phosphorylation signalling and promoting oxidative stress.[49,68] Simultaneous reductions in Hcy and quinolinic acid may reflect coordinated downregulation of neurotoxic signalling through shared excitatory pathways. Given their combined effects on NMDA receptor activation and neuroinflammation, these findings have broader implications for excitatory neurotransmission and neuronal survival, potentially offering new mechanistic insight into B vitamin-mediated neuroprotection. Dysregulation of the kynurenine pathway leads to quinolinic acid accumulation, observed, for example, in AD patient monocytes,[69] which may disrupt neurotransmitter homeostasis and promote neuroinflammation via microglia activation and cytokine release.[66,69,70] Additionally, quinolinic acid strongly correlated with glucose, consistent with evidence that altered glucose metabolism influences the kynurenine pathway and may exacerbate neurodegeneration in AD and Parkinson's disease.[71] Quinolinic acid was also positively correlated with TCA cycle intermediates, possibly owing to its conversion into NAD^+, which is utilised by pyruvate dehydrogenase (PDH) to generate acetyl-CoA for TCA cycle entry.[71] This process also requires α-lipoic acid, a PDH cofactor,[72] identified as a key element in pathway enrichment analysis, suggesting an interplay between the kynurenine pathway and the TCA cycle.[70] Notably, vitamin B6 supplementation reduced quinolinic acid levels despite its role as a cofactor in the kynurenine pathway. Although the atrophy progression model included both treatment arms and thus reflected a biologically heterogeneous cohort, multivariate modelling nonetheless identified consistent metabolic differences associated with brain atrophy, including elevated quinolinic acid levels. These findings were concordant with univariate and pathway-level analyses, reinforcing their mechanistic relevance. In the context of B vitamin treatment, this may reflect complex regulation of pathway enzymes, such as kynurenine-3-monooxygenase, or negative feedback whereby elevated vitamin B6 levels reduce quinolinic acid production despite its cofactor role.[71,73]

4.4 Limitations

Not all placebo-treated individuals exhibited increased atrophy progression, nor did all B vitamin-treated individuals show reduced atrophy rates. This variability suggests that treatment responses may not be uniform across individuals and could fluctuate over time. Stratifying participants by atrophy rate and treatment category enabled assessment of the distinct effects of B vitamins, atrophy progression, and temporal metabolomic changes. While modest subgroup sizes may have constrained statistical power, this approach provided valuable insights into metabolic responses. Baseline variability in dietary intake, microbiome composition, and serum folate levels may have contributed to metabolic heterogeneity

and modulated responses. Although our multi-platform approach provided broad metabolome coverage, it did not capture key lipid classes implicated in neurodegeneration, such as phospholipids and sphingolipids. Finally, pathway-level interpretation is inherently constrained by the limited metabolic coverage and the structure of existing reference libraries; however, enriched pathways were cross-referenced with prior literature to support biological plausibility.[74] Given the hypothesis-generating nature of untargeted metabolomics, further *in vitro* and *in vivo* studies are needed to validate B vitamin-induced metabolic changes and their relevance to neuroprotection.

4.5 Conclusion

This study provides a comprehensive analysis of serum metabolome alterations in MCI following B vitamin supplementation and associated Hcy-lowering. Leveraging an untargeted metabolomics strategy across complementary NMR and LC–MS platforms, we captured a broad spectrum of metabolic changes extending beyond tHcy. Our findings demonstrate that B vitamins, as essential enzyme cofactors, significantly influence central carbon metabolism, reducing glucose levels and TCA cycle intermediates, while also modulating the kynurenine pathway and lowering the neurotoxic metabolite quinolinic acid. These insights support the potential of B vitamin supplementation as an adjunctive strategy for MCI and reinforce its role in slowing progression to AD, as indicated by previous studies.

5 References

1. Fox NC, Schott JM. Imaging cerebral atrophy: normal ageing to Alzheimer's disease. Lancet. Jan 31 2004;363(9406):392-4. doi:10.1016/S0140-6736(04)15441-X

2. Jack CR, Jr., Weigand SD, Shiung MM, et al. Atrophy rates accelerate in amnestic mild cognitive impairment. Neurology. May 6 2008;70(19 Pt 2):1740-52. doi:10.1212/01.wnl.0000281688.77598.35

3. Pini L, Pievani M, Bocchetta M, et al. Brain atrophy in Alzheimer's Disease and aging. Ageing Res Rev. Sep 2016;30:25-48. doi:10.1016/j.arr.2016.01.002

4. Smith AD, Smith SM, de Jager CA, et al. Homocysteine-lowering by B vitamins slows the rate of accelerated brain atrophy in mild cognitive impairment: a randomized controlled trial. Plos One. Sep 8 2010;5(9):e12244. doi:10.1371/journal.pone.0012244

5. Wu Y, Smith AD, Refsum H, Kwok T. Effectiveness of B Vitamins and Their Interactions with Aspirin in Improving Cognitive Functioning in Older People with Mild Cognitive Impairment: Pooled Post-Hoc Analyses of Two Randomized Trials. Journal of Nutrition Health Aging. Dec 2021;25(10):1154-1160. doi:10.1007/s12603-021-1708-1

6. Koohpeyma H, Goudarzi I, Elahdadi Salmani M, Lashkarbolouki T, Shabani M. Postnatal Administration of Homocysteine Induces Cerebellar Damage in Rats: Protective Effect of Folic Acid. Neurotox Res. Apr 2019;35(3):724-738. doi:10.1007/s12640-018-9979-y

7. Oldreive CE, Doherty GH. Neurotoxic effects of homocysteine on cerebellar Purkinje neurons in vitro. Neurosci Lett. Feb 8 2007;413(1):52-7. doi:10.1016/j.neulet.2006.11.031

8. Smith AD, Refsum H. Vitamin B-12 and cognition in the elderly. Am J Clin Nutr. Feb 2009;89(2):707S-11S. doi:10.3945/ajcn.2008.26947D

9. Wang Q, Zhao J, Chang H, Liu X, Zhu R. Homocysteine and Folic Acid: Risk Factors for Alzheimer's Disease-An Updated Meta-Analysis. Front Aging Neurosci. 2021;13:665114. doi:10.3389/fnagi.2021.665114

10. Durand P, Prost M, Loreau N, Lussier-Cacan S, Blache D. Impaired homocysteine metabolism and atherothrombotic disease. Lab Invest. May 2001;81(5):645-72. doi:10.1038/labinvest.3780275

11. Ho PI, Ortiz D, Rogers E, Shea TB. Multiple aspects of homocysteine neurotoxicity: glutamate excitotoxicity, kinase hyperactivation and DNA damage. J Neurosci Res. Dec 1 2002;70(5):694-702. doi:10.1002/jnr.10416

12. Kruman, II, Culmsee C, Chan SL, et al. Homocysteine elicits a DNA damage response in neurons that promotes apoptosis and hypersensitivity to excitotoxicity. J Neurosci. Sep 15 2000;20(18):6920-6. doi:10.1523/JNEUROSCI.20-18-06920.2000

13. Morris MC, Schneider JA, Tangney CC. Thoughts on B-vitamins and dementia. Journal of Alzheimers Disease. Aug 2006;9(4):429-433.

14. Smith AD, Refsum H. Homocysteine - from disease biomarker to disease prevention. J Intern Med. Oct 2021;290(4):826-854. doi:10.1111/joim.13279

15. Costeira R, Evangelista L, Wilson R, et al. Metabolomic biomarkers of habitual B vitamin intakes unveil novel differentially methylated positions in the human epigenome. Clin Epigenetics. Oct 19 2023;15(1):166. doi:10.1186/s13148-023-01578-7

16. Parra M, Stahl S, Hellmann H. Vitamin B(6) and Its Role in Cell Metabolism and Physiology. Cells. Jul 22 2018;7(7)doi:10.3390/cells7070084

17. Smith AD. The worldwide challenge of the dementias: a role for B vitamins and homocysteine? Food Nutr Bull. Jun 2008;29(2 Suppl):S143-72. doi:10.1177/15648265080292S119

18. de Jager CA, Oulhaj A, Jacoby R, Refsum H, Smith AD. Cognitive and clinical outcomes of homocysteine-lowering B-vitamin treatment in mild cognitive impairment: a randomized controlled trial. Int J Geriatr Psychiatry. Jun 2012;27(6):592-600. doi:10.1002/gps.2758

19. Smith AD, Refsum H. Homocysteine, B Vitamins, and Cognitive Impairment. Annu Rev Nutr. Jul 17 2016;36:211-39. doi:10.1146/annurev-nutr-071715-050947

20. Hughes CF, Ward M, Tracey F, et al. B-Vitamin Intake and Biomarker Status in Relation to Cognitive Decline in Healthy Older Adults in a 4-Year Follow-Up Study. Nutrients. Jan 10 2017;9(1)doi:10.3390/nu9010053

21. Kwok T, Wu YY, Lee J, et al. A randomized placebo-controlled trial of using B vitamins to prevent cognitive decline in older mild cognitive impairment patients. Clinical Nutrition. Aug 2020;39(8):2399-2405. doi:10.1016/j.clnu.2019.11.005

22. Lefevre-Arbogast S, Feart C, Dartigues JF, Helmer C, Letenneur L, Samieri C. Dietary B Vitamins and a 10-Year Risk of Dementia in Older Persons. Nutrients. Nov 26 2016;8(12)doi:10.3390/nu8120761

23. Zhou H, Wu Y, Jiang B, et al. Metabolic Basis of Cognitive Improvement Associated With Active B Vitamin Supplementation in Cognitively Impaired Elderly Subjects - A Metabolomics Study. Front Med (Lausanne). 2022;9:864152. doi:10.3389/fmed.2022.864152

24. Ford TC, Downey LA, Simpson T, McPhee G, Oliver C, Stough C. The Effect of a High-Dose Vitamin B Multivitamin Supplement on the Relationship between Brain Metabolism and Blood Biomarkers of Oxidative Stress: A Randomized Control Trial. Nutrients. Dec 1 2018;10(12)doi:10.3390/nu10121860

25. Johnson CH, Ivanisevic J, Siuzdak G. Metabolomics: beyond biomarkers and towards mechanisms. Nat Rev Mol Cell Bio. Jul 2016;17(7):451-459. doi:10.1038/nrm.2016.25

26. Kennedy DO. B Vitamins and the Brain: Mechanisms, Dose and Efficacy–A Review. Nutrients. Jan 27 2016;8(2):68. doi:10.3390/nu8020068

27. Petersen RC, Roberts RO, Knopman DS, et al. Mild cognitive impairment: ten years later. Arch Neurol. Dec 2009;66(12):1447-55. doi:10.1001/archneurol.2009.266

28. Smith SM, Zhang Y, Jenkinson M, et al. Accurate, robust, and automated longitudinal and cross-sectional brain change analysis. Neuroimage. Sep 2002;17(1):479-89. doi:10.1006/nimg.2002.1040

29. Douaud G, Refsum H, de Jager CA, et al. Preventing Alzheimer's disease-related gray matter atrophy by B-vitamin treatment. Proc Natl Acad Sci U S A. Jun 4 2013;110(23):9523-8. doi:10.1073/pnas.1301816110

30. Stratmann B, Krepak Y, Schiffer E, et al. Beneficial Metabolic Effects of Duodenal Jejunal Bypass Liner for the Treatment of Adipose Patients with Type 2 Diabetes Mellitus: Analysis of Responders and Non-Responders. Horm Metab Res. Sep 2016;48(10):630-637. doi:10.1055/s-0042-115175

31. Yeo T, Probert F, Sealey M, et al. Objective biomarkers for clinical relapse in multiple sclerosis: a metabolomics approach. Brain Commun. 2021;3(4):fcab240. doi:10.1093/braincomms/fcab240

32. Luo YJ, Zhu JY, Gao YQ. Metabolomic analysis of the plasma of patients with high-altitude pulmonary edema (HAPE) using H NMR. Mol Biosyst. 2012;8(6):1783-1788. doi:10.1039/c2mb25044f

33. Probert F, Yeo T, Jurynczyk M, et al. Diagnosis and staging of multiple sclerosis using a metabolomics-based blood test: a simple method for monitoring progression independently of EDSS. Mult Scler J. Sep 2019;25:500-501.

34. Probert F, Yeo TR, Zhou YF, et al. Determination of CSF GFAP, CCN5, and vWF Levels Enhances the Diagnostic Accuracy of Clinically Defined MS From Non-MS Patients With CSF Oligoclonal Bands. Front Immunol. Feb 4 2022;12doi:ARTN 81135110.3389/fimmu.2021.811351 35. Wishart DS, Guo A, Oler E, et al. HMDB 5.0: the Human Metabolome Database for 2022. Nucleic Acids Res. Jan 7 2022;50(D1):D622-D631. doi:10.1093/nar/gkab1062

36. Kacerova T, Pires E, Walsby-Tickle J, Probert F, McCullagh JSO. Integrating NMR and Multi-LC-MS-Based Untargeted Metabolomics for Comprehensive Analysis of Blood Serum Samples. Anal Chim Acta. 2025;1356doi:10.1016/j.aca.2025.343979

37. Reinbold R, Hvinden IC, Rabe P, et al. Resistance to the isocitrate dehydrogenase 1 mutant inhibitor ivosidenib can be overcome by alternative dimer-interface binding inhibitors. Nat Commun. Aug 15 2022;13(1)doi:ARTN 478510.1038/s41467-022-32436-4

38. Walsby-Tickle J, Gannon J, Hvinden I, et al. Anion-exchange chromatography mass spectrometry provides extensive coverage of primary metabolic pathways revealing altered metabolism in IDH1 mutant cells. Commun Biol. May 20 2020;3(1):247. doi:10.1038/s42003-020-0957-6

39. Sumner LW, Amberg A, Barrett D, et al. Proposed minimum reporting standards for chemical analysis Chemical Analysis Working Group (CAWG) Metabolomics Standards Initiative (MSI). Metabolomics. Sep 2007;3(3):211-221. doi:10.1007/s11306-007-0082-2

40. Thonusin C, IglayReger HB, Soni T, Rothberg AE, Burant CF, Evans CR. Evaluation of intensity drift correction strategies using MetaboDrift, a normalization tool for multi-batch metabolomics data. J Chromatogr A. Nov 10 2017;1523:265-274. doi:10.1016/j.chroma.2017.09.023

41. Thevenot EA, Roux A, Xu Y, Ezan E, Junot C. Analysis of the Human Adult Urinary Metabolome Variations with Age, Body Mass Index, and Gender by Implementing a Comprehensive Workflow for Univariate and OPLS Statistical Analyses. J Proteome Res. Aug 7 2015;14(8):3322-35. doi:10.1021/acs.jproteome.5b00354

42. Yeo T, Sealey M, Zhou Y, et al. A blood-based metabolomics test to distinguish relapsing-remitting and secondary progressive multiple sclerosis: addressing practical considerations for clinical application. Sci Rep. Jul 24 2020;10(1):12381. doi:10.1038/s41598-020-69119-3

43. Pang ZQ, Lu Y, Zhou GY, et al. MetaboAnalyst 6.0: towards a unified platform for metabolomics data processing, analysis and interpretation. Nucleic Acids Res. Apr 8 2024;52(W1):W398-W406. doi:10.1093/nar/gkae253

44. Stipanuk MH, Ueki I. Dealing with methionine/homocysteine sulfur: cysteine metabolism to taurine and inorganic sulfur. J Inherit Metab Dis. Feb 2011;34(1):17-32. doi:10.1007/s10545-009-9006-9

45. Dewanjee S, Chakraborty P, Bhattacharya H, et al. Altered glucose metabolism in Alzheimer's disease: Role of mitochondrial dysfunction and oxidative stress. Free Radic Biol Med. Nov 20 2022;193(Pt 1):134-157. doi:10.1016/j.freeradbiomed.2022.09.032

46. Shah K, Desilva S, Abbruscato T. The role of glucose transporters in brain disease: diabetes and Alzheimer's Disease. Int J Mol Sci. Oct 3 2012;13(10):12629-55. doi:10.3390/ijms131012629

47. An Y, Varma VR, Varma S, et al. Evidence for brain glucose dysregulation in Alzheimer's disease. Alzheimers Dement. Mar 2018;14(3):318-329. doi:10.1016/j.jalz.2017.09.011

48. Pang R, Wang X, Pei F, et al. Regular Exercise Enhances Cognitive Function and Intracephalic GLUT Expression in Alzheimer's Disease Model Mice. J Alzheimers Dis. 2019;72(1):83-96. doi:10.3233/JAD-190328

49. Deep SN, Seelig S, Paul S, Poddar R. Homocysteine-induced sustained GluN2A NMDA receptor stimulation leads to mitochondrial ROS generation and neurotoxicity. J Biol Chem. May 2024;300(5):107253. doi:10.1016/j.jbc.2024.107253

50. Li H, Liu L, Cao Z, et al. Naringenin ameliorates homocysteine induced endothelial damage via the AMP-Kalpha/Sirt1 pathway. J Adv Res. Dec 2021;34:137-147. doi:10.1016/j.jare.2021.01.009

51. Bubber P, Haroutunian V, Fisch G, Blass JP, Gibson GE. Mitochondrial abnormalities in Alzheimer brain: mechanistic implications. Ann Neurol. May 2005;57(5):695-703. doi:10.1002/ana.20474

52. Sang C, Philbert SA, Hartland D, et al. Coenzyme A-Dependent Tricarboxylic Acid Cycle Enzymes Are Decreased in Alzheimer's Disease Consistent With Cerebral Pantothenate Deficiency. Front Aging Neurosci. 2022;14:893159. doi:10.3389/fnagi.2022.893159

53. Jia D, Wang F, Yu H. Systemic alterations of tricarboxylic acid cycle enzymes in Alzheimer's disease. Front Neurosci. 2023;17:1206688. doi:10.3389/fnins.2023.1206688

54. Dahlhoff C, Desmarchelier C, Sailer M, et al. Hepatic Methionine Homeostasis Is Conserved in C57BL/6N Mice on High-Fat Diet Despite Major Changes in Hepatic One-Carbon Metabolism. Plos One. Mar 5 2013;8(3)doi:ARTN e5738710.1371/journal.pone.0057387

55. Chen Z, Zhong C. Decoding Alzheimer's disease from perturbed cerebral glucose metabolism: implications for diagnostic and therapeutic strategies. Prog Neurobiol. Sep 2013;108:21-43. doi:10.1016/j.pneurobio.2013.06.004

56. Soares C, Da Ros LU, Machado LS, et al. The glutamatergic system in Alzheimer's disease: a systematic review with meta-analysis. Mol Psychiatry. Feb 16 2024;doi:10.1038/s41380-024-02473-0

57. Milos T, Rojo D, Nedic Erjavec G, et al. Metabolic profiling of Alzheimer's disease: Untargeted metabolomics analysis of plasma samples. Prog Neuropsychopharmacol Biol Psychiatry. Dec 20 2023;127:110830. doi:10.1016/j.pnpbp.2023.110830

58. Bukke VN, Archana M, Villani R, et al. The Dual Role of Glutamatergic Neurotransmission in Alzheimer's Disease: From Pathophysiology to Pharmacotherapy. Int J Mol Sci. Oct 2020;21(20)doi:ARTN 745210.3390/ijms21207452

59. Wang G, Zhou Y, Huang FJ, et al. Plasma metabolite profiles of Alzheimer's disease and mild cognitive impairment. J Proteome Res. May 2 2014;13(5):2649-58. doi:10.1021/pr5000895

60. Lerner V, Bergman J, Statsenko N, Miodownik C. Vitamin B6 treatment in acute neuroleptic-induced akathisia: a randomized, double-blind, placebo-controlled study. J Clin Psychiatry. Nov 2004;65(11):1550-4. doi:10.4088/jcp.v65n1118

61. Koh W, Kwak H, Cheong E, Lee CJ. GABA tone regulation and its cognitive functions in the brain. Nat Rev Neurosci. Sep 2023;24(9):523-539. doi:10.1038/s41583-023-00724-7

62. Carello-Collar G, Bellaver B, Ferreira PCL, et al. The GABAergic system in Alzheimer's disease: a systematic review with meta-analysis. Mol Psychiatry. Dec 2023;28(12):5025-5036. doi:10.1038/s41380-023-02140-w

63. Teruya T, Chen YJ, Kondoh H, Fukuji Y, Yanagida M. Whole-blood metabolomics of dementia patients reveal classes of disease-linked metabolites. Proc Natl Acad Sci U S A. Sep 14 2021;118(37)doi:10.1073/pnas.2022857118

64. Giil LM, Midttun O, Refsum H, et al. Kynurenine Pathway Metabolites in Alzheimer's Disease. J Alzheimers Dis. 2017;60(2):495-504. doi:10.3233/JAD-170485

65. Bakker L, Kohler S, Eussen S, et al. Correlations between kynurenines in plasma and CSF, and their relation to markers of Alzheimer's disease pathology. Brain Behav Immun. Jul 2023;111:312-319. doi:10.1016/j.bbi.2023.04.015

66. Ting KK, Brew BJ, Guillemin GJ. Effect of quinolinic acid on human astrocytes morphology and functions: implications in Alzheimer's disease. J Neuroinflammation. Dec 10 2009;6:36. doi:10.1186/1742-2094-6-36

67. Guillemin GJ, Brew BJ. Implications of the kynurenine pathway and quinolinic acid in Alzheimer's disease. Redox Rep. 2002;7(4):199-206. doi:10.1179/135100002125000550

68. Poddar R, Paul S. Homocysteine-NMDA receptor-mediated activation of extracellular signal-regulated kinase leads to neuronal cell death. J Neurochem. Aug 2009;110(3):1095-106. doi:10.1111/j.1471-4159.2009.06207.x

69. Busse M, Hettler V, Fischer V, et al. Increased quinolinic acid in peripheral mononuclear cells in Alzheimer's dementia. Eur Arch Psychiatry Clin Neurosci. Aug 2018;268(5):493-500. doi:10.1007/s00406-017-0785-y

70. van der Velpen V, Teav T, Gallart-Ayala H, et al. Systemic and central nervous system metabolic alterations in Alzheimer's disease. Alzheimers Res Ther. Nov 28 2019;11(1):93. doi:10.1186/s13195-019-0551-7

71. Gonzalez Esquivel D, Ramirez-Ortega D, Pineda B, Castro N, Rios C, Perez de la Cruz V. Kynurenine pathway metabolites and enzymes involved in redox reactions. Neuropharmacology. Jan 2017;112(Pt B):331-345. doi:10.1016/j.neuropharm.2016.03.013

72. Solmonson A, DeBerardinis RJ. Lipoic acid metabolism and mitochondrial redox regulation. J Biol Chem. May 18 2018;293(20):7522-7530. doi:10.1074/jbc.TM117.000259

73. Ueland PM, McCann A, Midttun O, Ulvik A. Inflammation, vitamin B6 and related pathways. Mol Aspects Med. Feb 2017;53:10-27. doi:10.1016/j.mam.2016.08.001

74. Pang Z, Chong J, Zhou G, et al. MetaboAnalyst 5.0: narrowing the gap between raw spectra and functional insights. Nucleic Acids Res. Jul 2 2021;49(W1):W388-W396. doi:10.1093/nar/gkab382

Contribution statement

A.D.S., D.C.A., and F.P. conceived and designed the study. A.D.S. and H.R. were responsible for study oversight and patient recruitment. D.S. oversaw the biobank management. T.K., A.G.Y., and J.D. performed the experiments. T.K. processed and analysed the data. E.P. and T.K. developed and optimised the sample processing methods. F.P., S.J., Q.G., and E.S. oversaw the NMR analysis. J.S.O.M. oversaw the LC-MS analysis. F.P and J.S.O.M provided supervision. T.K. drafted the manuscript. D.C.A., F.P., J.S.O.M., F.J., T.O., H.R., and A.D.S. provided critical feedback and guidance for experimental and analysis design. All authors provided input on the manuscript.

Declaration of competing interest

A.D.S. and H.R. are named as inventors on two patents held by the University of Oxford on the use of B-vitamins to treat cognitive disorders (US9364497 and US10966947). F.J. is named as an inventor on US10966947. These patents have been licensed to Elysium Health, NY. J.S.O.M. has a research contract and equipment loan from ThermoFisher Scientific, which manufactures IC-MS systems. S. de J., Q. G. and E. S. are employees of Numares AG (Am Biopark 9, 93053 Regensburg-Graß, Germany). All other authors report no conflicts of interest.

Funding

F.P. is funded by a Dorothy Hodgkin Early Career Fellowship in Chemistry in association with Somerville College. T.K. is funded by an EPSRC Doctoral Training Partnership (EP/W524311/1) and Numares AG (Am Biopark 9, 93053 Regensburg-Graß, Germany). This research was supported in part by the Aqua-Synapse EU framework (2022-2026) to D.A., funded by the European Union's Horizon 2020 Research and Innovation programme under the Marie Sklodowska-Curie Grant Agreement No. 101086453. The authors are solely responsible for the content of this publication, which does not necessarily represent the official views of the European Union or the European Research Executive Agency. The original VITACOG trial was supported by grants from Charles Wolfson Charitable Trust, Medical Research Council, Alzheimer's Research Trust, Henry Smith Charity, John Coates Charitable Trust, Thames Valley Dementias and Neurodegenerative Diseases Research Network of the National Institute for Health Research, UK, and the Sidney and Elizabeth Corob Charitable Trust.

Ethics approval and consent to participate

The trial, registered as VITACOG under the title "*Homocysteine and B Vitamins in Cognitive Impairment*" (ISRCTN 94410159), was conducted in accordance with the principles outlined in the Declaration of Helsinki. Ethical approval was granted by the local NHS research ethics committee (COREC 04/Q1604/100). Written informed consent was obtained from all participants prior to their enrolment in the study.

Data access and availability

Anonymised data will be made available by request from any qualified investigator.

Acknowledgement

The authors thank all MCI patients participating in this study and the NMR and MS Research Facility (Department of Chemistry, University of Oxford) for use of equipment and advice.

Supplementary Information – Manuscript 5

Supplementary Information

Role of B vitamins in modulating homocysteine and metabolic pathways linked to brain atrophy: metabolomics insights from the VITACOG trial

Tereza Kacerova[1], Abi G. Yates[1,2], Jiayi Dai[1], Dawn Shepherd[2], Elisabete Pires[1], Sebastian de Jel[3], Qingxia Gong[3], Eric Schiffer[3], Fredrik Jernerén[4], Thomas Olsen[5], Celeste A. De Jager Loots[6], Helga Refsum[2,5], A. David Smith[2], James S. O. McCullagh[1]*, Daniel C. Anthony[2]*, Fay Probert[1]

[1] Chemistry Research Laboratory, Department of Chemistry, University of Oxford, Mansfield Road, Oxford, OX1 3TA, UK
[2] Department of Pharmacology, University of Oxford, Mansfield Road, Oxford, OX1 3QT, UK
[3] numares AG, Am Biopark 9, Regensburg, 93053, Germany
[4] Department of Pharmaceutical Biosciences, Uppsala University, Husargatan 3, Uppsala, 752 37, Sweden
[5] Department of Nutrition, Institute of Basic Medical Sciences, Faculty of Medicine University of Oslo, Postboks 1046 Blindern, 0317 Oslo, Norway
6The Ageing Epidemiology Research Unit, School of Public Health, Imperial College London, Charing Cross Hospital, St Dunstan's Road, London, W6 8RP, UK

Corresponding author: James S.O. McCullagh james.mccullagh@chem.ox.ac.uk

Corresponding author: Daniel C. Anthony daniel.anthony@pharm.ox.ac.uk

Supplementary Information – Manuscript 5

CONSORT diagram

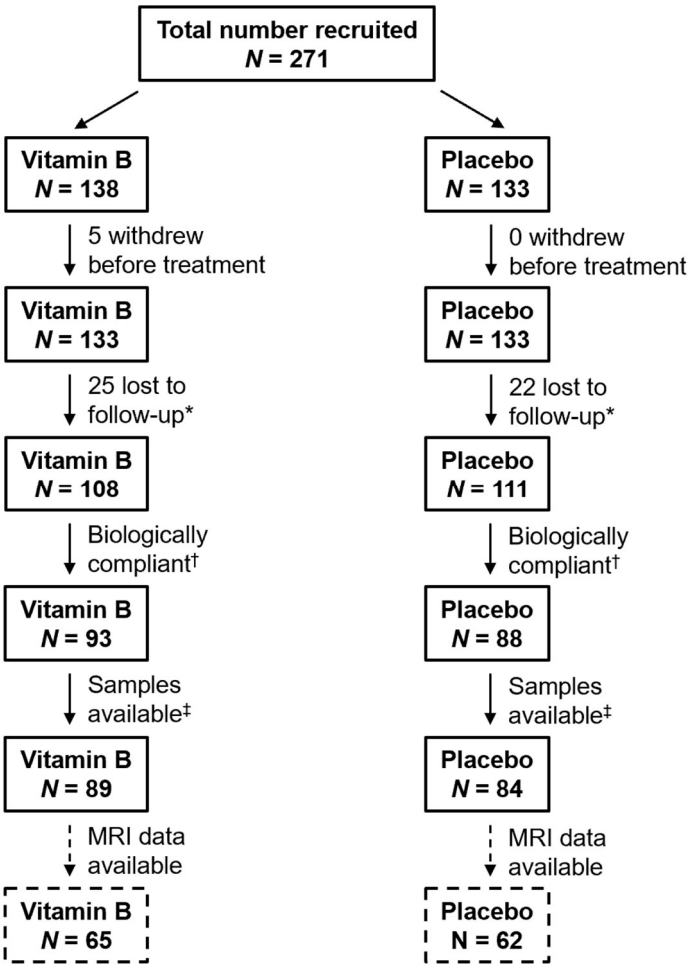

SI Figure 1 Participant flow through the trial (CONSORT diagram).[2] "Available samples" refers to the samples remaining in the biobank for this retrospective study. In this study, all B vitamin and placebo samples (baseline and follow-up for each participant) were analysed. For specific analyses focused on brain atrophy, only participants with available MRI scans were included.

Supplementary Information – Manuscript 5

Assessment of the potential confounding effect of treatment signature in the multivariate models

B vitamins (B6, B12, and folate), aspirin and their selected derivatives were analysed across all LC-MS platforms. Due to their low serum concentrations, these compounds were not detectable by NMR. In most cases, the compounds were either not detected in the VITACOG samples or failed to meet the quality curation criteria. Where compounds did pass the curation criteria (e.g., salicylic acid), the corresponding signals were removed from the multivariate model to prevent bias.

SI Table 1 List of parameters for B vitamins and homocysteine derivatives analysed using RPLC-MS (ESI^+)

Compound	Monoisotopic Molecular Weight	*Rt* (min)	*m/z*	Note
Vitamin B6	169.0739	0.83, 1.17	170.0829	/
Vitamin B12	1355.575	2.73, 3.21	678.2936	$[M+2H]^+$
Folic acid	441.1397	2.54, 3.17	442.1425	/
Pyridoxal 5'-phosphate	247.0246	0.86, 1.31	248.018	/
Pyridoxal	167.0582	0.84	150.5730, 168.0680	$[M-H_2O-H]^+$
4-Pyridoxic acid	183.0532	0.86, 1.67	166.0413, 184.0540	$[M-H_2O-H]^+$
Tetrahydrofolic acid	445.171	0.86, 1.89	267.0818	/
Homocysteine	135.0354	0.79	136.04	/
Cysteine	121.0197	0.74	122.0306	/
Salicylic acid	138.0317	4.70	139.0411*	/
Acetylsalicylic acid	180.0423	4.19	139.0411*	/

*The identical fragment ion at *m/z* 139.0411observed for both salicylic acid and acetylsalicylic acid results from the loss of the acetyl substituent under electrospray ionisation (ESI) conditions, yielding the salicylic acid core. Discrimination between the two compounds was therefore achieved on the basis of their distinct retention times.

Supplementary Information – Manuscript 5

SI Table 2 List of parameters for B vitamins and homocysteine derivatives analysed using RPLC-MS (ESI^-); some compounds were not detected (ND).

Compound	Monoisotopic Molecular Weight	*Rt* (min)	*m/z*	Note
Vitamin B6	169.0739	0.83, 1.17	168.8488	/
Vitamin B12	1355.575	ND	ND	/
Folic acid	441.1397	2.54, 3.17	440.1307	/
Pyridoxal 5'-phosphate	247.0246	0.86, 1.31	246.0171	/
Pyridoxal	167.0582	0.84	166.0556	/
4-Pyridoxic acid	183.0532	0.86, 1.67	182.0507	/
Tetrahydrofolic acid	445.171	0.86, 1.89	265.0859	/
Homocysteine	135.0354	0.79	134.0306	/
Cysteine	121.0197	0.74	120.0148	/
Salicylic acid	138.0317	4.70	137.0266*	/
Acetylsalicylic acid	180.0423	4.19	137.0266*	/

*The identical fragment ion at *m/z* 137.0266 observed for both salicylic acid and acetylsalicylic acid results from the loss of the acetyl substituent under electrospray ionisation (ESI) conditions, yielding the salicylic acid core. Discrimination between the two compounds was therefore achieved on the basis of their distinct retention times.

SI Table 3 List of parameters for B vitamins and homocysteine derivatives analysed using AEC-MS (ESI^-); some compounds were not detected (ND).

Compound	Monoisotopic Molecular Weight	*Rt* (min)	*m/z*	Note
Vitamin B6	169.0739	12.98	168.8472	/
Vitamin B12	1355.575	ND	ND	/
Folic acid	441.1397	ND	ND	/
Pyridoxal 5'-phosphate	247.0246	21.5	246.0175	/
Pyridoxal	167.0582	17.27	166.0512	/
4-Pyridoxic acid	183.0532	18.3	182.0462	/
Tetrahydrofolic acid	445.171	ND	ND	/
Homocysteine	135.0354	ND	ND	/
Cysteine	121.0197	ND	ND	/
Salicylic acid	138.0317	29.65	137.0247	/
Acetylsalicylic acid	180.0423	ND	ND	/

Supplementary Information – Manuscript 5

Assessment of Potential Confounding Factors

Renal function

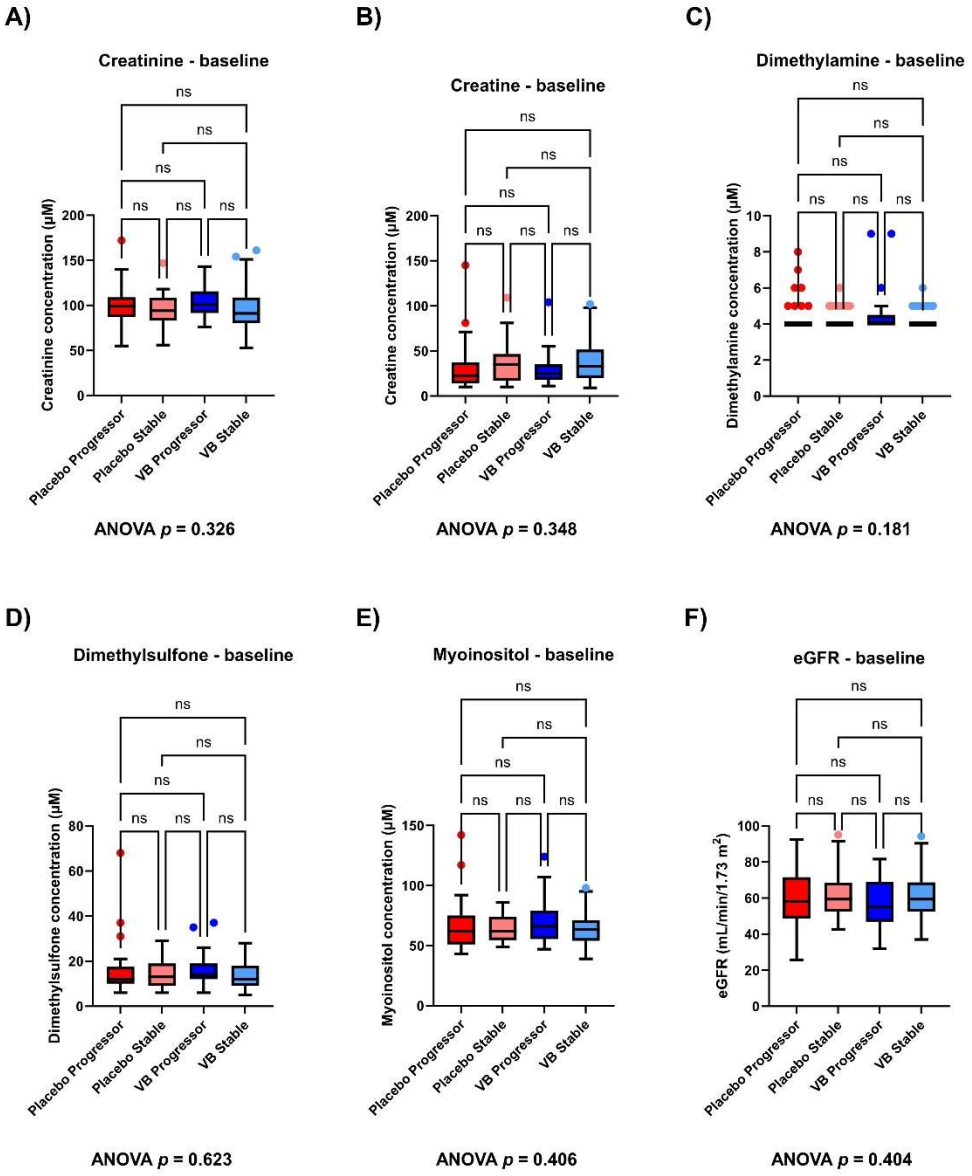

SI Figure 2 Assessment of renal and osmolyte markers at baseline across study groups. Boxplots show the distribution of serum **(A)** creatinine, **(B)** creatine, **(C)** dimethylamine, **(D)** dimethylsulfone, **(E)** myo-inositol, and **(F)** estimated glomerular filtration rate (eGFR) at baseline in placebo-progressors, placebo-stable, VB-progressors, and VB-stable groups. No significant differences were observed between groups for any marker (ANOVA, all $p > 0.18$), indicating baseline comparability and supporting the absence of renal or osmotic confounding.

Supplementary Information – Manuscript 5

Assessment of Potential Confounding Factors

Renal function

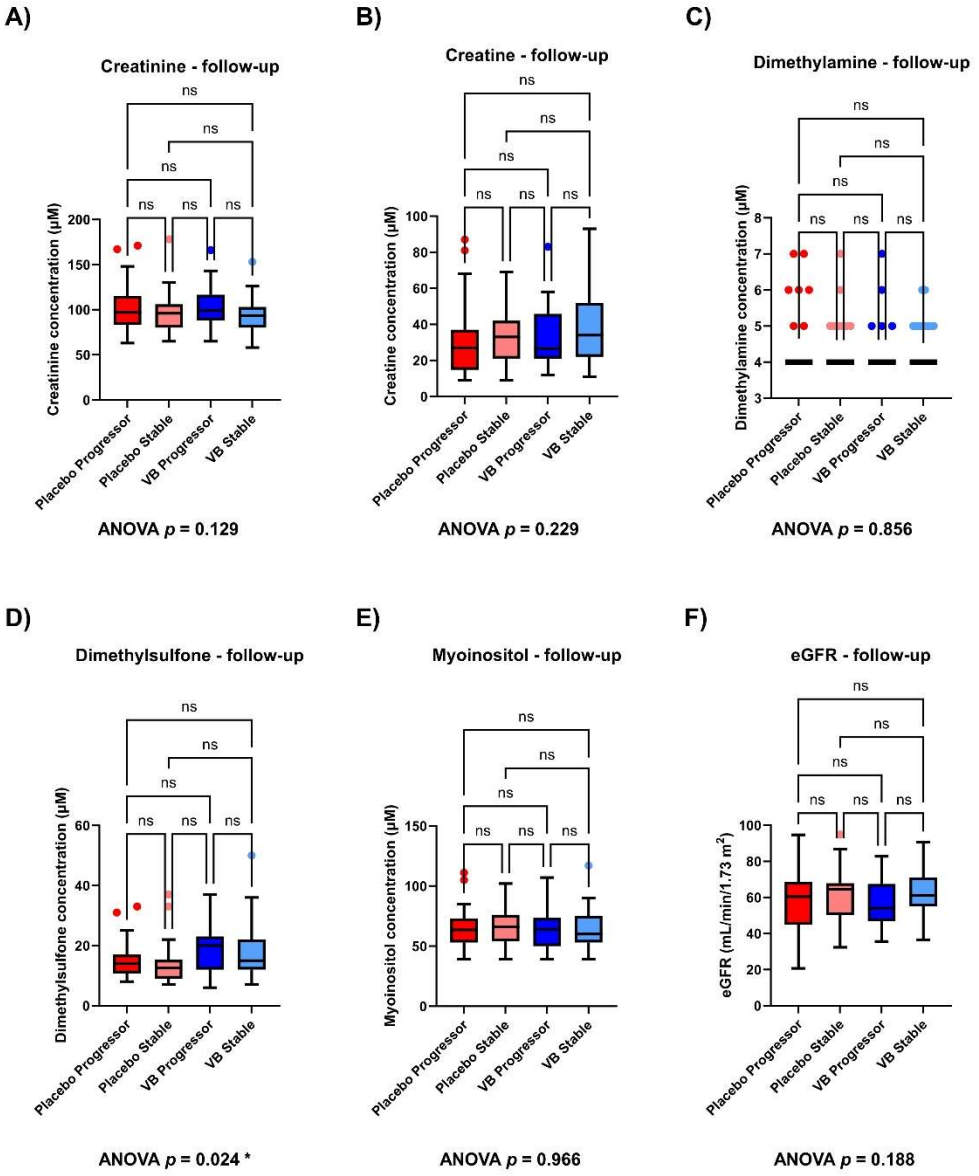

SI Figure 3 Assessment of renal and osmolyte markers at follow-up across study groups. Boxplots show the distribution of serum **(A)** creatinine, **(B)** creatine, **(C)** dimethylamine, **(D)** dimethylsulfone, **(E)** myo-inositol, and **(F)** estimated glomerular filtration rate (eGFR) at follow-up in placebo-progressors, placebo-stable, VB-progressors, and VB-stable groups. No significant differences were observed between groups for most markers (ANOVA, all $p > 0.12$), except for dimethylsulfone ($p = 0.024$), which showed a modest group effect. These findings support the absence of major renal or osmotic shifts following intervention.

Supplementary Information – Manuscript 5

Assessment of Potential Confounding Factors

Central Nervous System (CNS) Targeting Drugs

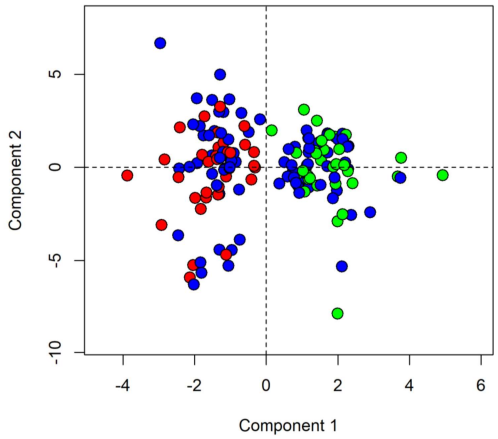

SI Figure 4 OPLS-DA scores plot illustrating the distribution of individuals treated with B vitamins (green) and placebo controls (red), with those who were co-administered CNS targeting drugs highlighted in blue. The blue datapoints are evenly distributed across the plot, indicating no discernible clustering related to CNS targeting drugs administration.

Cardiovascular System Targeting Drugs

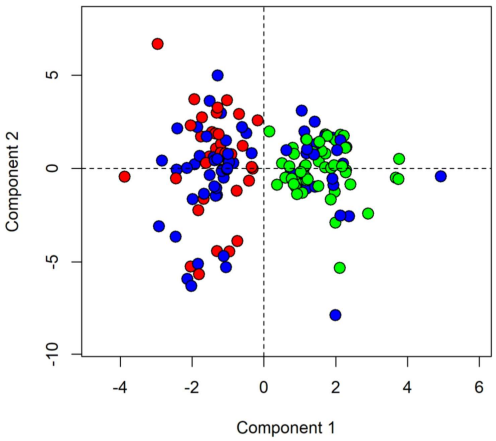

SI Figure 5 OPLS-DA scores plot illustrating the distribution of individuals treated with B vitamins (green) and placebo controls (red), with those who were co-administered cardiovascular system targeting drugs highlighted in blue. The blue datapoints are evenly distributed across the plot, indicating no discernible clustering related to cardiovascular system targeting drugs administration.

Supplementary Information – Manuscript 5

Aspirin

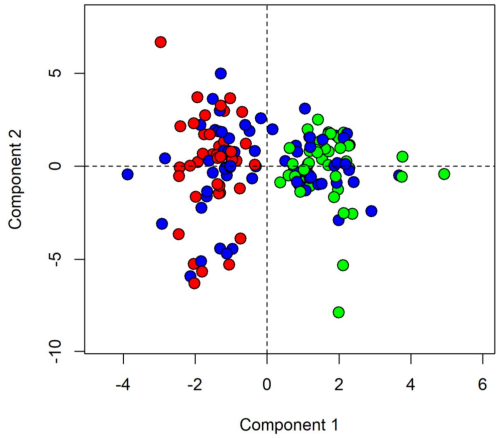

SI Figure 6 OPLS-DA scores plot illustrating the distribution of individuals treated with B vitamins (green) and placebo controls (red), with those who were co-administered aspirin highlighted in blue. The blue datapoints are evenly distributed across the plot, indicating no discernible clustering related to aspirin administration.

Supplementary Information – Manuscript 5

Polar metabolome allows discriminating between B vitamin-treated individuals and placebo controls

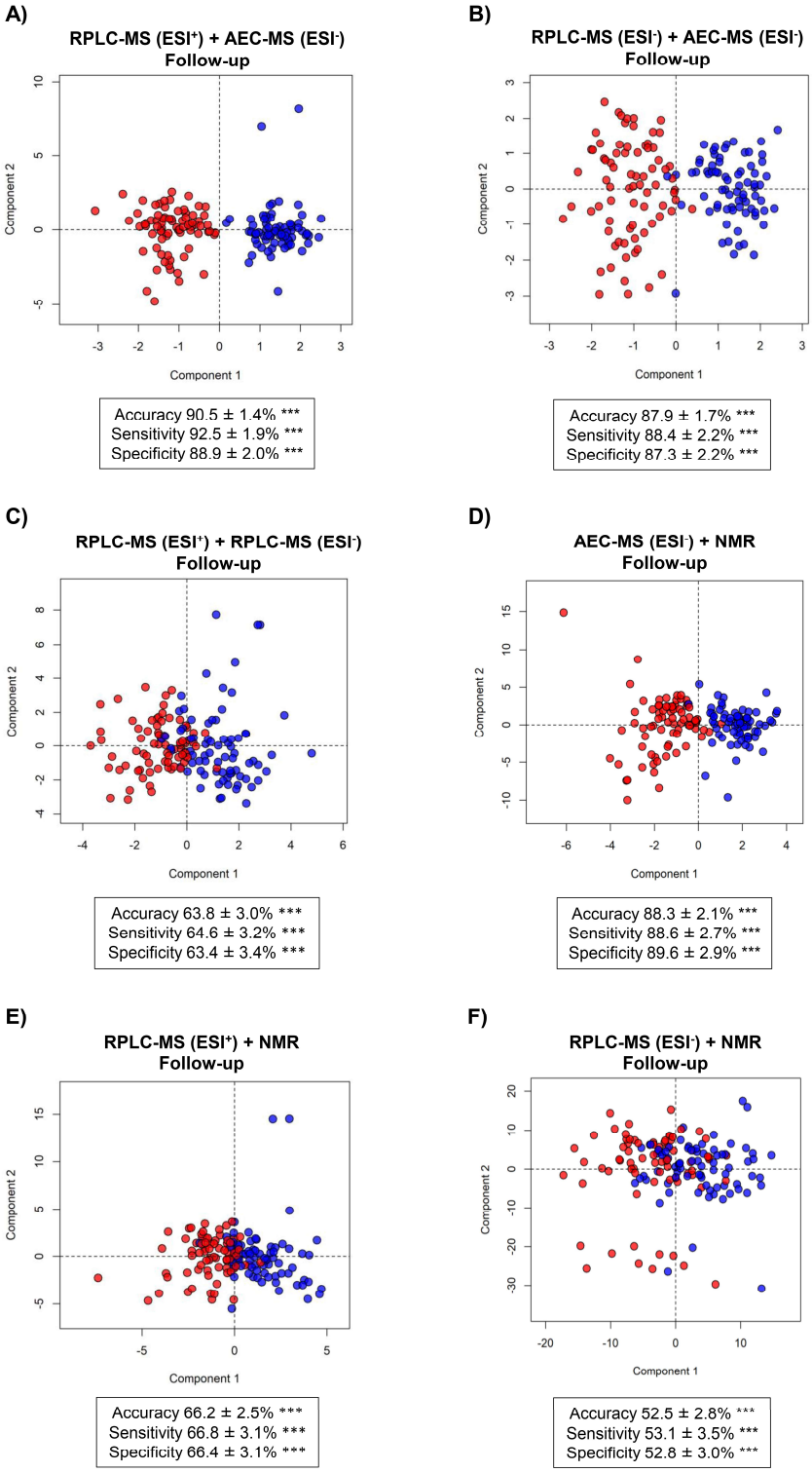

SI Figure 7 OPLS-DA score plots illustrating the separation between placebo-treated (red) and B vitamin-treated (blue) individuals based on serum metabolomic profiling at follow-up. Each panel displays results for a binary combination of analytical platforms: A) RPLC-MS (ESI^+) + AEC-MS (ESI^-); B) RPLC-MS (ESI^+) + AEC-MS (ESI^-) [duplicate of A to assess reproducibility]; C) RPLC-MS (ESI^+) + RPLC-MS (ESI^-); D) AEC-MS (ESI^-) + NMR; E) RPLC-MS (ESI^+) + NMR; F) RPLC-MS (ESI^-) + NMR. Each model includes accuracy, sensitivity, and specificity (mean ± SD) derived from cross-validation. Significance (***$p < 0.001$) was assessed relative to a random class ensemble using the Kolmogorov–Smirnov test. These results highlight the dominant contribution of the AEC-MS platform and the incremental value of complementary platform integration.

Supplementary Information – Manuscript 5

Polar metabolome allows discriminating between B vitamin-treated individuals and placebo controls

SI Table 4 List of compound-features and bins with the highest VIP score for the multiplatform metabolomics model discriminating between B vitamin-treated individuals and placebo controls at follow-up

Feature	Frequency	Average Rank	Overall Score	Overall Rank
9.49_372.2723	354	1.46	242.9	1
9.68_261.1482	858	3.66	234.2	2
9.68_239.1683	989	5.02	197.0	3
8.52_557.2365	919	4.93	186.5	4
Mannitol	298	1.92	155.5	5
7.39_229.1446	995	7.76	128.2	6
10.18_726.3464	642	5.93	108.3	7
0.77_365.1172	983	11.43	86.0	8
4.39_198.0581	1000	13.34	74.9	9
8.26_539.2501	314	4.65	67.6	10
5.54_360.2393	909	13.70	66.3	11
4.39_260.0292	964	15.82	60.9	12
10.01_491.8127	457	7.97	57.3	13
12.73_209.0820	605	10.79	56.1	14
[2.95....2.97]	423	7.67	55.1	15
4.77_266.9830	160	2.98	53.7	16
7.96_449.3099	583	12.25	47.6	17
Succinic acid	895	20.13	44.5	18
5.75_479.2639	524	11.97	43.8	19
5.49_427.1624	123	3.06	40.2	20
8.80_453.2498	819	20.36	40.2	21
13.84_452.0498	834	21.89	38.1	22
4.58_857.2492	890	24.00	37.1	23
3.62_121.0325	533	16.31	32.7	24
4.58_857.0491	949	29.11	32.6	25

Supplementary Information – Manuscript 5

Polar metabolome allows discriminating between B vitamin-treated individuals and placebo controls

SI Table 5 List of identified LC-MS-detected metabolites with the highest VIP scores for the multiplatform metabolomics model discriminating between B vitamin-treated individuals and placebo controls at follow-up. Note that only identified metabolites were used construct the used multivariate model constructed model accuracy: 63.5 ± 2.8%).
†† RPLC-MS (pos. ion mode); † RPLC-MS (neg. ion mode); no symbol AEC-MS (neg. ion mode).

Metabolite	Frequency	Average Rank	Overall Score	Overall Rank
Succinic acid	785	2.86	274.86	1
Arabitol	877	3.44	255.27	2
Lactose	970	4.44	218.51	3
Sugar-phosphate	997	7.06	141.25	4
Mannitol	808	7.82	103.33	5
α-Ketoglutaric acid	994	14.47	68.69	6
3,4-Dihydroxybenzylamine	982	17.41	56.40	7
α-Ketobutyric acid	159	2.96	53.79	8
2-Hydroxyhexanoic acid	993	19.19	51.73	9
Glucose	955	18.60	51.35	10
Ribulose	983	19.89	49.42	11
2-Hydroxybutyric acid	961	19.78	48.58	12
††Propionyl carnitine	244	5.03	48.48	13
Glycolic acid	323	7.11	45.46	14
Quinolinic acid	913	20.80	43.90	15
2-Methylcitric acid	513	11.75	43.66	16
Aspartate	965	22.19	43.48	17
†Citraconic acid	506	13.85	36.52	18
Pyruvic acid	759	21.05	36.06	19
3,3-Dimethylglutaric acid	827	23.79	34.76	20
Acetoacetate	850	26.15	32.51	21
Linoleic acid	696	21.42	32.49	22
N-acetylglutamic acid	910	28.68	31.73	23
Sorbitol	894	31.37	28.50	24
4-Methyl-2-oxovaleric acid	690	29.05	23.75	25

Supplementary Information – Manuscript 5

Three-way ANOVA reveals B vitamin-dependent changes and their association with brain atrophy

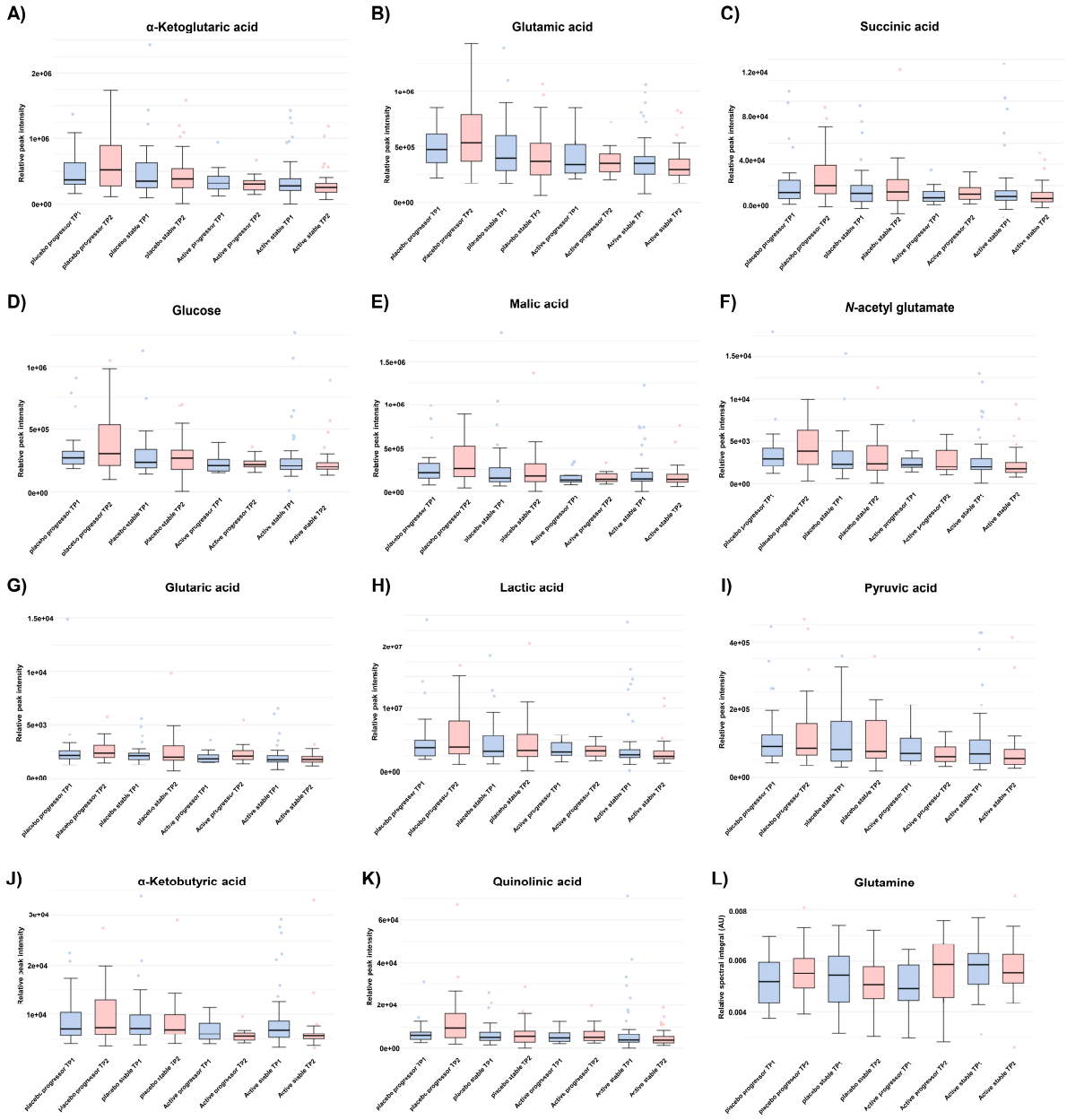

SI Figure 8 Three-way ANOVA assessing the effects of B vitamin treatment (active vs placebo), atrophy progression (stable vs progressor), and temporal effects (TP1 (baseline) vs TP2 (follow-up) in the VITACOG cohort. **A) 2-oxoglutaric acid:** treatment effect $p < 0.0001$ (0.002); atrophy effect $p = 0.10$ (0.46) ; timepoint effect $p = 0.23$ (0.62); **B) glutamic acid:** treatment effect $p < 0.0001$ (0.0004); atrophy effect $p = 0.03$ (0.21); timepoint effect $p = 0.59$ (0.85); **C) succinic acid:** treatment effect $p < 0.0015$ (0.03); atrophy effect $p = 0.18$ (0.55); timepoint effect $p = 0.41$ (0.75); **D) glucose:** treatment effect $p = 0.0001$ (0.008); atrophy effect $p = 0.07$ (0.39); timepoint effect $p = 0.40$ (0.75); **E) malic acid:** treatment effect $p = 0.0001$ (0.008); atrophy effect $p = 0.21$ (0.59); timepoint effect $p = 0.28$ (0.65); **F) *N*-acetylglutamate:** treatment effect $p = 0.0004$ (0.01); atrophy effect $p = 0.03$ (0.25); timepoint effect $p = 0.27$ (0.64); **G) glutaric acid:** treatment effect $p = 0.0002$ (0.009); atrophy effect $p = 0.10$ (0.46); timepoint effect $p = 0.69$ (0.91); **H) lactic acid:** treatment effect $p = 0.0004$ (0.01); atrophy effect $p = 0.12$ (0.50); timepoint effect $p = 0.16$ (0.54); **I) pyruvic acid:** treatment effect $p = 0.001$ (0.02); atrophy effect $p = 0.14$ (0.52); timepoint effect $p = 0.10$ (0.44); **J) 2-ketobutyric acid:** treatment effect $p = 0.002$ (0.03) ; atrophy effect $p = 0.62$ (0.87); timepoint effect $p = 0.03$ (0.23); **K) quinolinic acid:** treatment effect p =0.02 (0.19); atrophy effect $p = 0.03$ (0.24); timepoint effect $p = 0.27$ (.065); **L) glutamine:** treatment effect p = 0.04; atrophy effect $p = 0.67$; timepoint effect $p = 0.57$. One outlier was excluded from the graphical representation to enhance data clarity. This exclusion did not significantly impact the results.

Supplementary Information – Manuscript 5

Three-way ANOVA reveals B vitamin-dependent changes and their association with brain atrophy

SI Table 6 List of LC-MS identified metabolites and results of three-way ANOVA (main class effects).
†† RPLC-MS (pos. ion mode); † RPLC-MS (neg. ion mode); no symbol AEC-MS (neg. ion mode).

Metabolite	Class 1		Class 2		Class 3	
	p-value	FDR	*p*-value	FDR	*p*-value	FDR
†2-*C*-Methyl-*D*-Erythritol-4-phosphate	0.3349	0.6897	0.6486	0.8965	0.7487	0.9248
2-Hydroxybutyric acid	0.0061	0.0641	0.6330	0.8862	0.0477	0.3186
2-Hydroxyhexanoic acid	0.0823	0.4290	0.8176	0.9466	0.0178	0.1596
2-Ketobutyric acid	0.0017	0.0275	0.6178	0.8749	0.0295	0.2299
2-Ketoglutaric acid	<0.0001	0.0021	0.0996	0.4594	0.2346	0.6159
2-Methylcitric acid	0.0035	0.0422	0.1484	0.5267	0.1180	0.5026
3,3-Dimethyl glutarate	0.0032	0.0395	0.2172	0.5962	0.1261	0.5034
3,4-Dihydroxybenzylamine	0.0026	0.0341	0.2532	0.6347	0.4190	0.7529
3,4-Dihydroxyphenylacetic acid	0.2342	0.6159	0.3583	0.7014	0.6554	0.8965
3-Dehydroquinate	0.0021	0.0302	0.2608	0.6371	0.2909	0.6526
3-Ethylmalate	0.0009	0.0185	0.0712	0.3969	0.2286	0.6134
3-Hydroxyisovaleric acid	0.0003	0.0090	0.1311	0.5082	0.3802	0.7261
3-Isopropylmalic acid	0.0043	0.0499	0.0833	0.4290	0.2249	0.6060
3-Methoxyphenylacetic acid	0.0046	0.0513	0.0155	0.1404	0.4651	0.7808
4-Methoxybenzoic acid	0.0046	0.0513	0.5788	0.8468	0.9646	0.9940
5-Methoxyindoleacetate	0.1466	0.5267	0.1034	0.4699	0.4480	0.7707
Acetoacetate	0.0268	0.2149	0.2071	0.5838	0.4157	0.7529
Acetylglycine	0.0951	0.4488	0.2809	0.6526	0.2405	0.6179
Adonitol	0.0003	0.0090	0.1938	0.5757	0.5231	0.8224
Allantoin	0.0003	0.0090	0.0404	0.2830	0.3426	0.6924
α-Ketoisovaleric acid	<0.0001	0.0021	0.3924	0.7358	0.1053	0.4752
Arabinonic acid	0.0018	0.0281	0.1564	0.5380	0.1596	0.5401
Arabitol	<0.0001	0.0034	0.0138	0.1292	0.6639	0.8994
Ascorbate	0.0026	0.0341	0.1543	0.5374	0.3301	0.6897
††Aspartame	0.0243	0.2031	0.1203	0.5026	0.5995	0.8591
Aspartate	0.0010	0.0185	0.2658	0.6409	0.1820	0.5626
††Butyrylcarnitine	0.1706	0.5474	0.4550	0.7762	0.8548	0.9613
†Citraconic acid	0.7684	0.9279	0.9436	0.9895	0.5209	0.8224
Citramalic acid	0.0002	0.0083	0.1890	0.5641	0.4286	0.7573
Citric acid	0.0129	0.1228	0.3738	0.7226	0.2020	0.5838
†Deoxycholic acid	0.9806	0.9953	0.8044	0.9367	0.7333	0.9189
††Dopamine hydrochloride	0.9074	0.9780	0.1871	0.5641	0.3232	0.6875
Ethylmalonic acid	0.0369	0.2645	0.3445	0.6924	0.1661	0.5468
Fructose	0.0010	0.0185	0.2897	0.6526	0.5812	0.8468
Galactaric acid	0.0007	0.0157	0.2813	0.6526	0.4518	0.7750
Galacturonic acid	0.0442	0.3056	0.4398	0.7609	0.2396	0.6179
Gluconate	0.0024	0.0322	0.1373	0.5195	0.2054	0.5838
Gluconolactone	0.0067	0.0689	0.1496	0.5267	0.3513	0.6991
Glucose	0.0001	0.0079	0.0654	0.3903	0.4014	0.7466
Glucose-1-phosphate	0.0013	0.0227	0.3242	0.6875	0.0764	0.4079
Glucuronic acid	0.0019	0.0281	0.2173	0.5962	0.1688	0.5474

Glutamic acid	<0.0001	0.0004	0.0261	0.2116	0.5879	0.8505
Glutaric acid	0.0002	0.0087	0.0987	0.4589	0.6934	0.9091
Glyceric acid	0.0031	0.0393	0.3381	0.6907	0.3058	0.6722
Glycolic acid	0.0003	0.0094	0.2327	0.6159	0.3394	0.6907
Isocitrate	0.0195	0.1724	0.2046	0.5838	0.0891	0.4371
Lactic acid	0.0004	0.0104	0.1217	0.5026	0.1622	0.5427
Lactose	0.1863	0.5641	0.6548	0.8965	0.7925	0.9354
†Linoleic Acid	0.7065	0.9091	0.1958	0.5788	0.2095	0.5853
†*L*-Theanine	0.7648	0.9279	0.8779	0.9661	0.0115	0.1116
Malic acid	0.0001	0.0079	0.2089	0.5853	0.2825	0.6526
Malitol	0.0014	0.0236	0.0059	0.0632	0.8909	0.9741
Mannitol	0.0001	0.0045	0.0949	0.4488	0.4075	0.7466
Mannose	0.0004	0.0101	0.2960	0.6570	0.5431	0.8246
Methylglutaric acid	0.0152	0.1400	0.0690	0.3969	0.2416	0.6179
Methyl-phenylacetate	0.1175	0.5026	0.7895	0.9354	0.9389	0.9895
Mytilitol	0.0004	0.0104	0.1444	0.5267	0.2024	0.5838
N-Acetylaspartate	0.0004	0.0104	0.0385	0.2724	0.5087	0.8175
N-Acetylglutamate	0.0004	0.0104	0.0343	0.2549	0.2681	0.6409
N-Acetyl-L-alanine	0.0010	0.0185	0.1297	0.5082	0.3434	0.6924
††*N*-Acetyl-*L*-methionine	0.1596	0.5401	0.1736	0.5534	0.7783	0.9330
N-Acetylneuraminic acid	0.0069	0.0698	0.2055	0.5838	0.1242	0.5026
Nonate	0.0101	0.0996	0.2684	0.6409	0.3231	0.6875
Oxalic acid	0.0023	0.0322	0.3582	0.7014	0.4222	0.7529
Pantoic acid	0.0496	0.3211	0.5785	0.8468	0.8071	0.9381
Pantothenic acid	0.0019	0.0281	0.3403	0.6907	0.4358	0.7609
p-Hydroxyphenylacetic acid	0.9422	0.9895	0.9508	0.9895	0.1705	0.5474
Phytanic acid	0.9943	0.9976	0.8597	0.9613	0.4672	0.7817
††Propionylcarnitine	0.8977	0.9744	0.6817	0.9091	0.7954	0.9364
Protocatechuic acid	0.0002	0.0083	0.5411	0.8246	0.9145	0.9804
Pyroglutamic acid	0.0059	0.0632	0.2199	0.5978	0.1159	0.5026
Pyruvic acid	0.0010	0.0185	0.1391	0.5229	0.0974	0.4562
Quinic acid	0.0040	0.0475	0.3251	0.6875	0.7591	0.9279
Quinolinic acid	0.0235	0.1991	0.0369	0.2645	0.2865	0.6526
Raffinose	0.1102	0.4937	0.4881	0.8012	0.2139	0.5921
Ribulose	0.0002	0.0087	0.0254	0.2088	0.3074	0.6735
Sorbitol	0.0021	0.0302	0.1809	0.5620	0.4864	0.8005
†Stearic acid	0.7423	0.9208	0.1708	0.5474	0.2761	0.6493
Succinic acid	0.0015	0.0255	0.1749	0.5546	0.4053	0.7466
Tartaric acid	0.0481	0.3186	0.1452	0.5267	0.1782	0.5620
Taurine	0.0018	0.0281	0.1318	0.5082	0.0855	0.4304
††Theophylline	0.6534	0.8965	0.9687	0.9948	0.8489	0.9613
†Tryptamine	0.7161	0.9112	0.9538	0.9895	0.8532	0.9613
Uridine	0.0002	0.0083	0.0574	0.3569	0.4077	0.7466
††Vanillin	0.1314	0.5082	0.7921	0.9354	0.7223	0.9112
Xylulose	0.0009	0.0185	0.0845	0.4290	0.3243	0.6875

Supplementary Information – Manuscript 5

Three-way ANOVA reveals B vitamin-dependent changes and their association with brain atrophy

SI Table 7 List of LC-MS identified metabolites and results of three-way ANOVA (classes interactions). †† RPLC-MS (pos. ion mode); † RPLC-MS (neg. ion mode); no symbol AEC-MS (neg. ion mode).

Metabolite	Class 1:2 interaction		Class 1:3 interaction		Class 2:3 interaction	
	p-value	FDR	*p*-value	FDR	*p*-value	FDR
†2-*C*-Methyl-*D*-Erythritol-4-phosphate	0.5424	0.8246	0.5350	0.8246	0.5387	0.8246
2-Hydroxybutyric acid	0.1461	0.5267	0.3468	0.6940	0.2902	0.6526
2-Hydroxyhexanoic acid	0.0494	0.3211	0.9008	0.9744	0.0348	0.2554
2-Ketobutyric acid	0.0723	0.3969	0.4933	0.8055	0.7421	0.9208
2-Ketoglutaric acid	0.0941	0.4488	0.5026	0.8138	0.9183	0.9811
2-Methylcitric acid	0.1982	0.5804	0.8499	0.9613	0.9507	0.9895
3,3-Dimethyl glutarate	0.1646	0.5447	0.9526	0.9895	0.7697	0.9279
3,4-Dihydroxybenzylamine	0.2586	0.6371	0.5333	0.8246	0.4650	0.7808
3,4-Dihydroxyphenylacetic acid	0.0649	0.3903	0.8800	0.9661	0.8513	0.9613
3-Dehydroquinate	0.0879	0.4351	0.8964	0.9744	0.8580	0.9613
3-Ethylmalate	0.2543	0.6347	0.9871	0.9957	0.7008	0.9091
3-Hydroxyisovaleric acid	0.0734	0.3991	0.2851	0.6526	0.2721	0.6448
3-Isopropylmalic acid	0.1486	0.5267	0.9875	0.9957	0.7900	0.9354
3-Methoxyphenylacetic acid	0.4208	0.7529	0.6615	0.8992	0.5281	0.8246
4-Methoxybenzoic acid	0.7635	0.9279	0.9003	0.9744	0.4829	0.7988
5-Methoxyindoleacetate	0.6891	0.9091	0.1793	0.5620	0.3214	0.6875
Acetoacetate	0.0568	0.3567	0.0472	0.3186	0.1236	0.5026
Acetylglycine	0.0602	0.3702	0.8039	0.9367	0.5443	0.8246
Adonitol	0.0510	0.3236	0.9941	0.9976	0.2967	0.6570
Allantoin	0.0306	0.2360	0.9601	0.9917	0.6574	0.8965
α-Ketoisovaleric acid	0.1360	0.5195	0.2567	0.6356	0.5429	0.8246
Arabinonic acid	0.1496	0.5267	0.7376	0.9206	0.9000	0.9744
Arabitol	0.9209	0.9822	0.3323	0.6897	0.6397	0.8915
Ascorbate	0.5010	0.8138	0.7798	0.9330	0.8820	0.9661
††Aspartame	0.4356	0.7654	0.8317	0.9538	0.4072	0.7466
Aspartate	0.1213	0.5026	0.4325	0.7591	0.5761	0.8468
††Butyrylcarnitine	0.0002	0.0083	0.6228	0.8779	0.8653	0.9634
†Citraconic acid	0.2673	0.6409	0.2312	0.6148	0.2561	0.6356
Citramalic acid	0.0897	0.4371	0.5218	0.8224	0.3787	0.7261
Citric acid	0.8722	0.9657	0.3032	0.6690	0.3317	0.6897
†Deoxycholic acid	0.1367	0.5195	0.4396	0.7609	0.0909	0.4395
††Dopamine hydrochloride	0.0718	0.3969	0.7052	0.9091	0.5651	0.8393
Ethylmalonic acid	0.1672	0.5474	0.6268	0.8797	0.5068	0.8165
Fructose	0.0321	0.2447	0.7473	0.9248	0.2602	0.6371
Galactaric acid	0.0508	0.3236	0.1882	0.5641	0.5928	0.8534
Galacturonic acid	0.4150	0.7529	0.8777	0.9661	0.9437	0.9895
Gluconate	0.1300	0.5082	0.8101	0.9398	0.7314	0.9183
Gluconolactone	0.1544	0.5374	0.7606	0.9279	0.7085	0.9091
Glucose	0.0283	0.2239	0.9042	0.9764	0.7078	0.9091
Glucose-1-phosphate	0.2425	0.6179	0.5016	0.8138	0.5597	0.8375
Glucuronic acid	0.3352	0.6897	0.9160	0.9804	0.7250	0.9122

Glutamic acid	0.3117	0.6804	0.2515	0.6347	0.2368	0.6179
Glutaric acid	0.7091	0.9091	0.9770	0.9953	0.6202	0.8763
Glyceric acid	0.2296	0.6134	0.2914	0.6526	0.7172	0.9112
Glycolic acid	0.2188	0.5976	0.5201	0.8224	0.5708	0.8417
Isocitrate	0.1246	0.5026	0.9229	0.9826	0.7860	0.9354
Lactic acid	0.9943	0.9976	0.8943	0.9744	0.8566	0.9613
Lactose	0.1265	0.5034	0.8392	0.9606	0.8009	0.9367
†Linoleic Acid	0.0071	0.0713	0.6514	0.8965	0.7964	0.9364
†*L*-Theanine	0.7710	0.9279	0.9722	0.9951	0.5038	0.8138
Malic acid	0.0805	0.4264	0.7532	0.9266	0.7021	0.9091
Malitol	0.0462	0.3163	0.6845	0.9091	0.5582	0.8372
Mannitol	0.0339	0.2548	0.7568	0.9279	0.0205	0.1785
Mannose	0.1441	0.5267	0.6414	0.8918	0.5981	0.8590
Methylglutaric acid	0.2133	0.5921	0.2677	0.6409	0.1606	0.5404
Methyl-phenylacetate	0.3935	0.7358	0.3734	0.7226	0.4361	0.7609
Mytilitol	0.1968	0.5791	0.8818	0.9661	0.7392	0.9206
N-Acetylaspartate	0.0709	0.3969	0.4212	0.7529	0.8255	0.9524
N-Acetylglutamate	0.1556	0.5380	0.5246	0.8224	0.7221	0.9112
N-Acetyl-L-alanine	0.0000	0.0000	0.6357	0.8880	0.4384	0.7609
††*N*-Acetyl-*L*-methionine	0.1207	0.5026	0.8282	0.9524	0.9550	0.9895
N-Acetylneuraminic acid	0.0877	0.4351	0.5879	0.8505	0.9777	0.9953
Nonate	0.7126	0.9112	0.9713	0.9951	0.4746	0.7919
Oxalic acid	0.1452	0.5267	0.2018	0.5838	0.7178	0.9112
Pantoic acid	0.0702	0.3969	0.5141	0.8195	0.2907	0.6526
Pantothenic acid	0.1848	0.5641	0.5832	0.8477	0.9674	0.9948
p-Hydroxyphenylacetic acid	0.4294	0.7573	0.9980	0.9980	0.7080	0.9091
Phytanic acid	0.3874	0.7314	0.4302	0.7573	0.9824	0.9955
††Propionylcarnitine	0.0000	0.0021	0.7511	0.9260	0.8479	0.9613
Protocatechuic acid	0.6726	0.9002	0.1805	0.5620	0.6657	0.8994
Pyroglutamic acid	0.0678	0.3969	0.5688	0.8417	0.9089	0.9780
Pyruvic acid	0.1231	0.5026	0.9390	0.9895	0.4776	0.7948
Quinic acid	0.0661	0.3909	0.2490	0.6318	0.1203	0.5026
Quinolinic acid	0.0621	0.3784	0.8288	0.9524	0.9860	0.9957
Raffinose	0.2532	0.6347	0.5104	0.8179	0.2396	0.6179
Ribulose	0.0208	0.1786	0.8579	0.9613	0.8721	0.9657
Sorbitol	0.1034	0.4699	0.9797	0.9953	0.7022	0.9091
†Stearic acid	0.9491	0.9895	0.5524	0.8306	0.4228	0.7529
Succinic acid	0.0844	0.4290	0.3333	0.6897	0.4654	0.7808
Tartaric acid	0.2395	0.6179	0.5391	0.8246	0.5927	0.8534
Taurine	0.0836	0.4290	0.6949	0.9091	0.9768	0.9953
††Theophylline	0.1635	0.5441	0.3218	0.6875	0.8684	0.9651
†Tryptamine	0.0705	0.3969	0.4894	0.8012	0.7903	0.9354
Uridine	0.0757	0.4079	0.2696	0.6413	0.4051	0.7466
††Vanillin	0.1123	0.4954	0.6019	0.8605	0.3605	0.7014
Xylulose	0.1147	0.5025	0.9134	0.9804	0.8737	0.9657

Supplementary Information – Manuscript 5

Three-way ANOVA reveals B vitamin-dependent changes and their association with brain atrophy

SI Table 8 List of NMR identified metabolites and results of three-way ANOVA (main class effects).

Metabolite	Bin (ppm)	Class 1		Class 2		Class 3	
		p-value	FDR	*p*-value	FDR	*p*-value	FDR
High density lipoproteins	[0.85..0.87]	0.43	0.82	0.18	0.70	0.92	0.95
Very low-density lipoproteins	[0.87..0.89]	0.22	0.75	0.25	0.76	0.35	0.77
Isoleucine	[0.95..0.97]	0.52	0.85	0.09	0.57	0.71	0.89
Leucine	[0.97..0.99]	0.14	0.66	0.20	0.74	0.49	0.82
Hydroxybutyrate	[1.17..1.19]	0.75	0.89	0.04	0.40	0.47	0.82
Low density lipoproteins	[1.23..1.25]	0.75	0.89	0.39	0.79	0.33	0.77
Low/Very-low density lipoproteins	[1.29..1.31]	0.28	0.77	0.27	0.77	0.36	0.77
Alanine	[1.47..1.49]	0.13	0.66	0.36	0.77	0.11	0.59
βCH_2	[1.59..1.61]	0.49	0.83	0.57	0.86	0.43	0.82
$/=CH-CH_2-CH=$	[1.99..2.01]	0.68	0.89	0.14	0.66	0.58	0.86
Proline	[2.01..2.03]	0.35	0.77	0.17	0.70	0.63	0.89
N-acetyl glycoprotein A (NAC1)	[2.03..2.05]	0.53	0.85	0.30	0.77	0.87	0.92
N-acetyl glycoprotein B (NAC2)	[2.07..2.09]	0.07	0.54	0.89	0.93	0.75	0.89
Glutamine	[2.13..2.15]	0.04	0.40	0.70	0.89	0.57	0.86
Acetoacetate	[2.21..2.23]	0.45	0.82	0.67	0.89	0.03	0.40
Valine/Proline	[2.29..2.31]	0.53	0.85	0.60	0.87	0.70	0.89
Glutamate	[2.35..2.37]	0.37	0.77	0.75	0.89	0.22	0.75
Creatinine	[3.03..3.05]	0.22	0.75	0.86	0.92	0.14	0.66
Mobile $-N(CH_3)_3$/	[3.19..3.21]	0.44	0.82	0.63	0.89	0.48	0.82
mobile $-N(CH_3)_3$/free choline	[3.21..3.23]	0.10	0.57	0.86	0.92	0.71	0.89
Histidine	[3.31..3.33]	0.10	0.57	0.65	0.89	0.17	0.70
Glucose	[3.55..3.57]	0.48	0.82	0.37	0.77	0.70	0.89
Threonine	[3.59..3.61]	0.48	0.82	0.64	0.89	0.76	0.89
Myoinositol	[3.61..3.63]	0.21	0.75	0.76	0.89	0.13	0.66
Lactate	[4.11..4.13]	0.46	0.82	0.41	0.80	0.94	0.96
Unsaturated lipid	[5.30..5.32]	0.08	0.54	0.23	0.75	0.52	0.85
Tyrosine	[6.88..6.90]	0.28	0.77	0.99	0.99	0.04	0.40
Phenylalanine	[7.56..7.58]	0.11	0.61	0.63	0.89	0.23	0.75

Supplementary Information – Manuscript 5

Two-Way ANOVA *Post hoc* Results

A Two-Way ANOVA with Tukey's *post hoc* analysis of follow-up metabolite levels, adjusted for baseline, revealed that treatment (B vitamin administration) is the primary factor driving interclass differences; however, secondary effects associated with brain atrophy progression were also observed.

SI Table 9 Two-Way ANOVA *post hoc* results for the metabolites selected in the three-way ANOVA analysis. The follow-up levels adjusted for the baseline levels were used for each metabolite.

Metabolite	Combined class 1	Combined class 2	*p* value
2-Ketoglutaric acid	placebo stable	placebo progressor	0.4084
2-Ketoglutaric acid	placebo stable	vitamin stable	0.2008
2-Ketoglutaric acid	placebo stable	vitamin progressor	0.6047
2-Ketoglutaric acid	placebo progressor	vitamin stable	0.0192
2-Ketoglutaric acid	placebo progressor	vitamin progressor	0.2199
2-Ketoglutaric acid	vitamin stable	vitamin progressor	0.6183
Glutamic acid	placebo progressor	placebo stable	0.3476
Glutamic acid	placebo progressor	vitamin stable	0.0331
Glutamic acid	placebo progressor	vitamin progressor	0.1358
Glutamic acid	placebo stable	vitamin stable	0.4737
Glutamic acid	placebo stable	vitamin progressor	0.6458
Glutamic acid	vitamin stable	vitamin progressor	0.9612
Succinic acid	placebo progressor	placebo stable	0.2652
Succinic acid	placebo progressor	vitamin stable	0.0097
Succinic acid	placebo progressor	vitamin progressor	0.3804
Succinic acid	placebo stable	vitamin stable	0.1271
Succinic acid	placebo stable	vitamin progressor	0.9920
Succinic acid	vitamin stable	vitamin progressor	0.2043
Glucose	placebo progressor	placebo stable	0.0358
Glucose	placebo progressor	vitamin stable	0.0492
Glucose	placebo progressor	vitamin progressor	0.1621
Glucose	placebo stable	vitamin stable	0.5187
Glucose	placebo stable	vitamin progressor	0.6838
Glucose	vitamin stable	vitamin progressor	0.8848
Malic acid	placebo progressor	vitamin stable	0.0403
Malic acid	placebo progressor	placebo stable	0.4995
Malic acid	placebo progressor	vitamin progressor	0.2112
Malic acid	vitamin stable	placebo stable	0.1750
Malic acid	vitamin stable	vitamin progressor	0.7855
Malic acid	placebo stable	vitamin progressor	0.4239
N-Acetylglutamate	placebo progressor	vitamin stable	0.2045
N-Acetylglutamate	placebo progressor	placebo stable	0.3778
N-Acetylglutamate	placebo progressor	vitamin progressor	0.3011
N-Acetylglutamate	vitamin stable	placebo stable	0.6831
N-Acetylglutamate	vitamin stable	vitamin progressor	0.9842
N-Acetylglutamate	placebo stable	vitamin progressor	0.6848
Glutaric acid	placebo progressor	placebo stable	0.8056
Glutaric acid	placebo progressor	vitamin stable	0.0727

Glutaric acid	placebo progressor	vitamin progressor	0.9891
Glutaric acid	placebo stable	vitamin stable	0.1380
Glutaric acid	placebo stable	vitamin progressor	0.8504
Glutaric acid	vitamin stable	vitamin progressor	0.1390
Lactic acid	placebo progressor	placebo stable	0.4993
Lactic acid	placebo progressor	vitamin stable	0.0670
Lactic acid	placebo progressor	vitamin progressor	0.3424
Lactic acid	placebo stable	vitamin stable	0.1897
Lactic acid	placebo stable	vitamin progressor	0.5384
Lactic acid	vitamin stable	vitamin progressor	0.6871
Pyruvic acid	vitamin stable	placebo stable	0.3635
Pyruvic acid	vitamin stable	placebo progressor	0.2423
Pyruvic acid	vitamin stable	vitamin progressor	0.9134
Pyruvic acid	placebo stable	placebo progressor	0.6954
Pyruvic acid	placebo stable	vitamin progressor	0.5330
Pyruvic acid	placebo progressor	vitamin progressor	0.4765
2-Ketobutyric acid	placebo stable	placebo progressor	0.3326
2-Ketobutyric acid	placebo stable	vitamin stable	0.1647
2-Ketobutyric acid	placebo stable	vitamin progressor	0.8150
2-Ketobutyric acid	placebo progressor	vitamin stable	0.0300
2-Ketobutyric acid	placebo progressor	vitamin progressor	0.3534
2-Ketobutyric acid	vitamin stable	vitamin progressor	0.3477
Quinolinic acid	placebo stable	placebo progressor	0.3338
Quinolinic acid	placebo stable	vitamin stable	0.1245
Quinolinic acid	placebo stable	vitamin progressor	0.9387
Quinolinic acid	placebo progressor	vitamin stable	0.0091
Quinolinic acid	placebo progressor	vitamin progressor	0.3376
Quinolinic acid	vitamin stable	vitamin progressor	0.3020
Glutamine	vitamin stable	placebo stable	0.0232
Glutamine	vitamin stable	placebo progressor	0.0452
Glutamine	vitamin stable	vitamin progressor	0.0476
Glutamine	placebo stable	placebo progressor	0.4978
Glutamine	placebo stable	vitamin progressor	0.7058
Glutamine	placebo progressor	vitamin progressor	0.4270

Supplementary Information – Manuscript 5

The metabolomic differences are primarily associated with B vitamins rather than brain atrophy

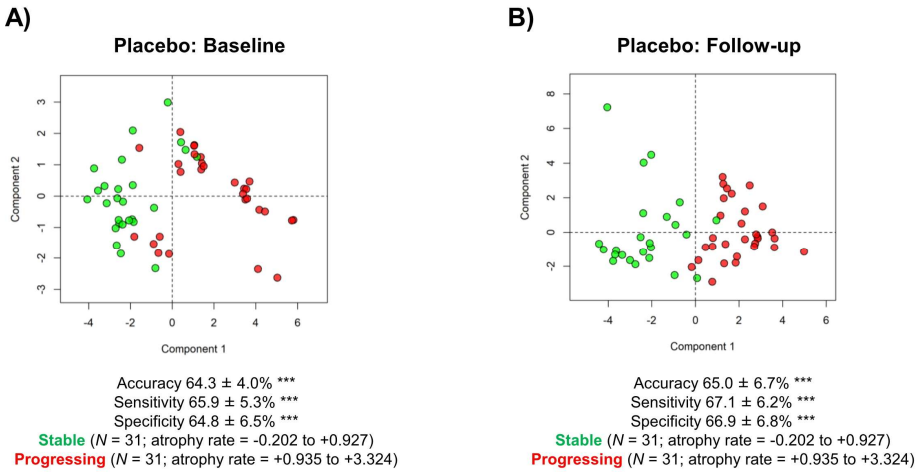

SI Figure 9 OPLS-DA scores plot showing the separation between stable placebo controls (green; $N = 31$; atrophy rate: -0.202 to +0.927) and progressing (worsening) placebo controls (red; $N = 31$; atrophy rate: +0.935 to +3.324) stratified based on the rate of brain atrophy progression. a) baseline samples; b) follow-up samples. The minimal differences in separation suggest that brain atrophy progression has only a limited impact on the metabolome. Consequently, the differences observed in the models presented in the main text (Fig. 1) are predominantly reflective of the treatment effect.

Supplementary Information – Manuscript 5

Pearson correlation analysis for B vitamin treated-individuals with slow rate of brain atrophy progression ("responders to treatment")

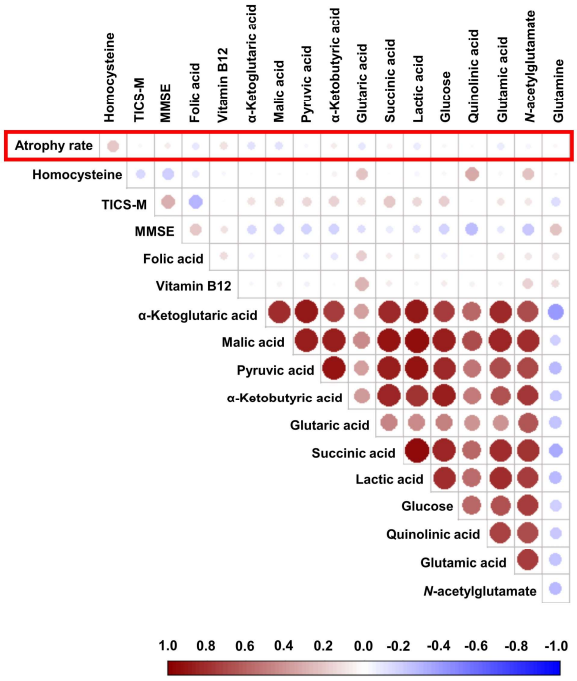

SI Figure 10 Pearson correlation analysis of significantly altered metabolites, homocysteine (total homocysteine), folate, and vitamin B12 (all follow-up levels), atrophy rate (highlighted in the red box), and cognitive test scores (MMSE and TICS-M). The discrepancy between TICS-M and MMSE may be attributed to the higher sensitivity of TICS-M, particularly in mild cognitive impairment (MCI). Data include all compliant individuals with available MRI scans at the follow-up time point who received B vitamins and were characterised by a slow rate of brain atrophy ("stable"; $N = 51$).

Supplementary Information – Manuscript 5

Metabolic pathway analysis reveals B vitamins effects on amino acid and central carbon metabolism

SI Table 10 Results of the metabolic pathway analysis comparing B vitamin-treated individuals and placebo controls, including pathway significance and impact.

Pathway	Total Compounds	Total Hits	Pathway p-value	Pathway impact
Biosynthesis of unsaturated fatty acids	36	2	0.0057	0.0000
Nicotinate and nicotinamide metabolism	15	2	0.0073	0.0000
Fatty acid degradation	33	3	0.0201	0.0000
Glycine, serine and threonine metabolism	21	1	0.0228	0.0000
Pentose metabolism	19	4	0.0313	0.2410
Lipoic acid metabolism	28	2	0.0361	0.0068
Alanine, aspartate and glutamate metabolism	28	6	0.0464	0.5072
Histidine metabolism	16	2	0.0578	0.0000
Glycolysis or Gluconeogenesis	26	3	0.0644	0.0442
Glyoxylate and dicarboxylate metabolism	32	6	0.0683	0.1400
Citrate cycle (TCA cycle)	20	5	0.0811	0.2586
Arginine biosynthesis	14	3	0.0830	0.1223
Galactose metabolism	27	7	0.1119	0.1871
Tyrosine metabolism	42	1	0.1477	0.0000
Pentose and glucuronate interconversions	19	4	0.1477	0.0000
Pyruvate metabolism	23	3	0.2028	0.2197
Arginine and proline metabolism	36	2	0.2671	0.0000
Glycerolipid metabolism	16	1	0.2706	0.0935
Pantothenate and CoA biosynthesis	20	3	0.3443	0.0979
Cysteine and methionine metabolism	33	2	0.3600	0.1785
Glutathione metabolism	28	2	0.3737	0.0268
Ascorbate and aldarate metabolism	9	1	0.4288	0.5238
Inositol phosphate metabolism	30	1	0.4288	0.0000
Tryptophan metabolism	41	1	0.4481	0.0139
Valine, leucine and isoleucine degradation	40	1	0.5563	0.0108
Valine, leucine and isoleucine biosynthesis	8	1	0.5563	0.0000
Fructose and mannose metabolism	20	3	0.6080	0.1308
Propanoate metabolism	22	1	0.6337	0.0000
Neomycin, kanamycin and gentamicin biosynthesis	2	1	0.6561	0.0000
Amino sugar and nucleotide sugar metabolism	42	3	0.6949	0.0637
One carbon pool by folate	26	1	0.7269	0.0449
Purine metabolism	70	1	0.7454	0.0000
Pyrimidine metabolism	39	1	0.8367	0.0399
Starch and sucrose metabolism	18	3	0.8779	0.5601
Butanoate metabolism	15	2	0.8794	0.0000
Taurine and hypotaurine metabolism	8	1	0.9250	0.4286
Primary bile acid biosynthesis	46	1	0.9250	0.0076
Porphyrin metabolism	31	1	0.9398	0.0000
Nitrogen metabolism	6	1	0.9398	0.0000

Chapter 7 Summary, Discussion, and Conclusions

7. 1 Integrated multi-omics strategies for blood-based biomarkers in neurological diseases

This thesis has investigated omics-based approaches, with a particular emphasis on comprehensive multi-platform metabolomics, method development, and their application to enhance diagnostic accuracy, prognostic modelling, and therapeutic monitoring in neurological disease. In addition to clinical applications, considerable emphasis was placed on methodological optimisation, particularly in developing robust, reproducible sample preparation protocols that are compatible with limited-volume serum and/or plasma specimens and suitable for multi-platform analytical workflows (**Chapters 2 and 3**). High-resolution NMR spectroscopy and LC-MS were employed in parallel to achieve complementary metabolome coverage, facilitating more comprehensive biomarker discovery across a spectrum of neurological conditions, including multiple sclerosis, Ab-mediated demyelinating diseases, and MCI. By applying untargeted metabolomic, lipidomic, and glycomic profiling alongside targeted proteomic markers across diverse, well-characterised patient cohorts, this work demonstrates how integrated multi-omics approaches can enhance the identification of disease-associated metabolic signatures, provide mechanistic insight into processes such as neuroinflammation and neurodegeneration, predict disease trajectory, and inform the development of scalable, serum-based tools for precision medicine.

The studies presented in this thesis build on a strong foundation of preclinical and clinical metabolomics research at the University of Oxford, extending prior in *vitro*[1, 2], *in vivo,*[3-5] and cohort-based studies[6-11] through the development and application of integrated multi-omics approaches. Given the complexity of human cohorts, sample preparation and analytical protocols (**Chapters 2 and 3**) were optimised to improve signal quality and enable detection of subtle metabolic changes linked to disease progression.[12-15]

A key contribution of this work was the demonstration that integrating complementary omics platforms can improve analytical resolution and deepen biological interpretation, consistent with findings from the Wishart group.[16, 17] This integration was achieved through both coordinated (direct) and sequential (indirect) strategies. Coordinated integration refers to the parallel analysis of the same samples across platforms. For example, in the extreme-phenotype multiple sclerosis cohort, NMR metabolomics was combined with

protein biomarker data to improve prognostic modelling (**Chapter 4**), while in the VITACOG MCI study, a fully integrated multiplatform metabolomics workflow was applied, using both NMR and LC-MS (**Chapter 6**). In contrast, sequential integration involves follow-up analyses informed by initial findings from a single platform. This is illustrated by the Oxford glycomics cohort,[18] where an NMR-identified signal (GlycA) was subsequently explored using a semi-targeted LC-MS glycomics approach to elucidate its structural basis and diagnostic relevance (**Chapter 5**).

Finally, to translate these analytical advances into clinically relevant insights, integrated omics analyses were combined with multivariate statistics and ML throughout the thesis (**Chapters 4-6**). Emphasis was placed on harmonising data processing and integrating clinical, biochemical, and omics variables to support robust biomarker discovery and translational analysis.

7. 2 Sample preparation and platform compatibility optimisation (Chapters 2 and 3)

The first two experimental chapters (**Chapter 2 and 3**) focused on the systematic optimisation of sample preparation workflows to enable reproducible, multi-platform metabolomics from restricted serum or plasma volumes. A key outcome was the demonstration that NMR-prepared samples - using deuterated aqueous solvents and phosphate buffering salts - can be efficiently reprocessed for LC-MS analysis with minimal modification. Importantly, no deuterium incorporation was detected in LC-MS data, and only minor metabolite alterations were associated with the phosphate buffer (**Chapter 2**).[19]

Building on these findings, the next chapter evaluated LC-MS extraction protocols, demonstrating that IC-MS profiling of polar and ionic metabolites is largely unaffected by protein removal;[2] however, sample filtration is recommended to minimise suppressor degradation from concentrated biological matrices.[20] In contrast, RPLC-MS workflows targeting less polar metabolites showed substantial loss of hydrophobic compounds after protein removal, consistent with findings from the Vuckovic group.[21] Less disruptive depletion methods may therefore be more appropriate, particularly given the higher protein tolerance of standard C18 and BEH silica columns commonly used in SFC and high-resolution LC separations.[22]

To further optimise extraction performance across platforms, several solvent systems were systematically evaluated. MeCN-based protein precipitation was found to be the most effective for reducing total protein

content while maintaining compatibility with RPLC, HILIC, SFC, and IC systems. However, MeCN-based protocols, particularly in RPLC-MS using positive ionisation, displayed poor reproducibility. To address this, a modified extraction approach was proposed, in which samples were pre-treated with formic acid to achieve 1% formate ion concentration prior to MeCN addition (Fig. 7.1). This strategy improved extraction reproducibility and enhanced the recovery of cationic metabolites (**Chapter 3**).

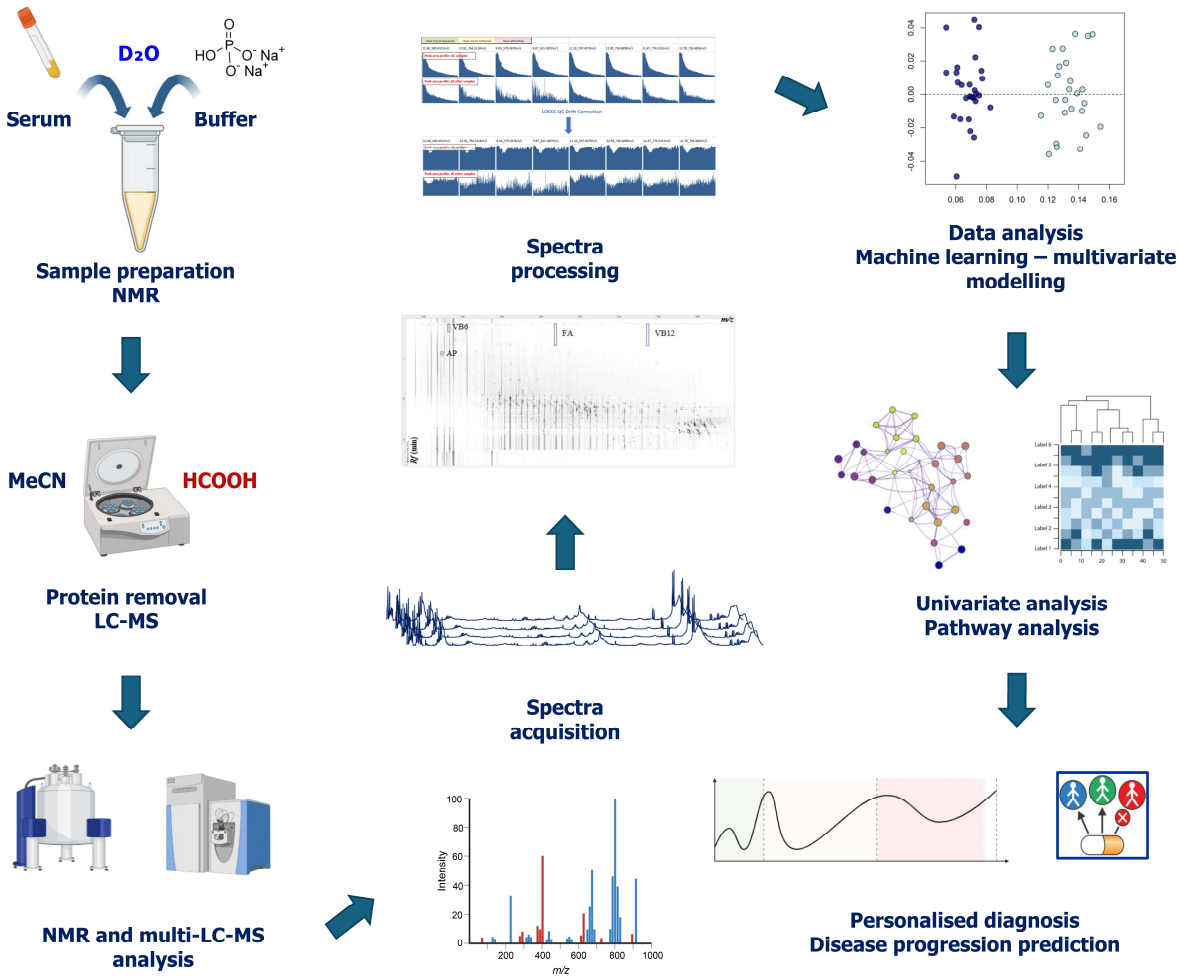

Figure 7.1. Overview of the analytical and data integration workflow. Developed in **Chapters 2 and 3** and applied to clinical cohorts in **Chapters 4–6**, the workflow combines NMR and LC-MS metabolomics for biomarker discovery and disease stratification. Serum samples were initially prepared for NMR analysis via the addition of deuterated phosphate buffer. Following NMR spectral acquisition, the same samples underwent protein removal and were reprocessed for multi-platform LC-MS analysis. For RPLC-MS specifically, acetonitrile-based protein precipitation - without mechanical filtration - enabled a more representative capture of the metabolome. Additionally, pre-treatment with formic acid significantly improved extraction reproducibility. After NMR and LC-MS data acquisition and processing, spectral bins and compound-features were used for multivariate modelling. Metabolites identified as discriminatory were further subjected to univariate testing and pathway enrichment analysis. Integrating multiple omics platforms within this workflow improved the performance of diagnostic and prognostic models.

Importantly, the optimised workflow improved reproducibility in test serum and plasma samples and increased classification accuracy in supervised multivariate diagnostic models, as demonstrated in two

independent human cohorts: OPTIMA and VITACOG (**Chapter 3**).[23, 24] Furthermore, the robustness and versatility of these optimised protocols (Fig. 7.1) were demonstrated by their successful application across multiple studies, including the VITACOG cohort (**Chapter 6**), the OPTIMA cohort (AD vs. VaD discrimination in early cognitive impairment, data not included), and a subset of the Oxford MS cohort, where they were used to evaluate metabolic effects of dimethyl fumarate (DMF) treatment compared to individuals not receiving disease-modifying therapies (non-DMT), in collaboration with the Schofield group at the University of Oxford.

7. 3 Development and validation of a reproducible multi-omics data analysis pipeline

Following optimisation of the sample preparation protocols, a robust and reproducible clinical metabolomics data analysis pipeline was established to support downstream interpretation (Fig. 7.1). This was particularly critical given the complexity of the human cohorts analysed in this work, many of which featured substantial clinical heterogeneity and comorbidities that could confound disease-specific metabolic signatures.[14]

Throughout this thesis, internal cross-validation was performed using stratified pseudo-random sampling, as outlined in **Chapter 1**.[25] Where feasible, external validation was conducted via cross-cohort comparisons to ensure model generalisability. Moreover, to minimise technical variability and account for sample quality, all datasets underwent standardised pre-processing and rigorous quality control procedures to ensure data integrity. Feature selection and biomarker refinement were guided by ML-based optimisation strategies. To improve model robustness and minimise overfitting, several classification algorithms - including random forest, elastic net regression, OPLS-DA, and logistic regression - were evaluated using stratified cross-validation. Predictive models incorporating multi-omics features were evaluated using standard performance metrics, including accuracy, sensitivity, specificity, and ROC AUC. Model performance was further validated through permutation testing and comparison across algorithmic outputs.

Biomarkers were evaluated both individually and within multivariate signatures, with discriminatory power assessed using variable importance in projection (VIP) scores and random forest-based rankings. Diagnostic models reaching ROC AUC values ≥ 0.82 were considered clinically relevant, in line with thresholds for translational utility (**Chapter 4**).[26] External validation, particularly within the multiple sclerosis cohorts,

confirmed reproducibility and identified complementary markers characterised by either high sensitivity or specificity, further supporting the clinical potential of the multi-omics strategy.

7. 4 Multi-omics biomarkers of disability progression in multiple sclerosis (Chapter 4)

The extreme-phenotype multiple sclerosis cohort, described in **Chapter 4**, employed a multi-omics approach to investigate biomarkers of disease progression.[27] Specifically, NMR-based metabolomics was used to profile a broad range of circulating small molecules - such as amino acids, sugars, and lipoprotein-associated lipid signals (HDLs and LDLs subclasses) - alongside targeted serum proteomics, measuring GFAP and NfL. The study focused on the predictive capacity of baseline serum samples, irrespective of clinical phenotype, aiming to identify metabolic signatures associated with disease progression.

Although the cohort size was modest (18 progressors vs. 19 stable individuals), the well-preserved longitudinal dataset provided a rare opportunity to investigate metabolic signatures specifically associated with disease progression.[27] This reflects a broader shift in multiple sclerosis research,[28, 29] which is moving beyond traditional phenotype-based classifications and conventional metrics such as EDSS or MRI lesion load,[28, 30] toward more sensitive, minimally invasive biomarkers. Recent efforts, particularly by the Kuhle group and others, have focused on blood-based protein markers including NfL, GFAP,[27, 31-33] CHI3L1,[34] neuron-specific enolase (NSE), and chemokine ligand 13 (CXCL13).[35, 36] While these markers provide valuable information on neuroaxonal damage and inflammation, metabolomics offers a complementary layer of insight by capturing broader, dynamic changes in biochemical pathways and may further improve the sensitivity and specificity of progression monitoring in multiple sclerosis.

In the analysis presented in **Chapter 4**, several metabolites previously associated with RRMS-SPMS classification, such as valine, LDLs, and HDLs,[10, 25, 37] also demonstrated predictive value in a progression-focused model. In addition, novel metabolites more closely linked to disability worsening rather than disease stage, such as alanine and glutamine, were identified. Importantly, these findings, initially derived from the Swiss multiple sclerosis cohort, were successfully validated in an independent British multiple sclerosis cohort, further supporting their generalisability.

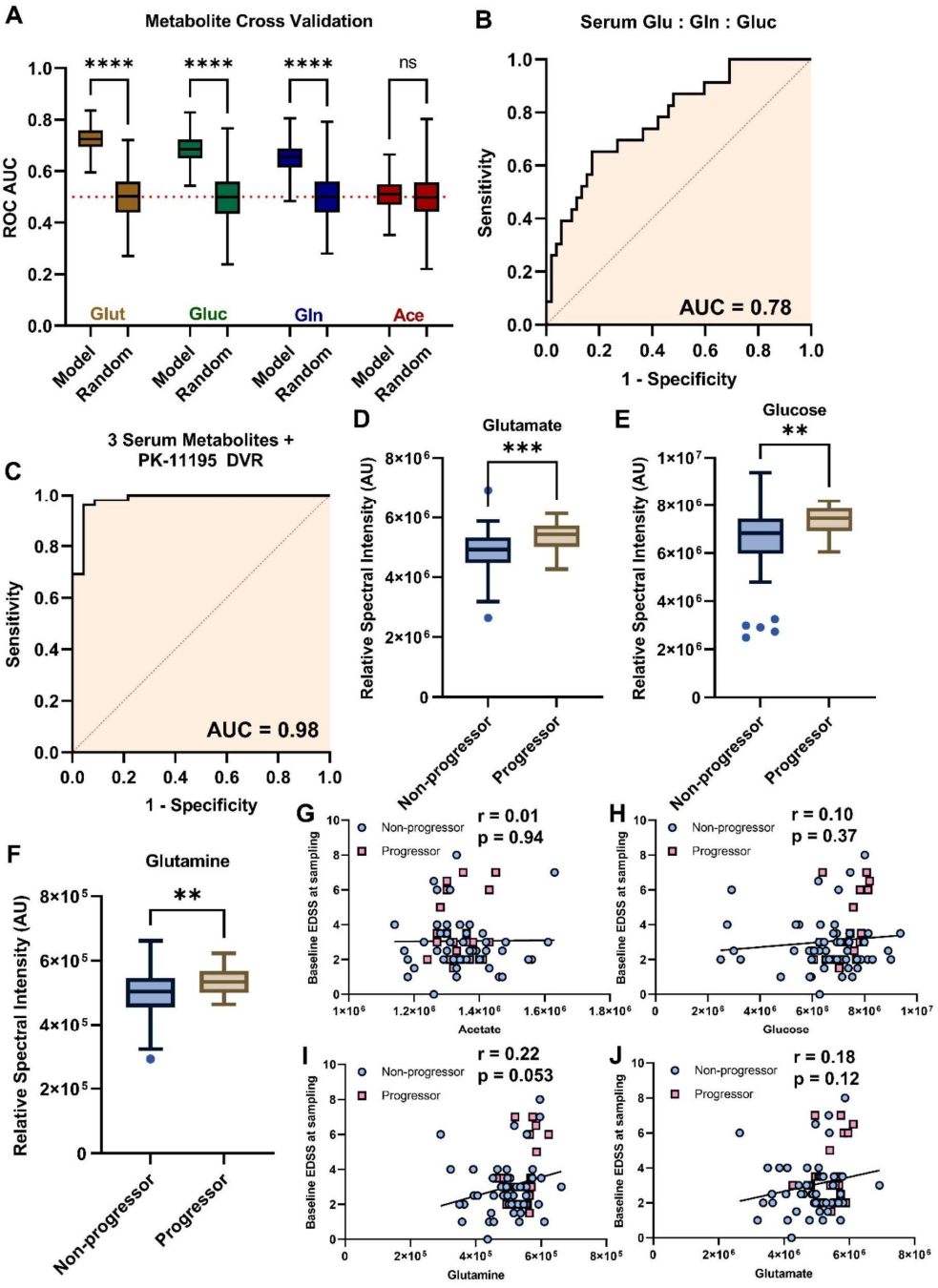

Figure 7.2. Integration of TSPO-PET and NMR metabolomics for predicting MS progression. Serum metabolites (glutamate, glucose, and glutamine) were highly predictive of future disease progression, defined as a confirmed increase in EDSS score of ≥0.5 over one year. Their predictive performance was further enhanced when integrated with TSPO-PET imaging data. **(A)** Cross-validated classification accuracy of glutamate, glucose, glutamine, and acetate for predicting progression status. Performance was assessed using 2-fold cross-validation, repeated 500 times with stratified class matching. The reported AUC reflects the mean performance across all runs, with significance evaluated against permuted data using unpaired *t*-tests. The four metabolites were selected based on their variable importance in projection (VIP) scores from a multivariable model (OPLS-DA). All, except for acetate, demonstrated significant predictive potential, outperforming randomly permuted models. **(B)** ROC curve for the combined three-metabolite model, and **(C)** ROC curve for the combined metabolite model integrated with ^{11}C-PK11195 TSPO-PET data. **(D–F)** Serum levels of glutamate, glucose, and glutamine in progressors versus non-progressors, showing significant group separation. **(G–J)** Pearson correlation between baseline EDSS and serum levels of acetate, glucose, glutamine, and glutamate. ** p <0.01, *** p <0.001, **** p <0.0001. Figure reproduced with permission from Reference [38], where the author contributed as a co-author.[38]

Building on this work, a parallel study integrated TSPO-PET imaging, primarily reflecting microglial activation, with NMR-based serum metabolomics in 87 MS patients from a Finnish cohort.[38] In this study, progression was defined as a confirmed ≥ 0.5-point increase in EDSS over one year, indicating clinically meaningful disability worsening within a relatively short interval. Three serum metabolites - glutamate, glutamine, and glucose (Fig. 7.2A) - were significantly associated with future progression and predicted outcomes with similar accuracy to TSPO-PET imaging alone (AUC = 0.78; $p = 0.0001$; Fig. 7.2B), further supporting key findings from **Chapter 4**. Notably, combining these three metabolites with TSPO-PET imaging substantially improved predictive performance (AUC = 0.98; $p < 0.0001$; Fig. 7.2C), highlighting the added value of integrating blood-based and imaging biomarkers.[38]

These results further underscore the scalability and affordability of NMR as a practical tool for personalised disease monitoring. Consistent with previous studies,[10, 39] the findings support its utility for patient stratification in clinical trials. Notably, several metabolites associated with progression - particularly glutamine and glucose - were identified across three independent cohorts in Switzerland, the UK, and Finland. This convergence across distinct populations and complementary methodologies strengthens the case for their adoption as robust, translational biomarkers of MS progression.

7. 5 *N*-Glycomics discriminates between MS and Ab-defined demyelinating disorders (Chapter 5)

Following the investigation of progression markers in multiple sclerosis (**Chapter 4**), the next stage of this work focused on early disease classification. Distinguishing multiple sclerosis from Ab-defined disorders such as AQP4-Ab NMOSD and MOGAD remains a significant clinical challenge, especially in cases where imaging and serological findings are inconclusive.[40] Expanding on diagnostic signals identified by NMR metabolomics, particularly the inflammation-associated GlycA peak,[18] LC-MS-based glycomics was employed to directly characterise plasma *N*-glycan structures (**Chapter 5**).

This approach demonstrated that distinct glycan signatures could accurately differentiate multiple sclerosis from Ab-mediated diseases, a clinically important distinction for guiding treatment decisions. While Cvetko *et al.* previously reported glycomic differences between multiple sclerosis and healthy individuals,[41] this is, to our knowledge, the first study to apply glycomics for distinguishing NMOSD from other demyelinating

disorders. By expanding from metabolomics to glycomics, the study moved beyond signal-based discrimination toward structural characterisation, enhancing diagnostic specificity. This complementary use of orthogonal platforms underscored the value of multi-omics integration in advancing both mechanistic insight and diagnostic accuracy in complex neurological disorders.

Although the glycomics analysis yielded promising diagnostic insights, it was conducted as an initial collaborative study with Ludger Ltd., and external validation was not yet available. Replication in an independent dataset will therefore be critical to confirm the reproducibility and diagnostic value of the identified glycan features. Importantly, the GlycA signal, initially identified via NMR, has also been implicated in other inflammatory and neurodegenerative conditions,[42-44] reinforcing the broader potential of integrated metabolomics and glycomics for cross-disease biomarker discovery.

Since LC-MS-based glycomics does not provide information on the protein carriers of glycan structures, integration with complementary glycoproteomic approaches would enable site-specific mapping of glycan alterations to individual proteins, thereby improving mechanistic interpretation and diagnostic specificity, as demonstrated in the work of the Bertozzi group.[45] Despite this limitation, the glycomics findings complement the progression-focused studies discussed earlier and further illustrate how targeted molecular profiling can advance precision medicine in neurological disorders.

7.6 Monitoring treatment response in MCI using a multi-omics approach (Chapter 6)

In the final research chapter, methodological advances from earlier multiple sclerosis studies were applied to a new clinical context - cognitive impairment as an early feature of AD and related neurodegenerative disorders. Cognitive impairment represents a growing clinical and societal burden, yet current diagnostic tools are constrained by invasiveness, high cost, limited accessibility, and suboptimal accuracy.[24, 46] The early detection of neurodegenerative disorders, including AD, VaD, and LBD, is further complicated by their gradual and heterogeneous onset.[47, 48] Clinical differentiation between these conditions is difficult due to overlapping features and a lack of reliable, accessible biomarkers capable of predicting progression or guiding long-term management.[48] Moreover, the scarcity of effective therapeutic options reinforces the need for molecular tools that support routine monitoring and disease stratification.

While most metabolomics studies in AD have employed LC-MS, its pathway-specific constraints highlight the value of an integrated, multi-platform omics approach.[49] To address these limitations, a comprehensive analysis was conducted using biobanked samples from the VITACOG trial - a double-blind, placebo-controlled study that monitored individuals with MCI over a two-year period (**Chapter 6**).[24] All participants entered the study with baseline MMSE scores ≥27, ensuring a well-characterised early-stage MCI population. Approximately 125 participants underwent serial MRI over two years, providing a framework to assess neurodegenerative biomarkers.[24, 50] Nevertheless, the trial primarily aimed to evaluate the effects of B vitamin supplementation on cognitive decline and brain atrophy. Earlier findings from the VITACOG trial, led by Prof. A. D. Smith, demonstrated that B vitamin treatment reduced circulating tHcy levels and significantly slowed the rate of brain atrophy progression.[24, 51] While these results support a neuroprotective role for B vitamins, some studies have questioned their broader efficacy in general populations,[52] indicating that further research is needed to clarify the underlying mechanisms and identify those most likely to benefit. A multi-platform untargeted metabolomics strategy, combining NMR, RPLC-MS, and AEC-MS, was therefore applied to characterise systemic metabolic changes associated with B vitamin supplementation (**Chapter 6**). The analysis revealed broad metabolic reprogramming, including reduced circulating glucose, altered TCA cycle intermediates, and modulation of the kynurenine pathway, offering mechanistic insights into how B vitamin-induced tHcy reduction may confer neuroprotection and support their potential as adjunctive therapy in MCI.

Furthermore, this study provided a proof-of-concept for the integrated multi-platform workflow developed in **Chapters 2 and 3**. While the preceding multiple sclerosis cohorts (**Chapters 4 and 5**) integrated multiple biomarker modalities, such as NMR with proteomic or imaging data, the VITACOG study highlighted the analytical efficiency and diagnostic utility of a streamlined, multi-platform metabolomics approach. In VITACOG (**Chapter 6**), NMR spectroscopy was combined with both RPLC-MS and AEC-MS to achieve broad metabolome coverage from limited serum volume (**Chapter 2**).[19] AEC-MS effectively captured B vitamin-related metabolic changes, while NMR performed comparably to RPLC-MS in modelling atrophy rate, highlighting the complementary strengths of each platform across biological contexts.

Together, these findings demonstrate the robustness and adaptability of the optimised workflow and support its broader application across neurodegenerative diseases. The same approach could be extended to

additional cohorts, such as OPTIMA, or applied to other neurological conditions where scalable, blood-based biomarkers remain unmet needs. Alternatively, drawing on the integrated design of the extreme-phenotype multiple sclerosis study, existing MCI metabolomics datasets (VITACOG, OPTIMA) could be further enriched with proteomic, lipidomic, or imaging data to improve predictive performance. Overall, the results not only underscore the feasibility of multi-omics profiling in cognitive impairment, but also establish a flexible and transferrable model for precision medicine across the neurodegenerative disease spectrum.

7. 7 Future directions

7. 7. 1 Scaling multi-omics for early diagnosis and progression modelling

The multi-platform omics workflows developed in this thesis establish a robust foundation for broader application across neurological disorders. The next phase of work should prioritise the validation and refinement of these methods in larger, more heterogeneous clinical cohorts, with the aim of developing scalable, clinically relevant tools for early disease detection and patient stratification.

Within the context of cohorts introduced in this thesis, a key opportunity lies in extending the analysis to the full Oxford multiple sclerosis cohort ($n \sim 700$),[10] thereby enhancing the progression models established in **Chapter 4**. Building on the extreme-phenotype subset used for model validation in the Swiss multiple sclerosis cohort, which focused on individuals with clearly stable or progressive disease, analysis of the full Oxford dataset could enhance model generalisability and facilitate the identification of subtler metabolic signatures associated with disease progression.

Similarly, the OPTIMA study offers a uniquely valuable resource for expanding these approaches. Founded in 1988, OPTIMA is among the very few longitudinal studies of ageing and memory to combine detailed clinical, neuroimaging, and *post-mortem* pathological data.[23, 53] With over 80% of participants donating their brains for autopsy, the cohort provides neuropathologically confirmed diagnoses across AD, VaD, and cognitively healthy controls.[53] Approximately 200 prodromal serum samples, collected prior to the onset of clinical dementia, are available and present a rare opportunity to investigate disease-specific metabolic alterations. This dataset could be used to develop early diagnostic models - such as discriminating between AD and VaD - or, following the approach used in the Swiss multiple sclerosis cohort, to model long-term progression. Moreover, since the OPTIMA cohort includes multiple MCI individuals with well-characterised

trajectories, findings could be externally validated using the placebo arm of the VITACOG trial, avoiding confounding effects from B vitamin supplementation. Such cross-validation would strengthen the clinical relevance of the biomarkers identified in this thesis for neurodegenerative disease research.

7. 7. 2 Future research will integrate metabolomics and proteomics for early stratification and progression modelling in AD

With a validated multi-omics framework in place, future research is well positioned to address major unresolved questions in neurology. Building on the successful application of integrative metabolomics and proteomics to multiple sclerosis, there is substantial potential to extend this approach to stratified AD cohorts. Such efforts could improve early-stage prediction, facilitate more accurate risk profiling, and support the development of personalised prevention strategies. As shown in the Swiss multiple sclerosis cohort, combining small-molecule metabolite profiles with protein biomarkers, such as GFAP and NfL, markedly enhances the predictive accuracy of progression models. In the context of AD, GFAP reflects astrocytic activation and neuroinflammation,[50] while NfL serves as a sensitive indicator of axonal injury;[54] both are measurable in serum or CSF and are known to be elevated during early neurodegenerative changes.

Additional protein candidates such as soluble TREM2 (sTREM2) and CHI3L1, associated with microglial activation and cognitive decline, may further strengthen predictive models. Core AD pathology can also be captured through tau-related markers, including phosphorylated tau isoforms (pTau181, pTau217, and pTau231), which reflect downstream neurofibrillary tangle formation and have demonstrated predictive value in several recent studies.[55-57] Similarly, the Aβ42/Aβ40 ratio, as reported by Trelle *et al*., is considered a reliable surrogate marker of early amyloid accumulation.[58] These markers are readily quantifiable using ultrasensitive immunoassay platforms such as Simoa,[59] enabling their integration into multi-omics pipelines alongside NMR and LC-MS-based metabolomics. Together, these tools offer a practical and scalable means of developing robust multivariate models for disease stratification and progression monitoring in AD.

7.7.3 Expanding platform coverage: lipidomics and proteomics integration

Given recent advances in high-throughput analytical platforms, future work could expand beyond current methods by incorporating additional LC-MS modalities. For instance, optimising RPLC-MS or implementing SFC-MS could enable targeted lipidomics, facilitating the detection of ceramides, phosphatidylcholines, and steroid hormones.[60] These lipid classes are increasingly implicated in neurological

diseases, as demonstrated by recent findings from Huynh *et al.*[61] and Kim *et al.*,[62] and their inclusion may therefore enhance the diagnostic sensitivity of existing models.

Similarly, HILIC-MS would complement the IC-MS system already employed in this thesis (Fig. 7.3). HILIC-MS is particularly suited for detecting small, polar compounds such as low-abundance amino acids, bile acids, and acylcarnitines - molecules that are poorly retained on RPLC or IC columns but have been implicated in AD-related mitochondrial dysfunction and lipid metabolic dysregulation.[63]

In parallel, expanding the proteomic dimension would further enrich the multi-omics pipeline. While immunoassay-based platforms such as Simoa provide high-sensitivity quantification of known protein markers, untargeted proteomics via nano-flow LC-MS-based bottom-up workflows offers the potential to identify broader, discovery-level protein alterations (Fig. 7.3).[64] Moreover, integrating metabolomics and proteomics datasets into joint pathway analysis can enhance the detection of disease signatures by increasing both diagnostic specificity and mechanistic insight.[65]

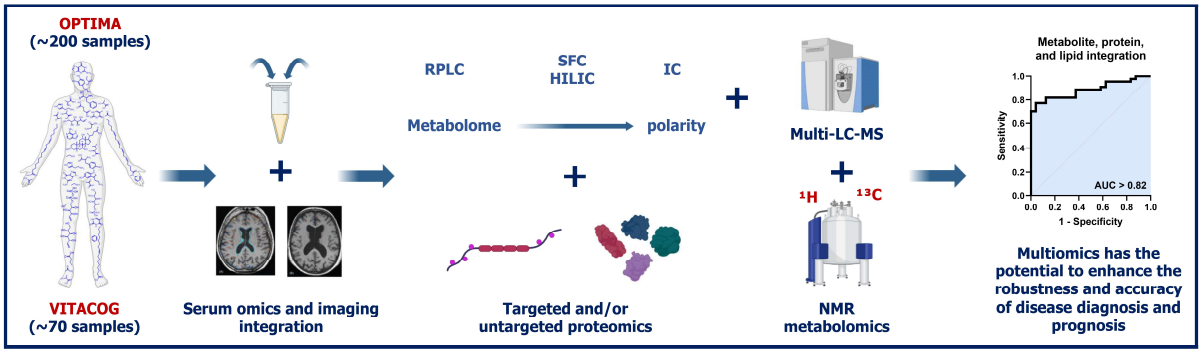

Figure 7.3. Future potential of integrative multi-omics approaches for disease diagnosis and prognosis. Building on the methodology developed in this thesis, serum samples from the VITACOG and OPTIMA cohorts can be analysed using a multi-omics strategy that integrates neuroimaging, NMR metabolomics, multi-platform LC-MS (RPLC, SFC, HILIC, IC), and targeted or untargeted proteomics. This comprehensive framework enables broad biochemical coverage and supports the construction of robust diagnostic and prognostic models (AUC > 0.82). The integration of metabolic, proteomic, and imaging data demonstrates the potential of multi-omics to improve diagnostic precision and inform personalised healthcare in neurodegenerative disease.

Notably, some of these multi-omics directions are already being explored. Pilot experiments using bottom-up proteomics are underway in a subset of the VITACOG cohort to evaluate protein changes associated with B vitamin supplementation and tHcy reduction. Additionally, the OPTIMA cohort is now being processed using the optimised multi-platform metabolomics pipeline, alongside high-throughput lipidomics. While these results are not included in the current thesis, they represent a direct extension of its methodologies and set the stage for a next generation of multi-omics applications in neurological disease research.

7. 8 Concluding remarks

This thesis demonstrates that an integrated multi-omics approach can support both mechanistic discovery and the development of clinically relevant biomarkers in neurological disease. By combining NMR and LC-MS metabolomics, this work enabled reproducible, high-resolution profiling from limited-volume clinical samples. The use of complementary platforms enhanced biomarker discovery, while the inclusion of additional omics modalities - such as proteomics, glycomics, and neuroimaging - extended the analysis beyond classification alone. This integrative strategy provided new insights into disease mechanisms and treatment response, supporting a systems-level understanding of neurological disorders with clear implications for early diagnosis and personalised intervention.

A central contribution of this work has been to show that multi-platform integration is not merely additive, but potentially transformative. Through the combination of complementary biochemical readouts and advanced multivariate modelling, I was able to capture complex, dynamic features of disease that would likely remain undetectable using single-modality approaches alone. Rather than focusing solely on isolated biomarker discovery, this thesis contributes to the development of integrated, hypothesis-driven multi-omics pipelines, capable of supporting early intervention, precise disease stratification, and personalised therapeutic strategies.

Taken together, the methodological and analytical advances developed throughout this research provide a foundation for future efforts to better understand the biological mechanisms and clinical progression of neurological disorders. By enabling integrated, high-resolution analysis of small-volume serum and plasma samples, this work establishes a practical foundation for the development of translatable biomarkers and robust patient stratification tools.

7. 9 References

(1) Reinbold, R.; Hvinden, I. C.; Rabe, P.; Herold, R. A.; Finch, A.; Wood, J.; Morgan, M.; Staudt, M.; Clifton, I. J.; Armstrong, F. A.; et al. Resistance to the isocitrate dehydrogenase 1 mutant inhibitor ivosidenib can be overcome by alternative dimer-interface binding inhibitors. *Nat Commun* **2022**, *13* (1). DOI: ARTN 478510.1038/s41467-022-32436-4.

(2) Walsby-Tickle, J.; Gannon, J.; Hvinden, I.; Bardella, C.; Abboud, M. I.; Nazeer, A.; Hauton, D.; Pires, E.; Cadoux-Hudson, T.; Schofield, C. J.; et al. Anion-exchange chromatography mass spectrometry provides extensive coverage of primary metabolic pathways revealing altered metabolism in IDH1 mutant cells. *Commun Biol* **2020**, *3* (1), 247. DOI: 10.1038/s42003-020-0957-6 From NLM Medline.

(3) Dunstan, I. K.; McLeod, R.; Radford-Smith, D. E.; Xiong, W.; Pate, T.; Probert, F.; Anthony, D. C. Unique pathways downstream of TLR-4 and TLR-7 activation: sex-dependent behavioural, cytokine, and metabolic consequences. *Front Cell Neurosci* **2024**, *18*, 1345441. DOI: 10.3389/fncel.2024.1345441 From NLM PubMed-not-MEDLINE.

(4) Radford-Smith, D. E.; Yates, A. G.; Rizvi, L.; Anthony, D. C.; Probert, F. HDL and LDL have distinct, opposing effects on LPS-induced brain inflammation. *Lipids Health Dis* **2023**, *22* (1), 54. DOI: 10.1186/s12944-023-01817-z From NLM Medline.

(5) Yeo, T.; Bayuangga, H.; Augusto-Oliveira, M.; Sealey, M.; Claridge, T. D. W.; Tanner, R.; Leppert, D.; Palace, J.; Kuhle, J.; Probert, F.; et al. Metabolomics detects clinically silent neuroinflammatory lesions earlier than neurofilament-light chain in a focal multiple sclerosis animal model. *J Neuroinflammation* **2022**, *19* (1), 252. DOI: 10.1186/s12974-022-02614-8 From NLM Medline.

(6) Lennox, B.; Xiong, W.; Waters, P.; Coles, A.; Jones, P. B.; Yeo, T.; May, J. T. M.; Yeeles, K.; Anthony, D.; Probert, F. The serum metabolomic profile of a distinct, inflammatory subtype of acute psychosis. *Mol Psychiatry* **2022**, *27* (11), 4722-4730. DOI: 10.1038/s41380-022-01784-4 From NLM Medline.

(7) Probert, F.; Yeo, T.; Zhou, Y.; Sealey, M.; Arora, S.; Palace, J.; Claridge, T. D. W.; Hillenbrand, R.; Oechtering, J.; Leppert, D.; et al. Integrative biochemical, proteomics and metabolomics cerebrospinal fluid biomarkers predict clinical conversion to multiple sclerosis. *Brain Commun* **2021**, *3* (2), fcab084. DOI: 10.1093/braincomms/fcab084 From NLM PubMed-not-MEDLINE.

(8) Radford-Smith, D. E.; Anthony, D. C.; Benz, F.; Grist, J. T.; Lyman, M.; Miller, J. J.; Probert, F. A multivariate blood metabolite algorithm stably predicts risk and resilience to major depressive disorder in the general population. *Ebiomedicine* **2023**, *93*, 104643. DOI: 10.1016/j.ebiom.2023.104643 From NLM Medline.

(9) Xiong, W.; Yeo, T.; May, J. T. M.; Demmers, T.; Ceronie, B.; Ramesh, A.; McGinty, R. N.; Michael, S.; Torzillo, E.; Sen, A.; et al. Distinct plasma metabolomic signatures differentiate autoimmune encephalitis from drug-resistant epilepsy. *Ann Clin Transl Neurol* **2024**, *11* (7), 1897-1908. DOI: 10.1002/acn3.52112 From NLM Medline.

(10) Yeo, T.; Probert, F.; Sealey, M.; Saldana, L.; Geraldes, R.; Hoeckner, S.; Schiffer, E.; Claridge, T. D. W.; Leppert, D.; DeLuca, G.; et al. Objective biomarkers for clinical relapse in multiple sclerosis: a metabolomics approach. *Brain Commun* **2021**, *3* (4), fcab240. DOI: 10.1093/braincomms/fcab240 From NLM PubMed-not-MEDLINE.

(11) Yeo, T.; Probert, F.; Sealey, M.; Saldana, L.; Geraldes, R.; Höckner, S.; Schiffer, E.; Claridge, T. D. W.; Leppert, D.; DeLuca, G.; et al. Objective Biomarkers for Clinical Relapse in Multiple Sclerosis: A Metabolomics Approach (vol 3, 240, 2021). *Brain Communications* **2021**, *3* (4). DOI: ARTN 28310.1093/braincomms/fcab283.

(12) Boernsen, K. O.; Gatzek, S.; Imbert, G. Controlled protein precipitation in combination with chip-based nanospray infusion mass spectrometry. An approach for metabolomics profiling of plasma. *Anal Chem* **2005**, *77* (22), 7255-7264. DOI: 10.1021/ac0508604.

(13) Bruce, S. J.; Tavazzi, I.; Parisod, V.; Rezzi, S.; Kochhar, S.; Guy, P. A. Investigation of Human Blood Plasma Sample Preparation for Performing Metabolomics Using Ultrahigh Performance Liquid Chromatography/Mass Spectrometry. *Anal Chem* **2009**, *81* (9), 3285-3296. DOI: 10.1021/ac8024569.

(14) Dunn, W. B.; Broadhurst, D.; Begley, P.; Zelena, E.; Francis-McIntyre, S.; Anderson, N.; Brown, M.; Knowles, J. D.; Halsall, A.; Haselden, J. N.; et al. Procedures for large-scale metabolic profiling of serum and plasma using gas chromatography and liquid chromatography coupled to mass spectrometry. *Nat Protoc* **2011**, *6* (7), 1060-1083. DOI: 10.1038/nprot.2011.335 From NLM Medline.

(15) Southam, A. D.; Haglington, L. D.; Najdekr, L.; Jankevics, A.; Weber, R. J. M.; Dunn, W. B. Assessment of human plasma and urine sample preparation for reproducible and high-throughput UHPLC-MS clinical metabolic phenotyping. *Analyst* **2020**, *145* (20), 6511-6523. DOI: 10.1039/d0an01319f.

(16) Psychogios, N.; Hau, D. D.; Peng, J.; Guo, A. C.; Mandal, R.; Bouatra, S.; Sinelnikov, I.; Krishnamurthy, R.; Eisner, R.; Gautam, B.; et al. The human serum metabolome. *Plos One* **2011**, *6* (2), e16957. DOI: 10.1371/journal.pone.0016957 From NLM Medline.

(17) Wishart, D. S.; Cheng, L. L.; Copie, V.; Edison, A. S.; Eghbalnia, H. R.; Hoch, J. C.; Gouveia, G. J.; Pathmasiri, W.; Powers, R.; Schock, T. B.; et al. NMR and Metabolomics-A Roadmap for the Future. *Metabolites* **2022**, *12* (8). DOI: ARTN 67810.3390/metabo12080678.
(18) Jurynczyk, M.; Probert, F.; Yeo, T.; Tackley, G.; Claridge, T. D. W.; Cavey, A.; Woodhall, M. R.; Arora, S.; Winkler, T.; Schiffer, E.; et al. Metabolomics reveals distinct, antibody-independent, molecular signatures of MS, AQP4-antibody and MOG-antibody disease. *Acta Neuropathol Com* **2017**, *5*. DOI: ARTN 9510.1186/s40478-017-0495-8.
(19) Kacerova, T.; Pires, E.; Walsby-Tickle, J.; Probert, F.; McCullagh, J. S. O. Integrating NMR and Multi-LC-MS-Based Untargeted Metabolomics for Comprehensive Analysis of Blood Serum Samples. *Anal Chim Acta* **2025**, *1356*. DOI: 10.1016/j.aca.2025.343979.
(20) Ngere, J. B.; Ebrahimi, K. H.; Williams, R.; Pires, E.; Walsby-Tickle, J.; McCullagh, J. S. O. Ion-Exchange Chromatography Coupled to Mass Spectrometry in Life Science, Environmental, and Medical Research. *Anal Chem* **2023**, *95* (1), 152-166. DOI: 10.1021/acs.analchem.2c04298.
(21) Vuckovic, D. Current trends and challenges in sample preparation for global metabolomics using liquid chromatography-mass spectrometry. *Anal Bioanal Chem* **2012**, *403* (6), 1523-1548. DOI: 10.1007/s00216-012-6039-y.
(22) Broughton, R.; Tocher, D. R.; Betancor, M. B. Development of a C18 Supercritical Fluid Chromatography-Tandem Mass Spectrometry Methodology for the Analysis of Very-Long-Chain Polyunsaturated Fatty Acid Lipid Matrices and Its Application to Fish Oil Substitutes Derived from Genetically Modified Oilseeds in the Aquaculture Sector. *ACS Omega* **2020**, *5* (35), 22289-22298. DOI: 10.1021/acsomega.0c02631 From NLM PubMed-not-MEDLINE.
(23) Razay, G.; Williams, J.; King, E.; Smith, A. D.; Wilcock, G. Blood pressure, dementia and Alzheimer's disease: the OPTIMA longitudinal study. *Dement Geriatr Cogn Disord* **2009**, *28* (1), 70-74. DOI: 10.1159/000230877 From NLM Medline.
(24) Smith, A. D.; Smith, S. M.; de Jager, C. A.; Whitbread, P.; Johnston, C.; Agacinski, G.; Oulhaj, A.; Bradley, K. M.; Jacoby, R.; Refsum, H. Homocysteine-lowering by B vitamins slows the rate of accelerated brain atrophy in mild cognitive impairment: a randomized controlled trial. *Plos One* **2010**, *5* (9), e12244. DOI: 10.1371/journal.pone.0012244 From NLM Medline.
(25) Probert, F.; Yeo, T. R.; Zhou, Y. F.; Sealey, M.; Arora, S.; Palace, J.; Claridge, T. D. W.; Hillenbrand, R.; Oechtering, J.; Kuhle, J.; et al. Determination of CSF GFAP, CCN5, and vWF Levels Enhances the Diagnostic Accuracy of Clinically Defined MS From Non-MS Patients With CSF Oligoclonal Bands. *Front Immunol* **2022**, *12*. DOI: ARTN 81135110.3389/fimmu.2021.811351.
(26) Mandrekar, J. N. Receiver operating characteristic curve in diagnostic test assessment. *J Thorac Oncol* **2010**, *5* (9), 1315-1316. DOI: 10.1097/JTO.0b013e3181ec173d From NLM Medline.
(27) Meier, S.; Willemse, E. A. J.; Schaedelin, S.; Oechtering, J.; Lorscheider, J.; Melie-Garcia, L.; Cagol, A.; Barakovic, M.; Galbusera, R.; Subramaniam, S.; et al. Serum Glial Fibrillary Acidic Protein Compared With Neurofilament Light Chain as a Biomarker for Disease Progression in Multiple Sclerosis. *JAMA Neurol* **2023**, *80* (3), 287-297. DOI: 10.1001/jamaneurol.2022.5250 From NLM Medline.
(28) Dobson, R.; Giovannoni, G. Multiple sclerosis - a review. *Eur J Neurol* **2019**, *26* (1), 27-40. DOI: 10.1111/ene.13819 From NLM Medline.
(29) Ziemssen, T.; Bhan, V.; Chataway, J.; Chitnis, T.; Campbell Cree, B. A.; Havrdova, E. K.; Kappos, L.; Labauge, P.; Miller, A.; Nakahara, J.; et al. Secondary Progressive Multiple Sclerosis: A Review of Clinical Characteristics, Definition, Prognostic Tools, and Disease-Modifying Therapies. *Neurol Neuroimmunol Neuroinflamm* **2023**, *10* (1). DOI: 10.1212/NXI.0000000000200064 From NLM Medline.
(30) Kalinowski, A.; Cutter, G.; Bozinov, N.; Hinman, J. A.; Hittle, M.; Motl, R.; Odden, M.; Nelson, L. M. The timed 25-foot walk in a large cohort of multiple sclerosis patients. *Mult Scler* **2022**, *28* (2), 289-299. DOI: 10.1177/13524585211017013 From NLM Medline.
(31) Barro, C.; Healy, B. C.; Liu, Y.; Saxena, S.; Paul, A.; Polgar-Turcsanyi, M.; Guttmann, C. R. G.; Bakshi, R.; Kropshofer, H.; Weiner, H. L.; et al. Serum GFAP and NfL Levels Differentiate Subsequent Progression and Disease Activity in Patients With Progressive Multiple Sclerosis. *Neurol Neuroimmunol Neuroinflamm* **2023**, *10* (1). DOI: 10.1212/NXI.0000000000200052 From NLM Medline.
(32) Benkert, P.; Maleska Maceski, A.; Schaedelin, S.; Oechtering, J.; Zadic, A.; Vilchez Gomez, J. F.; Melie-Garcia, L.; Cagol, A.; Galbusera, R.; Subramaniam, S.; et al. Serum Glial Fibrillary Acidic Protein and Neurofilament Light Chain Levels Reflect Different Mechanisms of Disease Progression under B-Cell Depleting Treatment in Multiple Sclerosis. *Ann Neurol* **2024**. DOI: 10.1002/ana.27096 From NLM Publisher.
(33) Benkert, P.; Meier, S.; Schaedelin, S.; Manouchehrinia, A.; Yaldizli, O.; Maceski, A.; Oechtering, J.; Achtnichts, L.; Conen, D.; Derfuss, T.; et al. Serum neurofilament light chain for individual prognostication of disease activity in people with multiple sclerosis: a retrospective modelling and validation study. *Lancet Neurol* **2022**, *21* (3), 246-257. DOI: 10.1016/S1474-4422(22)00009-6 From NLM Medline.

(34) Cubas-Nunez, L.; Gil-Perotin, S.; Castillo-Villalba, J.; Lopez, V.; Solis Tarazona, L.; Gasque-Rubio, R.; Carratala-Bosca, S.; Alcala-Vicente, C.; Perez-Miralles, F.; Lassmann, H.; et al. Potential Role of CHI3L1+ Astrocytes in Progression in MS. *Neurol Neuroimmunol Neuroinflamm* **2021**, *8* (3). DOI: 10.1212/NXI.0000000000000972 From NLM Medline.
(35) Comabella, M.; Montalban, X. Body fluid biomarkers in multiple sclerosis. *Lancet Neurol* **2014**, *13* (1), 113-126. DOI: 10.1016/S1474-4422(13)70233-3 From NLM Medline.
(36) Khademi, M.; Kockum, I.; Andersson, M. L.; Iacobaeus, E.; Brundin, L.; Sellebjerg, F.; Hillert, J.; Piehl, F.; Olsson, T. Cerebrospinal fluid CXCL13 in multiple sclerosis: a suggestive prognostic marker for the disease course. *Mult Scler* **2011**, *17* (3), 335-343. DOI: 10.1177/1352458510389102 From NLM Medline.
(37) Yeo, T.; Sealey, M.; Zhou, Y.; Saldana, L.; Loveless, S.; Claridge, T. D. W.; Robertson, N.; DeLuca, G.; Palace, J.; Anthony, D. C.; et al. A blood-based metabolomics test to distinguish relapsing-remitting and secondary progressive multiple sclerosis: addressing practical considerations for clinical application. *Sci Rep* **2020**, *10* (1), 12381. DOI: 10.1038/s41598-020-69119-3 From NLM Medline.
(38) Radford-Smith, D. E.; Yates, A. G.; Kacerova, T.; Nylund, M.; Sucksdorff, M.; Matilainen, M.; Willemse, E.; Oechtering, J.; Maleska Maceski, A.; Leppert, D.; et al. Integrating TSPO-PET imaging with metabolomics for enhanced prognostic accuracy in multiple sclerosis. *BMJ Neurol Open* **2025**, *7* (1), e001026. DOI: 10.1136/bmjno-2025-001026 From NLM PubMed-not-MEDLINE.
(39) Dickens, A. M.; Larkin, J. R.; Griffin, J. L.; Cavey, A.; Matthews, L.; Turner, M. R.; Wilcock, G. K.; Davis, B. G.; Claridge, T. D.; Palace, J.; et al. A type 2 biomarker separates relapsing-remitting from secondary progressive multiple sclerosis. *Neurology* **2014**, *83* (17), 1492-1499. DOI: 10.1212/WNL.0000000000000905 From NLM Medline.
(40) Matthews, L.; Marasco, R.; Jenkinson, M.; Küker, W.; Luppe, S.; Leite, M. I.; Giorgio, A.; De Stefano, N.; Robertson, N.; Johansen-Berg, H.; et al. Distinction of seropositive NMO spectrum disorder and MS brain lesion distribution. *Neurology* **2013**, *80* (14), 1330-1337. DOI: 10.1212/WNL.0b013e3182887957.
(41) Cvetko, A.; Kifer, D.; Gornik, O.; Klaric, L.; Visser, E.; Lauc, G.; Wilson, J. F.; Stambuk, T. Glycosylation Alterations in Multiple Sclerosis Show Increased Proinflammatory Potential. *Biomedicines* **2020**, *8* (10). DOI: ARTN 41010.3390/biomedicines8100410.
(42) Dierckx, T.; Verstockt, B.; Vermeire, S.; van Weyenbergh, J. GlycA, a Nuclear Magnetic Resonance Spectroscopy Measure for Protein Glycosylation, is a Viable Biomarker for Disease Activity in IBD. *J Crohns Colitis* **2019**, *13* (3), 389-394. DOI: 10.1093/ecco-jcc/jjy162 From NLM Medline.
(43) Liang, N.; Nho, K.; Newman, J. W.; Arnold, M.; Huynh, K.; Meikle, P. J.; Borkowski, K.; Kaddurah-Daouk, R.; Alzheimer's Disease Metabolomics, C. Peripheral inflammation is associated with brain atrophy and cognitive decline linked to mild cognitive impairment and Alzheimer's disease. *Sci Rep* **2024**, *14* (1), 17423. DOI: 10.1038/s41598-024-67177-5 From NLM Medline.
(44) Mokkala, K.; Houttu, N.; Koivuniemi, E.; Sorensen, N.; Nielsen, H. B.; Laitinen, K. GlycA, a novel marker for low grade inflammation, reflects gut microbiome diversity and is more accurate than high sensitive CRP in reflecting metabolomic profile. *Metabolomics* **2020**, *16* (7), 76. DOI: 10.1007/s11306-020-01695-x From NLM Medline.
(45) Palaniappan, K. K.; Bertozzi, C. R. Chemical Glycoproteomics. *Chem Rev* **2016**, *116* (23), 14277-14306. DOI: 10.1021/acs.chemrev.6b00023 From NLM Medline.
(46) de Jager, C. A.; Oulhaj, A.; Jacoby, R.; Refsum, H.; Smith, A. D. Cognitive and clinical outcomes of homocysteine-lowering B-vitamin treatment in mild cognitive impairment: a randomized controlled trial. *Int J Geriatr Psychiatry* **2012**, *27* (6), 592-600. DOI: 10.1002/gps.2758 From NLM Medline.
(47) Chouliaras, L.; O'Brien, J. T. The use of neuroimaging techniques in the early and differential diagnosis of dementia. *Mol Psychiatry* **2023**, *28* (10), 4084-4097. DOI: 10.1038/s41380-023-02215-8 From NLM Medline.
(48) Karantzoulis, S.; Galvin, J. E. Distinguishing Alzheimer's disease from other major forms of dementia. *Expert Rev Neurother* **2011**, *11* (11), 1579-1591. DOI: 10.1586/ern.11.155 From NLM Medline.
(49) Reveglia, P.; Paolillo, C.; Ferretti, G.; De Carlo, A.; Angiolillo, A.; Nasso, R.; Caputo, M.; Matrone, C.; Di Costanzo, A.; Corso, G. Challenges in LC-MS-based metabolomics for Alzheimer's disease early detection: targeted approaches versus untargeted approaches. *Metabolomics* **2021**, *17* (9), 78. DOI: 10.1007/s11306-021-01828-w From NLM Medline.
(50) Douaud, G.; Refsum, H.; de Jager, C. A.; Jacoby, R.; Nichols, T. E.; Smith, S. M.; Smith, A. D. Preventing Alzheimer's disease-related gray matter atrophy by B-vitamin treatment. *Proc Natl Acad Sci U S A* **2013**, *110* (23), 9523-9528. DOI: 10.1073/pnas.1301816110 From NLM Medline.
(51) Smith, A. D.; Refsum, H.; Bottiglieri, T.; Fenech, M.; Hooshmand, B.; McCaddon, A.; Miller, J. W.; Rosenberg, I. H.; Obeid, R. Homocysteine and Dementia: An International Consensus Statement. *J Alzheimers Dis* **2018**, *62* (2), 561-570. DOI: 10.3233/JAD-171042 From NLM Medline.
(52) Morris, M. C.; Schneider, J. A.; Tangney, C. C. Thoughts on B-vitamins and dementia. *J Alzheimers Dis* **2006**, *9* (4), 429-433. DOI: 10.3233/jad-2006-9409 From NLM Medline.

(53) Esiri, M. M.; Joachim, C.; Sloan, C.; Christie, S.; Agacinski, G.; Bridges, L. R.; Wilcock, G. K.; Smith, A. D. Cerebral subcortical small vessel disease in subjects with pathologically confirmed Alzheimer disease: a clinicopathologic study in the Oxford Project to Investigate Memory and Ageing (OPTIMA). *Alzheimer Dis Assoc Disord* **2014**, *28* (1), 30-35. DOI: 10.1097/WAD.0b013e31829b72f1 From NLM Medline.
(54) Giacomucci, G.; Mazzeo, S.; Bagnoli, S.; Ingannato, A.; Leccese, D.; Berti, V.; Padiglioni, S.; Galdo, G.; Ferrari, C.; Sorbi, S.; et al. Plasma neurofilament light chain as a biomarker of Alzheimer's disease in Subjective Cognitive Decline and Mild Cognitive Impairment. *J Neurol* **2022**, *269* (8), 4270-4280. DOI: 10.1007/s00415-022-11055-5 From NLM Medline.
(55) Giacomucci, G.; Mazzeo, S.; Ingannato, A.; Crucitti, C.; Bagnoli, S.; Padiglioni, S.; Romano, L.; Galdo, G.; Emiliani, F.; Frigerio, D.; et al. Future perspective and clinical applicability of the combined use of plasma phosphorylated tau 181 and neurofilament light chain in Subjective Cognitive Decline and Mild Cognitive Impairment. *Sci Rep* **2024**, *14* (1), 11307. DOI: 10.1038/s41598-024-61655-6 From NLM Medline.
(56) Gonzalez-Ortiz, F.; Kac, P. R.; Brum, W. S.; Zetterberg, H.; Blennow, K.; Karikari, T. K. Plasma phospho-tau in Alzheimer's disease: towards diagnostic and therapeutic trial applications. *Mol Neurodegener* **2023**, *18* (1), 18. DOI: 10.1186/s13024-023-00605-8 From NLM Medline.
(57) Horie, K.; Salvado, G.; Koppisetti, R. K.; Janelidze, S.; Barthelemy, N. R.; He, Y.; Sato, C.; Gordon, B. A.; Jiang, H.; Benzinger, T. L. S.; et al. Plasma MTBR-tau243 biomarker identifies tau tangle pathology in Alzheimer's disease. *Nat Med* **2025**. DOI: 10.1038/s41591-025-03617-7 From NLM Publisher.
(58) Trelle, A. N.; Young, C. B.; Vossler, H.; Ramos Benitez, J.; Cody, K. A.; Mendiola, J. H.; Swarovski, M. S.; Guen, Y. L.; Feinstein, I.; Butler, R. R., 3rd; et al. Plasma Abeta(42)/Abeta(40) is sensitive to early cerebral amyloid accumulation and predicts risk of cognitive decline across the Alzheimer's disease spectrum. *Alzheimers Dement* **2025**, *21* (2), e14442. DOI: 10.1002/alz.14442 From NLM Medline.
(59) Bayoumy, S.; Verberk, I. M. W.; den Dulk, B.; Hussainali, Z.; Zwan, M.; van der Flier, W. M.; Ashton, N. J.; Zetterberg, H.; Blennow, K.; Vanbrabant, J.; et al. Clinical and analytical comparison of six Simoa assays for plasma P-tau isoforms P-tau181, P-tau217, and P-tau231. *Alzheimers Res Ther* **2021**, *13* (1), 198. DOI: 10.1186/s13195-021-00939-9 From NLM Medline.
(60) van de Velde, B.; Guillarme, D.; Kohler, I. Supercritical fluid chromatography - Mass spectrometry in metabolomics: Past, present, and future perspectives. *J Chromatogr B Analyt Technol Biomed Life Sci* **2020**, *1161*, 122444. DOI: 10.1016/j.jchromb.2020.122444 From NLM Medline.
(61) Huynh, K.; Lim, W. L. F.; Giles, C.; Jayawardana, K. S.; Salim, A.; Mellett, N. A.; Smith, A. A. T.; Olshansky, G.; Drew, B. G.; Chatterjee, P.; et al. Concordant peripheral lipidome signatures in two large clinical studies of Alzheimer's disease. *Nat Commun* **2020**, *11* (1), 5698. DOI: 10.1038/s41467-020-19473-7 From NLM Medline.
(62) Kim, M.; Nevado-Holgado, A.; Whiley, L.; Snowden, S. G.; Soininen, H.; Kloszewska, I.; Mecocci, P.; Tsolaki, M.; Vellas, B.; Thambisetty, M.; et al. Association between Plasma Ceramides and Phosphatidylcholines and Hippocampal Brain Volume in Late Onset Alzheimer's Disease. *J Alzheimers Dis* **2017**, *60* (3), 809-817. DOI: 10.3233/JAD-160645 From NLM Medline.
(63) Meikopoulos, T.; Deda, O.; Karagiannidis, E.; Sianos, G.; Theodoridis, G.; Gika, H. A HILIC-MS/MS method development and validation for the quantitation of 13 acylcarnitines in human serum. *Anal Bioanal Chem* **2022**, *414* (9), 3095-3108. DOI: 10.1007/s00216-022-03940-9 From NLM Medline.
(64) Bian, Y.; Zheng, R.; Bayer, F. P.; Wong, C.; Chang, Y. C.; Meng, C.; Zolg, D. P.; Reinecke, M.; Zecha, J.; Wiechmann, S.; et al. Robust, reproducible and quantitative analysis of thousands of proteomes by micro-flow LC-MS/MS. *Nat Commun* **2020**, *11* (1), 157. DOI: 10.1038/s41467-019-13973-x From NLM Medline.
(65) Panyard, D. J.; McKetney, J.; Deming, Y. K.; Morrow, A. R.; Ennis, G. E.; Jonaitis, E. M.; Van Hulle, C. A.; Yang, C.; Sung, Y. J.; Ali, M.; et al. Large-scale proteome and metabolome analysis of CSF implicates altered glucose and carbon metabolism and succinylcarnitine in Alzheimer's disease. *Alzheimers Dement* **2023**, *19* (12), 5447-5470. DOI: 10.1002/alz.13130 From NLM Medline.